Radiogenic isotopes in the Mediterranean Sea: water mass exchange and precessional variability during the Messinian

Sevasti Eleni Modestou

Doctor of Philosophy

Scottish Universities Environmental Research Centre
College of Science and Engineering
University of Glasgow

November 2016

Abstract

During the late Miocene, exchange between the Mediterranean Sea and Atlantic Ocean changed dramatically, culminating in the Messinian Salinity Crisis (MSC). Understanding Mediterranean-Atlantic exchange at that time could answer the enigmatic question of how so much salt built up within the Mediterranean, while furthering the development of a framework for future studies attempting to understand how changes may have impacted global thermohaline circulation.

Due to their association with specific water masses at different scales, radiogenic Sr, Pb, and Nd isotope records were generated from various archives contained within marine deposits to endeavour to understand better late Miocene Mediterranean-Atlantic exchange. The archives used include foraminiferal calcite (Sr), fish teeth and bone (Nd), dispersed authigenic ferromanganese oxyhydroxides (Nd, Pb), and a ferromanganese crust (Pb). The primary focus is on sediments preserved at one end of the Betic corridor, a gateway that once connected the Mediterranean to the Atlantic through southern Spain, although other locations are investigated. The Betic gateway terminated within several marginal sub-basins before entering the Western Mediterranean; one of these is the Sorbas Basin, a well-studied location whose sediments have been astronomically tuned at high temporal resolution, providing the necessary age control for sub-precessional resolution records. Since the climatic history of the Mediterranean is strongly controlled by precessional changes in regional climate, the aim was to produce records at high (sub-precessional) temporal resolution, to be able to observe clearly any precessional cyclicity driven by regional climate which could be superimposed over longer trends. This goal was achieved for all records except the ferromanganese crust record.

The $^{87}Sr/^{86}Sr$ isotope record (Ch. 3) shows precessional frequency excursions away from the global seawater curve. As precessional frequency oscillations are unexpected for this setting, a numerical box model was used to determine the mechanisms causing the excursions. To enable parameterisation of model variables, regional Sr characteristics, data from general circulation model HadCM3L, and new benthic foraminiferal assemblage data are employed. The model results imply that the Sorbas Basin likely had a positive hydrologic budget in the late Miocene, very different to that of today. Moreover, the model indicates that the mechanism controlling the Sr isotope ratio of Sorbas Basin seawater was not restriction, but a lack of density-driven exchange with the Mediterranean. Beyond

improving our understanding of how marginal Mediterranean sub-basins may evolve different isotope signatures, these results have implications for astronomical tuning and stratigraphy in the region, findings which are crucial considering the geological and climatic history of the late Miocene Mediterranean is based entirely on marginal deposits.

An improved estimate for the Nd isotope signature of late Miocene Mediterranean Outflow (MO) was determined by comparing Nd isotope signatures preserved in the deeper Alborán Sea at ODP Site 978 with literature data as well as the signature preserved in the Sorbas Basin (Ch. 4; -9.34 to -9.92 ± 0.37 $\varepsilon_{Nd(t)}$). It was also inferred that it is unlikely that Nd isotopes can be used reliably to track changes in circulation within the shallow settings characteristic of the Mediterranean-Atlantic connections; this is significant in light of a recent publication documenting corridor closure using Nd isotopes. Both conclusions will prove useful for future studies attempting to understand changes in Mediterranean-Atlantic exchange.

Excursions to high values, with precessional frequency, are also observed in the radiogenic Pb isotope record for the Sorbas Basin (Ch. 5). Widening the scope to include locations further away from the gateways, records were produced for late Miocene sections on Sicily and Northern Italy, and similar precessional frequency cyclicity was observed in the Pb isotope records for these sites as well. Comparing these records to proxies for Saharan dust and available whole rock data indicates that, while further analysis is necessary to draw strong conclusions, enhanced dust production during insolation minima may be driving the observed signal. These records also have implications for astronomical tuning; peaks in Pb isotope records driven by Saharan dust may be easier to connect directly to the insolation cycle, providing improved astronomical tuning points.

Finally, a Pb isotope record derived using *in-situ* laser ablation performed on ferromanganese crust 3514-6 from the Lion Seamount, located west of Gibraltar within the MO plume, has provided evidence that plume depth shifted during the Pliocene. The record also suggests that Pb isotopes may not be a suitable proxy for changes in late Miocene Mediterranean-Atlantic exchange, since the Pb isotope signatures of regional water masses are too similar. To develop this record, the first published instance of laser ablation derived $^{230}Th_{excess}$ measurements are combined with ^{10}Be dating.

Table of Contents

Abstract *iii*
List of Tables *viii*
List of Figures *ix*
Acknowledgements *xvii*
Author's Declaration *xviii*
Glossary of Acronyms *xix*

1 Introduction **1**
1.1 Motivation 1
1.1.1 Understanding Earth's climate: the biggest jigsaw puzzle 1
1.1.2 Ocean forensics: radiogenic isotope 'fingerprints' 4
1.1.3 MEDGATE 5
1.2 Late Miocene Mediterranean geology: salt, sapropels, and cycles 5
1.2.1 History of MSC research 5
1.2.2 The Betic and Rifian palaeogateways 7
1.2.3 A mechanistic MSC timeline 9
1.2.4 Summary of MSC stratigraphy 12
1.2.5 Orbital cycles and Mediterranean sapropels 13
1.2.6 Cyclostratigraphy: precision, phase lags and breakthroughs in Messinian Mediterranean geochronology 19
1.2.7 Mediterranean-Atlantic exchange 21
1.3 Radiogenic isotopes as water mass tracers 24
1.3.1 Neodymium (Nd): $^{143}Nd/^{144}Nd$ 26
1.3.2 Lead (Pb) 33
1.3.3 Strontium: $^{87}Sr/^{86}Sr$ 36
1.3.4 ^{10}Be and ^{230}Th dating tools 40
1.4 Archives 41
1.4.1 FeMn crust 3514-6 41
1.4.2 Sedimentary successions 43
1.4.2.1 The Sorbas Basin 44
1.4.2.2 ODP Site 978 44
1.5 Summary 44
1.5.1 Thesis organization and key questions 46

2 Materials and Methods **49**
2.1 Overview 49
2.2 Sedimentology and chronology of sediment samples 50
2.2.1 Upper Abad Marls, Sorbas Basin 50
2.2.2 ODP Site 978 54
2.3 Methodology applied to sediment samples 55
2.3.1 Foraminiferal $^{87}Sr/^{86}Sr$ 55
2.3.2 $^{87}Sr/^{86}Sr$ mass spectrometry 57
2.3.3 Benthic foraminiferal assemblages 57
2.3.4 Seawater and sediment Nd and Pb 57
2.3.4.1 Acid-reductive leaching of bulk sediments 57
2.3.4.2 Strong leaching of bulk sediment 59
2.3.4.3 Total dissolution of bulk sediment 59
2.3.4.4 Fossil fish remains 60
2.3.5 Nd and Pb mass spectrometry 61
2.4 Methodology applied to ferromanganese crust 3516-4 63
2.4.1 High temporal resolution Pb isotope record 63
2.4.2 Cosmogenic ^{10}Be extraction procedure 64
2.4.3 Laser ablation MC-ICPMS procedure 67
2.4.4 $^{230}Th_{excess}$ measurement 69
2.5 Published data: ferromanganese crust chronology, correction of ^{10}Be values for new half-life, and conversion of published ε_{Nd} to $\varepsilon_{Nd(t)}$ 70

2.6 Numerical Box Modeling – Sorbas Basin 71
2.6.1 Equations 72
2.6.2 Parameter selection 74
2.6.3 Transient model 77
2.6.4 Volume and eustacy 79

3 Precessional variability of $^{87}Sr/^{86}Sr$ in the late Miocene Sorbas Basin: an interdisciplinary study of drivers of inter-basin exchange 81
3.1 Overview 81
3.2 Sources of Sr 81
3.3 Results 83
3.3.1 Sorbas Sr isotopic compositions 83
3.3.2 Potential effects of diagenesis on foraminiferal $^{87}Sr/^{86}Sr$ 84
3.3.3 Sorbas palaeodepth and bottom water oxygenation 86
3.3.4 Model results: steady-state approximations 88
3.3.5 Transient model results 89
3.3.6 Sensitivity of salinity parameters 92
3.3.7 Sensitivity to basin depth 92
3.4 Discussion 93
3.4.1 Processes affecting seawater $^{87}Sr/^{86}Sr$ in Sorbas 93
3.4.1.1 Eustatic sea level change 93
3.4.1.2 River runoff 94
3.4.1.3 Fluctuations in the hydrologic budget 95
3.4.1.4 Dust 96
3.4.2 The freshwater budget and vertical mixing 97
3.4.3 $^{87}Sr/^{86}Sr$ and vertical mixing 98
3.4.4 Temporal lags and implications for Mediterranean astronomical tuning 99
3.4.5 Implications for overlying Sorbas Basin deposits 100
3.5 Conclusions 101

4 Tracing circulation in the Western Mediterranean and Sorbas Basin with Nd isotopes: results and implications 105
4.1 Overview 105
4.2 Background oceanography 105
4.3 Late Miocene Western Mediterranean ε_{Nd}: ODP Site 978 107
4.3.1 Results 107
4.3.2 Discussion 108
4.3.2.1 Implications of late Miocene $\varepsilon_{Nd(t)}$ from ODP Site 978 108
4.3.2.2 Reliability of Site 978 data and implications for regional palaeoceanography and MO 109
4.3.2.3 Implications for previously published MO water mass estimates 111
4.3.2.4 Late Pliocene and Quaternary records: causes for consistently more radiogenic values? 112
4.4 Sorbas Basin ε_{Nd} signatures 114
4.4.1 Results: Nd isotope analyses 114
4.4.2 Elemental ratios: Al/Nd 117
4.4.3 Discussion 119
4.4.3.1 Reliability of the leaching process for Sorbas Basin sediment 119
4.4.3.2 Seawater $^{143}Nd/^{144}Nd$ in the Sorbas basin 120
4.4.3.3 Further issues: Eastern North Atlantic Central Water (ENACW) vs. North Eastern Atlantic Deep Water (NEADW) 122
4.5 Conclusions 123

5 Mediterranean and Mediterranean marginal basin seawater Pb isotopes: records of precessional climate variability 125
5.1 Overview 125
5.2 Results 125
5.2.1 Sorbas, Falconara, and Monte del Casino leachates 125

5.2.2 ODP Site 978 131
5.2.3 Reliability 131
5.3 Discussion 133
5.3.1 Sorbas Basin 134
5.3.2 Falconara section 134
5.3.3 Monte del Casino section 135
5.3.4 Potential mechanisms controlling seawater Pb isotope composition 136
5.3.4.1 Temporal variability in riverine runoff 137
5.3.4.2 Productivity-related U complexation or exclusion 139
5.3.4.3 Dust 141
5.3.4.4 Incongruent weathering 153
5.4 Conclusions 155

6 FeMn crust 3514-6: age model and long-term Pb isotope record outside the Gulf of Cadiz 159
6.1 Overview 159
6.2 Results: growth rate determination 159
6.2.1 $^{10}Be/^{9}Be$ method 159
6.2.2 $^{230}Th_{excess}$ method 163
6.3 Results: Pb isotope analyses 166
6.4 Age models 168
6.4.1 Assessment and application of growth rates: Th 168
6.4.2 Assessment and application of growth rates: Be 170
6.4.3 Growth rate differences and discrepancies 171
6.5 Palaeoceanographic interpretation of crust 3514-6 Pb isotope record 176
6.5.1 The Messinian Salinity Crisis 176
6.5.2 Effects of glaciation on MO plume settling depth 176
6.5.3 ^{9}Be flux and water mass changes 181
6.5.4 Inconsistencies 182
6.5.5 Further interpretation to the 65GTV record 184
6.6 Conclusions 185
6.6.1 Age model generation and cosmogenic beryllium: to normalize or not to normalize? 186
6.6.2 Insights from the Pb isotope record of crust 3514-6 187

7 Synopsis and future outlook 191
7.1 Overview 191
7.2 Challenges of applying radiogenic isotopes to understanding Mediterranean-Atlantic exchange in the late Miocene 191
7.3 North African Monsoon system and Mediterranean seawater radiogenic isotopes: application of Sr and Pb to astronomical tuning and the phase lag 193
7.4 Crust 65GTV: the most appropriate MO record for the late Miocene 196
7.5 Recommendations for future work 197
7.5.1 Lessons from an analytical point of view 197
7.5.2 Pb isotopes as a stratigraphic tool in the Mediterranean: where to sample? 198
7.5.3 What is needed for numerical modeling with Pb? 199
7.5.4 The importance of deep section recovery: the DREAM project 200
7.5.5 A better salinity proxy 201
7.5.6 Where can we find ideal records for reconstructing global ocean circulation? 202

References 203

Appendix 1: Letters of permission and credit to contributors 225
Appendix 2: Corrected secondary standard data 229
Appendix 3: Additional results: Nd and Pb across the Mediterranean 231
Appendix 4: Elemental ratio data 235

Appendix 5: Pb isotope data including individual measurements *263*
Appendix 6: $^{230}Th_{excess}$ plots *269*
Appendix 7: $^{87}Sr/^{86}Sr$ data for Fig. 1.19 (electronic format only) *----*

List of Tables

Table 1.1. Radiogenic isotopes used as tracers and for dating in this thesis. 26

Table 2.1. Summary of constants, including half-lifes ($t_{1/2}$, y), and references. 49

Table 2.2. Summary of published characteristics of crust 3514-6 [Muiños et al., 2008]. 64

Table 2.3. Cup configuration for LA-MC-ICPMS Pb isotope measurements. 68

Table 2.4. Locations and details of ferromanganese crusts discussed in this thesis. 71

Table 2.5. Summary of constraints used for box modeling. 75

Table 2.6. Estimated Late Miocene evaporation (E) and precipitation (P) for the Western and Eastern Mediterranean regions from orbital experiments of global circulation model HadCM3L [*Marzocchi,* 2016]. For Sorbas, values are scaled from surface area of Late Miocene Western Mediterranean ($9.21831x10^{11}$ m^2; model palaeogeography) to estimated Sorbas basin surface area ($1.2x10^9$ m^2, see Table 2.5.) 77

Table 3.1. $^{87}Sr/^{86}Sr$ isotope ratios measured from Sorbas Basin planktic foraminifera. 2SD external uncertainty = 0.000018. Location: 37°05'22"N 2°04'08"W. 84

Table 3.2. Selected benthic foraminifera (percentages, except total). 87

Table 4.1. ODP Leg 161 Site 978 $^{143}Nd/^{144}Nd$ ratios (uncertainty 2SD). 108

Table 4.2. $^{143}Nd/^{144}Nd$ ratios of Sorbas Basin samples (ratio uncertainty 2SE internal; ε_{Nd} uncertainty 2SD external). 115

Table 5.1. Pb isotopic compositions of acid-reductive leaches, all sections. 126

Table 5.2. Pb isotopic compositions, ODP Leg 161, Site 978. 131

Table 5.3. Strong leach and total dissolution Pb isotope compositions of Sorbas Basin sediments. 132

Table 5.4. Calculation of excess U and Th required to cause radiogenic compositions observed in-situ, assuming maximum $^{20x}Pb/^{204}Pb$ ratios represent present time and minimum ratios represent 'initial' ratios (6.6 Ma). Values in red do not match targets. 141

Table 6.1. Beryllium measurement results. All errors reported to 2σ (95% confidence interval), except depths, which correspond to linearly measured uncertainties. Depth assignments are estimated rather than measured for samples marked with * (see text, this section). Depth corresponds to distance from crust surface along the laser ablation profile. 160

Table 6.2. Growth rates for FeMn crust 3514-6 analysed in this project derived from either [^{10}Be] or $^{10}Be/^{9}Be$, and extrapolated crust surface values. 160

Table 6.3. Results of $^{230}Th_{excess}$ measurement. 2SD of sample mean. 164

List of Figures

Fig. 1.1. Representations of thermohaline circulation in the global oceans. (a) Simplistic bird's eye view of major currents and circulation, as well as locations of significant deep water formation, upwelling, and locations of surface waters significantly more or less saline than mean salinity. Modified to include MO from [*Kuhlbrodt et al.,* 2007]. (b) More accurate (although still simplified) three-dimensional view of ocean circulation centered about the Antarctic. Surface currents are purple, intermediate are red, deep are green, and bottom currents are blue. Modified from [*Schmitz*, 1996]. 2

Fig. 1.2. Modern dynamics of Mediterranean Outflow (MO), referred to as MOW in the figure. Main graphic shows horizontal pathways of MO, including the three branches, the most prominent flowing northwards along the Iberian margin. Boxes above and below the main figure summarize the vertical distribution of MO and its relationship to overlying and underlying water masses, both in the Atlantic and in the Mediterranean (TDW = Tyrrhenian Deep Water). From [*Hernández-Molina et al.,* 2011]. 3

Fig. 1.3. Correlation of marginal evaporite successions to deep basin seismic profiles. Note that the Lower Evaporites in the deep setting correspond only to the unit below the halite, while on Sicily they are composed of gypsum, evaporitic limestone and halite. M, K, and L refer to significant seismic reflectors discussed in *Lofi et al.* [2005]. Modified from *Krijgsman and Meijer* [2008]. 7

Fig. 1.4. Simplified reconstructions of the Betic and Rifian palaeocorridors linking the Atlantic to the Mediterranean prior to the MSC. (a) Modified satellite imagery; present day coastline in red. From *Duggen et al.* [2003], reconstruction based on *Esteban et al.* [1996]. (b) Approximately Tortonian stage reconstruction. Modified from *Ivanoviç* [2012], based on *Santisteban and Taberner* [1983]. (c) Reconstruction through time (Tortonian to Zanclean) from *Martín et al.* [2009]. 8

Fig. 1.5. (a) Astronomical tuning of the Molinos/Perales (S Spain), Metochia (Crete) and Gibliscemi/Falconara (Sicily) sections by *Krijgsman et al.* [1999a] leading to the determination of evaporite deposition at 5.96 Ma ± 20 ky (sourced from same publication). (b) Revised age of onset for evaporite precipitation by *Manzi et al.* [2013] based on astronomical tuning, also showing association to potential glacio-eustatic trigger for evaporite onset by correlation to the δ18O record of *van der Laan et al.* [2006] and associated glacial stages (source: *Manzi et al.* [2013]). 10

Fig. 1.6. Cyclostratigraphic and bioevent correlations (unbracketed numbers) for the key cyclically bedded sedimentary sequences around the Mediterranean basin used in dating MSC events. Locations correspond to map inset, which also shows locations of DSDP sampling. Locations shown refer to: (1) *Krijgsman et al.* [2004]; (2) *van Assen et al.* [2006]; (3-5) *Krijgsman et al.* [1999a]; (6) *Krijgsman et al.* [2002]; (7) *Manzi et al.* [2007]. Source: *Krijgsman and Meijer* [2008]. 11

Fig. 1.7. Summary of the MSC succession, divided into 3 major stages. Modified from *CIESM* [2008]. 13

Fig. 1.8. Orbital parameters and the relationship between ε (obliquity, blue), e (eccentricity, green), sin(ϖ) (purple), esin(ϖ) (climatic precession, red), and Qday (insolation, black). These are compared to the benthic δ18O record (LR04 stack) [*Lisiecki and Raymo,* 2005] and a record of relative temperature change from the Vostok ice core [*Petit et al.,* 1999]. 14

Fig. 1.9. Interpretations of palaeochannels through central North Africa, some of which may have transported water from Neogene Lake Chad to the Eastern Mediterranean basin. (a) Reconstruction comparing mapped palaeochannels to 16

modern-day Nile. Initials represent mountain ranges (HP – Hoggar Plateau; TM – Tibesti Mountains; EM – Ennedi Mountains). Symbols not relevant (indicate sampling locations for study from which reconstruction was taken). From *Osborne et al.* [2008]. (b) Reconstruction showing how main channel from Neogene Lake Chad may have connected it to the Mediterranean Sea, including along the way the Chad Basin, the Kufra Basin, and the Sirt Basin. From *Griffin* [2006].

Fig. 1.10. A comparison of several insolation curves applied in the literature to the sapropel pattern of the Mediterranean. Note the thick-thin pattern; for example, S3 is thicker than S4, and S6 is thicker than S7, although the insolation curve for low latitudes (23°N, black line) suggests the opposite should be occurring. The pattern fits to 65°N and SITIG much better, two curves which are nearly identical. See text for references for each curve. From *Bosmans et al.* [2015a]. 18

Fig. 1.11. Messinian age sections from outside the Mediterranean basin (Atlantic Morocco) correlated to intra-Mediterranean evaporitic sections on the basis of orbital tuning, benthic $\delta^{18}O$ and geochemical element (PC-1) records. Note the gap in the Mediterranean sequences which is thought to correspond to the deep halite unit, and seems to be linked temporally to TG12 and TG14. Source: *Krijgsman and Meijer* [2008]; modified from *Hilgen et al.* [2007]. 21

Fig. 1.12. Modern exchange through the Strait of Gibraltar. (a) Excess evaporation over the Mediterranean generates denser water which flows out (Q_{OUT}) beneath Atlantic inflow (Q_{IN}). (b) Cross section through the Gibraltar Strait with contours corresponding to salinity. Upper panel of (b) is a magnification of the top 300 m. Modified from *Flecker et al.* [2015]. 23

Fig. 1.13. Trace metal pathways including sources and sinks. Three major sources exist for particulate and dissolved trace metals in the ocean: aeolian, riverine, and hydrothermal. In addition, some metals such as Nd are probably supplied by partial dissolution of shelf sediments. Shaded and solid lines indicate surface and deep-water circulation (respectively) causing mixing of the dissolved metals. Modified from *Frank* [2002], to include Sr pathways as per *Veizer* [1989], and benthic flux as per *Abbott et al.* [2015b]. Processes in italics. 25

Fig. 1.14. W-E transect of the Mediterranean basin summarizing modern day surface and deep Nd isotopic composition (ε_{Nd}) and concentration (pmol/kg, italics). Arrows indicate circulation pathways. At Gibraltar, Atlantic inflow at the surface has ~ -11.4 ε_{Nd}, while Mediterranean water with ~ -9.4 ε_{Nd} flows out at the bottom. Modified from *Henry et al*. [1994]; Nile ε_{Nd} from *Scrivner et al.* [2004]; dust ε_{Nd} from *Scheuvens et al.* [2013] and references therein. 30

Fig. 1.15. Compilation of ε_{Nd} depth profiles around the Mediterranean. Note scales differ between groups of plots. 31

Fig. 1.16. Reproduction of Fig. 5 from *Ivanoviç et al.* [2013]. ε_{Nd} isotope record from the Rifian palaeocorridor region between ~7.7 and 5.0 Ma. Sample locations shown in inset. 'B/G' for upper evaporites (brackish water deposits and gypsum), 'H' for halite and 'Gypsum' for lower gypsum. Mediterranean outflow here denoted MOW (Mediterranean Outflow Water). Atlantic inflow ε_{Nd} from *Spivack and Wasserburg* [1988], *Henry et al.* [1994] and *Tachikawa et al.* [2004]. 32

Fig. 1.17. Decay chains for ^{238}U, ^{235}U, and ^{232}Th producing ^{206}Pb, ^{207}Pb, and ^{208}Pb respectively. Arrows between elements labeled with decay mode. α-decay: ejection of Helium nucleus, loss of 4 mass units. β-decay: loss of electron (or positron); changes atomic number ± 1 (no mass change). 35

Fig. 1.18: Sr seawater curve for (left) the past 200 Ma, and (right) to the beginning of the Neogene; grey bar indicates the MSC. Images reproduced directly from the LOWESS database [*Howarth and McArthur,* 1997]. Though the database has 37

been updated several times, changes to the curves shown here is negligible.

Fig. 1.19. Radiogenic isotope records for the Mediterranean and Mediterranean Outflow (MO) from 8 to 5 Ma. (a) Mediterranean water $^{87}Sr/^{86}Sr$ inferred from several archives [1, 2] plotted against global seawater $^{87}Sr/^{86}Sr$. Fossils divided by marginal or open locations. (b) $\varepsilon_{Nd(t)}$ bottom water values from the Rifian paleocorridor (diamonds, circles) [3]. Compare to estimates for MO (microfossils [squares, 3] and FeMn crusts [bands, 4, 5]) and North Eastern Atlantic Deep Water (NEADW) (crust 3511-1). 65GTV data corrected for ingrowth of ^{143}Nd. (c) Pb isotope ratio time series for crusts 65GTV, 3514-6, 3511-1 and 3513-14 [4, 5]. Errors 2SD external reproducibility, unless internal was larger (see Ch. 2 for explanation of error and 65GTV correction). [1] [*Roveri et al.,* 2014]; [2] [*Topper et al.,* 2011]; [3] [*Ivanoviç et al.,* 2013]; [4] [*Muiños et al.,* 2008]; [5] [*Abouchami et al.,* 1999]. Originally published in *Flecker et al.* [2015] (author's own work). 39

Fig. 1.20. (a) Plot of surface ε_{Nd} of crust 3514-6 [*Muiños et al.,* 2008] compared with nearby water column profiles. (b) Sampling locations. Crust 3514-6 was dredged from the Lion Seamount. 3514-6 surface ε_{Nd} is most similar to profiles from Stn 95 [*Piepgras and Wasserburg,* 1983] and USGT10-01 [*Stichel et al.,* 2015], though profile USGT10-03 [*Stichel et al.,* 2015] was sampled nearly at the same location. Crust 65GTV [*Abouchami et al.,* 1999] was sourced from essentially the same location as 3514-6, but from deeper in the water column (1500 m). 42

Fig. 1.21. Locations of sediment deposits around the Mediterranean used as archives for this thesis. Also indicated are names of smaller basins comprising the Mediterranean used in the text. Late Miocene seawater isotopic compositions measured for each location are listed. Sites for which Sr, Nd, and Pb were measured are noted by black symbols; for those where Nd and Pb were measured, red symbols are used; and for sites where only Pb isotope compositions are reported, green symbols are used. 43

Fig. 2.1. (a) Modern MO preferred pathways and sampling locations of archives referred to in the text. Circles: sediment or fish remains. Stars: ferromanganese crusts. Betic and Rifian palaeogateways shown in light blue; configuration spans approximately 8 – 6 Ma (corridors were closing through this period). Reconstruction adapted from *Ivanoviç et al.* [2013] based on S*antisteban and Taberner* [1983]. ODP Site 978 (36°13.9'N 2°3.4'W), Leg 161 Report; Sorbas Basin (37°05'22"N 2°04'08"W), this study; Messadît (35°17'38"N 2°59'55"W), *Ivanoviç et al.* [2013]. See Table 2.3 for crust locations. Note 121DK is off map; this crust is located ~500 km SW of the Canary Islands off NW Africa. (b) General geological map of the Almería region; Neogene and Quaternary cover coincides mainly with locations of palaeogateways and basins. Messinian reef deposits provide indication of basin size at that time. Adapted from *Krijgsman et al.* [2001]. (c) Idealized profile of Sorbas basin Upper Abad sediments showing quadripartite cycle. (d) Idealized cross section through Gibraltar showing approximate depths of relevant water masses and depths of various archives from (a). ENACW – Eastern North Atlantic Central Water; MAW – Modified Atlantic Water; MO – Mediterranean Outflow; NEADW – North Eastern Atlantic Deep Water; AAIW – Antarctic Intermediate Water; WMDW – Western Mediterranean Deep Water; LIW – Levantine Intermediate Water (also referred to as MIW – Mediterranean Intermediate Water). 51

Fig. 2.2. Appearance of Upper Abad Member sediments; image on right is interpretation of image on left. Cyclicity is not very obvious to the naked eye, though it is possible to see the difference between the sapropelic layers (reddish brown) compared to the other marls (grey). 52

Fig. 2.3. Flowchart of foraminiferal calcite cleaning procedure prior to Sr isotopic measurements. 56

Fig. 2.4. Flowchart of total dissolution procedure. 61

Fig. 2.5. (a) Spliced image of thick section of crust 3514-6 before analysis; image prepared using 5x objective and automatic stage to enable automatic splicing with Zeiss Axio software. (b) Location of subsamples removed for 10Be measurement (labelled CR1-13) and ablation tracks (arrows). Ablation for Pb in red; ablation for $^{230}Th_{excess}$ in blue at upper left (2 positions). (c) Major laminations highlighted to illustrate spatial arrangement. Black stars indicate laminations disappearing towards the right; white star indicates lamination disappearing towards the left. (d) High resolution scanned image of section of 3514-6 after drilling and ablating with respective areas highlighted as in (b) and (c); arrows indicate location of $^{230}Th_{excess}$ ablations. (e) Explanation of how depth assignments are made for Be subsamples, with detail of textures and subsample size. Red dashed lines indicate laminations followed from edges of Be subsample to ablation profile; midpoint of distance between the lines is the assigned Be subsample depth, while depth uncertainty is the total distance. Arrows 1, 2: single and groups of ablation lines respectively (ablated horizontally) for Pb; 3 indicates an area sampled for Be, with illustration of area of sample used for analysis (accidental chippings were discarded). (f) Detail of ablations performed for $^{230}Th_{excess}$ measurements (blue); f1, f2 correspond to arrows in (d). Arrow indicates group of 20 horizontal line scan Pb ablations. 65

Fig. 2.6. Spatial illustration of model parameters and their relationships. The Sorbas basin is treated as one box, with fluxes of Q_I and Q_O (inflow from and outflow to the Mediterranean respectively) and Q_R (river runoff), all with associated [Sr] and $^{87}Sr/^{86}Sr$ isotope ratio. Q_I and Q_O also have associated salinity. Fluxes E (evaporation) and P (precipitation) are assumed to have no associated salinity or Sr. All fluxes together compose the overall hydrologic budget of the Sorbas Basin box; only those with no associated salinity, E, P, and Q_R, make up the freshwater budget. 72

Fig. 3.1. $^{87}Sr/^{86}Sr$ isotope compositions of Sorbas basin water compared to lithology (Upper Abad marls, cycles UA5 to UA8), sedimentation rate (far right), insolation, and other available data. (a) Precession and (b) insolation [*Laskar et al.,* 2004]. (c) Ceara Rise (tropical W Atlantic) ODP Leg 154 Site 926 $\delta^{18}O$ [*Shackleton and Hall,* 1997]. (d) Sorbas Basin B/P and (e) *G. bulloides* records from identical samples [*Perez-Folgado et al.,* 2003]. (f) $^{87}Sr/^{86}Sr$ isotope compositions of Sorbas basin planktic foraminifera. Data points outside of analytical error are highlighted. Green bar indicates time span covered by GCM simulation data used in box model. 85

Fig. 3.2. Steady state model results. (a) Sorbas Basin Sr isotope ratio ($[^{87}Sr/^{86}Sr]_S$) vs Q_R:Q_I for riverine Sr concentrations ($[Sr]_R$) from 0.1 to 0.5 mg/L. Values on vertical lines indicate minimum ratio value where an anomaly can occur for each concentration. (b) Contour plot of $(E - P - Q_R) / Q_R$, with respect to Sorbas Basin salinity and $^{87}Sr/^{86}Sr$ ratio, using $[Sr]_R = 0.3$ mg/L. Sr anomaly requires $Q_R < E - P \pm \sim 1.7\%$, as indicated by shaded box. 88

Fig. 3.3. Transient model results. (a-c) Comparison of hydrologic budgets (upper curves), and effect on evolution of Q_I and Q_O (middle curves), basin salinity and $^{87}Sr/^{86}Sr$ ratio (lower curves); g = 12 m^3/s per g/L. $\Delta S=0$: Sorbas and Mediterranean salinities equal. Sr anomaly: minimum observable $^{87}Sr/^{86}Sr$ ratio anomaly ($\geq$ 0.709003; section 3.3). Freshwater budgets vary ideally through minimum and maximum E – P over 20 ky, applying constant Q_R to generate (a) mainly positive (average $E<P+Q_R$), (b) half positive/half negative (average $E=P+Q_R$), and (c) mainly negative (average $E>P+Q_R$) hydrologic budgets. Positive freshwater budget axes values indicate freshwater loss, as the term ($E-P-Q_R$) is positive in the model. Star-marked bars emphasize small time lag between peak hydrologic budget values, salinity, and $^{87}Sr/^{86}Sr$. (d-f) Peak $^{87}Sr/^{86}Sr$ isotope ratios encountered over a 20 ky model cycle for given g and 91

Q_R. (d) Higher resolution plot of boxed area in contour plot (e) showing only anomalies greater than 0.709003 for cycles with a mainly positive hydrologic budget (as in a). (e) Contour plot for all Q_R and g; red areas (outlined in black) indicate peak Sr isotope values > 0.709003; blue indicates no anomaly occurs. Q_R and g combinations employed for plots a-c are indicated. Area A: values of Q_R and g that do not allow between-peak $^{87}Sr/^{86}Sr$ ratios to return to global ocean value (allowing for 5 ppm margin, to $^{87}Sr/^{86}Sr$=0.708970); Sr isotope anomalies are observed in this region, but the foraminifera data pattern is not reproduced (Fig. 2). Area B: insufficient time near neutral hydrologic budget to generate an anomaly. (f) Higher resolution plot of boxed area in (e), emphasizing only anomalies above 0.709003 for cycles with a mainly negative hydrologic budget as in (c).

Fig. 4.1. $\varepsilon_{Nd(t)}$ from ODP Site 978 (squares) compared with published values for Mediterranean Outflow (MO) and North Eastern Atlantic Deep Water (NEADW) from FeMn crusts (65GTV, 121DK [*Abouchami et al.,* 1999]; 3514-6, 3511-1, [*Muiños et al.,* 2008]). Dashed lines at 6.12 and 6.62 Ma indicate age range of Messinian samples; boundaries are provided by last occurrence (LO) and first occurrence (FO) of R. rotaria (Ref, Leg 161 Results). Samples within the interval are assigned age uncertainty equal to this time span. Tan box emphasizes the maximum range of values observed in late Miocene Site 978 values (including analytical uncertainty), corresponding to Range C. Range A indicates modern MO values at Gibraltar [*Tachikawa et al.,* 2004]; Range B indicates values for the Holocene measured in sediments from the Iberian margin [*Stumpf et al.,* 2010]. See Ch. 2, Fig. 2.1 and Table 2.3 for locations. LIW – Levantine Intermediate Water. 107

Fig. 4.2. Map of structures in Alborán Sea and location of sites mentioned in this chapter. Inset shows the main mountainous regions of the area (Betic, Rif, and Tell). Cap des Trois Fourches and Gourougou areas are regions of volcanic rock with highly radiogenic ε_{Nd} signatures; Messadît is one outcropping sedimentary section from which *Ivanoviç et al.* [2013] used fossil fish teeth to estimate the palaeo-ε_{Nd} signature of MO. AMS – Al-Mansour Seamount; YR – Yusuf Ridge; MR – Maimonides Ridge; AR – Alboran Ridge; AI – Alboran Island; XB – Xauen Bank; DB - Djibouti Bank; ACH – Alboran Channel. Modified from [*Martínez-Ruíz et al.,* 1999]. 110

Fig. 4.3. Nd isotope results from Sorbas basin sediments. $\varepsilon_{Nd(t)}$ of fish remains, acid-reductive bulk sediment leachates, strong leachates, and total dissolution samples are compared with estimates of water mass Nd isotope signature estimates for MO and NEADW from *Ivanovic et al.* [2013], ODP Site 978, and FeMn crusts 65 GTV, 3514-6, and 3511-1 [*Abouchami et al.,* 1999; *Muiños et al.,* 2008]. 114

Fig. 4.4. Al/Nd ratios of bulk sediment leachates compared (a) by lithology, (b) by $\varepsilon_{Nd(t)}$, and (c) with insolation. Al/Nd uncertainty smaller than symbols. 118

Fig. 5.1. Pb isotope time series of acid-reductive leaches on bulk sediment from the Sorbas Basin (red), Falconara section (blue), and Monte del Casino section (black), compared with orbital parameters insolation, climatic precession, obliquity, and eccentricity. The ranges of Pb isotope compositions measured from late Miocene samples from ODP Site 978 are also shown. 129

Fig. 5.2. $^{206}Pb/^{204}Pb$ records from Monte del Casino (upper panels) and Falconara (lower panels) plotted against lithological variation. 130

Fig. 5.3. Ranges of Pb isotope compositions measured at each of the three sites (Sorbas Basin, Falconara, and Monte del Casino). Where it is visually clear, based on the correspondence shown in Fig. 5.1, which compositions tend to correlate to insolation maxima (+) and minima (-), this is noted. 130

Fig. 5.4. Pb/Pb crossplots of Sorbas Basin acid-reductive leachates (blue), strong 133

leachates (red), and total dissolutions (black). Arrows emphasize linear trend in data, from either leachates of sapropelic layer samples towards values consistent with insolation minima (dashed) or towards total dissolution values (dotted). Leachates from samples deposited near insolation minima essentially plot as separate population (tan areas). Errorbars represent 2SD external reproducibility unless internal was larger.

Fig. 5.5. Comparison of $^{87}Sr/^{86}Sr$ isotope results, benthic to planktic (B/P) ratio, % *G. bulloides* (of planktic foraminiferal assemblage), % Neogloboquadrinids (of planktic foraminiferal assemblage), and $^{206}Pb/^{204}Pb$ isotope ratios with lithology and precession/insolation. Faunal data from *Pérez-Folgado et al.* [2003]. The $^{206}Pb/^{204}Pb$ isotope ratio is selected as it shows the cyclicity most clearly; however, the temporal changes in all other Pb isotope ratios are identical relative to lithology, with the exception of $^{207}Pb/^{204}Pb$, as variability in the record of this ratio is obscured by the low natural variability compared to analytical uncertainty. 135

Fig. 5.6. $^{208}Pb/^{204}Pb$ vs. $^{206}Pb/^{204}Pb$ plot comparing Sorbas, Falconara, and Monte del Casino seawater values with other regional data. Sorbas Basin seawater signature (acid-reductive leachates, orange circles) strong leach and total dissolution results (diamonds) plot within a triangle bounded at the bottom by an array (dashed line), labeled the "Open-marine trend", described by ODP Site 978 (red triangles), and FeMn crusts (squares). To the bottom-left of the triangle, values associated with insolation maxima (+), and to the bottom-right, values associated with insolation minima (-). The top of the triangle likely represents the siliciclastic end-member. Monte del Casino plots on its own array (brown squares). An average value for Saharan dust compiled by *Abouchami and Zabel* [2003] from other literature data is shown; this average is contested in section 5.3.4.3. 138

Fig. 5.7. Annual aerosol deposition rates (g/m^2 $x10^3$) over the North Atlantic and Mediterranean. Modified from [*Goudie and Middleton,* 2001], data from [*Prospero,* 1996]. 142

Fig. 5.8. Astronaut photograph ISS042-E-244403 (acquired February 12, 2015) of a dust plume originating from the Bodélé Depression. Source: NASA. 143

Fig. 5.9. Modern-day dust transport from Africa during various seasons from major source locations. A – Chad Basin (Bodélé Depression included); B – Eljouf Basin (Mali/Mauritania border); C – Region near 33°N 7°E; D – Region near 25°N 18°E. Modified from *Israelevich et al.* [2003]. Sites A and B are the primary sources. Darker colours represent increased concentration of aerosols, although no scale is provided in the original publication. Additional sources include south of the Atlas Mountains (Morocco), the eastern Libyan desert, and large areas of Egypt and Sudan (the Nubian Desert) [*Engelstaedter et al.,* 2006]. 144

Fig. 5.10. Modern seasonal variability in dust over the Mediterranean, according to type, derived from MODIS satellite data. 'Maritime' is defined as aerosols lifted from the sea surface itself; 'continental' is defined as aerosol particulates, either anthropogenic or natural, originating over the European continent; desert dust is defined as mineral aerosol derived from Northern Africa. Each type has a specific and identical particle size distribution which allows the three sources to be seperable. Winter and spring shown here; summer and fall shown in Fig. 5.11. From [*Barnaba and Gobbi,* 2004]. 145

Fig. 5.11. As per Fig. 5.10. 146

Fig. 5.12. Sorbas Basin, Falconara and Monte del Casino Pb isotope results compared to (a, b) ODP Site 978, NE Atlantic FeMn crusts, and Sal Island (Cape Verde) loess; (c, d) Bodélé Depression diatomite, African dust, pelagic N Atlantic sediments; and (e, f) circum-Mediterranean whole rock data (GEOROC 147

database). Note differing axes between panel pairs. M08 - [*Muiños et al.,* 2008], A99 - [*Abouchami et al.,* 1999], A13 - [*Abouchami et al.,* 2013], S80 - [*Sun,* 1980]. "Open marine" trendline includes data from deep sites ODP Site 978 and all FeMn crusts. "Bodele" trendline includes only Bodélé Depression diatomites. Tetraethyl gasoline additive Pb isotope ratios for North Africa are $^{206}Pb/^{204}Pb$ 17.02-17.99, $^{207}Pb/^{204}Pb$ 15.53-15.60, $^{208}Pb/^{204}Pb$ 36.66-37.93, and for Europe are $^{206}Pb/^{204}Pb$ 17.03-18.2, $^{207}Pb/^{204}Pb$ 15.43-15.64, $^{208}Pb/^{204}Pb$ 36.82-38.10 [*Bollhofer and Rosman,* 2001].

Fig. 5.13. $^{208}Pb/^{204}Pb$ vs. $^{206}Pb/^{204}Pb$ (upper panel) and $^{207}Pb/^{204}Pb$ vs. $^{206}Pb/^{204}Pb$ plots comparing late Miocene seawater values from the Sorbas Basin, Falconara and Monte del Casino sections with Holocene marine sediments, Sal Island loess, and whole rock data from the Betic-Rif Arc and the Atlas Mountains, Northern Morocco. S80 - [*Sun*, 1980], A13 - [*Abouchami et al.,* 2013]. Solid line, "open marine" trendline; dashed line, Bodélé Depression samples trendline. 152

Fig. 6.1. (a) [^{10}Be] vs. depth in crust 3514-6. The extrapolated surface concentration is $1.97x10^{10}$ atoms/g. There are two distinct growth rate segments along the transect (Segments 1-2). Values used to calculate growth rates are derived from trendlines. (b) Depth vs. time relative to crust surface, calculated using extrapolated surface concentration determined in (a). In both plots, open symbols indicate data for which a precise depth could not be applied on the laser ablation transect due to the disappearance or 'pinching-out' of laminations (marked with * in Table 6.1). 161

Fig. 6.2. (a) $^{10}Be/^{9}Be$ vs. depth in crust 3514-6. The extrapolated surface ratio is $2.75x10^{-8}$. There are two distinct growth rate segments along the transect (Segments 1-2). Values used to calculate growth rates are derived from trendlines. (b) Depth vs. time relative to crust surface, calculated using extrapolated surface concentration shown in upper plot. In both plots, open symbols indicate data for which a precise depth could not be applied on the laser ablation transect due to the disappearance or 'pinching-out' of laminations (marked with * in Table 6.1). 162

Fig. 6.3. Results of $^{230}Th_{excess}$ measurements (left-hand plots from TH1; right-hand plots from TH6). (a, b) Activity ratios for ^{230}Th, ^{234}U, and ^{238}U normalized to ^{232}Th; secular equilibrium is reached after ~200 μm in (a) and ~ 300 μm in (b). (c, d) Calculation of growth rate from plot of ln($^{230}Th_{excess}$ activity) vs. depth; note y-axes differ. (e, f) ($^{234}U/^{238}U$) vs. depth plotted with lines for unity (black) and ($^{234}U/^{238}U$) seawater value (1.147). Uncertainty is estimated solely from counting statistics on ^{230}Th and ^{234}U; this is a minimum value only (see text for further explanation of error calculation). Parentheses denote activity as per convention. 165

Fig. 6.4. (a) Crust 3514-6 Pb isotope results versus depth with uncertainty (grey bars). (b) Data compared to those of *Muiños et al.* [2008]. Green circles, depths given in publication. Blue squares, depths converted by proportional correspondence of $^{10}Be/^{9}Be$ ratios from sample to sample (see text for further information). 167

Fig. 6.5. Depth ranges of growth rates applied to crust 3514-6 determined by $^{230}Th_{excess}$ and ^{10}Be atoms/g ([^{10}Be] 1 and 2). CR# labels indicate subsamples drilled for $^{10}Be/^{9}Be$ measurement; thin vertical red lines indicate laser ablation profile for Pb isotopes; blue (top right corner) indicates region of laser ablation profiles for $^{230}Th_{excess}$. See Tables 6.2, 6.3 and Figs. 6.1, 6.3 for calculation of rates. 173

Fig. 6.6. Crust 3514-6 Pb isotope time series using the combined $^{230}Th_{excess}$ and [^{10}Be] age model (0 to 0.2 Ma, no data; 0.2 to 0.38 Ma, $^{230}Th_{excess}$ rate; 0.38 to 4.1 Ma, [^{10}Be] rate 1; 4.1 Ma to end of record, [^{10}Be] rate 2). Green circles are previously published data [*Muiños et al.,* 2008]. 174

Fig. 6.7. Crust 3514-6 Pb isotope time series using the combined $^{230}Th_{excess}$ and $^{10}Be/^{9}Be$ age model (0 to 0.2 Ma, no data; 0.2 to 0.38 Ma, $^{230}Th_{excess}$ rate; 0.38 to 2.5 Ma, 175

$^{10}Be/^{9}Be$ rate 1; 2.5 Ma to end of record, $^{10}Be/^{9}Be$ rate 2). Green circles are previously published data [*Muiños et al.,* 2008].

Fig. 6.8. High resolution Pb isotope record of crust 3514-6, with comparison to other crusts from the NE Atlantic. For locations and water depths see Ch. 1, Fig. 1.20, Ch. 2, Fig 2.1, Ch. 2 Table 2.4. 65GTV represents MO at deeper location; 3511-1 represents NEADW, in vicinity of Gulf of Cadiz; 121DK represents NEADW at a more southern location far from MO influence. Late Pleistocene to recent Iberian coast bulk sediment leachate data [*Stumpf et al., 2010*] shown for reference; this data has maximum age of ~22 ky. 177

Fig. 6.9. The locations of the crusts discussed in this section. The column at the right shows the water depths each crust was collected from and indicates the water mass which is thought to have bathed the crusts. MO – Mediterranean Outflow, NEADW – North Eastern Atlantic Deep Water, AAIW – Antarctic Intermediate Water. 178

Fig. 6.10. High resolution $^{208}Pb/^{206}Pb$ record of crust 3514-6, compared with crust records from the NE Atlantic (as per Fig. 6.8) and open ocean records of major oceanographic changes. Record compilation (panel above Pb isotope record) modified from [*Hernández-Molina et al.,* 2014b]. 179

Fig. 6.11. (a) Comparison of fluctuations of [^{9}Be] in crust 3514-6 with (b-d) changes in Pb isotope compositions recorded in NE Atlantic crusts. Periods of fluctuating [^{9}Be] also consistent with irregularities in the $^{10}Be/^{9}Be$ ratio (Table 6.1, Fig. 6.2) are highlighted in blue and labeled with the relevant palaeoclimatic event which likely caused the fluctuations. Higher concentrations of [^{9}Be] after 8 Ma are not consistent with irregularities in the normalized $^{10}Be/^{9}Be$ ratio, and consequently do not constitute a change in water masses bathing the location. NH – northern hemisphere. 182

Fig. 7.1. Precipitation across the globe and monsoons. North Africa is particularly dry in the modern configuration, while the African monsoon system sits just to the south (area of African continent outlined with a dashed line). Modified from *Goudie and Middleton* [2001]. 194

ACKNOWLEDGEMENTS

To my supervisors, Dr. Rachel Flecker, Dr. Marcus Gutjahr, and Prof. Rob Ellam, you all have complementary strengths that have taught me a lot. I hope, like you, I never lose my passion for science. Thank you all, from the bottom of my heart, for everything you have done for me.

I have to place in very high regard the social support that ultimately means I haven't lost my mind. My SUERC office mates over the years (Ana, Brett, Domokos, Jess, Keiran, Kim, Leisa, Pete), many other SUERC friends with whom I've shared a beer and maybe some science (you know who you are), my softball mates (you know who you are too), and my MEDGATE mates (or MADLATE? Ali, Bas, Diana, Dirk, Evelina, Maria, Marlies, JP, Walter). MEDGATE was a whirlwind experiment in science as well as social engineering – and we had a blast, from the field to the pub. Even if sometimes Rachel didn't approve! To Ali, with whom I may (definitely) have shared too much, even from before our PhDs officially started. Somehow she still loves me (even after that smell? And the noises…). And Marlies, who shared her space with me and made me feel at home in Kiel. To Janett and Kristin, even though you were busy/stressed/trying to finish up, you still hosted me, and did an amazing job of it. All of you are always welcome in my home.

A special mention goes to our totally dedicated MEDGATE supervisory team who would always continue the scientific discussions and teaching late into the night (as long as there was beer to be had!) and gave up so much of their time (and sleep) for us students, whether we were "their own" or not. That is the meaning of true dedication to your profession. Also, Carla, aka Superwoman, we know you had a lot to put up with. You still managed to run the program efficiently and logically.

To Jan Fietzke, Tanja Kouwenhoven, Francisco Sierro and Frits Hilgen, who were very generous with analyses, samples, counting, teaching, data, and in general their time and knowledge. Emails out of the blue, asking for clarification of specific information (related or not to the samples) were always answered. For your dedication, and willingness to teach even when you have no responsibility to do so, thank you. In the lab, Anne and Vinnie were always willing to put up with me and my stupid questions; for showing me how to work and get results, thank you.

Near the end, I hatched a plan (read: harebrained scheme) to undertake a modeling study. And it happened! Thanks so much to Paul Meijer for the support in making it happen, and Dirk Simon for putting up with me and teaching me to use R and how to understand the math. Thanks also to the Jim Gatheral Scholarship Fund and the University of Glasgow for their financial generosity.

To all of my family: thank you for your never ending support, love, and editing skills. You don't know how much you mean to me (not that I show it very well – I keep leaving to go to another country).

I'd also like to thank the EU and the Marie Sklodowska Curie Actions for ultimately bringing me to Scotland (a country I'd never really considered before, but it turns out I like very much). I may have found a new home (if Brexit doesn't result in my deportation at some point in the next couple of years). Frits, I finally agree with you - technocracy.

AUTHOR'S DECLARATION

The material presented in this thesis is the result of research carried out between October 2012 and March 2016 at the Scottish Universities Environmental Research Centre, College of Science and Engineering, University of Glasgow, under the supervision of Professor Rob Ellam (SUERC); work was also performed at GEOMAR Helmholtz Centre for Ocean Research Kiel, Germany under the supervision of Dr Marcus Gutjahr; further co-supervision was provided by Dr Rachel Flecker (Department of Geographical Sciences, University of Bristol). This thesis is based on my own independent research and any published or unpublished material used here is given full acknowledgment.

Due to the interdisciplinary nature of my working group (MEDGATE, section 1.1.3), some data from other researchers has been incorporated into this thesis. Persons other than my supervisors have also mentored and assisted me with lab work, particularly mass spectrometry for isotope measurements, as well as computer programming to enable me to generate scripts for data reduction and model work. A summary of the relevant contributors beyond my immediate supervisors, including their specific contributions, is provided at the beginning of each results chapter. Letters of permission for the use of unpublished data are provided in Appendix 1.

_____

Sevasti Eleni Modestou
Monday November 7th, 2016

Glossary of Acronyms

General

MSC	Messinian Salinity Crisis
LE	Lower Evaporites
UE	Upper Evaporites
PLG	Primary Lower Gypsum (MSC Stage 1)
PLE	Primary Lower Evaporites (MSC Stage 1)
RLG	Resedimented Lower Gypsum
MES	Messinian Erosional Surface
FeMn	Ferromanganese (for crusts and dispersed material)
ε_{Nd}	epsilon Neodymium
REE	Rare Earth elements (heavy/middle/light: HREE/MREE/LREE)

Water Masses

AABW	Antarctic Bottom Water
AAIW	Antarctic Intermediate Water
AMOC	Atlantic Meridional Overturning Current
ENACW	Eastern North Atlantic Central Water
LDW	Levantine Deep Water
LIW	Levantine Intermediate Water
MAW	Modified Atlantic Water
MO	Mediterranean Outflow
NACW	North Atlantic Central Water
NADW	North Atlantic Deep Water
NEADW	North Eastern Atlantic Deep Water
WMDW	Western Mediterranean Deep Water

“Her intentions are good,” she said.
“And her information is bad,” Kenner said. “A prescription for disaster.”

State of Fear
Michael Crichton, 2004

1 Introduction

1.1 Motivation

1.1.1 Understanding Earth's climate: the biggest jigsaw puzzle

Earth's climate is the result of solar radiation reaching our planet, and the interaction of that energy with the various spheres, e.g. lithosphere, atmosphere, biosphere, hydrosphere. In particular, the oceans are fundamental in regulating the distribution of thermal energy; the 'conveyor belt' of thermohaline circulation spreads heat energy from the equator to the poles (Fig. 1.1) [*Broecker and Peng*, 1982]. Thus, understanding past ocean circulation is critical to our understanding of past changes in Earth's climate, as well as to predicting how climate may change in the future in response to anthropogenic or natural forcings.

Deep water formation in the oceans is a key climate process, as it is a major driver of thermohaline circulation. In the North Atlantic, referred to as Atlantic Meridional Overturning Circulation (AMOC), water masses progressively mix to become colder and saltier, eventually becoming denser than the surrounding water and sinking. This process provides the required energy to drive water all the way from the Arctic to the Antarctic in deep currents (referred to collectively as North Atlantic Deep Water, NADW; Fig. 1.1). Similar deep water formation processes near the south pole drive a dense water mass to flow northwards at the bottom of the Atlantic (i.e., Antarctic Bottom Water, AABW) which can be detected in a modified form all the way to the Rockall Trough near the British Isles.

The "puzzle piece" of ocean circulation investigated in this thesis is a current exiting the Mediterranean Sea, known as Mediterranean Outflow (MO)[1]. In the modern-day configuration, MO exits the Mediterranean Sea at depth and splits into three main branches, the most prominent of which flows northwards (Fig. 1.2). This salty branch of water is understood to impact AMOC, both today and in the past [e.g., *Bigg et al.*, 2003; *Rogerson et al.*, 2012; *Hamon et al.*, 2013; *Ivanoviç et al.*, 2014], pre-

[1] Mediterranean Outflow (MO) is considered any part of the plume of denser water exiting the Mediterranean past the Camarinal Sill, the shallowest part of the Strait. Elsewhere, this water mass may be referred to as Mediterranean Outflow Water, MOW.

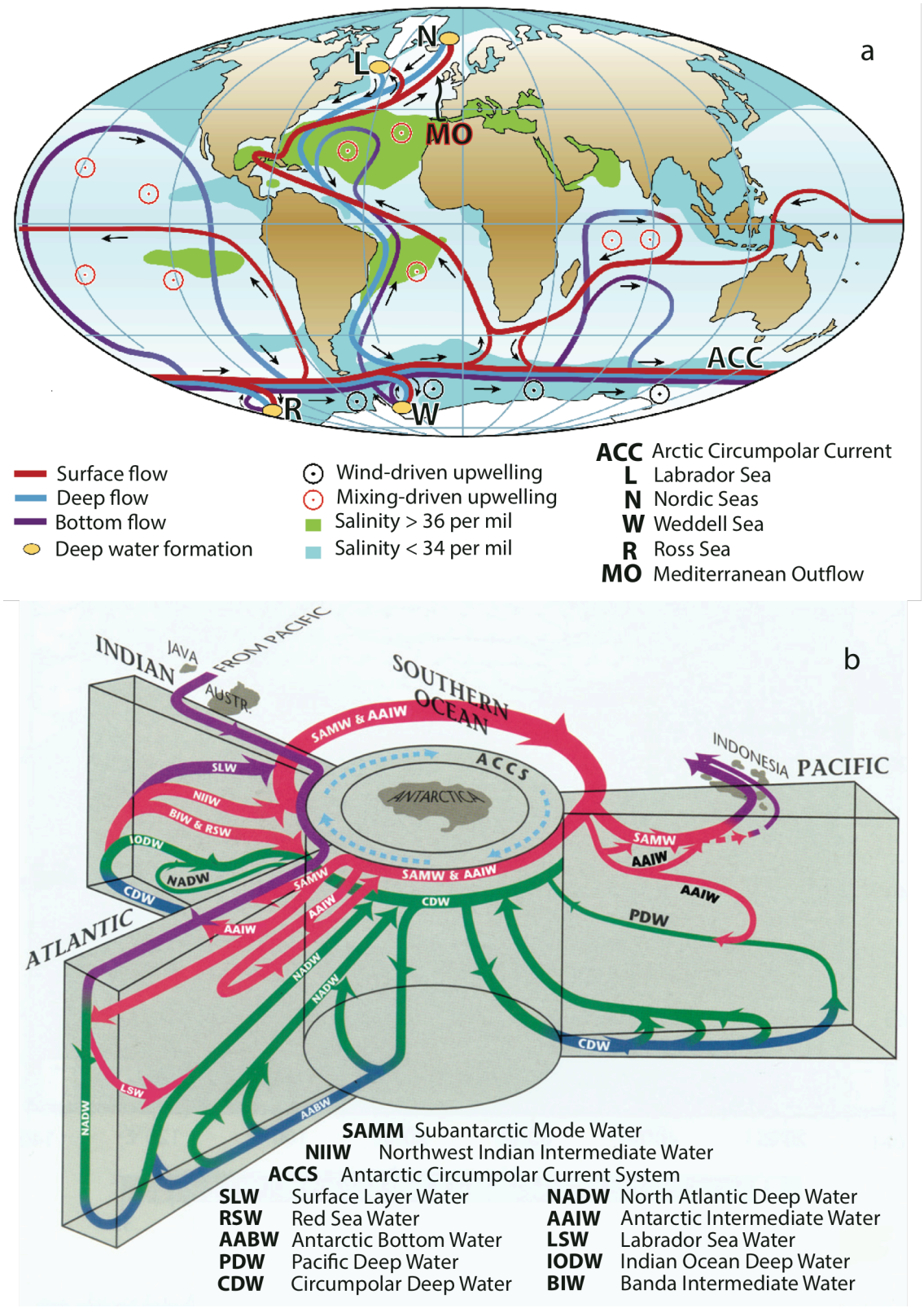

Fig. 1.1. Representations of thermohaline circulation in the global oceans. (a) Simplistic bird's eye view of major currents and circulation, as well as locations of significant deep water formation, upwelling, and locations of surface waters significantly more or less saline than mean salinity. Modified to include MO from [*Kuhlbrodt et al.,* 2007]. (b) More accurate (although still simplified) three-dimensional view of ocean circulation centered about the Antarctic. Surface currents are purple, intermediate are red, deep are green, and bottom currents are blue. Modified from [*Schmitz,* 1996].

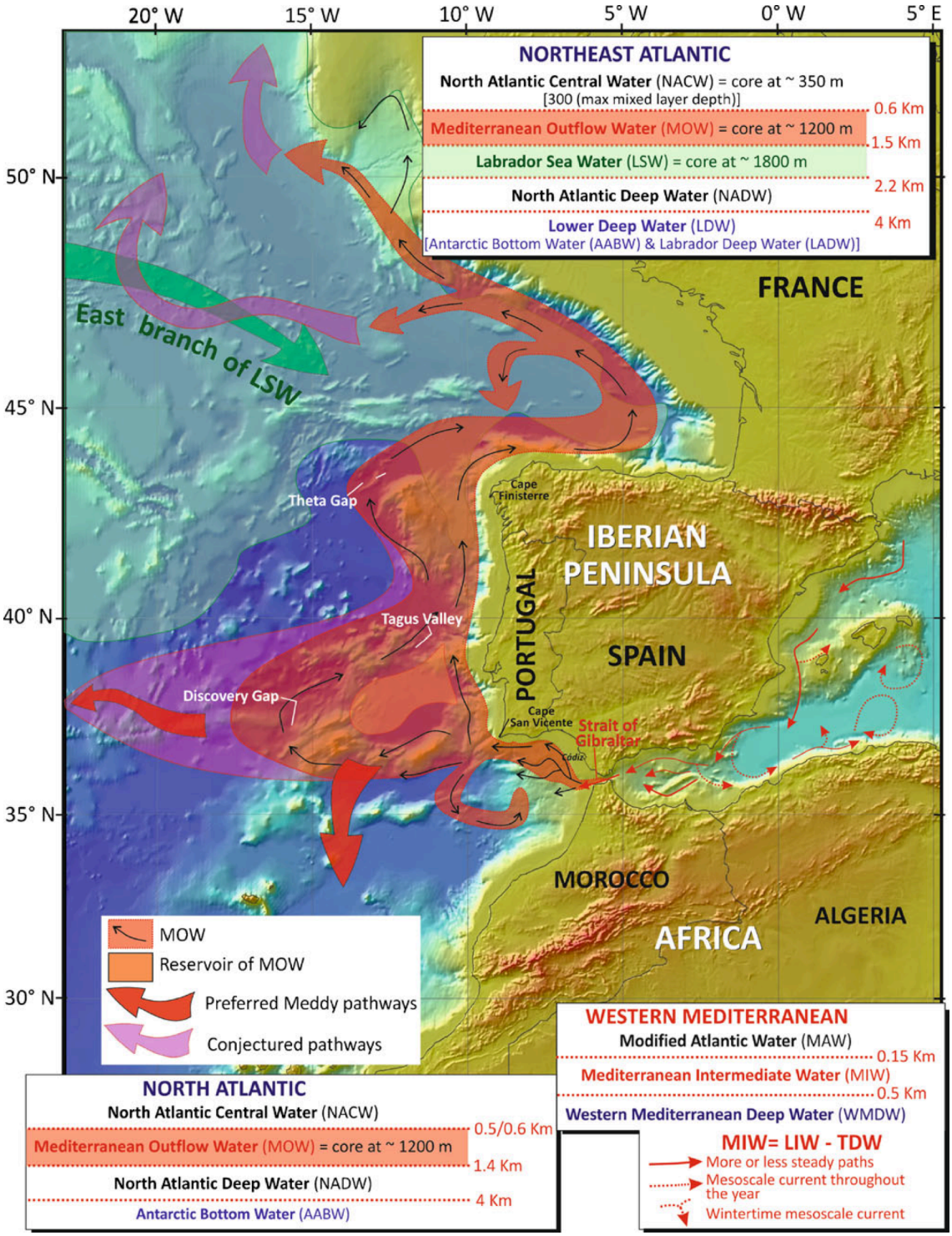

Fig. 1.2. Modern dynamics of Mediterranean Outflow (MO), referred to as MOW in the figure. Main graphic shows horizontal pathways of MO, including the three branches, the most prominent flowing northwards along the Iberian margin. Boxes above and below the main figure summarize the vertical distribution of MO and its relationship to overlying and underlying water masses, both in the Atlantic and in the Mediterranean (TDW = Tyrrhenian Deep Water). From [*Hernández-Molina et al.*, 2011].

conditioning water masses for deep water formation by increasing their salinity and thus density. It should be noted that the relative importance of MO is contested for modern day circulation [e.g., *Rahmstorf*, 1998; *Mauritzen et al.*, 2001].

Between about 5.33 and 6 Ma [*Lourens et al.*, 1996; *Manzi et al.*, 2013], at the end of the Messinian stage, an event termed the Messinian Salinity Crisis occurred in the Mediterranean Sea. At that time, the connections between the Mediterranean and Atlantic were severely disrupted. How did this event affect global climate? Was it significant enough to alter thermohaline circulation measurably? Is it possible to use past changes in exchange to quantify the effect of MO on AMOC? Before we can answer those questions, before we can facilitate our understanding of the effect changes in this current have had on AMOC and, in general, past climate, we must adequately define how MO has changed through time. As major changes to MO are expected during the MSC, this event provides an ideal time to study the impact of MO on AMOC in the past. However, the true extent and timing of the disruption to exchange is debated (discussed in sections 1.2.2 and 1.2.7 below). To date, answers to the questions of how much and when the MO plume into the North Atlantic changed have not been adequately resolved. Better constraints on the timing of closure of the corridors linking the Mediterranean and Atlantic prior to the MSC are required, as well as more direct evidence of when and with what properties outflow was reinitiated after the Mediterranean and Atlantic became re-connected at the Miocene-Pliocene boundary.

1.1.2 Ocean forensics: radiogenic isotope 'fingerprints'

This study was specifically motivated by preliminary results indicating that neodymium (Nd) isotopes could record the pattern of exchange between the Atlantic and Mediterranean during the Messinian [now published; see *Ivanoviç et al.*, 2013]. Isotopes of trace metals, such as Nd, are preserved within marine sediments, allowing identification of water masses present at a given location and time. Radiogenic daughter isotopes are produced by the decay of radioactive parents; thus, radiogenic and non-radiogenic isotopes of the same elements can be compared to understand changes. Similarly to the way radioactivity is used as a chronometer, rocks of different ages have varying radiogenic isotope signatures, allowing waters derived from specific locations to incorporate specific

(and sometimes, but not always, unique) radiogenic isotope signatures[2]. Records of these signatures, which illustrate changes (or not) through time, allow us to piece together the puzzle of when and how much circulation has changed, and infer causal mechanisms. *Ivanoviç et al.* [2013] interpreted their data as a record of gradual seaway closure, and also opened new possibilities for research into the Messinian Salinity Crisis.

1.1.3 MEDGATE

The research leading to the radiogenic isotope records described in this thesis was funded through the MEDGATE Project, a European Union funded Marie Curie Initial Training Network. MEDGATE's multi-disciplinary programme aimed to integrate geochemistry, micropalaeontology, field and lab based sedimentology, numerical modeling, structural geology, palaeoclimatology, palaeoceanography, and seismic data analysis to reconstruct gateway evolution and exchange dynamics before, during and after the Messinian Salinity Crisis and to examine the impact of the MSC on global climate. Ten researchers, nine doctoral and one postdoctoral, have focussed on one or more disciplines to examine Atlantic-Mediterranean exchange during the MSC from multiple angles and using different approaches. A large group of experienced researchers, acting as supervisors directly or partly, have also been involved with the project to provide expertise. At the end of the project, results were shared and combined in interdisciplinary work where possible; for this reason, this thesis incorporates data generated by or in concert with co-researchers. Contributions from other persons incorporated in this thesis are clearly indicated at the beginning of each results and discussion chapter (Chapters 3, 4, 5, and 6). Appendix 1 includes letters of permission from each individual who contributed unpublished data. Interdisciplinary integration provides the ability to reconstruct a more complete history of exchange than would otherwise be possible.

1.2 Late Miocene Mediterranean geology: salt, sapropels, and cycles

1.2.1 History of MSC research

The most recent case of basin-wide evaporite deposition in a large sea [*Rohling et al.*, 2008], the Messinian Salinity Crisis (MSC; 5.971 – 5.333 Ma; *Krijgsman et al.* [1999];

[2] This very simplistic statement is discussed in more appropriate detail in section 1.3, where specific radiogenic isotopes are individually introduced and their properties and sources outlined.

Manzi et al. [2013]; *Lourens et al.* [1996]) has been recognized as an extreme climate event for more than 40 years, yet its causes are poorly understood. The Late Miocene history of the Mediterranean may be one of the best studied on the globe, considering the wealth of palaeoclimate records generated from this region compared to elsewhere (see data compilation, Fig. 8 of *Marzocchi et al.* [2015]; see also [*Bradshaw et al.*, 2012]). Since discovery of the MSC, over 1000 articles have been published about the event [*CIESM*, 2008], yet we do not know how and where water entered the basin to support the sequestration of ~ 6% of global ocean salt [*McKenzie*, 1999] in basin-wide evaporite deposits which, in some locations, reach 3 km in thickness [*Hsü et al.*, 1973]. Also enigmatic is the history of the deep basins, and their relation to marginal successions outcropping on land today [e.g., *Ochoa et al.*, 2015].

The true extent of MSC evaporites was uncovered in 1970, when Deep Sea Drilling Program (DSDP) Leg 13 attempted to drill the deposits. Seismic data and partial cores suggested a layer of salt extending throughout the basin varying between 1,500 m to 3,000 m in thickness. After the discovery, *Hsü et al.* [1973] argued that evaporite samples recovered during the cruise indicated a shallow water depositional environment, at times becoming fully subaerial, punctuated by repeated marine incursions into a deep, isolated basin. As the hydrologic budget of the Mediterranean Sea today is strongly evaporative [*Mariotti et al.*, 2002], *Hsü et al.* [1973] assumed isolation from the Atlantic would result in evaporite deposition due to desiccation. From mass balance calculations, they concluded that one solitary desiccation event could produce an evaporite deposit in the range of 20 metres thick, leading them to suggest several marine incursions would be necessary to generate the volume of halite observed. This hypothesis requires, at minimum, an intermittent connection between the Atlantic and Mediterranean to provide the necessary salt. Dissent to the concept of complete desiccation was quick; other research groups immediately published alternatives, including a shallow basin model [*Nesteroff*, 1973] and a deep non-desiccated basin model [*Selli*, 1973]. Such dissent regarding various aspects of the causes and consequences of the MSC has continued to the present.

There are two separate Messinian evaporite successions: one of marginal settings, and one of deep settings (Fig. 1.3). The classical marginal sequence is defined by the Sicilian section [*Decima and Wezel*, 1973], separated into two units, the Lower Evaporites (LE) and the Upper Evaporites (UE). The former begins with open marine marls, organic-rich laminated layers, and diatomites, followed by evaporitic limestone (‘Calcare di Base’), gypsum, marls, and halite. The latter is composed of gypsum and marls, separated from the

former by an erosional and occasionally angular unconformity. Overlying the UE are the Lago Mare ('lake sea') facies, deposited in brackish water conditions. The Lago Mare sediments represent the final stage of the MSC; overlying these are Pliocene sediments indicating normal marine conditions. The deep marine succession is thought to be composed of similar lower gypsum, halite, and upper gypsum units. As the deep succession has only been recovered to within the top of the UE, seismic interpretations provide the majority of our understanding of the deep setting (Fig. 1.3; e.g. [*Hsü et al.*, 1973; *Lofi et al.*, 2005]).

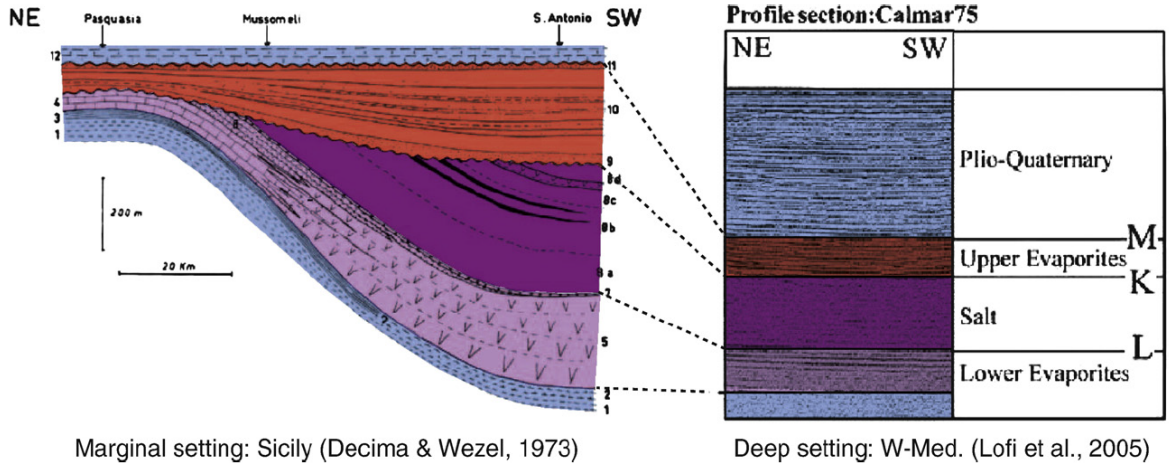

Fig. 1.3. Correlation of marginal evaporite successions to deep basin seismic profiles. Note that the Lower Evaporites in the deep setting correspond only to the unit below the halite, while on Sicily they are composed of gypsum, evaporitic limestone and halite. M, K, and L refer to significant seismic reflectors discussed in *Lofi et al.* [2005]. Modified from *Krijgsman and Meijer* [2008].

1.2.2 The Betic and Rifian palaeogateways

According to our current understanding, the opening of the seaway at Gibraltar did not occur until the end of the Messinian, at the Messinian/Zanclean boundary (eg. [*Hsü et al.*, 1973]). Prior to this, two gateways connected the Atlantic to the Mediterranean: the Betic corridor through Southern Spain, and the Rifian corridor through Northern Morocco (Fig. 1.4). It is commonly argued that the closure of these corridors played a central role for the MSC (e.g. [*Krijgsman et al.*, 1999b; *Flecker et al.*, 2002]).

Several palaeogeographic reconstructions (Fig. 1.4) suggest that the Betic corridor closed approximately 8.5 to 7.5 Ma [*Esteban et al.*, 1996; *Seidenkrantz et al.*, 2000; *Martin et al.*, 2001; *Betzler et al.*, 2006; *Martín et al.*, 2009], long before the onset of evaporite precipitation. *Krijgsman et al.* [1999b] found evidence to suggest that the closure of the Rifian corridor occurred by ~6.0 Ma at the latest; this finding led those authors to speculate that there may have been another connection, possibly a remnant through the Betics or a

channel underlying present day Gibraltar. Although the exact location of the Mediterranean-Atlantic connection during the MSC is still debated, it is clear that some connection must have existed to provide seawater to the Mediterranean during evaporite precipitation.

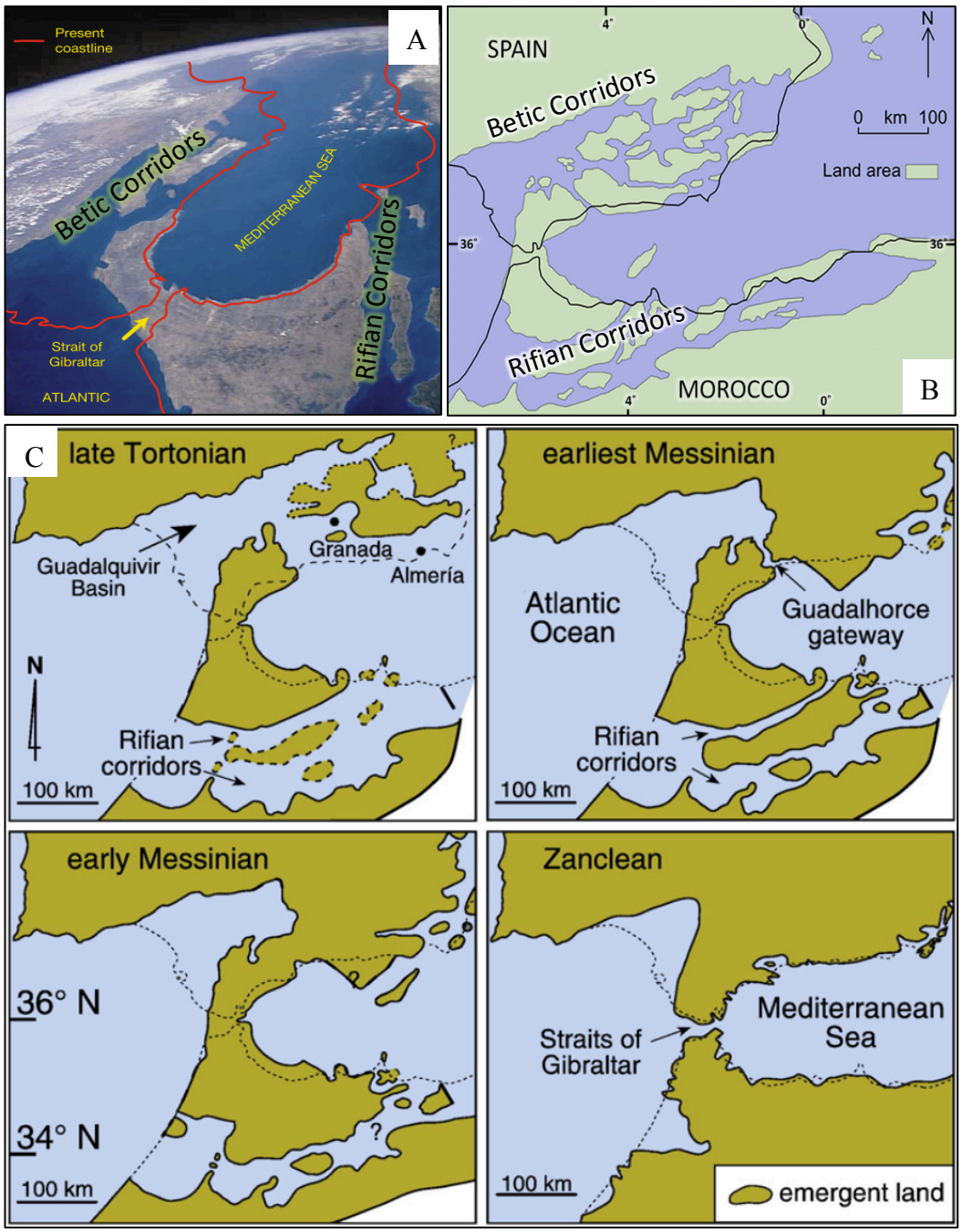

Fig. 1.4. Simplified reconstructions of the Betic and Rifian palaeocorridors linking the Atlantic to the Mediterranean prior to the MSC. (a) Modified satellite imagery; present day coastline in red. From *Duggen et al.* [2003], reconstruction based on *Esteban et al.* [1996]. (b) Approximately Tortonian stage reconstruction. Modified from *Ivanoviç* [2012], based on *Santisteban and Taberner* [1983]. (c) Reconstruction through time (Tortonian to Zanclean) from *Martín et al.* [2009].

1.2.3 A mechanistic MSC timeline

Duggen et al. [2003] summarized three possible mechanisms for the closure of the Betic and Rifian palaeocorridors: glacio-eustatic sea level drop [*Adams et al.*, 1977; *Hodell et al.*, 1986]; horizontal shortening due to crust movements [*Weijermars*, 1988], and/or tectonic uplift [*Hodell et al.*, 1989; *Garcés et al.*, 1998; *Krijgsman et al.*, 1999b]. Additionally, Govers (2009) suggested loading (due to evaporite deposition and the associated mass) may have generated isostatic uplift in the Gibraltar region.

Until recently, it was thought glacio-eustatic sea level changes did not contribute to MSC onset; initiation of evaporite deposition was thought to coincide with a deglaciated period in the benthic foraminiferal $\delta^{18}O$ record [*Krijgsman et al.*, 2004]. Using high-resolution stratigraphy incorporating orbital tuning with biostratigraphy and palaeomagnetism, [*Krijgsman et al.*, 1999a] was able to place the age of onset of evaporite deposition at 5.96 ± 0.02 Ma at several sites across the Mediterranean (Fig. 1.5a), indicating onset of the MSC was synchronous across the entire basin and that it did not coincide with glaciation. This figure was more recently revised by *Manzi et al.* [2013] to 5.971 Ma based on re-interpretation of the sedimentary contact between the underlying marls and the primary lower gypsum (PLG) in the Sorbas Basin, Southern Spain. *Manzi et al.* [2013] inferred that discontinuous lenses of gypsum, previously not considered as PLG, indicate the true onset of the MSC. This interpretation allows the age of MSC onset to be shifted by one precessional cycle back in time, and closely aligns MSC onset with glacial stage TG32 (Fig. 1.5b). Thus, current consensus is that a complex interplay between tectonism, leading to the uplift and closure of the Betic and Rifian corridors, and eustatic sea level change caused the Mediterranean to become sufficiently restricted from the Atlantic, leading to evaporite deposition.

Hilgen et al. [2007] determined that glacial stages TG12 and TG14 and their associated sea level drops coincide with the erosional gap between the PLG and UE in marginal settings. The erosional gap is an apparent desiccation phase, which seems to correlate to deep basin halite deposition [*Lofi et al.*, 2005; *Roveri et al.*, 2008]. Modeling results [*Krijgsman and Meijer*, 2008] corroborate this theory; those authors established that the deep halite unit could have been deposited under shallow conditions, assuming that its age corresponds to the approximately 70 ky time interval between glacial stages TG12 and TG14.

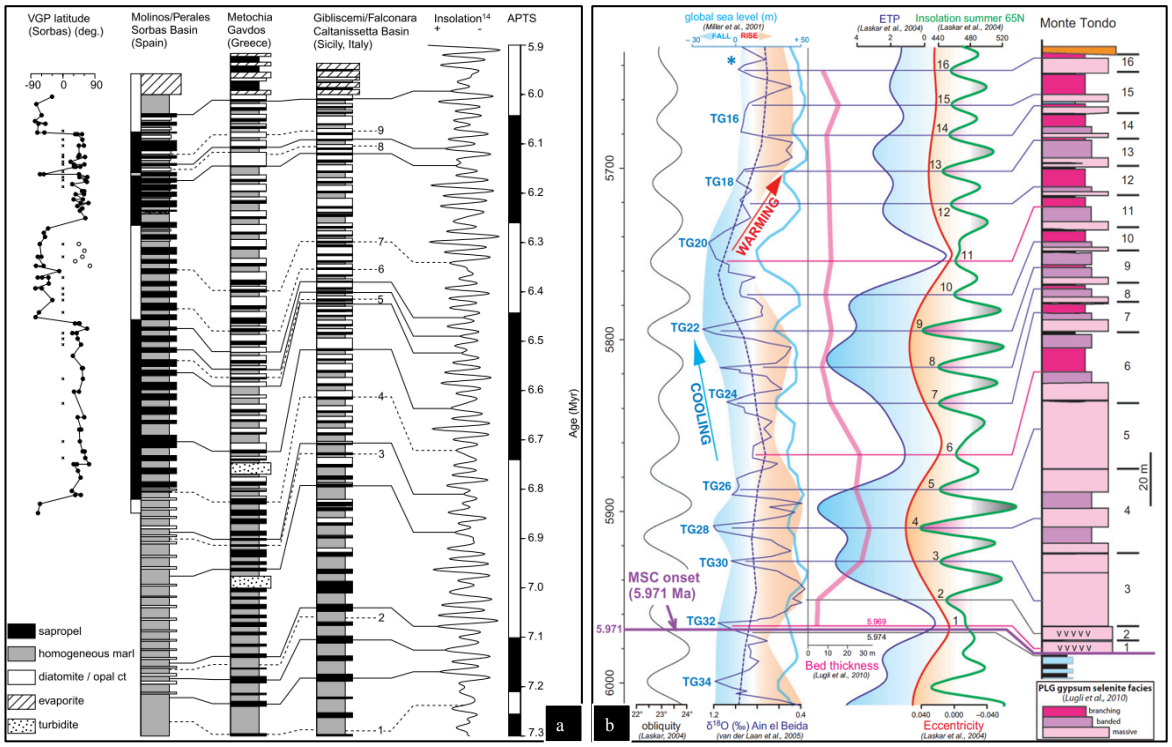

Fig. 1.5. (a) Astronomical tuning of the Molinos/Perales (S Spain), Metochia (Crete) and Gibliscemi/Falconara (Sicily) sections by *Krijgsman et al.* [1999a] leading to the determination of evaporite deposition at 5.96 Ma ± 20 ky (sourced from same publication). (b) Revised age of onset for evaporite precipitation by [*Manzi et al.* [2013] based on astronomical tuning, also showing association to potential glacio-eustatic trigger for evaporite onset by correlation to the $\delta^{18}O$ record of *van der Laan et al.* [2006] and associated glacial stages (source: *Manzi et al.* [2013]).

Hilgen et al. [2007] determined that deposition of the Upper Evaporites and Lago Mare facies should correspond to stages TG12 to TG9 and associated sea level rise, a further indication that changing climate played a major role in gateway exchange. The observation that beds of the UE onlap onto earlier, eroded MSC deposits implies sea level rise [*Roveri et al.*, 2008] and is consistent with the observations of *Hilgen et al.* [2007]. Minor sea level changes on a sub-orbital time scale could also be invoked to play a role [*Rohling et al.*, 2008].

The return to open marine conditions and the end of the MSC was revised to 5.333 Ma by *Lourens et al.* [1996]. Based on these dates, the crisis lasted approximately 640 ky (Fig. 1.7). Model studies confirm that evaporite precipitation could realistically initiate a few thousand years before the peak of a glaciation [*Meijer*, 2006], and that the volume of evaporites observed can be generated within this timespan [*Krijgsman and Meijer*, 2008], confirming the viability of this timing. The return to normal open marine conditions at 5.333 Ma does not seem to correspond to deglaciation [*van der Laan et al.*, 2006], leading those authors to suggest that tectonics may have played the primary role in returning the Mediterranean Sea to normal marine conditions.

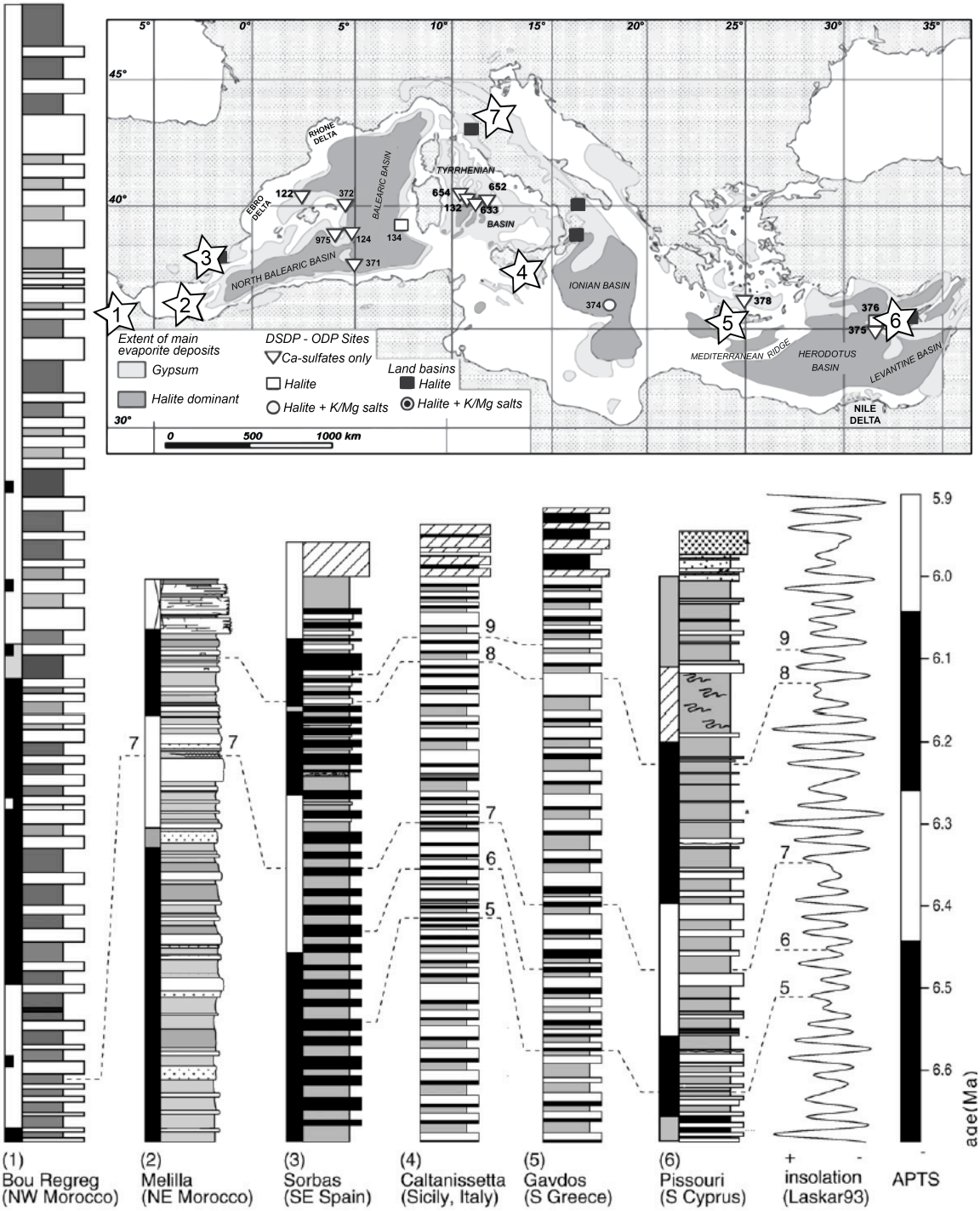

Fig. 1.6. Cyclostratigraphic and bioevent correlations (unbracketed numbers) for the key cyclically bedded sedimentary sequences around the Mediterranean basin used in dating MSC events. Locations correspond to map inset, which also shows locations of DSDP sampling. Locations shown refer to: (1) *Krijgsman et al.*, 2004; (2) *van Assen et al.*, 2006; (3-5) *Krijgsman et al.*, 1999a; (6) *Krijgsman et al.*, 2002; (7) *Manzi et al.*, 2007. Source: *Krijgsman and Meijer* [2008].

Marine marls exhibiting cyclical alternations between darker, laminated, organic rich and lighter homogenous layers underlie the evaporites (Fig. 1.6). Sections which are time-equivalent to, as well as younger than, the deposition of the evaporites exist in outcrops of similar cyclically bedded marine marls on the Atlantic side of Northern Morocco (Fig. 1.6, Ain el Beida and Loulja sections [*Krijgsman et al.*, 2004; *van der Laan et al.*, 2006]). These cyclically bedded marine successions are essential to our understanding of MSC chronology, as the cyclicity is controlled by climate cycles with precessional frequency.

1.2.4 Summary of MSC stratigraphy

Through a summary of the available literature (including that summarized above) and meetings with experts, a report of the Mediterranean Science Commission [*CIESM*, 2008] both summarized scientific consensus on the MSC and redefined the classical sequence in more logical terms. This report, and a related publication by Roveri et al. (2008), summarized the geological history of the MSC into three stages, incorporating basin-wide stratigraphy from both marginal and deep settings (see also Fig. 1.7; numbering updated to reflect [*Roveri et al.*, 2014]). A summary of the significant dates and stages in MSC stratigraphy, updated to include the latest adjustments, are as follows:

- *Stage 1, 5.971 – 5.61 Ma: Primary Lower Gypsum (PLG) deposition*. Shallow marginal basins like those found in Southern Spain and Sicily exhibit cyclical deposition of gypsum interbedded with organic rich, laminated marls. Deep water deposits, such as those observed on Gavdos (Crete) and other locations on Sicily, are composed of evaporitic carbonates and organic rich shales, barren of authigenic fossils. Onset in the Eastern and Western Mediterranean basins appears synchronous.
- *Stage 2, 5.61 – 5.55 Ma: MSC Acme and halite deposition.* This stage is characterized by massive primary halite deposition in deep basins, and a wide-spread erosional surface (the Messinian Erosional Surface, MES) in shallower locations indicative of a significant basin-wide sea level drop. Glacial stages TG12 and 14 are synchronous, indicating lowered global ocean sea level played a role.
- *Stage 3, 5.55 – 5.33 Ma: Upper Evaporites (UE; Stage 3.1) and Lago Mare (Stage 3.2).* The UE consist of gypsum-marl or gypsum-shale alternations best expressed on Sicily, the Ionian Islands, Crete, Cyprus, and the Nile delta area. The UE gypsum facies differ from those of the PLG and suggest deposition in very shallow (< 100 m) water. Onlapping sedimentary features over previously eroded rocks

implies a gradual transgression. The transition to Lago Mare (Stage 3.2) occurred ~5.42 Ma, coincident with the interglacial stage between TG7 and 9. The Lago Mare unit is characterized by brackish water deposits, indicating a major change in the overall Mediterranean hydrologic budget. Fauna from the Paratethys (today the Black and Caspian Seas) colonized locations across the Mediterranean.

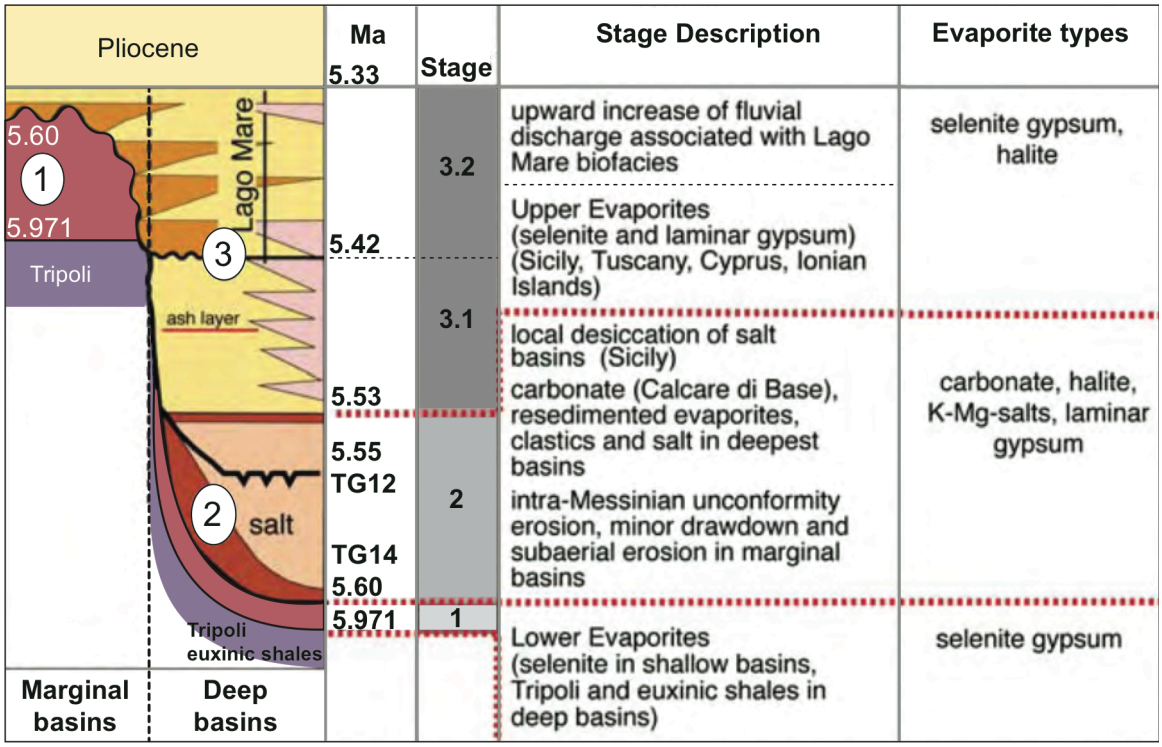

Fig. 1.7. Summary of the MSC succession, divided into 3 major stages. Modified from *CIESM* [2008].

1.2.5 Orbital cycles and Mediterranean sapropels

Earth's orbit and rotation control the amount of solar insolation received by the atmosphere at a given location. These include eccentricity (e), the shape of Earth's orbit; obliquity ($\in$), the tilt of Earth's axis; and precession, or the change in orientation of Earth's axis relative to the sun, affecting the phasing of the seasons compared to perihelion and apehelion (Fig. 1.8). These orbital cycles are recorded in Earth's geology by means of repetitive patterns in sediments. The preservation of these patterns is a result of insolation-driven climate change, which ultimately controls various Earth system responses. Biological (i.e., the abundance of certain species in the ocean) and sedimentological (i.e., continental weathering patterns) responses are archived in the geologic record. Specific frequencies for each orbital parameter have been determined: eccentricity has important frequencies at about 400 ky and 100 ky, obliquity has a frequency of about 42 ky, and precession a frequency in the range of ~19 to 26 ky [e.g., *Hays et al.*, 1976; *Zachos et al.*, 2001].

Lourens et al. [1996] determined that the astronomical solution for insolation best matching Mediterranean sedimentation from a geological point of view was La90 [*Laskar*, 1993] for summer insolation at 65°N due to the good empirical fit with the sapropel pattern [*Hilgen et al.*, 1999]. Astronomical solutions for insolation (Q^{day}, W/m^2, Fig. 1.8) are based on the calculation of climatic precession, $e \sin(\varpi)$, where ϖ is the longitudinal perihelion; insolation is calculated from climatic precession by accounting for longitude and season [Laskar, 1990, 1993; Berger and Loutre, 1992]. The amplitude of insolation is primarily controlled by eccentricity (e, Fig. 1.8); obliquity ($\in$, Fig. 1.8) is most visible at 65°N within the insolation curve as an interference pattern during times of eccentricity minima, although it exerts some influence throughout. Insolation minima correspond to precession maxima, and vice versa. The La90 solution has been updated, primarily to extend the solution further back in time; the version used in this thesis is La04 [*Laskar et al.*, 2004]. For the time periods relevant to this thesis, differences with the most recent solution are negligible (La2010) [*Laskar et al.*, 2011].

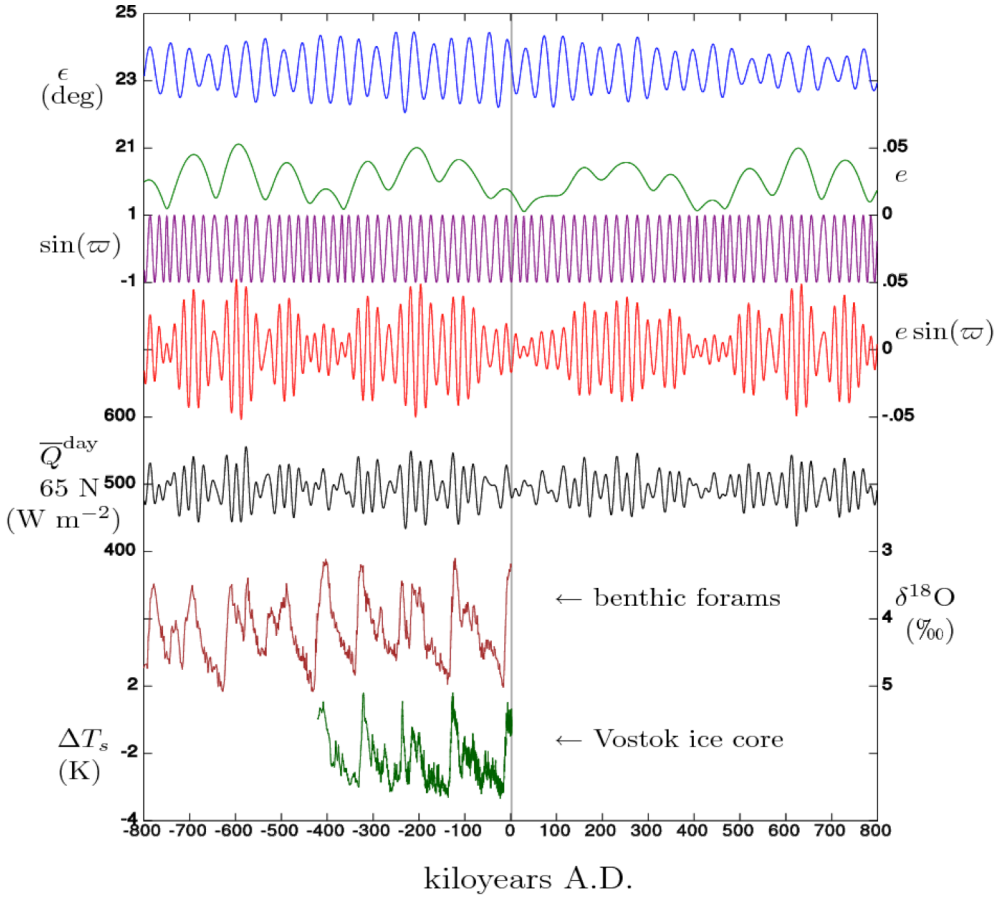

Fig. 1.8. Orbital parameters and the relationship between ε (obliquity, blue), e (eccentricity, green), sin(ϖ) (purple), $e$sin(ϖ) (climatic precession, red), and Q^{day} (insolation, black). These are compared to the benthic δ^{18}O record (LR04 stack) [*Lisiecki and Raymo*, 2005] and a record of relative temperature change from the Vostok ice core [*Petit et al.*, 1999].

For the Mediterranean region, there is a clear hypothesis of how climatic precession controls sedimentation, both for more recent geological history and for the Late Miocene. During insolation maxima, the North African monsoon system moves north compared to its present position; this causes much more precipitation to fall over North Africa [*Zhang et al.*, 2014; *Marzocchi et al.*, 2015], resulting in increased runoff to the Eastern Mediterranean basin, a phenomenon observed extensively in sedimentary records and modeling studies [e.g., *Rossignol-Strick*, 1985; *Rossignol-Strick and Planchais*, 1989; *Scrivner et al.*, 2004; *Osborne et al.*, 2010]. In addition to causing an increase in river runoff through the Nile, the now dry Sahabi/Eosahabi river system drained extra precipitation during wetter periods through the region of modern-day Libya into the Eastern Mediterranean basin through the Gulf of Sirte (Fig. 1.9) [*Osborne et al.*, 2008, 2010]. These palaeochannels may have reached far enough to form a connection to Megalake Chad [*Griffin*, 2002, 2011]. Although this connection could be debated [e.g., *Paillou et al.*, 2009; *Ghoneim et al.*, 2012], the Eosahabi/Sahabi palaeochannels are suggested to have provided, at their peak, as much water as the modern-day Nile [*Paillou et al.*, 2012].

Such drastically increased freshwater input to the Eastern Mediterranean generates lower salinity surface waters, halting deep water formation processes operating in the eastern basin, and preventing oxygenated waters from circulating to the bottom [see *Rohling et al.*, 2015 for a detailed review]. As water column stratification is enhanced, bottom water anoxia sets in, increasing organic matter preservation. It also appears that there is a coeval increase in organic matter production [*Rohling*, 1994] thought to be linked to the increase in nutrients derived from the rivers. These conditions lead to the deposition of sapropels, layers defined as laminated sediments with higher levels of organic matter (> 2%) [*Kidd et al.*, 1978]. The laminated texture, indicating lack of bioturbation, coincides with a lack of preserved benthic fauna suggesting bottom water anoxia was severe enough to prevent bottom dwellers from living in these layers [e.g., *Kidd et al.*, 1978; *Nolet and Corliss*, 1990; *Schmiedl et al.*, 2003, 2010; *Abu-Zied et al.*, 2008]. The relationship between benthic foraminifera and sapropelic layers also appears to extend to pre-MSC sediments; sapropelic layers found in the Sorbas Basin, a marginal sub-basin of the Western Mediterranean, show a similar lack of benthos in the sapropelitic layers of the Upper Abad Formation [*Sierro et al.*, 2001, 2003; *Pérez-Folgado et al.*, 2003].

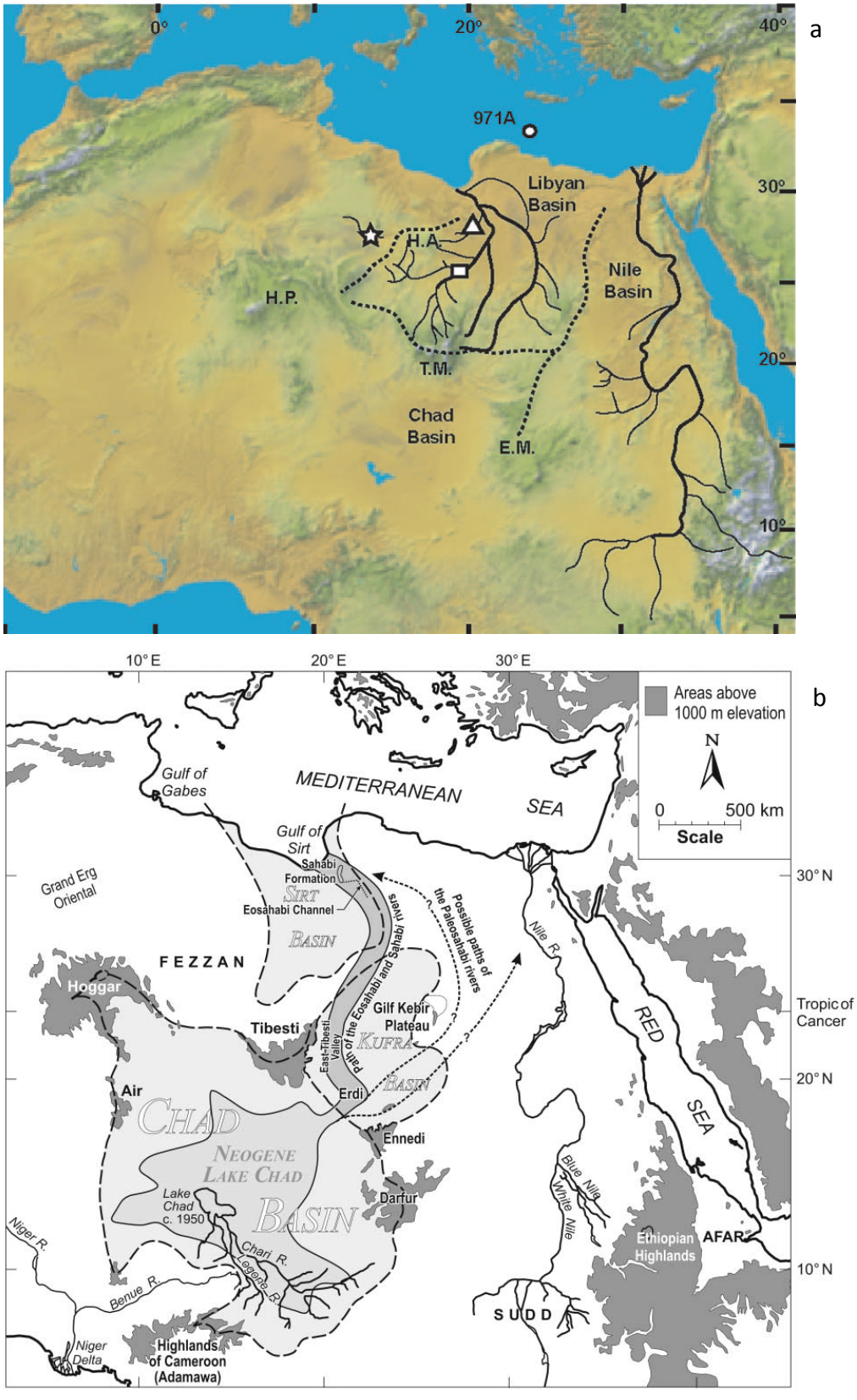

Fig. 1.9. Interpretations of palaeochannels through central North Africa, some of which may have transported water from Neogene Lake Chad to the Eastern Mediterranean basin. (a) Reconstruction comparing mapped palaeochannels to modern-day Nile. Initials represent mountain ranges (HP – Hoggar Plateau; TM – Tibesti Mountains; EM – Ennedi Mountains). Symbols not relevant (indicate sampling locations for study from which reconstruction was taken). From *Osborne et al.* [2008]. (b) Reconstruction showing how main channel from Neogene Lake Chad may have connected it to the Mediterranean Sea, including along the way the Chad Basin, the Kufra Basin, and the Sirt Basin. From *Griffin* [2006].

In antithesis, diatomite is often deposited at times of insolation minima, during which drier conditions favour evaporation, leading to increased surface water salinity driving enhanced water column mixing, which in turn promotes upwelling, enhanced nutrient availability and diatom production [*Sierro et al.*, 2003]. Diatom preservation often occurs in conjunction with evidence of enhanced bottom water oxygenation [e.g. *Pérez-Folgado et al.*, 2003; *Sierro et al.*, 2003]. Diatomite and sapropel layers are interspersed with homogeneous marls in varying combinations of repeating bipartite (sapropel-marl), tripartite (sapropel-diatomite-marl), or quadripartite cycles (sapropel-marl-diatomite-marl), depending on location. The homogenous marls are generally thought to be deposited on the transitions between insolation maxima and minima [e.g. *Pérez-Folgado et al.*, 2003]. These suggestions are corroborated by faunal assemblages in the host sediments [e.g., *Kouwenhoven et al.*, 1999; *Sierro et al.*, 1999].

Though this thesis uses the currently accepted method of comparing sedimentary patterns to insolation using the curve calculated for 65°N, this discussion would be incomplete without discussion of recent work assessing the mechanisms which cause this particular insolation curve to fit, visually, the sedimentation patterns in the Mediterranean. As explained above, precipitation over North Africa is responsible for the sapropel pattern, and the sapropel pattern fits an insolation curve showing clear influences of obliquity (see Fig. 1.10, comparing the first 12 sapropels to various insolation curves suggested in the literature). However, the Mediterranean straddles ~35°N; low latitude regions are not expected to show a clear obliquity interference pattern as precession exerts an effect ten times greater than obliquity on insolation over low latitudes (at 23°N or S, differences in insolation due to precession are up to 100 W/m^2, whereas those due to obliquity are only up to 10 W/m^2 [*Tuenter et al.*, 2003; *Bosmans et al.*, 2015b]). The fact that sapropel patterns match the high latitude curve well into the Miocene, before the onset of northern hemisphere glaciation, is an argument against the indirect control of high latitude ice caps on low latitude climate patterns such as the North African monsoon [*Bosmans et al.*, 2015a].

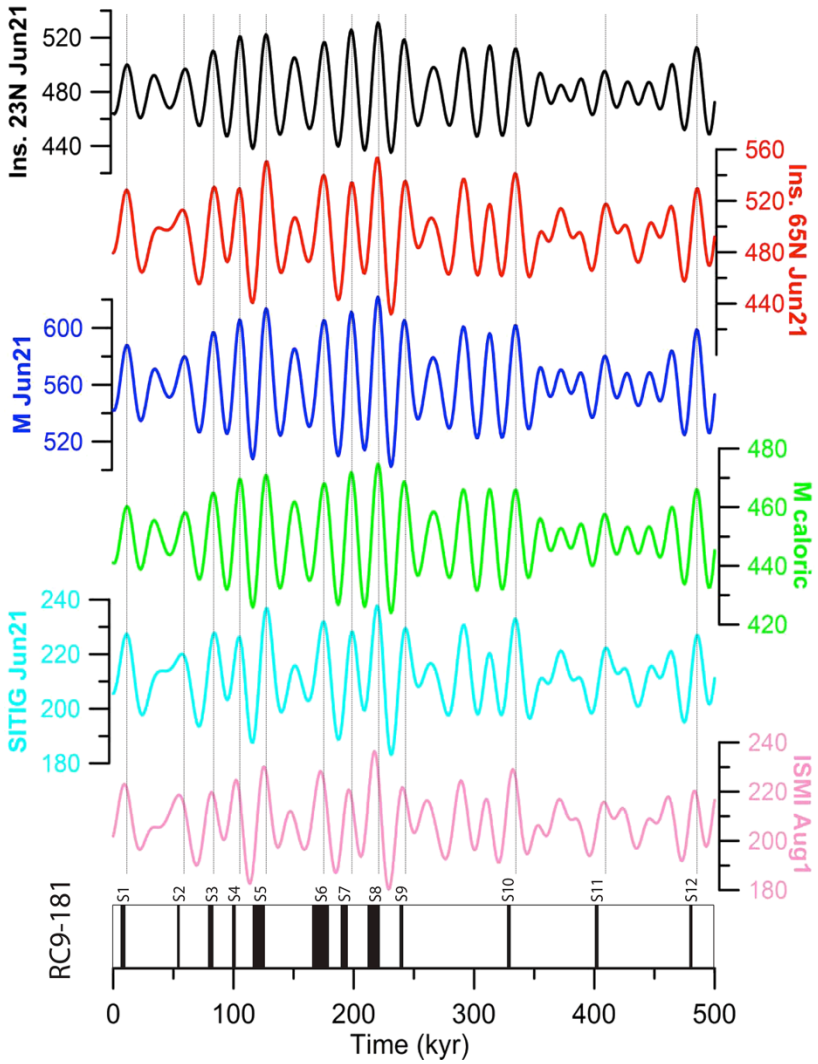

Fig. 1.10. A comparison of several insolation curves applied in the literature to the sapropel pattern of the Mediterranean. Note the thick-thin pattern; for example, S3 is thicker than S4, and S6 is thicker than S7, although the insolation curve for low latitudes (23°N, black line) suggests the opposite should be occurring. The pattern fits to 65°N and SITIG much better, two curves which are nearly identical. See text for references for each curve. From *Bosmans et al.* [2015a].

While several curves for insolation have been calculated and compared to Mediterranean sapropel patterns [e.g., 'M' curve, *Rossignol-Strick*, 1985; 'ISMI', *Leuschner and Sirocko*, 2003; blue, green, and pink lines, Fig. 1.10], the summer inter-tropical insolation gradient (SITIG; blue line, Fig. 1.10) [*Reichart*, 1997] has proven to be most robust because SITIG emphasizes the difference in insolation between the two hemispheres, $I_{23°N} - I_{23°S}$. Coincidentally, SITIG emphasizes the effect of obliquity nearly identically to insolation at 65°N. This difference in the effect of obliquity between hemispheres is mirrored in the differences observed in precipitation patterns over low latitudes in experiments comparing maximum and minimum obliquity while land ice, and vegetation, is held constant in high-resolution climate modelling [*Bosmans et al.*, 2015a] using EC-Earth [*Hazeleger et al.*, 2010]. Thus, *Bosmans et al.* [2015a] concluded that there is a direct mechanism causing the interference of obliquity to be expressed in low-latitude sedimentation patterns such as

those in the Mediterranean; specifically, that the gradient in insolation between the hemispheres due to obliquity drives wind, moisture transport, and other climate parameters. *Bosmans et al.* [2015a] suggested that astronomical tuning should be performed with the SITIG curve in future work.

1.2.6 Cyclostratigraphy: precision, phase lags and breakthroughs in Messinian Mediterranean geochronology

Sapropels are a distinguishing feature of Mediterranean sedimentation, occurring with quasi-precessional frequency since at least 13.5 Ma [*Rohling et al.*, 2015], up until the youngest sapropel, S1, the midpoint of which corresponds to ~8 ka [*Lourens et al.*, 1996]. As a consequence of precessional depositional cyclicity, many outcropping successions have been 'astronomically calibrated' or 'orbitally tuned' with relatively high temporal resolution. In practice, orbital tuning is an integrated process: first, magnetostratigraphy, biostratigraphy, and/or radiometric dating are used to determine initial tie points or marker ages. After ages are broadly resolved, patterns found in changes in sedimentation, colour, dominant grain size, stable isotope ($\delta^{18}O$, $\delta^{13}C$) and/or other geochemical records (i.e., elemental composition ratios such as Ti/Al) among others are used to correlate a given section to the astronomical solution for that time span. The results of astronomical tuning are often presented without age uncertainty [e.g. *Clauzon et al.*, 2015]. Errors in ages determined through radiometric dating are quantified by propagating sources of error such as internal counting statistics and the external uncertainties of decay constants; in contrast, the Mediterranean sapropel pattern over the last 7 Ma reproduces strongly the La04 solution, suggesting age uncertainty using this method may be less than 1 ky [*Rivera et al.*, 2011] if individual beds are tuned to the correct cycle.

With the exception of bed-cycle mismatch, the primary limitation for the precision of orbital tuning in the Mediterranean is the incomplete understanding of phasing between sedimentation, climate, and insolation throughout a precessional cycle. *Weber and Tuenter* [2011] determined from general circulation model (GCM) results that little to no time lag exists for precessional climate forcing at mid-latitudes. In contradiction with the findings of *Rivera et al.* [2011] and *Weber and Tuenter* [2011], *Lourens et al.* [1996] determined a ~ 3 ky lag from precession minima to the midpoint of youngest Eastern Mediterranean sapropel S1 based on ^{14}C dating. Variability in temporal lags and leads has also been suggested. *Pérez-Folgado et al.* [2003] determined pre-MSC sapropelic layers deposited in

a restricted sub-basin of the Mediterranean may coincide with the transition from insolation minima to insolation maxima. This would imply some sapropelic layer midpoints lead insolation maxima, in contrast to the 3 ky lag observed by *Lourens et al.* [1996] for sapropel S1. *Pérez-Folgado et al.* [2003] also found that the relationship between cyclicity in faunal assemblages and lithology was different in the restricted basin compared to an open Mediterranean site (Gavdos, Crete), implying phasing differs at the two sites. Comparing datasets from different sites for the same sapropels, *Rohling et al.* [2015] found that specific details match over only short distances, highlighting the dynamic nature of the climate-deposition feedback system. In general the mismatch is understood to be the time required for climate to respond to changes in solar insolation at a given location [*Lourens et al.*, 2004], though clearly the mechanisms are still debated [*Rohling et al.*, 2015].

Though it has now been revised, the age model generated by [*Krijgsman et al.*, 1999a] using orbital tuning was a major step forward in the understanding of the environmental processes leading to the crisis, while simultaneously allowing bed-by-bed correlation of Messinian sequences all over the Mediterranean [*Krijgsman and Meijer*, 2008]. This led to a more complete understanding of the synchronicity of MSC onset between the western and eastern basins, a still-debated but generally accepted hypothesis [e.g., *Manzi et al.*, 2016]. This approach has also allowed the correlation of Moroccan sections bordering the Atlantic to the Mediterranean MSC sections [*Krijgsman et al.*, 1999b, 2004; *Hilgen et al.*, 2007]. Such correlations are significant since Atlantic sections provide complete sequences from pre- to post-MSC time. Sections on the Mediterranean side of the gateway are incomplete due to the large unconformity between the LE and UE (Fig. 1.11). Astronomical tuning of Mediterranean MSC sections is challenging as the sediments are not ideal for palaeomagnetic reconstruction due to the minerals present and the amount of weathering [*Krijgsman et al.*, 1999b]. Likewise, biostratigraphy is nearly impossible as these layers are essentially barren. The time equivalent Atlantic sections include a complete biological record [e.g., *Sierro et al.*, 1999; *van Assen et al.*, 2006], presenting a solution to the problem of dating the MSC successions. Unfortunately, this is a trade-off situation, as Atlantic successions record the environmental conditions of the Atlantic Ocean rather than those of the Mediterranean.

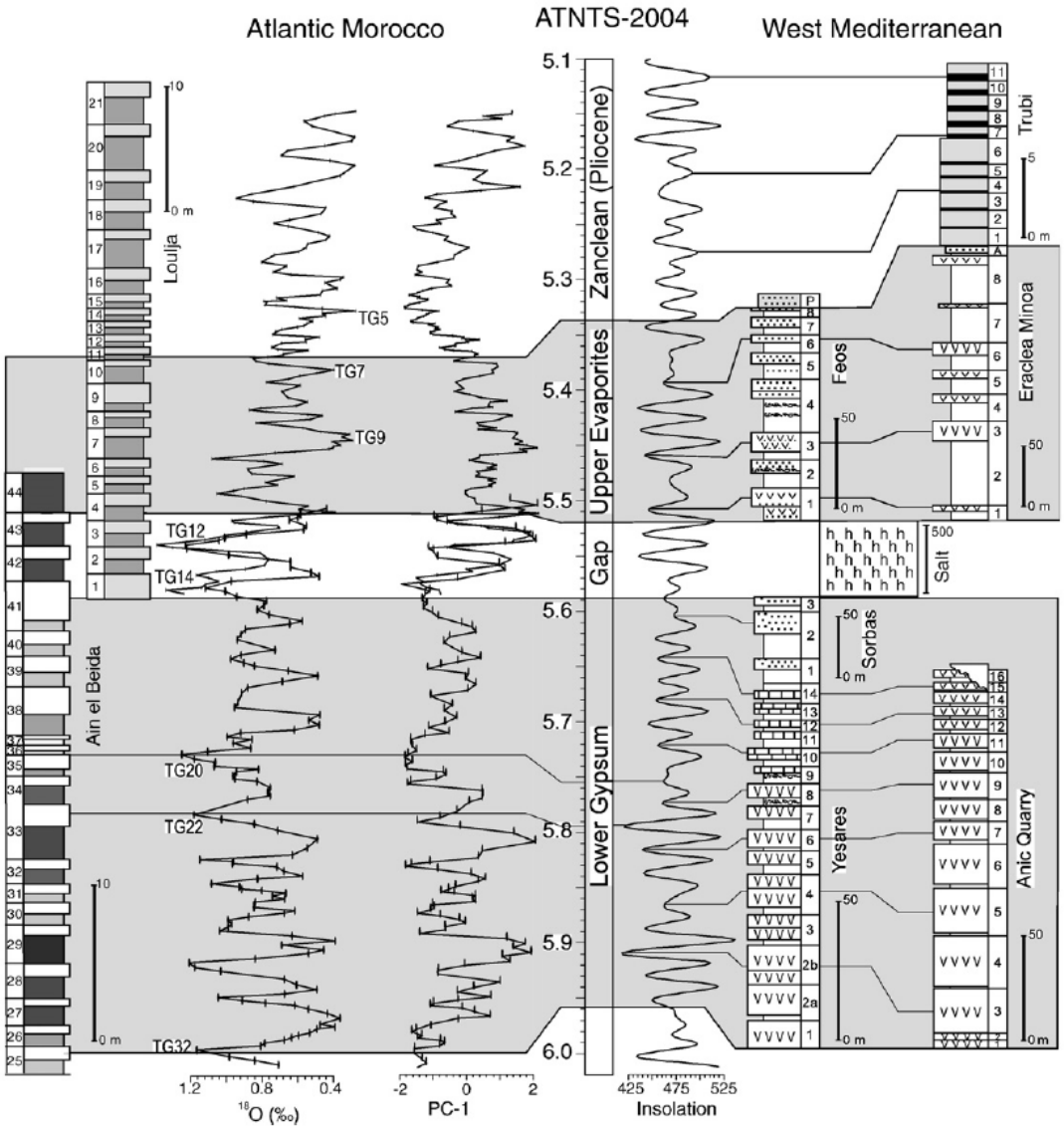

Fig. 1.11. Messinian age sections from outside the Mediterranean basin (Atlantic Morocco) correlated to intra-Mediterranean evaporitic sections on the basis of orbital tuning, benthic $\delta^{18}O$ and geochemical element (PC-1) records. Note the gap in the Mediterranean sequences which is thought to correspond to the deep halite unit, and seems to be linked temporally to TG12 and TG14. Source: *Krijgsman and Meijer* [2008]; modified from *Hilgen et al.* [2007].

1.2.7 Mediterranean-Atlantic exchange

Investigating past changes in Mediterranean hydrology, including those causing the MSC and changes in sedimentation, necessitates an understanding of modern Atlantic-Mediterranean exchange. This exchange today is a combination of two processes. First, the negative hydrologic budget of the Mediterranean basin leads to an excess of evaporation (Fig. 1.9a), requiring input from the Atlantic to make up the water loss. Second, density contrast exchange occurs, whereby the vigor of exchange increases proportionally with the density difference between Mediterranean and Atlantic water [e.g. *Bryden and Stommel*, 1984; *Bryden and Kinder*, 1991; *Meijer*, 2006]. The first process increases the salinity, and

thus density, of Mediterranean water compared to Atlantic water. Today, the Mediterranean experiences evaporative losses ranging from about 0.4 to 1.2 m/y [*Rohling et al.*, 2015 and references therein], or approximately 0.03 to 0.1 Sv (1 Sv = 10^6 m^3/s). Atlantic inflow is much larger at about 0.8 Sv [*Tsimplis and Bryden*, 2000]. The majority of inflow balances denser Mediterranean Outflow (MO; ~ 0.7 Sv) [*Tsimplis and Bryden*, 2000; *Garcia-Lafuente et al.*, 2011]. A combination of forces (including displacement, mixing, and Bernoulli suction) results in the evaporative losses over the Mediterranean generating a denser water mass which is driven to exchange at Gibraltar in much greater volumes than that required simply to replace the freshwater loss.

Hypotheses from the literature concerning circulation patterns through the Betic and Rifian gateways are largely untested. Bi-directional, anti-estuarine flow similar to that in operation today (Fig. 1.12) through the Gibraltar Straits is thought to have occurred through both corridors for most of the time [*Ivanoviç et al.*, 2013]. A notable exception is the 'Siphon Event': on the basis of the sudden appearance of deep-water Atlantic ostracods in the Morrocan corridor, *Benson et al.* [1991] suggested that between 6.4 and 5.3 Ma all Atlantic inflow occurred through the Rifian corridor while Mediterranean outflow was exclusively funneled through the Betic gateway. *Betzler et al.* [2006] found sedimentological evidence to support this theory in Southern Spain. Recently, *de la Vara et al.* [2015] concluded that the Siphon Event is highly unlikely, based on flow dynamics observed from intermediate complexity model studies of exchange through the Betic and Rifian corridors.

According to *Meijer* [2006], *Debenedetti* [1976] first suggested that deep outflow could have been blocked due to shallowing of the gateways while inflow to the Mediterranean persisted. While this hypothesis answers the question of salt provenance, it also creates new problems. Results of more recent modeling studies indicate that a very shallow inlet on the order of only a few metres deep would be required to completely interrupt outflow, while the precipitation of the observed evaporites may still require 6 to 8 ky [*Meijer*, 2006]. The probability that such shallow conditions could prevail for that long is clearly low. Evidently, understanding the flow configuration of the Betic and Rifian palaeogateways will be a substantial challenge. However, understanding the configuration of these gateways and circulation through them is essential to constrain the causes and consequences of the MSC itself.

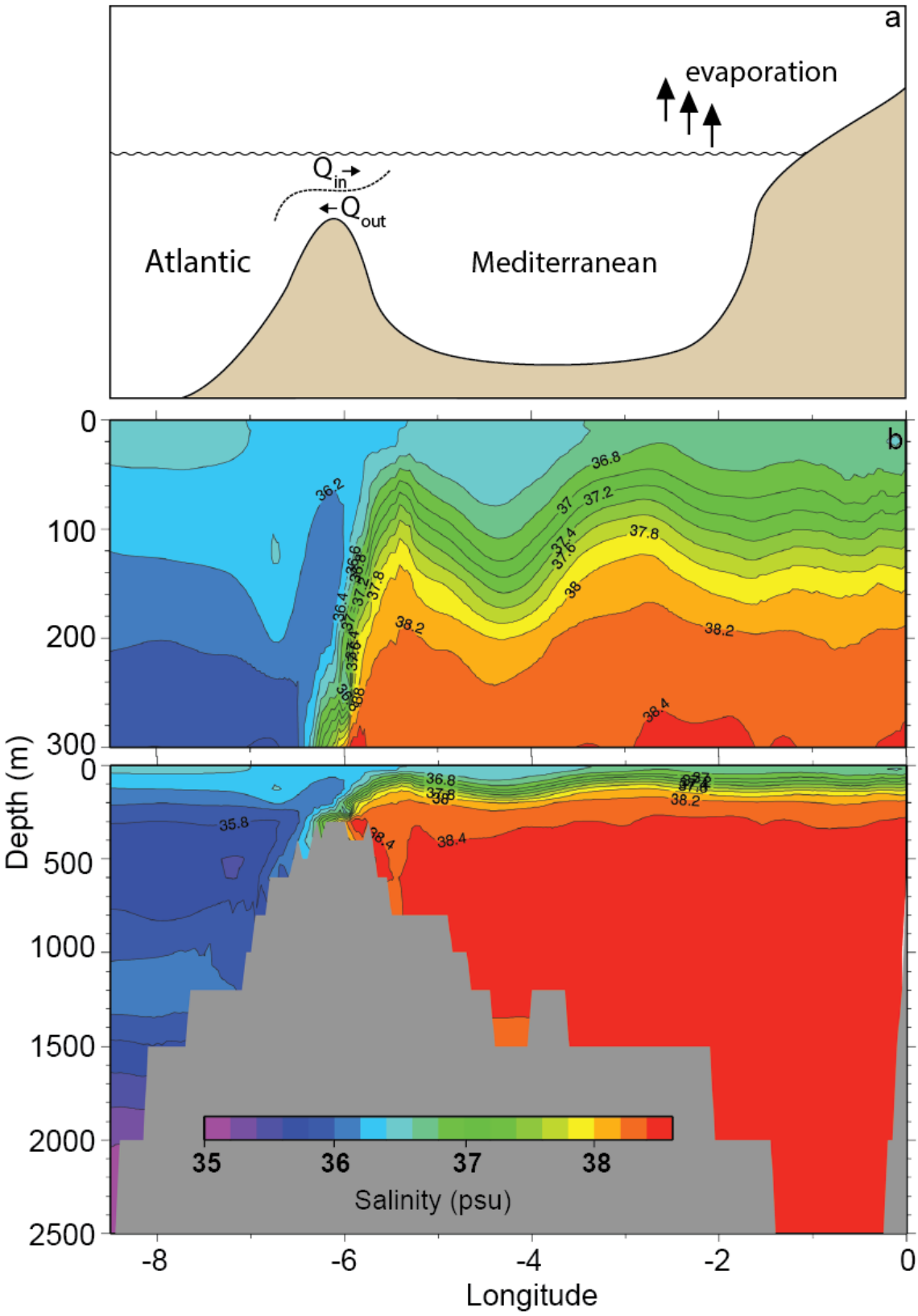

Fig. 1.12. Modern exchange through the Strait of Gibraltar. (a) Excess evaporation over the Mediterranean generates denser water which flows out (Q_{OUT}) beneath Atlantic inflow (Q_{IN}). (b) Cross section through the Gibraltar Strait with contours corresponding to salinity. Upper panel of (b) is a magnification of the top 300 m. Modified from *Flecker et al.* [2015].

There are several important research steps that need to be taken in order to solve the MSC paradox. First, it is clear that drilling the deep Mediterranean basins and recovering a complete MSC succession is essential. Plans to do this with the International Ocean Discovery Program's (IODP) Chikyu platform are ongoing, but in reality this is unlikely to be achieved within a decade. Second, developing a thorough understanding of the Late Miocene marine corridors linking the Mediterranean with the Atlantic is critical to quantifying palaeo-inflow and -outflow fluxes and hence constraining the hydrologic budget at different times during the MSC. Recent developments in the use of Nd isotopes [*Ivanoviç et al.*, 2013] and earlier papers using Sr isotopes [*Flecker et al.*, 2002; *Flecker and Ellam*, 2006] have provided potential mechanisms for reconstructing these properties with time.

1.3 Radiogenic isotopes as water mass tracers

Radiogenic isotopes are daughter products of radioactive decay, for example ^{143}Nd from ^{147}Sm or ^{87}Sr from ^{87}Rb. While some primordial concentration of these elements existed from the initial formation of the solar system, the property that they are also generated by decay allows them to be monitors for several processes. Rocks develop unique radiogenic isotope ratios due to a combination of age and factors influencing elemental distribution during petrogenesis and weathering [*Dickin*, 2005]. Due to these properties, radiogenic isotopes can be used as geochronometers, or in provenance studies. Similarly, radiogenic isotope signatures may be used to track water mass circulation. Water masses develop specific signatures dependent partly on the geology of the location of their source waters. Through various sources (see Fig. 1.13), radiogenic isotopes are input to the hydrologic cycle; under the right conditions, they will be advected conservatively or quasi-conservatively with particular water masses, and in this context can be used as water mass tracers by palaeoceanographers [*Frank*, 2002 and references therein]. The radiogenic isotopes employed in this thesis (^{87}Sr, ^{143}Nd, ^{206,207,208}Pb) are products of radioactive parents with relatively long half-lives compared to the age of the Earth; therefore changes due to decay can be neglected over the time scales of ocean circulation which is approximately 1500 y [*Broecker and Peng*, 1982].

Isotope signatures of water masses are influenced by several factors (Fig. 1.13, Table 1.1), some more important than others depending on the individual element and its physicochemical characteristics. Riverine and aeolian inputs are most important for the

trace metals Nd and Pb [*Frank*, 2002]. Hydrothermal inputs are not significant for Nd [*Halliday et al.*, 1992] while they can be significant for Pb [*van de Flierdt et al.*, 2004] and Sr [*Palmer and Edmond*, 1989]. It has also been determined that the continental shelf is an important source for Nd [*Jeandel et al.*, 2007].

While some fractionation due to environmental processes has been observed in some stable isotopes of heavy elements (e.g. Tl, Hg), the level to which it occurs is not significant enough to cause interference affecting the interpretation of records in terms of input sources and changes through time, at least for the Pb isotope system [*Noble et al.*, 2015 and references therein]. In the case of Nd, fractionation should be accounted for during the process of data normalization to the primordial $^{146}Nd/^{144}Nd$ ratio, a fundamental part of generating useable isotopic measurements. Pb does not have a suitable non-radiogenic isotope pair to permit internal correction, but mass bias is corrected using other means (i.e. standard sample bracketing, Ch. 2, section 2.3.5). Both Pb and Nd have residence times shorter than the ocean mixing time of ~ 1500 y [*Broecker and Peng*, 1982], due to their particle reactivities and low solubilities; short enough that individual ocean water masses can develop distinct signals, but long enough to be useful for tracing water currents over distances [*Frank*, 2002].

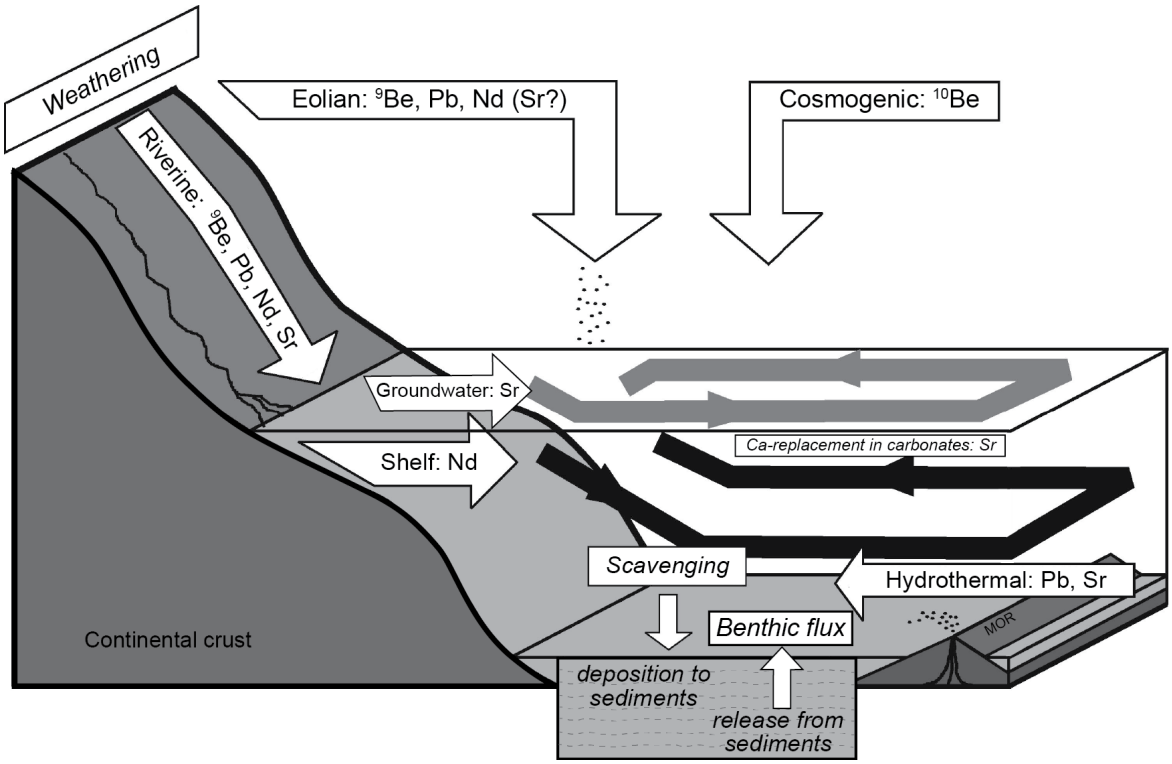

Fig. 1.13. Trace metal pathways including sources and sinks. Three major sources exist for particulate and dissolved trace metals in the ocean: aeolian, riverine, and hydrothermal. In addition, some metals such as Nd are probably supplied by partial dissolution of shelf sediments. Shaded and solid lines indicate surface and deep-water circulation (respectively) causing mixing of the dissolved metals. Modified from *Frank* [2002], to include Sr pathways as per *Veizer* [1989], and benthic flux as per *Abbott et al.* [2015b]. Processes in italics.

Table 1.1. Radiogenic isotopes used as tracers and for dating in this thesis.

Element	Radiogenic isotope	Parent isotope	Primordial isotopes	Common ratios	Primary sources
Nd	^{143}Nd	^{147}Sm	$^{142}Nd^{*}$, ^{144}Nd, ^{145}Nd, ^{146}Nd, ^{148}Nd, ^{150}Nd	$^{143}Nd/^{144}Nd$	continental crust erosion
Pb	^{206}Pb ^{207}Pb ^{208}Pb	^{238}U ^{235}U ^{232}Th	^{204}Pb	$^{20x}Pb/^{204}Pb$, $^{207}Pb/^{206}Pb$, $^{208}Pb/^{206}Pb$	continental crust weathering; minor hydrothermal inputs
Sr	^{87}Sr	^{87}Rb	^{88}Sr, ^{86}Sr, ^{84}Sr	$^{87}Sr/^{86}Sr$	continental crust weathering; hydrothermal inputs; marine carbonate dissolution
Be	$^{10}Be^{+}$	--	^{9}Be		cosmogenic production
Th	^{230}Th	^{234}U			decay of ^{234}U in seawater
	--	--	^{232}Th		continental crust erosion

* Some of ^{142}Nd comes from the decay of ^{146}Sm, an extinct nuclide due to the relatively short half-life. $^{+}$ ^{10}Be is produced from interaction of cosmic rays, primarily with nitrogen and oxygen. Table expanded from *Frank* [2002] to include Th and all primordial isotopes of Sr.

Sr is relatively soluble and has a long residence time; thus, it is fully mixed in the global oceans. This precludes its use as an ocean water mass tracer in a conventional sense; however, this tracer can be used as an indication of connectivity, as disconnected water bodies will evolve Sr isotope signatures which deviate from global ocean ratios [*Flecker and Ellam*, 1999; *Flecker et al.*, 2002]. Table 1.1 provides a summary of the radiogenic isotopes used in this thesis and their properties, including two used for chronology rather than tracing water masses (^{10}Be, ^{230}Th).

1.3.1 Neodymium (Nd): $^{143}Nd/^{144}Nd$

Differences between individual $^{143}Nd/^{144}Nd$ isotopic ratios are very small due to the long half-life of ^{147}Sm ($t_{1/2}$ = 106 Gyr; see Table 1.1). ε (epsilon) notation is employed to express Nd isotope values in a useable format, calculated as the ratio of a sample relative to a reference ratio [1.1]:

$$\varepsilon_{Nd} = \left(\left\{\frac{(^{143}Nd/^{144}Nd)_{sample}}{(^{143}Nd/^{144}Nd)_{CHUR}}\right\} - 1\right) x\ 10^{4} \qquad [1.1]$$

where CHUR stands for CHondritic Unfractionated (originally 'Uniform') Reservoir. This value is thought to represent the bulk $^{143}Nd/^{144}Nd$ value of the Earth. The current value of CHUR is 0.512638, normalized to $^{146}Nd/^{144}Nd$ = 0.7219 [*Jacobsen and Wasserburg*,

1980]. Very low (very negative) ε_{Nd} values are referred to as 'non-radiogenic' or 'unradiogenic', whereas higher (less negative to positive) values are referred to as relatively 'radiogenic' isotope ratios. This statement applies also to Sr and Pb isotopes; higher values are considered radiogenic, while low values are considered unradiogenic.

In the open ocean, Nd generally follows a trend of very low concentration at the surface to higher concentrations at depth. This concentration profile is typical for elements which behave like nutrients: Nd is particle reactive, with rapid vertical transfer via scavenging commonly reported [e.g., *Henry et al.*, 1994; *Jeandel et al.*, 2007], possibly during the process of manganese oxide particle coating as particles settle out of suspension [*Tachikawa et al.*, 1999]. In the Mediterranean, the concentration does not follow this convention, instead remaining nearly constant throughout the depth profile [*Tachikawa et al.*, 2004]. The average concentration of Nd in the North Atlantic ranges from approximately 10 to 35 pmol/kg [*Lambelet et al.*, 2015; *Stichel et al.*, 2015], whereas the Mediterranean has slightly higher concentrations, from about 15 to 55 pmol/kg [*Henry et al.*, 1994; *Tachikawa et al.*, 2004]. In previous decades, to generate a sufficiently concentrated sample of Nd^{+} from seawater for analysis, it was necessary to process samples on the order of 5 to 10 L [e.g., *Tachikawa et al.*, 2004]. For this reason, as well as other technical difficulties, Nd data are somewhat limited compared with other isotopic tracers such as Sr [*Goldstein and Hemming*, 2003]. This deficit is currently being addressed by the GEOTRACES program, whose mandate is to improve the quality and quantity of available geochemical tracer data in the oceans [*van de Flierdt et al.*, 2012].

Nd is a quasi-conservative water mass tracer in the open ocean. At individual locations, where there is a significant Nd isotopic contrast between water masses with depth, Nd isotope ratios vary coherently [*Goldstein and Hemming*, 2003]. Throughout the open ocean, Nd ratios in seawater vary systematically:

- ratios associated with water masses are conserved over long advective pathways;
- ratios are variable in depth profiles containing different water masses;
- surface seawater Nd ratios vary more widely since they are easily modified by partial dissolution of particulates such as aeolian dust.

Relationships between the ε_{Nd} values of various water masses and their geographical location are not always direct. There are several sources for seawater Nd: continental runoff, interaction with continental shelf, and aeolian dust (Fig. 1.13). Differential

weathering rates of different substrates should also be taken into account; volcanic basalts (i.e. Mid-Oceanic Ridge Basalt, MORB and Ocean Island Basalt, OIB) tend to weather more rapidly and therefore contribute more material to the water column than resistant continental rocks such as granite [*Goldstein and Hemming*, 2003]. Nd fractionates more readily into magma than Sm, leading to lower Sm/Nd ratios in continental crust compared to the mantle. This fractionation also leads to a general relationship between geologic history and ε_{Nd}: young mantle-derived volcanic rocks tend to exhibit radiogenic ε_{Nd}, whereas old cratons are characterized by unradiogenic ε_{Nd} [*Dickin*, 2005]. Since MORB and OIB are derived more directly from the mantle, they tend to be characterized by radiogenic ε_{Nd}. Sinks include interaction with continental shelf and scavenging from the water column by adhesion to particles; deposition in marine sediment is the most important [*Frank*, 2002]. Estuaries can fractionate the dissolved rare earth element (REE) component of fresh water entering the oceans, with light REE such as Nd being preferentially removed relative to heavy REE. These are complex processes which function differently depending on salinity; low salinity causes a removal of light REE such as Nd, while shifts to higher salinity will cause re-dissolution [*Sholkovitz and Szymczak*, 2000; *Rousseau et al.*, 2015]. Of particular importance for this thesis (Ch. 4) is the interaction which occurs between dissolved trace metals in the water column and lithogenic particles, occurring at the sediment-water interface, for which the term 'boundary exchange' is applied [*Bacon et al.*, 1988; *Lacan and Jeandel*, 2005]. The precise mechanisms operating during boundary exchange to cause transfer of Nd between particles and seawater are a current topic of research [e.g., *Pearce et al.*, 2013]. This term specifically conveys an isotopic shift, not a shift in concentration; for example, when the Nd isotopic composition of a water mass has clearly shifted towards compositions of local lithic particles it has come in contact with, compared to the same water mass in the open ocean [e.g., *Rickli et al.*, 2014]. Boundary exchange is of primary importance in near-shore, marginal settings, with significant fluxes of Nd attributed to this process at ocean-continent boundaries [*Lacan and Jeandel*, 2005]. This includes settings where currents continually remobilize sediments [*Gutjahr et al.*, 2008], near sediments with significant quantities of volcanic minerals [*Roberts et al.*, 2010; *Elmore et al.*, 2011; *Wilson et al.*, 2013] or relatively unweathered glacially-eroded material [*Rickli et al.*, 2014]. As up to 99% of the global flux of Nd to the oceans is via particulates [*Oelkers et al.*, 2011], boundary exchange is understandably a very important process contributing to the dissolved Nd budget in seawater. A similar type of exchange has been considered for dust-seawater interactions [e.g., *Tachikawa et al.*, 1999; *Bayon et al.*, 2004], where dust inputs have been observed to alter the ε_{Nd} of seawater but not the dissolved [Nd].

A process known as benthic flux is another significant source of Nd to the oceans [*Pearce et al.*, 2013; *Abbott et al.*, 2015a, 2015b]. This process is recognized to occur with rare earth elements (REE) in general, and, similarly to boundary exchange, is of particular concern because Nd isotopes are used to interpret changes in ocean circulation in the past. While both boundary exchange and benthic flux processes may alter the preserved Nd isotope signature in archives, affecting their interpretation, benthic flux specifically denotes an input source, whereas boundary exchange may not be accompanied by an increase in Nd concentration. Of particular importance are regions with a significant non-authigenic component in the underlying marine sediment, such as detrital siliciclastics or volcanic rocks; in such cases, the isotopic composition of the sediment may be very different to the overlying water. This creates a situation where the release of Nd upwards to the water column can significantly shift its isotopic composition, away from the water mass signal. This is a similar process to boundary exchange, but here mass of Nd is added to the water column. In cases where the sediments are dominated by authigenic and biogenic components, the benthic flux is not as likely to change the overall Nd isotopic composition as the sediment and water column will be similar in this regard [*Abbott et al.*, 2015a].

Additionally, near interfaces between large rivers and the ocean, ε_{Nd} may be significantly hindered; the seawater signature can be overwhelmed by local input sources, due to delivery of large amounts of pre-formed riverine allogenic FeMn oxyhydroxides [*Bayon et al.*, 2004]. The depositional environment of the sedimentary sequences investigated here ranges from deep and distal to proximal and relatively shallow. Thus, processes affecting seawater ε_{Nd} such as boundary exchange must be considered seriously in the context of this project. Though there are several issues, Nd has been successfully applied to palaeo-gateway studies at intermediate water depths for other locations such as the Panama seaway [e.g., *Osborne et al.*, 2014a, 2014b].

In the Gibraltar Straits today, there is an approximately 2 ε_{Nd} unit difference between outgoing MO and inflowing Atlantic water (Fig. 1.14). MO has a signature of approximately -9.4 ε_{Nd} [*Tachikawa et al.*, 2004], while Atlantic inflow has a signature between -11.4 and -11.8 ε_{Nd} [*Piepgras and Wasserburg*, 1983; *Spivack and Wasserburg*, 1988; *Henry et al.*, 1994; *Tachikawa et al.*, 2004]. This difference is important for detecting individual influences of Atlantic inflow and MO, given that typical analytical uncertainty for Nd isotope ratio measurements is about an order of magnitude smaller.

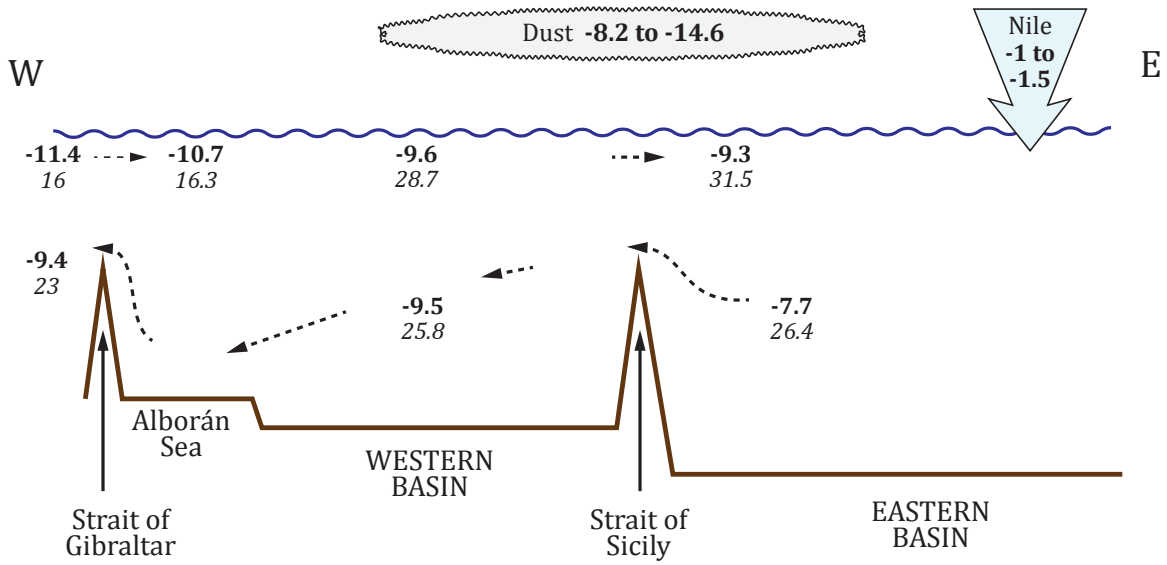

Fig. 1.14. W-E transect of the Mediterranean basin summarizing modern day surface and deep Nd isotopic composition (ε_{Nd}) and concentration (pmol/kg, italics). Arrows indicate circulation pathways. At Gibraltar, Atlantic inflow at the surface has ~ -11.4 ε_{Nd}, while Mediterranean water with ~ -9.4 ε_{Nd} flows out at the bottom. Modified from *Henry et al.* [1994]; Nile ε_{Nd} from *Scrivner et al.* [2004]; dust ε_{Nd} from *Scheuvens et al.* [2013] and references therein.

Within the modern Mediterranean, it has been shown that ε_{Nd} values generally follow the anti-estuarine circulation pattern (Fig. 1.14) [*Henry et al.*, 1994], shifting to higher ε_{Nd} values as water flows through the eastern end of the Mediterranean basin [*Tachikawa et al.*, 2004]. In general, surface waters are slightly less radiogenic than deep waters, with a difference on the order of approximately one ε_{Nd} unit for the western basin and 1.5 to 2.5 ε_{Nd} for the eastern basin [*Tachikawa et al.*, 2004]. Flow back towards the western end becomes less radiogenic again yet never fully recovers to the Atlantic inflow value (Fig. 1.14). In the eastern basin, it is thought that radiogenic Nile input (-1 to -1.5 ε_{Nd}, [*Scrivner et al.*, 2004]) is the most significant source, while less radiogenic sources include Saharan dust and river runoff from elsewhere [*Spivack and Wasserburg*, 1988; *Henry et al.*, 1994; *Tachikawa et al.*, 2004]. Mediterranean ε_{Nd} depth profiles from the literature are compiled in Fig. 1.15.

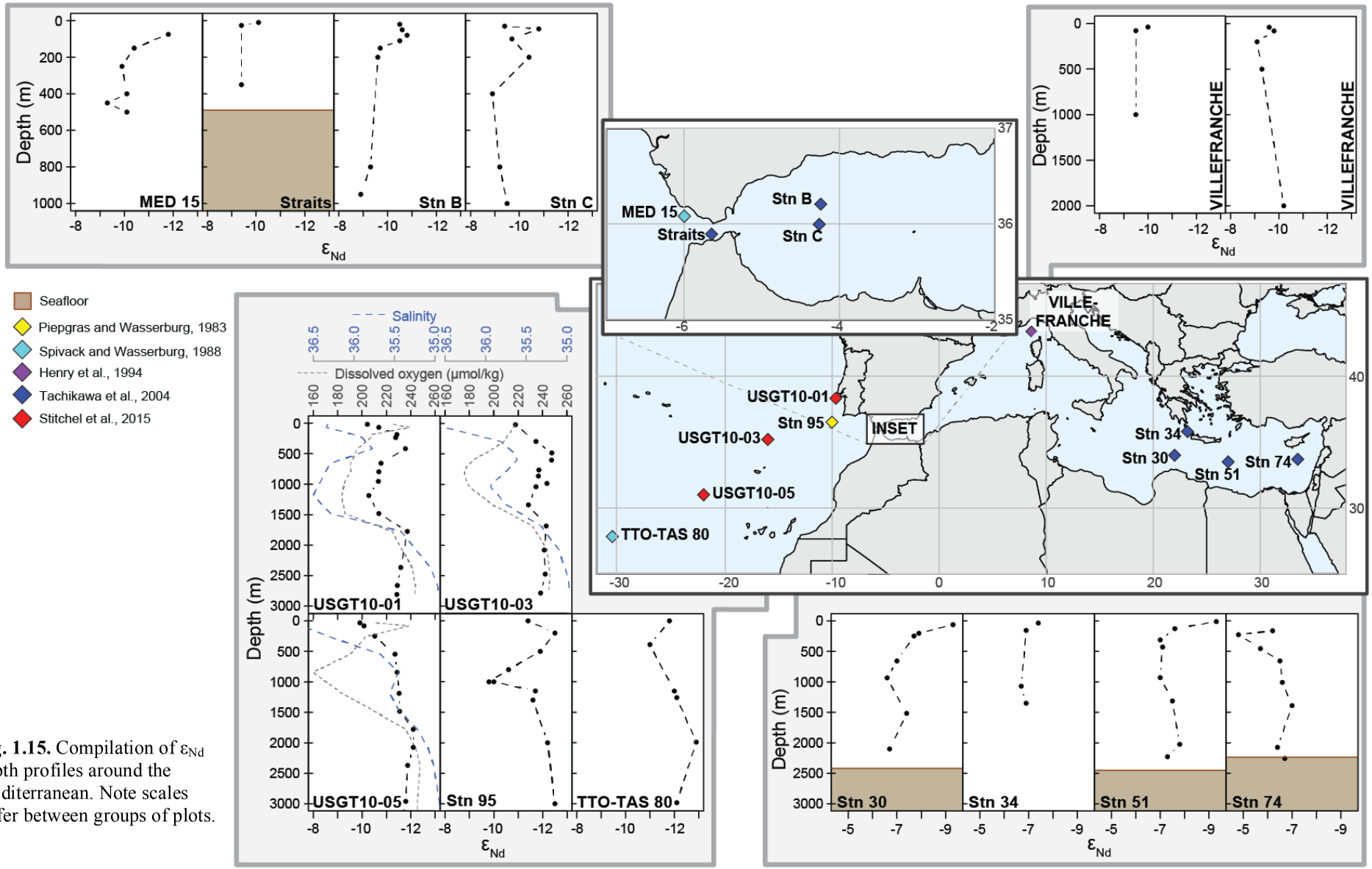

Fig. 1.15. Compilation of ε_{Nd} depth profiles around the Mediterranean. Note scales differ between groups of plots.

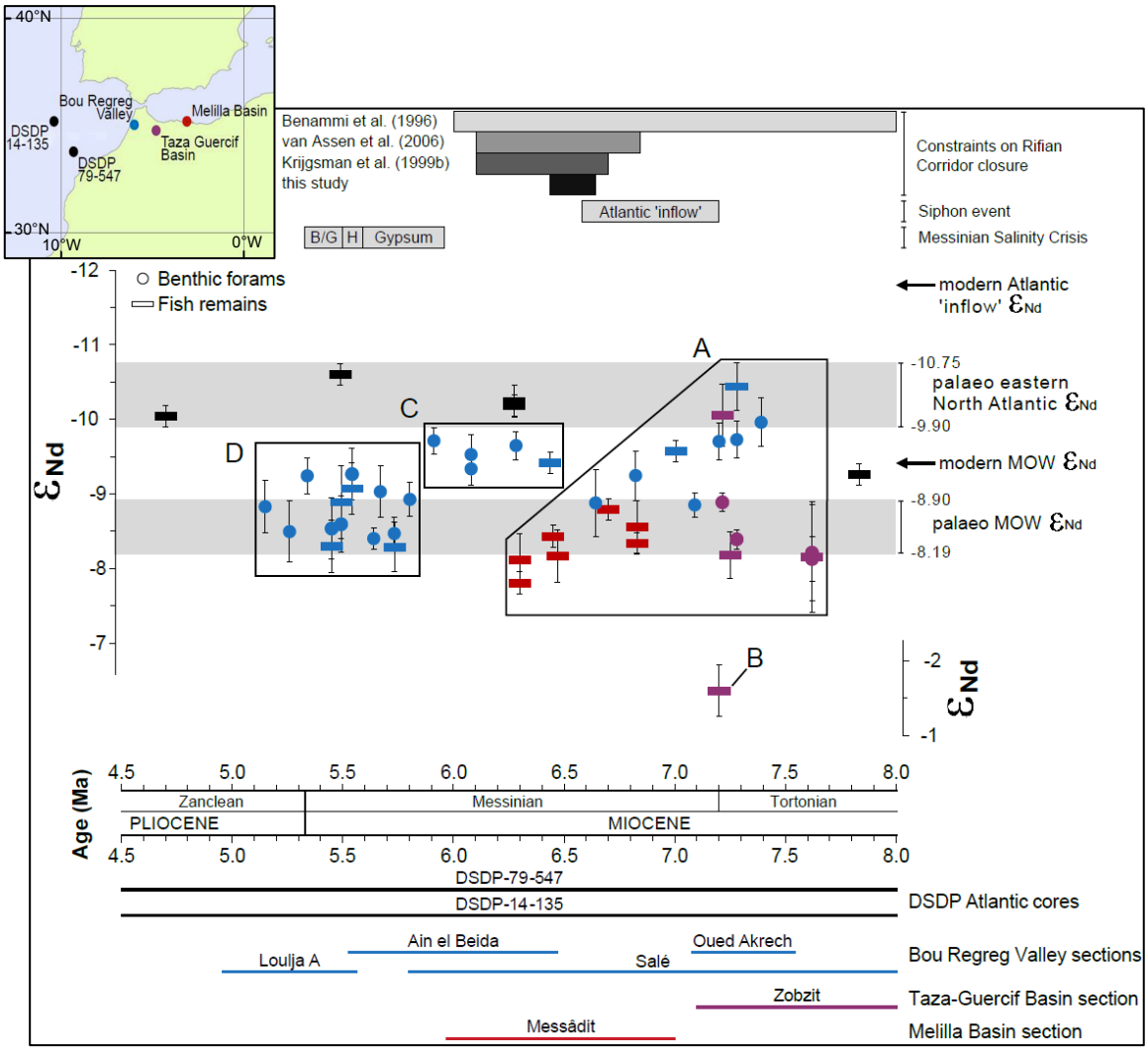

Fig. 1.16. Reproduction of Fig. 5 from *Ivanoviç et al.* [2013]. ε_{Nd} isotope record from the Rifian palaeocorridor region between ~7.7 and 5.0 Ma. Sample locations shown in inset. 'B/G' for upper evaporites (brackish water deposits and gypsum), 'H' for halite and 'Gypsum' for lower gypsum. Mediterranean outflow here denoted MOW (Mediterranean Outflow Water). Atlantic inflow ε_{Nd} from *Spivack and Wasserburg* [1988], *Henry et al.* [1994] and *Tachikawa et al.* [2004].

Only one bottom water Nd isotope record exists regarding MSC gateway exchange; this was published in *Ivanoviç et al.* [2013], and relies heavily on sites from the Rifian palaeocorridor. The main findings are summarized here and reproduced in Fig. 1.16. In the figure, Box A indicates a progressive transition towards more radiogenic ε_{Nd}. *Ivanoviç et al.* [2013] interpret this as a shift over time from an Atlantic signal towards a signal dominated by local (continental) inputs, probably caused by regional uplift. The data excursion at B is interpreted as related to the relatively rapid shallowing of the Taza-Guercif basin (located in the interior region of the Rifian corridor area, inset, Fig. 1.16). This rapid shallowing was observed by *Krijgsman et al.* [1999b] from palaeodepth reconstructions using foraminifera assemblages. On the Atlantic side of the gateway region, a shift towards less radiogenic values is supported by the data in Box C. The authors interpret this shift to indicate a closed or minimally flowing Rifian corridor by

approximately 6.39 Ma. Finally, the ε_{Nd} data in Box D are interpreted as being derived from more continental, more radiogenic material being input to the basin area as continuing tectonic uplift in the region brought terrestrial land-masses closer to the Atlantic Corridor side of the gateway (Salé, Loulja A, Ain el Beida and Oued Akrech sites; inset Fig. 1.16). The authors alternatively suggest that a minimal MO presence could also explain this younger part of the record.

1.3.2 Lead (Pb)

Pb is useful as a proxy for determining local changes to continental inputs and palaeocirculation patterns, particularly at high temporal resolution (Ch. 5, 6), due to its short residence time in seawater. Owing to its particularly low solubility and high particle reactivity, the residence time of Pb in seawater is much shorter than Nd, far shorter than ocean mixing, and is dependent on location and water depth. Surface water residence times of only a few years have been observed [*Bacon et al.*, 1976; *Nozaki et al.*, 1976]. In deeper waters, the residence time of Pb appears to be significantly longer, from ~50 to 400 years, with the Atlantic generally showing much shorter times than the Pacific [*Frank*, 2002 and references therein]. Modeling has corroborated these observations, indicating a global average of about 50 years, with areas of high and low productivity exhibiting an order of magnitude difference [*Henderson and Maier-Reimer*, 2002]. Significantly, the results of *Henderson and Maier-Reimer* [2002] also indicated that even in the absence of anthropogenic input (discussed below), Pb exhibits water column profiles with concentration maxima at the surface followed by very low concentrations (~ 2.2 pmol/kg, or 0.45 ng/L) in deeper waters. Riverine input is likely to be the most important source, while aeolian dust can explain only about 10–12% of the preanthropogenic Pb budget of the ocean [*Frank*, 2002 and references therein]. Hydrothermal input is considered to be a minor contributor (<2%) for the total oceanic budget [*Chen et al.*, 1986], although it is of significance near thermally active areas such as mid oceanic ridges [*Barrett et al.*, 1987]. Anthropogenic Pb contamination, mainly due to the use of alkyl-lead additives in gasoline, has obscured the natural Pb signal in the modern oceans [e.g., *Settle and Patterson*, 1982 and references therein]. This has implications for the interpretation of natural Pb isotope records from the past as, unlike the Nd system, patterns of Pb isotope distributions in the modern oceans do not reflect natural sources. Due to the 1980's U.S. led phase-out of alkyl-lead additives [*Kerr and Newell*, 2003], surface ocean Pb isotope signatures appear to be shifting to those of other industrial sources, while deep waters in the North Atlantic now exhibit typical North American alkyl-lead additive signatures [*Noble et al.*, 2015].

Natural Pb isotope signatures derived from continental sources may be a result of incongruent weathering, a process which fractionates lead isotopes, preferentially releasing radiogenic isotopes compared to primordial ^{204}Pb. During the radioactive decay of parent nuclides (such as ^{238}U, ^{235}U, ^{232}Th), alpha recoil damages host minerals causing the daughter isotopes (^{206}Pb, ^{207}Pb, ^{208}Pb, respectively) to be loosely bound in the crystal lattice and easier to mobilize. The decay chains from radioactive parent to stable radiogenic daughter isotope are shown in Fig. 1.17. Note that other isotopes from these decay chains, ^{230}Th, ^{234}U, will be touched upon in this thesis in relation to determining growth rates in an archive investigated for this project (Ch. 6). In addition to easily mobilized radiogenic Pb released by alpha recoil, accessory minerals which are more easily weathered than feldspar and other major rock forming minerals may contribute large amounts of radiogenic Pb during early weathering [*Harlavan and Erel*, 2002]. These types of minerals, such as apatite, sphene, or allanite, tend to be uranium-rich, and will accumulate high concentrations of radiogenic Pb with time after crystallization. Thus, the dominant weathering regime can affect the isotopic composition of Pb transported to the oceans [*Erel et al.*, 1994; *Harlavan et al.*, 1998; *Harlavan and Erel*, 2002]. For example, major deglaciations have been associated with significant shifts towards more radiogenic compositions in seawater Pb isotope records from the North Atlantic [*Gutjahr et al.*, 2009; *Kurzweil et al.*, 2010]. These changes are attributed to the exposure of glacially ground sediments, sediments which preferentially release their more loosely bound radiogenic component during incipient weathering phases after they are uncovered. Pb isotope ratios in seawater are also affected by the relative availability of fresh and/or radiogenic material, changes in detrital input volume, or hydrologic cycling and runoff; and changes may be recorded in archives over shorter time scales due to the short residence time [*Gutjahr*, 2006 and references therein]. Due to these properties, Pb isotope ratios have been used as a proxy for changes in continental weathering regimes in the context of glacial-interglacial periods and other climate-induced signals, regardless of the difficulties imposed by modern anthropogenic contamination [e.g., *Christensen et al.*, 1997; *Foster and Vance*, 2006; *Gutjahr et al.*, 2009; *Harlavan et al.*, 2009]. Continentally-derived Pb can usually be distinguished from marine-derived Pb [*Goldstein and Hemming*, 2003]. In plots of ^{206}Pb/^{204}Pb versus ^{207}Pb/^{204}Pb, evolved continental crust generally falls above oceanic basalts. This is a consequence of two factors: higher U/Pb ratios in the crust over the first half of earth's history as a result of elemental fractionation during magmatic processes, and the much shorter $t_{1/2}$ of ^{235}U compared to ^{238}U [*Dickin*, 2005].

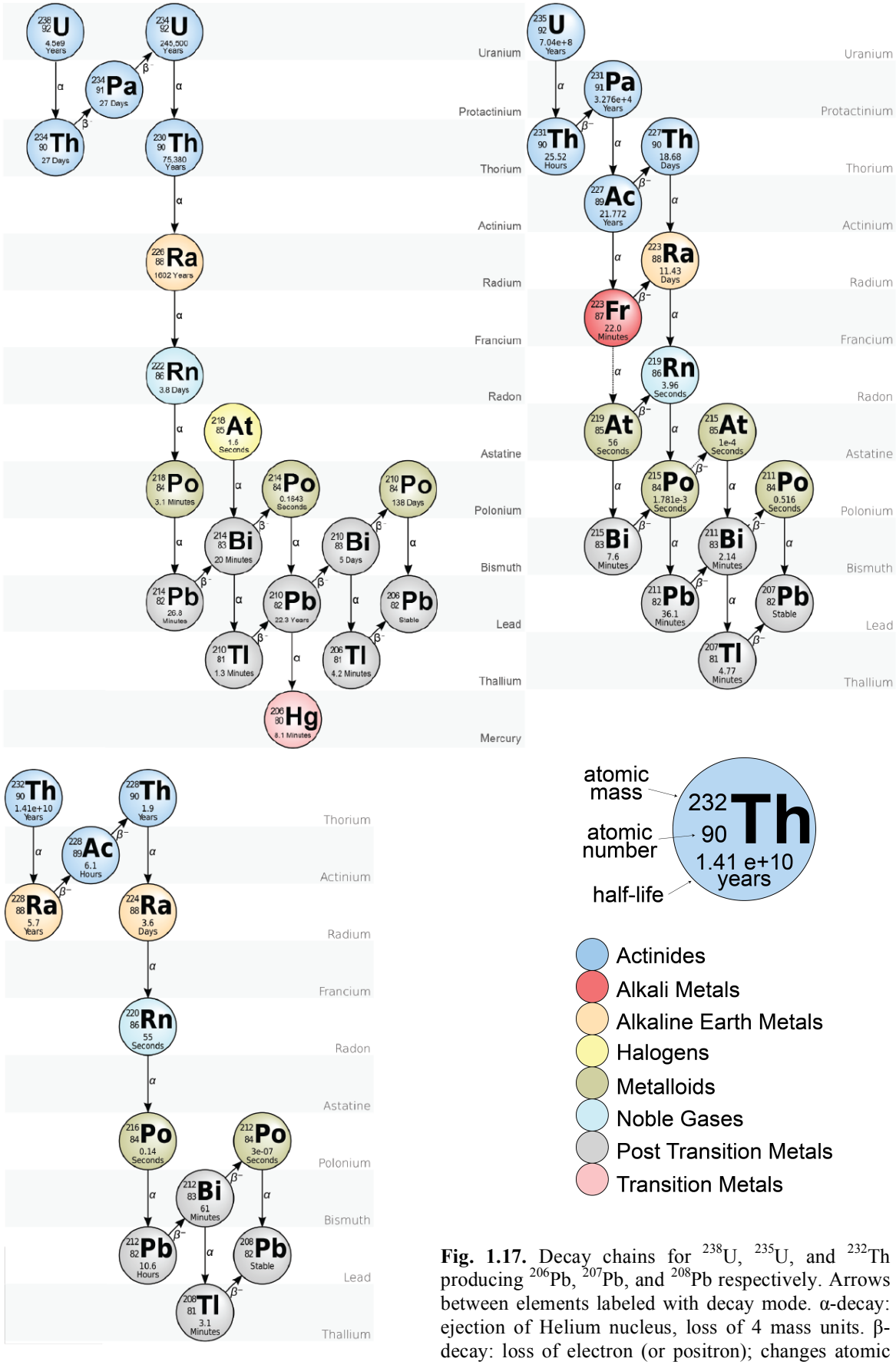

Fig. 1.17. Decay chains for ^{238}U, ^{235}U, and ^{232}Th producing ^{206}Pb, ^{207}Pb, and ^{208}Pb respectively. Arrows between elements labeled with decay mode. α-decay: ejection of Helium nucleus, loss of 4 mass units. β-decay: loss of electron (or positron); changes atomic number ± 1 (no mass change).

Pb isotope records derived from marine sediment archives, similar to those presented in Ch. 5, are relatively novel. The first sedimentary-derived Pb isotope records began appearing as recently as 2006 [*Gutjahr*, 2006]. Generally, Pb and Nd isotope time series have differences making these two systems complementary, owing to their different isotope system characteristics and general chemistry. The short residence time of Pb may allow changes to be recorded with higher temporal resolution when extracted from marine sediments. The Pb isotope system may prove useful for inferring evolution of Atlantic-Mediterranean exchange, but also may prove more useful than Nd in detecting short-lived events such as precessional changes in weathering regimes or tectonic uplift. Pb has a very high affinity to hydrous manganese oxide [*Gadde and Laitinen*, 1974]; thus, after deposition within authigenic FeMn oxyhydroxides it is much less likely to be remobilized than REE. Furthermore, processes such as reverse scavenging and diagenetic exchange have yet to be observed for Pb.

Published information regarding the Pb isotope composition of MO is very scarce. It is limited to records derived from two FeMn crusts, 3514-6 and 65GTV, dredged from ~ 800 m and 1500 m water depth, respectively [*Abouchami et al.*, 1999; *Muiños et al.*, 2008]. Both crusts provide records of Pb and Nd isotope ratios of the seawater which bathed them; the published record for 65GTV appears to have captured changes in MO around the time of the MSC, but the record for 3514-6 does not show changes at this time (Fig. 1.19) [*Abouchami et al.*, 1999; *Muiños et al.*, 2008]. Both were sourced from the same location, the Lion Seamount, outside the Gulf of Cadiz (Fig. 1.20). Neither crust shows significant changes in the Pb isotope signature of the water bathing the Lion Seamount during the late Miocene; however, both records have very coarse temporal resolution due to the methods employed to derive the record.

1.3.3 Strontium: $^{87}Sr/^{86}Sr$

Radiogenic $^{87}Sr/^{86}Sr$ isotope ratios are commonly used as a stratigraphic tool for carbonates formed in open marine settings [*Elderfield*, 1986; *McArthur et al.*, 2012]. The $^{87}Sr/^{86}Sr$ seawater curve may provide ages with a precision of up to +/- 1 My, depending on their position on the curve (Fig. 1.18). Though it varies slightly with depth, the accepted seawater concentration of Sr is 7.85 ± 0.03 ppm [*Veizer*, 1989 and references therein]. $^{87}Sr/^{86}Sr$ is not useful as a water mass tracer as it is fully mixed in the open ocean [*Frank*,

2002] due to its long residence time, on the order of millions of years [*Hodell et al.*, 1990; *McArthur et al.*, 2012].

Sr is chemically similar to Ca and is therefore easily incorporated in the carbonate crystal lattice; due to this, fossilized biogenic carbonates are the primary archive for past seawater Sr isotope reconstructions. In addition to stratigraphy, applications for water Sr isotope signatures include lacustrine and estuarine salinity reconstructions, generally based on idealized two end member mixing between ocean and river water [*Vonhof et al.*, 1998; *Peros et al.*, 2007]. This type of reconstruction does not apply to the Mediterranean basin [*Flecker et al.*, 2002] due to the strongly evaporative hydrologic budget [*Mariotti et al.*, 2002]. $^{87}Sr/^{86}Sr$ can also be used in tandem with other isotopes, such as those of Nd and Pb, to determine if the proxy archives used have a detrital or marine origin [*Bayon et al.*, 2002], accomplished by comparing values to the global seawater curve (Fig. 1.15).

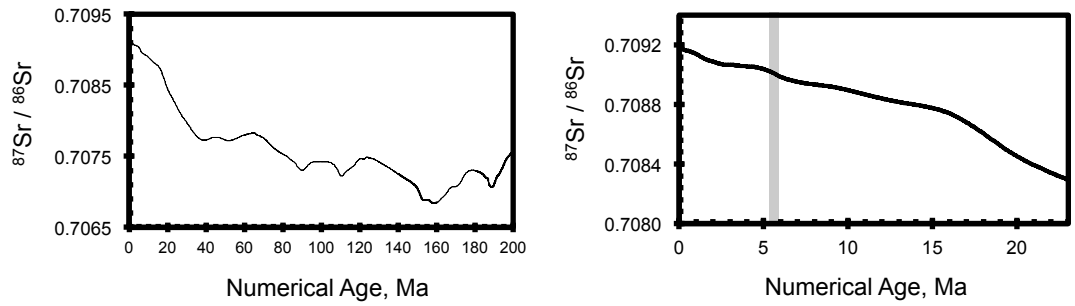

Fig. 1.18: Sr seawater curve for (left) the past 200 Ma, and (right) to the beginning of the Neogene; grey bar indicates the MSC. Images reproduced directly from the LOWESS database [*Howarth and McArthur,* 1997]. Though the database has been updated several times, changes to the curves shown here is negligible.

In the context of the MSC, the $^{87}Sr/^{86}Sr$ ratio has been used to examine inter-basin connectivity and the hydrologic budgets of landlocked basins such as the Mediterranean [e.g. *Flecker and Ellam*, 1999; *Flecker et al.*, 2002; *Topper et al.*, 2011, 2014; *Roveri et al.*, 2014]. Due to the long residence time and high concentration of Sr in seawater, marginal basins can maintain global ocean isotope signatures even with a relatively restricted connection to the open ocean [*McArthur et al.*, 2012 and references therein]. Basins must have little ocean input or be completely isolated from the global ocean to develop $^{87}Sr/^{86}Sr$ isotope signatures which diverge towards local continental Sr inputs [e.g., *Flecker and Ellam*, 1999]. As such, $^{87}Sr/^{86}Sr$ is useful in determining the connectivity history of marginal basins with the open ocean (Ch. 3). Independent salinity constraints are necessary for such studies, since salinity and riverine dilution can be decoupled when

evaporative water loss meets or exceeds freshwater input [*Flecker et al.*, 2002; *Flecker and Ellam*, 2006]. In such a situation, basins containing normal marine fauna can exhibit seawater $^{87}Sr/^{86}Sr$ ratios deviating from ocean values. Though changes in Mediterranean circulation are recognized well before MSC onset, coeval Sr isotope records from open locations plot on the global ocean Sr seawater curve (see compilations in *Topper et al.* [2011] and *Roveri et al.* [2014]). Only a few marginal sub-basins of the Mediterranean region are known to have deviated from global ocean Sr values prior to the MSC (Fig. 1.16a; e.g. Southern Turkey [*Flecker and Ellam*, 1999]; Monte dei Corvi [*Montanari et al.*, 1997]; Tyrrhenian Sea [*Müller and Mueller*, 1991]). *Flecker et al.* [2002] have inferred that gypsum deposition during Stage 1 of the MSC could have been caused by a marine transgression from $^{87}Sr/^{86}Sr$ measurements coupled with salinity estimates in a steady-state box model. Using a transient box model, *Topper et al.* [2011] demonstrated that increased restriction and greatly increased Nile runoff was more likely. Fig. 1.19 summarizes available late Miocene Mediterranean isotope records for Sr, Pb, and Nd.

Due to its applicability as a basin connectivity indicator, $^{87}Sr/^{86}Sr$ is an ideal tracer to investigate climatic and depositional conditions during the MSC, providing complementary information to compare with Nd and Pb isotope ratios. One of the most prominent hypothesis from the literature regarding Mediterranean sapropel formation is that boreal insolation maxima influenced monsoonal conditions, causing much greater river runoff to the Eastern Mediterranean, generating a less saline water cap and inducing water column stratification. Such conditions should be accompanied by increased continental Sr inputs. In the west, GCM simulations show increased precipitation during the same part of the insolation cycle, although the magnitude of variability of change in precipitation is smaller [*Marzocchi*, 2016]. As such, if particularly extreme climatic conditions prevailed in the last few precessional cycles leading up to evaporite precipitation, precessional variability away from the global seawater curve could be expected in the Sr isotope record.

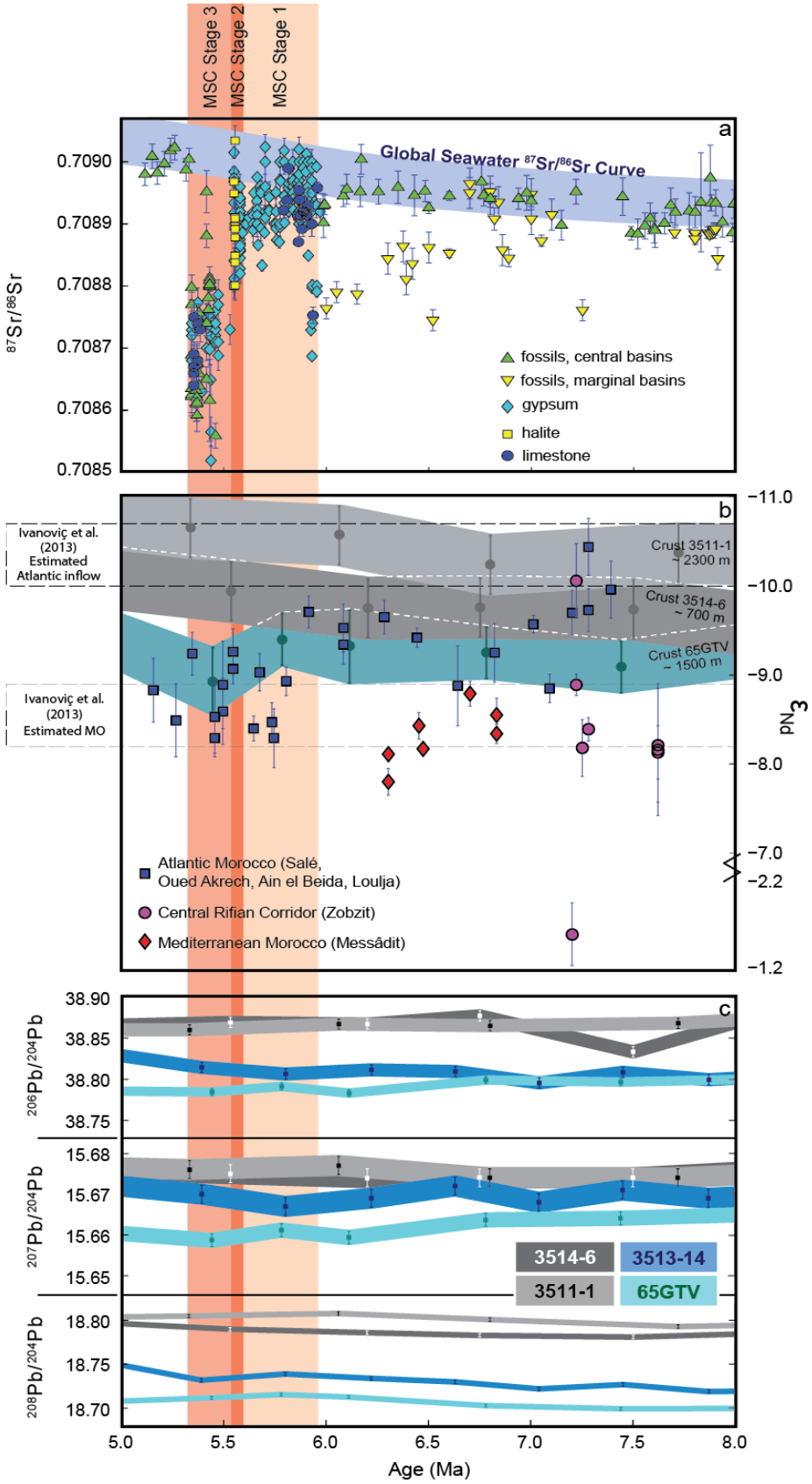

Fig. 1.19. Radiogenic isotope records for the Mediterranean and Mediterranean Outflow (MO) from 8 to 5 Ma. (a) Mediterranean water $^{87}Sr/^{86}Sr$[1,2] plotted against global seawater $^{87}Sr/^{86}Sr$. (b) $\varepsilon_{Nd(t)}$ bottom water values[3] from the Rifian paleocorridor (diamonds, circles) [3]. Compare to estimates for MO (microfossils[3] [squares] and FeMn crusts[4,5] [bands]) and North Eastern Atlantic Deep Water (NEADW) (crust 3511-1). 65GTV data corrected for ingrowth of ^{143}Nd. (c) Pb isotope ratio time series for crusts 65GTV[5], 3514-6, 3511-1 and 3513-14[4]. Error bars 2SD external reproducibility, unless internal was larger (see Ch. 2 for explanation of uncertainty and 65GTV correction). [1] [*Roveri et al.*, 2014]; [2] [*Topper et al.*, 2011]; [3] [*Ivanoviç et al.*, 2013]; [4] [*Muiños et al.*, 2008]; [5] [*Abouchami et al.*, 1999]. Originally published in *Flecker et al.* [2015] (author's own work). See Appendix 7 for Sr isotope data (included electronically only).

1.3.4 ^{10}Be and ^{230}Th dating tools

The most important records of long-term changes in oceanic circulation have come from ferromanganese crusts (FeMn crusts; e.g., *Abouchami et al.* [1997]; *O'Nions et al.* [1998]; *Frank et al.* [1999a]; *van de Flierdt et al.* [2003]). There are three primary methods for dating hydrogenetic FeMn crusts (section 1.4.1); these employ the concentrations of cosmogenic ^{10}Be, excess ^{230}Th, or cobalt incorporated into the material. Cosmogenic, radioactive ^{10}Be is produced in the atmosphere by interaction of cosmic rays with atmospheric gas molecules, and introduced to the oceans via fallout in precipitation. Although the atmospheric production rate is not constant over relatively short time spans [e.g., *Berggren et al.*, 2009] it is assumed that for the coarse, million-year time scales relevant to FeMn crust records, changes in flux are negligible [*Frank*, 2002]. The concentration of ^{10}Be is most often normalized to that of ^{9}Be. While this normalization strategy has been a topic of discussion related to age model generation with ^{10}Be [e.g., *Segl et al.*, 1984], it appears to be a good approximation as the flux of ^{9}Be into the large ocean basins seems to have been relatively stable over the Cenozoic [*Willenbring and von Blanckenburg*, 2010]. The long half-life of ^{10}Be (1.37 ± 0.012 My) [*Chmeleff et al.*, 2010] allows the ^{10}Be method to be effective up to 10 Ma [*Frank*, 2002 and references therein].

Due to the low temporal resolution associated with ^{10}Be/^{9}Be derived growth rates, it is common for growth rates for the upper few mm of a crust to be estimated by the $^{230}Th_{excess}$ method [e.g., *Lalou et al.*, 1979; *Chabaux et al.*, 1995; *Claude et al.*, 2005]. Thorium is less soluble and more effectively scavenged in seawater than uranium; thus, Th precipitates from the water column and is incorporated in sediments and FeMn crusts at faster rates than U. This leads to ^{230}Th radioactivity (hereafter 'activity') which is much greater than (unsupported by) that generated solely by the *in-situ* decay of ^{234}U. Partitioning of Th into crusts from seawater is also ~ 10^6 times higher than U [*Dickin*, 2005]. Due to the shorter half-life of ^{230}Th (~75 ky) compared to its parent ^{234}U (~ 246 ky) [*Cheng et al.*, 2013] (Fig. 1.14), after the system becomes closed to new Th inputs, the activities of the two elements will eventually return to secular equilibrium (ie, A(^{230}Th/^{234}U) = 1, where A(^{xx}I/^{xx}I) denotes activity rather than atom ratio following conventional notation). $^{230}Th_{excess}$ is thus defined as ^{230}Th activity less ^{234}U activity; specifically, A(^{230}Th) within the crust which is in excess of that produced by ^{234}U decay. The use of this excess ^{230}Th allows dating of crust materials up to ~400 ka [*Frank*, 2002 and references therein].

The "Co wt %" method involves the assumption that incorporation of Co has been constant through time. Two empirical relationships have been inferred for age determination using this method [*Manheim*, 1980; *Puteanus and Halbach*, 1988]. This is often used to extend the age model past the 10 My limit of the ^{10}Be method [*Frank et al.*, 1999a; *Frank*, 2002]. The Co wt % method is not employed as this research project is concerned with palaeoceanographic changes related to the MSC, an event at ~ 5 to 6 Ma and within the limit of the ^{10}Be method.

1.4 Archives

Mediterranean and Atlantic waters have distinctly different physical and chemical characteristics. These characteristics are incorporated into marine sediment components such as fossils (e.g., fish remains, foraminifera tests), and authigenic ferromanganese (FeMn) oxyhydroxides which deposit onto sediment grains or form crusts. Such components can be exploited to extract past isotope signatures of Sr, Nd, and Pb. Analysis of the isotopic composition of these extracted elemental fractions can then be used to deduce information such as the presence of a specific water mass at certain times, or changes to regional inputs to the hydrologic system. A general overview of each archive exploited for this thesis is outlined below; further details for each are provided in the methodology (Ch. 2).

1.4.1 FeMn crust 3514-6

One issue in examining palaeocirculation between the Atlantic and Mediterranean using radiogenic isotopes is that Nd and Pb isotopic compositions of palaeo-MOW are not well constrained. Few estimates exist, notably those found in *Ivanoviç et al.* [2013], who place the Atlantic end-member at approximately -9.90 to -10.75 ε_{Nd}, and the Mediterranean end-member at approximately -8.19 to -8.90 ε_{Nd}. These values are approximately 1.5 and 0.9 ε_{Nd} units, respectively, more radiogenic than today. Several assumptions were required in order to derive these values, indicating a need to perform further investigation to confirm these palaeo-end-member values.

Hydrogenetic FeMn crusts are natural marine materials which accrete very slowly (rates of 1 – 15 mm/My; [*Frank*, 2002]) on hard substrates, in areas with relatively fast bottom currents precluding sediment deposition [*Frank et al.*, 1999a]. Trace metals are co-

precipitated directly from seawater with mixed Fe and Mn colloids as oxides or oxyhydroxides [*Koschinsky and Halbach*, 1995]. Their composition and slow formation make them ideal archives for past Pb and Nd isotope compositions of seawater, particularly over timescales of millions of years [e.g., *Abouchami et al.*, 1997, 1999; *O'Nions et al.*, 1998; *Frank et al.*, 1999a; *Muiños et al.*, 2008]. FeMn crusts are not suitable archives for Sr, which has a high rate of diffusivity in FeMn crusts, unlike Pb and Nd [*Henderson and Burton*, 1999].

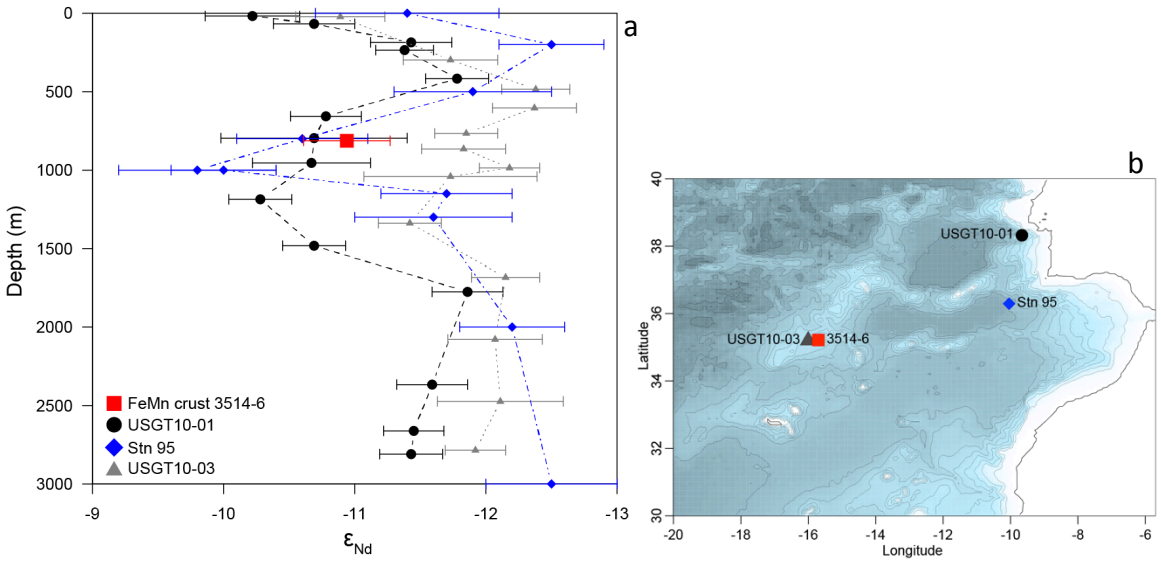

Fig. 1.20. (a) Plot of surface ε_{Nd} of crust 3514-6 [*Muiños et al.*, 2008] compared with nearby water column profiles. (b) Sampling locations. Crust 3514-6 was dredged from the Lion Seamount. 3514-6 surface ε_{Nd} is most similar to profiles from Stn 95 [*Piepgras and Wasserburg*, 1983] and USGT10-01 [*Stichel et al.*, 2015], though profile USGT10-03 [*Stichel et al.*, 2015] was sampled nearly at the same location. Crust 65GTV [*Abouchami et al.*, 1999] was sourced from essentially the same location as 3514-6, but from deeper in the water column (1500 m).

A thick section of FeMn crust 3514-6, obtained during Meteor Cruise 51/1 in 2001 [*Hoernle et al.*, 2003] was acquired for the purpose of high temporal resolution analysis of Pb and Nd isotopes. The provenance of sample 3514-6 is ideal for measuring MO characteristics as it formed between ~ 700 and 900 m water depth on the Lion Seamount, a location bathed by the MO plume today [*Koschinsky et al.*, 1996]. This is confirmed by the surface Nd isotopic composition of 3514-6 (Fig. 1.20) [*Muiños et al.*, 2008]. Published coarse resolution data for this crust show little to no variation in Pb and Nd isotope compositions during the MSC [*Muiños et al.*, 2008]; however, the temporal resolution of these measurements is on the order of 0.75 My, far too coarse to show variation in the time scale of the MSC.

1.4.2 Sedimentary successions

The majority of the archives exploited in this thesis to investigate changes in radiogenic isotopes of seawater through time are marine sediment deposits exposed in outcrops on land (Fig. 1.21). The most important is the Upper Abad Formation of the Sorbas Basin (near Almería, Spain; details given in Ch. 2, section 2.2.1). From marine sediments, authigenic fractions such as foraminiferal calcite and FeMn oxyhydroxides are exploited to produce records of seawater Sr, Pb, and Nd and investigate patterns of water mass circulation, exchange, and climate signals.

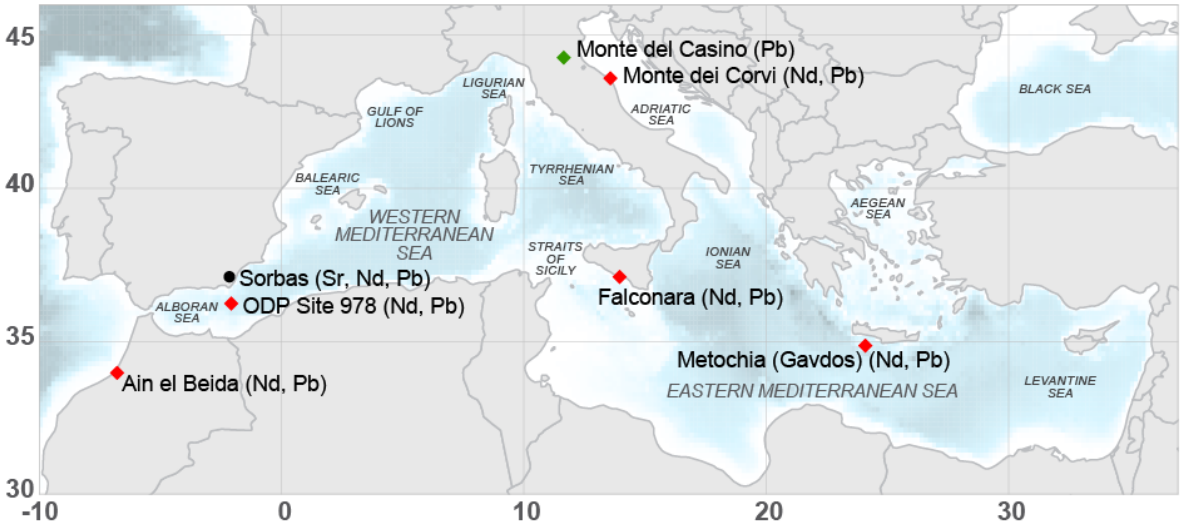

Fig. 1.21. Locations of sediment deposits around the Mediterranean used as archives for this thesis. Also indicated are names of smaller basins comprising the Mediterranean used in the text. Late Miocene seawater isotopic compositions measured for each location are listed. Sites for which Sr, Nd, and Pb were measured are noted by black symbols; for those where Nd and Pb were measured, red symbols are used; and for sites where only Pb isotope compositions are reported, green symbols are used.

Based on the outcome of Pb isotope analyses performed on sediments from the Sorbas Basin, it was deemed useful to attempt to generate similar records for the same time frame from other locations around the Mediterranean. Four sections from within the Mediterranean (Monte dei Corvi, Monte del Casino, Falconara, and Metochia) and one from the Atlantic (Ain el Beida) were selected for preliminary analysis (Fig. 1.21). From the initial results, two were selected for high-resolution analysis, Monte del Casino and Falconara.

The primary reason the Sorbas Basin sediments were chosen for this study, other than that detailed below, was to work with a sample set for which a significant amount of data has been previously published (section 2.2.1). Selection of samples from other locations was based on several criteria. For obvious reasons, samples of the same age as the interval investigated from the Sorbas Basin were preferred. In addition to age, clear sedimentary cyclicity and a high resolution age model were prerequisites. If the same age interval was not available but a location was desireable to enable wide spatial coverage, the nearest time span which also coincided with a section of cycles deposited near eccentricity maxima were preferred. At eccentricity maxima, insolation has a high amplitude and precessional sedimentary cyclicity is most clearly preserved.

1.4.2.1 The Sorbas Basin

As the previous Nd isotope study dealing with Mediterranean-Atlantic exchange focused on the Rifian corridor [*Ivanoviç et al.*, 2013], a location for the Betic corridor was preferred for this project. To enable this study to be performed within a reasonable timescale, a section with previously determined high-resolution age control was mandatory. Furthermore, a section which is well-studied in other respects helps facilitate interpretation of new results, particularly considering the shallow nature of gateways and the known issues in using the Nd isotope tracer in shallow settings. Detailed sedimentological and chronological information regarding the Sorbas Basin is provided in Ch. 2, section 2.2.1.

1.4.2.2 ODP Site 978

To enable comparison of the data from the shallow and marginal Sorbas Basin, and provide further constraints on the late Miocene characteristics of Western Mediterranean water, measurements from a deep site within the Mediterranean are required. Site 978 (Fig. 1.21) was drilled during Leg 161 of the Ocean Drilling Program (ODP) in 1995 [*Shipboard Scientific Party*, 1996]. This site is significant as it provides the only pre-MSC deep marine sediment available from the Alborán Sea, the closest sub-basin of the Mediterranean to the Sorbas Basin. Other samples from the region have been recovered, but no other cores have the requisite late Miocene marine sediments for the methodology applied here (Ch. 2), or adequate age control. Sedimentological and chronological characteristics of the section of core sampled for analysis are provided in Ch. 2, section 2.2.2.

1.5 Summary

The purpose of this introductory chapter was three-fold: (1) to provide the non-specialist with background into the key disciplines involved in this project; (2) to provide a summary of the available information already published related to radiogenic isotopes and Mediterranean-Atlantic exchange; (3) and to outline the organization of this thesis.

Ocean circulation is an integral part of the climate system; it regulates Earth's climate by distributing heat energy between the equator and poles. Different sources and sinks of heat and salinity drive water masses to circulate, producing a feedback system. One potentially important feedback is the interplay of Mediterranean Outflow (MO) on Atlantic Meridional Overturning Circulation (AMOC), which is driven by deep water formation in the North Atlantic. The Mediterranean is a net sink of heat from the Atlantic [*Rogerson et al.*, 2012]; this water body releases denser (both cooler and saltier) water back to the Atlantic which travels northwards, preconditioning water for overturning [*Ivanoviç et al.*, 2014]. Thus, an important step in understanding past global climate is to reconstruct exchange between the Atlantic and Mediterranean. This thesis focuses specifically the latest Miocene, during which the Messinian Salinity Crisis (MSC) occurred, which is expected to have caused significant changes to MO.

To reconstruct such exchange, background is required in several key areas. To this end, this introduction has covered the critical aspects of late Miocene palaeogeography and stratigraphy, and the interrelated concepts of astronomical tuning, climate forcing, and the current understanding of the feedback system between precessional shifts in the North African monsoon system, sedimentation in the open Mediterranean Sea, and modern Atlantic-Mediterranean exchange. Section 1.2.6 highlighted the current debate on climate lags and leads within a precessional cycle, illustrating the knowledge gap in this area and the difficulties in correlating specific lithologies at one location to another in terms of time. This issue is relevant to the results discussed in Chapters 3 and 5.

Application of radiogenic isotopes of Sr, Nd, and Pb to reconstructing exchange between basins is the scientific focus of this thesis. To support this goal, background on the physicochemical characteristics, sources, sinks, and behaviour of these geochemical tools is provided, following the general background section on the Mediterranean region and stratigraphy. Differences in behaviour are highlighted, to foster an understanding of how

each can be used individually and how each may be complementary to the other. In general, Sr is applied to reconstruct basin connectivity, Nd is applied as a tracer to detect the presence or estimate the relative influence of water masses, and Pb is applied primarily to estimate the change in regional climatic factors such as continental weathering regimes which may affect the seawater isotope signature.

1.5.1 Thesis organization and key questions

This thesis is organized into seven chapters. The general background presented here (Ch. 1) is followed by the analytical methodology and all relevant methodological background (Ch. 2) required to produce the data presented in the subsequent results and discussion chapters (Ch. 3 – 6). The methodology for all analytical and modeling work performed is concentrated Chapter 2, as many results were determined from the same methodologies. The results and discussion chapters (Ch. 3 – 6) outline the results and discuss their implications. Each focuses on a specific set of results from one isotope system and one type of archive, and the information that can be inferred from those results relevant to the scientific questions posed. This thesis is completed with a short chapter summarizing the useful conclusions and insights gained through this project; this final chapter also synthesizes inferences by combining data from different chapters.

A general aim of this thesis project was to produce and interpret radiogenic isotope records from locations near the Atlantic-Mediterranean gateway(s). The records are used to address, where possible, a number of key research questions:

- Ch. 3: What is the nature of connection between the Sorbas Basin, the primary source for the seawater records produced during this project, and the open Mediterranean during the study interval? In understanding the nature of the connection, can we better understand the relationship between organic rich layers deposited in marginal Mediterranean settings and open Mediterranean settings?
- Ch. 4, 5, 6: Can radiogenic Nd and Pb isotopes be applied to understanding Mediterranean-Atlantic water mass exchange in the late Miocene? If so, what caveats are there? Can the Nd isotope record generated for the Rifian corridor [*Ivanoviç et al.*, 2013] be reproduced for the Betic corridor?
- Ch. 5: Given that sedimentation in the Mediterranean region is strongly controlled by precessional climate fluctuations, do radiogenic isotopes also respond to these climate signals? Is there high-frequency (i.e., precessional) variability in radiogenic

isotope records from late Miocene Mediterranean deposits? If so, what are the causes or drivers, and can we separate these short-term variations from any longer-term trends? Can such records give us insight into the nature of deposition across precessional cycles?

- Ch. 6 (see also Ch. 2): Using laser ablation measurements, which provide improved temporal resolution, can more information about Mediterranean-Atlantic exchange be determined from crust 3514-6? In parallel, is it possible to generate a higher precision age model to accompany such records? What information can be garnered from such a high-resolution record, relevant to both events in the late Miocene and beyond this period?

2 Materials and Methods

2.1 Overview

This chapter describes the materials and methods employed in this project. The materials are discussed first, including sedimentology, chronology, and other relevant background. This is followed by a description of the laboratory methods used for analysis. A brief summary is provided indicating modifications to published data used to enable data inter-comparison. Finally, an explanation of the numerical box modeling methods is provided. Several constants (e.g. half-lives, bulk earth isotope ratios) are required for calculations such as growth rates and mass spectrometer data normalization; these are summarized in Table 2.1. Canonical values are used [e.g., *Steiger and Jager*, 1977; *Begemann et al.*, 2001; *Dickin*, 2005], unless literature consensus exists for newer values.

Table 2.1. Summary of constants, including half-lifes ($t_{1/2}$, y), and references.

Element	Daughter isotope	Parent, $t_{1/2}$	Ref
Nd	^{143}Nd, stable	^{147}Sm, 1.06 x 10^{11}	a
	^{144}Nd, stable, primordial		
	^{143}Nd/^{144}Nd CHUR = 0.512638		b
	^{147}Sm/^{144}Nd CHUR = 0.1966		b
	^{146}Nd/^{144}Nd = 0.7219		c
Pb	^{208}Pb, stable	^{232}Th, 75,584 ± 110	d
	^{207}Pb, stable	^{235}U, 7.03 x 10^{8}	e
	^{206}Pb, stable	^{238}U, 4.4680 x 10^{9}	e
	^{204}Pb, observationally stable, primordial		
Sr	^{87}Sr, stable	^{87}Rb, 4.94 ± 0.3 x 10^{10}	f, *
	^{86}Sr/^{88}Sr = 0.1194		
Th	^{230}Th, radioactive	^{234}U, 245,620 ± 260	d
	^{232}Th, radioactive, primordial		
U	^{234}U, radioactive	^{238}U, 4.4680 x 10^{9}	e
Be	^{10}Be, cosmogenic	^{10}Be, 1.387 ± 0.012 x 10^{6}	g
	^{9}Be, stable	(primordial)	

References: a, *Lugmair and Marti* [1978]; b, *Hamilton et al.* [1983]; c, *O'Nions et al.* [1977]; d, *Cheng et al.* [2013]; e, *Jaffey et al.* [1971]; f, *Minster et al.* [1982] (post-depositional ingrowth of Rb in calcite is negligible; this value is included here solely for completeness); g, *Chmeleff et al.* [2010], note that ^{10}Be is cosmogenic and does not have one individual parent isotope. * This half-life differs from the conventionally accepted decay constant for ^{87}Rb (1.42 x 10^{-11}; *Steiger and Jager*, 1977).

2.2 Sedimentology and chronology of sediment samples

2.2.1 Upper Abad Marls, Sorbas Basin

The Sorbas Basin formed in a series of extensional depressions at the Eastern end of the Betic corridor (Fig. 2.1a, b). It is a well-studied marginal sub-basin of the Western Mediterranean providing an ideal opportunity to study exchange using radiogenic isotopes. Although Mediterranean-Atlantic exchange through the Betic gateway is thought to have ceased by ~ 7 Ma [*Esteban et al.*, 1996; *Martín et al.*, 2001, 2009; *Betzler et al.*, 2006], marine sedimentation persisted in this area into Stage 1 of the MSC. The pre-MSC successions of interest are known as the Abad Marls, separated into two parts (Lower and Upper) based on cyclicity. The Lower Abad is characterized by bipartite cycles consisting of dark blue-grey homogenous marls punctuated by more indurated layers. The Upper Abad, a main focus of this thesis, is characterized quadripartite cyclicity, described below.

Deposition of the Abad Member began at approximately 7.25 Ma until the onset of evaporite deposition at 5.971 Ma, marking the beginning of the Messinian Salinity Crisis (MSC) [*Sierro et al.*, 2001; *Manzi et al.*, 2013]. The quadripartite sedimentary cyclicity characterizing the Upper Abad begins at approximately 6.71 Ma (Fig. 2.1c) [*Sierro et al.*, 1999, 2001, 2003]. These cycles consist of brownish-grey layers exhibiting faint laminations termed ‘sapropelic’; bioturbated, homogenous grey marl (hereafter ‘marl 1’); diatomaceous marl (hereafter diatomite); and another grey homogenous marl (hereafter ‘marl 2’; Fig. 2.2).

Although exchange between the Sorbas Basin and the Western Mediterranean is expected to have been relatively restricted during deposition of the Upper Abad [*Sierro et al.*, 1999], the lithological cyclicity is attributed to similar climate forcing as the more general Mediterranean case with water column stratification emphasized as a major influence [*Sierro et al.*, 2001, 2003]. For the overall Mediterranean, stratification is the main factor controlling sapropel formation, enhanced by export production [*Rohling*, 1994]. During insolation maxima, precipitation over North Africa is greatly increased, leading to a significant increase in freshwater runoff to the Eastern Mediterranean [*Marzocchi et al.*, 2015]. Increased freshwater input decreases the salinity of surface waters, resulting in lower density surface water and water column stratification, leading to bottom water anoxia [*Rohling*, 1994; *Matthiesen and Haines*, 2003]. Bioturbation does not occur due to a lack of benthos, and organic matter is thus well preserved in laminated sediments during

insolation maxima. On a larger scale, stratification reduced convective overturning in the Eastern Mediterranean, impacting Levantine Deep Water formation, and decreasing flow of Levantine Intermediate Water (LIW) back towards the Atlantic through the Western Mediterranean, leading to similar if somewhat less pronounced effects as observed in the East [e.g., *Rohling*, 1994; *Murat*, 1999].

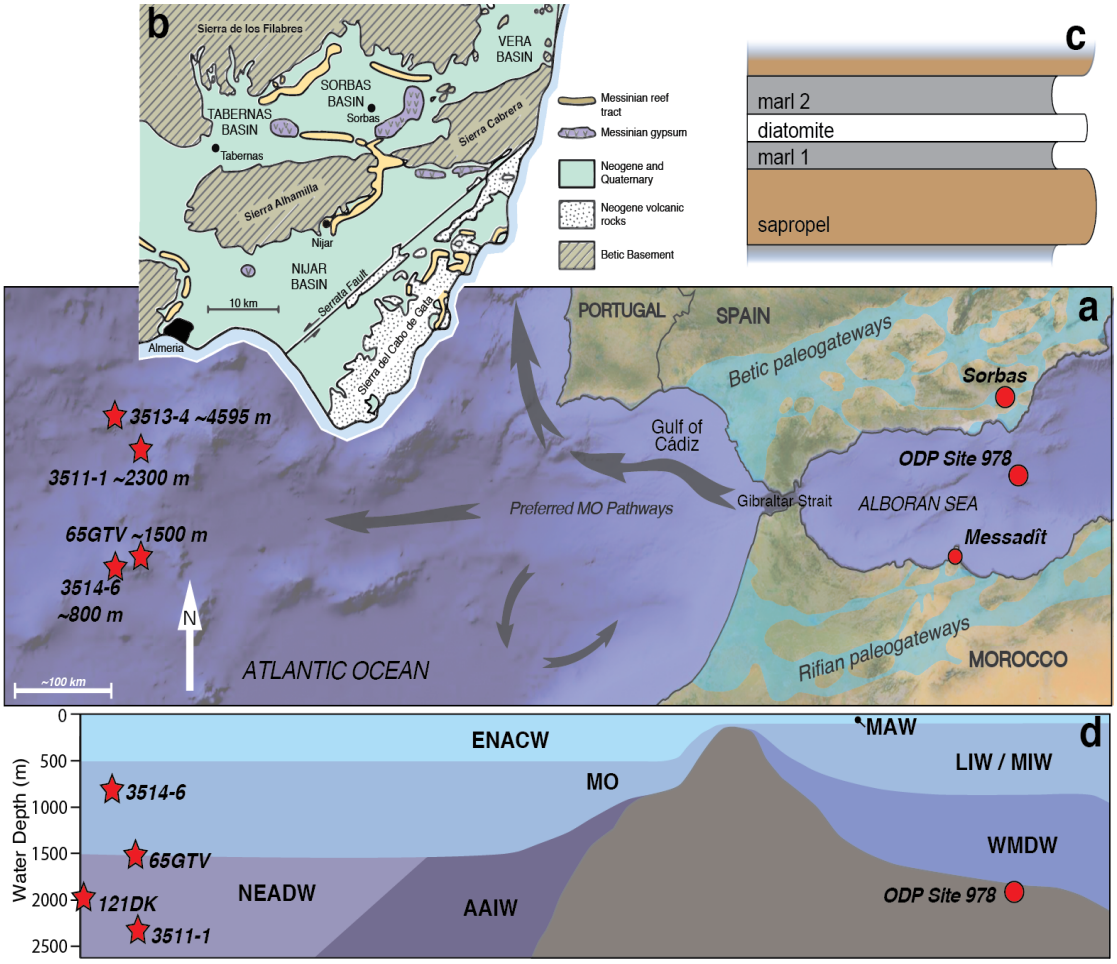

Fig. 2.1. (a) Modern MO preferred pathways and sampling locations of archives referred to in the text. Circles: sediment or fish remains. Stars: ferromanganese crusts. Betic and Rifian palaeogateways shown in light blue; configuration spans approximately 8 – 6 Ma (corridors were closing through this period). Reconstruction adapted from *Ivanoviç et al.* [2013] based on *Santisteban and Taberner* [1983]. ODP Site 978 (36°13.9'N 2°3.4'W), Leg 161 Report; Sorbas Basin (37°05'22"N 2°04'08"W), this study; Messadît (35°17'38"N 2°59'55"W), *Ivanoviç et al.* [2013]. See Table 2.3 for crust locations. Note 121DK is off map; this crust is located ~500 km SW of the Canary Islands off NW Africa. (b) General geological map of the Almería region; Neogene and Quaternary cover coincides mainly with locations of palaeogateways and basins. Messinian reef deposits provide indication of basin size at that time. Adapted from *Krijgsman et al.* [2001]. (c) Idealized profile of Sorbas basin Upper Abad sediments showing quadripartite cycle. (d) Idealized cross section through Gibraltar showing approximate depths of relevant water masses and depths of various archives from (a). ENACW – Eastern North Atlantic Central Water; MAW – Modified Atlantic Water; MO – Mediterranean Outflow; NEADW – North Eastern Atlantic Deep Water; AAIW – Antarctic Intermediate Water; WMDW – Western Mediterranean Deep Water; LIW – Levantine Intermediate Water (also referred to as MIW – Mediterranean Intermediate Water).

Fig. 2.2. Appearance of Upper Abad Member sediments; image on right is interpretation of image on left. Cyclicity is not very obvious to the naked eye, though it is possible to see the difference between the sapropelic layers (reddish brown) compared to the other marls (grey).

High total organic carbon (TOC) is a characteristic of sapropels of Pliocene and Pleistocene age; in the open Mediterranean, highest sapropel TOC decreases from east to west with the lowest percentages found in the Alboran Sea (maximum TOC 2%, [*Murat*, 1999]). Similar mechanisms have been invoked to explain the Sorbas sediments although TOC is even lower, as shown by measurements of sediments from the Upper Abad section indicating the sapropelic layers contain a maximum of 1.8% TOC compared to 0.6% in the marls [*Vázquez et al.*, 2000]. At the other extreme in the insolation cycle, diatomite formation in the Sorbas Basin is attributed to insolation minima [*Pérez-Folgado et al.*, 2003; *Sierro et al.*, 2003], when drier conditions led to an increase in the net fresh water loss due to decreased precipitation and runoff and increased evaporation, increasing the salinity of surface waters, destabilizing the water column and promoting vertical mixing. Such conditions lead to nutrient upwelling and enhanced phytoplankton production. Diatoms are only present during the diatomite layer, or immediately before or after in the transition from marl to diatomite and back [*Sierro et al.*, 2003]. The homogeneous marl preceeding the diatomite (marl 1) marks the onset of mixed conditions, while marl 2 marks the onset of nutrient depletion [*Sierro et al.*, 1999, 2003; *Filippelli et al.*, 2003]. For the interval studied in this project, the mechanisms controlling sedimentation are corroborated by high-resolution planktic foraminifera assemblage data and resulting ecological interpretation [*Pérez-Folgado et al.*, 2003]. Some of these foraminiferal records are used in Ch. 3 to interpret the Sorbas Basin $^{87}Sr/^{86}Sr$ isotope record generated during this project.

While the Upper Abad is composed of marls described as open marine, it has been suggested the basin was shallower at this time relative to the underlying Lower Abad sediments, based on sedimentological field observations and foraminiferal assemblages

[*Troelstra et al.*, 1980; *Sierro et al.*, 1997; *Krijgsman et al.*, 2006]. Palaeobathymetry of other late Miocene sections, generally open-marine, has been assessed using the benthic to planktic foraminifera ratio (B/P), where planktic forams tend to increase in relative proportion towards deeper water [*van der Zwaan et al.*, 1990]. However, palaeobathymetry of the Sorbas Basin, as for Mediterranean sediments in general, is difficult to determine with this proxy due to the strongly cyclical nature of climate effects on basin hydrology, such as bottom water anoxia [*Van Hinsbergen et al.*, 2005; *Krijgsman et al.*, 2006]. Existing estimates, based on various sedimentological observations and other factors, span a range of 200 to 1000 m [*Dronkert*, 1976; *Troelstra et al.*, 1980; *Poisson et al.*, 1999; *Baggley*, 2000]. Benthic foraminiferal assemblages (section 2.3.3 below) from the interval studied in this thesis are used to provide better constraints on palaeobathymetry (results in Ch. 3, section 3.3.3). Fringing carbonate reefs associated with the basin were deposited coevally with the sediments of interest (e.g.[*Martin and Braga*, 1994; *Braga and Martin*, 1996] and constrain horizontal basin dimensions to approximately 40 x 30 km^2 (Fig. 2.1b; see geological maps of [*Krijgsman et al.*, 2001; *Do Couto et al.*, 2014]). Connections to the Western Mediterranean were relatively long and complex, to the west through the Tabernas and Nijar Basins, and through the Vera Basin to the west (Fig. 2.1b).

40 samples were selected for this study from the lower section of the Upper Abad, cycles UA5 to UA8 (~6.61 to 6.55 Ma), from a preexisting sample set. These were originally collected from a section approximately 10 m high by graduate researchers from the University of Salamanca in 1999 from the Los Molinos section (37°05'22"N 2°04'08"W) for high temporal resolution studies of fauna and stable isotopes (published by *Pérez-Folgado et al.* [2003]). During collection, tens of cm of surface sediment were removed to collect fresh, uncontaminated material (pers. comm., Prof. F. Sierro, 2013). These samples were chosen for this project because a wealth of information is already available, including planktic foraminiferal assemblages, stable isotope data, total organic carbon, and some major element concentrations. Using leftover material from these samples enables a direct comparison requiring no assumptions about age or differential sample preservation.

A high resolution astronomically tuned age model for the Abad Member was published by *Krijgsman et al.* [1999a] and *Sierro et al.* [2001]. It was derived via integrated cyclo-, magneto- and biostratigraphy and tuned to La90 [*Laskar*, 1990]. For this work, the astronomical tuning was updated to La04 [*Laskar et al.*, 2004] based on the previous age model, assigning the age of insolation maxima peaks to the midpoints of sapropelic layers.

Sedimentation rate is extrapolated as constant between midpoints as further constraints are currently unavailable; this issue is discussed in Ch. 1, section 1.2.6.

2.2.2 ODP Site 978

ODP Leg 161 Site 978 (36°13.867'N, 2°3.424'W; Fig. 2.1) was drilled at a water depth of 1930 m. This core provides the only appropriate material available for the Messinian Western Mediterranean Sea, as this study requires authigenic marine sediments in order to apply an acid-reductive leaching methodology (section 2.3.4). Four Messinian and two early Pliocene samples from ODP Site 978 were selected for analysis, selecting samples near or between bioevents to enable age assignment.

For the Messinian age section, the sediment was likely to have been deposited by low to high density currents of a submarine lobe or apron, based on sediment textures, although the clay size fraction dominates [*Shipboard Scientific Party*, 1996]. The nannofossil assemblage indicates open marine conditions, but foraminifera are reworked and unreliable [*Shipboard Scientific Party*, 1996]. Age constraints for this section are based on two bioevents, the LO of *Reticulofenestra rotaria* at 6.12 Ma and the FO of the same nannofossil at 6.62 Ma [*Shipboard Scientific Party*, 1996]; intermediate sample ages are assigned assuming a constant sedimentation rate between the bioevents.

The Miocene age sediments are capped by a hiatus marked by a gravel bed of 10 to 25 m thickness that caused low core recovery, and foraminifera are poorly preserved throughout the interval. Furthermore, the bioevents of *R. rotaria* have been excluded from the latest revision of biostratigraphic events used to compile the Geologic Time Scale [*Gradstein et al.*, 2012] due to large spatial variability causing unreliability [*Raffi et al.*, 2003]. *Lourens et al.* [2004] report that the maximum time interval where *R. rotaria* is observed in the Eastern Mediterranean is 5.99 – 7.41 Ma. These issues result in difficulties generating robust age constraints. All Miocene age data from Site 978 are thus assigned an age uncertainty equal to the time between the two bioevents of *R. Rotaria,* according to the original ODP publications for Site 978 (6.12 to 6.62 Ma, *Shipboard Scientific Party* [1996]). It is intended that the large age uncertainty assigned to the samples will partially counter this age assignment issue, although this problem must be considered when comparing data between locations. In the following chapters, the range defined by the

Messinian age samples will be considered as general ranges only when comparing data from Site 978 to high temporal resolution data of other sites.

Pliocene sedimentation, including at the two sampled intervals, is characterized by normal open marine conditions. Pliocene preservation of foraminifera is good, enabling straight-forward age assignment [*Shipboard Scientific Party*, 1996]. Both samples for radiogenic isotope analysis were taken at depths of specific biostratigraphic events to enable direct age assignment, the first at the Top Common Occurrence (TCO) of *G. margaritae* at 3.98 Ma; [*Lourens et al.*, 2004]. The second sample was taken at the First Occurrence (FO) of *G. punticulata* at 4.52 Ma [*Shipboard Scientific Party*, 1996; *Lourens et al.*, 2004]. A conservative age uncertainty of 0.05 Ma is assigned to both Pliocene samples.

2.3 Methodology applied to sediment samples

All reagents used in the following procedures were either in-house distilled from analytical grade or ultraclean quality, except in the case of ammonium acetate, $MgCl_2$, and ethanol, which were of analytical grade. Hotplates used for drying samples were situated within separate chambers and supplied with filtered air to minimize contamination; no other materials or samples were allowed in the chamber during drying periods.

2.3.1 Foraminiferal $^{87}Sr/^{86}Sr$

Sr extraction and isotope analysis was performed for samples from the Sorbas Basin. Mixed planktic foraminifera (primarily *Orbulina universa* and *Globigerina* forms) were picked under a microscope in conventional laboratory conditions from previously disaggregated and washed samples (see *Pérez-Folgado et al.* [2003] for details). Foraminifera were gently crushed between glass plates under the microscope to ensure all chambers were opened before cleaning. Cleaning, dissolution, and purification for Sr was performed in clean lab conditions.

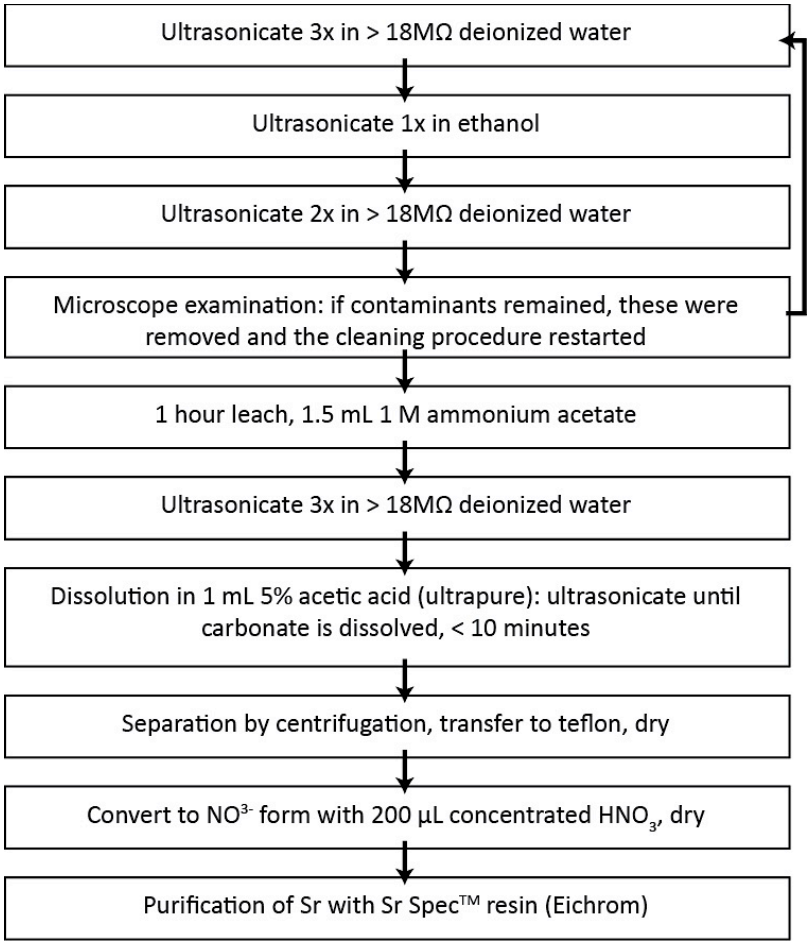

Fig. 2.3. Flowchart of foraminiferal calcite cleaning procedure prior to Sr isotopic measurements.

The cleaning procedure consisted of multiple ultrasonifications in > 18.2 MΩ deionized water, once in ethanol, and again in deionized water. The liquid from each step was removed by pipette, ensuring the final water rinse before the ethanol step was clear and free from clays. Foraminifera were examined under a binocular microscope for cleanliness; if any discoloration or dark minerals remained, these were removed and the cleaning procedure started anew. Foraminifera were leached in 1.5 mL 1 M ammonium acetate for 1 h to remove Sr not bound within the original calcite matrix [*Melezhik et al.*, 2001 and references therein]. The solution was removed by pipette and ultrasonicated a further three times in deionized water before dissolution. Foraminiferal calcite was digested in 5% acetic acid with ultrasonification for a minimum of 3 minutes and maximum of ten minutes, visually checking calcite dissolution at regular intervals to ensure minimum ultrasonification time. The liquid was separated by centrifugation, dried, and converted to nitrate form with 200 µL concentrated HNO_3. Sr was separated following standard column chromatography using Eichrom Sr Spec™ resin [*Henderson et al.*, 1994]. A flowchart of the foraminiferal calcite cleaning procedure is shown in Fig. 2.3.

2.3.2 $^{87}Sr/^{86}Sr$ mass spectrometry

Sr samples were analyzed with a VG Sector 54-30 multiple collector thermal ionization mass spectrometer (TIMS) at SUERC (East Kilbride, UK). Samples were loaded on single Re filaments with a Ta activator similar to that described by *Birck* [1986]. An ^{88}Sr intensity of $\sim 1 \times 10^{-11}$ A ± 10% was maintained. $^{87}Sr/^{86}Sr$ ratio was corrected for mass fractionation to $^{86}Sr/^{88}Sr = 0.1194$ using the exponential law [*Nier*, 1938]. The mass spectrometer was operated in dynamic mode with data collected in 15 blocks of 10 ratios. Total procedural blanks for Sr were < 164 pg. NIST SRM 987 (Strontium carbonate) gave 0.710259 ± 0.000018 (2 S.D., n=24) during the course of the analyses, within error of the recommended value of 0.710248. The 2 standard error internal precision on individual analyses was between 0.000012 and 0.000017 (smaller than external reproducibility).

2.3.3 Benthic foraminiferal assemblages

To enable modeling, a more accurate estimate of palaeobathymetry for the Sorbas Basin was required. A method commonly used to estimate palaeobathymetry is the benthic to planktic foraminifera ratio (B/P), wherein deeper water is associated with lower ratios. Benthic foraminifera are sensitive to bottom water oxygenation, such that during extended periods of anoxia, sediments can become completely devoid of these bottom-dwellers, irrespective of basin depth. To determine palaeobathymetry of the Upper Abad for the studied interval, due to the cyclical pattern of bottom water anoxia, the B/P ratio cannot be applied [*Van Hinsbergen et al.*, 2005; *Krijgsman et al.*, 2006]. Benthic foraminiferal assemblages, however, can provide constraints on palaeodepth, as well as more specific information about bottom water conditions. Twelve samples spanning UA5-7 were counted for benthic foraminifera species by Dr Tanja Kouwenhoven at Utrecht University, Netherlands. Details regarding the benthic foraminiferal assemblages have not previously been published; the results are shown in Ch. 3, section 3.3.3.

2.3.4 Seawater and sediment Nd and Pb

2.3.4.1 Acid-reductive leaching of bulk sediments

Nd and Pb extraction and isotope measurement was performed on sediments from the Sorbas Basin, Falconara, Monte del Casino, Monte dei Corvi, Metochia, and Ain el Beida

(Ch. 1, Fig. 1.21). A weak acid-reductive leach was applied to bulk sediment to extract the bottom water mass signal for Nd and Pb isotope analyses, a process which has been shown to be efficient and reliable in many cases [e.g. *Rutberg et al.* 2000; *Piotrowski et al.* 2004; *Piotrowski et al.* 2005; *Gutjahr et al.* 2007; *Gutjahr et al.* 2008; *Gutjahr et al.* 2009; *Böhm et al.* 2015]. This leaching process extracts FeMn oxyhydroxides which precipitate on and dispersed within sediment grains as they are deposited; REE and other trace metals are bound to these authigenic oxyhydroxides in the highest concentrations at the sediment-water interface and in the upper pore waters [*Palmer and Elderfield*, 1985; *Haley et al.*, 2004; *Roberts et al.*, 2012]. Thus, this authigenic oxyhydroxide component records the trace metal composition of ambient bottom water, assuming no major perturbations due to anoxia, although suboxic conditions do not always reset the isotope signature [e.g., *Haley et al.*, 2004; *Gutjahr et al.*, 2007]. Fine-grained sediment deposited under relatively quiet conditions is the most appropriate for this type of leaching. Approximately 300 mg of disaggregated, bulk unwashed sediment was used for neodymium isotope analysis. A weak leaching procedure was employed following [*Gutjahr et al.*, 2007] without prior decarbonation. Disaggregated sediment samples were agitated in 0.9 M $MgCl_2$ for two hours to remove easily exchangeable ions via cation exchange. While studies suggest that ammonium acetate is most appropriate for cleaning calcite for Sr analysis [*Melezhik et al.*, 2001], $MgCl_2$ has been shown to be more appropriate to bulk sediment for removing easily exchangeable or surficially adhered trace metals [*Tessier et al.*, 1979]. After multiple rinses with > 18.2 MΩ deionized water and separation via centrifugation, 10 mL of a leaching solution composed of 0.05M hydroxylamine hydrochloride, 15% v/v acetic acid, and 0.03 M EDTA (concentrations after combination of reagents) was allowed to agitate with samples for 2 hours. The leachate was separated, processed and purified using column chromatography following standard methods. A small aliquot of leachate was retained after separation to determine elemental ratios by Q-ICPMS. Disaggregation and leaching was performed in conventional laboratory conditions, while the processing and purification of the leachates was performed under clean lab conditions at GEOMAR Helmholtz Centre for Ocean Research Kiel (Germany) and SUERC (Scottish Universities Environmental Research Centre, East Kilbride, UK). Column chromatography was performed sequentially on the samples as follows: (1) lead was purified using BioRad AG1-X8 resin; (2) cation exchange with BioRad AG50W-X12 (200-400μm) resin was then employed to separate rare earth elements; and finally (3) Eichrom Ln resin was used to separate Nd from other REE.

2.3.4.2 *Strong leaching of bulk sediment*

To evaluate the effect of boundary exchange on the extracted bottom water signal, strong leaching as well as total dissolution were performed on a subset of the same samples from the Sorbas Basin (results in Ch. 4, section 4.4.1). A strong leach is necessary to assess the potential contribution of Nd or Pb from non-seawater derived components which may more readily exchange with the leaching solution, such as volcanic minerals, which tend to be more radiogenic than the overall bulk composition [*Wilson et al.*, 2013]. For the strongly leached samples, removal of the seawater signal was performed by repeated acid-reductive leaches with the same solution described in the previous section, first for 2 hours, then twice for 24 hours, centrifuging and removing the supernatant after each leach. Following leaching, the samples were rinsed three times with > 18.2 MΩ deionized water before agitating the material with a 5 mL solution of 3M HCl - 3M HNO_3 for 24 h.

2.3.4.3 *Total dissolution of bulk sediment*

The total dissolution procedure was more involved due to the persistence of organic matter within the samples which was highly resistant to oxidation. Similarly to the previous section, the seawater signal was removed by leaching first for 3 hours, then for 24 hours with centrifugation and removal of the leaching solution at each step. After rinsing twice and transferring to Teflon screw-top vials, organic matter in the samples was oxidized by step-wise addition of a total of 2 mL H_2O_2 combined with ultrasonification and refluxing overnight at 100°C. Vials were left with tops only lightly screwed down to allow degassing at room temperature until bubbling ceased, and refluxing was performed with sealed vials. After drying at 120°C, samples were oxidized following a process using the following procedure (flowchart, Fig. 2.4). 2 mL aqua regia was added and allowed to react on a hotplate at 100°C for 12 hours with vials open to allow degassing. Samples were dried overnight at 120°C. The following day, 3 mL aqua regia were added and allowed to react on a hotplate starting at 100°C followed by an increase in temperature to 130°C for reaction overnight. Vials were cooled, opened for degassing, resealed and left at 145°C again overnight; vials were again briefly cooled, opened for degassing, resealed and left overnight at 180°C. The next morning, vials were briefly cooled, opened for degassing, resealed and left for 48 h at 185°C. The samples were cooled then transferred with 5 mL 16 M HNO_3, 2 mL 12 M HCl, and 3 mL 29 M HF into specialized microwave digestion vessels. Temperature/pressure conditions were as follows: a ten minute ramp time was

allotted to reach 140°C and pressure between 10 to 15 bar; these conditions were maintained for 1 h, then the containers were left to cool. Samples were transferred back to teflon vials and dried. 350 μL of 9.5 M $HClO_4$ and 2 mL of 16 M HNO_3 were added and the samples were refluxed overnight at 120°C. Samples were then dried at 170°C, and the following sequence was performed three times to evaporate $HClO_4$: 1 mL concentrated HNO_3 was added, the samples were refluxed at 120°C for 7 h, then dried at 170°C overnight. Dissolution was confirmed by redissolving in 2 mL 8 M HNO_3; samples were dried down, then refluxed twice with 2 mL 1M HCl. Both the strong leach solutions and totally dissolved samples were processed and purified following standard column chromatography chemistry as above.

2.3.4.4 Fossil fish remains

Finally, to assess the impact of artefacts due to the acid-reductive leaching process as well as boundary exchange, fossil fish teeth and bone were analysed. Fish remains are arguably the most reliable archive of bottom water Nd isotope signatures [*Martin and Scher*, 2004], while Pb and Sr are not reliably recorded in fossil fish remains [*Martin and Scher*, 2004; *Basak et al.*, 2011]. Fossil fish teeth and bone fragments were hand picked under the microscope for samples from the same sediments described in section 2.2.1 above. Picked fish remains were vigorously cleaned by repeated ultrasonication in ultraclean deionized water and once in ethanol; they were then soaked in 0.9 M $MgCl_2$ for 1 h; this reagent was selected to maintain consistency between procedures applied for Nd extraction from both bulk sediment and fish teeth. Samples were thoroughly rinsed by repeated ultrasonication in deionized water, quickly rinsed once with 0.05M HNO_3, and dissolved in 0.5 mL 1M HCl in Teflon vials at 80°C. After drying, samples were purified as above, omitting the Pb purification column chromatography.

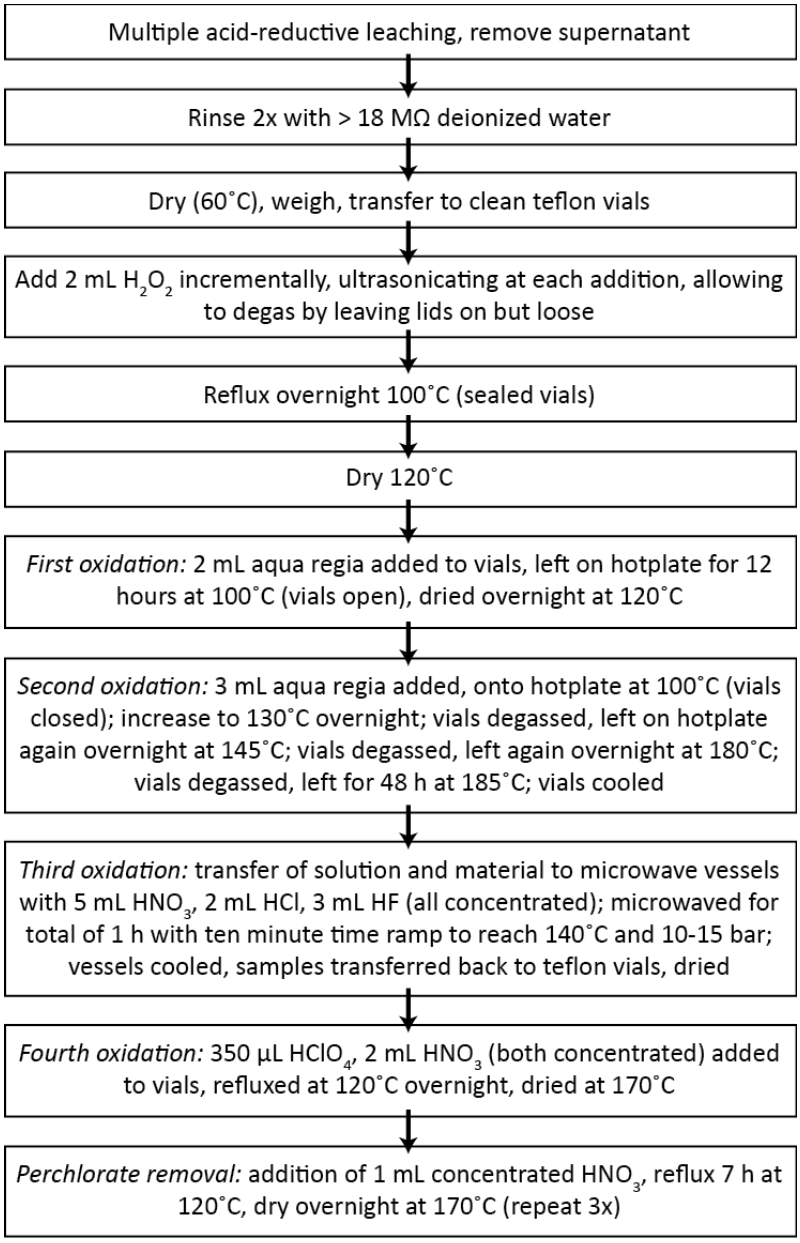

Fig. 2.4. Flowchart of total dissolution procedure.

2.3.5 Nd and Pb mass spectrometry

Neodymium and lead isotope analysis was performed on a Nu Plasma MC-ICPMS (multi-collector inductively coupled plasma mass spectrometer) or a Neptune Plus MC-ICPMS at GEOMAR Helmholtz Centre for Ocean Research Kiel (Germany). Nd samples were diluted to 50 ppb. All $^{143}Nd/^{144}Nd$ results were mass bias corrected to a $^{146}Nd/^{144}Nd$ ratio of 0.7219 and subsequently normalized to the accepted $^{143}Nd/^{144}Nd$ via adjustment of the consistency standard JNdi-1 $^{143}Nd/^{144}Nd$ to 0.512115 [*Tanaka et al.*, 2000]. External reproducibility (2 standard deviations, 2SD) for samples measured on the Nu Plasma machine was 0.42 ε_{Nd} based on repeated measurements of the secondary standard USGS-NOD-A-1 (n=11). For samples measured on the Neptune, external reproducibility for acid-

reductive and strong leach samples was 0.18 ε_{Nd} based on USGS-NOD-A-1 (n=22), and 0.13 ε_{Nd} for total dissolution samples based on Merck SPEX Nd standard (n=6). Procedural Nd blanks were as follows: less than 1.4 ng for acid-reductive leaching, less than 0.18 ng for strong leaching, and less than 0.12 ng for total dissolution; all are less than 1% of sample mass and therefore negligible.

The Nd isotopic signature is reported as ε_{Nd}, which corresponds to the deviation of a measured $^{143}Nd/^{144}Nd$ of a sample from CHUR in parts per 10^4 (0.512638, *Jacobsen and Wasserburg* [1980]). ε_{Nd} was calculated using equation 1.1 (Ch. 1). ε_{Nd} was further converted to $\varepsilon_{Nd(t)}$ to correct for ingrowth of ^{144}Nd due to ingrowth of ^{147}Sm after deposition using equation 2.1:

$$(^{143}Nd/^{144}Nd)_{(t)} = (^{143}Nd/^{144}Nd)_{(measured)} - \left(\frac{^{147}Sm}{^{144}Nd} * e^{\lambda t - 1}\right) \qquad [2.1]$$

where λ is the decay constant of ^{147}Sm (6.54×10^{-12}, *Dickin* [2005]) and t is time in years. This calculation is required to compare accurately samples of different ages, particularly where the samples are Miocene age or older. A $^{147}Sm/^{144}Nd$ ratio for the bulk earth of 0.1966 was used [*Dickin*, 2005], while for samples a $^{147}Sm/^{144}Nd$ ratio of 0.13915 was employed. This ratio was adopted from measurements of fish teeth and cleaned foraminifera by *Ivanoviç et al.* [2013]. Both fish teeth and foraminifera are dominated by the authigenic oxyhydroxide component. For this reason, and also because this value was measured on samples from the Atlantic-Mediterranean gateway region, it is assumed that ratio is adequate for use here.

Lead samples were diluted to 28 ppb and doped with NBS 997 Thallium solution to 7 ppb, aiming for an approximate Pb/Tl ratio of 4. All Pb results from the Nu Plasma were corrected using standard sample bracketing, correcting to the accepted value of primary standard NBS 981 [*Baker et al.*, 2004], while Neptune data were internally corrected using the $^{205}Tl/^{203}Tl$ ratio of 2.3897. External reproducibility for samples measured on the Nu Plasma are as follows: $^{208}Pb/^{204}Pb$ = 0.014, $^{207}Pb/^{204}Pb$ = 0.006, $^{206}Pb/^{204}Pb$ = 0.018, $^{208}Pb/^{206}Pb$ = 0.0004, and $^{207}Pb/^{206}Pb$ = 0.00013, based on secondary standard NBS 982 (n=53). External reproducibility for samples measured on the Neptune are as follows: $^{208}Pb/^{204}Pb$ = 0.007, $^{207}Pb/^{204}Pb$ = 0.002, $^{206}Pb/^{204}Pb$ = 0.002, $^{208}Pb/^{206}Pb$ = 0.0002, and $^{207}Pb/^{206}Pb$ = 0.00004, based on secondary standard USGS NOD-A-1 (n=32). Procedural Pb blanks were less than 0.7 ng for acid-reductive and strong leaching samples, lower than

1% and therefore negligible. The procedural blank for the total dissolution samples was 1.22 ng, between 0.8 and 3.4% of sample mass, necessitating blank correction. Monitoring for both Nd and Pb between analytical sessions and for matrix effects was performed using standard ferromanganese nodule powders USGS-Nod-A-1 and Nod-P-1 [*Flanagan and Gottfried*, 1980] with all results falling well within analytical error between sessions.

2.4 Methodology applied to ferromanganese crust 3516-4

Ferromanganese (FeMn) crust 3514-6, dredged from the Lion Seamount (35˚ 13'N, 15˚ 42'W) from a water depth of approximately 800 m, 3516-4 is thought to be suitable for measuring palaeo-MOW characteristics (Ch. 1, section 1.4.1) [*Hoernle et al.*, 2003; *Muiños et al.*, 2008]. Previously published Nd isotope data (Table 2.2; see also Ch. 1, Fig. 1.20) suggest crust 3514-6 was bathed by the MOW plume in the modern environment (see also Fig. 2.1d) and accreted in a separate water mass to the other major regional water masses, NE Atlantic Deep Water (NEADW) and Antarctic Intermediate Water (AAIW) [*Muiños et al.*, 2008].

2.4.1 High temporal resolution Pb isotope record

Due to the extremely slow growth rates of FeMn crusts (a few mm per Ma), the previously published Nd and Pb isotope data derived from 3514-6 using solution-based processing methods are of a resolution too coarse to detect events on the time scale of the MSC. Therefore, a thick section of crust 3514-6 was sampled via Laser Ablation Multi-Collector ICPMS (LA-MC-ICPMS). The temporal resolution of LA-MC-ICPMS is dependent on the laser spot size and material growth rate. Laser ablation is capable of providing data with ~ 15 ky time resolution for this material, compared to approximately 0.75 My between measurements from the previous solution-based analyses. One drawback of the LA-MC-ICPMS method is the inability to remove some isobaric interferences. For this project, only Pb isotopes have been measured accurately since interference, most likely with $^{130}Ba^{16}O$ and/or $^{130}Te^{16}O$, prevented accurate measurement of Nd isotopes. Such isobars can present a significant interference on mass 146 that is highly problematic as the Nd isotope ratios are internally mass bias corrected using the $^{146}Nd/^{144}Nd$ ratio. Though relative abundance of ^{130}Ba is small relative to the other isotopes of this element, the concentration of Ba in crusts in the North East Atlantic is observed to be 3 to 7 times higher than Nd [*Muiños et al.*, 2013]. Te is also commonly highly enriched in hydrogenous FeMn crusts with

concentrations up to ~ 200 ppm [*Hein et al.*, 2003]. For eighteen crusts from the North Eastern Atlantic, Te concentrations ranged from 11 to 71 ppm (average 48 ppm), compared to Nd concentrations of 55 to 339 ppm (average 238 ppm) [*Muiños et al.*, 2013].

Table 2.2. Summary of published characteristics of crust 3514-6 [*Muiños et al.*, 2008].

Origin	Coordinates	Water depth	Published Growth Rates
Lion Seamount, cone at SW margin	35° 12.7 – 13.0' N 15° 42.03 – 42.36' W	688 to 938 m	0 – 9.5 mm, 1.37 mm/Ma 9.5 – 17 mm, 2.45 mm/Ma 17 – 23.5 mm, 1.25 mm/Ma

2.4.2 Cosmogenic ^{10}Be extraction procedure

Using cosmogenic beryllium (^{10}Be) dating, [*Muiños et al.*, 2008] found growth rates between 1.25 to 2.45 mm/Ma for crust 3514-6 (Table 2.1). FeMn crusts exhibit a botryoidal, undulating laminated texture (Fig. 2.5). Therefore, it cannot be assumed that the growth pattern of the portion of crust 3514-6 used for previous analyses is identical to the sample procured for this project. Thus, a sample specific growth model was generated. Furthermore, considering the high temporal resolution which can be achieved with the *in-situ* laser ablation methodology compared to solution-based methodology, it was important to attempt to provide higher resolution age constraints. Contrary to the conventional method of drilling a profile perpendicular to growth, subsamples were removed at regular intervals parallel to laminations using a microdrill fitted with a 0.5 mm diametre tool (Fig. 2.5b). This method was chosen to enable extraction of a larger number of samples than normally possible by the conventional method. Approximately 15 to 60 mg of material was removed, with aliquot size increasing with depth in the crust to account for lower ^{10}Be concentrations due to decay. As the material is brittle, some closely-spaced drill tracks generated chips (Fig. 2.5e). These were removed and discarded.

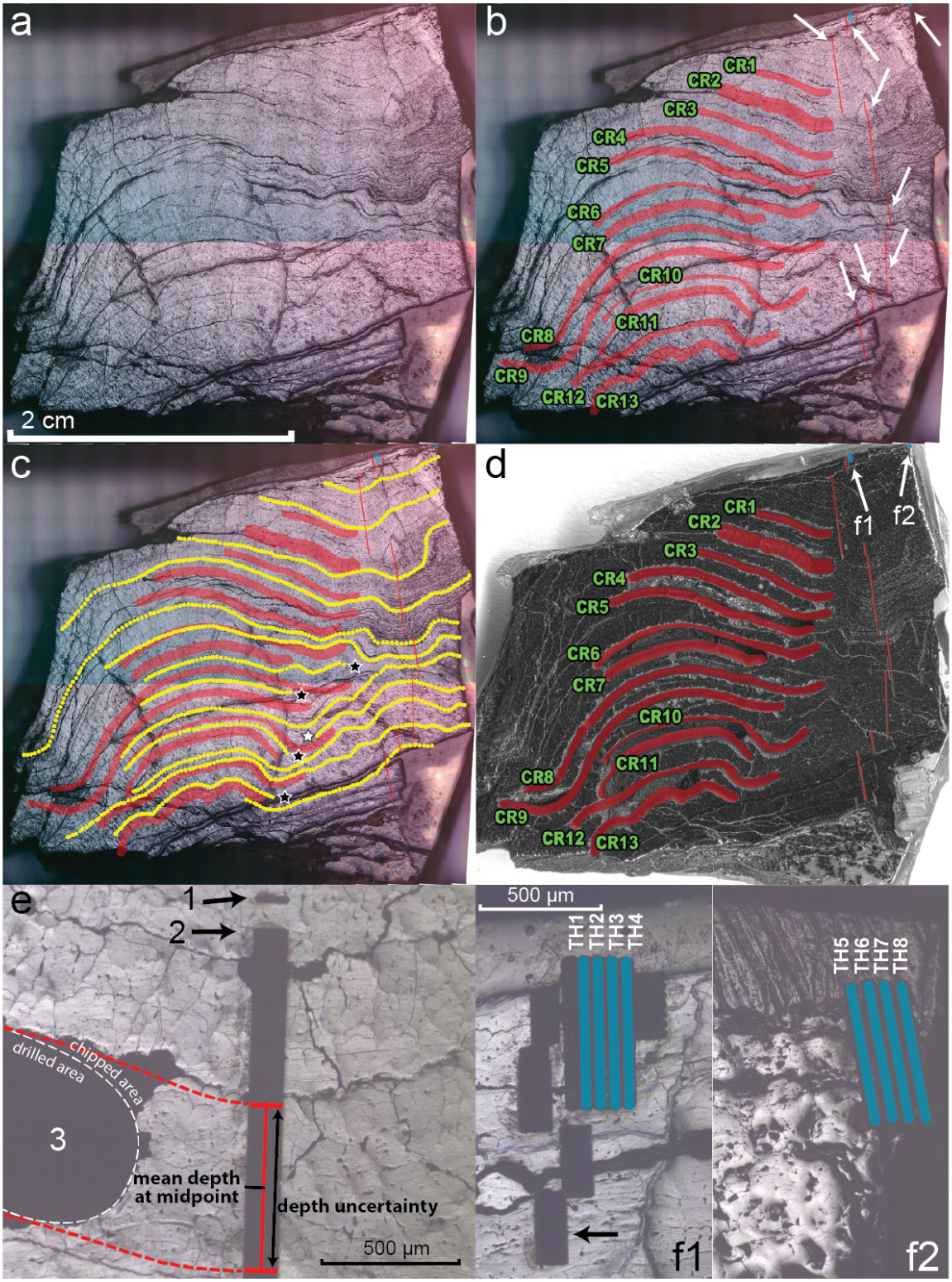

Fig. 2.5. (a) Spliced image of thick section of crust 3514-6 before analysis; image prepared using 5x objective and automatic stage to enable automatic splicing with Zeiss Axio software. (b) Location of subsamples removed for ^{10}Be measurement (labelled CR1-13) and ablation tracks (arrows). Ablation for Pb in red; ablation for $^{230}Th_{excess}$ in blue at upper left (2 positions). (c) Major laminations highlighted to illustrate spatial arrangement. Black stars indicate laminations disappearing towards the right; white star indicates lamination disappearing towards the left. (d) High resolution scanned image of section of 3514-6 after drilling and ablating with respective areas highlighted as in (b) and (c); arrows indicate location of $^{230}Th_{excess}$ ablations. (e) Explanation of how depth assignments are made for Be subsamples, with detail of textures and subsample size. Red dashed lines indicate laminations followed from edges of Be subsample to ablation profile; midpoint of distance between the lines is the assigned Be subsample depth, while depth uncertainty is the total distance. Arrows 1, 2: single and groups of ablation lines respectively (ablated horizontally) for Pb; 3 indicates an area sampled for Be, with illustration of area of sample used for analysis (accidental chippings were discarded). (f) Detail of ablations performed for $^{230}Th_{excess}$ measurements (blue); f1, f2 correspond to arrows in (d). Arrow indicates group of 20 horizontal line scan Pb ablations.

Fig. 2.5 shows the sample of crust 3514-6 used for this project, the locations of the subsamples removed for beryllium extraction, the locations of the ablation tracks, and the structure of the laminations. Individual depths of each Be sample were assigned by determining the corresponding depth in the laser ablation profile (Fig. 2.5). Extrapolation in some way is required as the ablation profile was performed to the right of the Be samples; as is shown in Fig. 2.5a, the laminations are quite variable across the sample and simply measuring depth from the surface along two separate profiles is inadequate. It is assumed that obvious laminations which can easily be traced from one place to another are the most accurate markers of equal time from one location in the crust to another. The ablation depth information is more precise and accurate than the Be sample location, due to the precision automatic stage controlling the laser ablation cell which allows for movement in sub-micrometre increments. In particular, the depth relative to the crust surface at the location of the ablation profile, and the ablation spot depths relative to each other, are much better known in comparison to the Be subsamples. To perform the extrapolation, the laminations bordering above and below each Be subsample were identified and followed to the ablation profile. The two ablations corresponding to each 'marker' lamination were identified, allowing determination of two boundary depths for each Be sample. The depth assigned to each Be sample is the mid-point between these boundaries. The uncertainty assigned is the distance from mid-point to boundary (Fig. 2.5e); thus, depth uncertainty is a linear measurement rather than a calculated value. In some instances, depths could not be assigned in this manner due to the fact that laminations disappeared. This has implications for the age model as this suggests that material is missing, due to either dissolution a hiatus in growth. The depths for these samples were estimated roughly by using a similar process as above; rather than employing laminations immediately adjacent to the subsamples, the closest available continuous laminations were used. The depth uncertainty is, appropriately, expanded for these samples but their relative order is correct in terms of age.

Between 11 and 58 mg of the Be subsamples were dissolved in 1 mL of 6M HCl in Teflon vials on a hotplate (T=100ºC) for 1 h. After cooling, a 50 µL aliquot was taken to measure the natural ^{9}Be concentrations by ICPMS. Afterwards, the remaining solutions and corresponding procedural blanks were spiked with between 260 and 350 µg of ^{9}Be carrier. At each step, samples, aliquots and/or additions were carefully weighed. The solutions were passed through anion exchange columns to remove Fe, precipitated by increasing pH to ~8.5 with ammonia, and the Mg-containing supernatant was removed. The precipitated hydroxides were redissolved by addition of H_2SO_4 dropwise until all material was dissolved. Be was extracted using cation exchange chromatography. The separate Be

fractions were again precipitated as $Be(OH)_2$ by taking the solution to pH 8-8.5 with ammonia, dried, and baked at 900ºC to form BeO. BeO samples were mixed with Nb and analysed by AMS. Natural ^{9}Be concentrations were measured by quadrupole ICPMS (Q-ICPMS) after initial digestion but before addition of the ^{9}Be carrier necessary for AMS measurements or any other processing. In total, thirteen subsamples were removed and purified over two analytical sessions. Beryllium samples were measured at the Accelerator Mass Spectrometry (AMS) facility at SUERC. ^{10}Be concentrations were derived from comparison of measured ratios to the certified 2.79 x 10^{11} $^{10}Be/^{9}Be$ ratio of NIST SRM4325 standard [*Maden et al.*, 2007; *Xu et al.*, 2010]. The processed blank ratios were between 0.04 and 1% of the sample $^{10}Be/^{9}Be$ ratios. The uncertainty of this correction is included in the stated standard uncertainties.

The age model is generated using the most recently determined half-life ($t_{1/2}$) for ^{10}Be of 1.387 ± 0.012 My [*Chmeleff et al.*, 2010] and the generic exponential decay equation [2.2]:

$$N_{(t)} = N_{(0)}\, e^{-\lambda t} = N_{(0)}\, e^{-\lambda (d/GR)} \qquad [2.2]$$

where $N_{(t)}$ is the concentration of ^{10}Be at time t, $N_{(0)}$ is the initial concentration of ^{10}Be extrapolated for the surface of the crust, and λ is the decay rate, equal to $\ln(2) / t_{1/2}$. The relationship t = d / GR, where d is depth and GR is growth rate, is substituted to calculate growth rate. Thus ages can be assigned to each ablation data point.

The common method of calculating growth rates for FeMn crusts using cosmogenic beryllium is to normalize the concentration of ^{10}Be to that of the natural ^{9}Be in the crust. In this case, the extrapolated $^{10}Be/^{9}Be$ ratios are substituted for ^{10}Be atoms/g of crust in the exponential decay equation. A discussion of both approaches accompanies the data in Ch. 6, section 6.4.1.

2.4.3 Laser ablation MC-ICPMS procedure

Ablation of the FeMn crust material was carried out with a New Wave UP193fx ArF excimer laser (λ = 193 nm, pulse length < 4 ns) equipped with a LFC (large format cell) using a laser fluence of 2.5 J/cm^2. Ablations consisted of 120 μm lines parallel to laminations with a spot size of 15 μm, a scan speed of 2 μm per second and a frequency of 20 Hz. Ablated material was carried from the ablation cell with Helium carrier gas (flow

rate 0.45 – 0.5 L/min) and mixed with Ar (flow rate ~ 1 L/min) before plasma ionization and induction into a VG Axiom MC-ICPMS. Cool gas and auxiliary gas flow rates were 17 and 0.9 L/min respectively. Cup configuration is shown in Table 2.3; signal was integrated over 5 s intervals.

NIST SRM 610 was the primary standard employed to correct the LA Pb isotope data for mass bias and drift. This standard is a homogenized glass wafer with well-characterized elemental and isotopic compositions commonly used for laser ablation measurements. USGS standard reference materials, NOD-A-1 and NOD-P-1 are prepared standard powders made from ferromanganese nodules from the Atlantic and Pacific, respectively; thus, these standards have a similar matrix to the sample, crust 3514-6. These materials were pressed into pellets at 30 psi, dehydrated at 40°C for several days, and subsequently used as secondary standards to monitor the ablation process and the mass bias correction procedure. Due to heterogeneity at the length scale of the ablation settings, these secondary standards do not produce a mass bias correction as accurate and precise as that produced using NIST 610.

Table 2.3. Cup configuration for LA-MC-ICPMS Pb isotope measurements.

Cup	L3	L2	L1	Axial	H1	H2	H3
Mass	202	203	204	205	206	207	208

Over 2,000 sample ablations were performed; data were reduced using a script written in Matlab. The calculations performed were as follows: initially, ratios were calculated from the slope of a regression of the intensities of the two isotopes involved; the intensity of ^{204}Pb for ^{204}Hg interference was corrected in the same step by subtracting a value equal to 0.2334 times the appropriate ^{202}Hg intensity. The regression also provides a 95% confidence interval to estimate measurement uncertainty for each ratio. Standard-sample bracketing was used to correct the ratios for mass bias and drift effects using NIST 610, with ten sample ablations performed between standard measurements. The correction calibration was performed by linear interpolation between successive NIST 610 measurements, providing a better correction for drift effects than a simple average between points. The reported uncertainty of corrected sample data is calculated by propagating together the 95% confidence interval, derived from the counting statistics of individual measurements in the regression, with the same uncertainty calculated for the relevant calibration standards (NIST 610). Corrected secondary standard measurements (n = 214 for both NOD-A and NOD-P) are shown in Appendix 2.

2.4.4 $^{230}Th_{excess}$ measurement

In the following section A($^{xx}I/^{xx}I$) denotes activities or activity ratios, rather than concentrations or isotope ratios, following convention. $^{230}Th_{excess}$ is defined as ^{230}Th activity less ^{234}U activity. Again employing the general equation for exponential decay, the growth rate determined from $^{230}Th_{excess}$ can be calculated from [2.3]:

$$\ln A = \ln A_0 - (\lambda_{230}\, t) = \ln A_0 - (\lambda_{230}(d/GR)) \qquad [2.3]$$

where A is the activity at time t, A_0 is the initial activity, λ_{230} is the decay constant for ^{230}Th, and substituting GR = d/t where GR is growth rate and d is the depth in the crust. [2.3] can be simplified to calculate directly from the slope of a semi-logarithmic plot of $^{230}Th_{excess}$ versus depth [2.4]:

$$GR = \lambda_{230} / \text{slope} \qquad [2.4]$$

This is likely the first application of LA-MC-ICPMS to estimate $^{230}Th_{excess}$ in FeMn crusts; the author has not found any similar methodologies in the published literature. Profiles were measured with the same instruments and similar laser settings as for Pb. The use of He (in comparison to Ar) in the ablation cell has been shown to improve the relative sensitivity of Th [*Stirling et al.*, 2000; *Jackson et al.*, 2004]. Eight ablation tracks were performed from the surface of the material perpendicular to laminations; each track was 600 μm using a spot size of 50 μm, a scan speed of 5 μm/s and a frequency of 50 Hz. ^{232}Th and ^{238}U intensities were measured on Faraday cups, while ^{230}Th and ^{234}U intensities were measured on single (or continuous) dynode multipliers ('channeltrons') during which the signal was integrated over 2 s intervals. Standard NIST 610 was employed to tune the instrument for optimal sensitivity. This standard has a Th/U elemental concentration ratio of ~ 1 (NIST certified values: Th 457.2 ± 1.2 ppm, U 461.5 ± 1.1 ppm); the measured Th/U elemental ratio was 0.54 after optimization. This large elemental fractionation, and its potential effect on determined growth rates, is discussed further here. Relative collector yields or other mass bias effects were not independently estimated. Rather, a novel approach was used to estimate an overall correction factor for relative collector efficiency, elemental fractionation, and any mass bias effects based on the portion of data acquired on the section of material at secular equilibrium. Th/U elemental fractionation measured using NIST SRM610 was factored into the measured $^{232}Th/^{238}U$ intensities, which were then converted from mass into activity ratios using their respective half-lives. The overall

calculated correction factor for (^{232}Th/^{238}U) was thus ~ 1.67. Following this, the activity ratios for the remaining activities of interest A(^{230}Th/^{232}Th), A(^{234}U/^{232}Th), and A(^{234}U/^{238}U) were corrected for fractionation effects and converted to activities iteratively, determining the factor necessary to force the data from the portion of crust in secular equilibrium to give the expected value of unity (ie, A(^{230}Th/^{238}U) = A(^{234}U/^{238}U) = 1). At minimum, the final 250 μm of the ablation tracks generated for these measurements are in secular equilibrium; this is shown in the results section (Ch. 6, Fig 6.3a, b).

2.5 Published data: ferromanganese crust chronology, correction of ^{10}Be values for new half-life, and conversion of published ε_{Nd} to $\varepsilon_{Nd(t)}$

In addition to data generated from crust 3514-6 through this project, published Nd and Pb isotope records from FeMn crusts 3514-6, 3511-1, 3513-14 [*Muiños et al.*, 2008], and 121DK and 65GTV [*Abouchami et al.*, 1999] are used to constrain Miocene isotopic water mass signatures (see Fig. 2.1a, d and Table 2.4 for locations and details for all crusts discussed here). The original age model for these crusts used a half-life of 1.5 My for ^{10}Be, corrected here using the updated half-life for ^{10}Be of 1.387 My [*Chmeleff et al.*, 2010]. As for 3514-6, 65GTV was dredged from the Lion Seamount, also from water depths consistent with the Mediterranean outflow plume (approximately 1500 m water depth). 3511-1 was sourced from about 2300 m water depth, consistent with North Eastern Atlantic Deep Water (NEADW), the current flowing beneath Mediterranean outflow outside the Gulf of Cadiz. 3513-14 was sampled deeper still (~ 4595 m) and is likely to have recorded Antarctic Intermediate water (AAIW). 121DK grew on the Tropic Seamount off NE Africa, approximately 500 km southwest of the Canary Islands, at about 2000 m water depth. It is used to provide further estimates for palaeo-NEADW, as this location is farther from Gibraltar and should not be influenced by MO. See Fig. 2.1d for an idealized diagram of water mass spatial distribution. A glossary of acronyms for water masses is included in the front matter of this thesis.

Published data for 65GTV and 121DK [*Abouchami et al.*, 1999] were not originally converted to $\varepsilon_{Nd(t)}$; this is necessary to enable comparison to other data including that generated for this project. In absence of direct measurements, a ^{147}Sm/^{144}Nd ratio of 0.115 was applied to correct for post-depositional ingrowth of ^{146}Nd from the decay of ^{147}Sm. This value was chosen as it is commonly employed in studies of FeMn crusts for this correction [e.g., *Frank et al.*, 2003; *Muiños et al.*, 2008]. This ratio may not be accurate as

evidenced by the range of $^{147}Sm/^{144}Nd$ ratios observed in NE Atlantic FeMn crusts, from 0.137 to 0.174 [*Muiños et al.*, 2013]. However, considering a large range of $^{147}Sm/^{144}Nd$ values reported for crusts (0.115 to 0.174, *Muiños et al.* [2008, 2013]) the difference generated in the absolute $\varepsilon_{Nd(t)}$ value is less than 0.05 ε_{Nd} units for the age range of interest. This is negligible relative to analytical uncertainty, and for consistency with the literature the value 0.115 is employed.

Table 2.4. Locations and details of ferromanganese crusts discussed in this thesis.

Crust	Coordinates	Location	Water depth, m	Water Mass	Ref
3514-6	35˚ 13'N, 15˚ 42'W	Lion Seamount	688 to 938	MOW	1, 2
3511-1	36˚ 31'N, 14˚ 13'W	Josephine Seamount	2436 to 2161	NEADW	2
3513-14	36˚ 58'N, 15˚ 45'W	Madeira-Tore Rise	4586 to 4603	NEADW, AABW	2
121DK	24˚ 53'N, 21˚ 42'W	Tropic Seamount	2000	NEADW	3
65GTV	35° 20'N, 15° 20'W	Lion Seamount	1500	MOW	3

Ref: 1 – this study; 2 – [*Muinos et al.,* 2008]; 3 – [*Abouchami et al.,* 1999].

2.6 Numerical Box Modeling – Sorbas Basin

To explore the relative hydrological flux implications of the Sr isotope data (Ch. 3) for the Sorbas Basin, numerical box modeling was performed. According to *Bryden and Kinder* [1991], *Nielsen* [1912] was the first to use numerical relationships to estimate fluxes at Gibraltar. The work presented here is based on relationships described by *Flecker et al.* [2002], *Meijer* [2006] and *Topper et al.* [2011, 2014] and provides quantitative constraints on the hydrologic budget and inter-basin exchange required to reproduce the Sr data. These authors examined the Sr isotope and salinity evolution, as well as exchange, for the Mediterranean during the Messinian by coupling mass balance equations for water, salinity and $^{87}Sr/^{86}Sr$ ratio. The $^{87}Sr/^{86}Sr$ data (Ch. 3), as well as previously observed patterns in lithology and ecology, are used to validate the model results.

Steady state solutions provide initial estimates of the inflow (Q_I), outflow (Q_O), and river water (Q_R), evaporation (E) and precipitation (P) fluxes required to effect change in the $^{87}Sr/^{86}Sr$ ratio of the basin while maintaining appropriate salinities. Here, we consider all terms to contribute to the overall hydrologic budget of the Sorbas Basin box (including exchange, Q_I and Q_O, between the Mediterranean and Sorbas Basin), whereas Q_R, E and P define the freshwater budget of the basin box. Transient solutions are required to assess the amount of time required to reach a Sr isotope anomaly and to investigate the dynamic

temporal evolution of hydrologic budget parameters. The equations used in the box model are detailed in the following section.

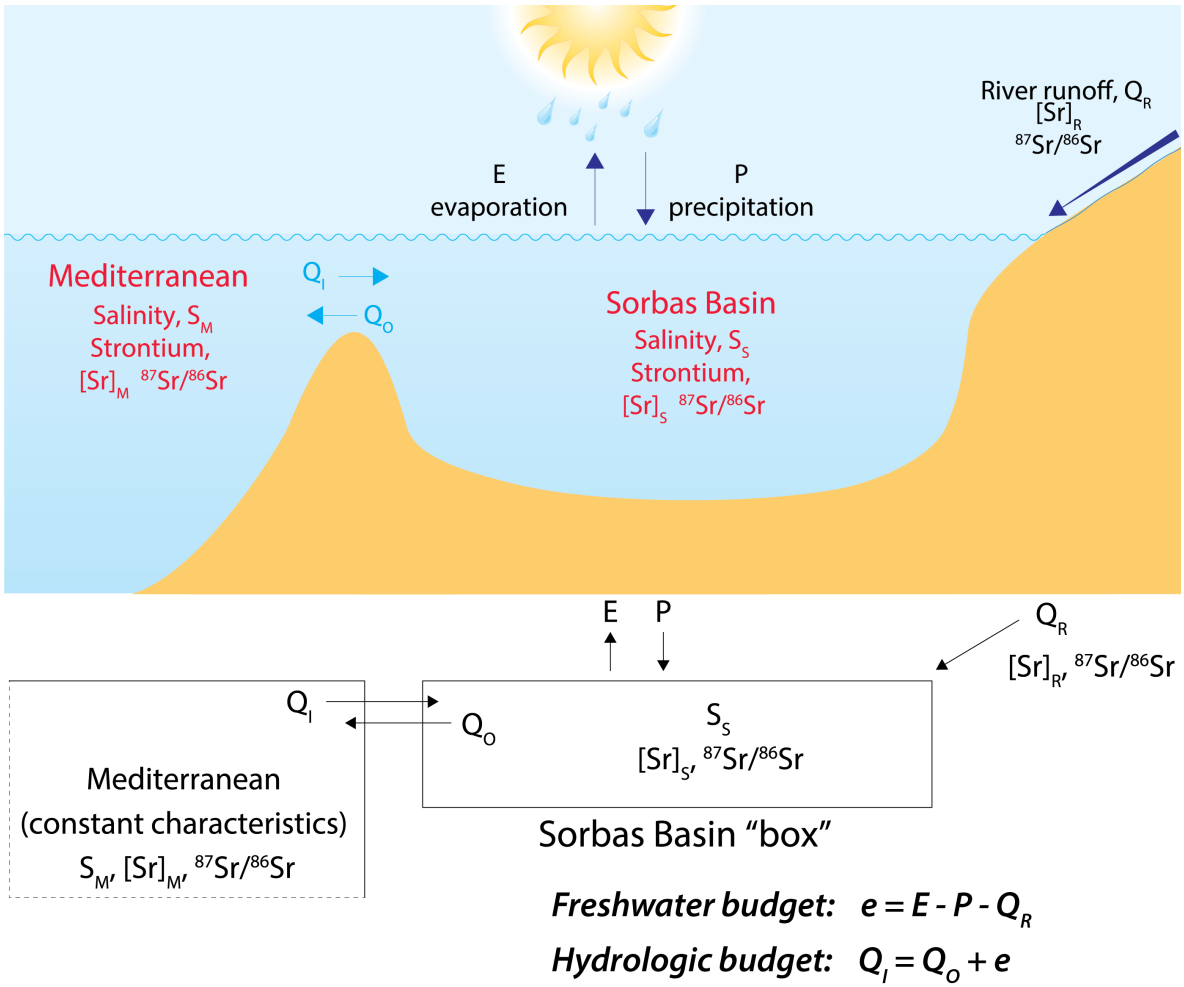

Fig. 2.6. Spatial illustration of model parameters and their relationships. The Sorbas basin is treated as one box, with fluxes of Q_I and Q_O (inflow from and outflow to the Mediterranean respectively) and Q_R (river runoff), all with associated [Sr] and $^{87}Sr/^{86}Sr$ isotope ratio. Q_I and Q_O also have associated salinity. Fluxes E (evaporation) and P (precipitation) are assumed to have no associated salinity or Sr. All fluxes together compose the overall hydrologic budget of the Sorbas Basin box; only those with no associated salinity, E, P, and Q_R, make up the freshwater budget.

2.6.1 Equations

The previously published equations are modified here to describe flow in and out of one basin (represented by one box, Fig. 2.6) and appropriate geometric and isotopic constraints appropriate for the Sorbas Basin at ~ 6.57 Ma, the interval mid-point, are applied. Fig. 2.6 illustrates the relationship between each parameter spatially. In the following, subscript S denotes a property relevant to the water in the Sorbas basin; subscript M, Mediterranean; and subscript R, rivers flowing into the Sorbas Basin.

Fluxes are denoted by Q and have units m^3/s; note that E and P are also fluxes. Inflow (Q_I) is the rate of Mediterranean water entering the Sorbas basin, while (Q_O) is the rate of Sorbas Basin water flowing back into the Mediterranean:

$$dV_S / dt = Q_O + (E - P - Q_R) - Q_I = Q_O + e - Q_I \quad [2.5]$$

where V is volume and e [m^3/s] = evaporation (E) minus precipitation (P) minus river influx (Q_R), or the total freshwater budget. For a steady state system, the dV_S/dt term goes to zero resulting in:

$$Q_I = Q_O + e \quad [2.6]$$

As sea level, and thus the volume of the Sorbas Basin, is assumed constant (see discussion Ch. 3, section 3.4.1.1), the steady state equation [2.6] is used in both steady state and transient simulations. Note that a positive value of e indicates a negative freshwater budget; i.e., when freshwater loss due to evaporation exceeds input by precipitation and river inflow, e is positive. This condition of positive e is the general case for a landlocked basin such as the Mediterranean due to the fact that evaporation exceeds precipitation at mid-latitudes [*Peixoto and Kettani*, 1973]. Outflux is controlled by a difference in density between exchanging water masses, and is approximated as per *Meijer* [2006] and references therein:

$$Q_O = g\,*(S_S - S_M) = g*\Delta S \quad [2.7]$$

where ΔS is the difference in salinity [g/L], between the two connected basins. The constant *g* is a linear exchange coefficient related to the efficiency of exchange between the basins and has units of m^3/s per g/L. When no salt deposition occurs, a condition appropriate for pre-MSC Sorbas, the following applies:

$$V_S*dS_S / dt = (Q_I*S_M) - (Q_O*S_S) \quad [2.8]$$

In steady state:

$$Q_O*S_S = Q_I*S_M \quad [2.9]$$

The concentration of Sr in the basin is described by:

$$V_S * d[Sr]_S / dt = Q_I * [Sr]_M + Q_R * [Sr]_R - Q_O * [Sr]_S \quad [2.10]$$

In steady state:

$$Q_O * [Sr]_S = Q_I * [Sr]_M + Q_R * [Sr]_R \quad [2.11]$$

where Q_R is the influx from rivers with associated [Sr]. The Sr isotope ratio is described by:

$$V_S * [Sr]_S * dRatio_S / dt = (Ratio_R - Ratio_S) * Q_R * [Sr]_S + (Ratio_M - Ratio_S) * Q_I * [Sr]_M \quad [2.12]$$

In steady state:

$$Ratio_S = [^{87}Sr]_S / [^{86}Sr]_S = (Q_I * [^{87}Sr]_M + Q_R * [^{87}Sr]_R) / (Q_I * [^{86}Sr]_M + Q_R * [^{86}Sr]_R) \quad [2.13]$$

where $Ratio_S$ refers to the $^{87}Sr/^{86}Sr$ ratio of the water in the Sorbas Basin. Equation 2.13 is based on the identity that the concentration of the isotopes and concentration of the element are related by the following:

$$[^{87}Sr] = ((^{87}Sr/^{86}Sr) / (1 + (^{87}Sr/^{86}Sr)) * [Sr] \quad [2.14]$$

$$[Sr] = [^{87}Sr] + [^{86}Sr] \quad [2.15]$$

Square brackets denote concentration; round brackets surround the ratio for readability in [2.14]. The final equation neglects the presence of ^{84}Sr and ^{88}Sr as the only isotopes of interest in the system are ^{87}Sr and ^{86}Sr, and the only isotope whose concentration changes relative to the concentration of the other isotopes is ^{87}Sr (via beta decay of ^{87}Rb). All other isotope concentrations remain fixed relative to each other, and thus can be neglected.

2.6.2 Parameter selection

Several parameters must be estimated to enable modeling of the Sorbas Basin system, as direct measurements are unavailable. Available and assumed constraints used are summarized in Table 2.5. Only Sorbas Basin Sr isotopic compositions that fall outside the contemporaneous global marine Sr isotope range (0.708965±20 [*McArthur et al.*, 2012]),

including their respective analytical uncertainty, are considered anomalous. The minimum anomalous $^{87}Sr/^{86}Sr$ isotope ratio is therefore 0.709003 as analytical uncertainty for the set of Sr isotope measurements presented in Ch. 3 is 18 x 10^{-6}. Basin surface area is estimated from constraints on Sorbas Basin palaeogeography (section 2.2.1) and depth is estimated from benthic foraminiferal assemblages (section 2.3.2, results in Ch. 3, section 3.3.3).

Table 2.5. Summary of constraints used for box modeling.

Parameter	Value	Reference
Sorbas basin geometry		
Surface area	1.2 x10^9 m^2 (30,000 m x 40,000 m)	[*Krijgsman et al.*, 2001; *Do Couto et al.*, 2014]
Depth	200 m	Ch. 3, section 3.3.3
Volume	2.4 x 10^{11} m^3	Section 2.2.1
[Sr]		
Mediterranean	8 mg/L	Palmer and Edmond, 1989; Frank, 2002
Sorbas basin	8 mg/L (initial)	
River	0.3 mg/L (0.1 – 0.5 mg/L)	Ch. 3, section 3.2
$^{87}Sr/^{86}Sr$		
Mediterranean	0.708965	[*McArthur et al.*, 2012]
River	0.709097	Ch. 3, section 3.2
Salinity		
Mediterranean	35 - 37 g/L	Section 2.2.6
Sorbas basin	30 – 49 g/L	Section 2.2.6
River	0 g/L	
Sorbas Basin Freshwater Budget		
Evaporation (E)	41.77 – 43.27 m^3/s	Section 2.2.6
Precipitation (P)	8.85 – 12.11 m^3/s	(min – max; annual means)

Planktic foraminifera are present throughout the entire interval studied [*Pérez-Folgado et al.*, 2003] suggesting salinity in the basin during this interval never exceeded 49 g/L, a concentration tolerance determined from modern-day foraminifera and salinity measurements in the Red Sea [*Fenton et al.*, 2000]. Faunal assemblages reported here and published previously [*Pérez-Folgado et al.*, 2003; *Sierro et al.*, 2003] also indicate that the basin did not decline to brackish conditions. Laboratory experiments have shown that some species of planktic foraminifera thrive at salinities as low as ~ 25 g/L [*Bijma et al.*, 1990]; however the atlas of *Hillbrecht* [1996] indicates the natural abundance of extant planktic foraminifera drops to zero between 32 and 33 g/L. For the box model constraint, a minimum salinity of 30 g/L was chosen; this is an intermediate value between the available constraints, but slightly nearer the value observed in the modern environment and therefore likely more realistic than the experimental value. Thus, the salinity of the Sorbas 'box'

must remain within the range 30 to 49 g/L for model results to be considered. Mediterranean salinity is assumed to be constant through time at 37 g/L based on the modern Alboran Sea average [*Levitus and Boyer*, 1994]. The assumption of constant salinity is not entirely correct, but is not as critical as for other Mediterranean regions due to the fact that the proximity to Gibraltar, and the constant mixing of incoming Atlantic water with outgoing Mediterranean water, causes much smaller salinity fluctuations in the Alboran Sea compared to that observed in other Mediterranean subbasins further east. The upper water mass in the Alboran Sea (westernmost Mediterranean, Fig. 2.1d) is aptly named Modified Atlantic Water (MAW) as it consists of Atlantic water which has been partially modified by mixing with MO [*Millot*, 1999]. As the Alboran is most proximal to Gibraltar, and thus is strongly influenced by Atlantic water, the westernmost Mediterranean has experienced smaller changes in salinity than the rest of the Mediterranean basin over the past 16,000 years [*Emeis et al.*, 2000]. The sensitivity of the model to this salinity selection is considered further in Ch. 3, section 3.3.6.

Values for freshwater budget terms E and P are taken from results from global general circulation model (GCM) HadCM3L (UK Hadley Centre Coupled Model, version 4.5). experiments performed by Dr Alice Marzocchi at the University of Bristol. Twenty-two steady-state snap-shot simulations were evenly distributed in time at 1 ky intervals over a real precessional cycle between 6.568 and 6.589 Ma [*Marzocchi et al.*, 2015]. This particular precessional cycle falls within the interval studied here; furthermore, the precession cycles both preceding and following are relatively similar in their insolation values. While there are other datasets available estimating values of evaporation and precipitation for the Late Miocene Mediterranean region [e.g., *Gladstone et al.*, 2007; *Bosmans et al.*, 2015c], the HadCM3L results employed here are the only dataset available which quantifies the variability (maximum, minimum, and intermediate values) of late Miocene E and P throughout a precessional cycle. Orbital parameters for the GCM experiments for each simulation were selected from the orbital solution of *Laskar et al.* [2004], allowing each snapshot to use the true insolation forcing for that time, and thus the true variability throughout a precessional cycle is tested and expressed. The full experimental design is published in *Marzocchi et al.* [2015]. The values of P and E for both the Western and Eastern Mediterranean basins from each simulation are shown Table 2.6. Maximum and minimum annual means for the Western Mediterranean basin are employed as these should represent the conditions over Southern Spain; the values are scaled down to the surface area of the Sorbas Basin. Actual precessional cycle lengths over the interval vary from ~20 to ~29 ky; for simplicity, we employed a sine function to vary

between the hydrologic budget extremes over 20 ky cycles, similarly to *Topper et al.* [2014].

Table 2.6. Estimated Late Miocene evaporation (E) and precipitation (P) for the Western and Eastern Mediterranean regions from orbital experiments of global circulation model HadCM3L [*Marzocchi*, 2016]. For Sorbas, values are scaled from surface area of Late Miocene Western Mediterranean (9.21831×10^{11} m^2; model palaeogeography) to estimated Sorbas Basin surface area (1.2×10^9 m^2, see Table 2.5.)

Snapshot Age (Ma)	West E (m^3/s)	West P (m^3/s)	West Q_R (m^3/s)	East E (m^3/s)	East P (m^3/s)	East Q_R (m^3/s)
6.568	32,919	8,529	4,763	78,678	21,168	10,590
6.569	32,722	9,305	4,254	78,599	20,929	8,429
6.570	32,704	8,826	3,991	78,627	20,487	8,062
6.571	32,840	8,711	3,832	78,726	20,073	7,529
6.572	32,891	8,352	3,928	78,803	18,795	7,414
6.573	32,822	8,278	4,281	78,775	18,564	7,631
6.574	32,846	8,027	4,621	78,769	18,196	8,184
6.575	32,209	7,498	4,348	78,248	16,904	9,137
6.576	32,456	7,228	4,584	78,893	16,134	11,930
6.577	32,210	7,183	4,087	78,296	15,683	14,273
6.578	32,087	6,979	4,319	77,982	15,738	19,228
6.579	32,277	6,802	4,675	77,979	15,813	21,613
6.580	32,414	7,101	4,947	78,044	16,717	27,597
6.581	33,131	7,915	5,145	77,882	17,748	34,985
6.582	32,930	8,359	5,740	77,969	18,770	36,647
6.583	32,817	8,982	5,684	78,290	19,496	37,021
6.584	33,165	9,080	5,838	78,729	19,852	34,945
6.585	33,173	9,221	5,974	78,932	20,253	30,170
6.586	33,236	9,277	5,728	79,029	21,657	26,963
6.587	32,795	9,082	5,598	78,837	20,659	20,385
6.588	32,708	8,615	5,092	78,292	20,842	14,890
6.589	32,667	8,455	4,445	78,225	21,535	11,098
Min	*32,087*	*6,802*	3,832	*77,882*	*15,683*	7,414
Max	*33,236*	*9,305*	5,974	*79,029*	*21,657*	37,021
Difference	***1,149***	***2,503***	**2,142**	***1,147***	***5,974***	**29,607**
Sorbas Average	***42.60***	***10.76***				
Sorbas Min	***41.77***	***8.85***				
Sorbas Max	***43.27***	***12.11***				

2.6.3 Transient model

The only significant deviation in the transient model applied here from *Topper et al.* [2011] is the introduction of a Sr concentration limit at 8 mg/L; this approximates ocean water [Sr] [7.85 ± 0.03 mg/L; *Veizer*, 1989], and essentially represents the solubility limit

of Sr in seawater of normal marine salinity. Imposing this limit prevents the model from generating artificially high [Sr] not representative of the natural environment. With respect to the Sorbas Basin box, the consequence of this limit is that riverine Sr input has a nominally greater impact on the Sr isotope ratio. In different systems, such as those with larger differences between seawater and riverine Sr isotope ratios, or greater riverine [Sr], the impact may be quite significant. No assumptions or controls are imposed on deposition or precipitation of Sr, as these processes do not affect basin connectivity or basin water $^{87}Sr/^{86}Sr$ ratios; any potential isotopic fractionation between seawater and calcite, such as during calcification of the foraminifer test, is compensated for during mass fractionation correction of the raw mass spectrometer data [*McArthur et al.*, 2012].

The GCM results indicate that the primary source of variability in the Western Mediterranean's freshwater budget is driven by P (Table 2.6), which varies with precession due to shifts in the latitude of North Atlantic storm tracks [*Bosmans et al.*, 2015; *Toucanne et al.*, 2015; *Marzocchi*, 2016]. Since precession drives river discharge, this suggests that riverine runoff (Q_R) should also vary with precession. Since Q_R is the only freshwater flux which also delivers Sr to the basin, the sensitivity of model results to the selection of the parameter used to vary the hydrologic budget was explored by comparing model results (not shown) with the same overall freshwater budget, achieved by varying either E, P, Q_R, or various combinations of these three. The range of Sr isotope ratios and salinities resulting from these tests were very similar regardless of which freshwater budget parameter(s) varied. This is probably because the range of values for P, or the combined EP term, is relatively small (8.85 to 12.11 m^3/s, or 30.48 to 33.16 m^3/s, respectively; Table 2.6). Consequently, although varying Q_R with precession is more realistic, it was kept constant for any one model run in order to simplify the temporal changes in mass flux to the basin, and make the model results easier to interpret.

For both steady state and transient simulations, salinity is assumed to be an adequate approximation for density as per *Meijer* [2006]. The linear exchange coefficient, g (m^3/s per g/L) is relevant for transient simulations (see equation 3). This parameter expresses gateway efficiency, and can be related to gateway dimensions; small, long, or tortuous gateways will have lower g values (see *Simon and Meijer* [2015] for discussion of the impact of gateway dimensions on exchange). No estimate of g for the connections between the Sorbas Basin and the Mediterranean is available. Thus, the model results are used to find the range of g values consistent with periodic Sr isotope anomalies and discuss the implications (discussed in Ch. 3, section 3.3.5). To determine optimum values of Q_R and g,

the transient model was run for a large range of Q_R and *g* in order to predict the optimal combinations required to generate a Sr anomaly. Based on initial transient model sensitivity tests, the ranges selected were Q_R from 29 to 35 m^3/s, and *g* from 0.5 to 250 m^3/s per g/L.

2.6.4 Volume and eustacy

For the modeling performed here, a constant volume is assumed for the Sorbas Basin, which may appear to be an oversimplification. Relatively small changes in sea level could have a large impact on basin volume and connectivity (*g*) due to the relatively shallow geometries of the Sorbas Basin itself as well as its connections to the Mediterranean. The most likely factor to cause volume variations consistent with orbital cycles is eustatic sea level change, as the Mediterranean was connected to the Atlantic during this interval (~6.5 Ma) [*Krijgsman et al.*, 1999b]. Adequate records with the requisite temporal resolution on which to base sea level and thus basin volume changes for this interval are currently lacking, though studies with lower temporal resolution have linked changes in Antarctic ice volume to MSC onset [e.g. *Ohneiser et al.*, 2015]. *Kouwenhoven et al.* [2003] observed no major sea level fluctuations at open Mediterranean settings (Gavdos, Crete) based on foraminiferal assemblages between ~ 8.2 and 6.5 Ma. However, the methods used by those authors are not sensitive to changes on the order of a few tens of metres. This issue is discussed alongside the results in section 3.4.1.1.

3 Precessional variability of $^{87}Sr/^{86}Sr$ in the late Miocene Sorbas Basin: an interdisciplinary study of drivers of inter-basin exchange

3.1 Overview

Following an outline of the sources and sinks of Sr, the first sub-precessional record of seawater $^{87}Sr/^{86}Sr$ ratios for the Mediterranean region is presented, derived from foraminifera of the late Miocene Sorbas Basin (SE Spain). The record exhibits brief excursions with precessional cyclicity to values more radiogenic than coeval ocean water. Using numerical box modeling, the hydrologic conditions in the Sorbas Basin required to generate the observed record is investigated. The results highlight the significance of density contrast between water masses as a significant driver of inter-basin exchange. The hydrologic budget of the Sorbas Basin must have been fundamentally different compared to the open Mediterranean to support the observed temporal patterns of lithological variations and $^{87}Sr/^{86}Sr$ isotope excursions; it is postulated that the hydrologic budget of the Sorbas Basin was generally positive, suggesting that the temporal relationship between bathyal Mediterranean sapropels and Sorbas Basin sapropelic layers is not identical; both appear precessional but may be out of phase with respect to each other.

CHAPTER NOTES

Materials and methods: Ch. 2, sections 2.2, 2.3.1 to 2.3.1, 2.6
Sample location maps: Ch. 1, Fig. 1.21; Ch. 2, Fig. 2.1
Contributions: Tanja J. Kouwenhoven, benthic foraminifer counting; Dirk Simon, assistance with box model setup; Alice Marzocchi, Western and Eastern freshwater budget data from GCM HadCM3L

3.2 Sources of Sr

Before presenting the data, it is necessary to review the sources of Sr to the Sorbas Basin to contextualize the mechanisms driving the observed values. This section outlines and justifies the selection of Sr isotope ratios and concentration values used in the Sorbas Basin Sr and hydrologic budget numerical box model (see Ch. 2, section 2.6, for methodology). The interval covered by the data presented in this study spans 6.60 – 6.55 Ma, parts of cycles UA 5-8. The average global ocean seawater $^{87}Sr/^{86}Sr$ isotope ratio for this time was 0.708965 ± 0.000020 [*McArthur et al.*, 2012], the mean changing only slightly from 0.708964 to 0.708966 over the interval. Because the concentration of Sr in seawater (8

mg/L) is more than an order of magnitude greater than in river water (global riverine average is 0.2 mg/L; up to ~ 0.5 mg/L for major rivers entering the Mediterranean [*Brass*, 1976; *Albarede and Michard*, 1987; *Palmer and Edmond*, 1989; *Reinhardt et al.*, 1998]), a measurable deviation from global ocean $^{87}Sr/^{86}Sr$ must be accompanied by a substantial increase in the source of non-marine Sr relative to marine Sr. This is generally only observed in very restricted marginal settings. The magnitude of riverine influx required to cause a Sr isotope anomaly also depends on the difference between the $^{87}Sr/^{86}Sr$ ratios of the combining water masses. Both the Sr concentration and isotopic ratio of river water are controlled by catchment geology. Many southern European rivers entering the Mediterranean have catchments dominated by Mesozoic carbonate with a Sr isotopic composition less radiogenic (lower) than Miocene global ocean Sr isotope ratios [*Flecker et al.*, 2002; *McArthur et al.*, 2012] and relatively high concentrations (e.g., Rhone, 0.52 mg/L, $^{87}Sr/^{86}Sr$ 0.708719 [*Albarede and Michard*, 1987]). The Mediterranean's largest river, the Nile, has a basalt-dominated catchment which supplies very unradiogenic $^{87}Sr/^{86}Sr$, although the Sr concentration, [Sr], is lower (0.235 mg/L, $^{87}Sr/^{86}Sr$ 0.7060 [*Brass*, 1976]). As a result the Sr anomalies observed in pre-MSC marginal settings and across the Mediterranean during the MSC itself are dominated by deviations towards ratios less radiogenic (lower) than coeval ocean $^{87}Sr/^{86}Sr$.

The Internal Betic Cordillera of SE Spain contains rocks with higher (more radiogenic) Sr isotopic ratios [*Powell and Bell*, 1970; *Hebeda et al.*, 1980; *Zeck et al.*, 1989; *de Jong*, 2003; *Conticelli et al.*, 2009]. The Sierras surrounding the Sorbas Basin (Ch. 2, Fig. 2.1) form the eastern end of this Cordillera. The fine-grained nature of the Abad Marls impedes provenance analysis; however, clasts derived from the Sierras are found both within the underlying Azagador Member [*Braga et al.*, 2001] and the overlying Zorreras member [*Aufgebauer and McCann*, 2010]. Available evidence for the Sierra de los Filabres, the range bounding the Sorbas basin to the North, indicates that exhumation due to rock (not surface) uplift stopped well before the Messinian (12-15 Ma, *Vazquez et al.* [2011]), suggesting that drainage network reorganization exposing significantly different geology is unlikely to have occurred since the Serravallian. Regional volcanics, active during the late Miocene, also exhibit radiogenic $^{87}Sr/^{86}Sr$ [*Toscani et al.*, 1990; *Benito et al.*, 1999; *Duggen et al.*, 2008; *Conticelli et al.*, 2009].

The $^{87}Sr/^{86}Sr$ of rivers feeding the Sorbas Basin during the Messinian can be constrained using published data from ostracods recovered from the overlying lacustrine Zorreras

member. The Zorreras member has a latest Messinian to earliest Pliocene age [*Martin and Braga*, 1994; *Fortuin et al.*, 1995; *Braga and Martin*, 1996; *Riding et al.*, 1998; *Roep et al.*, 1998; *Martin-Suarez et al.*, 2000; *Krijgsman et al.*, 2001; *Hilgen et al.*, 2007; *Aufgebauer and McCann*, 2010]. The Zorreras sediments are continental with some intercalation of marine sediments [*Roep et al.*, 1998; *Aufgebauer and McCann*, 2010] suggesting periodic ingress of seawater to the basin. The ostracod-bearing levels are brackish water deposits [*Roep et al.*, 1998], indicating that the ostracod $^{87}Sr/^{86}Sr$ ratios provide a conservative minimum estimate for Sorbas river water Sr isotope compositions. The ostracods have an $^{87}Sr/^{86}Sr$ ranging from 0.709066 to 0.709131 (average = 0.709097; n = 4; [*McCulloch and Deckker*, 1989], originally published in [*Roep and van Harten*, 1979]), higher than coeval ocean water values, and consistent with the radiogenic values anticipated from the catchment.

The concentration of Sr in river water correlates with the mineralogy of the catchment and its solubility; carbonate-rich drainage basins tend to exhibit higher concentrations, around ~0.5 mg/L. Catchments dominated by siliciclastic rocks tend to have lower [Sr] [e.g. *Blum et al.*, 1998; *English et al.*, 2000; *Jacobson and Blum*, 2000]. Considering the dominantly non-carbonate catchment and the lack of direct measurements on modern day analogs, we assume a [Sr] ~ 0.3 mg/L as a maximum estimate for water flowing into the Sorbas Basin in the late Miocene. Implications for a range (0.1 to 0.5 mg/L) of Sr concentrations will also be addressed.

3.3 Results

3.3.1 Sorbas Sr isotopic compositions

All but four of the measured $^{87}Sr/^{86}Sr$ ratios are within error of the coeval global seawater curve (Table 3.1, Fig. 3.1). These four anomalous Sr isotope ratios all have higher ratios than coeval seawater and occur in the non-sapropelic layers, within or immediately after the diatomite (Fig. 3.1). The Sr anomalies occur coevally with a maximum in the percentage of *Globigerina bulloides* (Fig. 3.1e). The anomalies are also consistently preceded by elevated B/P ratios compared with generally low background ratios (Fig. 3.1d). Both faunal oscillations, like the regular lithological change, are thought to fluctuate with insolation [*Pérez-Folgado et al.*, 2003; *Sierro et al.*, 2003] (Fig. 3.1b). The potential effects of diagenesis are considered below, but because of the regular pattern of Sr isotope

anomalies which are consistent with insolation, we suggest that the foraminiferal $^{87}Sr/^{86}Sr$ ratios are largely unaffected by diagenetic alteration.

Table 3.1. $^{87}Sr/^{86}Sr$ isotope ratios measured from Sorbas Basin planktic foraminifera. 2SD external uncertainty = 0.000018. Location: 37°05'22"N 2°04'08"W.

Sample	Age (Ma)	$^{87}Sr/^{86}Sr$	2SE error	Lithology
34-06	6.5958	0.708974	0.000013	D
34-12	6.5928	0.708979	0.000017	M2
34-14	6.5916	0.709009	0.000012	M2
34-17	6.5905	0.708982	0.000013	M2
34-20	6.5894	0.709004	0.000014	M2
34-29	6.5857	0.708976	0.000012	S
34-44	6.5799	0.708992	0.000014	S
34-50	6.5767	0.708957	0.000012	S
35-05	6.5741	0.708975	0.000013	M1
35-08	6.5726	0.708978	0.000016	D
35-11	6.5711	0.708990	0.000015	M2
35-14	6.5701	0.709032	0.000015	M2
35-26	6.5658	0.708990	0.000014	S
35-38	6.5619	0.708950	0.000014	S
35-44	6.5598	0.708944	0.000014	S
36-06	6.5549	0.708969	0.000014	M1
36-09*	6.5536	0.709003	0.000014	M1
36-11	6.5529	0.709007	0.000013	D

**Average; individual sample results: 0.708994, 0.709011*

3.3.2 Potential effects of diagenesis on foraminiferal $^{87}Sr/^{86}Sr$

Diagenetic alteration may affect the $^{87}Sr/^{86}Sr$ ratio preserved in biogenic calcite. During the interval in question, the Sr seawater curve does not change significantly (6.55 Ma, 0.708966; 6.60 Ma, 0.708964 [*McArthur et al.*, 2012]), so it is not possible to use the stratigraphic compatibility of the Sr isotope results as a test for diagenesis [*Beets and De Ruig*, 1992; *Flecker et al.*, 1998]. However, although some degree of diagenetic alteration of the primary $^{87}Sr/^{86}Sr$ ratio cannot be entirely excluded, the fact that the majority of the samples are within error of coeval seawater values implies that any effect on the preserved $^{87}Sr/^{86}Sr$ ratio for these samples is likely to be smaller than analytical error. Early calcite recrystallization is generally isochemical [*Baker et al.*, 1982], such that it should reflect pore waters with the same $^{87}Sr/^{86}Sr$ isotope composition as syn-depositional seawater. Sr is well mixed in seawater, thus unlike Nd, no gradients are expected between bottom water or upper pore water Sr isotopic compositions and surface waters where planktic foraminifera live.

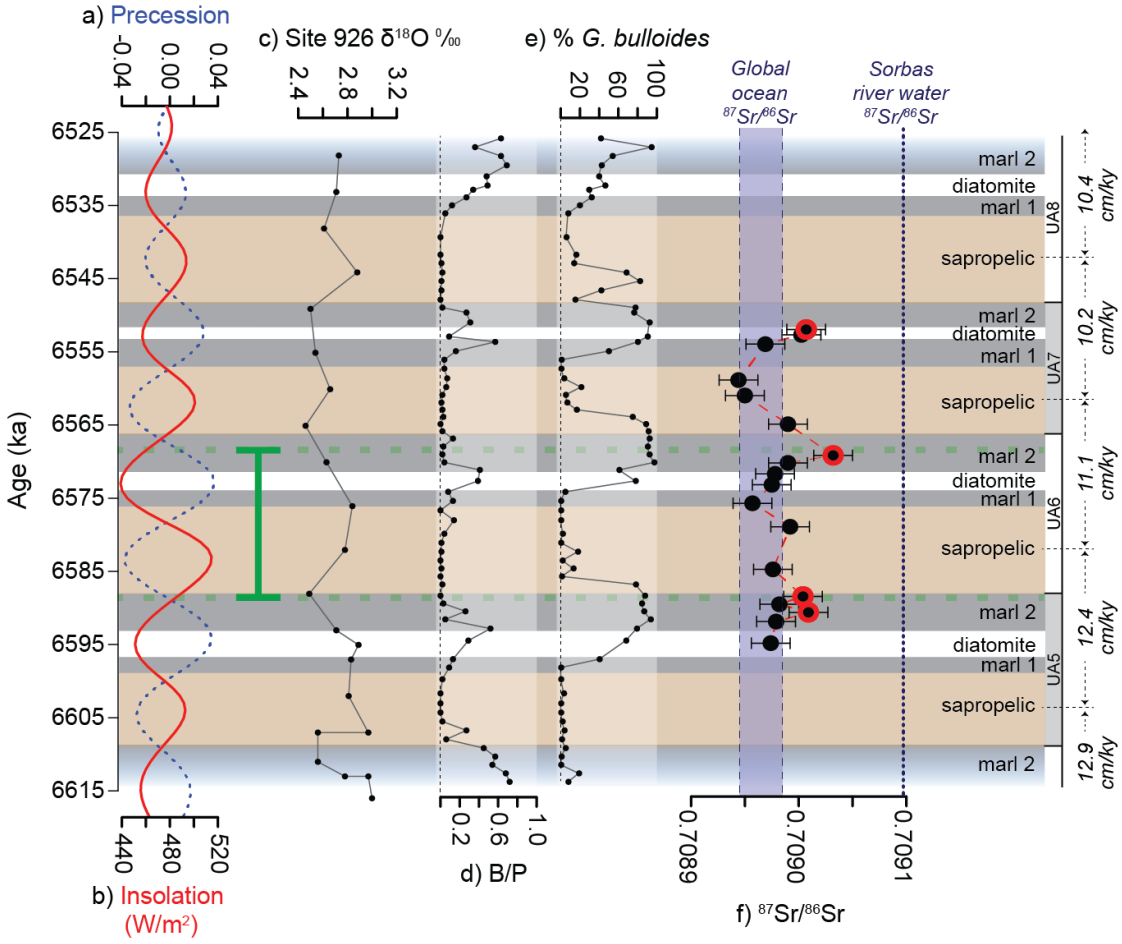

Fig. 3.1. $^{87}Sr/^{86}Sr$ isotope compositions of Sorbas basin water compared to lithology (Upper Abad marls, cycles UA5 to UA8), sedimentation rate (far right), insolation, and other available data. (a) Precession and (b) insolation [*Laskar et al.,* 2004]. (c) Ceara Rise (tropical W Atlantic) ODP Leg 154 Site 926 $\delta^{18}O$ [*Shackleton and Hall,* 1997]. (d) Sorbas Basin B/P and (e) G. bulloides records from identical samples [*Perez-Folgado et al.,* 2003]. (f) $^{87}Sr/^{86}Sr$ isotope compositions of Sorbas basin planktic foraminifera. Data points outside of analytical error are highlighted. Green bar indicates time span covered by GCM simulation data used in box model.

Adherent mineral phases could also result in radiogenic isotopic compositions; clay minerals and micas in particular are 'sticky' and tend to incorporate radiogenic Sr. In the case of the Sorbas Basin, transported siliciclastics are likely to contain radiogenic Sr (section 3.2). However, thorough cleaning following well-established methods was employed to avoid such contamination, followed by dissolution in very weak acid such that mineral phases other than calcite should not interact (Ch. 2, section 2.3.1). Moreover, contamination of this type should affect all data in a similar way, but values outside analytical error of the coeval seawater curve are only observed for 4 of 18 samples. Moreover, anomalies are observed within marl 2 for the first two cycles, whereas the third occurs within diatomite, implying the values are independent of sediment composition. Furthermore, the match between the regular cyclicity in the Sr isotope record and the faunal assemblages (compare Fig. 3.1d, e and f) suggests that the data are more likely to

coincide with changes in Sorbas Basin water. Therefore, the foraminiferal Sr isotope ratios are considered reliable indicators of Sorbas Basin water $^{87}Sr/^{86}Sr$ isotope compositions.

3.3.3 Sorbas palaeodepth and bottom water oxygenation

The benthic foraminiferal assemblages found in marls 1 and 2 are indicative of shelf edge or outer shelf conditions and suggest a water depth range of approximately 150 – 250 m (Table 3.2). Our estimate is in good agreement with *Troelstra et al.* [1980] who suggested the Upper Abad marls experienced shallowing from about ~ 200 m water depth at the base of the section to ~ 100 m near the top. Our estimate is specifically applicable to cycles UA5 to 8 in the lower part of the Upper Abad.

The majority of the sapropelic samples contain no benthic foraminifera (Figs. 2b, c in *Pérez-Folgado et al.* [2003]). Our analysis indicates that when benthic foraminifera are present, even while they comprise a relatively high percentage of the overall foraminiferal assemblage, the populations are dominated by stress-tolerant species (*Bolivina*, *Bulimina,* (*Rect-*) *Uvigerina*, and *Globobulimina* spp.) indicative of hypoxic conditions [*Kouwenhoven et al.*, 2003; *Van Hinsbergen et al.*, 2005; *Koho et al.*, 2011; *Koho and Piña-Ochoa*, 2012; *Langlet et al.*, 2014]. Stress tolerant species percentages range from 40% to 100%, with the majority of samples containing more than 50%. This systematic pattern of benthic occurrence suggests that during sapropelic layer deposition anoxia was extreme enough to prevent benthic foraminiferal survival, while during marl and diatomite deposition anoxia lessened to hypoxic conditions. For the marl and diatomite layers, the B/P ratio therefore indicates episodes of increased seafloor oxygenation where the most oxygenated conditions commonly immediately precede the Sr anomalies (Fig. 3.1d and f).

Table 3.2. Selected benthic foraminifera (percentages, except total).

Sample number	Age (Ma)	Lithology	***Bolivina dilatata***	***B. spathulata***	***B. dentellata***/spp.	***Bulimina aculeata***	*Bulimina costata*	***B. elongata/ echinata***	*Bulimina elegans*	*Cassidulina crassa/laevigata*	*Cibicides dutemplei*	*C. lobatulus*	*C. pachyderma*	*C. ungerianus*	*Elphidium* spp.	***Globobulimina* spp.**	*Globocassidulina* spp.	*Gyroidina* spp.	*Hanzawaia boueana*	lenticulinids	nodosariids	*Nonion fabum*	*Planulina ariminensis*	***Rectuvigerina bononiensis***	***R. cyclindrica***	*Sphaeroidina bulloides*	*Textularia* spp.	***Valvulineria bradyiana***	total	split**	**% stress tolerant taxa**
36-0	6.557	S	10.0	0.7		4.4	0.7	6.1	3.6	1.9	0.5	4.1	1.9	4.1	3.6	0.5		0.5	4.4	4.6	2.2	1.2	0.7	30.2	3.9	0.5	0.5	0.5	411	1/4	**60**
35-23	6.567	M2	1.4	23.8		0.5		0.3																3.7	69.7			0.6	623	1/8	**100**
35-20	6.568	M2	0.4	0.9		2.7		2.2				1.3		13.8	0.4	7.6			24.4			1.8		0.4	20.4			23.1	225	1/2	**58**
34-3	6.597	M1	7.8	1.9	1.7	4.5	1.4	9.0	0.9	1.4	2.4	1.9	1.7	2.8	4.7	1.9		4.0	6.4	0.2	0.2	13.2	0.7	1.2	24.3	0.2			424	1/4	**53**
34-0	6.598	M1	3.7	12.3		2.5	3.2	4.2	0.7	7.6	1.7	2.2	2.0	6.6	3.9	2.9		7.9	2.9	0.5	1.7	3.2	2.5	2.5	11.5	2.0	2.0		407	1/4	**40**
33-27	6.603	S*																											4	1/1	**n/a**
33-21	6.606	S*																											4	1/1	**n/a**
33-15	6.608	S*																											2	1/1	**n/a**
33-12	6.609	M2	0.8	4.2		0.8		0.3		0.3	0.3	0.8	0.3		0.3	0.3		0.8	0.3				0.3		87.2			0.8	359	1/1	**94**
33-9	6.610	M2	1.6	1.0	0.5	5.8		3.1		1.6				10.5	0.5	50.3	0.5	0.5	10.5		1.0	0.5			3.1			7.9	191	1/1	**73**
33-6	6.611	M2										2.4				78.6	2.4		2.4	2.4	11.9								42	1/1	**79**
33-3	6.613	M2	8.9	0.2	4.5	3.9				5.4		0.9		4.8	0.2	32.8	1.7		18.4	0.2	1.7	0.2		0.4	4.1			6.7	463	1/1	**62**

Stress tolerant taxa in boldface. Occurrences <2% not included. S = sapropelic, M = marl, * near-barren, ** proportion of washed residue counted.

3.3.4 Model results: steady-state approximations

For the Mediterranean Sea, *Topper* [2013] calculated that at least 25% of the water flux into the basin during the late Miocene must be riverine to generate a measureable Sr anomaly; e.g., a Q_R:Q_I ratio of ~ 1:3. Assuming the $^{87}Sr/^{86}Sr$ ratio of Nile runoff was similar to today, this implies a 2965 ppm difference between the late Miocene global ocean $^{87}Sr/^{86}Sr$ ratio and that of the freshwater source dominating the runoff to the Mediterranean. The late Miocene Sorbas fluvial Sr isotope ratio (0.709097, Ch. 2, Table 2.5) differs from the global ocean value at 6.57 Ma by only 132 ppm, so a larger Q_R:Q_I ratio is required to generate a measureable Sr anomaly. Assuming riverine Sr concentrations of 0.5 mg/L, 0.3 mg/L, and 0.1 mg/L, the Q_R:Q_I ratios required to observe a Sr isotope anomaly in the Sorbas Basin are 6.5:1, 10.8:1, and 32.8:1 respectively (Fig. 3.2a). In order to attain a Sr isotope anomaly while maintaining a salinity suitable for foraminifera, for $[Sr]_R$ = 0.3 mg/L, Q_R must be very small i.e. $Q_R \leq$ E-P ± 1.7%, or within 1.7% of a neutral freshwater budget (Fig. 3.2b).

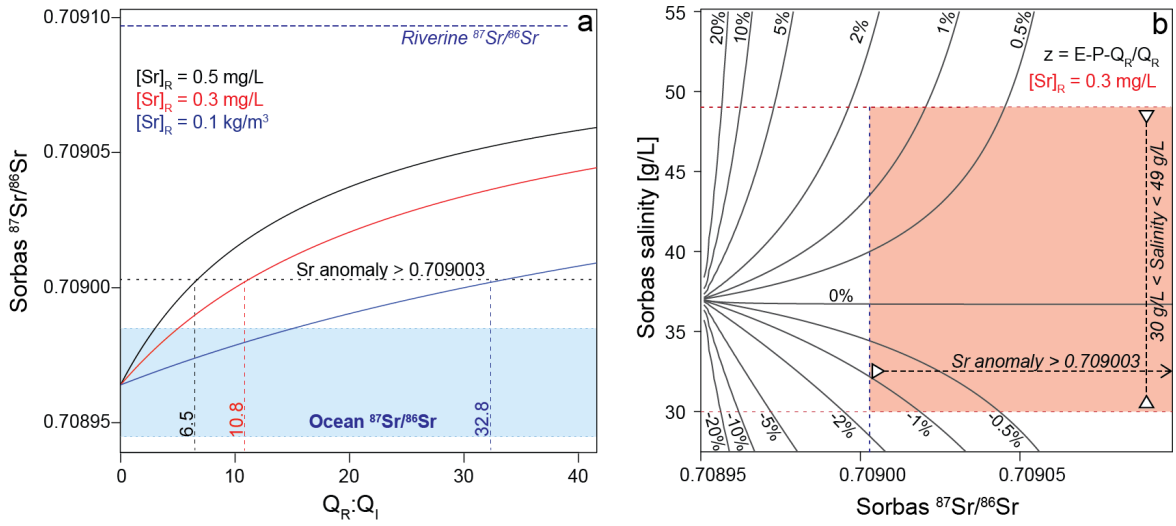

Fig. 3.2. Steady state model results. (a) Sorbas Basin Sr isotope ratio ($[^{87}Sr/^{86}Sr]_S$) vs Q_R:Q_I for riverine Sr concentrations ($[Sr]_R$) from 0.1 to 0.5 mg/L. Values on vertical lines indicate minimum ratio value where an anomaly can occur for each concentration. (b) Contour plot of (E – P – Q_R) / Q_R, with respect to Sorbas Basin salinity and $^{87}Sr/^{86}Sr$ ratio, using $[Sr]_R$ = 0.3 mg/L. Sr anomaly requires Q_R < E – P ± ~1.7%, as indicated by shaded box.

Combining these results with minimum and maximum E and P from the GCM data (Ch. 2, Table 2.6) allows us to calculate an expected range of river runoff (Q_R) into the basin for the salinity range required. For $[Sr]_R$ = 0.5 mg/L, Q_R = 29.6 to 34.2 m^3/s; for lower concentrations, the range narrows slightly ($[Sr]_R$ = 0.3 mg/L, Q_R = 30.0 to 33.8 m^3/s; $[Sr]_R$ = 0.1 mg/L, Q_R = 30.3 to 33.4 m^3/s). These ranges in discharge are comparable with the

annual discharge for small modern rivers in Southern Spain such as the Segura (~ 26 m^3/s, SAGE database). The Rio de Aguas, the main river draining the Sorbas Basin today, has a median annual discharge of only ~1 m^3/s [*Pulido-Bosch*, 1997], although significant catchment reorganization is suspected during the early Pleistocene, leading to diversion of water to other areas [*Mather*, 2000]. The modeled values are a total runoff estimate for the basin, and may have comprised discharge from more than one river. Consistent with the low predicted discharge is the absence of Messinian large-scale deltaic or fluvial deposits in the pre-MSC successions of the Sorbas Basin.

3.3.5 Transient model results

The combinations of the linear exchange coefficient *g* and riverine influx Q_R capable of generating a Sr isotope anomaly in the transient model are shown in Fig. 3.3a. Only a relatively small number of combinations of Q_R and *g* reproduce Sorbas' temporal pattern of oceanic ($^{87}Sr/^{86}Sr \leq 0.708970$) and anomalous ($^{87}Sr/^{86}Sr \geq 0.709003$) Sr isotope values. Area A (Fig. 3.3a) represents the combinations of Q_R and *g* where the Sr isotope ratios do not return to global ocean values between anomalies, while Area B highlights the range of Q_R values which never become anomalous due to insufficient time near the neutral fresh water budget ($\Delta S=0$).

A striking result of the transient model is that the freshwater budget must remain either positive ($E<P+Q_R$) or negative ($E>P+Q_R$) throughout the majority of a precessional cycle (Fig. 3.3b, d) in order to generate a single Sr ratio anomaly 'peak' per cycle and correctly reproduce the temporal pattern observed (compare Fig. 3.1f to Sr isotope evolution in Fig. 3.3b-d). Where the freshwater budget becomes neutral twice per cycle (e.g. where the freshwater budget is positive for half a cycle and negative the other half, so that on average $E=P+Q_R$; Fig. 3.3c), two $^{87}Sr/^{86}Sr$ peaks per precessional cycle occur. In addition to producing a different pattern than the data, these peaks are analytically indistinguishable from ocean water, and therefore are not anomalies.

As the difference in salinity (ΔS) between the Sorbas and Mediterranean basins approaches zero, Q_I and Q_O also approach zero. In Fig. 3.3c no Sr isotope anomaly is generated because ΔS is not maintained near zero for long enough. There are only two cases which produce Sr isotope anomaly patterns similar to the data: (1) when the freshwater budget is mainly positive and approaches neutral or briefly becomes negative once per cycle (Fig.

3.3b); and (2) when the freshwater budget is mainly negative and approaches neutral or briefly becomes positive once per cycle (Fig. 3.3d).

These two sets of Q_R and *g* combinations coincide with the mainly positive hydrologic budget case (Fig. 3.3b, or where *g* ranges from 11.3 to 33.5 m^3/s per g/L; and Q_R from 33.05 to 33.13 m^3/s) and the mainly negative hydrologic budget case (Fig. 3.3d, or where *g* ranges from 7.4 to 24.2 m^3/s per g/L; and Q_R from 30.57 to 30.67 m^3/s). From these results, it is clear that only two narrow ranges of Q_R values generate a Sr isotope anomaly compared with a relatively wide range of *g*. These narrow Q_R ranges are again a result of the time required to generate an anomaly and the sensitivity of salinity in a small basin to freshwater fluxes. The Sorbas-Mediterranean exchange coefficient, g, is very small by comparison with the modern Gibraltar strait (~ 10^5 m^3/s per g/L) and the *g* required at Gibraltar to effect measureable changes in Mediterranean Sr isotope ratios (< 10^3 m^3/s per g/L; *Topper et al.* [2011]). The relatively wide range of values for Sorbas' *g* is because, irrespective of gateway efficiency, as ΔS approaches zero, the Q_I and Q_O exchange fluxes decrease.

~~~ FACING PAGE ~~~

Fig. 3.3. Transient model results. (a) Contour plot, using 200 m basin depth, for Q_R and *g* parameter space generating a Sr isotope anomaly; orange areas (outlined by dotted line) indicate peak Sr isotope values > 0.709003. Q_R and *g* combinations employed for plots b-d are indicated by red dots. Area A: values of Q_R and *g* that do not allow minimum (between-peak) $^{87}Sr/^{86}Sr$ ratios to return to global ocean value (allowing for 5 ppm margin, to $^{87}Sr/^{86}Sr$=0.708970); Sr isotope anomalies are observed in this region, but the foraminifera data pattern is not reproduced (Figure 2). Area B (space between anomaly regions): insufficient time near neutral hydrologic budget to generate an anomaly. (b-d) Time series for Q_R and *g* combinations indicated in (a). Hydrologic budgets (upper curves), evolution of Q_I and Q_O (middle curves), basin salinity and $^{87}Sr/^{86}Sr$ ratio (lower curves); g = 12 m^3/s per g/L for all time series (this value of *g* was selected as it generates easily visible anomalies, but 7.4 < g < 33.5 m^3/s per g/L can generate an anomaly at this basin depth/volume). ΔS=0: Sorbas and Mediterranean salinities equal. Sr anomaly: minimum observable $^{87}Sr/^{86}Sr$ ratio anomaly (≥ 0.709003; section 3.3). Freshwater budgets vary cyclically through minimum and maximum E – P over 20 ky to generate (b) mainly positive (average $E<P+Q_R$), (c) half positive/half negative (average $E=P+Q_R$), and (d) mainly negative (average $E>P+Q_R$) hydrologic budgets. Positive freshwater budget axes values indicate freshwater loss, as the term ($E-P-Q_R$) is positive in the model (see supplement). Star-marked bars emphasize small time lag between peak hydrologic budget values, salinity, and $^{87}Sr/^{86}Sr$. (e,f) Contour plots illustrating model sensitivity to basin depth.
~~~

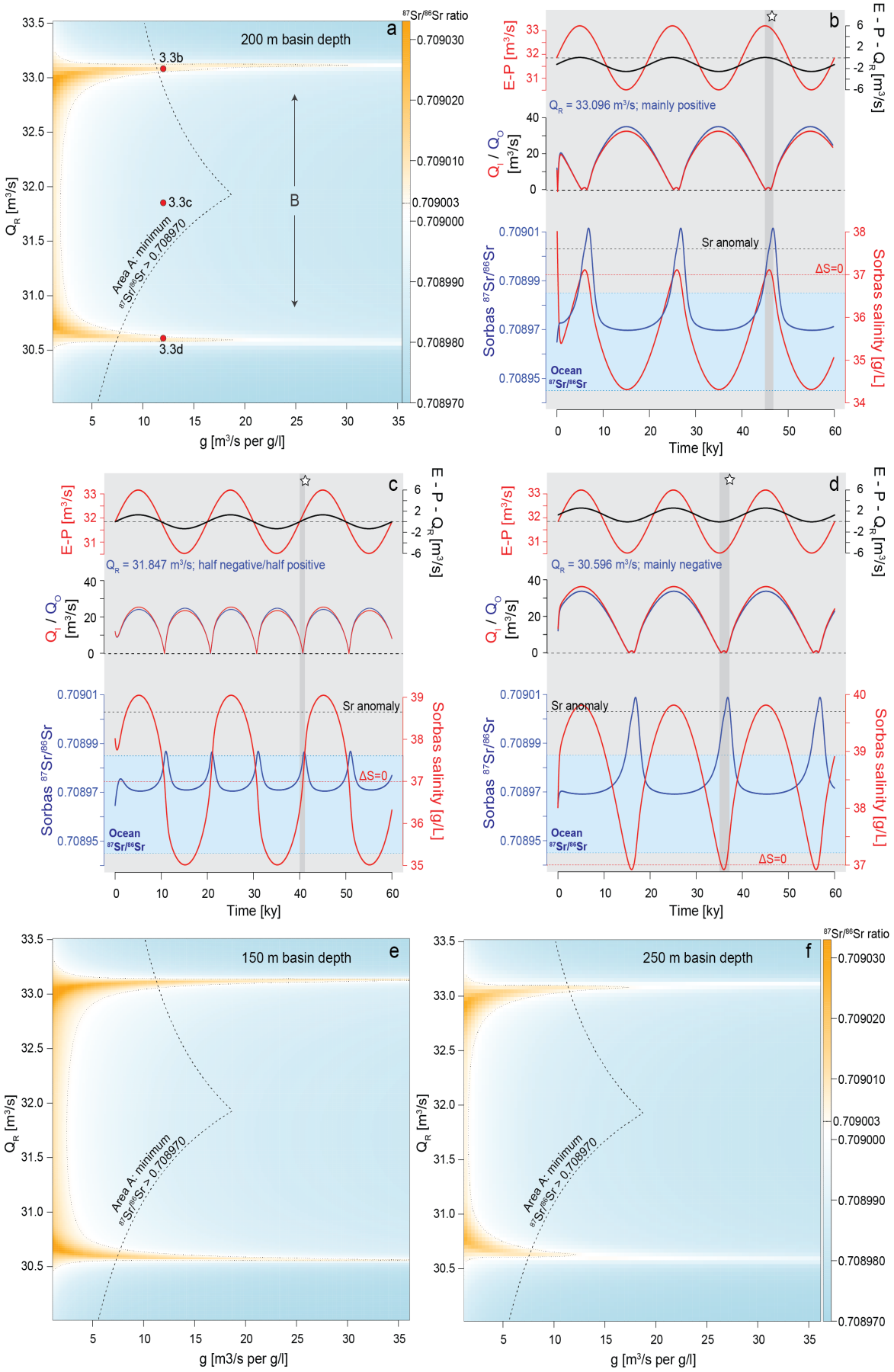
a
200 m basin depth
3.3b
3.3c
3.3d
B
Area A: minimum 87Sr/86Sr > 0.708970
QR [m3/s]
g [m3/s per g/l]
87Sr/86Sr ratio
0.709030
0.709020
0.709010
0.709003
0.709000
0.708990
0.708980
0.708970
b
E-P [m3/s]
QR = 33.096 m3/s; mainly positive
QI / QO [m3/s]
Sorbas 87Sr/86Sr
Sr anomaly
ΔS=0
Ocean 87Sr/86Sr
Sorbas salinity [g/L]
E - P - QR [m3/s]
Time [ky]
c
QR = 31.847 m3/s; half negative/half positive
d
QR = 30.596 m3/s; mainly negative
e
150 m basin depth
f
250 m basin depth

3.3.6 Sensitivity of salinity parameters

Regardless of the initial salinity selected for the Sorbas Basin 'box', Sorbas salinity comes into dynamic equilibrium with changes driven by the freshwater budget of the basin and the salinity selected for the Mediterranean in less than 2 ky (Fig. 3.3b-d, see stars and shaded bars). The selection of Mediterranean salinity does control the absolute value of Sorbas salinity, but not the amplitude of the salinity response across a cycle. For example, the results shown in Fig. 3.3b-d are for a Mediterranean salinity of 37 g/L; adjusting Mediterranean salinity to 39 g/L will shift the salinity curves two units higher, but all other parameters (Q_I, Q_O, $^{87}Sr/^{86}Sr$ ratio and amplitude of Sorbas 'box' salinity) remain the same. Consequently, a relatively wide range of Mediterranean salinity (~ 33 to 45 g/L) will satisfy the requirement that the Sorbas Basin remains within salinity tolerance of planktic foraminifera, and result in the same relationship between the freshwater budget and Sr isotope ratio. The primary significance of this result is that major changes in salinity observed in marginal basins are driven by the salinity of the main Mediterranean basin. This explains why the onset of gypsum precipitation at the start of the MSC is, on the scale of a single precession cycle, synchronous throughout the Mediterranean region in both marginal and deeper water settings [*Krijgsman et al.*, 1999a, 2002]. It also means that salinity data obtained from marginal settings reflect salinity in the more inaccessible open Mediterranean.

3.3.7 Sensitivity to basin depth

As indicated by the benthic foraminiferal assemblages, the depth of the Sorbas Basin during this interval may have been 150 - 250 m, affecting the basin volume and thus potentially the box model results. Figure 3.3e, f show the results of the transient box model simulations for these depths. While the range of *g* increases with decreasing basin depth, the ranges of Q_R which can generate Sr isotope anomalies remain very consistent. Consequently, inferences regarding the hydrologic budget of the Sorbas Basin derived from our box model results are very robust for a wide range of basin depths. Anomalies are generated from very shallow up to over 300 m basin depth.

3.4 Discussion

3.4.1 Processes affecting seawater $^{87}Sr/^{86}Sr$ in Sorbas

The regular pattern of Sr anomalies observed, their temporal cyclicity and relationship to lithology, suggest precessional changes to the Sorbas Basin source waters. Tectonic, magmatic and hydrothermal controls can be excluded because no regular temporal cyclicity is expected for these mechanisms. Orbitally-forced climate processes which could exert control on our record include eustatic sea-level fluctuations impacting the Mediterranean-Sorbas gateway, river runoff or changes to the overall freshwater budget, and/or shifts in continental weathering regimes.

3.4.1.1 Eustatic sea level change

The benthic foraminiferal assemblages, modeling results for *g* and palaeogeographic reconstructions [*Braga and Martin*, 1996; *Esteban et al.*, 1996] indicate that the Sorbas Basin was small and shallow (150 – 250 m), with connections to the open Mediterranean that were shallower still, as well as narrow and relatively long (Ch. 2, Fig. 2.1b). Long, shallow gateways are particularly sensitive to small changes in gateway size [*Simon and Meijer*, 2015] such as those that result from eustatic sea level variation. Eustacy certainly would have impacted the Sorbas-Mediterranean gateway as the Mediterranean was fully connected to the Atlantic prior to the MSC [*Roveri et al.*, 2014 and references therein]. At issue then is whether eustatic variation in sea level can modulate *g* to generate precessional changes in the Sr isotope record.

Thus, an important factor to address with respect to the numerical model is the use of constant volume. Relatively small changes in sea level could have had a large impact on both basin volume and connectivity (*g*) due to the relatively shallow geometry of both basin and gateway. Although studies have linked changes in Antarctic ice volume to MSC onset [e.g. *Ohneiser et al.*, 2015], adequate records with the requisite temporal resolution on which to base sea level, and thus changes to basin volume or *g* for the interval under study are lacking. *Kouwenhoven et al.* [2003] indicate that no major sea level fluctuations are observed at open Mediterranean settings between ~ 8.2 and 6.5 Ma, although the methods used by those authors are not sensitive to changes on the order of a few tens of

metres. For open ocean stable isotope records, obliquity strongly dominates eustatic sea level change in the Plio-Pleistocene [*Lisiecki and Raymo*, 2005; *Westerhold et al.*, 2005]. During the late Miocene, some benthic $\delta^{18}O$ records appear to contain other orbital frequencies including precession (e.g., ODP Leg 154 Site 926, Ceara Rise, western equatorial Atlantic [*Shackleton and Hall*, 1997]; ODP Leg 162 Site 982 North Atlantic [*Hodell et al.*, 2001]; ODP Site 659, Cape Verde, eastern equatorial Atlantic [*Colin et al.*, 2014]); unfortunately, pre-Pliocene $\delta^{18}O$ datasets tend to be low resolution by comparison. One of the highest resolution records available covering our interval is the Ceara Rise benthic $\delta^{18}O$ dataset (Fig. 3.1c), which has an average of 4 samples per precessional cycle. At this resolution, Ceara Rise data show no obvious variation with either obliquity or precession and no correlation with the Sorbas Basin Sr isotope data (Fig. 3.1f), lithology or faunal record (Fig. 3.1d, e). Without higher resolution late Miocene benthic $\delta^{18}O$ records it is not possible to reconstruct eustatic sea level changes to evaluate the impact on the Sorbas Basin on precessional timescales. Consequently, while acknowledging that if eustatic sea level changes occurred they will have modified the cross-section of the Sorbas-Mediterranean gateway and possibly affected Sorbas Basin $^{87}Sr/^{86}Sr$, we cannot currently attribute any of the systematic variation in the Sorbas data to eustacy.

3.4.1.2 River runoff

For river runoff to drive $^{87}Sr/^{86}Sr$ ratios in the Sorbas Basin, an increase in Q_R would need to occur at the same orbital phase as the anomaly e.g. during or just after the precession maxima (Fig. 3.1). GCM simulations of Late Miocene climate exhibit strong precessional shifts in the position of the Intertropical Convergence Zone (ITCZ) [*Bosmans et al.*, 2015a; *Marzocchi et al.*, 2015], shifting the position of the North African monsoonal rain belt and causing related changes to river discharge into the Mediterranean [*Gladstone et al.*, 2007; *Bosmans et al.*, 2015b; *Marzocchi*, 2016]. Maximum precipitation occurs during precession minima and reached the Eastern Mediterranean via the Nile, as well as Miocene palaeochannels, which flowed through modern-day Libya to the Gulf of Sirt draining a more humid Sahara [*Griffin*, 2002, 2011; *Paillou et al.*, 2009, 2012; *Ghoneim et al.*, 2012]. Enhanced fluvial run-off during precession minima dominates the Mediterranean's freshwater budget [*Marzocchi*, 2016] and is consistent with spikes in productivity, water column stratification and sapropel formation [e.g., *Rohling*, 1994; *Matthiesen and Haines*, 2003]. Were Mediterranean runoff the driver of the Sr anomalies observed, the $^{87}Sr/^{86}Sr$ excursion should therefore occur within or near the sapropelic layer, the layer associated

temporally with precession minima, rather than within the diatomite and marl 2 layers as observed (Fig. 3.1).

The GCM results indicate that in the western Mediterranean, maximum precipitation also occurs during precession minima. However, by comparison with the eastern basin, the variation in precipitation and river runoff between precession minima and maxima is less than half (compare eastern and western values, Ch. 2, Table 2.6), resulting from precessional shifts in Atlantic storm tracks [*Toucanne et al.*, 2015; *Marzocchi*, 2016]. This is consistent with relatively constant Al/Ti ratios over the four precessional cycles studied [*Filippelli et al.*, 2003]; in this context, changes in Al/Ti ratios would have indicated changes in river discharge recorded by changes in fluvially-derived clays. Consequently, neither the timing nor the amplitude of local runoff variability are consistent with a direct Q_R control on the Sorbas Basin $^{87}Sr/^{86}Sr$.

The relationship between discharge rate and Sr concentration also precludes river runoff as the driving mechanism. Low flow rates increase the time available to dissolve and incorporate ions into river water (e.g. Avon and Murchison of Western Australia, up to 1 mg/L, *Goldstein and Jacobsen* [1987]) so that rivers draining arid regions with low rainfall tend to have relatively high Sr concentrations. Thus, higher Q_R should be associated with lower Sr concentrations, decreasing the potency of the fluvially-derived Sr isotope signal (Fig. 3.3b) and reducing its ability to generate an anomaly. Another potential driver of the observed changes related to variability in runoff is weathering; the Sr isotopic composition transferred from minerals to runoff or groundwater can vary with weathering intensity due to the preferential breakdown of Sr- and Rb-rich phases such as mica [e.g. *Nesbitt et al.*, 1980; *Blum and Erel*, 1997; *Li et al.*, 2007]. Again, because small regional variations in precipitation and river runoff are expected for the Iberian region, shifts in weathering intensity are unlikely to explain the observations.

3.4.1.3 Fluctuations in the hydrologic budget

While the mass of Sr added to the basin per unit time is constant in the box model (e.g. constant Q_R), the only time that an anomaly occurs is during periods of significantly reduced exchange (Q_I, Q_O near 0; Fig. 3.3). During these periods, the hydrologic budget of the basin is close to neutral, maintaining marginal basin salinity near that of the open Mediterranean, and resulting in minimal density difference to drive exchange between the

Mediterranean and Sorbas (Fig. 3.3b-d). Because there is negligible export of riverine Sr to the Mediterranean under these near neutral hydrologic budget conditions, and negligible import of oceanic Sr into Sorbas, a buildup of river-derived Sr occurs in the Sorbas Basin which, given sufficient time, produces a Sr isotope anomaly. As *g* is held constant during any one model run (Fig. 3.3b-d), the mechanism suppressing exchange is not controlled by a reduction in physical connectivity, but driven by the local freshwater budget, which controls the density contrast.

The exchange at Gibraltar today provides a good analogy to the relative significance of density-contrast driven exchange compared to other drivers. Modern exchange between the Atlantic and Mediterranean is controlled by both evaporation and density contrast exchange, where exchange increases proportionally with density difference between Mediterranean and Atlantic water [e.g. *Bryden and Stommel*, 1984; *Bryden and Kinder*, 1991; *Meijer*, 2006]. Today, the Mediterranean experiences evaporative losses ranging from about 0.4 to 1.2 m/y [*Rohling et al.*, 2015 and references therein], or approximately 0.03 to 0.1 Sv (1 Sv = 10^6 m^3/s). However, Atlantic inflow is much larger, at about 0.8 Sv [*Tsimplis and Bryden*, 2000]. The majority of inflow balances denser Mediterranean Outflow (MO) (~ 0.7 Sv) [*Tsimplis and Bryden*, 2000; *Garcia-Lafuente et al.*, 2011], which is much saltier and thus denser than Atlantic water due to the evaporative losses. The evaporative losses over the Mediterranean generate a denser water mass which is driven to exchange at Gibraltar in much greater volumes than that required simply to replace the freshwater loss.

3.4.1.4 Dust

A final mechanism available which may affect seawater Sr isotope compositions is dust. Increased dust production and transport from North Africa is consistent with precession maxima when a southward shift of the ITCZ and increased aridity over North Africa is predicted [*Larrasoaña et al.*, 2003; *Zhang et al.*, 2014; *Marzocchi et al.*, 2015]. African dust is generally radiogenic with respect to Sr [*Scheuvens et al.*, 2013 and references therein]; in particular, the more proximal Moroccan and Mauritanian dust sources have $^{87}Sr/^{86}Sr > 0.722$ [*Grousset et al.*, 1988]. As the Sr anomalies occur just after the driest part of the insolation cycle (Fig. 3.1a, f), there is a mechanism for this source to play a role in the Sr isotope pattern. A high dust load in the water column could also be associated with high G. *bulloides* abundances as this species is adapted to low light or more turbid

conditions [*Ortiz and Mix*, 1992; *Ortiz et al.*, 1995]. However, dust is not considered a significant source of Sr to marine budgets [e.g. *Frank*, 2002; *Goldstein and Hemming*, 2003], as a small amount of Sr is transferred to seawater relative to the already high seawater Sr concentration.

3.4.2 The freshwater budget and vertical mixing

The freshwater budget of a basin controls, to a large extent, stratification and vertical mixing of the water body. Increased surface water salinity caused by evaporation leads to increased surface density and water column destabilization. This process will occur when the freshwater budget becomes negative (E>P+R), and vertical mixing increases as the freshwater budget becomes more negative. It should be noted that an important mechanism which is capable of producing mixing in the water column is wind, resulting in processes such as Ekman spirals down through the water column, or providing energy to promote upwelling in coastal areas. Unfortunately the information which is necessary to infer whether or not wind was a contributing factor in the basin during periods of bottom water oxygenation have not been preserved. For this reason, the classical interpretation of the Sorbas Basin Upper Abad sediments does not include wind as a factor. Instead, the explanation for sapropel formation in the open Mediterranean basins (water column stratification due to a less saline water cap) is more commonly invoked as the Sorbas Basin was connected to the open Mediterranean prior to the deposition of the evaporites.

The box model provides no insights into water column structure as it assumes fully mixed conditions. However, considerable information about changes in stratification and vertical mixing can be inferred from Sorbas' lithological and faunal patterns. In summary:

- the sapropelic layers, with preserved laminations and minimal benthic foraminifera, are thought to be deposited under stratified conditions which inhibited bottom water oxygenation and bioturbation [*Sierro et al.*, 2001, 2003];
- diatom blooms are linked to nutrient availability or upwelling; in the Sorbas Basin, upwelling is most likely [*Filippelli et al.*, 2003; *Sierro et al.*, 2003]. Our box model prediction of small variations in Q_R are consistent, implying changes to runoff are not sufficient to explain the observations;
- the increase in benthic relative to planktic fauna (the B/P ratio) suggests enhanced bottom water oxygenation coinciding with the non-sapropelic layers [*Pérez-Folgado et al.*, 2003]. Specifically, the B/P ratio increases through marl 1, peaks

somewhere near or during the diatomite, and decreases through marl 2 back to near zero at the base of the sapropel (Fig. 3.1d);

- *Globigerina bulloides* is a planktic foraminifer associated with cooler, more turbid upwelling waters [*Pérez-Folgado et al.*, 2003]; this species does not bear symbionts, and as such, is suited to lower light levels in the water column [*Ortiz et al.*, 1995]. The abundance of *G. bulloides* increases through marl 1, and peaks during or just after the diatomite.

Taken together, these factors indicate that strong vertical mixing was initiated during marl 1, reached a maximum either during diatomite deposition or the peak in *G. bulloides* abundance in marl 2, and decreased back to stratified conditions at the base of the sapropelic layers.

In detail, the relationship between the fauna and lithologies in the non-sapropelic layers is more complex (Fig. 3.1d, e) probably as a result of biological feedbacks. For example, bioavailable phosphorus is at maximum throughout the non-sapropelic layers and particularly during the diatomite [*Filippelli et al.*, 2003]. This suggests productivity was very high in these layers, potentially causing oxygen depletion in the bottom waters as a result of organic matter decomposition. The nutrient availability proxy, P/Ti, drops off at the top of the diatomite layers [*Filippelli et al.*, 2003]. These authors suggest that the transition from diatomite to marl 2 may be controlled primarily by nutrient depletion in the upwelling waters rather than a decrease in the vigor of upwelling itself. *G. bulloides* abundance may be affected by dust or other causes of turbidity in the water column, as well as temperature and food availability, and thus changes in its abundance may also be influenced by factors other than upwelling [*Pérez-Folgado et al.*, 2003]. However, the general faunal pattern is consistent throughout the entire Upper Abad marl succession, not just the four cycles studied here (Fig. 3.1), and supports most intense vertical mixing around or just after the time of diatomite deposition [*Sierro et al.*, 2003].

3.4.3 $^{87}Sr/^{86}Sr$ and vertical mixing

The Sr anomalies occur at the same time as the maximum in *G. bulloides* in all cycles (Fig. 3.1e,f). This implies that the isotope anomaly was produced during strong vertical mixing of the water column, i.e. during the most negative part of the hydrologic cycle. This phase relationship is simulated in Fig. 3.3b. In this case, the Sorbas Basin freshwater budget is positive except for a brief period when the hydrologic budget becomes negative (E >

$P+Q_R$), immediately preceding the Sr anomaly. This scenario is also consistent with the most positive hydrologic budget conditions during sapropelic layer deposition, when water column stratification is required. The case illustrated in Fig. 3.3d, where Sorbas has a mostly negative freshwater budget, causes the Sr anomaly peaks to be out of phase by half a precessional cycle with the salinity and implied water column stratification. We conclude therefore, that in contrast with the negative late Miocene freshwater budget for the main Mediterranean basin [*Blanc*, 2000; *Ryan*, 2008; *Marzocchi*, 2016], the Sorbas Basin is likely to have had a primarily positive freshwater budget in order to generate the observed phase relationship between the Sr anomalies and faunal data.

3.4.4 Temporal lags and implications for Mediterranean astronomical tuning

The transient model results (Fig. 3.3) indicate that while changes in Sorbas salinity lag changes in its freshwater budget by ~1 kyr, the Sr peak in each cycle lags changes in salinity by a similar interval (Fig. 3.3b-d, star-marked vertical bars). The lag between the Sr anomaly and salinity peak results from the time required to introduce enough riverine Sr to alter the basin isotopic composition while exchange between Sorbas and the Mediterranean is suppressed. Assuming maximum vertical mixing is synchronous with maximum salinity, this temporal relationship suggests that the Sr isotope anomaly should lag behind maximum vertical mixing of the water column by ~1ky and should lag the most negative hydrologic budget by ~ 2 ky. The time lag observed is smaller than the 3.3 ± 2.6 ky figure determined by *Topper and Meijer* [2015]. The difference in lag time is attributable to differences in the model set up. Firstly, these authors used a two-box model in which a smaller 'marginal' box exchanges with a Mediterranean 'deep' box, which then exchanges with the Atlantic. Both boxes evolve with precession and there is a phase lag related to each connection. Secondly, the selection of volume is different; *Topper and Meijer* [2015] adopted a volume of 300 km^3 on the basis that this figure is a suitable average for marginal basins across the entire Mediterranean region [*Topper et al.*, 2014]. The smaller box (240 km^3) we have used here is more appropriate for Sorbas and evolves faster than a larger volume marginal basin in response to identical forcing. This suggests that basin volume plays a key role in the duration of the temporal lags between climate and sedimentation and that therefore, within a single precessional cycle, changes in salinity and associated sedimentation seen in marginal basins may not be synchronous either with each other or with the main Mediterranean basin.

Phase lags between climate, lithology, and climate proxies have implications for the appropriate location of astronomical tuning tie points within each precessional cycle. Previous research has suggested that orbital tuning of the Abad Marls by tying precession minima to the midpoint of sapropelic layers [e.g., *Krijgsman et al.*, 1999a] is incorrect as sapropelic layers were deposited during the transition to precession minima, rather than being centered symmetrically around it *Pérez-Folgado et al.* [2003]. The Sr anomalies are associated with enhanced vertical mixing during the deposition of diatomite and/or marl 2 (Fig. 3.1) and just after maximum salinity (Fig. 3.3b). This supports the suggestion that astronomical tuning of the Abad Marls can be achieved most accurately by tying the diatomite layers to precession maxima. Tying precession maxima to cyclical diatomites has also been suggested for other Mediterranean successions (e.g. Tripoli Formation [*Hilgen and Krijgsman*, 1999]). However, the precise point within the diatomite to which precession maxima should be pinned cannot be deduced from our results as the diatomite is a product of mixing, and mixing is not included in the box model.

3.4.5 Implications for overlying Sorbas Basin deposits

Higher up the Abad succession (from UA 17, ~6.35 Ma), the marl 2 layer becomes nearly devoid of planktic foraminifera, leading to the term 'aplanktic marls' [*Sierro et al.*, 2003]. This is thought to result from surface water salinities above the tolerance of planktic foraminifera (> 49 g/L, *Fenton et al.* [2000]). The box model results indicate two controlling factors on Sorbas Basin salinity so long as two-way exchange is maintained: Western Mediterranean salinity controls average salinity in the Sorbas Basin, while the freshwater budget controls the amplitude of salinity change throughout a cycle. In the absence of a change in Mediterranean salinity, to maintain the lithological cyclicity observed throughout the Abad formation while generating salinity >49 g/L requires either increased salinity in the Western Mediterranean, or that part of Sorbas' hydrologic cycle becomes very negative. The latter requires very high amplitude shifts of the hydrologic budget within a precessional cycle, approximately three times greater amplitude than that shown in Fig. 3.3. Such a change would suggest an overall drying trend in the region, but this is not observed in other records. Pollen records from across the Mediterranean, including southern Spain, do not indicate any significant long-term drying trends during the Messinian or early Zanclean [*Fauquette et al.*, 2006], although sub-precessional cyclicity cannot be inferred. Thus, it is more likely that increasing salinity in the open Mediterranean is the primary driver. Indications of increasing salinity immediately prior to

MSC onset is observed in other marginal sections (e.g., Piedmont Basin, Italy [*Dela Pierre et al.*, 2011]). High resolution records of sea surface salinity, from open Mediterranean locations (far from the influence of river runoff), between 6.5 Ma and MSC onset are required to test this inference. A continued high-resolution Sr isotope record into UA17 and beyond could also differentiate the primary driver, as very high amplitude shifts would be inconsistent with Sr anomalies. In such a case, the amount of time near a neutral hydrologic budget would be insufficient to allow a Sr anomaly to develop in the basin.

The inference that Mediterranean salinity controls salinity in Sorbas is consistent with the accepted model of a deep Mediterranean basin during MSC Stage 1 [*CIESM*, 2008; *Roveri et al.*, 2008]. $^{87}Sr/^{86}Sr$ ratios measured from the Primary Lower Evaporite (PLE) gypsum in Sorbas are within error of the global ocean curve [*Lugli et al.*, 2010; *Roveri et al.*, 2014; *Evans et al.*, 2015]. Given that Sorbas fluvial $^{87}Sr/^{86}Sr$ continued to be relatively radiogenic after the MSC, oceanic $^{87}Sr/^{86}Sr$ signatures indicate that sea level in the open Mediterranean was maintained above the Sorbas Basin connections.

Interestingly, two studies have shown that PLE gypsum may have been affected by meteoric water since deposition. *Natalicchio et al.* [2014] found that the salinity of crystal inclusions in PLE gypsum from the Piedmont Basin (northwest Italy) is very low, while gypsum inclusions from the Conti Vecchi solar salt works (Sardinia, Italy), where seawater is evaporated in a series of ponds to concentrate gypsum and halite as commercial products, have high salinity, matching that of brine from which gypsum precipitates. *Evans et al.* [2015] observed seawater $\delta^{34}S$, $\delta^{18}O_{SO4}$ and $^{87}Sr/^{86}Sr$ isotope signatures in gypsum crystals from one cycle of Sorbas' PLG which also had $\delta^{18}O$ and δD values consistent with meteoric water. Both studies suggest that dissolution and re-precipitation are necessary for such a combination of characteristics. The results of our box model provide a plausible mechanism, as both studies can be explained by a primarily positive freshwater budget over the course of a precessional cycle, leading to incorporation of meteoric water post gypsum deposition.

3.5 Conclusions

The interval studied in the Sorbas Basin, approximately 0.5 Ma prior to the MSC, is characterized by regularly occurring $^{87}Sr/^{86}Sr$ anomalies more radiogenic than coeval global ocean values. These anomalies vary in phase with precession and are consistent

with the local continental Sr isotope signature. The precessional frequency indicates a climate-driven mechanism for the record, in parallel with cyclical changes in sedimentation and faunal assemblages.

Steady-state and transient numerical box modeling indicate that the Sr isotope anomalies are driven by restriction of exchange through Sorbas' marine connection with the Western Mediterranean. This restriction is not controlled by gateway size, but by precessional fluctuations in the freshwater budget driving changes in the Mediterranean-Sorbas density contrast and in turn impacting flux between basins. Both import of oceanic Sr and export of the local Sr signal are inhibited during minimal density contrast, enhancing the contribution of the fluvially-transported local continental Sr signal, relative to periods of active exchange. This is significant for many reasons, one of which is that this mechanism is often neglected in studies of basin connectivity relating to the MSC. Generally speaking, it is assumed that physical gateway closure is the primary mechanism causing Sr isotope ratios to fall away from the global ocean curve. Clearly, the case of the Sorbas Basin illustrates that the mechanism of density contrast driving (or impeding) exchange must also be taken into consideration.

The model results also demonstrate that the average Sorbas Basin salinity is controlled by Mediterranean salinity. This means that major changes in marginal basin salinity, such as the transition to gypsum precipitation at the onset of the MSC, reflect changes in the salinity of the main Mediterranean basin on the scale of a single precessional cycle. This result supports the hypothesis of a synchronous MSC onset between the Western and Eastern Mediterranean basins, where this hypothesis is based on outcrops primarily from marginal settings.

At sub-precessional timescales, however, the timing of salinity change and hence the lithological response to salinity and vertical mixing or stratification is likely variable, as sedimentation is a result of the individual basin freshwater budget and volume. In the case of the Sorbas Basin, the numerical model results are consistent with a primarily positive hydrologic budget; only this regime is capable of causing vertical mixing coincident with the correct lithologies at the same time as the observed Sr isotope anomalies. Conversely, it is understood that the open Mediterranean generally had a negative hydrologic budget during the late Miocene, similar to today [*Marzocchi et al.*, 2015; *Marzocchi*, 2016].

Although the results of *Pérez-Folgado et al.* [2003] have already suggested that sedimentation in the Sorbas Basin may have a different phasing to an open Mediterranean site (Gavdos, Crete), the difference in hydrologic budget indicated by the numerical model results provides a mechanism for this observation. The sapropelic layers in Sorbas appear to precede insolation maxima [*Pérez-Folgado et al.*, 2003], compared to a 3 ky lag observed for sapropel S1 in the Eastern Mediterranean [*Lourens et al.*, 1996]. The different phasing has significant implications for astronomical tuning tie points, since common practice in the literature is to assume that cycle-equivalent sapropel midpoints from multiple basins link to insolation maxima [e.g., *Krijgsman et al.*, 1999a], or that they should lag 3 kyr behind insolation maxima [e.g., *Sierro et al.*, 2001]. The Sr isotope results shown in Ch. 3, combined with the lithological and faunal data, suggest that it may be more accurate to tune the diatomite layers to insolation minima, although the Sr data set and model work does not allow the determination of exactly which part of the layer should correspond to the insolation trough. This is less problematic for sites with thin diatomite layers, but could be more problematic for sites such as Falconara (Sicily) with very thick diatomites. The volume of a basin also clearly exerts control over the magnitude of the lag, as observed when comparing the results from the small volume used here to represent the Sorbas Basin and larger volumes used in previous numerical modeling studies [*Topper and Meijer*, 2015]. Larger basin volumes apparently cause larger lags.

The box model also provides insight into conditions of the basin during later episodes. The results suggest that open Mediterranean salinity was the primary control on the high salinities inferred for the aplanktic marls (Abad cycles UA17 and above, from ~6.4 Ma to the MSC), implying Mediterranean salinity approached values near the limit for foraminiferal growth before MSC onset. To test this hypothesis, it is again necessary to recover pre-evaporite material from the deep basins, and develop age models for these samples allowing for temporal resolution better than precession; to date, this has not been accomplished, due to technical issues drilling underneath the deep salt layers as well as reworking and other complications affecting biostratigraphy and palaeomagnetic studies of the latest Miocene sediments in the Mediterranean.

Finally, the implications for the hydrologic budget of the Sorbas Basin provide an explanation for the observation of essentially fresh, meteoric water trapped in gypsum inclusions. Primary Lower Gypsums at Sorbas and the Piedmont Basin (Northern Italy) contain several characteristics suggesting the influence of meteoric water [*Natalicchio et*

al., 2014; *Evans et al.*, 2015]. While it is essentially accepted that the brine was sourced from the open Mediterranean (section 3.4.5 above), a positive freshwater budget for the individual marginal basins provides a mechanism to incorporate a post-depositional (or potentially syndepositional) freshwater signal.

4 Tracing circulation in the Western Mediterranean and Sorbas Basin with Nd isotopes: results and implications

4.1 Overview

This chapter outlines the results and discusses the implications of the neodymium (Nd) isotope compositions determined over the course of this project. Before it is possible to discuss gateway dynamics and exchange, it is necessary to establish a reliable estimate of the late Miocene Nd isotope signature for the Alboran Sea. To this end, data from ODP Site 978 are discussed initially, compared to literature data, and an estimate is provided for the Alboran Sea bottom water $\varepsilon_{Nd(t)}$ composition in the late Miocene. Nd isotope results derived from late Miocene Sorbas Basin sediments follow, and the implications of this dataset are discussed. This discussion includes an examination of the reliability of the leaching process for the specific case of the Sorbas Basin, including a comparison between different sediment fractions (bulk sediment leachates, fish teeth, strong leaches and total dissolution of sediment samples), and a comparison of the Al/Nd elemental ratio of the bulk sediment acid-reductive leachates with their ε_{Nd}. An updated assessment of the palaeo-signature of MO for the late Miocene is provided, and Nd as an isotopic proxy for investigating exchange between the Mediterranean and Atlantic prior to and during the MSC is re-examined. Nd isotope data from other locations, which does not fit with this chapter, is provided in Appendix 3.

CHAPTER NOTES

Materials and methods: Ch. 2, sections 2.2, 2.3.4, 2.5
Sample location maps: Ch. 1, Fig. 1.21; Ch. 2, Fig. 2.1
Contributions: Marlies van der Schee, ODP Site 978 Nd isotope data

4.2 Background oceanography

In the modern environment, as Mediterranean water flows out into the Atlantic, it settles into a plume between approximately 500 and 1500 m water depth [*Ambar et al.*, 2002] (Ch. 2, Fig. 2.1d). The Mediterranean Outflow (MO) plume is easily distinguished by its salinity and temperature characteristics from Eastern North Atlantic Central Water (ENACW) above, a significant amount of which is entrained within the MO plume as it travels west past Cape St. Vincent [*Baringer and Price*, 1999]. Due to this entrainment,

MO becomes neutrally buoyant and settles with a salinity maximum at approximately 1200 m [*Baringer and Price*, 1999; *Ambar et al.*, 2002]. In deeper settings, North Eastern Atlantic Deep Water (NEADW) is recognizable below the Mediterranean outflow plume flowing southwards, while Antarctic Bottom Water (AABW) lies deeper yet and flows northwards. One final water mass, Antarctic Intermediate Water (AAIW) also flows northwards, and can be found at relatively shallow depths along the African coast [*Jeandel*, 1993; *Rickli et al.*, 2009]. These water masses are distinguished from each other by several properties over and above salinity and temperature (potential density), including dissolved oxygen and nutrient content, stable isotope composition, suspended particulate matter, ε_{Nd} signature, and dissolved aluminium concentration [*Hydes*, 1983; *Piepgras and Wasserburg*, 1983; *Ambar et al.*, 2002; *Criado-Aldeanueva et al.*, 2006; *Stichel et al.*, 2015; *Voelker et al.*, 2015].

MO is a mixture of Levantine Intermediate Water (LIW) and Western Mediterranean Deep Water (WMDW) [*Kinder and Parrilla*, 1987; *Measures and Edmond*, 1988; *Greaves et al.*, 1991]. ODP Site 978 sits at approximately 2000 m water depth today, bathed by the upper part of Western Mediterranean Deep Water (WMDW; Ch. 2, Fig. 2.1a, d). It has been shown that WMDW may contribute less than 10% to MO [*Measures and Edmond*, 1988]; however, complete renewal of the WMDW mass has been observed on short time scales of just a few years [e.g., *Schroeder et al.*, 2008, 2016] suggesting that it is possible that WMDW contributes a more significant volume to MO during short lived turnover events. LIW is more radiogenic with respect to ε_{Nd} than WMDW, with published measurements as high as -4.8 ε_{Nd} in the Eastern Mediterranean, likely owing to the strongly radiogenic Nile input near the source of LIW formation [*Frost et al.*, 1986; *Weldeab et al.*, 2002; *Tachikawa et al.*, 2004]. Aeolian dust also contributes Nd to Mediterranean seawater, with a signature of about -10 ε_{Nd} in the Eastern Mediterranean [*Greaves et al.*, 1991, 1994; *Henry et al.*, 1994; *Tachikawa et al.*, 2004]. The ε_{Nd} signature of LIW in the Alboran Sea matches that of MO within the Gibraltar Strait itself [*Tachikawa et al.*, 2004]. WMDW is formed during periods of intense cooling, primarily in the Gulf of Lions, from a combination of LIW and surface water [*Wu and Haines*, 1996; *Schröder et al.*, 2006 and references therein]. As such, the Nd isotope signature of WMDW is a mixture of the two sources. In the past, WMDW formation has also been shown to vary on millennial timescales, owing primarily to changes to surface water density due to climate [*Frigola et al.*, 2008].

4.3 Late Miocene Western Mediterranean ε_{Nd}: ODP Site 978

4.3.1 Results

The Nd isotopic compositions measured from the four late Miocene samples from ODP Site 978 in the Alboran Sea range from -9.34 to -9.92 ± 0.37 $\varepsilon_{Nd(t)}$ between 6.12 and 6.62 Ma (Range C, Fig. 4.1, Table 4.1). The $\varepsilon_{Nd(t)}$ values for the early Pliocene are very similar, at -9.25 ± 0.51 (3.98 ± 0.05 Ma) and -9.35 ± 0.37 (4.52 ± 0.05 Ma), well within analytical error. One of the four late Miocene samples is slightly less radiogenic, at -9.92 $\varepsilon_{Nd(t)}$; all analyses were repeated to ensure the reported values are accurate. Excluding this unradiogenic datum, the average of all other data is -9.37 $\varepsilon_{Nd(t)}$, essentially the same as the modern value. At the Gibraltar Straits today, MO is approximately -9.4 ε_{Nd} (Range A, Fig. 4.1) while inflowing Atlantic water is around -11.8 ε_{Nd} [*Piepgras and Wasserburg*, 1983; *Spivack and Wasserburg*, 1988; *Tachikawa et al.*, 2004].

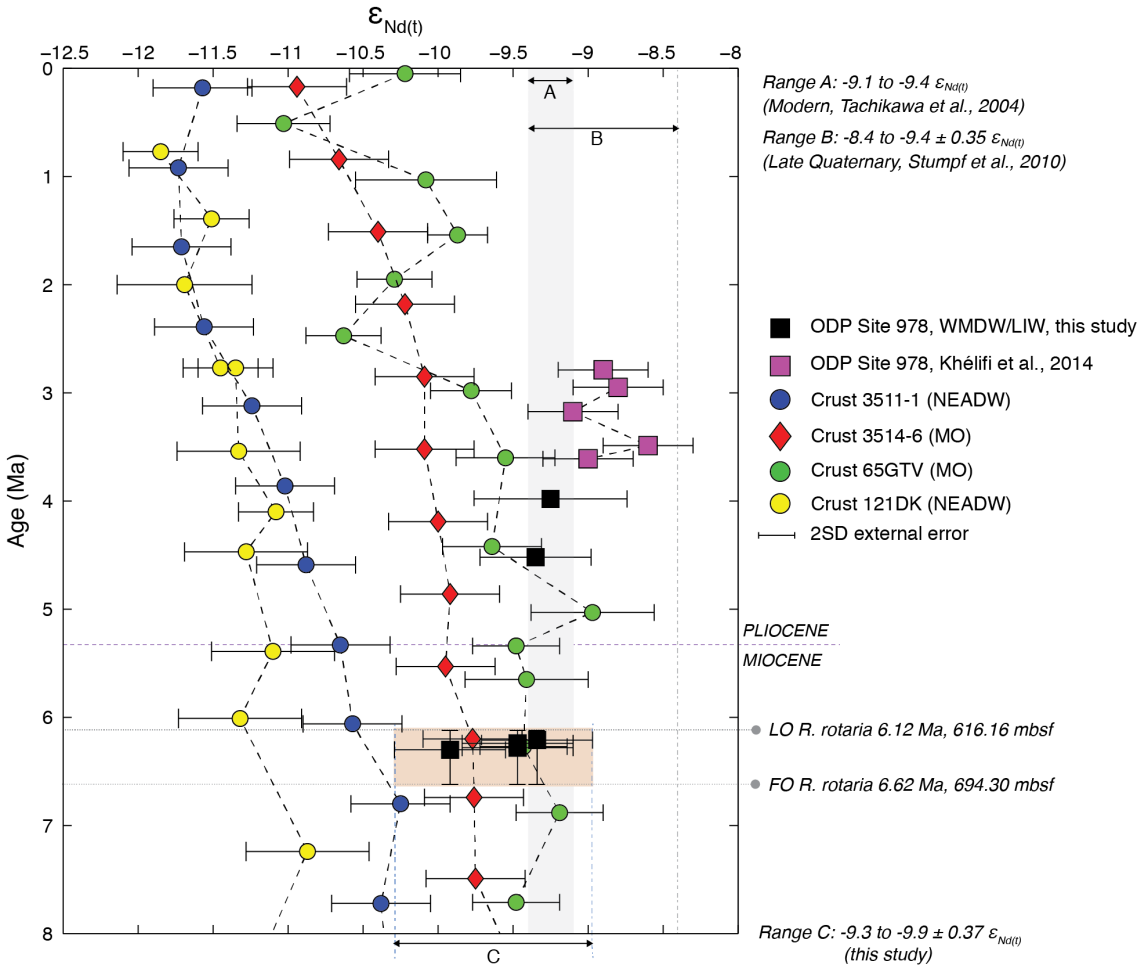

Fig. 4.1. $\varepsilon_{Nd(t)}$ from ODP Site 978 (squares) compared with published values for Mediterranean Outflow (MO) and North Eastern Atlantic Deep Water (NEADW) from FeMn crusts (65GTV, 121DK [*Abouchami et al.*, 1999]; 3514-6, 3511-1, [*Muiños et al.*, 2008]). Dashed lines at 6.12 and 6.62 Ma indicate age range of Messinian samples; boundaries are provided by last occurrence (LO) and first occurrence (FO) of R. Rotaria (Ref, Leg 161 Results). Samples within the interval are assigned age uncertainty equal to this time span. Tan box emphasizes the maximum range of values observed in late Miocene Site 978 values (including analytical uncertainty), corresponding to Range C. Range A indicates modern MO values at Gibraltar [*Tachikawa et al.*, 2004]; Range B indicates values for the Holocene measured in sediments from the Iberian margin [*Stumpf et al.*, 2010]. See Ch. 2, Fig. 2.1 and Table 2.3 for locations. LIW – Levantine Intermediate Water.

Table 4.1. ODP Leg 161 Site 978 $^{143}Nd/^{144}Nd$ ratios (uncertainty 2SD).

Age (Ma)	Maximum (Ma)	Minimum (Ma)	Sample Name	$\varepsilon_{Nd(t)}$	
6.30	6.62	6.12	48R-3W 121-123-15 cm	-9.92	± 0.37
6.28	6.62	6.12	48R-1W 13-15 cm	-9.61	± 0.37
6.28	6.62	6.12	48R-1W 13-15 cm	-9.32	± 0.37
6.24	6.62	6.12	47R-3W 122-124 cm	-9.55	± 0.37
6.24	6.62	6.12	47R-3W 122-124 cm	-9.40	± 0.37
6.21	6.62	6.12	47R-1W 16-18 cm	-9.34	± 0.37
6.21	6.62	6.12	47R-1W 16-18 cm	-9.33	± 0.37
4.52	4.57	4.47	35R-3W 65-67 cm	-8.91	± 0.51
4.52	4.57	4.47	35R-3W 65-67 cm	-9.35	± 0.37
3.98	4.03	3.93	29R-6W 30-32 cm	-9.25	± 0.51

4.3.2 Discussion

4.3.2.1 Implications of late Miocene $\varepsilon_{Nd(t)}$ from ODP Site 978

The configuration of water masses in the Alboran Sea during the late Miocene is unknown, and therefore the assessment here is based on the assumption that circulation patterns at that time were similar to today. Considering that the late Miocene range determined from Site 978 is within error of coeval values from FeMn crusts 65GTV and 3514-6, both thought to have been deposited in the MO plume [*Abouchami et al.*, 1999; *Muiños et al.*, 2008], it is likely that the Nd isotope compositions recorded at Site 978 indeed reflect the ε_{Nd} signature of MO. Since these FeMn crust data integrate water mass signatures over tens to hundreds of thousand years, shorter-term variability is averaged out (e.g., seasonal, decadal, precessional), providing more general estimates of MO. The precise signature recorded by the crusts is certainly the result of an admixture of MO and overlying NACW, and potentially NEADW, as the plume mixes with the water masses it contacts on exiting the Mediterranean. However, all other significant water masses in the region (i.e., NACW, NEADW, AAIW, AABW), with the exception of surface water, are expected to be significantly less radiogenic (< -11.5 εNd) [*Tachikawa et al.*, 1999; *Rickli et al.*, 2009; *Stichel et al.*, 2015].

4.3.2.2 *Reliability of Site 978 data and implications for regional palaeoceanography and MO*

The sediments recovered in the late Miocene Site 978 core segments are described as turbiditic deposits, implying sediment-water interaction as well as sediment redistribution is a factor for consideration (Ch. 1, section 1.3.1). Where suspended particulates are dense in bottom water layers, such as nepheloid clouds and turbidites, more vigorous exchange between particle Nd and dissolved Nd is suspected [*Gutjahr et al.*, 2008]. Today, Site 978 is pelagic at nearly 2000 m water depth and approximately 50 km from the nearest shoreline. During the late Miocene, palaeogeography suggests this distance was similar or greater (Ch. 2, Fig. 2.1a). Site 978 is located within an east-west trending graben, bounded by the Maimonides Ridge to the north and the Yusuf Ridge to the south (Fig. 4.2). Located southwards and nearer than the Yusuf Ridge is the Al-Mansour seamount, a volcanic mount related to the Alboran Arc. All these prominences are fully submersed and pre-date the late Miocene Site 978 sediments based on stratigraphic relationships observed from seismic images [*Shipboard Scientific Party*, 1996; *Iaccarino and Bossio*, 1999, see their Fig. 9], while the Al-Mansour Seamount formed approximately 8.7 Ma [*Duggen et al.*, 2008 and references therein]. The Maimonides Ridge is likely to have diminished the amount of continental sediment from Southern Spain reaching Site 978; likewise, the Yusuf Ridge and longer distance to the African coast likely prevented ingress of siliciclastics from southern continental sources. The sediment deposited by density currents during the late Miocene at Site 978 therefore likely originated from the adjacent ridges and/or seamounts, transporting marine sediments already possessing a marine signature, specifically that of LIW. Downslope transport of sediments is an advantage in this case, as this mechanism would transport sediments recording the shallower LIW signature to deeper water at Site 978, resulting in LIW and WMDW water mass signature integration or even a primarily LIW signature.

The depositional facies could also explain the variability in the late Miocene Nd isotope data from Site 978. Sedimentation is described as 'low to high density currents' [*Shipboard Scientific Party*, 1996] deposited in a 'submarine fan lobe deposit' [*Iaccarino and Bossio*, 1999]. Variability in the intensity and amount of flow downslope could affect the final archived signature in terms of the proportion of sediment sourced from within LIW or WMDW. In this case, the less radiogenic value may represent quieter conditions and a more direct recording of WMDW ε_{Nd}. The nearby Al-Mansour Seamount (Fig. 4.2) contains highly radiogenic volcanic rocks (+2 to +9 ε_{Nd} [*Duggen et al.*, 2008]). This

radiogenic signature implies that it is unlikely that the single late Miocene data point of less radiogenic signature (relative to both the modern signature and other Site 978 data) was caused by local boundary exchange but rather another source of slightly less radiogenic Nd. Significant interaction via boundary exchange with volcanic minerals originating from Al-Mansour would be expected to produce more radiogenic signatures than those observed, and can therefore be eliminated as a factor for the least radiogenic data; it is more likely that the least radiogenic sample from Site 978 was deposited during a period in which downslope transport was reduced, enhancing the contribution of the less radiogenic signature of WMDW. It is unknown what the impact of the underlying radiogenic rocks may be on the data from Site 978 overall; if circulation during the late Miocene, prior to the MSC, were similar to today (with water being pulled up from the depths through the Alboran Channel (ACH), Fig. 4.2) any signature deriving from the bottom may mix into LIW and contribute to the overall signature of MO.

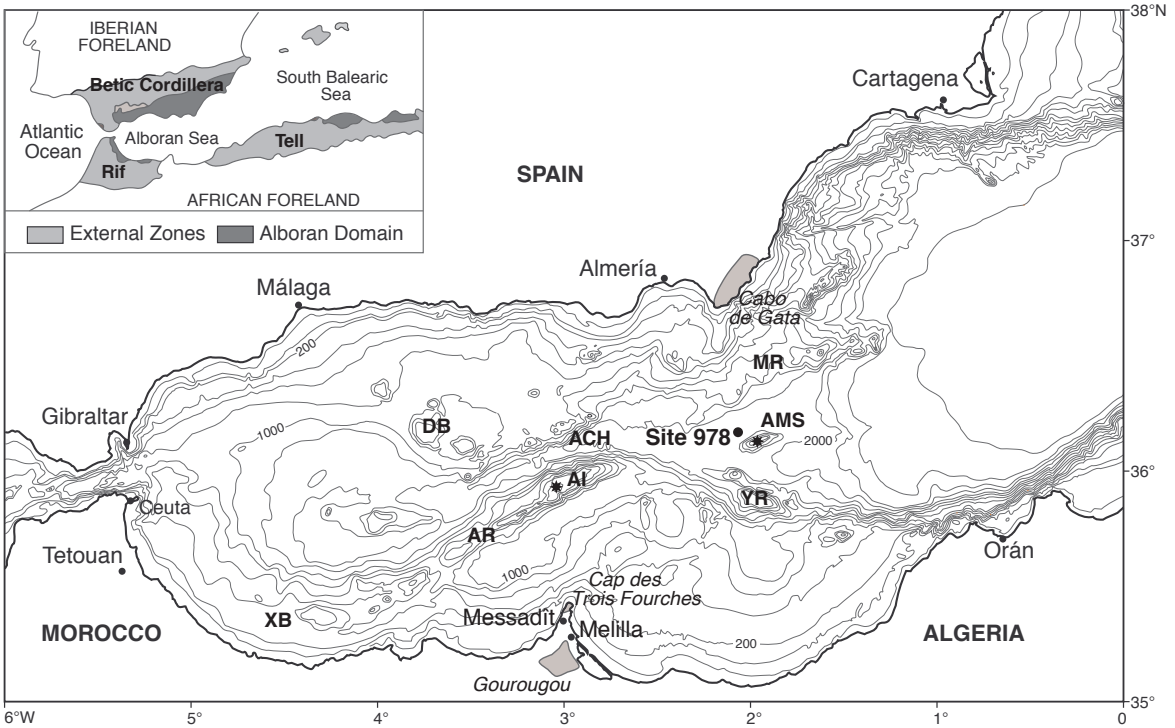

Fig. 4.2. Map of structures in Alboran Sea and location of sites mentioned in this chapter. Inset shows the main mountainous regions of the area (Betic, Rif, and Tell). Cap des Trois Fourches and Gourougou areas are regions of volcanic rock with highly radiogenic ε_{Nd} signatures; Messadît is one outcropping sedimentary section from which *Ivanoviç et al.* [2013] used fossil fish teeth to estimate the palaeo-ε_{Nd} signature of MO. AMS – Al-Mansour Seamount; YR – Yusuf Ridge; MR – Maimonides Ridge; AR – Alboran Ridge; AI – Alboran Island; XB – Xauen Bank; DB - Djibouti Bank; ACH – Alboran Channel. Modified from [*Martínez-Ruiz et al.*, 1999].

Climate variability causing changes in the intensity and volume of WMDW formation could also be responsible for the observed variability in late Miocene Site 978 ε_{Nd}. The age model of the late Miocene section of Site 978 is poor (Ch. 2, section 2.2.2), negating the ability to associate orbital cycles or other relatively short-term climate variability to the

data. However, for future work and to foster a comprehensive analysis of contributing factors, changes in climatic factors and the ε_{Nd} signatures such changes could cause is of merit for discussion. Sediment samples taken for isotope analysis integrate much shorter periods than FeMn crusts, on the order of a few ky at most; in comparison, the data from *Abouchami et al.* [1999] and *Muiños et al.* [2008] for the crusts is 10,000 to 100,000 years. The Nd isotopic compositions from Site 978 data appear to reflect reliably bottom water signatures, suggesting it is possible to generate a reliable ε_{Nd} record for MO given appropriate age constraints. Two processes known to have occurred in the late Miocene, operating on precessional timescales, could have significantly affected the overall physical oceanography of the Mediterranean and thus the ε_{Nd} signature of Mediterranean water masses: (1) changes in the quantity of runoff derived from North Africa, and, consequent to this, (2) changes in circulation patterns of the basin [*Rohling*, 1994; *Matthiesen and Haines*, 2003; *Scrivner et al.*, 2004; *Marzocchi et al.*, 2015; *Rohling et al.*, 2015]. The first process changes the overall proportion of water coming from various sources characterized by specific ε_{Nd} derived from their catchment geology, a process which on its own may affect overall basin ε_{Nd}. In addition to increased radiogenic Nile input during insolation maxima, the ancient Libyan Eosahabi river system likely provided another source of radiogenic Nd to the Eastern Mediterranean ($\varepsilon_{Nd} \sim -2$; Ch. 1, Fig. 1.9) [*Osborne et al.*, 2008, 2010]. Changes in freshwater input also affect circulation through the basin as density of surface water is altered, affecting the amount of LIW formed and its properties as it flows back through the Western Mediterranean. All water masses which incorporate LIW should therefore be affected, including both MO and WMDW. Hopefully, future drilling campaigns such as the DREAM project [*Camerlenghi et al.*, 2014], which propose to recover MSC deposits and beyond, will be able to provide appropriate late Miocene material from deep locations which could be used to apply the Nd isotope tracer with sub-precessional temporal resolution.

4.3.2.3 Implications for previously published MO water mass estimates

[*Ivanoviç et al.*, 2013] determined a much more radiogenic end-member for late Miocene to Pliocene MOW (-8.2 to -8.9 ε_{Nd}; Fig. 4.3). Those authors used ε_{Nd} compositions derived from fish remains from the Messadît section, Morocco (Fig. 4.2) as a basis for this estimate. Fish remains reliably incorporate Nd from near the sediment-water interface during deposition at concentrations high enough to maintain the Nd isotope signature incorporated at that time even during later episodes of diagenesis [*Martin and Scher*,

2004]. However, the Messadît section contains several prominent volcanic ash layers. It is likely that these volcanic sediments are characterized by radiogenic Nd as the nearby Gourougou and Cap des Trois Fourches volcanic deposits, which bound the Messadît site to the south and north respectively (Fig. 4.2), exhibit a range of -6.6 to +3.2 ε_{Nd} [*Maury et al.*, 2000 and references therein]. Thus, boundary exchange acting at this site would cause pore and bottom waters to shift towards more radiogenic (less negative) ε_{Nd} signatures than the overlying water mass. The Messadît site was relatively shallow and shoaling [*van Assen et al.*, 2006 and references therein] at the same time that ε_{Nd} trends towards more radiogenic values in the *Ivanoviç et al.* [2013] record. Consequently, this trend may be a result of increasing boundary exchange as the site became more shallow; therefore, the record of *Ivanoviç et al.* may not show changes in exchange, but rather uplift of the Rifian gateway. In this regard, their record is consistent with sedimentological studies suggesting a similar time frame of closure due to uplift [*Krijgsman et al.*, 1999b; *van Assen et al.*, 2006]. It is currently understood that boundary exchange increases with proximity to ocean margins [*Lacan and Jeandel*, 2005; *Jeandel et al.*, 2007], and in particular in the presence of easily weathered volcanic material [*Wilson et al.*, 2013]. More problematic, however, is that the estimate for the palaeo-ε_{Nd} signature of MO suggested by *Ivanoviç et al.* [2013] does not agree with any of the three alternative late Miocene MO estimates (Site 978 results here or published values for crusts 3514-6 and 65GTV). ODP Site 978 is significantly deeper (~1930 m) and more distal. These factors and the coincidence with modern-day MO ε_{Nd}, as well as the late Miocene values of extra-Mediterranean crusts 65GTV and 3514-6, therefore lends more confidence in values predicted from Site 978 than with those predicted by *Ivanoviç et al.* [2013].

4.3.2.4 Late Pliocene and Quaternary records: causes for consistently more radiogenic values?

[*Khélifi et al.*, 2009, 2014] also published ε_{Nd} for the Plio-Pleistocene (3.7 – 2.7 Ma) from Site 978. These data are are slightly more radiogenic, ranging from -9.1 to -8.6 ± 0.3 ε_{Nd} (values not corrected to $\varepsilon_{Nd(t)}$ as the difference is negligible), compared to our late Miocene and Pliocene data. For the Quaternary, sediments deposited within the MO pathway along the Iberian margin were of a very similar range to the Khelifi et al. values (Range B, Fig. 4.1) [*Stumpf et al.*, 2010].

There are two main factors that could have caused this shift towards more radiogenic ε_{Nd}. Oceanographic factors such as water mass extent, water mass mixing, and headwater sources may have been such that seawater at Site 978 maintained a slightly more radiogenic ε_{Nd} signature than the late Miocene or the modern signature. The other cause could be a difference in methodology. In contrast to earlier studies, for the current project samples were not decarbonated prior to leaching. [*Stumpf et al.*, 2010] and [*Khélifi et al.*, 2009, 2014] all used a decarbonation step prior to leaching. [*Stumpf et al.*, 2010] also performed leaching for a longer duration (3 hours versus 2 hours for this thesis). According to [*Wilson et al.*, 2013], two factors which are significantly responsible for causing artefacts, or bias towards unreliable values, in leachate data are the length of leaching time and prior decarbonation. Those authors showed that shorter leaching times and no decarbonation are preferable to minimize the time allowed for attack of phases other than those carrying the seawater signal, while carbonate provides a buffer to further protect detrital siliciclastics [*Blaser et al.*, 2016]. Furthermore, authigenic carbonates preserve the bottom water signal and therefore should record the same ε_{Nd} value as authigenic oxyhydroxides [*Roberts et al.*, 2012; *Tachikawa et al.*, 2014]. As previously discussed, the Al-Mansour seamount is proximal to Site 978 and would provide highly radiogenic volcanogenic material, mineral phases shown to be particularly reactive and easily weathered [*Pearce et al.*, 2013; *Wilson et al.*, 2013; *Rickli et al.*, 2014].

This difference in methodology increases the uncertainty in understanding changes to the ε_{Nd} of the Western Mediterranean and Alboran Sea through time. It may be the case that the Mediterranean basin and thus MO experienced a shift towards more radiogenic values from the latest Pliocene until the Holocene. It may also be the case that [*Stumpf et al.*, 2010] and [*Khélifi et al.*, 2009, 2014] reported values that were slightly more radiogenic than the true water mass signal due to partial contributions from the detrital siliciclastic fraction. If indeed methodology is the cause for the slightly more radiogenic values observed by [*Stumpf et al.*, 2010] and [*Khélifi et al.*, 2009, 2014], then the Western Mediterranean and MO have most likely been characterized by a very consistent ε_{Nd} signature since the late Miocene.

4.4 Sorbas Basin ε_{Nd} signatures

4.4.1 Results: Nd isotope analyses

The results from bulk sediment acid-reductive leaching and fish remains from the Sorbas Basin range from -9.14 to -10.65 ± 0.42 $\varepsilon_{Nd(t)}$, showing only 1.51 ± 0.42 $\varepsilon_{Nd(t)}$ units of variability across the study interval (Fig. 4.3; Table 4.2). These values are within error of the range determined from ODP Site 978. There is no consistent pattern or cyclicity in the data. The least radiogenic values of the acid reductive leachates overlap with estimated values for NEADW.

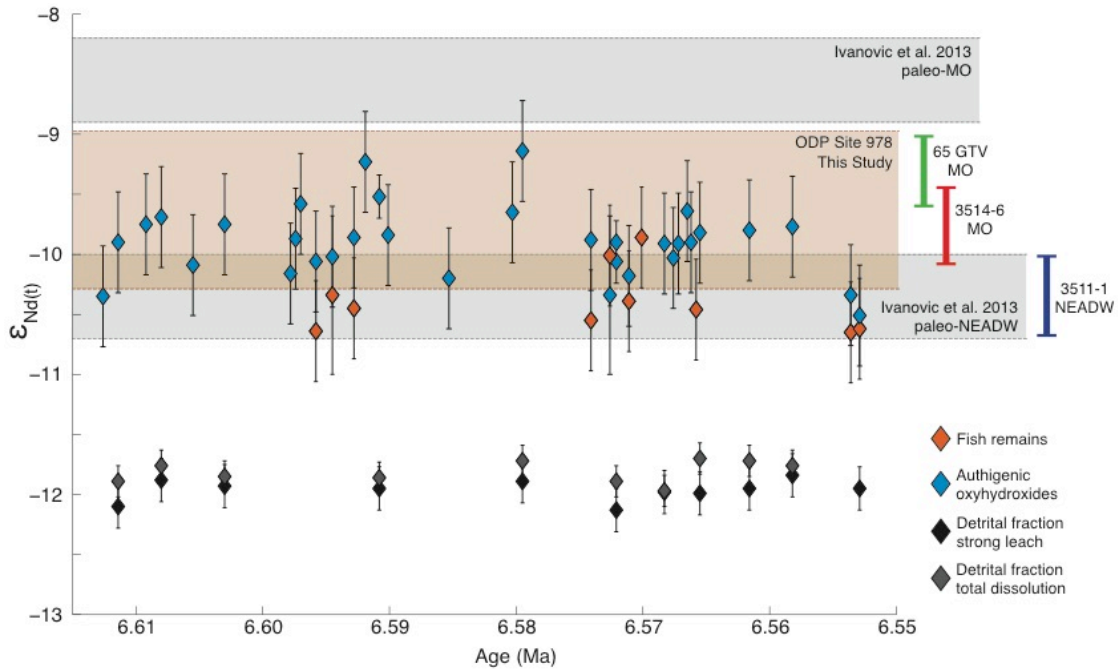

Fig. 4.3. Nd isotope results from Sorbas basin sediments. $\varepsilon_{Nd(t)}$ of fish remains, acid-reductive bulk sediment leachates, strong leachates, and total dissolution samples are compared with estimates of water mass Nd isotope signature estimates for MO and NEADW from *Ivanoviç et al.* [2013], ODP Site 978, and FeMn crusts 65 GTV, 3514-6, and 3511-1 [*Abouchami et al.,* 1999; *Muiños et al.,* 2008].

As shown in the lower part of Fig. 4.3, the strong leach and total dissolution $\varepsilon_{Nd(t)}$ is very similar, ranging from -11.7 to -12.1 ± 0.18. These unradiogenic values imply that a significant amount of easily weatherable minerals containing radiogenic Nd, such as volcanic ash, are not present. This isotopic range is also consistent with suspended detrital material, constituted in large part by eolian dust with unradiogenic ε_{Nd}, measured at several sites across the open Mediterranean [*Henry et al.*, 1994; *Tachikawa et al.*, 2004]. Relatively unradiogenic values in the strong leach and total dissolution samples are consistent with the observation that marine sediments are primarily composed of clay minerals derived from older rocks with relatively unradiogenic Nd in comparison to young volcanic minerals [e.g., *Wilson et al.*, 2013; *Osborne et al.*, 2014b].

Table 4.2. $^{143}Nd/^{144}Nd$ ratios of Sorbas Basin samples (ratio uncertainty 2SE internal; ε_{Nd} uncertainty 2SD external).

Sample	Age (Ma)	$^{143}Nd/^{144}Nd_{(t)}$	$\varepsilon_{Nd(t)}$		Session
(fish teeth and bone)					
34-06 FT	6.5958	0.512084 ±13	-10.64	± 0.42	1
34-09 FT	6.5945	0.512099 ±34	-10.34	± 0.66	1
34-12 FT	6.5928	0.512094 ±11	-10.45	± 0.42	1
35-05 FT	6.5741	0.512089 ±14	-10.55	± 0.42	1
35-08 FT	6.5726	0.512117 ±21	-10.01	± 0.42	1
35-11 FT	6.5711	0.512097 ±15	-10.39	± 0.42	1
35-14 FT	6.5701	0.512124 ±20	-9.86	± 0.42	1
35-26 FT	6.5658	0.512093 ±18	-10.46	± 0.42	1
36-09 FT	6.5536	0.512084 ±14	-10.65	± 0.42	1
36-11 FT	6.5529	0.512085 ±16	-10.62	± 0.42	1
(bulk sediment acid-reductive leaches)					
33-03 BSL2	6.6126	0.512099 ±13	-10.35	± 0.42	2
33-06 BSL2	6.6114	0.512103 ±11	-10.28	± 0.42	2
33-06 SL L1	6.6114	0.512134 ±4	-9.66	± 0.18	4
33-06 TD L1	6.6114	0.512133 ±3	-9.68	± 0.18	4
33-06 TD L1	6.6114	0.512126 ±4	-9.83	± 0.18	4
		Average 33-06	-9.90	± 0.42	
33-12 BSL2	6.6092	0.512130 ±10	-9.75	± 0.42	2
33-15 BSL2	6.6080	0.512135 ±15	-9.65	± 0.42	2
33-15 BSL3	6.6080	0.512125 ±15	-9.83	± 0.42	3
33-15 SL L1	6.6080	0.512134 ±4	-9.66	± 0.18	4
33-15 TD L1	6.6080	0.512135 ±3	-9.64	± 0.18	4
33-15 TD L1	6.6080	0.512138 ±3	-9.60	± 0.18	4
		Average 33-15	-9.69	± 0.42	
33-21 BSL2	6.6055	0.512112 ±10	-10.09	± 0.42	2
33-27 BSL2	6.6030	0.512120 ±13	-9.94	± 0.42	2
33-27 BSL3	6.6030	0.512139 ±14	-9.56	± 0.42	3
33-27 SL L1	6.6030	0.512131 ±4	-9.73	± 0.18	4
		Average 33-27	-9.75	± 0.42	
34-01 BSL2	6.5978	0.512109 ±18	-10.16	± 0.42	2
34-02 BSL2	6.5974	0.512123 ±9	-9.87	± 0.42	2
34-03 BSL2	6.5970	0.512138 ±11	-9.58	± 0.42	2
34-06 BSL1	6.5958	0.512114 ±15	-10.06	± 0.42	1
34-09 BSL1	6.5945	0.512116 ±15	-10.02	± 0.42	1
34-12 BSL1	6.5928	0.512124 ±16	-9.86	± 0.42	1
34-13 BSL2	6.5919	0.512156 ±13	-9.23	± 0.42	2
34-16 SL L1	6.5908	0.512146 ±4	-9.43	± 0.18	4
34-16 SL L1	6.5908	0.512139 ±3	-9.56	± 0.18	4
34-16 TD L1	6.5908	0.512139 ±3	-9.57	± 0.18	4
34-16 TD L1	6.5908	0.512141 ±3	-9.52	± 0.18	4
		Average 34-16	-9.52	± 0.18	
34-18 BSL2	6.5901	0.512125 ±14	-9.84	± 0.42	2
34-30 BSL3	6.5853	0.512107 ±13	-10.20	± 0.42	3

Session indicates analytical session (1 = August 2013, 2 = February 2014, 3 = November 2014, GEOMAR Nu Plasma MC-ICPMS; 4 = September 2015, 5 = November 2015, GEOMAR Neptune Plus MC-ICPMS).

Table 4.2 (cont'd). $^{143}Nd/^{144}Nd$ ratios of Sorbas Basin samples (ratio uncertainty 2SE internal; ε_{Nd} uncertainty 2SD external).

Sample	Age (Ma)	$^{143}Nd/^{144}Nd_{(t)}$	$\varepsilon_{Nd(t)}$		Session
34-43 BSL3	6.5803	0.512135 ±16	-9.65	± 0.42	3
34-45 BSL3	6.5795	0.512157 ±13	-9.22	± 0.42	3
34-45 SL L1	6.5795	0.512164 ±3	-9.08	± 0.18	4
34-45 SL L1	6.5795	0.512162 ±3	-9.12	± 0.18	4
34-45 TD L1	6.5795	0.512163 ±4	-9.10	± 0.18	4
		Average 34-45	-9.41	± 0.42	
35-05 BSL1	6.5741	0.512123 ±16	-9.88	± 0.42	1
35-08 BSL1	6.5726	0.512099 ±34	-10.34	± 0.66	1
35-09 SL L1	6.5721	0.512122 ±3	-9.90	± 0.18	4
35-09 SL L1	6.5721	0.512114 ±3	-10.06	± 0.18	4
35-11 BSL1	6.5711	0.512108 ±15	-10.18	± 0.42	1
35-19 BSL3	6.5683	0.512122 ±15	-9.90	± 0.42	3
35-19 SL L1	6.5683	0.512123 ±3	-9.89	± 0.18	4
35-19 SL L1	6.5683	0.512121 ±3	-9.92	± 0.18	4
35-19 TD L1	6.5683	0.512121 ±4	-9.92	± 0.18	4
		Average 35-19	-9.91	± 0.42	
35-21 BSL2	6.5676	0.512118 ±10	-9.98	± 0.42	2
35-21 BSL3	6.5676	0.512113 ±15	-10.08	± 0.42	3
		Average 35-21	-10.03	± 0.42	
35-22 BSL2	6.5672	0.512122 ±11	-9.91	± 0.42	2
35-24 BSL2	6.5665	0.512135 ±10	-9.64	± 0.42	2
35-25 BSL2	6.5662	0.512122 ±12	-9.90	± 0.42	2
35-27 BSL2	6.5655	0.512124 ±14	-9.86	± 0.42	2
35-27 SL L1	6.5655	0.512117 ±3	-10.00	± 0.18	4
35-27 SL L1	6.5655	0.512130 ±3	-9.74	± 0.18	4
35-27 TD L1	6.5655	0.512131 ±4	-9.73	± 0.18	4
		Average 35-27	-9.82	± 0.42	
35-39 BSL2	6.5616	0.512110 ±12	-10.13	± 0.42	2
35-39 SL L1	6.5616	0.512126 ±3	-9.82	± 0.18	4
35-39 SL L1	6.5616	0.512140 ±4	-9.56	± 0.18	4
35-39 TD L1	6.5616	0.512138 ±3	-9.59	± 0.18	4
		Average 35-39	-9.80	± 0.42	
35-48 BSL2	6.5582	0.512128 ±13	-9.78	± 0.42	2
35-48 SL L1	6.5582	0.512123 ±3	-9.88	± 0.18	4
35-48 SL L1	6.5582	0.512127 ±4	-9.80	± 0.18	4
35-48 TD L1	6.5582	0.512133 ±4	-9.69	± 0.18	4
		Average 35-48	-9.77	± 0.42	
36-09 BSL1	6.5536	0.512100 ±15	-10.34	± 0.42	1
36-11 BSL1	6.5529	0.512077 ±15	-10.78	± 0.42	1
36-11 SL L1	6.5529	0.512093 ±3	-10.46	± 0.18	4
36-11 SL L1	6.5529	0.512103 ±4	-10.28	± 0.18	4
		Average 36-11	-10.51	± 0.42	

Session indicates analytical session (1 = August 2013, 2 = February 2014, 3 = November 2014, GEOMAR Nu Plasma MC-ICPMS; 4 = September 2015, 5 = November 2015, GEOMAR Neptune Plus MC-ICPMS).

Table 4.2 (cont'd). $^{143}Nd/^{144}Nd$ ratios of Sorbas Basin samples (ratio uncertainty 2SE internal; ε_{Nd} uncertainty 2SD external).

Sample	Age (Ma)	$^{143}Nd/^{144}Nd_{(t)}$	$\varepsilon_{Nd(t)}$		Session
(strong leachates)					
33-06 SL	6.6114	0.512009 ±3	-12.10	± 0.18	4
33-15 SL	6.6080	0.512021 ±4	-11.88	± 0.18	4
33-27 SL	6.6030	0.512018 ±4	-11.93	± 0.18	4
34-16 SL	6.5908	0.512017 ±4	-11.95	± 0.18	4
34-45 SL	6.5795	0.512020 ±3	-11.89	± 0.18	4
35-09 SL	6.5721	0.512008 ±4	-12.13	± 0.18	4
35-19 SL	6.5683	0.512015 ±4	-11.98	± 0.18	4
35-27 SL	6.5655	0.512015 ±5	-11.99	± 0.18	4
35-39 SL	6.5616	0.512017 ±4	-11.95	± 0.18	4
35-48 SL	6.5582	0.512023 ±4	-11.84	± 0.18	4
36-11 SL	6.5529	0.512017 ±3	-11.95	± 0.18	4
(total dissolution)					
33-06 TD	6.6114	0.512020 ±3	-11.89	± 0.13	5
33-15 TD	6.6080	0.512027 ±3	-11.76	± 0.13	5
33-27 TD	6.6030	0.512022 ±3	-11.85	± 0.13	5
34-16 TD	6.5908	0.512021 ±3	-11.86	± 0.13	5
34-45 TD	6.5795	0.512028 ±2	-11.72	± 0.13	5
35-09 TD	6.5721	0.512020 ±3	-11.89	± 0.13	5
35-19 TD	6.5683	0.512016 ±4	-11.97	± 0.13	5
35-27 TD	6.5655	0.512030 ±3	-11.70	± 0.13	5
35-39 TD	6.5616	0.512029 ±3	-11.72	± 0.13	5
35-48 TD	6.5582	0.512027 ±3	-11.76	± 0.13	5

Session indicates analytical session (1 = August 2013, 2 = February 2014, 3 = November 2014, GEOMAR Nu Plasma MC-ICPMS; 4 = September 2015, 5 = November 2015, GEOMAR Neptune Plus MC-ICPMS).

4.4.2 Elemental ratios: Al/Nd

Elemental concentrations were measured in the acid-reductive leachates of the Sorbas Basin sediments, for a subset of samples. These measurements were also performed on the second and third leaches for sediment samples being prepared for strong leaching and total dissolution so that changes over successive leaches could be compared, although ε_{Nd} was only measured for the first leach. Elemental ratios were calculated from concentrations measured by Q-ICPMS (Ch. 2 section 2.3.4.1). There are no obvious trends for any elemental ratio pair, including the elements Sr, Ca, Ti, Mn, Fe, Ba or Ce. The results are tabulated in Appendix 4.

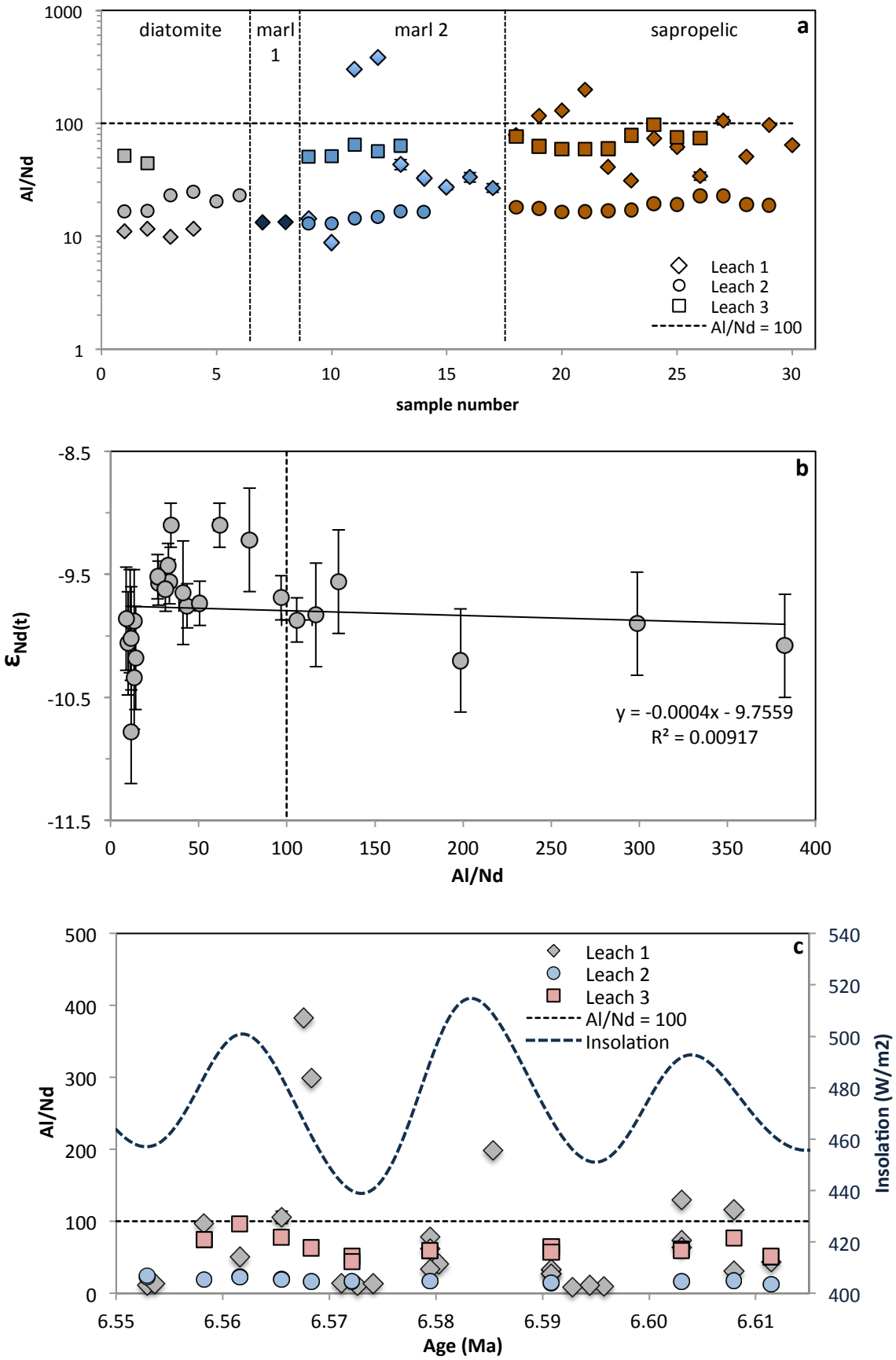

Fig. 4.4. Al/Nd ratios of bulk sediment leachates compared (a) by lithology, (b) by $\varepsilon_{Nd(t)}$, and (c) with insolation. Al/Nd uncertainty smaller than symbols.

In particular, Al/Nd has been suggested for use in monitoring the reliability of the leaching process [*Gutjahr et al.*, 2007; *Blaser et al.*, 2016]. Because Al tends to correlate well with increased input of the aluminosilicate fraction (clays), the Al/Nd elemental ratio may be useful in tracking the level of contamination by detrital siliciclastics during leaching. Higher ratios may signify more dissolution of, or interaction with, the unwanted non-authigenic fraction during leaching. For this reason, this ratio is presented here in more detail with respect to lithology, time and $\varepsilon_{Nd(t)}$. There is no apparent relationship between lithology and the Al/Nd ratio (Fig. 4.4a), implying no particular lithology is more or less susceptible to extraction of non-authigenic phases during leaching. Comparing results between successive leaches, the greatest variability in Al/Nd occurs during the first leach. The second and third leaches both show relatively low Al/Nd values, with ranges between ~13 to 25 and ~44 to 97, respectively. There is no evidence of a relationship between $\varepsilon_{Nd(t)}$ and Al/Nd ratio (Fig. 4.4b). While it could be tentatively suggested that a temporal relationship between Al/Nd and insolation exists (Fig. 4.4c), not all samples follow the pattern, in particular the two highest ratios at ~6.568 Ma.

4.4.3 Discussion

4.4.3.1 Reliability of the leaching process for Sorbas Basin sediment

The fish remains are all within error of the acid reductive ('weak') leachates, but tend to have slightly less radiogenic mean values. Fish remains provide the most reliable archive of syn-depositional bottom water Nd used in this research. As the fish and weak leach results are within error of each other, this suggests that the weak leach protocol is extracting the authigenic oxyhydroxide coating and not the detrital fraction within the sediment, the value of which is indicated by the total dissolution and strong leach data. Moreover, the fact that the leachate data mean values are consistently more radiogenic than the fish remains suggests the ferromanganese oxyhydroxide coatings sampled are likely to be of marine rather than riverine origin, since riverine particulates with preformed oxyhydroxide coatings generally have compositions more similar to the strong leach or total dissolution samples [*Charbonnier et al.*, 2012; *Kraft et al.*, 2013].

[*Blaser et al.*, 2016] found a relationship between ε_{Nd} and Al/Nd during successive leaching experiments performed on a variety of marine sediments. This result led those authors to suggest that Al/Nd > 100 may indicate contamination from detrital siliciclastics, although those authors were also careful to note that higher ratios are not always caused by

contamination during leaching. This cutoff value is indicated in Fig. 4.4. The great majority of the samples exhibit Al/Nd ratios much lower than 100. Assuming the relationship determined by [*Blaser et al.*, 2016] is representative, then widespread contamination from detrital siliciclastics is not expected for the acid-reductive leachates of Sorbas Basin sediments. The few samples exhibiting Al/Nd ratios greater than 100 correspond to identical ε_{Nd} as the samples with the lowest Al/Nd (Fig. 4.4b). Interestingly, the second leach consistently exhibits low ratios, with values comparable to the lowest Al/Nd of the first leach. The third leach consistently exhibits higher ratios than the second, though these are still well below the Al/Nd = 100 cutoff suggested by *Blaser et al*. The fact that the latter leaches show more consistent Al/Nd ratios may indicate that there is a large variability in the natural Al/Nd ratio of the authigenic oxyhydroxides in the Sorbas Basin, as a result of close proximity to the coast and/or the shallow water depth (~150 – 250 m, Ch. 3, section 3.3.3). The sediments examined by *Blaser et al*. were derived from cores extracted from very deep settings (> 2700 m water depth) several hundreds of km from any coast. Furthermore, these deep water samples did not exhibit falling Al/Nd ratios, even after ten leaches.

4.4.3.2 Seawater $^{143}Nd/^{144}Nd$ in the Sorbas basin

The Nd isotopic compositions of the Sorbas Basin sediment acid-reductive leaches represent bottom water isotopic compositions. These data are consistent with the Nd isotopic composition predicted from ODP Site 978 of water in the Alboran Sea, implying this was the main source of water to the Sorbas Basin throughout the period (Fig. 4.3). Orbital climatic influences on Sorbas, which resulted in clear precessional cyclicity shown by sedimentological and ecological studies [e.g., *Sierro et al.*, 1999, 2003; *Pérez-Folgado et al.*, 2003], as well as the Sr isotope results presented in Ch. 3 (Fig. 3.1), are not apparently recorded by seawater Nd isotope compositions. No obvious fluctuations corresponding to orbital parameter frequencies such as precession are observed. There is some minor variability in the data, but this variability is within analytical uncertainty.

It was expected that the Sorbas Basin should primarily record Western Mediterranean Nd isotopic compositions, as the Betic corridor is thought to have closed completely by ~ 7 Ma [*Esteban et al.*, 1996; *Seidenkrantz et al.*, 2000; *Martin et al.*, 2001; *Betzler et al.*, 2006; *Martín et al.*, 2009] (Ch. 1, section 1.2.2). The findings presented here support this hypothesis, as the majority of values plot well within the range of Site 978. The least

radiogenic of the Sorbas Nd isotope results appear to suggest that a minor influence of a source comparable to North Eastern Atlantic Deep Water (NEADW) or Modified Atlantic Water (MAW, Atlantic inflow at the surface east of Gibraltar; [*Millot*, 1999]) was present in the Sorbas Basin periodically. However, the detrital sediment components, represented by the strong leach results and the total dissolution results, are much less radiogenic than MOW. Even though the comparison of strong leach and total dissolution suggests that easily weathered minerals are not present, the basin was shallow during this interval (~150 to 250 m; Ch. 3 section 3.3.3), proximal to the coast, and anoxia was prevalent, conditions which apparently enhance the influence of boundary exchange [*Lacan and Jeandel*, 2005]. The fact that the sedimentary component is much less radiogenic than the recorded seawater signal is an issue as MAW is expected to be less radiogenic than MO. Even a small influence of boundary exchange, or other diagenetic processes caused by anoxia, occurring between detrital phases and bottom water would shift the recorded signal to less radiogenic values. It is therefore simply not possible to identify either Atlantic influence or boundary exchange as the cause of any unradiogenic signal in the Sorbas Basin.

Boundary exchange (Ch. 1, section 1.3.1) could also affect the preservation of minor variations of seawater Nd isotope compositions due to climate variability. The relatively short residence time of Nd (~200 – 1400 y [*Tachikawa et al.*, 1999; *Bayon et al.*, 2004]) should allow the preservation of variability on precessional timescales. While the basin is known to have experienced significant climate shifts [Ch. 3, this work; *Sierro et al.*, 1999, 2001, 2003; *Krijgsman et al.*, 2001; *Filippelli et al.*, 2003; *Pérez-Folgado et al.*, 2003], no such variability in the preserved Nd isotopes is observed. Benthic foraminiferal assemblages indicate that anoxia alternated between extreme anoxia and hypoxia over precessional timescales [*Pérez-Folgado et al.*, 2003; *Sierro et al.*, 2003] (Ch. 3 section 3.3.3); this could result in regular fluctuations in preservation, but again there is no clear evidence of this in the elemental ratios measured from the leachates. Complex relationships operate between seawater REE (including Nd) and salinity; as river water enters a basin, REE are first observed to precipitate then redissolve with increasing salinity [*Sholkovitz*, 1993; *Sholkovitz and Szymczak*, 2000; *Rousseau et al.*, 2015]. It appears that Nd is in general not an appropriate proxy to investigate water mass exchange in marginal sediments, particularly in the case of pre-MSC Mediterranean-Atlantic exchange, and that consequently the *Ivanoviç et al.* [2013] estimate of the ε_{Nd} palaeosignature of MO is not robust.

4.4.3.3 *Further issues: Eastern North Atlantic Central Water (ENACW) vs. North Eastern Atlantic Deep Water (NEADW)*

A further complication to understanding Atlantic-Mediterranean exchange using Nd isotopes, besides the fact that marginal marine sediments are, by their nature, relatively shallow deposits proximal to the coast and hence prone to boundary exchange, lies in the fact that archives for past water masses are found at deeper water depths; for example, archives consistent with modern NEADW or AAIW. Fish remains and foraminifera record bottom water or sediment-water interface Nd, while ferromanganese crusts record the characteristics of the water depth they are deposited at; the records referenced above recorded information at water depths which are therefore consistent with these deeper water masses. Planktic foraminifera incorporate Nd into their tests during their lifetime near the surface; however, it is extremely difficult to extract the primary water signal as ferromanganese oxyhydroxides become finely interspersed in foraminiferal calcite during deposition and burial [*Elmore et al.*, 2011; *Roberts et al.*, 2012; *Tachikawa et al.*, 2014]. Approximately 80% of the Nd associated with foraminiferal tests is derived from syn-depositional ferromanganese oxyhydroxides [*Roberts et al.*, 2012]. *Ivanoviç et al.* [2013] used proxies recording palaeo-NEADW to assess the Nd isotope signature of late Miocene Atlantic inflow to the Mediterranean; however, inflow is actually derived from ENACW rather than NEADW.

Today, ENACW and NEADW exhibit similar Nd isotope ratios (~ -11 to -11.5 ε_{Nd}) [*Piepgras and Wasserburg*, 1983; *Stichel et al.*, 2015]. However, these water masses do not have the same source. Upper NEADW in this region derives from Labrador Sea Water (LSW) while the lower part derives from Iceland Scotland Overflow Water (ISOW; *Stichel et al.* [2015] and references therein) and is considered the product of deep water formation processes. ENACW derives from the near-Arctic Atlantic surface convection processes ([*Van Aken*, 2001], and references therein). As these sources are not truly the same we cannot assume the similarity in ε_{Nd} extends to the past; therefore archives that recorded NEADW are not necessarily representative of the Nd isotopic composition of Atlantic inflow. If possible, suitable archives recording appropriate inflow characteristics must be found in order to properly assess the Nd isotope signature of inflowing Atlantic water.

4.5 Conclusions

This chapter has presented and discussed Nd isotope results from two sites, ODP Site 978 and the Sorbas Basin, and discussed them in the context of Atlantic-Mediterranean exchange and the existing literature. It appears likely that Site 978 faithfully recorded late Miocene to Pliocene Western Mediterranean water mass signatures, suggesting that the Alboran Sea and MO water masses had a neodymium isotopic signature in the range of -9.3 to -9.9 ε_{Nd}, similar to modern compositions. This assessment is important for future research assessing changes to or onset of Mediterranean Outflow into the NE Atlantic associated with the Messinian Salinity Crisis when significant changes to MO occurred [*Hernández-Molina et al.*, 2014b]. The data suggest the Nd isotope signature of the MO plume as been relatively constant since the late Miocene with an average composition of -9.3 to -9.5 ± 0.37 $\varepsilon_{Nd(t)}$, or about -8.9 to -9.9 ε_{Nd} including uncertainty.

Based on an assessment of depth (~ 2000 m), distance from coast (> 50 km), and protection from continental detrital siliciclastic influence by topography, it appears likely that the data from Site 978 are reliable. The late Miocene values recorded at this site are consistent with more recent and modern values; records from the Plio-Pleistocene and Holocene are generally within error, although their means are slightly more radiogenic ε_{Nd}. However, these studies used a methodology including decarbonation before leaching, which has been suggested to enhance contamination by easily weathered, generally more radiogenic minerals [*Wilson et al.*, 2013]. Decarbonation does not automatically lead to biased records [e.g., *Böhm et al.*, 2015]; however, the fact that Site 978 is located near a volcanic seamount which was active during the late Miocene indicates a high possibility of the type of material likely to contaminate bulk sediment leachates will be present in samples from this location (as in the case of *Khélifi et al*, [2009, 2014], even though their samples are of Plio-Pleistocene age). Combined, these factors provide confidence that the intermediate Alboran Sea (Levantine Intermediate Water, LIW) and MO water masses have had a very consistent Nd isotope signature since ~ 7 Ma, in the range of -9.3 to -9.9 ε_{Nd} units. The previous MO $\varepsilon_{Nd(t)}$ estimate published by *Ivanoviç et al.* [2013] is significantly more radiogenic than that suggested here, but this value was likely biased. Those authors based their estimate on samples from a concurrently shallowing location dominated by volcanic ash with very radiogenic Nd, factors known to enhance boundary exchange and thus shift bottom water Nd isotope compositions away from those of the overlying water mass.

$\varepsilon_{Nd(t)}$ obtained by acid-reductive leaching of bulk sediments from the Sorbas Basin also appears to reliably record the bottom water signature. This assessment is based on a comparison of measurements from fish teeth (the most reliable archive of bottom water ε_{Nd} [*Martin and Scher*, 2004]), strong leaching and total dissolution of duplicate bulk sediment samples, and the Al/Nd ratios measured from the leachate solutions. While the Al/Nd ratios are quite variable, the great majority are relatively low (< 100) and there is no correlation between ε_{Nd} and Al/Nd. The $\varepsilon_{Nd(t)}$ results are relatively invariant (-9.14 to -10.65 ± 0.42), with most variability within analytical uncertainty, and show no patterns or cyclicity. Superficially, the compositions measured in Sorbas appear to be similar to that which would be expected for the upper water mass in the Alboran Sea today (MAW, Modified Atlantic Water) which is an admixture of relatively radiogenic MO and less radiogenic, inflowing Eastern North Atlantic Central Water (ENACW; palaeo-signature estimated from proxies for North Eastern Atlantic Deep Water, NEADW). Unfortunately, because the detrital siliciclastic fraction incorporates much less radiogenic Nd isotope compositions (determined directly from total dissolutions and strong leachates), it is impossible to ascertain the true cause of the signal observed. In shallow gateway settings, such as the Sorbas Basin (~ 200 m; see Ch. 3, section 3.3.3) and those used by *Ivanoviç et al.* [2013], boundary exchange has been shown to be quite significant, and thus cannot be ruled out.

In general, it appears that the Neodymium isotope tracer is not appropriate for investigation of exchange through shallow basins or seaways such as the palaeocorridors which once connected the Mediterranean to the Atlantic. However, deeper locations such as Site 978 do appear to be reliable. If truly reliable, such sites could also be capable of recording millennial scale variability, assuming a deep sea core with appropriate age control could be retrieved. Beyond the boundary exchange issue, which plagues shallow environments, a suitable archive for ENACW (or MAW) would be preferable to the current assumption that proxies for NEADW are suitable for estimating the Nd isotope signature of inflowing Atlantic water.

5 Mediterranean and Mediterranean marginal basin seawater Pb isotopes: records of precessional climate variability

5.1 Overview

In this chapter, sub-precessional temporal resolution Pb isotope records are presented. These records were derived from bulk sediment leachates from three Mediterranean sections, including Sorbas Basin (southern Spain), Falconara (Sicily) and Monte del Casino (northern Italy). In addition to presenting the first Pb isotope records with this level of temporal resolution, this is also the first time that seawater Pb isotopes are observed to vary with precessional cyclicity, similarly to the lithological and faunal cyclicity consistently observed across the Mediterranean. These data are compared to new data from ODP Site 978 as well as data from the literature, in an effort to determine the mechanism(s) causing the observed variability. To this end, potential drivers are presented and discussed. Some additional Pb isotope data from other locations, which did not fit within the topic of this chapter, is given in Appendix 3.

CHAPTER NOTES

Materials and methods: Ch. 2, sections 2.2, 2.3.4, 2.3.5
Sample location maps: Ch. 1, Fig. 1.21
Contributions: Marlies van der Schee, ODP Site 978 Pb and Nd isotope data

5.2 Results

5.2.1 Sorbas, Falconara, and Monte del Casino leachates

The Pb isotopic compositions of the leachates from all three Mediterranean sections (Table 5.1) show regular cyclicity and generally appear to change broadly in phase (Fig. 5.1, 5.2), with the exception of the $^{207}Pb/^{204}Pb$ ratio where the low natural variability expected relative to analytical uncertainty obscures any potential cyclicity. The cyclicity of the Sorbas Basin and Falconara section results show more radiogenic values in the diatomite layers and less radiogenic values in the sapropelic layers consistently over the measured interval, while at Monte del Casino the ratios are less radiogenic at these times (Fig. 5.2).

Table 5.1. Pb isotopic compositions of acid-reductive leaches, all sections.

Sample	Age (Ma)	$^{208}Pb/^{204}Pb$		$^{207}Pb/^{204}Pb$		$^{206}Pb/^{204}Pb$		$^{208}Pb/^{206}Pb$		$^{207}Pb/^{206}Pb$	
Sorbas Basin											
33-03	6.6126	38.911	±14	15.692	±6	18.806	±18	2.0692	±4	0.83443	±13
33-06*	6.6114	38.899	±14	15.686	±6	18.795	±18	2.0698	±4	0.83459	±13
33-12	6.6092	38.876	±14	15.686	±6	18.776	±18	2.0707	±4	0.83547	±13
33-15*	6.6080	38.916	±14	15.690	±6	18.793	±18	2.0709	±4	0.83488	±13
33-21	6.6055	38.859	±14	15.676	±6	18.766	±18	2.0708	±4	0.83530	±13
33-27*	6.6030	38.909	±14	15.685	±6	18.798	±18	2.0699	±4	0.83443	±13
34-01	6.5978	38.906	±14	15.685	±6	18.776	±18	2.0722	±4	0.83538	±13
34-02	6.5974	38.948	±14	15.682	±6	18.789	±18	2.0730	±4	0.83465	±13
34-06	6.5958	38.957	±14	15.694	±6	18.848	±18	2.0669	±4	0.83267	±13
34-09	6.5945	38.944	±14	15.701	±6	18.913	±18	2.0591	±4	0.83014	±13
34-10	6.5939	38.895	±14	15.682	±6	18.815	±18	2.0673	±4	0.83349	±13
34-12	6.5928	38.933	±14	15.691	±6	18.843	±18	2.0663	±4	0.83274	±13
34-13	6.5919	38.889	±14	15.687	±6	18.793	±18	2.0694	±4	0.83471	±13
34-15	6.5912	38.835	±14	15.675	±6	18.774	±18	2.0687	±4	0.83497	±13
34-16*	6.5908	38.906	±14	15.684	±6	18.784	±18	2.0714	±4	0.83498	±13
34-18	6.5901	38.885	±14	15.685	±6	18.781	±18	2.0705	±4	0.83517	±13
34-19	6.5897	38.881	±14	15.682	±6	18.790	±18	2.0693	±4	0.83457	±13
34-21	6.5890	38.896	±14	15.685	±6	18.782	±18	2.0710	±4	0.83512	±13
34-28	6.5861	38.893	±14	15.688	±6	18.773	±18	2.0719	±4	0.83568	±13
34-30	6.5853	38.901	±14	15.685	±6	18.787	±18	2.0705	±4	0.83487	±13
34-43	6.5803	38.922	±14	15.689	±6	18.806	±18	2.0697	±4	0.83429	±13
34-45*	6.5795	38.917	±14	15.690	±6	18.858	±18	2.0637	±4	0.83203	±13
35-05	6.5741	38.903	±14	15.683	±6	18.869	±18	2.0617	±4	0.83113	±13
35-08	6.5726	38.972	±14	15.696	±6	18.887	±18	2.0634	±4	0.83104	±13
35-09	6.5721	38.909	±14	15.690	±6	18.892	±18	2.0597	±4	0.83050	±13
35-09	6.5721	38.901	±14	15.688	±6	18.875	±18	2.0610	±4	0.83112	±13
35-11	6.5711	38.954	±14	15.696	±6	18.873	±18	2.0641	±4	0.83169	±13
35-19*	6.5683	38.911	±14	15.685	±6	18.802	±18	2.0695	±4	0.83423	±13
35-21*	6.5676	38.884	±14	15.683	±6	18.770	±18	2.0715	±4	0.83551	±13
35-22	6.5672	38.891	±14	15.685	±6	18.786	±18	2.0703	±4	0.83488	±13
35-24	6.5665	38.876	±14	15.683	±6	18.787	±18	2.0694	±4	0.83478	±13
35-25	6.5662	38.864	±14	15.686	±6	18.768	±18	2.0710	±4	0.83585	±13
35-27*	6.5655	38.893	±14	15.685	±6	18.784	±18	2.0706	±4	0.83502	±13
35-39*	6.5616	38.881	±14	15.677	±6	18.769	±18	2.0717	±4	0.83529	±13
35-48*	6.5582	38.911	±14	15.685	±6	18.795	±18	2.0704	±4	0.83456	±13
36-09	6.5536	38.952	±14	15.694	±6	18.868	±18	2.0644	±4	0.83176	±13
36-11**	6.5529	38.948	±14	15.696	±6	18.878	±18	2.0632	±4	0.83145	±13
Monte del Casino											
JT 17.776*	6.6223	38.871	±7	15.698	±2	18.993	±2	2.0466	±2	0.82651	±4
JT 17.777	6.6183	38.870	±7	15.693	±2	18.909	±2	2.0556	±2	0.82991	±4
JT 17.779	6.6142	38.864	±7	15.693	±2	18.907	±2	2.0555	±2	0.83002	±4
JT 17.780	6.6075	38.844	±7	15.693	±2	18.948	±2	2.0500	±2	0.82821	±4
JT 17.781	6.6019	38.854	±7	15.695	±2	18.960	±2	2.0492	±2	0.82777	±4
JT 17.782	6.5982	38.865	±7	15.696	±2	18.982	±2	2.0474	±2	0.82686	±4

Table 5.1 (cont'd).

Sample	Age (Ma)	$^{208}Pb/^{204}Pb$		$^{207}Pb/^{204}Pb$		$^{206}Pb/^{204}Pb$		$^{208}Pb/^{206}Pb$		$^{207}Pb/^{206}Pb$	
Monte del Casino (cont'd)											
JT 17.783	6.5963	38.872	±7	15.692	±2	18.904	±2	2.0563	±2	0.83007	±4
JT 17.784	6.5941	38.881	±7	15.694	±2	18.918	±2	2.0552	±2	0.82961	±4
JT 17.785	6.5877	38.871	±7	15.698	±2	18.997	±2	2.0462	±2	0.82634	±4
JT 17.786	6.5781	38.841	±7	15.696	±2	19.003	±2	2.0439	±2	0.82596	±4
JT 17.787	6.5728	38.861	±7	15.695	±2	18.945	±2	2.0512	±2	0.82845	±4
JT 17.788	6.5708	38.874	±7	15.694	±2	18.910	±2	2.0557	±2	0.82992	±4
JT 17.789*	6.5688	38.873	±7	15.695	±2	18.939	±2	2.0526	±2	0.82871	±4
JT 17.790	6.5644	38.859	±7	15.696	±2	18.987	±2	2.0467	±2	0.82672	±4
JT 17.791	6.5594	38.850	±7	15.694	±2	18.962	±2	2.0489	±2	0.82770	±4
JT 17.792*	6.5538	38.861	±7	15.694	±2	18.949	±2	2.0508	±2	0.82819	±4
JT 17.793	6.5522	38.873	±7	15.697	±2	18.993	±2	2.0468	±2	0.82648	±4
JT 17.794	6.5506	38.869	±7	15.696	±2	18.975	±2	2.0484	±2	0.82722	±4
JT 17.795	6.5451	38.853	±7	15.696	±2	18.994	±2	2.0455	±2	0.82638	±4
JT 17.796*	6.5394	38.866	±7	15.700	±2	19.057	±2	2.0395	±2	0.82386	±4
JT 17.797	6.5334	38.874	±7	15.697	±2	18.988	±2	2.0473	±2	0.82670	±4
JT 17.798	6.5310	38.877	±7	15.698	±2	19.020	±2	2.0440	±2	0.82533	±4
Falconara											
18.887	6.6122	38.922	±7	15.696	±2	18.871	±2	2.0625	±2	0.83175	±4
18.888	6.6112	38.941	±7	15.695	±2	18.861	±2	2.0646	±2	0.83214	±4
18.889	6.6098	38.959	±7	15.697	±2	18.875	±2	2.0641	±2	0.83163	±4
18.890	6.6082	38.965	±7	15.698	±2	18.857	±2	2.0664	±2	0.83249	±4
18.891	6.6068	38.963	±7	15.698	±2	18.852	±2	2.0668	±2	0.83272	±4
18.893	6.6045	38.941	±7	15.700	±2	18.897	±2	2.0607	±2	0.83082	±4
18.894	6.6026	38.934	±7	15.699	±2	18.866	±2	2.0637	±2	0.83212	±4
18.895	6.6004	38.935	±7	15.698	±2	18.857	±2	2.0648	±2	0.83250	±4
18.896	6.5989	38.941	±7	15.703	±2	18.935	±2	2.0565	±2	0.82933	±4
18.897	6.5973	38.939	±7	15.700	±2	18.894	±2	2.0609	±2	0.83097	±4
18.897	6.5973	38.939	±7	15.700	±2	18.894	±2	2.0609	±2	0.83097	±4
18.898	6.5958	38.939	±7	15.701	±2	18.901	±2	2.0601	±2	0.83072	±4
18.900	6.5929	38.928	±7	15.699	±2	18.893	±2	2.0604	±2	0.83095	±4
18.901	6.5911	38.945	±7	15.698	±2	18.875	±2	2.0633	±2	0.83168	±4
18.902	6.5899	38.965	±7	15.699	±2	18.872	±2	2.0646	±2	0.83183	±4
18.903	6.5883	38.959	±7	15.697	±2	18.858	±2	2.0659	±2	0.83234	±4
18.904	6.5865	38.961	±7	15.698	±2	18.857	±2	2.0661	±2	0.83249	±4
18.905	6.5844	38.944	±7	15.698	±2	18.849	±2	2.0661	±2	0.83285	±4
18.906	6.5838	38.944	±7	15.700	±2	18.866	±2	2.0642	±2	0.83219	±4
18.907	6.5824	38.908	±14	15.690	±6	18.862	±18	2.063	±4	0.83182	±13
18.908	6.5807	38.935	±7	15.699	±2	18.859	±2	2.0646	±2	0.83248	±4
18.909	6.5796	38.935	±7	15.701	±2	18.894	±2	2.0606	±2	0.83096	±4
18.910	6.5781	38.932	±7	15.699	±2	18.880	±2	2.0621	±2	0.83151	±4
18.911	6.5762	38.941	±7	15.702	±2	18.922	±2	2.0580	±2	0.82980	±4
18.912	6.5742	38.965	±7	15.699	±2	18.921	±2	2.0593	±2	0.82972	±4
18.914	6.5708	38.943	±7	15.698	±2	18.863	±2	2.0645	±2	0.83220	±4
18.915	6.5697	38.929	±7	15.693	±2	18.855	±2	2.0647	±2	0.83231	±4

Table 5.1 (cont'd).

Sample	Age (Ma)	$^{208}Pb/^{204}Pb$		$^{207}Pb/^{204}Pb$		$^{206}Pb/^{204}Pb$		$^{208}Pb/^{206}Pb$		$^{207}Pb/^{206}Pb$	
Falconara (cont'd)											
18.915	6.5697	38.929	±7	15.693	±2	18.855	±2	2.0647	±2	0.83231	±4
18.916	6.5684	38.939	±7	15.694	±2	18.848	±2	2.0659	±2	0.83264	±4
18.917	6.5670	38.944	±7	15.695	±2	18.844	±2	2.0667	±2	0.83287	±4
18.918	6.5657	38.949	±7	15.696	±2	18.849	±2	2.0663	±2	0.83273	±4
18.919	6.5645	38.952	±7	15.698	±2	18.870	±2	2.0643	±2	0.83189	±4
18.920	6.5630	38.943	±7	15.699	±2	18.866	±2	2.0641	±2	0.83210	±4
18.921	6.5624	38.940	±7	15.698	±2	18.865	±2	2.0642	±2	0.83212	±4
18.922	6.5610	38.941	±7	15.697	±2	18.847	±2	2.0662	±2	0.83289	±4
18.923	6.5597	38.937	±7	15.697	±2	18.872	±2	2.0632	±2	0.83177	±4
18.924	6.5579	38.941	±7	15.700	±2	18.935	±2	2.0565	±2	0.82916	±4

* average of duplicate measurements (individual analyses in Appendix 5). Uncertainty is 2SD (external analytical reproducibility) unless 2SE (internal) was larger.

In contrast to the quadripartite cyclicity observed in the Sorbas Basin sediments (sapropelic layer, first homogenous marl, diatomite, second homogenous marl) the other two sections are characterized differently. At Falconara, the sedimentary cyclicity is tripartite (sapropel – marl – diatomite), and at Monte del Casino, the sediments are bipartite (sapropel – marl) [*Krijgsman et al.*, 1997; *Hilgen and Krijgsman*, 1999]. To enable the comparison between sites (Fig. 5.1, 5.2), the age models for Falconara and Monte del Casino have been updated to La04 [*Laskar et al.*, 2004] using sapropel midpoints as tuning tie points as for Sorbas (see Ch. 2, section 2.2.1, and known issues in Ch. 1, section 1.2.6). Pb isotope values at Falconara became relatively more radiogenic at about the same time as at the Sorbas Basin (e.g., $^{206}Pb/^{204}Pb$ ~ 18.9 compared to $^{206}Pb/^{204}Pb$ ~18.85 at Falconara and $^{206}Pb/^{204}Pb$ ~18.8 at Sorbas, Fig. 5.1), while these more radiogenic values generally observed in the diatomite layers at both sites. The values for Monte del Casino have the opposite relationship, with more radiogenic values generally observed within sapropels. As values reach their most radiogenic in Sorbas and at Falconara, the values at Monte del Casino reach their least radiogenic; at this time, the values from all three sites tend to become very similar, particularly with ratios containing ^{206}Pb (e.g., $^{206}Pb/^{204}Pb$ ~ 18.9; Figs. 5.1, 5.3). The range of Pb isotope compositions measured from each site, alongside an indication of which compositions correspond to insolation maxima and minima (where this is possible) is shown diagrammatically in Fig. 5.3.

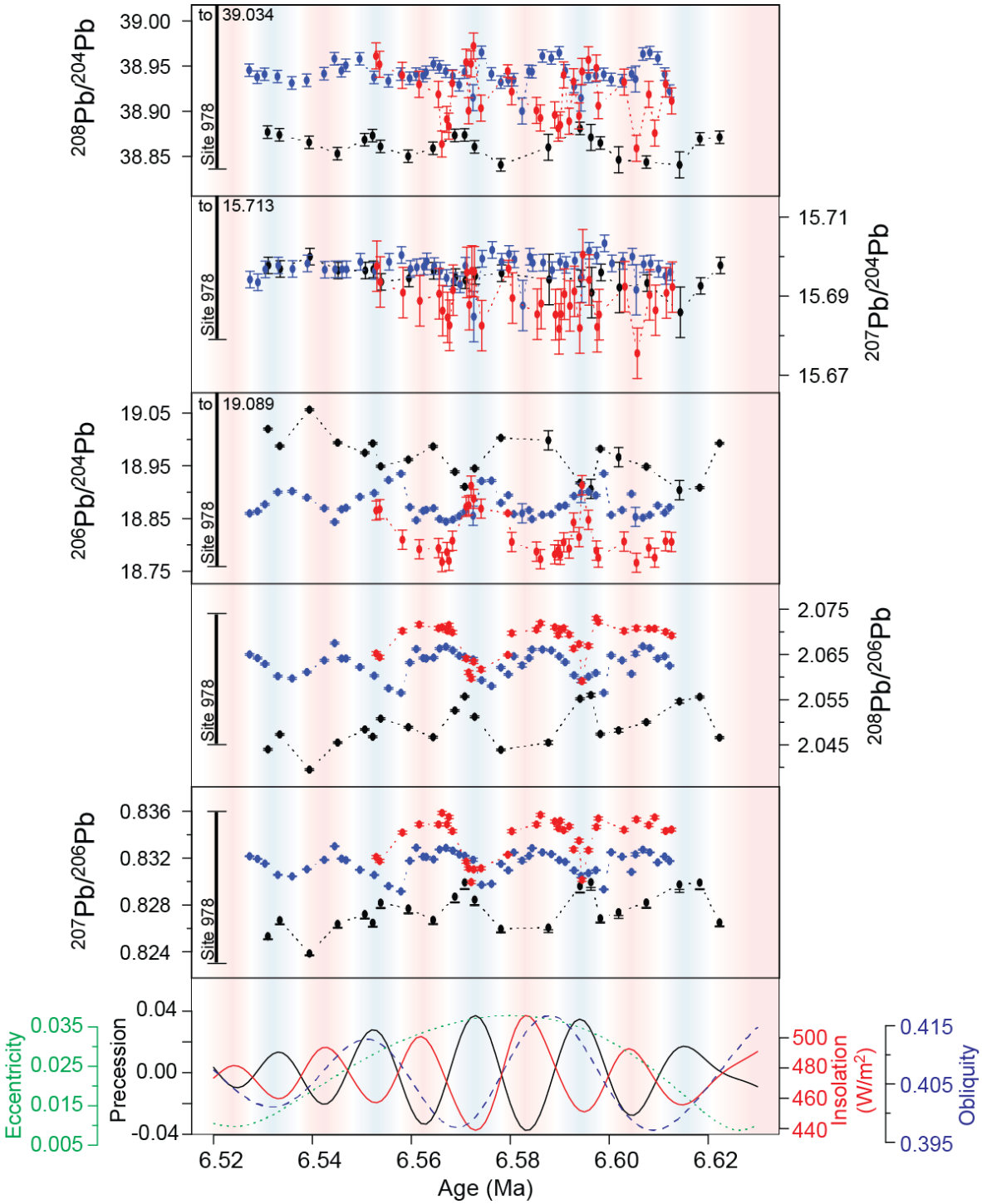

Fig. 5.1. Pb isotope time series of acid-reductive leaches on bulk sediment from the Sorbas Basin (red), Falconara section (blue), and Monte del Casino section (black), compared with orbital parameters insolation, climatic precession, obliquity, and eccentricity. The ranges of Pb isotope compositions measured from late Miocene samples from ODP Site 978 are also shown.

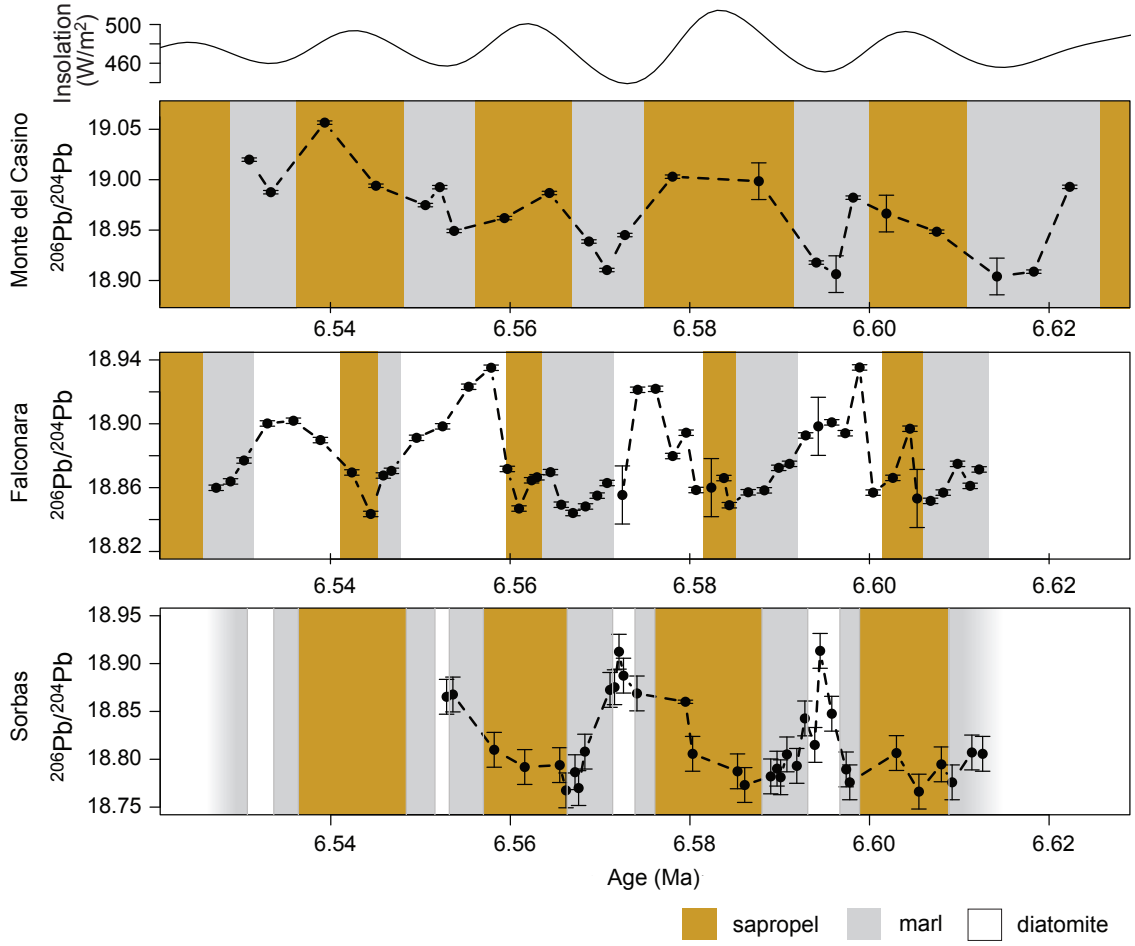

Fig. 5.2. $^{206}Pb/^{204}Pb$ records from Monte del Casino (upper panels) and Falconara (lower panels) plotted against lithological variation.

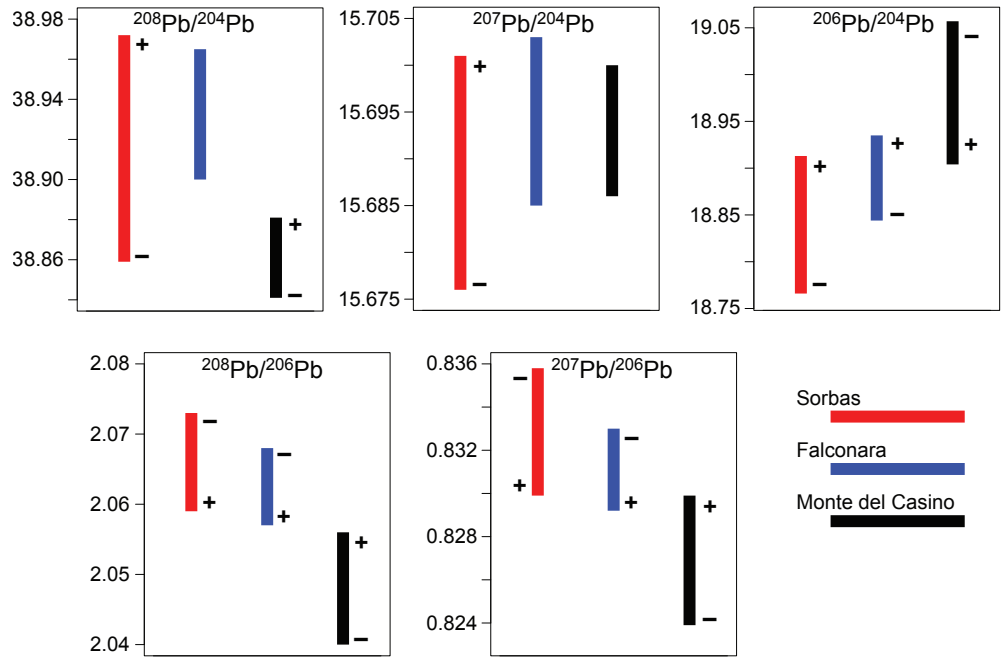

Fig. 5.3. Ranges of Pb isotope compositions measured at each of the three sites (Sorbas Basin, Falconara, and Monte del Casino). Where it is visually clear, based on the correspondence shown in Fig. 5.1, which compositions tend to correlate to insolation maxima (+) and minima (-), this is noted.

5.2.2 ODP Site 978

The results of acid-reductive leachates of samples from ODP Site 978 are listed in Table 5.2. Generally, the compositions are similar to the less radiogenic values observed at Sorbas, except for one sample (48R-1W 13-15 cm) which shows a very radiogenic value compared to the others. Analysis of this sample was repeated on a new portion of material and the elevated Pb isotopic composition was confirmed. The average of the two measurements is shown in Table 5.2. The large uncertainty regarding age for the samples from ODP Site 978 (Ch. 2, section 2.2.2) precludes presenting these data as a time series and directly comparing with the outcrop data from Sorbas, Falconara, and Monte del Casino; only ranges are shown in Fig. 5.1.

Table 5.2. Pb isotopic compositions, ODP Leg 161, Site 978.

Sample	Age (Ma)*	$^{208}Pb/^{204}Pb$	$^{207}Pb/^{204}Pb$	$^{206}Pb/^{204}Pb$	$^{208}Pb/^{206}Pb$	$^{207}Pb/^{206}Pb$
29R-6W 30-32	3.93-4.03 (3.98)	38.836 ±14	15.679 ±6	18.759 ±18	2.0703 ±4	0.83577 ±13
35R-3W 65-67	4.47-4.57 (4.52)	38.872 ±14	15.686 ±6	18.791 ±18	2.0687 ±4	0.83473 ±13
47R-1W 16-18	6.12-6.62 (6.21)	38.892 ±14	15.687 ±6	18.764 ±18	2.0727 ±4	0.83602 ±13
47R-3W 122-124	6.12-6.62 (6.24)	38.912 ±14	15.690 ±6	18.765 ±18	2.0736 ±4	0.83615 ±13
48R-1W 13-15	6.12-6.62 (6.28)	39.034 ±14	15.713 ±6	19.089 ±18	2.0449 ±4	0.82311 ±13
48R-3W 121-123-15	6.12-6.62 (6.30)	38.896 ±14	15.686 ±6	18.778 ±18	2.0713 ±4	0.83532 ±13

Uncertainty is 2SD (external analytical reproducibility) unless 2SE (internal) was larger. *Ages given in the format minimum-maximum (calculated).

5.2.3 Reliability

As the behaviour of Pb isotopes in seawater are not as well constrained as Sr and Nd, it is important to discuss the origin of the extracted signal as well as the reliability of the method. The reliability of the acid-reductive leach process (the method by which both Nd and Pb was extracted) was initially discussed in Ch. 4 alongside the Nd results (section 4.2.2.2). As outlined in that section, the sediment fraction sampled (authigenic Fe-Mn oxyhydroxides) has been shown to be both authigenic and of marine origin. There is also no substantive evidence that detrital phases have been accessed during the leaching process, or that anoxia has had a significant effect on the results, when considering the Al/Nd elemental ratios of the leachates (section 4.2.2.2, Fig. 4.3).

It is also useful to compare the Pb isotope compositions of the acid-reductive leaches, strong leaches and total dissolutions (Table 5.3). The Sorbas Basin leachate Pb isotope

values plot along an essentially linear array in Pb/Pb space (Fig. 5.4, 5.6), with samples deposited during insolation minima shifting towards more radiogenic values. The strong leach and total dissolution results plot away from this trend, with values more radiogenic in $^{208}Pb/^{204}Pb$ and $^{207}Pb/^{204}Pb$, and less so in $^{206}Pb/^{204}Pb$. Thus, fluctuations in preservation or bottom water conditions in phase with precession are not likely to have caused the bottom water compositions to be affected by detrital siliciclastics to a significant degree. If this were the case, all results (leachates and total dissolution) would be expected to plot on the same array. Therefore, the shifts are most likely caused by climatic factors affecting the overall water mass Pb isotope signatures bathing the location, and the acid-reductive leach results can be considered to represent seawater values.

Table 5.3. Strong leach and total dissolution Pb isotope compositions of Sorbas Basin sediments.

Sample	Age (Ma)	$^{208}Pb/^{204}Pb$		$^{207}Pb/^{204}Pb$		$^{206}Pb/^{204}Pb$		$^{208}Pb/^{206}Pb$		$^{207}Pb/^{206}Pb$	
33-6 SL	6.6114	39.059	±7	15.690	±2	18.815	±2	2.0760	±2	0.83391	±4
33-15 SL	6.6080	38.996	±7	15.690	±2	18.792	±2	2.0752	±2	0.83494	±4
33-27 SL	6.6030	38.988	±7	15.691	±2	18.789	±2	2.0751	±2	0.83514	±4
34-16 SL	6.5908	39.034	±7	15.690	±2	18.810	±2	2.0752	±2	0.83413	±4
34-45 SL	6.5795	38.988	±7	15.689	±2	18.795	±2	2.0743	±2	0.83472	±4
35-9 SL	6.5721	39.054	±7	15.693	±2	18.841	±2	2.0728	±2	0.83291	±4
35-19 SL	6.5683	38.996	±7	15.690	±2	18.799	±2	2.0744	±2	0.83461	±4
35-27 SL	6.5655	38.993	±7	15.692	±2	18.792	±2	2.0749	±2	0.83502	±4
35-39 SL	6.5616	38.985	±7	15.691	±2	18.780	±2	2.0759	±2	0.83553	±4
35-48 SL	6.5582	38.994	±7	15.690	±2	18.786	±2	2.0757	±2	0.83517	±4
36-11 SL	6.5529	39.064	±7	15.694	±2	18.822	±2	2.0755	±2	0.83383	±4
33-6 TD*	6.6114	39.071	±7	15.700	±2	18.797	±2	2.0785	±2	0.83521	±4
33-15 TD*	6.6080	39.066	±7	15.700	±2	18.813	±2	2.0765	±2	0.83454	±4
33-27 TD*	6.6030	39.072	±7	15.701	±2	18.810	±2	2.0772	±2	0.83473	±4
34-16 TD*	6.5908	39.061	±7	15.698	±2	18.806	±2	2.0771	±2	0.83471	±4
34-45 TD	6.5795	39.060	±7	15.702	±2	18.817	±2	2.0758	±2	0.83442	±4
35-9 TD	6.5721	39.047	±7	15.700	±2	18.775	±2	2.0797	±2	0.83621	±4
35-19 TD*	6.5683	39.073	±7	15.700	±2	18.804	±2	2.0780	±2	0.83493	±4
35-27 TD*	6.5655	39.053	±7	15.699	±2	18.809	±2	2.0763	±2	0.83464	±4
35-39 TD*	6.5616	39.048	±7	15.698	±2	18.795	±2	2.0776	±2	0.83523	±4
35-48 TD	6.5582	39.056	±7	15.701	±2	18.797	±2	2.0778	±2	0.83529	±4

SL – strong leach. TD – total dissolution. * average of duplicate measurements (individual analyses in Appendix 5). Uncertainty is 2SD (external analytical reproducibility) unless 2SE (internal) was larger.

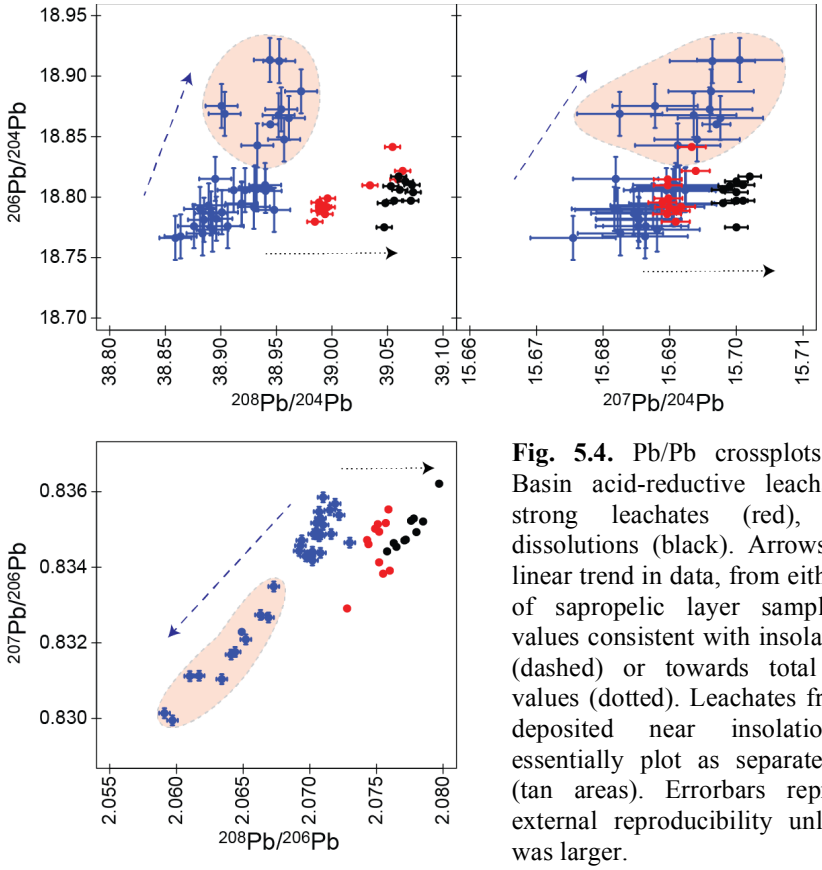

Fig. 5.4. Pb/Pb crossplots of Sorbas Basin acid-reductive leachates (blue), strong leachates (red), and total dissolutions (black). Arrows emphasize linear trend in data, from either leachates of sapropelic layer samples towards values consistent with insolation minima (dashed) or towards total dissolution values (dotted). Leachates from samples deposited near insolation minima essentially plot as separate population (tan areas). Errorbars represent 2SD external reproducibility unless internal was larger.

5.3 Discussion

Erel et al. [1994] observed that soil Pb isotope compositions were related to both the weathering regimes producing the soils and their relative age. This combination of properties has led several authors to note that seawater Pb isotopes can record changes in continental weathering regimes related to climate [e.g., *Chow and Patterson*, 1962; *Sun*, 1980; *Foster and Vance*, 2006; *Gutjahr et al.*, 2009]. The Pb isotopic compositions of Sorbas, Falconara, and Monte del Casino seawater preserved in authigenic oxyhydroxides exhibit the characteristic precessional frequency observed across the Mediterranean in sedimentation patterns (Figs. 5.1, 5.2, 5.5). The near landlocked nature of the Mediterranean reduces the buffering effect of the Atlantic, rendering the system sensitive to regional climatic change [*Gladstone et al.*, 2007]. As outlined in the introduction (Ch. 1, section 1.2.5) Mediterranean climate is strongly influenced by precessional frequency climate shifts. In particular, the hydrologic budget is controlled primarily by shifts of the African monsoon system over North Africa, driven by a northward movement of the ITCZ [e.g., *Marzocchi et al.*, 2015], with a much larger amount of riverine runoff discharging into the Eastern Mediterranean from North Africa during precession minima (insolation maxima) [*Rohling et al.*, 2015 and references therein].

5.3.1 Sorbas Basin

The cyclicity observed in the Pb isotope records in the Sorbas Basin is similar to the cyclicity observed in Sr isotopes (Ch. 3) although the two are sometimes out of phase (Fig. 5.5). Peaks in the Pb isotope compositions ($^{206}Pb/^{204}Pb \sim 18.9$) occur within the diatomite layer, before the Sr anomalies, in cycles UA5 and UA6. Cycle UA7 is the exception with the anomalies occurring at the same time. The maximum excursions observed in the Pb isotope compositions occur consistently within the diatomite layer, while the Sr isotope anomalies do not consistently plot with the same lithology. The difference in phasing observed for the two isotope systems suggests that two different climate-related mechanisms are being recorded. This may be related to the very different residence times of these two elements in seawater, but also to different mechanisms driving the changes.

The peaks in Pb isotope ratios are also slightly out of phase with the faunal cyclicity at this location (Fig. 5.5). The peaks in Pb isotope composition lag slightly behind Neogloboquadrinid maxima while they lead the shift towards a dominance of *Globigerina bulloides* (both expressed as a percentage of total planktic foraminiferal assemblage). The temporal match is better with the increase in benthic foraminifera (expressed as a ratio of benthic/planktic foraminifera). Cyclicity in several factors (e.g., $^{87}Sr/^{86}Sr$, see Ch. 3; fauna, [*Pérez-Folgado et al.*, 2003; *Sierro et al.*, 2003], lithology, [*Sierro et al.*, 1997, 1999, 2001]) has been attributed to precessional oscillations in environmental conditions. Although the mechanisms controlling the Pb isotope ratios are not identical to those controlling the $^{87}Sr/^{86}Sr$ ratios, or the planktic foraminiferal communities, there is still a strong coincidence with insolation. This indicates another precessional environmental oscillation controls the Pb isotope compositions preserved in the Sorbas Basin.

5.3.2 Falconara section

The Pb isotope compositions measured from the Falconara section are quite similar to those of Sorbas, albeit the range is smaller ($^{206}Pb/^{204}Pb$ from 18.844 to 18.935, compared to $^{206}Pb/^{204}Pb$ from 18.766 to 18.913 at Sorbas). For both sections, the more radiogenic ratios tend to be associated with the non-sapropelic layers, in particular, the diatomite. The relationship between lithology and climate at Falconara is also thought to be similar to Sorbas: diatomite deposition coincides with insolation minima, while sapropel deposition coincides with insolation maxima [*Hilgen and Krijgsman*, 1999]. Thus, for Falconara as

for Sorbas, it can be assumed that the source of Pb during colder, drier periods (insolation minima/precession maxima) is more radiogenic, while during wetter, warmer periods (insolation maxima/precession minima) the source is less radiogenic (Figs. 5.1, 5.2).

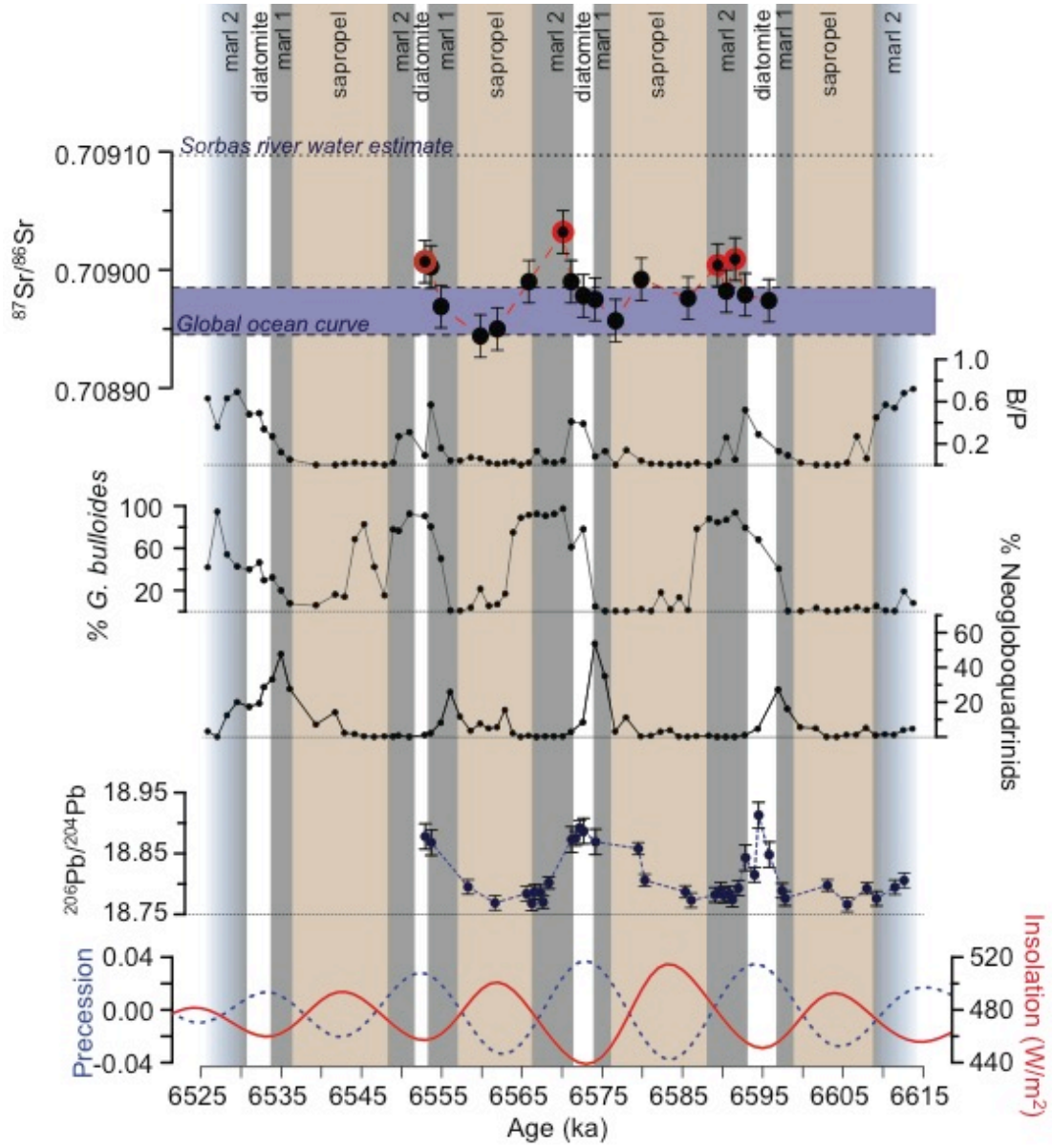

Fig. 5.5. Comparison of $^{87}Sr/^{86}Sr$ isotope results, benthic to planktic (B/P) ratio, % *Globigerina bulloides* (of planktic foraminiferal assemblage), % Neogloboquadrinids (of planktic foraminiferal assemblage), and $^{206}Pb/^{204}Pb$ isotope ratios with lithology and precession/insolation. Faunal data from *Pérez-Folgado et al.* [2003]. The $^{206}Pb/^{204}Pb$ isotope ratio is selected as it shows the cyclicity most clearly; however, the temporal changes in all other Pb isotope ratios are identical relative to lithology, with the exception of $^{207}Pb/^{204}Pb$, as variability in the record of this ratio is obscured by the low natural variability compared to analytical uncertainty.

5.3.3 Monte del Casino section

The opposite relationship is observed for Monte del Casino (Figs. 5.1, 5.2). The data also plot on an entirely different array (Fig. 5.6), although during times of insolation minima

the isotope compositions in $^{206}Pb/^{204}Pb$ appear to converge with those of the other two sites ($^{206}Pb/^{204}Pb \sim 18.9$). In general, the lithological cyclicity is thought to be similar to the other two sections; sapropels are thought to be deposited during insolation maxima, and the homogeneous marls during insolation minima [*Krijgsman et al.*, 1997; *Hüsing et al.*, 2009]. No diatomite layers are observed at this section. Thus, for Monte del Casino, the observed Pb isotopic compositions trend towards more radiogenic values during wetter periods (e.g., $^{206}Pb/^{204}Pb >19$, at insolation maxima) and less radiogenic values during drier periods (e.g., $^{206}Pb/^{204}Pb \sim 18.9$, at insolation minima), opposite to Sorbas and Falconara. This implies the sources affecting Sorbas and Falconara may be similar, while those controlling Monte del Casino are likely to be very different.

5.3.4 Potential mechanisms controlling seawater Pb isotope composition

The coincidence between the variability observed in the high-temporal resolution Pb isotope records presented here with precession suggests that precessional climate shifts are influencing the Pb isotopic compositions of seawater at Sorbas, Falconara and Monte del Casino. As discussed with respect to the Sr isotope results (Ch. 3, section 3.4.1), mechanisms such as volcanism, tectonism, and hydrothermal activity do not operate on precessional timescales, and therefore are unlikely to be responsible. Thus, the marginal marine sections of Sorbas, Falconara, and Monte del Casino are likely to have preserved climate-driven changes in seawater Pb isotopes which are a direct reflection of changes in local weathering regimes. That these signals are recorded by changes in Pb isotopes and not in Nd isotopes (Ch. 4) is likely enabled by the short residence time and high particle reactivity of this element in seawater. Unlike Nd, an element for which boundary exchange (and the related process of benthic flux) has been observed to shift seawater ε_{Nd} nearer to that of solid phases close to the sediment-water interface (see Ch. 1, section 1.3.1) [e.g., *Lacan and Jeandel*, 2005; *Jeandel et al.*, 2007; *Wilson et al.*, 2012, 2013; *Pearce et al.*, 2013; *Abbott et al.*, 2015b], Pb is not likely to be remobilized once deposited due to its very high affinity for manganese oxyhydroxides, leading this element to adsorb very strongly [*Gadde and Laitinen*, 1974]. Climate-driven mechanisms which could generate the Pb isotope variations include changes in dust production, temporal variability in riverine runoff, and changes to the continental Pb isotope signal caused by incongruent weathering. As stated in the previous section, it is unlikely that temporal variability in riverine runoff is the primary driver of the observed precessional cyclicity in the Sorbas, Falconara and Monte del Casino Pb isotope records. Compared to Sr, Pb has a much lower

solubility and residence time, allowing sources such as dust to impact seawater isotope compositions to a much greater degree (Ch. 1, section 1.3.2, Fig. 1.13). Another mechanism may be related to changes in productivity and/or bottom water oxygenation, as both these processes have been observed to affect uranium complexation and precipitation in marine sediments. As uranium and thorium decay results in the production of radiogenic Pb (Ch. 1, Fig. 1.17), processes affecting the flux of these elements to marine sediments should also be considered.

5.3.4.1 Temporal variability in riverine runoff

There is an apparent linear array across open marine sites (including all FeMn crusts and ODP Site 978; a linear trendline through data from all these sites is plotted and labeled "open marine" trend, Fig. 5.6, 5.12). Linear arrays in Pb/Pb isotope space indicate binary mixing of two end members or sources; this open marine trend could be considered to represent a mixture of Pb inputs to the Mediterranean Sea (at the far right) and the Pb inputs to the NE Atlantic (at the far left). As a large input to the Mediterranean occurs via exchange through the Gibraltar region, the water within the Mediterranean should be an admixture of the inputs directly to the basin and the NE Atlantic signature. This "open marine" array also describes a great deal of variability in the Sorbas and Falconara data.

Plotted in Pb/Pb space (Figs. 5.2, 5.6), the Sorbas leachate data form two statistically distinct groups, with the more radiogenic group containing the data consistent with insolation minima. The entirety of the array trends parallel to the "open marine" trendline. Variability not described by the "open marine" array for the Sorbas Basin samples could be explained by local inputs from siliciclastic weathered material as indicated by the strong leach and total dissolution samples, which plot in a tight cloud above the trend (Sorbas Basin siliciclastic end-member, upper corner of triangle, Fig. 5.5). The influence of the siliciclastic end-member does not appear to have any relationship to precession, as values from both the insolation minima and insolation maxima groups appear equally affected (Fig. 5.6, also section 5.3.3). This latter observation suggests that riverine input to the basin did not vary greatly, consistent with the Sr isotope modeling results (Ch. 3) that indicate little absolute change in river runoff with precession to the Sorbas Basin. In comparison to the general Mediterranean case, in which the overall hydrology is driven by changes in North Africa, past climate fluctuations over Spain, and in general southern Europe, appear to be controlled by precessional changes in Atlantic storm track systems

[*Toucanne et al.*, 2015; *Marzocchi*, 2016]. While these systems cause changes in the hydrologic budget in phase with the shift of the ITCZ over North Africa (i.e., wetter conditions during precession minima/insolation maxima and drier conditions during precession maxima/insolation minima), the magnitude of variation is much less. Comparing the hydrologic budget for the Western and Eastern Mediterranean basins, the difference in riverine runoff is more than an order of magnitude smaller between wet and dry extremes, due principally to the enhanced river fluxes from North Africa, while the variation in precipitation is less than half (see Table 2.6, Ch. 2, and discussion in Ch. 3; [*Marzocchi et al.*, 2015, 2016]).

In combination, these factors indicate that the Sorbas Basin seawater Pb isotope compositions can be explained by three end-members: a degree of influence from local siliciclastic input, on a relatively constant basis, regardless of insolation; and open seawater values transitioning between two end-members depending on climate (precession/insolation). The open Atlantic data tend to plot towards the less radiogenic end of the array, suggesting a regional Mediterranean source(s) for the more radiogenic end-member.

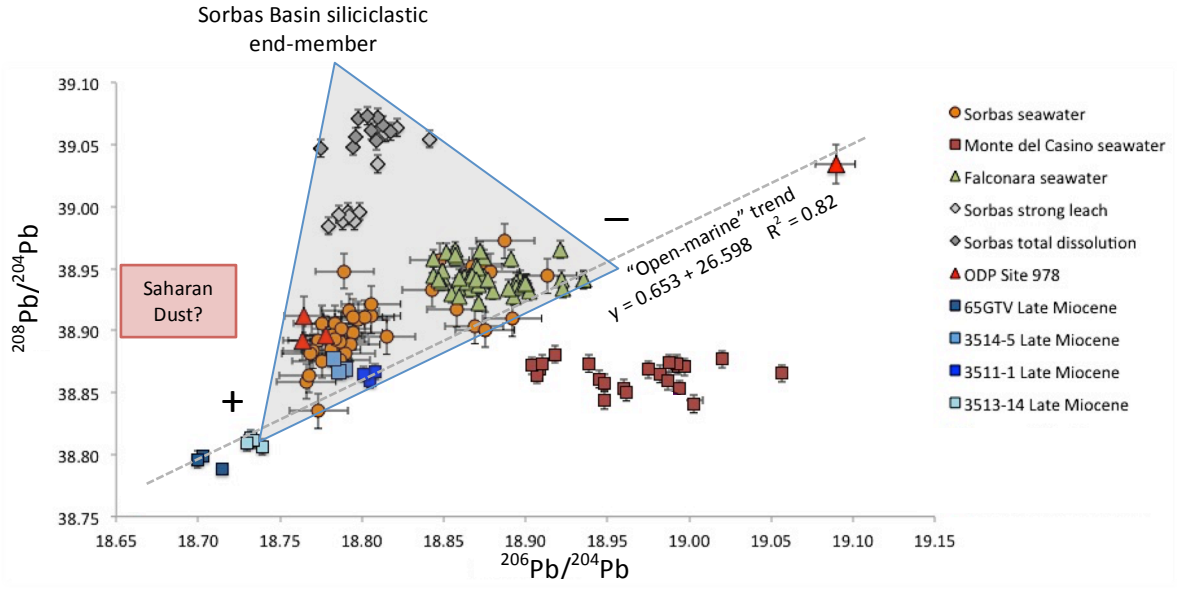

Fig. 5.6. $^{208}Pb/^{204}Pb$ vs. $^{206}Pb/^{204}Pb$ plot comparing Sorbas, Falconara, and Monte del Casino seawater values with other regional data. Sorbas Basin seawater signature (acid-reductive leachates, orange circles) strong leach and total dissolution results (diamonds) plot within a triangle bounded at the bottom by an array (dashed line), labeled the "Open-marine trend", described by ODP Site 978 (red triangles), and FeMn crusts (squares). To the bottom-left of the triangle, values associated with insolation maxima (+), and to the bottom-right, values associated with insolation minima (-). The top of the triangle likely represents the siliciclastic end-member. Monte del Casino plots on its own array (brown squares). An average value for Saharan dust compiled by *Abouchami and Zabel* [2003] from other literature data is shown; this average is contested in section 5.3.4.3.

5.3.4.2 *Productivity-related U complexation or exclusion*

Differential deposition or complexation of the radioactive parent isotopes of U and Th could explain some of the observed variability in the seawater records. The amount of U, Th and K contained in sedimentary rocks is most commonly related to grain size, as fine particles like clays adsorb these elements readily. Gamma ray well logs, which reflect varying activities of these elements in rock strata, are often used for cyclostratigraphy due to the good correlation between sediment grain size, weathering regimes, and orbital changes in climate [e.g., *Baumgarten and Wonik*, 2014; *Cantalejo and Pickering*, 2015]; sand and gravel units tend to show low γ-ray values, while clays typically have high values. For the Sorbas Upper Abad sediments, the cyclicity in Pb isotope ratios cannot be explained in this manner, as non-biogenic grains of all lithologies are dominated by the fine fraction (< 63 μm, *Vázquez et al.* [2000]).

Changes in the concentration of uranium deposited in marine sediments is also attributed to changes in oxygen levels [e.g., *Zheng et al.*, 2002; *Hayes et al.*, 2014]. This phenomenon is related to oxygenation at the seafloor, as anoxia leads to greater deposition of uranium under redox conditions. It is well understood that in anoxic conditions, soluble U(VI) is reduced to insoluble U(IV), leading to precipitation of uranium and removal from the water column [*Langmuir*, 1978; *Klinkhammer and Palmer*, 1991; *Cochran*, 1992]. Differences in [U] between sedimentary layers can be explained by the link between bioturbation and oxygenation; in a generally anoxic environment, periods of increased oxygenation lead to more vigorous bioturbation, exposing deposited uranium and allowing it to revert to the soluble phase, reducing the [U] in the bioturbated layers [*Zheng et al.*, 2002]. This explanation could fit with the pattern observed at Monte del Casino, where the sapropelic layers generally preserved more radiogenic Pb isotope compositions. At Monte del Casino, as for the other sections, the sapropelic layers are associated with anoxia due to stagnant basin conditions reinforced by enhanced hydrological cycling during insolation maxima, as is the general Mediterranean case [*Krijgsman et al.*, 1997; *Hüsing et al.*, 2009].

In addition, organic matter is known to be capable of complexing uranium [*Ivanovich and Harmon*, 1992]. *Mann and Fyfe* [1985] found that green algae can concentrate U by factors of 10^3 to 10^5 above background levels, although this study was carried out in freshwater mine tailings ponds containing high uranium concentrations. A review by *Santschi et al.* [2006] highlights the role that biologically produced polysaccharide gel films, commonly found on the outside of diatom frustules, bacteria, and other organisms, plays in

complexing thorium in seawater. The diatomites at Sorbas and Falconara are thought to form during periods of high productivity, and the most radiogenic Pb isotope values are found in these layers, suggesting biological complexation could play a role (Fig. 5.2).

Although U, Th and Pb concentration measurements have not been made, it is possible to estimate if biological complexation could produce the amount of *in-situ* ingrowth of radiogenic daughter products using general radioactive decay equations. Average concentrations were estimated from literature values for marine sediments from different environments (anoxic to oxic, Table 5.4). Initial and present day Pb isotope ratios were assumed to be the least radiogenic (lowest) and most radiogenic (highest) ratios, respectively, from Sorbas and Monte del Casino; consequently, the calculated concentration corresponds to the excess over background concentration required to generate the isotopic difference. Calculations were made by both keeping the ratio of Th/U the same as that suggested from the literature, as well as by adjusting it, to quantify how much of a shift is necessary to produce target (initial, or minimum) values.

Even if the factors of 10^3 – 10^5 above background levels [*Mann and Fyfe*, 1985] overestimate biological complexation for the marine environment, the factors in Table 5.4 are well below the range of enrichment suggested by those authors. Thus, it could be feasible to produce the $^{208}Pb/^{204}Pb$ and $^{206}Pb/^{204}Pb$ ratios observed in the Sorbas Basin, although it is necessary to adjust the Th/U ratio. From the literature compilation, it appears that the Th/U ratios used (Table 5.4) to estimate the values in Sorbas are within the natural range (Th/U 1.78 to 2.44), while that required to estimate similar values for Monte del Casino is too low (Th/U 0.84). However, a more serious problem is encountered when considering the $^{207}Pb/^{204}Pb$ ratio; a much higher concentration of U is required to generate the $^{207}Pb/^{204}Pb$ ratio observed than that required to generate the $^{206}Pb/^{204}Pb$ ratios. As both ^{206}Pb and ^{207}Pb are products of U, this would necessitate fractionation of the parent isotopes, ^{238}U and ^{235}U. In terms of the values observed at Monte del Casino, the enrichment in ^{235}U would need to be at least double that of ^{238}U, while the enrichment at Sorbas would need to be at least three times greater. While some fractionation has been observed between these U isotopes [*Stirling et al.*, 2007; *Weyer et al.*, 2008], this tends to be associated with only a very slight enrichment of ^{235}U (on the order of 0.5 per mil) into sediments under anoxic conditions [*Andersen et al.*, 2014]. Thus, *in-situ* radiogenic decay in layers which have incorporated differing U and Th concentrations (due to biological complexation or any other reason) is very unlikely to explain the observed ratios.

Table 5.4. Calculation of excess U and Th required to cause radiogenic compositions observed in situ, assuming maximum $^{20X}Pb/^{204}Pb$ ratios represent present time and minimum ratios represent 'initial' ratios (6.6 Ma). Values in red do not match targets.

Marine sediment U, Th, P concentrations* (ppm)							Sorbas			
	U	Th	Pb	Pb/U	Th/U		$^{206}Pb/^{204}Pb$	$^{207}Pb/^{204}Pb$	$^{208}Pb/^{204}Pb$	
Average	9	16	32	3.6	1.78	*Present*	*18.913*	*15.701*	*38.972*	*(input)*
Range	0.6 - 41	4.2 - 40	1 - 65			*Initial*	*18.766*	*15.676*	*38.859*	*(target)*
Additional U and Th to reach target (Sorbas):										
6 x U	54	96	32	0.59	1.78		18.766	15.694	38.890	
22 x U	198	352	32	0.16	1.78		18.374	15.676	38.672	
6 x U	54	132	32	0.59	2.44		18.766	15.694	38.859	
22 x U	198	484	32	0.16	2.44		18.374	15.676	38.559	
							Monte del Casino			
						Present	*19.057*	*15.700*	*38.881*	*(input)*
						Initial	*18.904*	*15.686*	*38.841*	*(target)*
Additional U and Th to reach target (Monte del Casino):										
6.2 x U	56	47	32	0.57	0.84		18.904	15.693	38.841	
12 x U	108	47	32	0.30	0.44		18.763	15.686	38.841	

* References used to compile marine sediment concentration data: Mo et al., 1973; Cochran and Krishnaswami, 1980; Cochran et al., 1986; Ben Othman et al., 1989; Windom et al., 1989; Klinkhammer and Palmer, 1991; Zheng et al., 2002; Brumsack, 2006.

5.3.4.3 Dust

Abouchami and Zabel [2003] noted cyclicity in Pb isotopes measured from sediment cores from the Ceará Rise and Sierra Leone Rise, and suggested precessional changes to dust production from the Sahara and Sahel may be responsible. Today, somewhere between 130 - 1600 Tg/yr of dust are emitted per year from North Africa, with an estimated 140 – 260 Tg/yr deposited in the North Atlantic Ocean [*Engelstaedter et al.*, 2006 and references therein]. Considerable amounts of dust are also deposited over the Mediterranean, although the values decrease by over an order of magnitude from east to west (Fig. 5.7) [*Prospero*, 1996]. At present, the Sahara is the source of over half of mineral aerosol particulates in the Earth's atmosphere [*Goudie and Middleton*, 2001]. The terrigenous particles transported depend on several factors; the ones relevant to wet/dry climate oscillations include particle size, particle exposure, soil moisture and cohesion, and vegetative cover [*Rodrigo-Gámiz et al.*, 2015 and references therein].

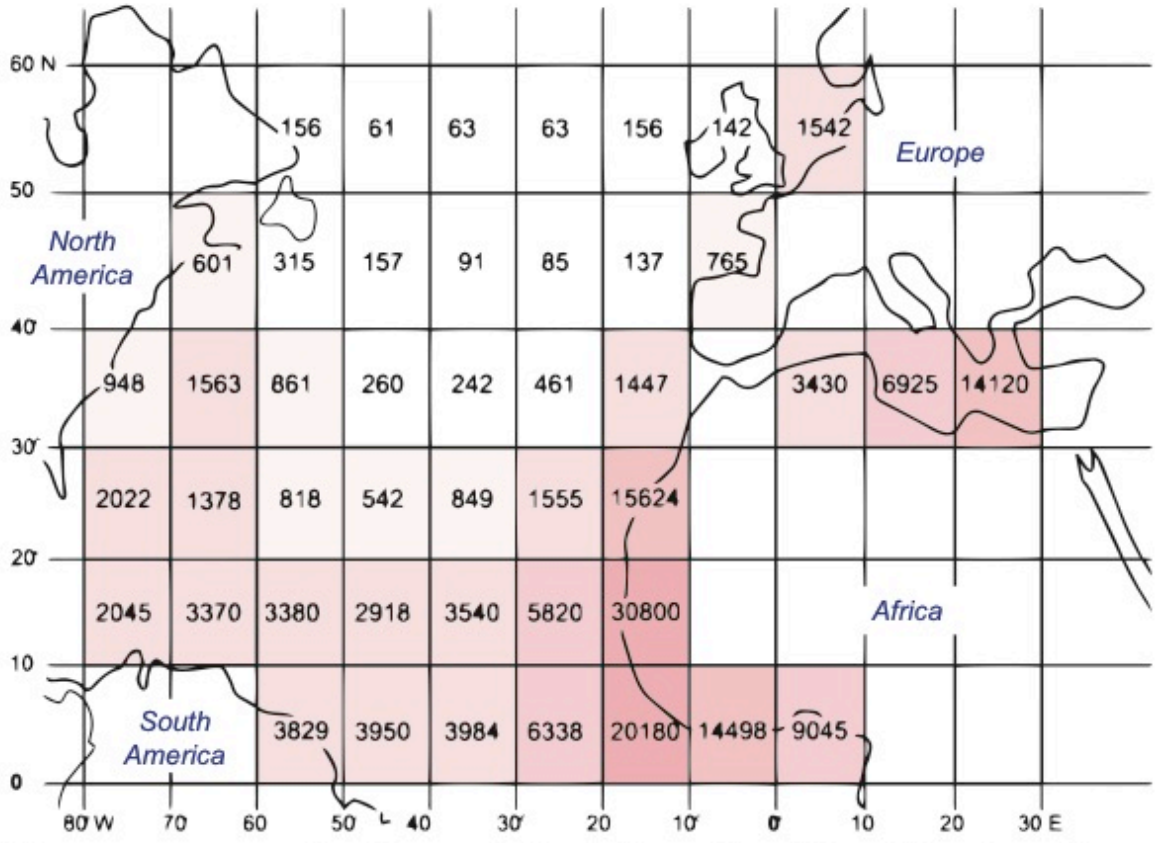

Fig. 5.7. Annual aerosol deposition rates (g/m^2 $x10^3$) over the North Atlantic and Mediterranean. Modified from [*Goudie and Middleton*, 2001], data from [*Prospero*, 1996].

A summary of available estimates for the Pb isotope composition of Saharan dust does not plot on the array of Sorbas or Falconara seawater values (Fig. 5.6) [*Abouchami and Zabel*, 2003 and references therein], seemingly suggesting that Saharan dust is not likely to represent the radiogenic end member of the system. However, the scarce data available for Pb isotope compositions of Saharan dust are considered suspect due to anthropogenic contamination [*Scheuvens et al.*, 2013]. Furthermore, some authors have found that the Pb isotope composition of Saharan dust sources is more variable than previously thought; for example, diatomite from the Bodélé Depression has relatively radiogenic compositions compared to modern-day dust [*Abouchami et al.*, 2013]. The Bodélé Depression (Fig. 5.8) is widely recognized as the single largest source of atmospheric dust in the world [e.g., *Prospero et al.*, 2002; *Washington et al.*, 2003, 2009]. Fig. 5.9 illustrates modern-day dust trajectories and their seasonal variability, including dust derived from the Bodélé Depression (location A). Figs. 5.10 and 5.11 show seasonal modern-day dust transport over the Mediterranean, separated by origin. Assuming that past dust inputs were similar, the amount of dust deposited over the Mediterranean today suggests that this source should have a significant effect on seawater Pb isotope ratios, particularly considering the importance of dust to the oceanic Pb budget [*Frank*, 2002; *Henderson and Maier-Reimer*, 2002]. Significant dust influxes during insolation minima to the Eastern Mediterranean are preserved to at least 3 Ma [*Larrasoaña et al.*, 2003].

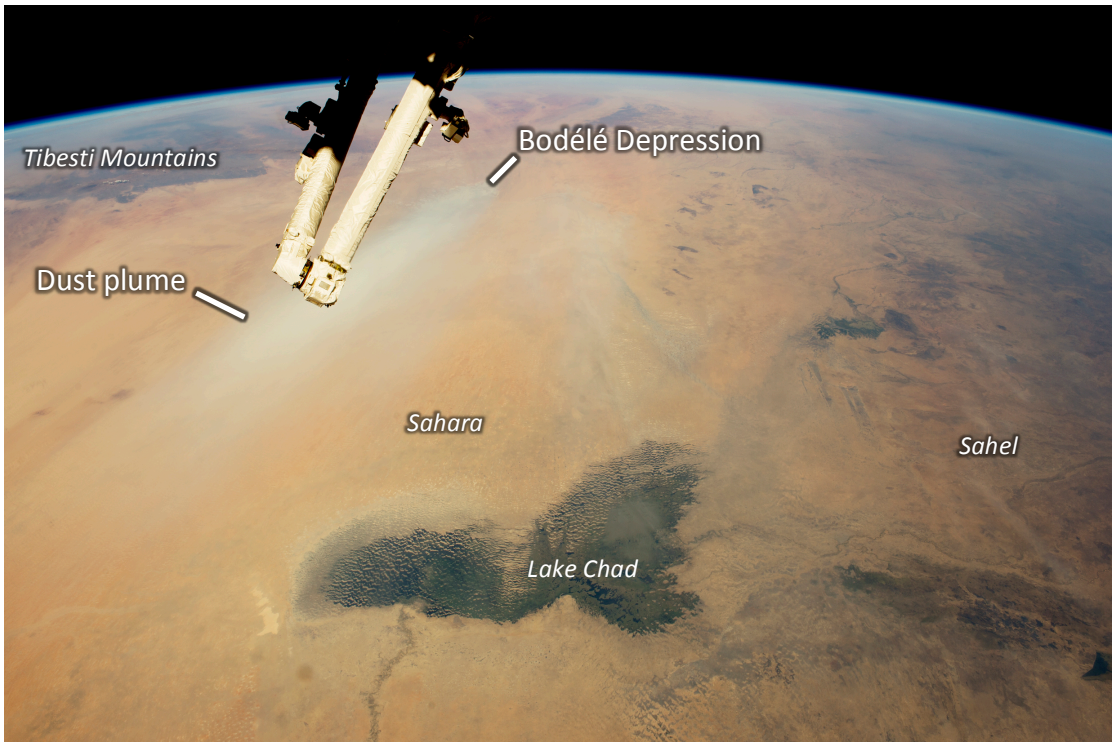

Fig. 5.8. Astronaut photograph ISS042-E-244403 (acquired February 12, 2015) of a dust plume originating from the Bodélé Depression. Source: NASA.

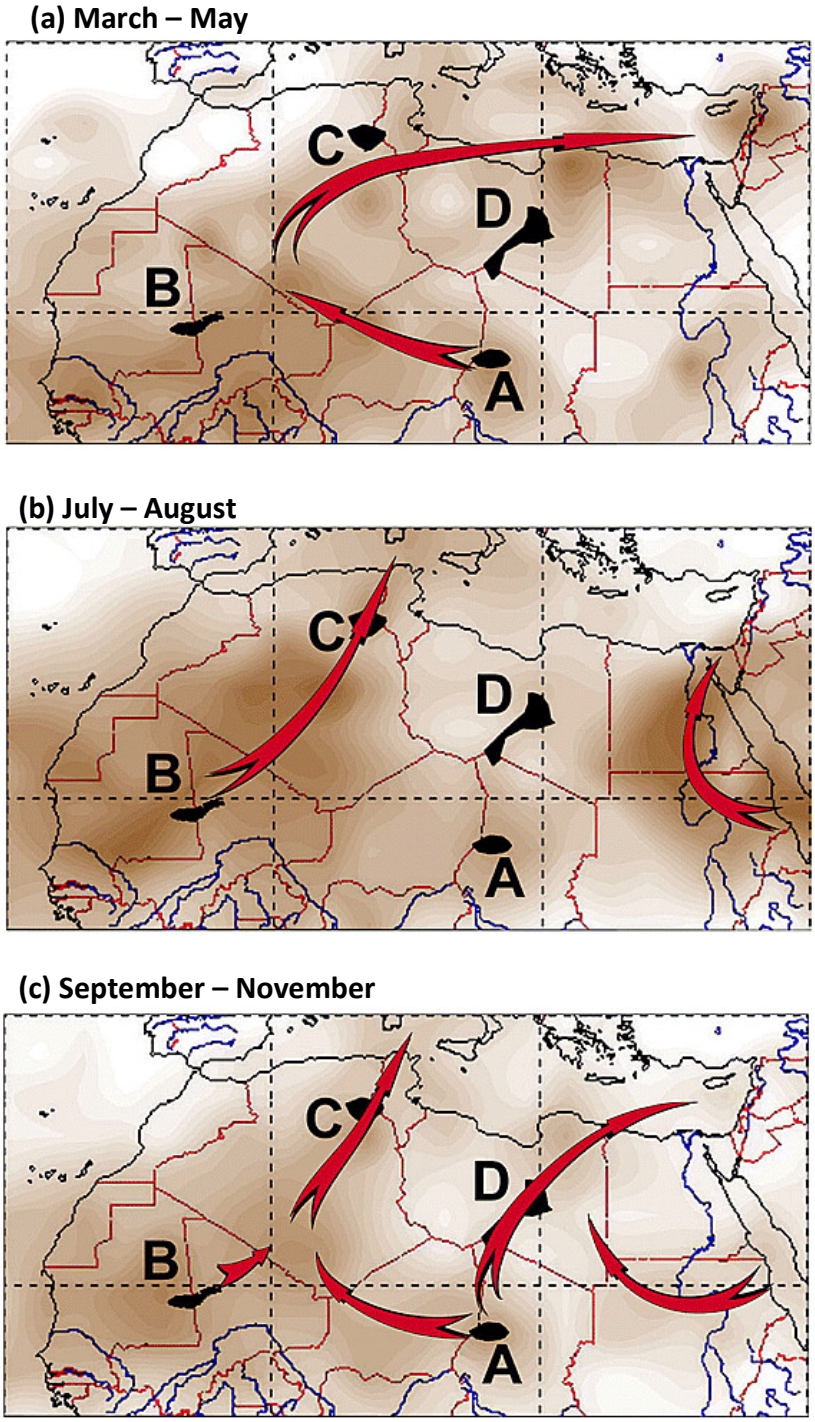

Fig. 5.9. Modern-day dust transport from Africa during various seasons from major source locations. A – Chad Basin (Bodélé Depression included); B – Eljouf Basin (Mali/Mauritania border); C – Region near 33°N 7°E; D – Region near 25°N 18°E. Modified from *Israelevich et al.* [2003]. Sites A and B are the primary sources. Darker colours represent increased concentration of aerosols, although no scale is provided in the original publication. Additional sources include south of the Atlas Mountains (Morocco), the eastern Libyan desert, and large areas of Egypt and Sudan (the Nubian Desert) [*Engelstaedter et al.*, 2006].

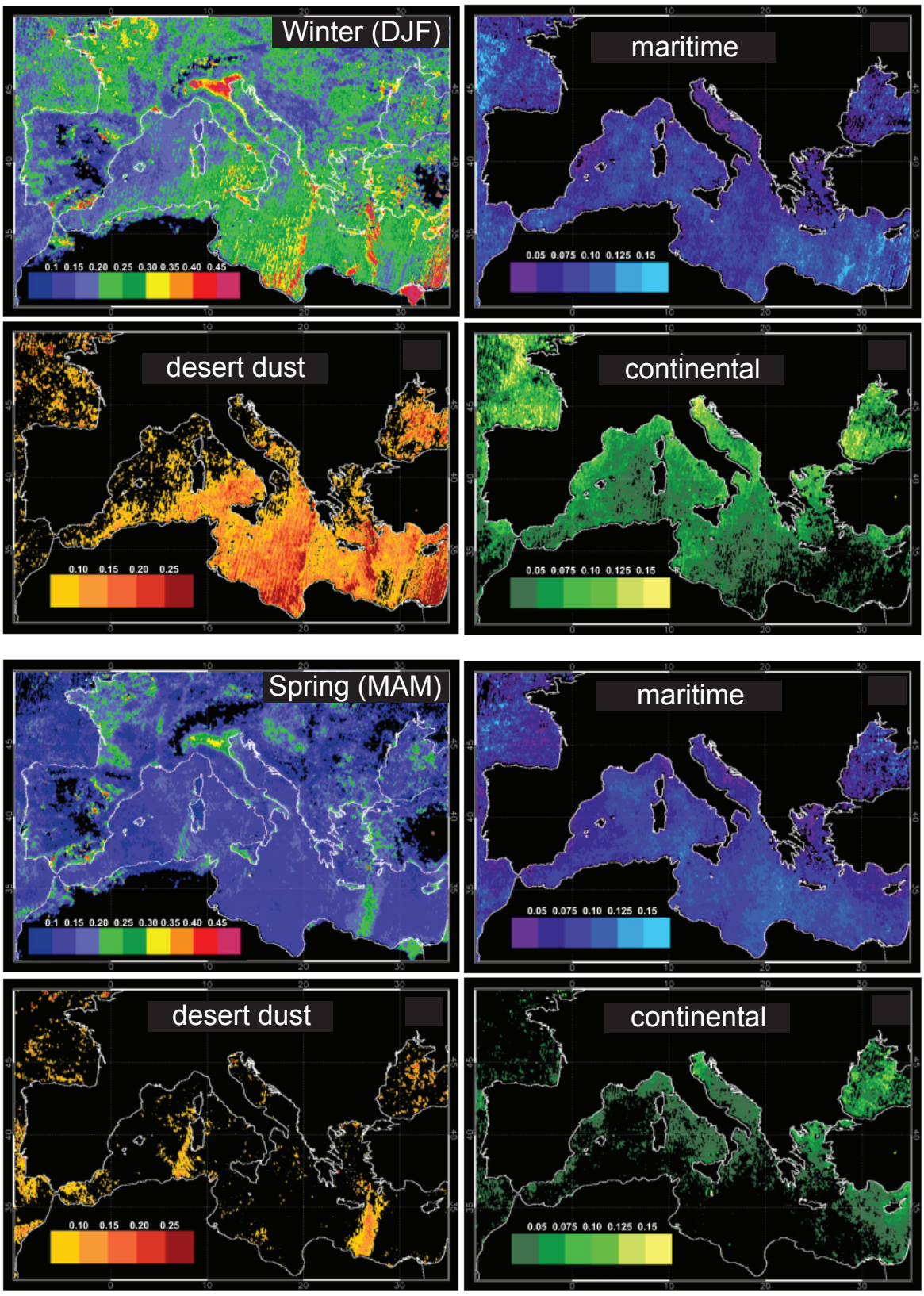

Fig. 5.10. Modern seasonal variability in dust over the Mediterranean, according to type, derived from MODIS satellite data. 'Maritime' is defined as aerosols lifted from the sea surface itself; 'continental' is defined as aerosol particulates, either anthropogenic or natural, originating over the European continent; desert dust is defined as mineral aerosol derived from Northern Africa. Each type has a specific and identical particle size distribution which allows the three sources to be seperable. Winter and spring shown here; summer and fall shown in Fig. 5.11. From [*Barnaba and Gobbi*, 2004].

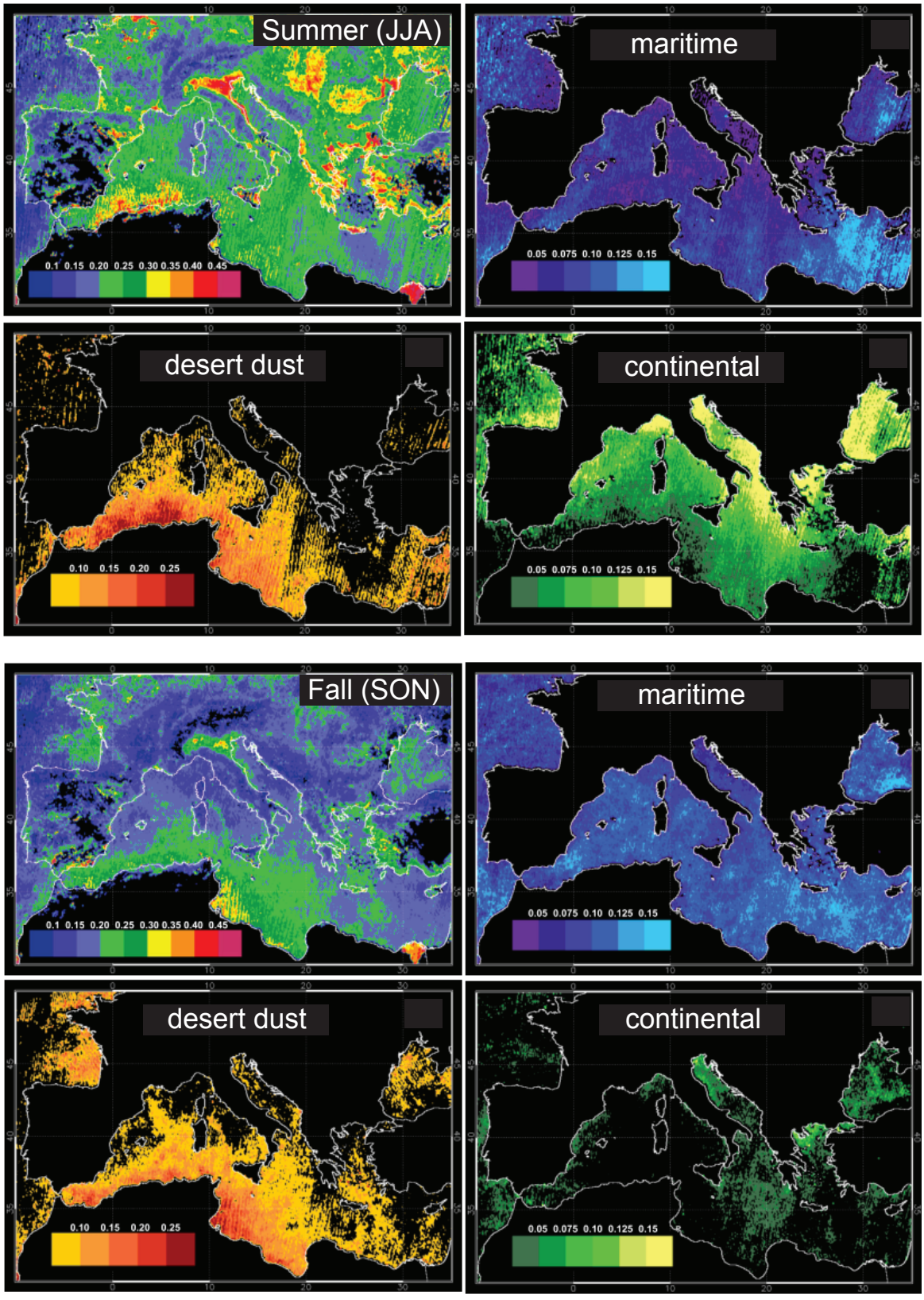

Fig. 5.11. As per Fig. 5.10.

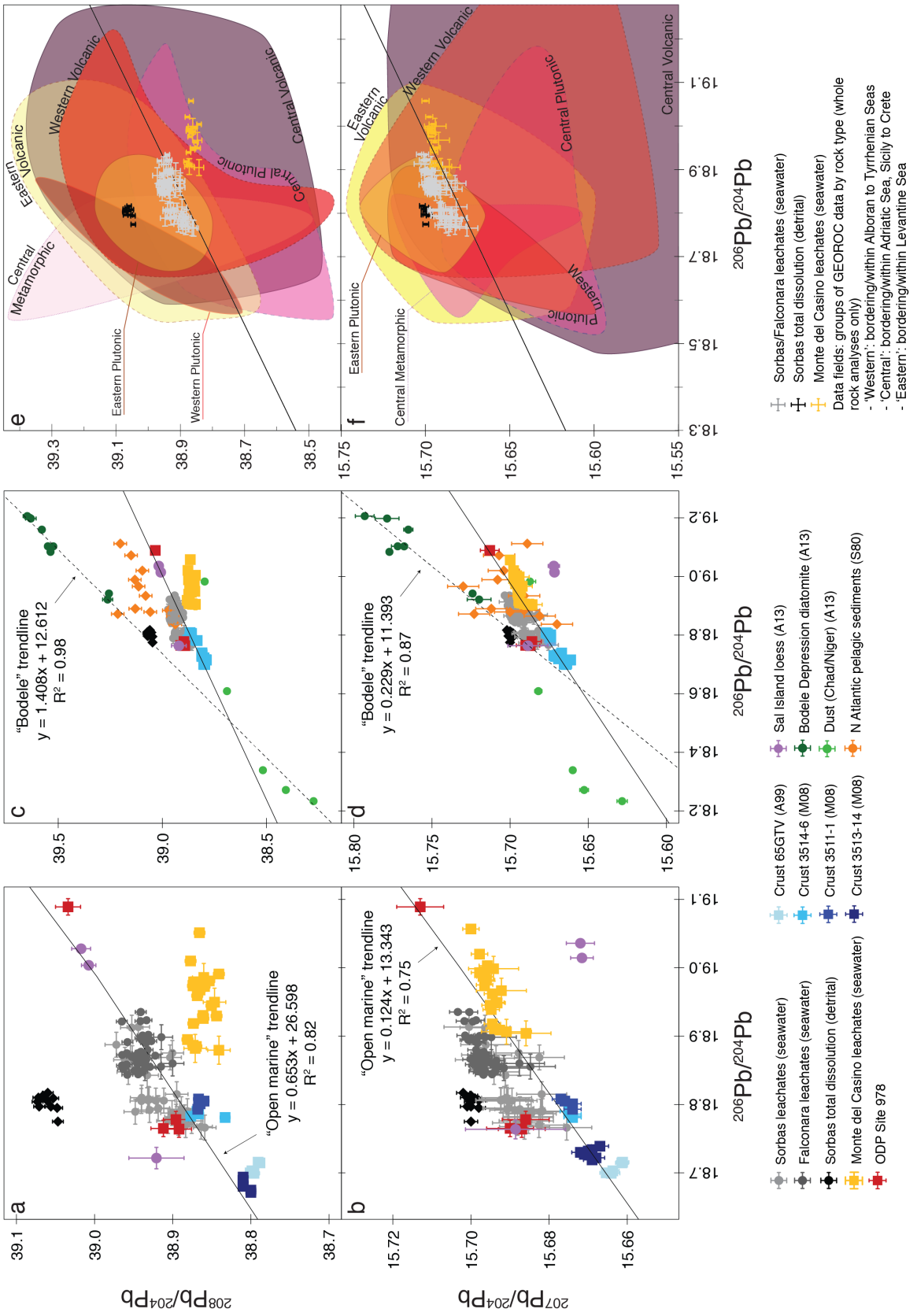

Fig. 5.12. Sorbas Basin, Falconara and Monte del Casino Pb isotope results compared to (a, b) ODP Site 978, NE Atlantic FeMn crusts, and Sal Island (Cape Verde) loess; (c, d) Bodélé Depression diatomite, African dust, pelagic N Atlantic sediments; and (e, f) circum-Mediterranean whole rock data (GEOROC database). Note differing axes between panel pairs. M08 - [*Muiños et al.*, 2008], A99 - [*Abouchami et al.*, 1999], A13 - [*Abouchami et al.*, 2013], S80 - [*Sun*, 1980]. “Open marine” trendline includes data from deep sites ODP Site 978 and all FeMn crusts. “Bodele” trendline includes only Bodélé Depression diatomites. Tetraethyl gasoline additive Pb isotope ratios for North Africa are $^{206}Pb/^{204}Pb$ 17.02-17.99, $^{207}Pb/^{204}Pb$ 15.53-15.60, $^{208}Pb/^{204}Pb$ 36.66-37.93, and for Europe are $^{206}Pb/^{204}Pb$ 17.03-18.2, $^{207}Pb/^{204}Pb$ 15.43-15.64, $^{208}Pb/^{204}Pb$ 36.82-38.10 [*Bollhofer and Rosman,* 2001].

Though limited, some direct evidence exists for significant precessional shifts between wet and dry conditions in late Miocene North Africa. As discussed previously with respect to Sr (Ch. 3, section 3.4.7), Saharan-like conditions have been inferred from aeolian dune deposits [*Schuster et al.*, 2006]. The Bodélé Depression itself was part of Mega Lake Chad during the Neogene [*Griffin*, 2006]. Lacustrine sedimentation began in the region of the Bodélé Depression and greater Lake Chad Basin as early as the mid-Miocene [*Griffin*, 2006]. Diatomaceous and argillaceous sediments deposited in the Mega Lake Chad area are interbedded with thick sandstones which contain aeolian dune characteristics [*Vignaud et al.*, 2002], suggesting cyclicity between wetter and dryer conditions [*Griffin*, 2006]. These sediments are exposed locally by erosion across large areas to approximately Miocene age [*Griffin*, 2006 and references therein], though these deposits have not been studied at a resolution which would allow conclusions about the frequency of shifts between wet and dry conditions to be drawn. Less direct evidence comes from combined model-data studies, suggesting conditions in North Africa changed dramatically from relatively wet to Saharan-like conditions over precessional cycles in the late Miocene, reflected not only in the cyclicity of sapropel deposition but also in dust deposition in Plio-Pleistocene Mediterranean sediment cores [*Larrasoaña et al.*, 2003; *de Menocal*, 2004]. These deductions have been reinforced by GCM results predicting wet/dry oscillations with precessional frequency [*Zhang et al.*, 2014; *Marzocchi et al.*, 2015].

Fig. 5.12 plots the Pb isotope results from all three sections against the data representing dust compositions and sourced from the GEOROC database. As direct dust measurements are considered suspect due to anthropogenic contamination, the available data most likely to reflect natural African dust Pb isotope compositions are sediment samples taken from the sources themselves, or loess or other sedimentary deposits known to be composed to a large degree by dust from North Africa. Lacustrine sediments (primarily diatomite) from the Bodélé Depression and loess from Sal Island (Cape Verde, off the coast of NW Africa) published by *Abouchami et al.* [2013] fit these categories, as well as North Atlantic pelagic marine sediments published by *Sun* [1980]. Although the Bodélé Depression is ranked as the largest single source [*Goudie and Middleton*, 2001; *Washington et al.*, 2003, 2009], there are other centers of Saharan Dust (Fig. 5.8) that contribute significantly to overall dust production, locations for which there are no direct data. Provenance analysis using Nd and Sr isotopes indicates that 80 to 95% of Sal Island loess originates from the Sahara [*Rognon et al.*, 1996], while back trajectory analysis suggests the dust deposited here may be sourced from a relatively large geographical area [*Chiapello et al.*, 1997], integrating the isotopic signal from a wide area. The North Atlantic sediment sample locations are

argued to have low sedimentation rates, thus Saharan dust is considered to contribute strongly to their Pb isotope compositions [*Sun*, 1980]. These Atlantic marine sediments have a roughly mid-Holocene age, and near-surface sediment which may have been contaminated by anthropogenic Pb was not included in the analyses. Saharan dust is known to traverse the entire Atlantic (Fig. 5.7), with provenance studies tracking it to the Caribbean and the Amazon [e.g., *Hamelin et al.*, 1989; *Abouchami and Zabel*, 2003; *Grousset and Biscaye*, 2005].

For the following discussion, it should be noted that no age information is provided for the Sal Island and Bodélé Depression samples [*Abouchami et al.*, 2013] used here for comparison. Due to the paucity of relevant data in the literature, these samples are used in absence of more suitable information, although an intrinsic assumption must be made that they are not older than the late Miocene in order to be relevant. The benefit of using the Sal Island and the Bodélé Depression data is that the degree of anthropogenic contamination is considerably less than that for modern dust samples. Though sampled from locations relatively near the Bodélé Depression, the dust data shown in Fig. 5.12 (c, d) plot towards values observed for dust heavily influenced by tetra-ethyl lead additives in Europe ($^{206}Pb/^{204}Pb$: 17.03-18.20, $^{207}Pb/^{204}Pb$: 15.43-15.64, $^{208}Pb/^{204}Pb$: 36.82-38.10) and North Africa and the near East ($^{206}Pb/^{204}Pb$: 17.02-17.99, $^{207}Pb/^{204}Pb$: 15.53-15.60, $^{208}Pb/^{204}Pb$: 36.66-37.93) [*Bollhofer and Rosman*, 2001]. The clear trend in the dust data towards such compositions compounds the suspicion that modern dust measurements are not reliable.

Panels a and b (Fig. 5.12) compare the "open marine" trendline (consisting of data from ODP Site 978 and all FeMn crusts sourced relatively near Gibraltar, 65GTV, 3514-6, 3511-1, 3513-14 [*Abouchami et al.*, 1999; *Muiños et al.*, 2008]) with the Falconara, Sorbas, Monte del Casino, and Sal Island data. The linear correlation of the "open marine" samples is high in both plots (Fig. 5.12a, $R^2 = 0.82$; Fig. 5.12b, $R^2 = 0.75$). Based on the relationship between the Sorbas and Falconara seawater values, the "open marine" trendline, and the Sal Island samples in $^{208}Pb/^{204}Pb$ vs. $^{206}Pb/^{204}Pb$ space, the argument for an increased contribution of Saharan dust during times of insolation minima appears valid. However, this correlation breaks down in $^{207}Pb/^{204}Pb$ vs. $^{206}Pb/^{204}Pb$ space, although the data from Sorbas and Falconara still fit within the limits suggested by the "open marine" trendline and Sal Island samples.

The second set of panels (Fig. 5.12c, d) include the Bodélé Depression data as well as dust samples from Niger and Chad [data from *Abouchami et al.*, 2013], alongside the North

Atlantic marine sediments. A trendline through the Bodélé samples has a high linear correlation ("Bodele" trendline, dashed line). The variability observed here, and the relationship between datasets, mimics the dichotomy between $^{208}Pb/^{204}Pb$ vs. $^{206}Pb/^{204}Pb$ space and $^{207}Pb/^{204}Pb$ vs. $^{206}Pb/^{204}Pb$ space seen in the first two panels (compare 5.11c, d to 5.11a, b). In $^{208}Pb/^{204}Pb$ vs. $^{206}Pb/^{204}Pb$ space, the marine sediment samples fall consistently between the two trendlines; in $^{207}Pb/^{204}Pb$ vs. $^{206}Pb/^{204}Pb$ space, the marine sediments fall between the region defined by the "Bodele" trendline and those of Sal Island. The discrepancy between the relationships observed in $^{208}Pb/^{204}Pb$ vs. $^{206}Pb/^{204}Pb$ space and $^{207}Pb/^{204}Pb$ vs. $^{206}Pb/^{204}Pb$ potentially suggests another source is contributing to the signal, one which is more radiogenic in terms of ^{207}Pb. Several of the pelagic sediment samples from the NE Atlantic are consistent with both the data from Falconara and Sorbas, as well as the Bodélé and Sal Island samples. Assuming that these Atlantic samples are indeed composed of a significant amount of dust, this corroborates the link between the isotopic compositions observed at Falconara and Sorbas during insolation minima, and suggests that there are sources of dust contributing to all these regions which are not accounted for by the available data.

Panels shown in Fig. 5.12 (e, f) combine the acid-reductive leach data from both the Sorbas Basin and Falconara section as one Western Mediterranean seawater group and, with the total dissolution samples from Sorbas and the leachates from Monte del Casino, are plotted against all circum-Mediterranean data available from the GEOROC database (http://georoc.mpch-mainz.gwdg.de/georoc/; note that only whole rock analyses have been employed). In these final panels, the Pb isotope compositions are divided between three main rock types (plutonic, volcanic, and metamorphic) and three regions (west, central, and east; regions defined in Fig. 5.12 legend). The seawater Pb isotope signatures from Sorbas and Falconara fall near the general average of all the whole rock data in $^{208}Pb/^{204}Pb$ vs. $^{206}Pb/^{204}Pb$ space, suggesting that the seawater Pb isotope compositions observed at these two sites are an average signal from circum-Mediterranean geology. In $^{207}Pb/^{204}Pb$ vs. $^{206}Pb/^{204}Pb$ space, the relationship is again inconsistent. While the great majority of whole rock samples in in $^{207}Pb/^{204}Pb$ vs. $^{206}Pb/^{204}Pb$ space converge near the zone in which the seawater values fall, there is still a considerable number of data for central and western volcanic rock, as well as central plutonic rocks, which plot towards more radiogenic compositions in $^{206}Pb/^{204}Pb$ but less radiogenic $^{207}Pb/^{204}Pb$ values. Arguably, the Monte del Casino data plot much nearer to compositions expected for an average of Central Mediterranean rock values.

A different approach is to consider more local geology rather than that of the entire Mediterranean region. Fig. 5.13 plots a subset of the GEOROC data against the dust estimates and outcrop leachate compositions. The first subset include only those belonging to the Betic Cordillera and Alboran Arc magmatic rocks, located within the Alboran Sea or from Spain. The second subset includes values from extrusive rocks of continental Morocco; this set consists primarily of rocks related to Alboran Arc magmatism although a few are from other Miocene age deposits. A connection between arc related magmatism and seawater values is not intended; this is simply the nature of available whole rock data. The suite of Northern Moroccan rocks essentially extends the trend defined for Sal Island loess in both $^{208}Pb/^{204}Pb$ and $^{207}Pb/^{204}Pb$ vs. $^{206}Pb/^{204}Pb$ space (Fig. 5.13). These Moroccan data thus provide a potential approximation for the dust end member which is more radiogenic in terms of ^{206}Pb but invariant in ^{207}Pb which formed the loess deposits. This confirms that sources are available to explain the compositions observed at Sal Island as well as those North Atlantic sediment samples which are less radiogenic in ^{207}Pb. Based on back trajectory calculation and major elemental concentrations, dust from Morocco is a significant source to Sal Island [*Chiapello et al.*, 1997]; Morocco also supplies dust to locations further north (and nearer Gibraltar) such as the Canary Islands [*Coude-Gaussen et al.*, 1987; *Bergametti et al.*, 1989]. The comparison in Fig. 5.13 suggests that the Sal Island loess samples have compositions closer to Moroccan sources, while the North Atlantic marine samples could be a mixture of the Pb isotope composition expected for Moroccan dust and the Bodélé source, as well as other, at the moment undefined, North African sources which may plot somewhere in between. As the Sorbas and Falconara sites are located considerably further north and east than Sal Island, it is logical that the relative composition of the dust reaching these sites is not identical, and that other locations are contributing relatively more dust.

It appears that during insolation minima, all three sites, Sorbas, Falconara, and Monte del Casino, converge towards similar Pb isotope compositions (in particular, in $^{206}Pb/^{204}Pb$; Fig. 5.1). This supports the concept of a common source at this extreme point in the insolation cycle; the most likely candidate, for such disparate sites, separated by very long distances, should be dust. As shown in Figs. 5.10 and 5.11, modern day aerosol transport patterns over the Mediterranean generally indicate much less African dust reaching Northern Italy compared to the rest of the region. However, our current climate state with respect to insolation is approximately ¼ of the way along the transition from insolation maxima to insolation minima [*Imbrie and Imbrie*, 1980]; thus, it can be reasoned that dust production during insolation minima, times of drier, colder climates particularly around the

Mediterranean, could be much more extreme relative to today, and account for an impact of this source at the northernmost location (Monte del Casino). Considering the pattern of dust transport images in Figs. 5.10 and 5.11, it is clear that the open Mediterranean is consistently supplied with large quantities of dust, both throughout the seasons as well as likely throughout precessional cycles. The fact that the composition of seawater at Falconara, an open, central Mediterranean site, maintains Pb isotope compositions nearer to those argued here for North African dust, while the two basins which are marginal and isolated diverge more strongly from these values away from insolation maxima, is consistent with this conclusion.

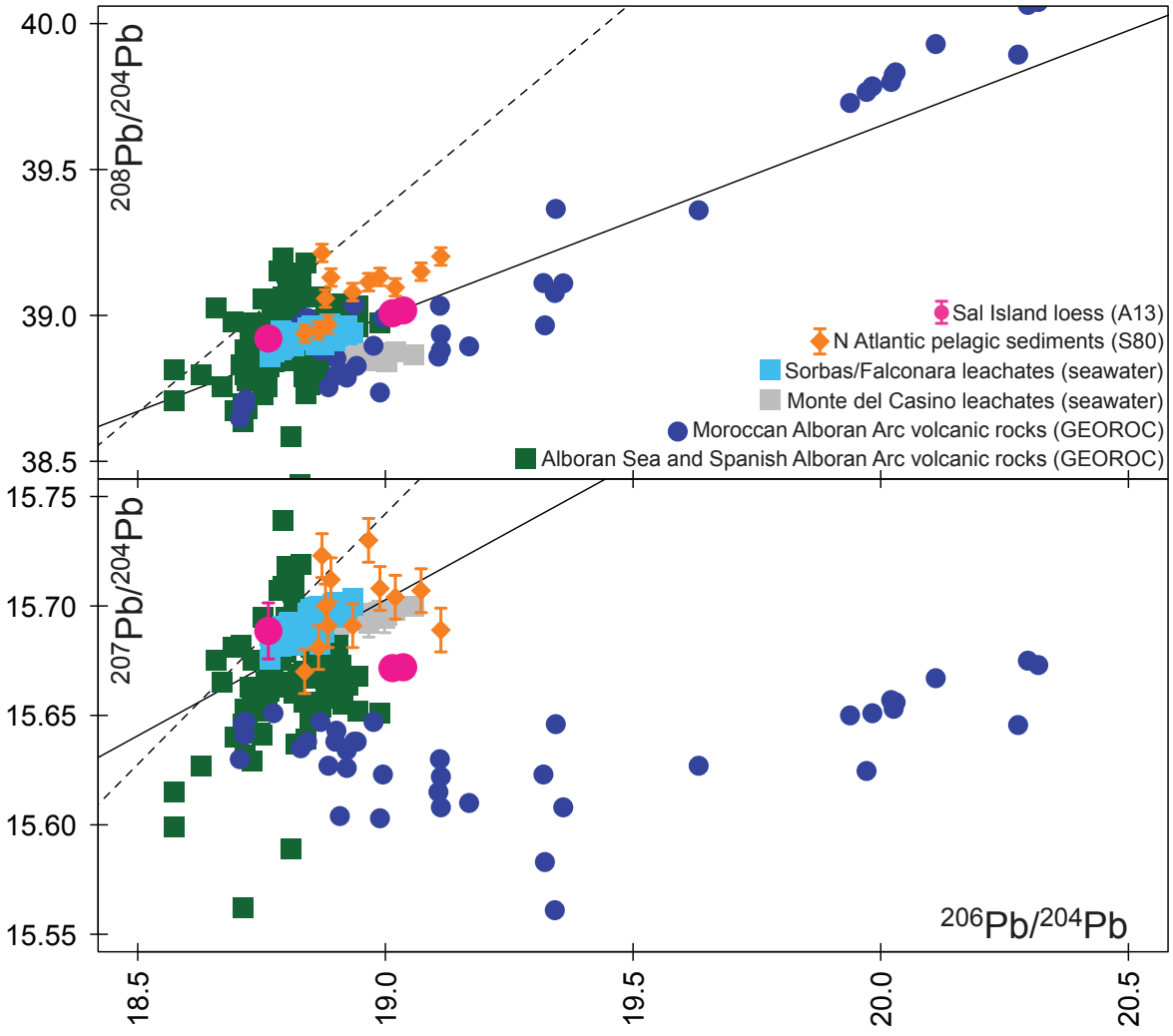

Fig. 5.13. $^{208}Pb/^{204}Pb$ vs. $^{206}Pb/^{204}Pb$ (upper panel) and $^{207}Pb/^{204}Pb$ vs. $^{206}Pb/^{204}Pb$ plots comparing late Miocene seawater values from the Sorbas Basin, Falconara and Monte del Casino sections with Holocene marine sediments, Sal Island loess, and whole rock data from the Betic-Rif Arc and the Atlas Mountains, Northern Morocco. S80 - [*Sun*, 1980], A13 - [*Abouchami et al.*, 2013]. Solid line, "open marine" trendline; dashed line, Bodélé Depression samples trendline.

While the hypothesis of precessional changes in African dust production and export as a control on Mediterranean seawater Pb isotope cyclicity certainly requires further study to prove or disprove, it may have significant implications for astronomical tuning. The currently accepted model of tuning in the Mediterranean tends to associate insolation maxima with the mid-point of sapropel layers [e.g., *Hilgen and Krijgsman*, 1999; *Krijgsman et al.*, 1999a], or to shift sapropel midpoints to 3 ka after insolation maxima [e.g., *Lourens et al.*, 1996; *Sierro et al.*, 2001] based on the radiometrically dated age of the sapropel S1 midpoint, and the assumption that this relationship holds for all sapropels (Ch. 1, section 1.2.6). However, complex biological processes partially mediate sapropel deposition, and it is currently not understood whether there are lags between maximum precipitation over North Africa, riverine runoff to the Eastern Mediterranean, and sapropel deposition (see discussion, Ch. 3). If a more direct link could be provided between dust production and insolation minima in the Mediterranean region, this proxy could have enormous potential for stratigraphy and astronomical tuning, in particular in marginal Mediterranean basins. For sediments such as those encountered at Sorbas, a much more accurate and precise tie point would be provided by the sharp peak observed in the diatomites (Figs. 5.1, 5.2, 5.5). As highlighted in Ch. 3, deposition of sapropels in the Sorbas Basin is more likely controlled by the local hydrologic budget, which may differ in terms of phasing from the open Mediterranean [*Pérez-Folgado et al.*, 2003]. Dust, however, appears to be a common regional factor for all three sites of Monte del Casino, Falconara, and Sorbas; moreover, dust production is not mediated to any significant degree by biological processes, and may respond much more quickly to changes in insolation. The primary drawback to using Pb isotope records for this purpose would be the large volume of work involved with the measurement; relatively high temporal precision on the order of ten samples or more per precessional cycle is required to identify potential peaks and troughs. This work could be minimized by identifying which lithologies are likely to contain peaks or troughs, allowing the sampling resolution to be decreased in other lithologies.

5.3.4.4 Incongruent weathering

As introduced in Ch. 1, section 1.3.2, incongruent weathering is another mechanism by which changes in climate may be reflected in seawater Pb isotope compositions. Accessory mineral phases rich in radioactive parents U and Th will suffer damage to their crystal lattices during radioactive decay events; radiogenic daughter products are easily liberated

from these damaged areas relative to non-radiogenic ions in tightly-bound crystal lattice sites. Combined with this mechanism, accessory minerals such as allanite, apatite, and sphene are more easily weathered than plagioclase [*Harlavan et al.*, 1998], a mineral which tends to make up a large proportion of the bulk rock. Such accessory phases tend to be rich in U and Th compared to major rock forming minerals; with time, they develop higher concentrations of radiogenic Pb due to decay of the radioactive parents. Both of these mechanisms cause the isotopic composition of the Pb released to the labile pool, during the early stages of weathering, to be radiogenic relative to the bulk parent rock [*Erel et al.*, 1994; *Harlavan et al.*, 1998; *Harlavan and Erel*, 2002]. Thus, the interplay of efficient physical and incipient chemical weathering favours the release of the products of decay as it generally increases the exposed surface area of minerals, whereas bulk dissolution on mature soils tends to release Pb with an isotopic composition similar to the bulk rock. Effective release of radiogenic Pb compared to bulk rock compositions are thought to extend to a maximum of 300 ky, after which time the labile Pb pool generally reflects the same isotopic compositions as the bulk rock [*Erel et al.*, 1994; *Harlavan et al.*, 1998]. Such variation in weathering mechanisms, leading to incongruent release of radiogenic Pb, have led several authors to interpret changes in deep water Pb isotope compositions in the North Atlantic in terms of glacial-interglacial cycles, where more radiogenic compositions are observed to coincide with glacial terminations [e.g., *Foster and Vance*, 2006; *Gutjahr et al.*, 2009; *Kurzweil et al.*, 2010].

While it is unlikely that incongruent release of Pb can explain the variability in compositions observed for the Sorbas Basin or Falconara section, the consistent uplift of the Northern Apennines provides an explanation for the Pb isotope compositions observed at Monte del Casino. At times other than insolation minima, the values at this section are generally more radiogenic, while the record also exhibits a long-term shift towards more radiogenic compositions, particularly visible in the $^{206}Pb/^{204}Pb$ ratio (Figs. 5.1, 5.2). The seawater compositions estimated from the leachates of the Monte del Casino sediments are somewhat different to the Sorbas and Falconara values, although the whole rock data for the entire Mediterranean region appears very similar (Fig. 5.12e, f). The sediments of the Monte del Casino section were deposited above calcareous turbidites of the Marnoso-Arenacea Formation [*Negri et al.*, 1999] in a marine basin created by the Northern Apennine foredeep. The Apennines began forming during the Oligocene [*Lucchi*, 1986], while activity continues to this day; over the past 3 Ma, uplift of up to 2.5 km, at fast rates of about 1 km/Ma, and similarly fast rates of subsidence (~ 2.5 km/Ma) have been observed [*Vai and Martini*, 2001]. The uppermost nappes of the Northern Apennines

include ophiolitic rocks and oceanic sediments of Jurassic to Eocene age, and sub-oceanic sediments of Cretaceous/Oligocene age. These, as well as some Middle Triassic volcanic rocks are found emplaced above the Romagna-Umbria thrust units [*Vai and Martini*, 2001] which contain the siliciclastic and marine sediments exposed at Monte del Casino. Regionally, Messinian age volcanics are present [*Carmignani and Kligfield*, 1990], while numerous ash layers are present within the Monte del Casino open marine succession [*Negri et al.*, 1999]. The basement of the Northern Apennines, poorly preserved rocks of the Hercynian orogeny, are thought to be sandwiched between Mesozoic carbonate [*Vai and Martini*, 2001]; however, the basement is not exposed [*Lucchi*, 1986].

The succession at Monte del Casino includes several low angle shear planes and deformation near the top of the sequence [*Krijgsman et al.*, 1997]; the turbidites below and deformation above this sedimentary succession suggest that uplift was active around the time of deposition. Although the majority of studies espousing incongruent weathering as the cause of changes in seawater Pb isotope records focus on deglaciation as the primary mechanism, continuous uplift also provides a mechanism for continuous exposure of fresh, unweathered rock surfaces which could enhance the release of radiogenic Pb. Rapid uplift, causing relatively rapid mechanical denudation and exposing young weathering surfaces has been associated with the release of radiogenic material, in addition to deglaciation, with respect to release of radiogenic Sr during very early weathering phases [*Blum and Erel*, 1995, 1997]. While the units exposed above the Monte del Casino section are certainly complex, they are also relatively young; younger rocks tend to be relatively invariable in ^{207}Pb. This helps justify the relatively flat profiles observed in $^{207}Pb/^{204}Pb$, while there are relatively more radiogenic $^{206}Pb/^{204}Pb$ compositions.

5.4 Conclusions

This chapter presented and discussed the results of marine bulk sediment leaching from three disparate locations across the Mediterranean. The Pb isotope records generated through this study are quite significant. The marginal successions investigated here in high resolution indicate that Pb isotopes are a sensitive recorder of climate-driven shifts in inputs to the marine system.

As the Nd isotope results in Ch. 4 show, the acid-reductive leachates from bulk sediment from the Sorbas Basin are likely to have reliably recorded bottom water characteristics.

This conclusion is also supported by a comparison of the strong leach and total dissolution Pb isotope compositions and the acid-reductive leachate Pb isotope compositions from Sorbas; there may be influence from detrital siliciclastics, but this appears to be a consistent influence across the entire precessional cycle. This is in agreement with the box modeling results suggesting that riverine runoff into the Sorbas basin did not change drastically throughout a precessional cycle. The reliability of Pb isotope values derived from acid-reductive leaching of bulk sediments, designed to retrieve the bottom water signal stored in the authigenic ferromanganese oxyhydroxide fraction, is also supported by the fact that Pb in this fraction is not complicated by effects such as boundary exchange and benthic flux which are problematic for Nd isotope signatures. This may be related to the fact that the authigenic phase released during leaching is the primary Pb-carrying component in seawater [*Basak et al.*, 2011], but could also be due to the very low solubility and severely particle-reactive nature of Pb, leading to no observation of reversible scavenging effects to date for this element.

Moving forward from this important distinction, the most obvious and immediate observation concerning the bottom water Pb isotope results from the Sorbas Basin, Falconara, and Monte del Casino sections is that there are cyclic precessional variations, similar in phase to those observed with Sr (Ch. 3). Determining the cause of this variability is more difficult, due to the poorly constrained nature of seawater Pb isotope variability, primarily caused by the lack of reliable modern day analogues due to anthropogenic contamination. Considering first the Sorbas Basin, the results from the acid-reductive leaches compared to the total dissolution and strong leaches are insightful, as is the comparison to the Sr isotope results (Fig. 5.6 and 5.5 respectively). The peaks in radiogenic Sr and Pb do not occur at the same time with respect to each other in each cycle (i.e., the time between the Pb "excursion" and Sr anomaly decreases with each successive cycle; Ch. 5, Fig. 5.4). This suggests changes in the Sorbas Basin hydrologic budget do not control the seawater Pb isotope compositions observed in this basin, because if the same processes were responsible, a clear pattern resulting in a similar offset (or none at all) at each cycle should be observed. This implication is supported by the comparison between the Pb isotope compositions of the total dissolution and acid-reductive leachates. It seems that a similar amount of locally-derived Pb is pulling the seawater signature of this basin away from the marine end-members throughout the entire precessional cycle (Fig. 5.5). This is further supported by the fact that the Sr isotope box modeling results presented here as well as general circulation model studies [*Marzocchi et al.*, 2015, 2016] support only

small changes in the riverine runoff to the Western Mediterranean region between insolation maxima and minima.

All three sections exhibit cyclicity coincident with precession (insolation). Comparing the the relatively different 'background' compositions observed during periods of insolation maxima, both Sorbas and Falconara exhibit more radiogenic compositions during insolation minima (precession maxima), while Monte del Casino exhibits less radiogenic values; however, the isotopic compositions, particularly in terms of $^{206}Pb/^{204}Pb$, actually converge to similar absolute ratios for all three sections at insolation minima. This supports the argument that localized effects cannot be the source of the Pb isotope values observed at insolation minima; a Pb isotope signal capable of being transported across the region is necessary to explain the observations. The three sites are separated by hundreds of kilometres, two of them are associated with marginal basin deposition and one is associated with more open conditions, yet they all display nearly identical $^{206}Pb/^{204}Pb$ ratios during insolation minima. Thus, regional-scale climate-driven mechanisms which fluctuate on precessional timescales are the most probable drivers.

Since insolation minima also coincide with the driest time in North Africa, and most likely the time of greatest dust production, this mechanism was investigated in more detail. An overview of literature isotope data for modern Saharan dust suggests that dust Pb isotope compositions are too unradiogenic to explain the values at these three sites. However, published values have been questioned due to anthropogenic contamination [*Scheuvens et al.*, 2013]. A comparison of source sediment from the Bodélé Depression in northern Chad with dust samples from the nearby town of Faya Largeau supports this claim, suggesting that anthropogenic Pb has a strong influence even over short distances. In contrast, a comparison of samples from locations known to have a very significant influx of Saharan dust (or, more generally, dust from North Africa) generally show much more radiogenic compositions, supporting the hypothesis that the more radiogenic compositions observed near insolation minima at Sorbas and Falconara are likely a result of Saharan or North African dust. The fact that seawater Pb isotope compositions at insolation minima in Monte del Casino appear to become less radiogenic akin to compositions recorded at Falconara and Sorbas corroborates this hypothesis further, particularly due to the fact that significant amounts of dust from North Africa are not expected to be transported to northern Italy except during the extreme conditions of insolation minima. Samples which can be considered proxies for the Pb isotope composition of uncontaminated North African dust (diatomite from the Bodélé Depression, loess from Sal Island (Cape Verde), and

North Atlantic marine sediments) are more radiogenic than the previously reported ranges measured directly from African dust. Data from these locations show trends in Pb/Pb isotope space which suggest that dust sources can indeed explain the seawater compositions determined at all three sites during insolation minima. While in Pb/Pb isotope space $^{206}Pb/^{204}Pb$ versus $^{207}Pb/^{204}Pb$ appears to suggest a slightly different relationship between the sample groups than $^{206}Pb/^{204}Pb$ versus $^{208}Pb/^{204}Pb$, the dataset available to approximate Saharan dust Pb isotope compositions for the past is certainly not exhaustive, and whole rock data from Northern Morocco (another significant source of dust) may provide the potential missing source of unradiogenic ^{207}Pb. Increased complexation and sequestration of the radioactive parents U and Th at times of insolation minima due to biological productivity or otherwise can also be ruled out, as the correct proportion of isotopes necessary to generate the observed shifts is essentially impossible.

A summary of circum-Mediterranean whole rock Pb isotope values indicates that all regions have overlapping ranges of Pb isotope compositions, regardless of rock type (metamorphic, plutonic, volcanic). This fact causes difficulties when attempting to understand the very different apparent local signal observed in the Monte del Casino Pb isotope values. However, considering the significant and relatively continuous uplift experienced in the Northern Apennines during deposition of the Monte del Casino sediments, it is possible that incongruent release of radiogenic Pb was significant at this location and sufficiently explains the observed seawater values at this location outwith insolation minima. Further comparison to the detrital fraction at this location would be required to fully corroborate this suggestion.

If the hypothesis that a dust signal is accepted as the driving mechanism for the Pb isotope compositions of seawater during insolation minima, seawater Pb isotopes in marginal and open Mediterranean sedimentary successions could become a very powerful stratigraphic tool. A signal driven by dust could provide a regional mechanism which responds to precession yet is likely to suffer much less from temporal lags and individual sub-basin dependent hydrologic conditions. Pb isotope compositions could be a truly basin-wide means of tying sedimentary layers in disparate locations to each other, enabling bed-to-bed correlation at sub-precessional resolution, and improving the available precision of the astronomical tuning method. In this context, it is worth highlighting that reductive leaching of bulk sediments is a relatively quick method to produce extensive Pb isotope data sets.

6 FeMn crust 3514-6: age model and long-term Pb isotope record outside the Gulf of Cadiz

6.1 Overview

This chapter presents and discusses the results of analyses performed on ferromanganese (FeMn) crust 3514-6. Formed west of the Gulf of Cadiz (Ch. 1, Fig. 1.20; Ch. 2, Fig. 2.1) at a depth consistent with Mediterranean outflow, this crust is a candidate for recording changes to Mediterranean Outflow (MO) in the NE Atlantic. Two methods were applied to determine the crust growth rate, using $^{230}Th_{excess}$ and cosmogenic ^{10}Be. The results pertaining to growth rate determination are presented and discussed first; following this, the age model[3] is assigned to generate the Pb isotope time series. Palaeoceanographic interpretation and implications are then presented and discussed.

CHAPTER NOTES

Materials and methods: Ch. 2, sections 2.4, 2.5
Sample maps and figures: Ch. 1, Fig. 1.20; Ch. 2, Figs. 2.1, 2.4
Contributions: Marlies van der Schee, ODP Site 978 Pb and Nd isotope data; Jan Fietzke, mass spectrometry with LA-MC-ICPMS; Angel Rodes, assistance with Be extraction and Matlab script to reduce data

6.2 Results: growth rate determination

6.2.1 $^{10}Be/^{9}Be$ method

Two growth rate models have been calculated from the beryllium data, one using ^{10}Be atoms/g of crust (denoted [^{10}Be]) and the other using the normalized $^{10}Be/^{9}Be$ ratio. The data and calculations are shown in Fig. 6.1 and 6.2 and Tables 6.1 and 6.2. Time is plotted relative to the crust surface. Thus, time zero equals the initial time of the record, without making the assumption that the crust is completely intact (i.e., surface layers could be missing). The locations of subsamples removed for beryllium extraction are shown in Ch. 2, Fig. 2.4.

[3]Notation: time passed is denoted by S.I. prefix–a (e.g., Ma, million years ago) while length of time is denoted prefix–y (e.g., My, million years). Also note that activity (rather than isotope ratio) is indicated using the notation $A(^{x}I/^{x}I)$.

Table 6.1. Beryllium measurement results. All errors reported to 2σ (95% confidence interval), except depths, which correspond to linearly measured uncertainties. Depth assignments are estimated rather than measured for samples marked with * (see text, this section). Depth corresponds to distance from crust surface along the laser ablation profile.

Sample	Depth (mm)	negative error (mm)	positive error (mm)	[^{9}Be] (x10^{17} atoms/g)	Error (x10^{17} atoms/g)	[^{10}Be] (x10^{6} atoms/g)	error (x10^{6} atoms/g)	^{10}Be/^{9}Be (x10^{-7})	error (x10^{-7})
CR1	4.31	0.30	0.30	5.252	0.243	9300	170	17.71	0.882
CR2	6.97	0.55	0.55	3.690	0.074	5906	264	16.01	0.392
CR3	8.873	0.35	0.35	3.760	0.124	3719	152	9.892	0.260
CR4	10.36	0.55	0.55	3.100	0.091	3390	192	10.93	0.349
CR5	10.93	0.20	0.20	2.920	0.069	2834	98	9.71	0.204
CR6	12.57	0.35	0.35	3.210	0.083	1281	42	3.99	0.083
CR7*	12.66	0.09	3.54	5.286	0.095	1101	52	2.08	0.053
CR8*	12.69	0.12	3.51	2.373	0.046	764	16	3.22	0.046
CR9*	13.11	0.54	3.09	1.349	0.045	509	22	3.77	0.103
CR10	16.20	0.35	0.35	5.012	0.018	343	14	0.68	0.019
CR11*	16.51	0.32	0.32	5.175	0.019	305	15	0.59	0.018
CR12	16.83	0.30	0.30	5.355	0.139	269	13	0.50	0.014
CR13	17.05	0.35	0.35	5.537	0.150	263	13	0.48	0.014

Table 6.2. Growth rates for FeMn crust 3514-6 analysed in this project derived from either [^{10}Be] or ^{10}Be/^{9}Be, and extrapolated crust surface values.

[^{10}Be] (atoms/g) growth rates (mm/My)		^{10}Be/^{9}Be growth rates (mm/My)	
Section 1, 0 - 10.57 mm	2.82	Section 1, 0 - 10.85 mm	5.22
Section 2, 10.57 – 17.05 mm	1.30	Section 2, 10.85 – 17.05 mm	1.01
Age (Ma, extrapolated) 21 mm:	11.8	Age (Ma, extrapolated) 21 mm:	12.1
Extrapolated surface [^{10}Be]	1.97 x10^{10}	Extrapolated surface ^{10}Be/^{9}Be	2.75 x10^{-8}

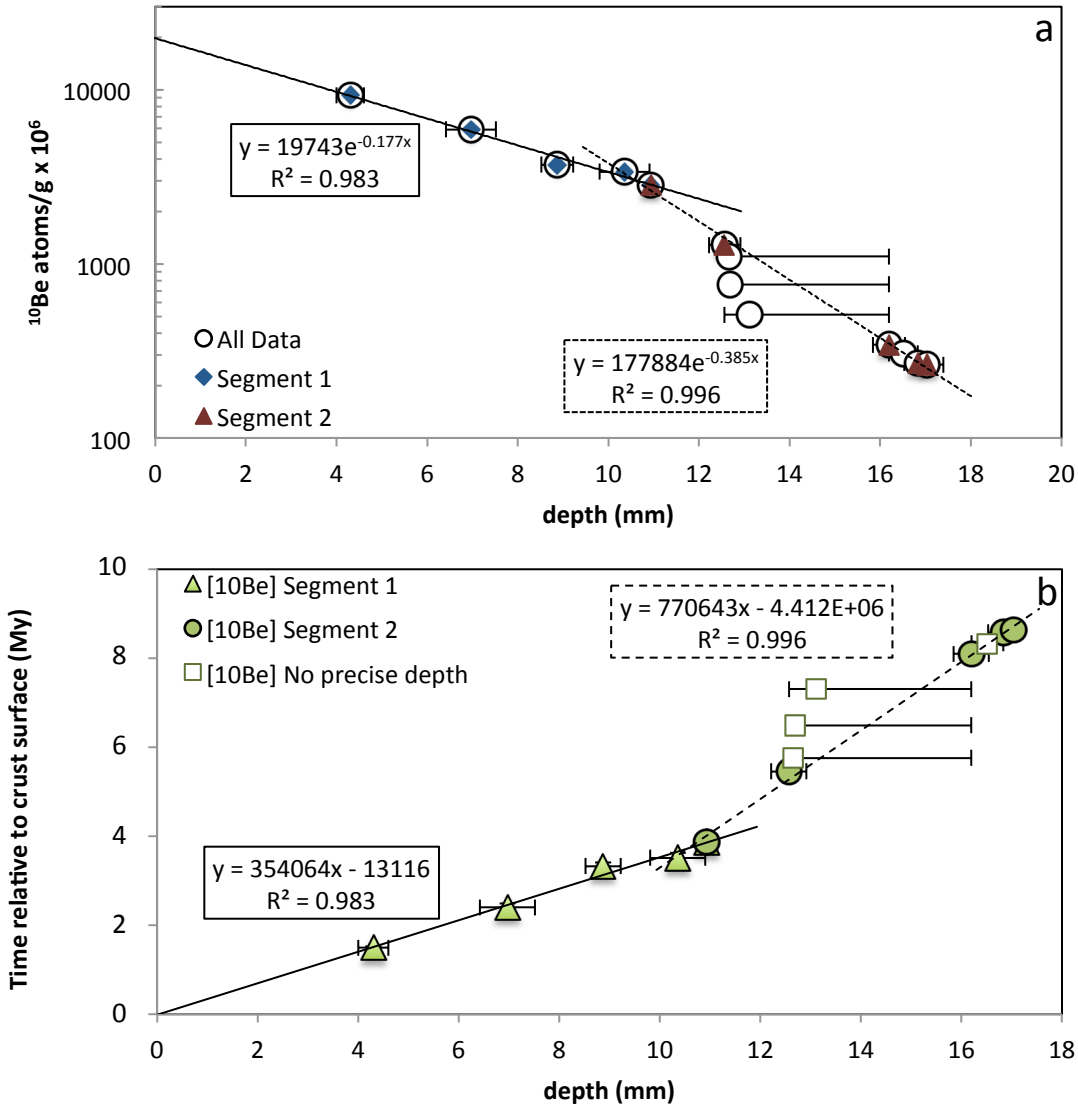

Fig. 6.1. (a) [^{10}Be] vs. depth in crust 3514-6. The extrapolated surface concentration is 1.97x10^{10} atoms/g. There are two distinct growth rate segments along the transect (Segments 1-2). Values used to calculate growth rates are derived from trendlines. (b) Depth vs. time relative to crust surface, calculated using extrapolated surface concentration determined in (a). In both plots, open symbols indicate data for which a precise depth could not be applied on the laser ablation transect due to the disappearance or 'pinching-out' of laminations (marked with * in Table 6.1).

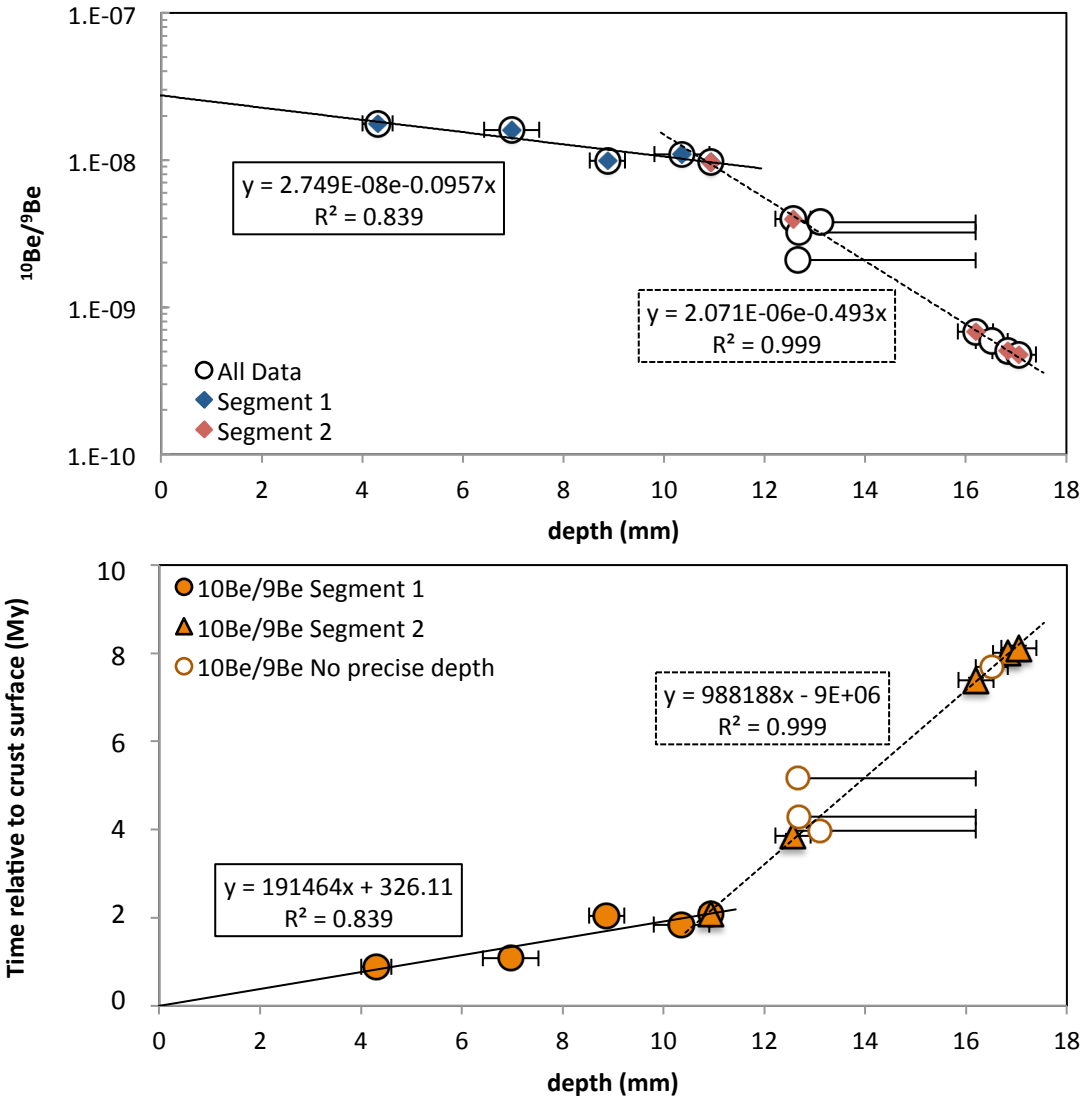

Fig. 6.2. (a) $^{10}Be/^{9}Be$ vs. depth in crust 3514-6. The extrapolated surface ratio is $2.75x10^{-8}$. There are two distinct growth rate segments along the transect (Segments 1-2). Values used to calculate growth rates are derived from trendlines. (b) Depth vs. time relative to crust surface, calculated using extrapolated surface concentration shown in upper plot. In both plots, open symbols indicate data for which a precise depth could not be applied on the laser ablation transect due to the disappearance or 'pinching-out' of laminations (marked with * in Table 6.1).

Data which could not be assigned depths on the laser ablation transect are denoted by open symbols in Figs. 6.1 and 6.2. Some laminations could not be traced from the location of drilling to the laser ablation profile due to the fact that they pinched-out and disappeared completely (Ch. 2, Fig. 2.4c) owing to natural variations in the crust texture. For these data, only minimum and maximum depths were determined by finding the nearest laminations which could be followed to the ablation transect, and relative depths were assigned in order of the depth at the drilling area. Thus, regardless of the inability to assign an accurate central depth on the laser ablation transect, the order of relative age is known for every sample. In the case of [^{10}Be], these data plot in the correct order in terms of both concentration (Fig. 6.1a) and extrapolated age (Fig. 6.1b). In terms of the ^{10}Be/^{9}Be ratio, this is not the case for samples CR7 to CR9. These data plot in reverse of that expected; this is particularly evident in Fig. 6.2b, where CR7 appears to be oldest of the three. This is impossible as CR7 was clearly drilled from a location in the crust closer to the surface than CR8 and CR9 (Ch. 2, Fig. 2.4).

The other outlier in the ^{10}Be/^{9}Be dataset is CR4. This sample also generates a younger age than the previous sample based on the ^{10}Be/^{9}Be ratio. For the corresponding crust depth (~10.358 mm), there were no issues in assigning depths to the laser ablation transect and no obvious sections of pinching-out or otherwise anomalous growth are apparent.

6.2.2 $^{230}Th_{excess}$ method

Overall, the average growth rate determined by this method is 0.41 ± 0.12 mm/My (Table 6.3), much lower than rates determined with the ^{10}Be/^{9}Be or [^{10}Be] method. This may be due to the material truly having extremely slow growth closer to modern times, although reported crust growth rates generally range from about 1 to 15 mm/My [*Frank*, 2002]. While the beryllium data span essentially the entire depth of the crust (~2.5 cm), the $^{230}Th_{excess}$ data span a maximum of 600 μm from the surface inwards.

For ^{230}Th the crust was ablated in 2 groups, consisting of 4 lines each, with TH1 to 4 near the Pb isotope ablation region about 1 cm from the top right corner of the crust, and TH5 to 8 performed at the outermost right corner (Ch. 2, Fig. 2.4f). There is a clear difference in the surface A(^{230}Th/^{232}Th) of the first group (TH1 to TH4; TH1 A(^{230}Th/^{232}Th) ~4.1) and the second group (TH5 to TH8; TH6 A(^{230}Th/^{232}Th) ~14.4), with the second group showing much higher values on average (Table 6.3). The $^{230}Th_{excess}$ measurements were

organized in this manner for the purpose of testing whether or not surface layers have been lost from this sample, as visually it appears that laminations are truncated, in particular towards the left of the crust surface (Ch 2, Fig. 2.4c). Fig. 6.3a, b show activity profiles for A(^{230}Th/^{232}Th), A(^{234}Th/^{232}Th) and A(^{238}U/^{232}Th) for ablation lines TH1 and TH6. These plots are typical of the respective groups, and indicate that surface $^{230}Th_{excess}$ is diminished in the first group compared to the second. This is evidence that surface layers are missing, at least from the location of the first group of ablations; however, it does not affect the calculation of growth rate significantly as this growth rate is based on slope, and both ablations have a very similar slope calculation (Table 6.3; compare Fig. 6.3c, d). The amount of time missing from the left group of ablations is approximately 0.2 My, assuming 80 μm thickness is missing and a growth rate of 0.407 mm/Ma. Activity ratio profiles and growth rate calculation plots for all profiles are shown in Appendix 6.

Table 6.3. Results of $^{230}Th_{excess}$ measurement. 2SD of sample mean.

Sample	Slope	1σ SE	Growth Rate (mm/My)	2σ SE	Maximum (^{230}Th/^{232}Th) (measured)	Surface (^{230}Th/^{232}Th) (extrapolated)
TH1	0.021	± 0.002	0.431	± 0.088	3.1	4.1
TH2	0.020	± 0.003	0.470	± 0.130	2.2	3.8
TH3	0.031	± 0.002	0.298	± 0.029	5.2	7.1
TH4	0.027	± 0.001	0.341	± 0.028	9.2	13.3
TH5	0.023	± 0.001	0.402	± 0.028	8.5	10.6
TH6	0.020	± 0.001	0.465	± 0.050	13.7	14.4
TH7	0.022	± 0.001	0.419	± 0.033	11.5	14.4
TH8	0.021	± 0.001	0.430	± 0.040	6.0	7.43
Average	**0.023**	**± 0.001**	**0.407**			
2 SD	**0.008**		**0.119**			

Present-day seawater A(^{234}U/^{238}U) is ~ 1.147 (dashed line, Fig. 6.3e, f) [*Andersen et al.*, 2010] due to the preferential leaching of ^{234}U from continental crust. This is primarily a result of preferential release of the ^{234}U isotope from lattice sites damaged by decay of ^{238}U, or due to ejection during α-recoil during the decay process itself [*Ivanovich and Harmon*, 1992]. Therefore it should be possible to use this activity ratio to corroborate the indication from $^{230}Th_{excess}$ that surface material has been lost. Unfortunately, the method used here does not have the requisite precision to interpret such a relationship; the measurement of highly precise ^{234}U/^{238}U is not trivial and cannot be easily achieved with a laser ablation mass spectrometric approach. The calculated minimum analytical uncertainty is hence larger than the difference between secular equilibrium and the seawater activity ratio. This is particularly apparent in the outermost crustal data points, which are of the greatest relevance (Fig. 6.3e, f).

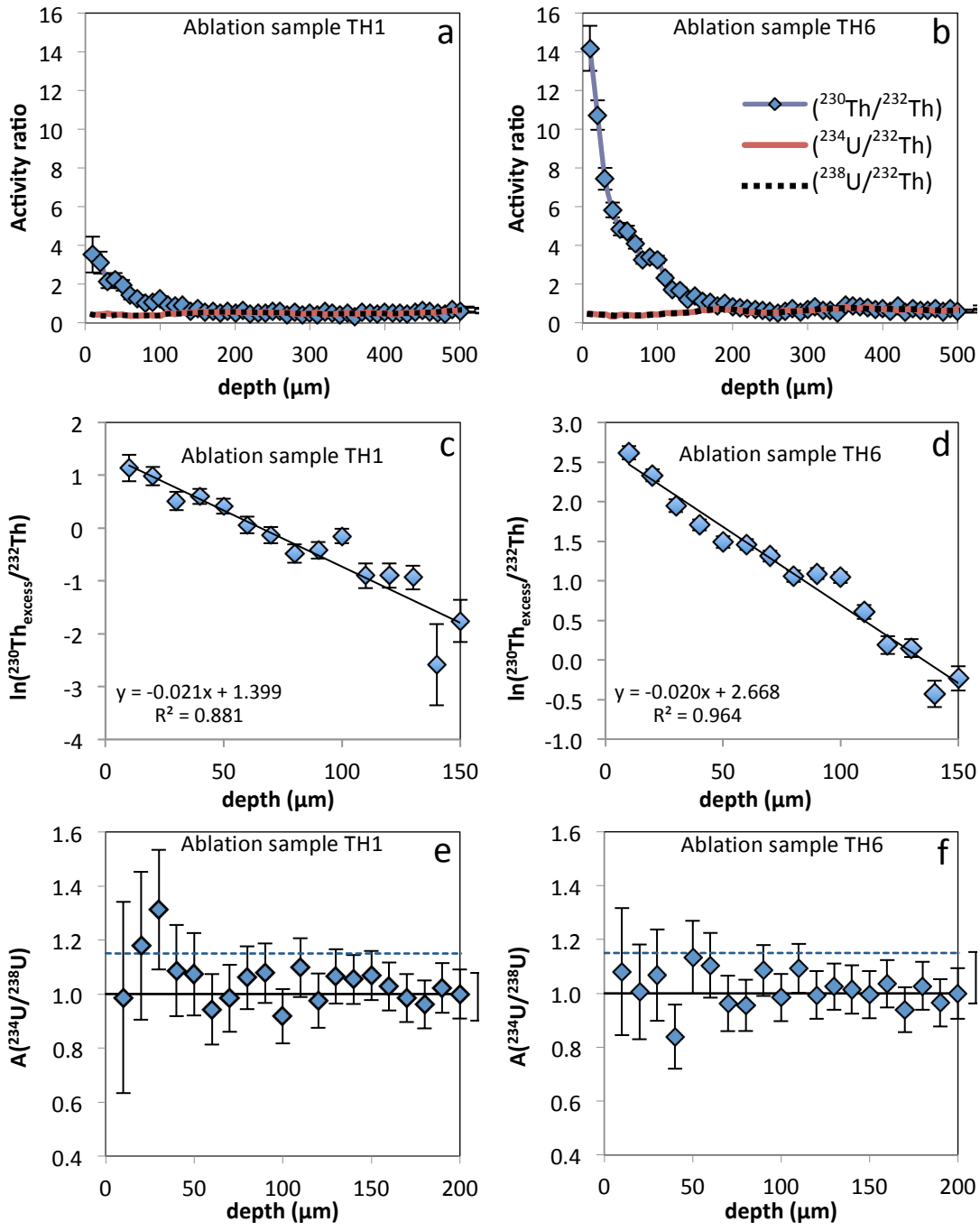

Fig. 6.3. Results of $^{230}Th_{excess}$ measurements (left-hand plots from TH1; right-hand plots from TH6). (a, b) Activity ratios for ^{230}Th, ^{234}U, and ^{238}U normalized to ^{232}Th; secular equilibrium is reached after ~200 µm in (a) and ~ 300 µm in (b). (c, d) Calculation of growth rate from plot of ln($^{230}Th_{excess}$ activity) vs. depth; note y-axes differ. (e, f) ($^{234}U/^{238}U$) vs. depth plotted with lines for unity (black) and ($^{234}U/^{238}U$) seawater value (1.147). Uncertainty is estimated solely from counting statistics on ^{230}Th and ^{234}U; this is a minimum value only (see section 2.4.4 and this section for additional information about uncertainty calculation). Parentheses denote activity as per convention.

As a thorough characterization of analytical error through repeated measurements over time on standards could not be performed, the errors on measurements shown in Fig. 6.3 are twice the relative standard deviation (2RSD) based solely on counting statistics of ^{230}Th and ^{234}U, propagated through consequent activity ratio calculations. Uncertainties in counting statistics on the much more abundant ^{232}Th and ^{238}U are negligible in comparison. This method of estimating the analytical uncertainty represents a minimum estimate. Nevertheless, comparisons between values are valid as analytical or machine bias should affect all measurements in more or less the same manner. As ablations TH1 to 8 were performed over a period of less than 20 minutes, it is unlikely that effects such as drift would greatly affect the measurements.

6.3 Results: Pb isotope analyses

The final LA-MC-ICPMS Pb isotope record (Fig. 6.4a) consists of 1,440 data points, after data rejection due to low voltage intensities or apparent instability. Overall, the record is in excellent agreement with the previously published record derived through wet-based chemistry by *Muiños et al.* [2008] (Fig. 6.4b). This agreement indicates that the method used here is reliable and comparable with other solution-based data sets. Compared to the previous record, some shorter scale variability is observed due to the fine spatial resolution of the laser ablation method. Initially, between 0 and ~1 mm, there appear to be some small scale variations or 'cycles'; these are particularly visible in the ^{208}Pb/^{206}Pb ratio, but also in the ^{207}Pb/^{206}Pb ratio and to a lesser degree in the ^{204}Pb normalized ratios. All five ratio pairs suggest that a slight trend is apparent over the first millimetre. Some minor variations around ~13 mm and ~16.3 mm are also visible, again particularly in the ^{208}Pb/^{206}Pb ratio; outside of these depths, any apparent variations are well within the calculated uncertainty and thus likely to be a reflection of analytical bias rather than variability in the material. The apparent outliers at ~10 mm in the ^{20X}Pb/^{204}Pb normalized ratios were performed on a crack in the crust; the large uncertainty in these measurements, and the lack of their appearance in the ^{20X}Pb/^{206}Pb ratios suggests that the material in this feature affected the accuracy of the applied Hg correction. As they are within analytical uncertainty, they are not suggestive of any particular change, as is the case for the apparent change at ~20 mm.

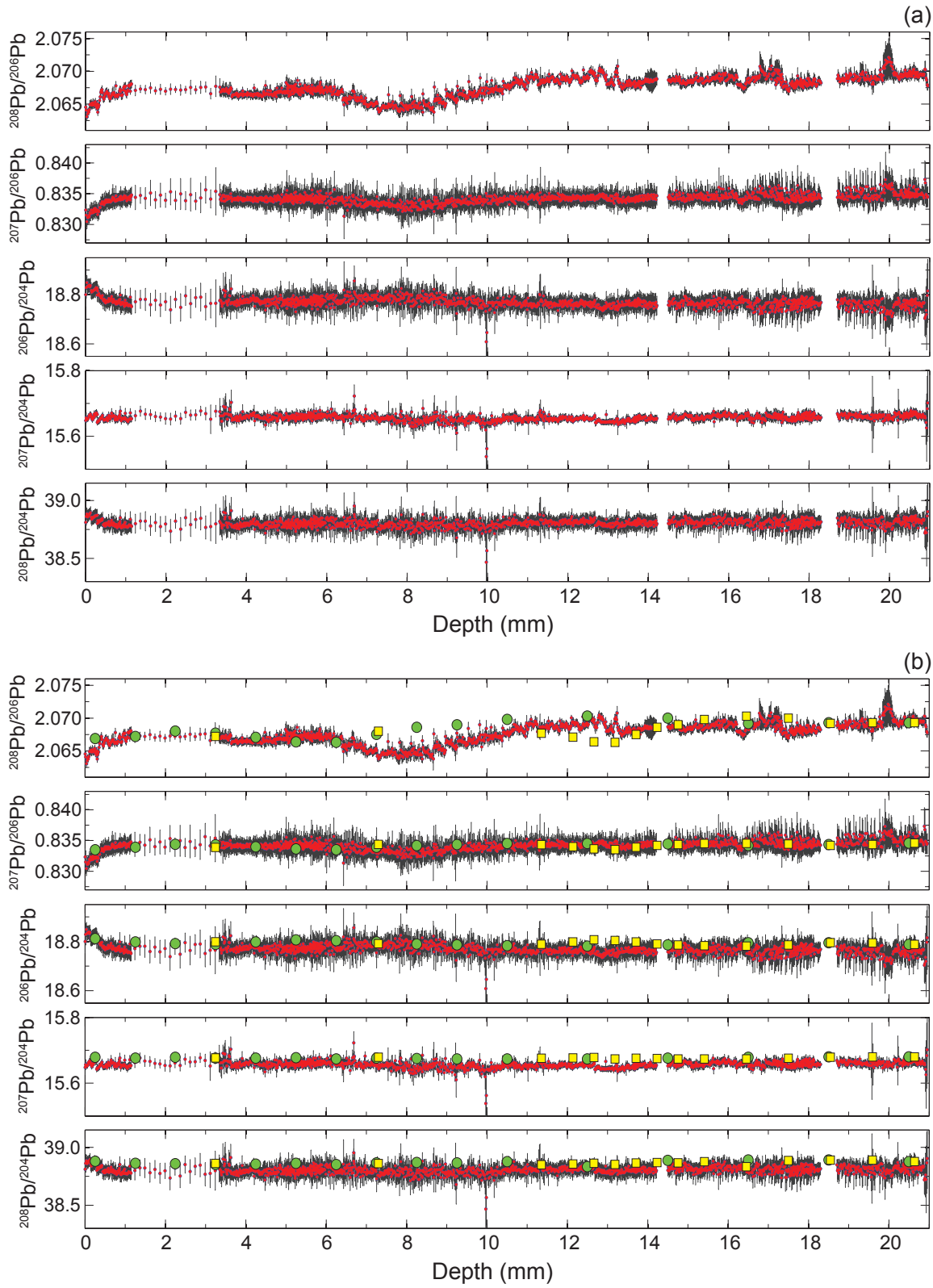

Fig. 6.4. (a) Crust 3514-6 Pb isotope results versus depth with uncertainty (grey bars). (b) Data compared to those of *Muiños et al.* [2008]. Green circles, depths given in publication. Yellow squares, depths converted by proportional correspondence of $^{10}Be/^{9}Be$ ratios from sample to sample (See text for further information).

The corresponding positions (depths) of the previously published record for crust 3514-6 were correlated by interpolation of the measured natural $^{10}Be/^{9}Be$ ratios in both crusts, and

assuming proportional correspondence in variations of growth. The only feature in the record itself which could be used to align the data is a long-term dip in the $^{208}Pb/^{206}Pb$ ratio. For the data generated by this project, this dip is observed between 6 and 10.2 mm, with its lowest value around 8 mm. A similar dip is also observed in the previously published $^{208}Pb/^{206}Pb$ ratio record. However, this feature does not occur at the same depth, either using the published depths or the depths converted to the growth profile of the section of material employed here.

The age model implemented by *Muiños et al.* [2008] includes three different growth rates. Initially, those authors calculated a singular $^{10}Be/^{9}Be$ growth rate based on three measurements, and adjusted this rate according to a larger number of Co wt % data, allowing refinement of their age model beyond that possible using only three $^{10}Be/^{9}Be$ data points. The empirical Co wt % method is based on the assumption that Co is incorporated at a constant rate according to crust growth, such that high concentrations correlate to slow growth and vice versa [*Manheim*, 1980; *Puteanus and Halbach*, 1988]. The depth correlation shown in Fig. 6.4b (blue squares) based on correlation of the $^{10}Be/^{9}Be$ ratio/depth profile does not align the records, if it is assumed that the long-term dip in the $^{208}Pb/^{206}Pb$ ratio observed in both records is the same event. It is not possible to perform an age correlation using Co, as no Co wt % measurements were made for the section of crust 3514-6 used here. Using this 'wiggle-matching' approach, the original ages assigned to the Muinos et al. data appear to give a better fit (Fig. 6.6), thus the original age model is applied for further comparisons. For other crust data (65GTV, 121DK, 3511-1, 3514-13) compared below, the original age models are also employed. It should be noted that comparing data with age models based on growth rates using different methods may be problematic ($[^{10}Be]$-based vs. $^{10}Be/^{9}Be$ ratio-based or Co wt % growth rates); however the requisite information with which to convert the other age models to one based on $[^{10}Be]$ is not available.

6.4 Age models

6.4.1 Assessment and application of growth rates: Th

Unlike $^{234}U/^{238}U$ or $^{10}Be/^{9}Be$, common seawater $^{230}Th/^{232}Th$ or $^{230}Th/^{234}U$ ratios do not exist. Primarily, this is due to the very different particle reactivity of U and Th, the latter being scavenged quickly from the water column. Additionally, the two isotopes of Th have different sources; the majority of seawater ^{230}Th in the open ocean is produced *in-situ* from

^{234}U decay, while ^{232}Th derives from continental inputs. Continentally-sourced ^{232}Th is not transported in large quantities out into the open marine environment, as Th is scavenged out of the water column alongside riverine particulates as they settle out near their source [*Cochran et al.*, 1986]. The different sources, combined with the high particle reactivity of Th, lead to higher near shore ^{232}Th/^{230}Th ratios compared to pelagic sites [*Cochran*, 1992]. Hence, water column concentration profiles of the two isotopes (^{232}Th, ^{230}Th) show differing patterns with depth at the same location, while profiles and concentrations differ from location to location [e.g., *Broecker and Peng*, 1982; *Ivanovich and Harmon*, 1982 and references therein; *Chen et al.*, 1986; *Roy-Barman et al.*, 2002]. Consequently, it is not possible to compare the crust surface A(^{230}Th/^{232}Th) or A(^{230}Th/^{234}U) to some general seawater constant to assess the validity of our ^{230}Th$_{excess}$ results.

Fortunately, the ability to use material which has reached secular equilibrium deeper within the same crust provides an adequate raw data correction mechanism to ensure that the calculated A(^{230}Th$_{excess}$/^{232}Th) are reliable, at least for comparative purposes between ablation profiles and for growth rate calculation. The measured Th/U elemental ratio during measurement for NIST 610 of 0.54, compared to its known ratio of ~1, indicates several processes may be occurring to fractionate Th and U, either during the ablation process, transport of the volatilized material, ionization efficiency, or ion 'transfer' efficiency. Here, the term 'transfer efficiency' encompasses the relative ability to move ions into the mass spectrometer from the sample encompassing all processes occurring during measurement, including but not limited to ionization potential. U and Th have relatively similar first ionization potentials (Th ~6.95 eV, U ~6.08 eV), which are well within the capability of an ICP to ionize; thus, phenomena other than ionization efficiency may play a significant role. It is known that the matrix of the material being ablated and laser settings such as power and spot geometry can strongly affect elemental fractionation [*Jackson et al.*, 2004]. Thus, the characterization of Th/U elemental fractionation based on the standard reference material is limited as the matrices of the sample (a natural FeMn crust) and the standard (a prepared fused glass wafer) are very different. To examine the effect of differential fractionation between standard and sample on growth rate calculation, a range of Th/U elemental fractionation values were tested, ranging from 50% greater to 50% less Th transmission (relative to U). The range of overall correction factors tested ranged from 0.85 to 2.54 (compare to factor based on observed fractionation of 1.67). Absolutely no difference in final calculated growth rate is observed. This is ultimately due to the fact that the calibration of individual measurements and conversion to activity ratios before calculation of the growth rate is entirely dependent on a single-step iterative

calculation which forces the values measured deeper in the crust (at secular equilibrium) to the expected activity ratio of 1. The availability of material in secular equilibrium to make this correction is confirmed by the measured activity ratios falling to the same value below a certain depth; this is shown in Fig. 6.3a, b. Therefore, even though the upper growth rate calculated from A($^{230}Th_{excess}/^{232}Th$), ~0.4 mm/My, is quite different from that calculated from either [^{10}Be] or $^{10}Be/^{9}Be$ ratio (~2.8 and 5.4 mm/My, respectively), it appears that this result is reliable. Though the method employed here certainly requires more work to fully characterize the uncertainty, for the first time a direct, *in-situ* measurement of $^{230}Th_{excess}$ using laser ablation has been performed successfully to calculate FeMn crust growth rate.

6.4.2 Assessment and application of growth rates: Be

The two approaches using Be also generate significantly different growth rates from each other (Table 6.1; Fig. 6.1, 6.2; [^{10}Be] growth rates 2.82 and 1.30 mm/My; $^{10}Be/^{9}Be$ growth rates 5.22 and 1.01 mm/My). The age discrepancy observed for samples CR4 and CR7 to CR9 indicates that the seawater $^{10}Be/^{9}Be$ ratio was fluctuating at this location. This fluctuation could be due to reorganizations in currents originating from the Mediterranean. Recent studies suggest normalizing ^{10}Be with ^{9}Be should be an appropriate means of generating growth rates for crusts as open-ocean locations suggest very little change in the flux of ^{9}Be to at least 12 Ma [*Willenbring and von Blanckenburg,* 2010; *von Blanckenburg et al.,* 2015]. However, as the Mediterranean has a large amount of riverine input relative to its surface area and volume, there is a much larger input of ^{9}Be compared to ^{10}Be in this basin relative to larger basins. This leads to a large difference between the modern day $^{10}Be/^{9}Be$ ratio in the Mediterranean Sea (~ $0.1 – 0.3 \times 10^{-7}$) compared to that in the North Atlantic (~ $0.3 – 0.7 \times 10^{-7}$; see Fig. 1 in *von Blanckenburg et al.* [2015]). Thus, the assumption of a constant supply of ^{9}Be may not be applicable in some locations; in particular, locations bathed by different water masses at different times, if those water masses have significantly different $^{10}Be/^{9}Be$ ratios. Significant changes to MO are likely to have occurred during the MSC, which, due to the different $^{10}Be/^{9}Be$ ratios of Atlantic and Mediterranean water, could lead to inconsistencies in the $^{10}Be/^{9}Be$ ratio recorded in crust 3514-6. It is very likely that such a mechanism is responsible for the fluctuating $^{10}Be/^{9}Be$ ratios observed in crust 3514-6 (Table 6.1; Fig. 6.2). The palaeoceanographic event of a blockage to MO, which was the scientific target of the high-resolution isotope analyses performed here, compromises the use of the $^{10}Be/^{9}Be$ ratio to calculate growth rates for

crust 3514-6. Assuming that the exponential relationship observed for [^{10}Be] (Fig. 6.1; see also Fig. 6.11a, section 6.5.3, discussion, this chapter) within the crust is solely due to radioactive decay relies on two further assumptions: that diffusion is not occurring to any significant rate given the time interval under discussion, and that there was a constant supply of ^{10}Be over time. The former assumption has been shown to be valid due to extremely low diffusion rates of Be in FeMn crusts (< 10^{-9} cm/y) [*Henderson and Burton*, 1999]; this low diffusivity also applies for Th. The second assumption is clearly not valid over short timescales [e.g., *Berggren et al.*, 2009] but is assumed to be valid for the long periods integrated in single crust measurements [*Frank*, 2002 and references therein]. Applying a [^{10}Be]-derived growth rate can therefore be justified.

6.4.3 Growth rate differences and discrepancies

The discrepancy between the ^{230}Th-derived and ^{10}Be-derived growth rates (Fig. 6.1, 6.2; Tables 6.2, 6.3; ^{10}Be growth rates 2.82 and 1.30 mm/My; $^{232}Th_{excess}$ growth rate 0.407 mm/My) can be attributed to variable growth; changes in growth rates are commonly observed in crust samples [e.g., *Frank et al.*, 1999, 2003; *Muiños et al.*, 2008]. While the ^{10}Be method covers nearly the entire depth of the sample (extrapolated to ~21 mm), the $^{230}Th_{excess}$ rate can be applied to only the outermost 150 μm, the depth corresponding to the data used in the calculation (Ch 2, Fig. 2.4). Considering the general picture, this will not greatly affect interpretation as the Pb isotope record is essentially invariable. However, two significant issues generate large uncertainties affecting the ability to interpret any small-scale variations in the Pb isotope record. The first is the depth range at which the growth rate shifts from the slow Th-derived rate at the surface to the faster Be-derived rate. The location of this change cannot be defined with the data available, and thus an arbitrary change from the Th-derived growth rate to the Be-derived growth rate must be assigned. An abrupt shift from 0.4 mm/My to 2.82 mm/My (or 5.22 mm/My in the case of the ^{10}Be/^{9}Be derived growth rate) is clearly not realistic for a natural material such as this FeMn crust.

The second concern is the amount of time missing from the crust surface. The extrapolated surface [^{10}Be] and ^{10}Be/^{9}Be ratio are critical for the Be-derived growth rates, and they depend directly on the assumed position of the surface and the shallowest concentrations. As indicated by the Th data, the time missing from the surface at the point the Pb isotope measurements were performed can be estimated at ~0.2 Ma (section 6.2.2), relative to

further right in the sample (compare Fig. 6.3a, b). The greatest depth to reach secular equilibrium is about 0.18 mm (TH6); the least depth to secular equilibrium is about 0.1 mm (TH1). Applying the individual ablation Th-derived growth rates, these lengths suggest time spans of 0.39 My and 0.23 My for TH6 and TH1 respectively. The limit of the Th excess method is constrained to about 0.4 Ma [*Frank*, 2002] due to the half-life of ^{230}Th; thus, it appears that the longest Th excess depth at TH6 is approaching the limit of the method, suggesting that this profile has captured relatively intact surface material.

Missing surface material from the location of the Pb isotope ablation profile (next to TH1) is consistent with the extrapolated surface ^{10}Be/^{9}Be ratio, as the value calculated is lower than for other crusts in the NE Atlantic [*von Blanckenburg et al.*, 1996]. *Muiños et al.* [2008] state that there was no visual evidence of missing surface material for their sample of crust 3514-6. Those authors also state that their extrapolated ^{10}Be/^{9}Be ratio of 2.7 x 10^{-8} is consistent with an admixture of low ^{10}Be/^{9}Be Mediterranean water and higher ^{10}Be/^{9}Be NW Atlantic water. The extrapolated ratio determined for the sample of crust 3514-6 employed here is only slightly higher (2.75 x 10^{-8}), but there is some visual evidence of material missing from the surface to the left of the laser ablation profile (Ch. 2, Fig. 2.3). NE Atlantic ^{10}Be/^{9}Be FeMn crust surface ratios range from ~4 to 5 x 10^{-8} [*von Blanckenburg et al.*, 1996]. As sample CR4, and for similar reasons potentially sample CR5, have higher ^{10}Be/^{9}Be ratios than the previous measurement, the extrapolated surface ^{10}Be/^{9}Be ratio was recalculated for comparative purposes, based only on samples CR1 to CR3. The value obtained is 3.19 x 10^{-8}; compare to the extrapolated value employing CR1 to CR5 of 2.75 x 10^{-8} (Table 6.2, Fig. 6.2b). The higher value is within the range of ^{10}Be/^{9}Be water mass ratios for the North Atlantic tabulated by von Blanckenburg et al. (2015) (3 to 7 x 10^{-8}), and closer to the ^{10}Be/^{9}Be surface ratio of nearby crust Gibraco CH30 (4 x 10^{-8}; 36°35' N 11°43'W, water depth 1300 m, *von Blanckenburg et al.* [1996]) which formed near the Gulf of Cadiz at a depth consistent with MO. Considering the Gibraco crust ^{10}Be/^{9}Be surface ratio for the true surface of crust 3514-6, the amount of time missing would be 7 Ma (assuming 3514-6 surface ^{10}Be/^{9}Be ratio is 2.75 x 10^{-8} based on CR1 to CR5) or 2.2 Ma (assuming 3514-6 surface ^{10}Be/^{9}Be ratio is 3.19 x 10^{-8} using only CR1 to CR3). These long time periods are not supported by the $^{230}Th_{excess}$ excess data; after this amount of time, no $^{230}Th_{excess}$ would be observed, as all material would be at secular equilibrium. Therefore, the estimate of missing surface material corresponding to ~0.2 My at the location of the laser ablation profile is the most plausible. Furthermore, this conclusion supports an initial surface [^{10}Be] and ^{10}Be/^{9}Be ratio similar to that determined here, as the higher ^{10}Be/^{9}Be ratio for the Gibraco crust clearly suggests far too much time

is missing. 0.2 My of missing surface material corresponds to an initial surface [^{10}Be] of 2.05 x 10^{10} or a ^{10}Be/^{9}Be ratio of 3.27 x 10^{-8}, employing CR1 to CR3, or 2.82 x 10^{-8} employing CR1 to CR5.

The Pb isotope data are presented as time series in Fig. 6.6 and 6.7. As the ^{10}Be/^{9}Be derived growth rate is considered highly suspect for crust 3514-6, application of the growth rates derived with this ratio is shown only for interest (Fig. 6.7); the [^{10}Be]-derived age model (Fig. 6.6) will be employed for interpretation. The ^{230}Th$_{excess}$-derived rate is applied to the topmost 150 μm; after this, the [^{10}Be] derived rates are applied (Fig. 6.5). The record begins with a 0.2 My gap as suggested by the ^{230}Th$_{excess}$ data. The time integrated into each data point is as follows: initially, with the ^{230}Th$_{excess}$ derived rate (0.41 mm/My), ~37 ky; with the first [^{10}Be] derived rate (2.82 mm/My), ~5 ky; with the second [^{10}Be] derived rate (1.30 mm/My), ~12 ky.

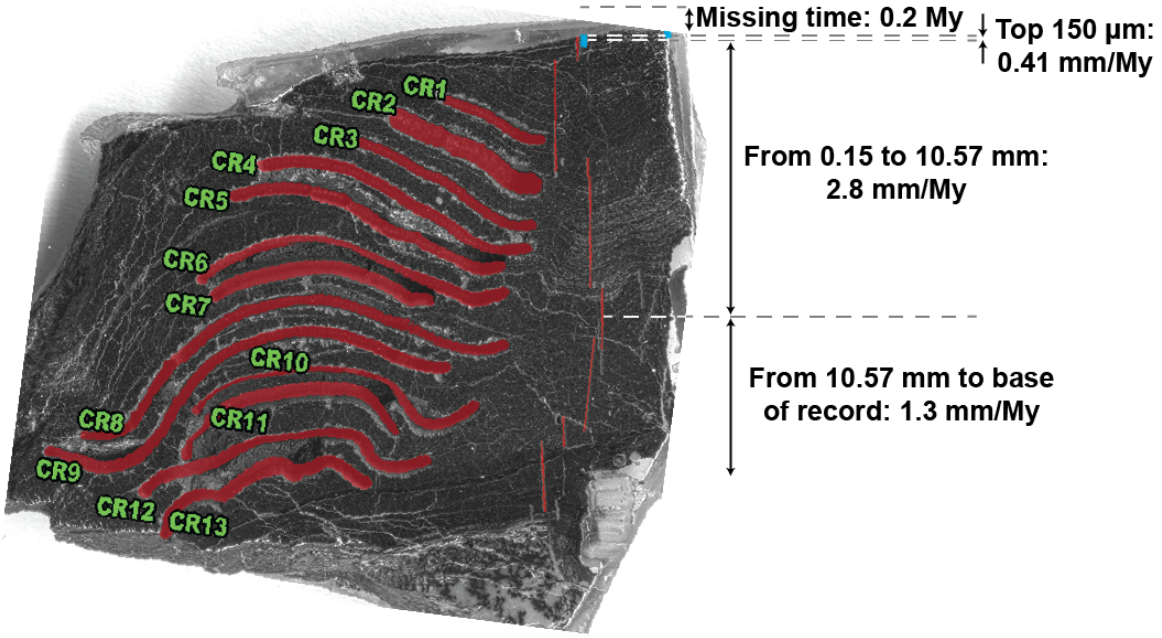

Fig. 6.5. Depth ranges of growth rates applied to crust 3514-6 determined by ^{230}Th$_{excess}$ and ^{10}Be atoms/g ([^{10}Be] 1 and 2). CR# labels indicate subsamples drilled for ^{10}Be/^{9}Be measurement; thin vertical red lines indicate laser ablation profile for Pb isotopes; blue (top right corner) indicates region of laser ablation profiles for ^{230}Th$_{excess}$. See Tables 6.2, 6.3 and Figs. 6.1, 6.3 for calculation of rates.

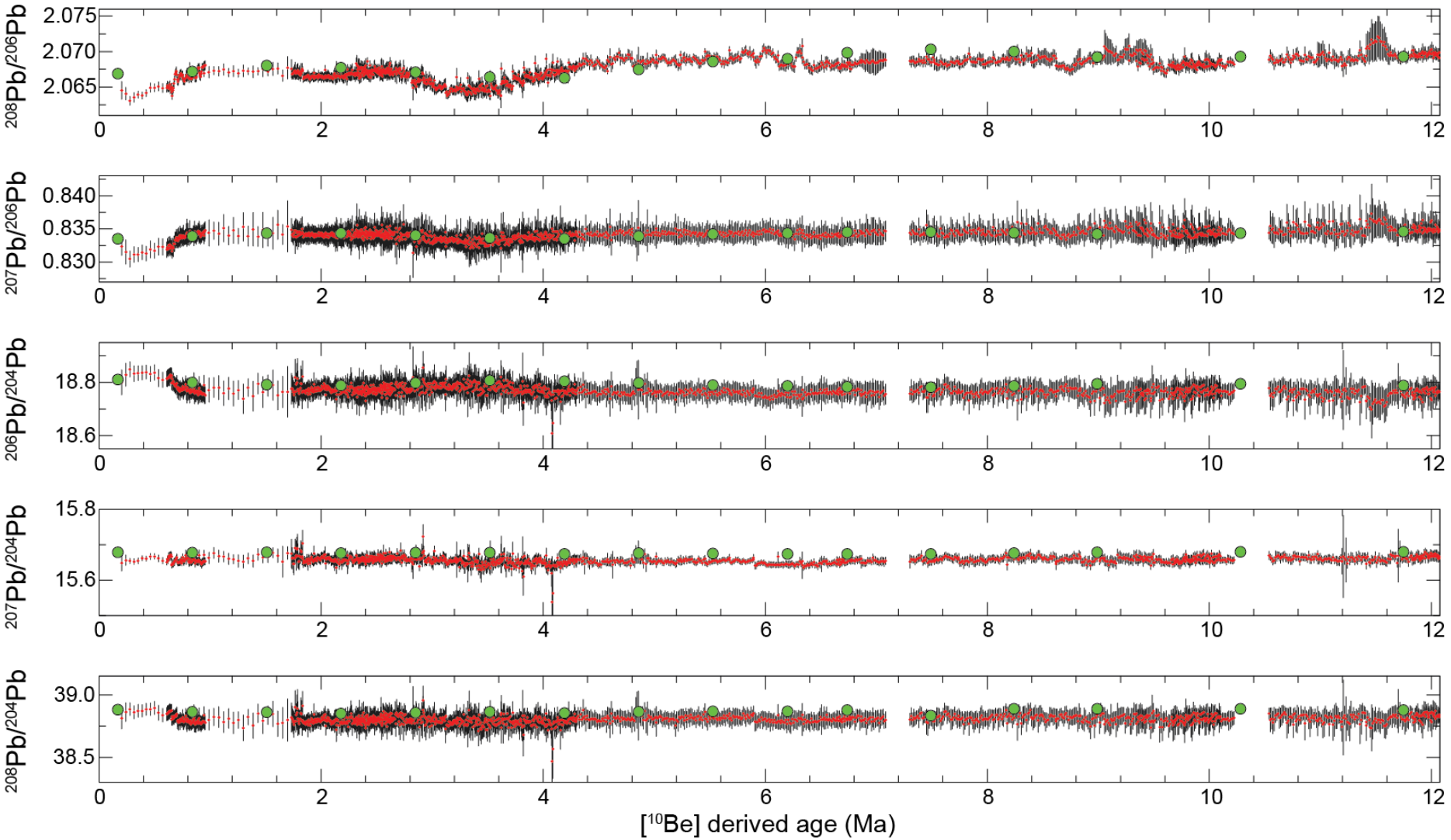
208Pb/206Pb
2.075
2.070
2.065
207Pb/206Pb
0.840
0.835
0.830
206Pb/204Pb
18.8
18.6
207Pb/204Pb
15.8
15.6
208Pb/204Pb
39.0
38.5
0
2
4
6
8
10
12
[10Be] derived age (Ma)

.38 to 2.5 Ma,

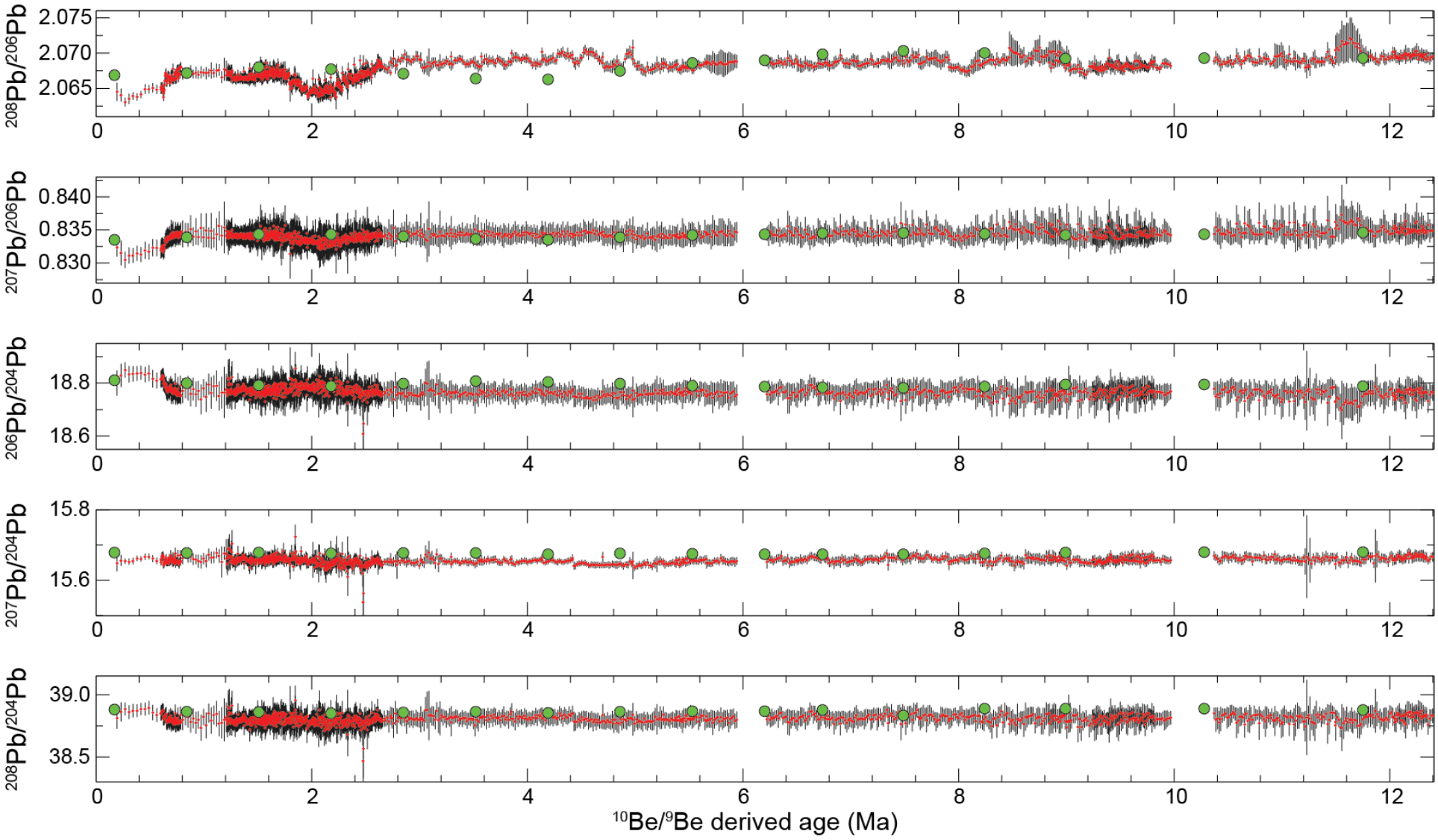
208Pb/206Pb
2.075
2.070
2.065
207Pb/206Pb
0.840
0.835
0.830
206Pb/204Pb
18.8
18.6
207Pb/204Pb
15.8
15.6
208Pb/204Pb
39.0
38.5
0
2
4
6
8
10
12
10Be/9Be derived age (Ma)

6.5 Palaeoceanographic interpretation of crust 3514-6 Pb isotope record

6.5.1 The Messinian Salinity Crisis

Except for some small fluctuations observed only in the $^{208}Pb/^{206}Pb$ record between ~5.5 and 6 Ma, no clear, consistent changes are observed to occur in crust 3514-6 in relation to the MSC, even with the increased temporal resolution of laser ablation (Fig. 6.8). This is likely primarily due to the fact that, according to the other crusts from the vicinity, the Pb isotope signatures of different water masses throughout the water column in the late Miocene were very similar. Only crust 121DK, sourced from further afield off the coast of West Africa, differs significantly from the other crusts between 4.5 and 8 Ma. The comparison is also hampered by the relatively poor precision of the laser ablation measurements compared to the published values generated using solution-based chemistry. The previously published crust data compared to the laser ablation record in Fig. 6.8 have associated uncertainties smaller than the symbol size. The locations of the crusts used in the following discussion are shown in Fig. 6.9.

6.5.2 Effects of glaciation on MO plume settling depth

The youngest part of the record is more insightful. In general, hydrogenetic crust records from major ocean basins indicate the past 1 Ma has been the period of time with the most pronounced isotopic differences over the past 60 Ma, mainly as a consequence of a distinct change in the isotopic composition of deep waters in the North Atlantic [e.g., *Abouchami et al.*, 1999; *Frank et al.*, 1999a, 1999b; *Reynolds et al.*, 1999]. This change has been attributed to a strong shift in weathering regimes affecting the isotopic composition of source waters to the North Atlantic after the onset of northern hemisphere glaciation, which began approximately 3 Ma [*Frank*, 2002 and references therein]. This shift in weathering regime was compounded beginning ~ 1 Ma during the middle Pleistocene transition (MPT) when the material being eroded by glaciers changed from primarily regolith material to the granitic bedrock of the Canadian Shield [*Clark et al.*, 2006]. Crust 3514-6 follows this trend, with the strongest isotopic shift observed ~ 1 Ma (Fig. 6.8). This shift is not as clear in the previously published record.

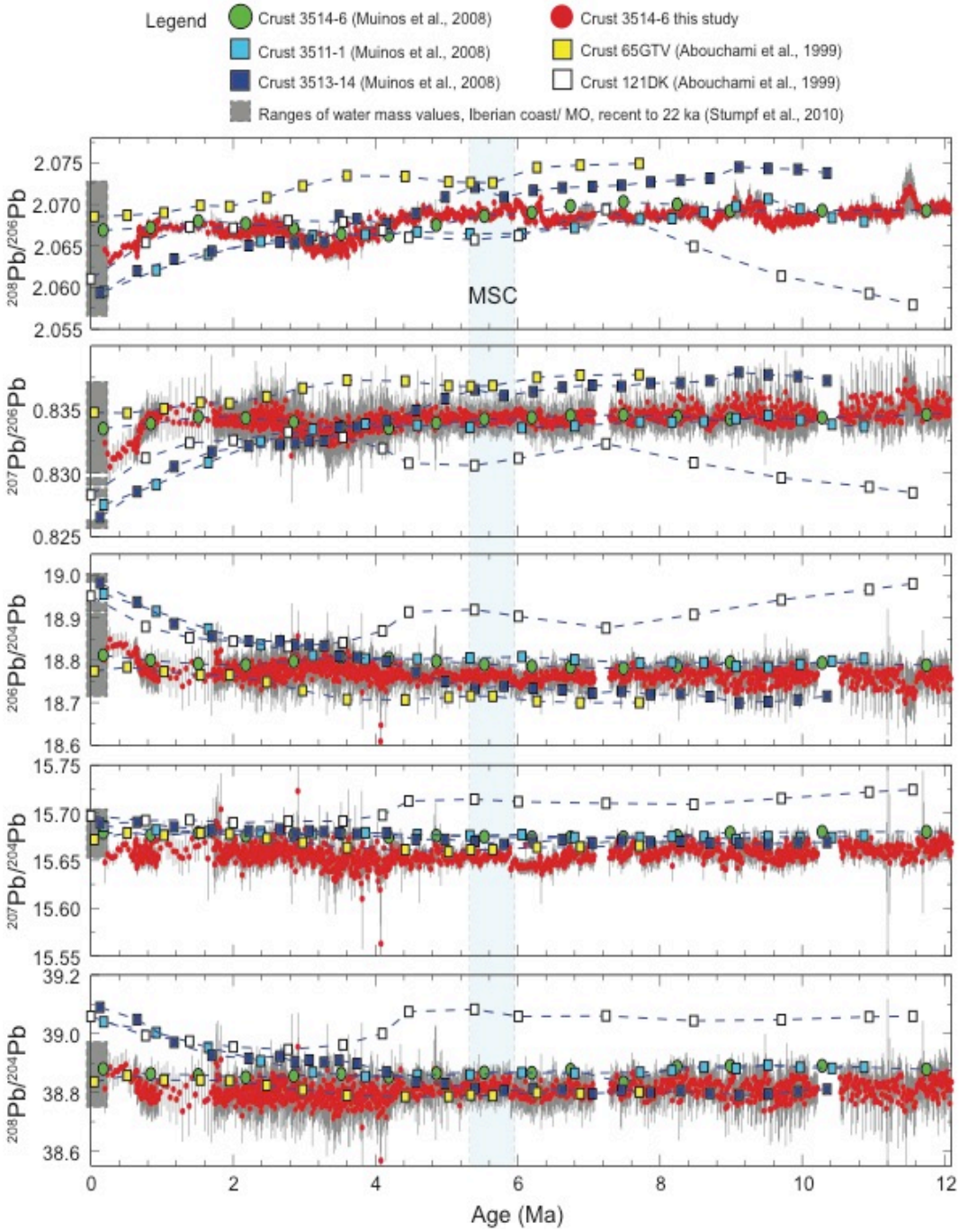

Fig. 6.8. High resolution Pb isotope record of crust 3514-6, with comparison to other crusts from the NE Atlantic. For locations and water depths see Ch. 1, Fig. 1.20, Ch. 2, Fig 2.1, Ch. 2 Table 2.4. 65GTV represents MO at deeper location; 3511-1 represents NEADW, in vicinity of Gulf of Cadiz; 121DK represents NEADW at a more southern location far from MO influence. Late Pleistocene to recent Iberian coast bulk sediment leachate data [*Stumpf et al.*, 2010] shown for reference; this data has maximum age of ~22 ky.

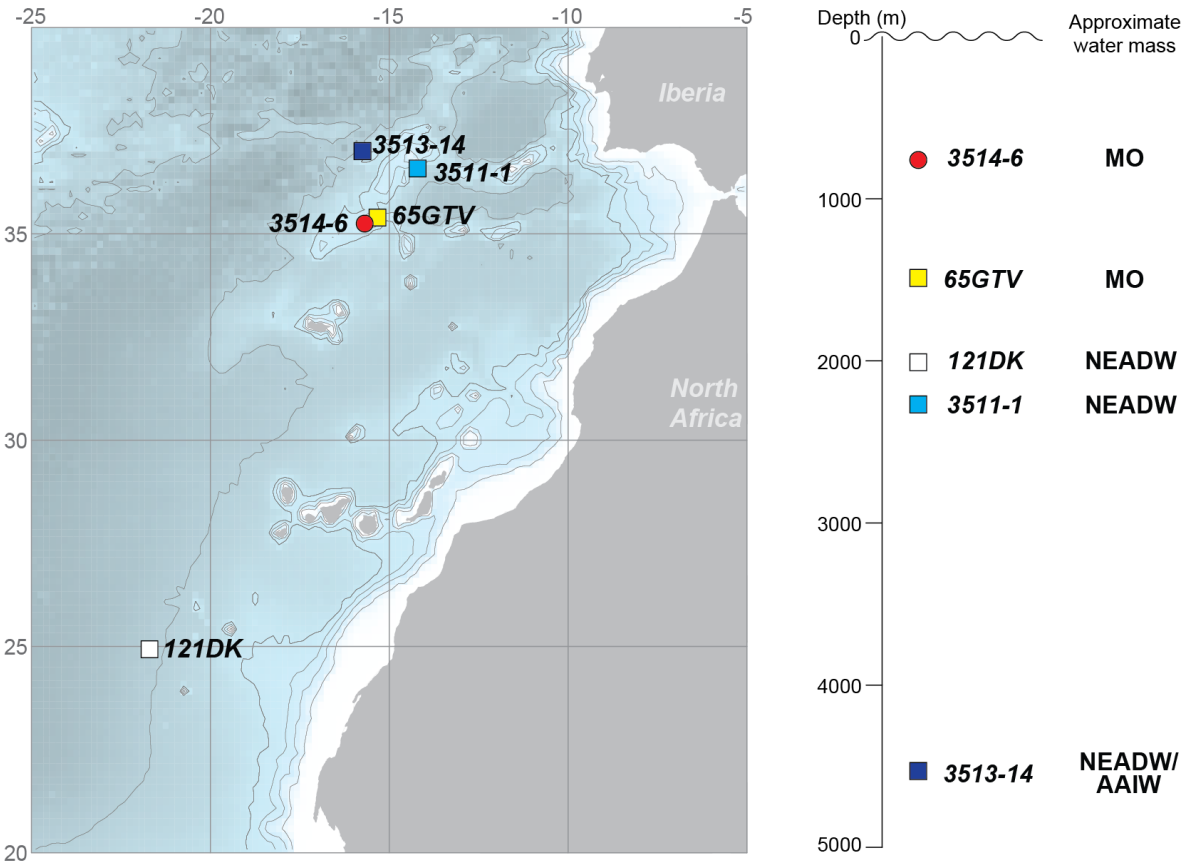

Fig. 6.9. The locations of the crusts discussed in this section. The column at the right shows the water depths each crust was collected from and indicates the water mass which is thought to have bathed the crusts. MO – Mediterranean Outflow, NEADW – North Eastern Atlantic Deep Water, AAIW – Antarctic Intermediate Water.

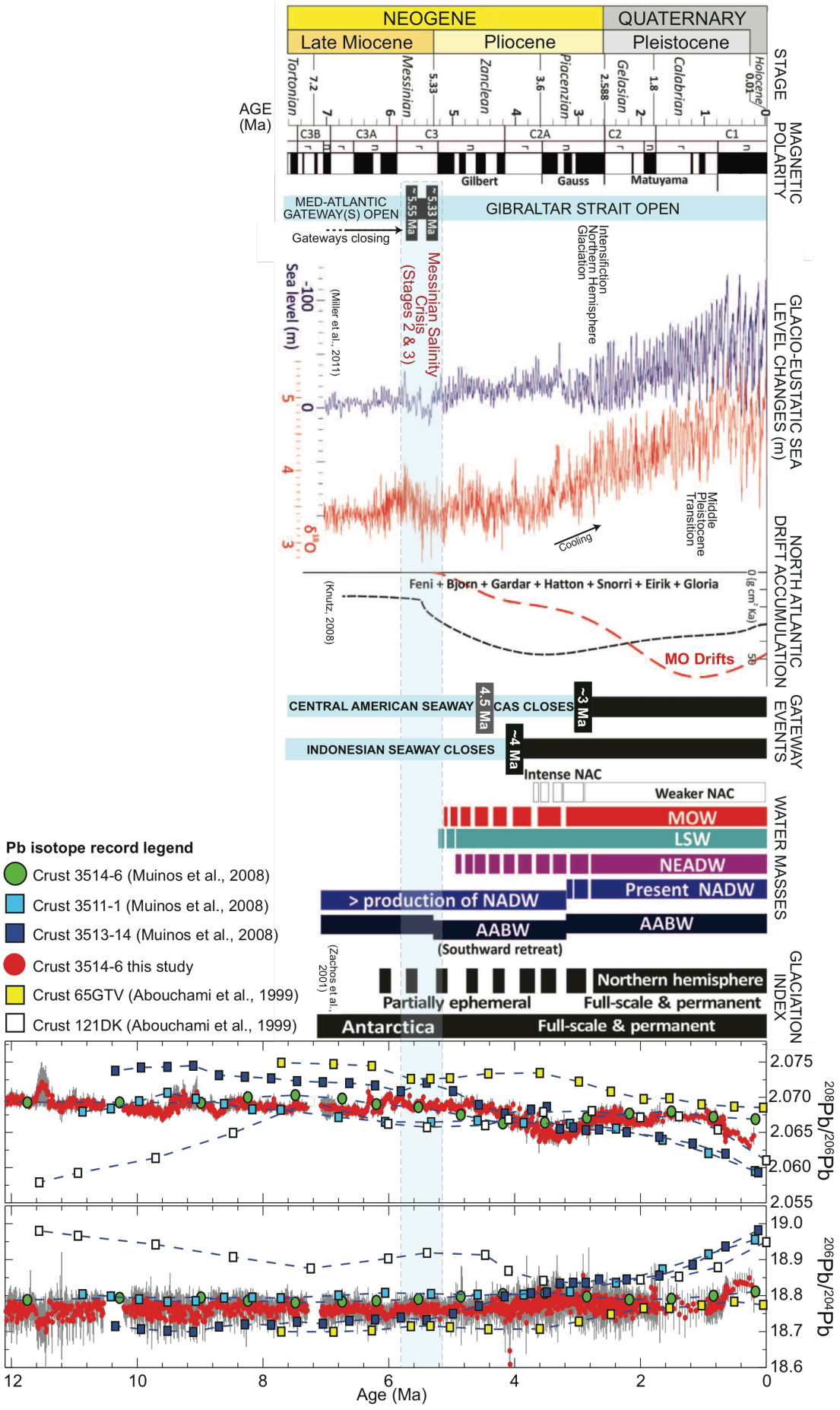

Fig. 6.10. High resolution $^{208}Pb/^{206}Pb$ record of crust 3514-6, compared with crust records from the NE Atlantic (as per Fig. 6.8) and open ocean records of major oceanographic changes. Record compilation (panel above Pb isotope record) modified from [*Hernández-Molina et al.*, 2014b].

To discuss changes in MO over time, it is critical to clarify the mechanisms controlling the settling depth of the MO plume. As detailed in a modeling study by *Rogerson et al.* [2012], MO plume settling depth is not controlled by Mediterranean density, but rather by the density profile of the Atlantic. The density contrast between MO and the Atlantic water masses it comes in contact with causes mixing; changes in the density of MO will cause changes to the vigor of mixing, resulting in a stable plume settling depth regardless of MO salinity or density. The buoyancy of the resulting admixture of Mediterranean and ambient Atlantic waters relative to the density of the Atlantic dictates settling depth; saltier, denser Atlantic waters will increase the buoyancy of the MO plume, causing it to settle higher in the water column. This counterintuitive mechanism is important for understanding the differences in the records of crusts 3514-6 and 65GTV, both of which precipitated at the Lion Seamount. Crust 3514-6 accumulated somewhere between 688 and 938 m water depth, while crust 65GTV was collected from ~1500 m (Ch. 2, Fig. 2.1, Table 2.4).

Over the youngest ~3 My of the record, deep water masses NEADW (3511-1, 121DK) and AABW (3513-14) have very similar Pb isotope signatures (Fig. 6.8, 6.9; with the exception of 121DK in the $^{208}Pb/^{206}Pb$ normalized ratio, discussed below). In the case of the $^{207}Pb/^{204}Pb$ ratio, little difference between water masses is apparent; however, this is most likely due to low natural variability controlled by the shorter half-life of parent isotope ^{235}U. Crust 65GTV, on the contrary, retains a significantly less radiogenic isotope signature over the entire record compared to other regional water masses. Beginning from ~3 Ma and continuing towards present day, both the previously published and newly generated records for 3514-6 begin to shift from signatures similar to NEADW, as indicated by 3511-1, towards a signature comparable to that recorded in 65GTV. 65GTV is also the only local water mass record in which trace metal isotope changes are observed around the time of the MSC (Fig. 6.8, $^{20X}Pb/^{206}Pb$ ratios; see also Nd record, Ch. 4, Fig. 4.1).

The apparent change at 3 Ma is coeval with intensification in northern hemisphere glaciation and increased sediment accumulation associated with MO flow in the Gulf of Cadiz (Fig. 6.10; see *Hernández-Molina et al.* [2014a, 2014b] for an explanation of MO-related contourite deposits). Increased glaciation causes a rise in ocean salinity due to greater retention of freshwater in high latitude ice shields; this would have the effect of increasing the relative buoyancy of the MO plume, allowing it to settle higher in the water column. Thus, prior to ~3 Ma, the MO plume may have settled deeper in the water column, missing the upper part of the Lion Seamount and crust 3514-6. This explains why no clear

signal is recorded during the MSC in either record of 3514-6. This may also explain the irregularity in the Nd isotope record of deeper crust 65GTV for the youngest 3 Ma (Ch. 4, Fig. 4.1); during intense northern hemisphere glaciation, the MO plume may have occasionally risen above this crust entirely. The youngest 3 My of the record is also consistent with the onset of the major currents in the Atlantic that are observed to compose the majority of circulation in this ocean (Fig. 6.10).

6.5.3 ^{9}Be flux and water mass changes

The major changes observable in the Pb isotope record of 3514-6 and 65GTV (intensification of northern hemisphere glaciation and changes to MO during the MSC) are coincident with the irregularities observed in the ^{10}Be/^{9}Be ratio (samples CR 4, CR7 to CR9). These fluctuations are compared to changes in the [^{9}Be] in crust 3514-6 in Fig. 6.11. Such fluctuations are consistent with fluctuations in the ^{10}Be/^{9}Be ratio of water masses bathing crust 3514-6, and thus fluctuations in the source of the water masses themselves. The fact that changes in the Pb isotope compositions (and Nd, Ch. 4) of 3514-6 do not mirror that of 65GTV earlier than ~3.5 Ma, while still recording a change in ^{9}Be flux, can be explained by the fact that the water mass signature recorded by 3514-6 was an admixture of both NEADW and MO, with the relative amounts of contributions from each water mass changing through time, while local Pb sources seem to have caused all major water masses outside the Gulf of Cadiz to have remarkably similar Pb isotope compositions. The observation that the flux of ^{9}Be to crust 3514-6 has changed, at times consistent with major palaeoceanographic changes, supports the hypothesis that the MO plume has changed settling depth according to the North Atlantic density profile as well as highlighting the problematic nature of employing the normalized ^{10}Be/^{9}Be ratio for the age model in this crust.

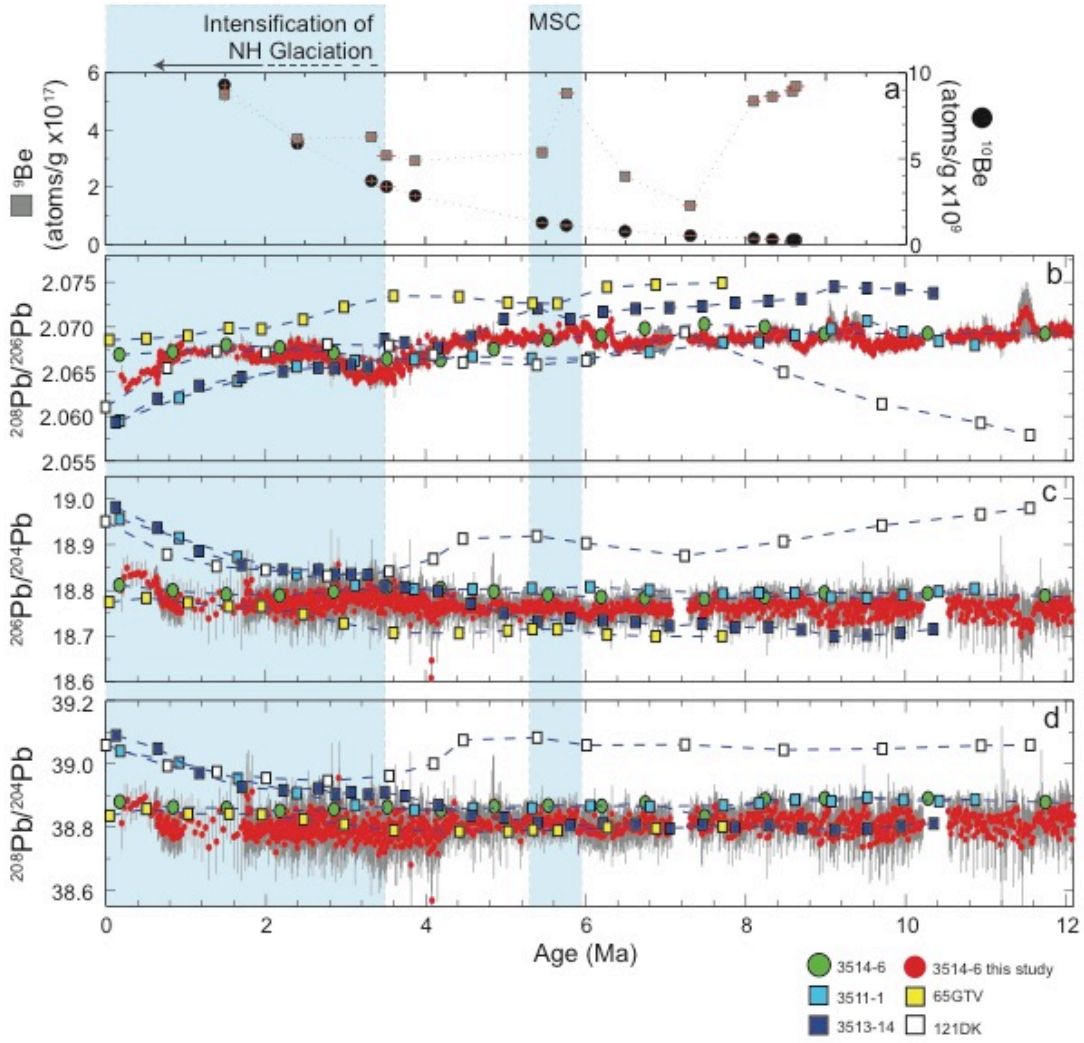

Fig. 6.11. (a) Comparison of fluctuations of [^{9}Be] in crust 3514-6 with (b-d) changes in Pb isotope compositions recorded in NE Atlantic crusts. Periods of fluctuating [^{9}Be] also consistent with irregularities in the ^{10}Be/^{9}Be ratio (Table 6.1, Fig. 6.2) are highlighted in blue and labeled with the relevant palaeoclimatic event which likely caused the fluctuations. Higher concentrations of [^{9}Be] after 8 Ma are not consistent with irregularities in the normalized ^{10}Be/^{9}Be ratio, and consequently do not constitute a change in water masses bathing the location. NH – northern hemisphere.

6.5.4 Inconsistencies

The Nd and Pb isotope records for 65GTV are not entirely consistent. The upper ~2.5 Ma in the Nd record (Ch. 4, Fig. 4.1) suggest significant fluctuations in the water bathing the site; this is not observed in the Pb isotope records of this crust. This may be related to the relative importance of local effects, particularly dust, for Pb. Open ocean locations are more favourable for reliably recording the Nd isotope signature of overlying currents. Both the Mediterranean and North Atlantic region to the west of North Africa receive a great deal of input from Saharan dust (Ch. 5, Fig. 5.7) [e.g., *Hamelin et al.*, 1989; *Grousset et al.*, 1990, 1992; *Abouchami and Zabel*, 2003]. This dust input may have a greater effect on local water masses in terms of Pb as the concentration of this element in seawater is much

lower (deep water [Pb] ~2pmol/kg; compare to [Nd] up to 45 pmol/kg; Ch. 1, section 1.4). A recent assessment of the relative impact of sources to the global ocean Nd budget indicates that dust contributes only about 5%, while riverine input makes up about 7% and boundary exchange at continental margins makes up about 88% [*Rempfer et al.*, 2012 and references therein]. In comparison, it is thought that dust contributes about 12% to the oceanic Pb budget, with riverine input making up the rest [*Henderson and Maier-Reimer*, 2002]. While both elements are quickly scavenged from surface waters, scavenging in the case of Pb is non-reversible [*Craig et al.*, 1973; *Henderson and Maier-Reimer*, 2002 and references therein], meaning that once an atom of the element has adhered to or become incorporated into the particulate phase, it has been removed from the system permanently. Nd scavenging, on the other hand, is considered reversible [*Tachikawa et al.*, 1999; *Siddall et al.*, 2008] indicating that there is constant exchange between particulates and dissolved Nd, potentially diluting new inputs. Seawater Pb isotope compositions are also likely to be more affected in regions of the ocean which receive a large dust flux, as is the case for the equatorial and northern Atlantic and Mediterranean Sea [*Duce et al.*, 1991; *Prospero*, 1996; *Henderson and Maier-Reimer*, 2002]. Based on comparisons with Al, an element that correlates well to natural aluminosilicate mineral compositions, it has been estimated that anywhere from 13 to 90% of the Pb contained in mineral dust may dissolve into seawater [*Maring and Duce*, 1990]. The high end of this range may be an overestimation due to the nature of anthropogenic contamination; while concentrations of Pb and Nd in mineral aerosols are noted to be slightly enriched compared to crustal average concentrations, the enrichment in Pb is generally considered by be caused by anthropogenic contamination [*Scheuvens et al.*, 2013]. Nevertheless, the amount of Pb dissolution into the water column from dust is likely to be higher than that for Nd, as only about 2% of Nd is thought to dissolve from mineral aerosols into seawater [*Goldstein et al.*, 1984; *Rempfer et al.*, 2012].

Additionally, different Pb isotope ratios suggest slightly different relationships when comparing the records of some of the crusts. For example, the record of 121DK and 3514-6 in $^{208}Pb/^{206}Pb$ and $^{206}Pb/^{204}Pb$ show slightly different trends (Fig. 6.10). Before 3 Ma, the $^{208}Pb/^{206}Pb$ isotope record of both 121DK and 3514-6 lies between 3511-1/3513-14 and 65GTV. The same part of the $^{206}Pb/^{204}Pb$ record suggests that the water mass recorded in 121DK was more similar to the water masses recorded by 3511-1 and 3513-14, while 3514-6 still plots between those crusts and 65GTV. In terms of Nd, the record of 121DK is very consistent with that of 3511-1 during more recent times until about ~4 Ma (Ch. 4, Fig. 4.1). In general, examining the 121DK record in all Pb isotope pairs (Fig. 6.10), ratios

normalized to ^{204}Pb have different trends compared to ratios normalized to ^{206}Pb, particularly the timing of when 121DK and 3511-1 recorded the same Pb isotope ratios (note that both crusts are thought to have recorded NEADW). This again apparently points to different sources supplying Pb to the region 121DK was located (Tropic Seamount, west coast of Africa) and highlights the importance of local inputs for this isotope system. Although the palaeoclimatic changes which caused this discrepancy is unclear, it appears that some event ~ 7 to 7.5 Ma caused the ^{206}Pb normalized ratios to briefly become more similar to 3511-1, while this is not supported in ratios not containing ^{206}Pb.

The fact that the Nd and Pb isotope records of some crusts do not covary has been observed before; for example, *Foster and Vance* [2006] observed secular changes in Pb isotopes tracking glacial-interglacial cycles while the Nd isotope record remained relatively constant in FeMn crust BM1969.05 from the San Pablo seamount in the Northwest Atlantic. Those authors attributed this to the fact that seawater Pb isotope compositions are more susceptible to local changes (in that case, the release of freshly weathered glacial till and associated highly radiogenic Pb) exacerbated by the short residence time of Pb, while such local effects are more diluted by the longer residence time and higher concentration of Nd already in the marine system. In this case, the Pb isotopic changes in 121DK which are not observed in other crust records could also be due to a change in inputs to seawater off the coast of West Africa, since the Nd isotope record of this crust does not show significant shifts at the same time (Ch. 4, Fig. 4.1).

6.5.5 Further interpretation to the 65GTV record

The record of 65GTV includes a brief peak towards an even more radiogenic value in the Nd isotope signature of MO around 5.5 Ma. If MO were to cease, the intuitive assumption about the behaviour of Nd in crust 65GTV would be to trend towards less radiogenic values, because the water masses which could replace MO are all understood to be less radiogenic [*Rickli et al.*, 2009]. However, a more radiogenic signature is observed, and at no point near the time of the MSC does the record of 65GTV become significantly less radiogenic. Firstly, it should be acknowledged that the uncertainty on ages determined using the beryllium method (the growth rate of 65GTV was determined via ^{10}Be/^{9}Be) may be large, on the order of 0.5 to 1 My. Thus, it can be argued that this radiogenic peak actually coincides with the end of the MSC, at the moment the Mediterranean fully reconnected with the Atlantic through Gibraltar, and exchange as we understand it today

became reestablished. It is reported that the residence time of water in the Mediterranean began to increase as early as 6.7 to 6.8 Ma, based on changes in stable oxygen and carbon isotope signatures of carbonate fossils [*Sierro et al.*, 2003]. This observation is believed to be a result of increasing restriction between the Mediterranean and Atlantic, an effect also observed in changes to benthic foraminiferal assemblages [*Kouwenhoven et al.*, 1999, 2003; *Seidenkrantz et al.*, 2000] well before MSC onset at 5.971 Ma. The effect of increasing the residence time of Mediterranean water, while restricting exchange with the Atlantic during the MSC, should be to enhance the contribution of river water to the Nd budget of the basin relative to the unradiogenic signatures of the NE Atlantic. The Nile, and likely the Eosahabi river system [*Osborne et al.*, 2010], the largest contributors of freshwater to the Mediterranean Sea, have very radiogenic compositions ($\geq$ -2 ε_{Nd}, [*Osborne et al.*, 2010; *Scrivner et al.,* 2004]. While salinity in the basin can be maintained due to the freshwater budget, restriction should result in an overall increase towards more radiogenic Nd compositions overall in the basin. This signature is not likely to have reached 65GTV in any significant amount until effective communication with the Atlantic was re-established. Re-establishment of exchange would also lead to a flushing of the radiogenic Nd signature from the Mediterranean, followed by a return to pre-MSC values. Thus, the radiogenic spike in the ε_{Nd} record of 65GTV may actually reflect the opening of the Gibraltar Strait and re-establishment of normal marine conditions in the Mediterranean.

6.6 Conclusions

A higher resolution age model than that previously published, using both $^{230}Th_{excess}$ and cosmogenic ^{10}Be, has been generated for crust 3514-6. To the best of the author's knowledge, this is the first published instance of *in-situ* $^{230}Th_{excess}$ growth rate determination on a FeMn crust using laser ablation. The age model was required to convert a high resolution Pb isotope record for this crust into a time series with relatively high accuracy. The Pb isotope record was generated on crust 3514-6 *in-situ*, via laser ablation multi-collector inductively-coupled plasma mass spectrometry (LA-MC-ICPMS). The resulting record is of variable resolution (between ~5 and 37 ky per data point) depending on the corresponding growth rate, and contains 1,440 data points.

The original scientific objective, to capture changes in Mediterranean Outflow (MO) using radiogenic isotopes recorded in crust 3514-6, was not achieved. Besides analytical issues with isobaric interference prevented measurement of Nd by laser ablation on this sample

(Ch. 2, section 2.4.1), this is due to two factors: (1) the neighboring water mass Pb isotope signatures were too similar to allow differentiation around the time of the MSC; and (2) it appears likely that 3514-6 was not bathed by MO during that time, or was bathed by a weak admixture of NEADW and MO such that the precision in the method used here precludes variability being outside uncertainty.

By comparing the new record with existing records, changes in the upper 3 My of the record produced here are placed into context with changes in the Atlantic that would affect the settling depth of the MO plume. Onset and intensification of northern hemisphere glaciation may have allowed the MO plume to settle higher in the water column due to changes in the North Atlantic density profile. This effect, and other changes to overall MO output (i.e., closure of the Betic and Rifian gateways), has probably affected the incorporation of the two isotopes of beryllium in crust 3514-6 as water from the Mediterranean and North Atlantic have significantly different $^{10}Be/^{9}Be$ ratios. This has led to inconsistencies in the $^{10}Be/^{9}Be$ ratio at specific times in 3514-6, indicating a need to exercise caution when using this ratio to calculate growth rates, and suggesting that using [^{10}Be] is the more reliable option.

6.6.1 Age model generation and cosmogenic beryllium: to normalize or not to normalize?

FeMn crust 3514-6 was investigated in much higher temporal resolution than has been previously accomplished for the purpose of determining changes in MO during the late Miocene. Two methods, one based on $^{230}Th_{excess}$, the other on cosmogenic beryllium, were used to generate a sample-specific age model for a thick section of this crust. While the two methods generate significantly different growth rates, they both appear robust, and differences are likely due to the different sections of crust to which each corresponds. A very slow rate of growth was estimated for the upper layers, while rates well within the average was determined for the rest of the material.

A comparison of data and growth models contrasting the use of the non-normalized [^{10}Be] to the $^{10}Be/^{9}Be$ ratio suggests that, in the case of this particular crust, normalization is problematic. The inherent assumption of normalization, that the flux of incorporation of the cosmogenic ^{10}Be is more accurately represented in normalized form because of relatively constant input of ^{9}Be to the oceans, is flawed in the case of locations bathed by

water masses from different basins. This is because different basins may have significantly different natural $^{10}Be/^{9}Be$ ratios, in large part a result of the ratio of riverine input to basin volume [*Willenbring and von Blanckenburg*, 2010; *von Blanckenburg et al.*, 2015]. In the case of crust 3514-6, changes to the volume, depth, and intensity of the MO plume, as well as changes in its settling depth controlled by changes to the North Atlantic density profile, would have an effect on the water bathing the crust's location. North Atlantic water has a significantly higher $^{10}Be/^{9}Be$ ratio than Mediterranean water, and this is reflected in inconsistencies in the $^{10}Be/^{9}Be$ depth profile of crust 3514-6. Using the age model derived by combining the $^{230}Th_{excess}$ and [^{10}Be] methods, it appears that the oldest inconsistencies in the $^{10}Be/^{9}Be$ ratio (~ 5.5 Ma) coincide with the MSC, while the youngest coincide with major changes in the North Atlantic density profile due to intensification of northern hemisphere glaciation (~ 3.5 Ma).

While fluctuations in the preserved $^{10}Be/^{9}Be$ ratio is a problem for age model generation using this method, it is also potentially useful. For example, this mechanism could be applied to longstanding palaeoceanographic problems such as the timing of closure of the Panama gateway, if a suitable crust were identified. The North Atlantic and Pacific Ocean basins have a comparable difference in their natural $^{10}Be/^{9}Be$ ratio to that observed between Mediterranean and North Atlantic seawater, such that a similar phenomenon as that observed in crust 3514-6 might be observed. Indeed, crust "Antilles", deposited to the east of the Panama gateway, could be argued to show a trend towards increasing $^{10}Be/^{9}Be$ ratios at the oldest end of the published beryllium data [*Reynolds et al.*, 1999]. Unfortunately, the maximum age of this crust is only ~ 4 Ma, not long enough to provide sufficient data before the closure of the Panama gateway to enable reliable interpretation.

6.6.2 Insights from the Pb isotope record of crust 3514-6

In general, the ~ 12 My long Pb isotope record is relatively invariant, showing little variability outside of analytical uncertainty. Compared with other crust records, this relative invariance shows the stability of the Pb isotope signature of the NE Atlantic outside the Gibraltar region, which appears to have been stable with depth as well as through time. This stability and constancy with depth (as observed when comparing the records from several crusts from the area, including 65GTV, 3514-13, and 3511-1) does not support using Pb isotopes to distinguish changes to MO in the late Miocene, as the signatures from all water masses in the region appear to have been very similar at this time.

The primary changes observed in the Pb isotope time series of crust 3514-6, also more obvious when comparing with other crust records, likely correspond to the intensification of northern hemisphere glaciation around 3.5 Ma and related changes in the density profile of the North Atlantic. This mechanism is the most plausible because the settling depth of the MO plume outside Gibraltar is controlled by the density profile of the Atlantic water masses, rather than the salinity of Mediterranean waters exiting the strait. The observation that the MO plume settling depth was likely lower during the late Miocene relative to the modern environment also explains why deeper crust 65GTV appears to have captured changes in seawater Nd isotope signatures during the MSC, while 3514-6 did not. This conclusion also supports the hypothesis that the Nd isotope results from ODP Site 978 (Ch. 4) are a more reliable estimate for late Miocene MO than those previously published, as the ε_{Nd} of crust 65GTV is very similar to that of Site 978 during this period. Three of the four samples from the Site 978 core have essentially identical ε_{Nd} values as crust 65GTV.

The temporal resolution and precision of the LA-MC-ICPMS method should also be noted. The resolution achieved here is not quite precise enough (in terms of the age model) or of high enough resolution (in terms of the isotope measurements) to determine if precessional variability in seawater Pb isotopes could have occurred outside the Gulf of Cádiz as is observed inside the Mediterranean.

As indicated by the $^{230}Th_{excess}$ ablation data, a more intact portion of crust 3514-6 is likely to be found at the location of ablation TH6. If it were desirable to generate a high resolution record for the most recent portion of this crust, that would be the location to perform the measurements. Such a record could be compared to the glacial-interglacial cycles observed for crusts BM1969.05 and ALV539 from the NW Atlantic [*Foster and Vance*, 2006]. If the patterns of the different records match, this could provide information about the path length/distance of transportation of the radiogenic Pb signal during glacial maxima and glacial retreat. If not, this could indicate more recent fluctuations of the MO plume in the water column at this location, or could be suggestive of other processes. High resolution records of the early part of 65GTV, 121DK, 3511-1 and 3514-15 would also be useful, in order to differentiate the signal produced from glacial-interglacial cycles and shifts in MO plume height. Finally, the results from crust 3514-6 suggest that high temporal resolution laser ablation studies are not likely to provide useful information about changes in the Mediterranean-Atlantic gateways prior to ~ 3.5 Ma, unless precision could be improved greatly, as very little is observed in the way of variability before this time,

and the Pb isotope signatures in the region were very similar. This chapter has highlighted the fact that local inputs must always be considered when interpreting seawater Pb isotope variations, particularly compared to Nd isotope variations which, in the case of FeMn crusts, are less likely to be diluted by local signals.

7 Synopsis and future outlook

7.1 Overview

This final chapter synthesizes the key conclusions derived from this project. Initially, the overall goal of assessing late Miocene Atlantic-Mediterranean exchange with the various isotope systems is assessed. This section is followed by a series of inferences determined by considering individual isotope systems together. The final section includes recommendations for future work.

7.2 Challenges of applying radiogenic isotopes to understanding Mediterranean-Atlantic exchange in the late Miocene

The geochemical tracers Sr, Nd, and Pb have specific physicochemical properties enabling their use in palaeoceanographic contexts as water mass tracers or as indicators of basin connectivity. However, those same physicochemical characteristics also place limitations on these tracers, and in the context of directly determining exchange through the Betic and Rifian gateways, various difficulties with Pb and Nd have been identified, affecting the ability to infer past changes from isotope records of these elements.

In the case of Nd, the shallow nature of the Betic and Rifian gateway sediments are prime candidates for boundary exchange. In the open ocean, the concentration profile of Nd is nutrient-like, with lower concentrations near the surface (Ch. 1, section 1.3.1); thus, the relatively higher concentrations expected at depth can easily dominate the preserved Nd isotope signatures. In the Mediterranean, the concentration profile is essentially constant, which could partially counter this issue. Regardless, in shallow and high-energy environments such as the Mediterranean-Atlantic gateway regions investigated in this thesis, care must be taken to ensure that the bottom water signal preserved is representative of the water masses being studied. The results in Chapter 4 show no particular change in Nd isotope signatures over the interval measured, and boundary exchange cannot be ruled out. Comparing new late Miocene results for deep, distal Site 978 to the previously published Nd record from the Rifian corridor [*Ivanoviç et al.*, 2013] indicates that the

estimate for the palaeo-MO end-member inferred by these authors was too radiogenic. A more appropriate value is likely -9.3 to -9.9 ± 0.37 $\varepsilon_{Nd(t)}$; this is quite similar to the ε_{Nd} observed in the Alborán Sea and at the Gibraltar Strait today [*Tachikawa et al.*, 2004]. This comparison also implies that the record of *Ivanoviç et al.* [2013] more likely reflects shoaling/shallowing of the Rifian corridor, and that boundary exchange and/or benthic flux was very likely a strong factor in the Nd isotope signatures preserved during corridor closure. As these effects cannot be separated, Nd cannot be used reliably in shallow marginal environments, and thus it is unlikely to be a useful tracer for Mediterranean-Atlantic exchange.

Measurement of a Nd isotope record was attempted for FeMn crust 3514-6, which accreted on the Lion Seamount outside the Gulf of Cadiz and far from sedimentary contamination; unfortunately, this was unsuccessful due to analytical challenges. The Pb isotope record was measured successfully; however, it does not show significant changes during the late Miocene which are consistent with changes to Mediterranean Outflow (MO). This is partially due to the fact that the Pb isotope signature of other water masses outside Gibraltar had very similar Pb isotopic compositions prior to 4 Ma. If MO ceased, the signal from this water mass would be replaced by another with a very similar composition. To separate such signals, high precision measurements are necessary; however, high temporal resolution in-situ methods such as LA-MC-ICPMS are not generally capable of the same precision as solution-based MC-ICPMS or TIMS. With these latter methods there is a trade-off, as the high temporal resolution required to capture a relatively short-lived event such as the MSC is very difficult to accomplish due to the slow growth rates inherent to FeMn crusts. Thus, in terms of understanding changes in MO outside Gibraltar, the simple conclusion is that the stable Pb isotope signatures of the various water masses in the area are quite similar, requiring both high precision as well as high temporal resolution. Despite these challenges what the Pb record does show is that crust 3514-6 was bathed by a water mass with a much smaller proportion of MO during the late Miocene, and that therefore this crust is not likely to record clearly changes in the water masses at that time. Records from the deeper crust, 65GTV, from the same location also barely register any significant changes over the interval 5.33 – 6 Ma in Pb isotopes [*Abouchami et al.*, 1999].

Strontium is a more thoroughly studied isotope tracer in the context of the MSC, having been used to investigate the Mediterranean-Atlantic connection and basin hydrology in several studies [e.g., *Flecker et al.*, 2002; *Flecker and Ellam*, 2006; *Lugli et al.*, 2007; *Roveri et al.*, 2014; *Topper et al.*, 2014]. In most instances, reliable estimates are available

due to the well-studied nature of this isotope system, which does not suffer from anthropogenic contamination like Pb. Due to this, Sr can provide insight not only into exchange between basins, but also allows for modeling of the hydrologic budget of a basin (Ch. 3). The only other prominent issue to keep in mind when using this isotope system is that it does not register excursions from global values until fairly extreme restriction occurs. Nevertheless, compared to $^{143}Nd/^{144}Nd$ and $^{208,207,206}Pb/^{204}Pb$, $^{87}Sr/^{86}Sr$ remains the most viable radiogenic isotope system available to promoting our understanding of Atlantic-Mediterranean exchange in the late Miocene. The main difficulty currently preventing the discovery of more direct information about connectivity during the later stages of the MSC (Stages 2 and 3) is the lack of material recovered from deep basin locations.

7.3 North African Monsoon system and Mediterranean seawater radiogenic isotopes: application of Sr and Pb to astronomical tuning and the phase lag

As outlined in the Introduction (section 1.2.5), precessional latitudinal shifts in the North African monsoon system (Fig. 7.1) are an important control on the Mediterranean hydrologic budget and patterns of sedimentation. During insolation maxima, increased freshwater input to the Eastern Mediterranean generates lower salinity surface waters, halting deep water formation, causing bottom water anoxia and sapropel deposition. This regularly repeating climate shift is the primary reason precessional resolution astronomical tuning is so successful in the Mediterranean region, currently limited by an incomplete understanding of precisely when each part of the sedimentary cycle should be tied to the insolation curve (Ch. 1, section 1.2.6).

Like the sedimentary cyclicity, both the Sr and Pb isotope compositions of seawater from the Sorbas Basin, and Pb isotope compositions from elsewhere, appear to vary with insolation. Both isotope systems also appear to react or track changes in the climate system near insolation minima. Thus, both Sr and Pb isotopes may provide more reliably consistent tie points between lithology and the insolation cycle than the mid-point of sapropels currently used for most astronomical tuning in the Mediterranean [e.g., *Hilgen and Krijgsman*, 1999; *Krijgsman et al.*, 1999a]. However, it appears that two different mechanisms are responsible: for Sr, the Sorbas Basin hydrologic budget; for Pb, dust from North Africa.

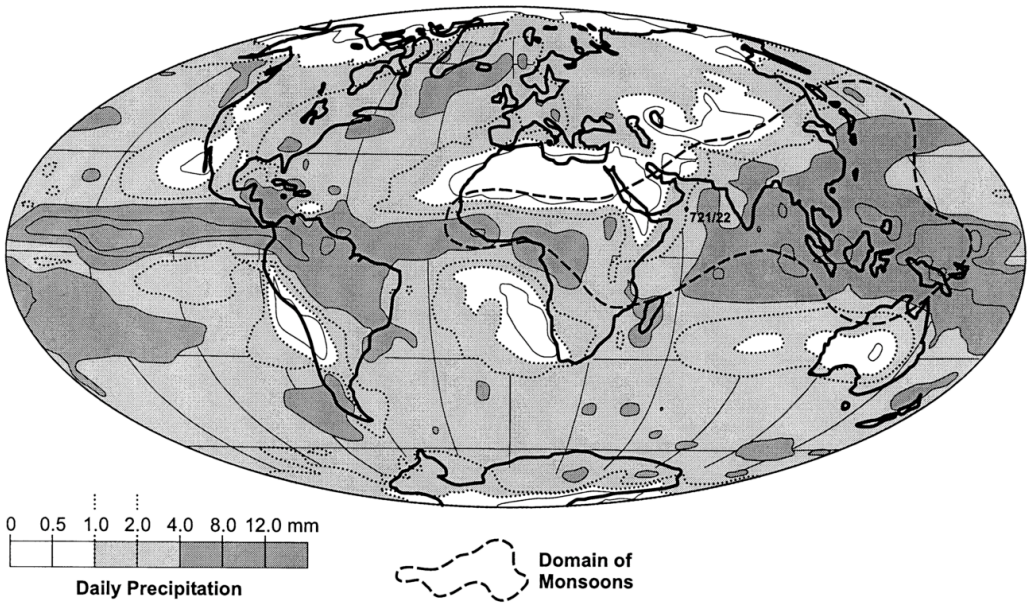

Fig. 7.1. Precipitation across the globe and monsoons. North Africa is particularly dry in the modern configuration, while the African monsoon system sits just to the south (area of African continent outlined with a dashed line). Modified from *Goudie and Middleton* [2001].

In the case of Sr, the signal being captured is caused by the effect of the basin hydrologic cycle affecting the vigour of exchange between the Sorbas Basin and the Western Mediterranean. The Sr anomalies lag the minimum in the hydrologic budget, which is likely to coincide more precisely to insolation minima (though there could be a lag between insolation minima and the minimum in the hydrologic budget which is not possible to capture with the simple box model). As the Sr anomalies generally lag the diatomite layers, this suggests that the diatomite is closely related to insolation minima, supporting the tuning of this layer to that part of the cycle. However, the precise time at which point the insolation minima should be tied to this layer is more difficult to discern. One cause of this is that the transition from diatomite to marl 2 may be triggered by a depletion of nutrients [*Filippelli et al.*, 2003] rather than an increase in freshwater to the basin affecting vertical mixing coinciding with an increase in insolation. The other issue to consider is that the lag between minimum exchange and the Sr anomaly will be dependent on the basin volume, and thus would have to be determined on a basin by basin case.

Other factors complicate the use of Sr isotopes in astronomical tuning; primarily, very minimal exchange is required for a Sr anomaly to occur. Sr anomalies are not likely to happen in all marginal basins all the time, so Sr isotopic excursions are not going to occur consistently, and are thus not going to be useful in a large range of locations and times. This isotope system is definitely more useful in terms of enabling modeling the local

hydrologic budget in semi-enclosed Mediterranean sub-basins; in this respect, very specific quantitative constraints can be attained. One basin, which has potential to preserve precessional Sr isotope anomalies, could be the Piedmont Basin (Northern Italy). This is a likely candidate since freshwater inclusions were preserved in gypsum deposited during MSC Stage 1, suggesting that this basin also had a positive freshwater budget during the late Miocene.

In the case of Pb, the consistent timing at different locations of a shift towards similar Pb isotope compositions suggests that a regional mechanism, common across the Mediterranean, is the cause. This is certainly more useful in astronomical tuning, especially when correlating sections from different marginal and open Mediterranean locations. It may be possible that peak dust production correlates more closely to insolation minima, although this requires more careful study, for example using a GCM model coupled with dust simulations. If this is the case and the lag is minimal to non-existent, this mechanism could be very useful in improving the accuracy of determining tie points and intercorrelation between sections, particularly due to the very short residence time of Pb in seawater. This characteristic allows seawater Pb isotope signatures to react very quickly to inputs, such that changes in isotopic compositions may reflect changes within a few years to a few decades. One caveat is that this relatively fast change could appear essentially instantaneous in areas of low sedimentation, but could appear more significant in sections with high sedimentation rates. For example, relatively sharp peaks (or troughs) are observed at Monte del Casino and the Sorbas Basin, but broader peaks are observed at Falconara. This could potentially be due to a high sedimentation rate within the diatomite layer at this location, causing a 'spreading' of the signal relative to the other sites. Currently, the information available does not allow deduction of differing sedimentation rates within a precessional cycle. Although it is clear that more work must be done to provide confidence in dust as the real cause, this mechanism seems to tick all the necessary boxes, including the fact that dust is a regional signal which affects sections across a wide geographical area, and a signal that appears regardless of marginal basin connectivity. A modeling study determining the timing of response between insolation and dust production would allow for the determination of when exactly the peaks in the Pb isotope composition of Mediterranean seawater should coincide with insolation. Moreover, more sections must be examined, particularly in the Eastern Mediterranean, to ensure the same relationships are observed and that the same assumptions can be made. Finally, the link between dust and Pb isotope compositions suggest seawater Sr isotopes are not a result of dust. If dust

were the mechanism driving both signals, the peaks in Sr and Pb would be expected to occur at the same time.

The radiogenic signal inferred here for Saharan dust, in combination with removal of the unradiogenic Pb isotope signal of the Atlantic, should cause the expected Pb isotope signature of the open Mediterranean to become more radiogenic after corridor closure. Thus, studies with Pb isotopes continued across MSC onset and intra-MSC Stage boundaries could provide information about corridor closure. Similarly to that seen with Nd, an increase in residence time of Mediterranean water should correlate to an overall more radiogenic Pb isotope signature in the basin. This type of study would require both high temporal resolution, on the order of several samples per precessional cycle, while also examining several cycles across the MSC due to the fact that both the influence of the Atlantic over the ~ 640 ky of the MSC needs to be separated from the precessional scale influence of dust.

7.4 Crust 65GTV: the most appropriate MO record for the late Miocene

The high temporal resolution Pb isotope record from crust 3514-6, combined with the late Miocene Nd isotope data from ODP Site 978, has helped determine which Atlantic locations were likely to have recorded MO around the time of the MSC. The connections between plume depth, $^{10}Be/^{9}Be$, and the Pb isotope record for crust 3514-6 indicate that this crust was not likely to have been bathed by the MO plume as effectively as deeper crust 65GTV in the late Miocene. The majority of Nd isotope compositions from Site 978 plot directly on top of the 65GTV compositions, while 3514-6 is less radiogenic. This appears reversed for the more recent part of the isotope records of these crusts, where the variability the Nd isotope record of crust 65GTV suggests that the MO plume shallowed to less than 1500 m, bathing this location in the less radiogenic Nd isotope signature of NEADW (Ch. 4, Fig. 4.1, compare 121DK and 3511-1 to 65GTV and 3514-6). However, during the late Miocene, 3514-6 is less radiogenic than 65GTV, plotting between the values for this crust, 3511-1, and 121DK. Out of these four records, 121DK is clearly the least radiogenic, best reflecting the unradiogenic Nd isotope signature expected for NEADW, a water mass derived in large part from waters of the very unradiogenic Labrador Sea. In the modern environment, 1500 m is thought to be very near the deepest limit of the MO plume; the most recent (relative to the Miocene) northern hemisphere glacial maxima likely would have increased the density of ocean water, particularly in the North Atlantic, allowing the MO plume to settle higher in the water column, above the

depth of crust 65GTV. Conversely, in the past, the lack of northern hemisphere glaciation would have led to less saline waters in the North Atlantic, and potentially a deeper settling depth of the MO plume, supporting 65GTV as the most appropriate record of MO Nd and Pb isotope signatures outside the Gulf of Cadiz prior to onset and intensification of northern hemisphere glaciation. Thus, the isotope signatures archived in crust 65GTV are likely to be the best open ocean record for the MO water mass during the Miocene and early Pliocene.

7.5 Recommendations for future work

7.5.1 Lessons from an analytical point of view

There are several caveats to understanding Mediterranean-Atlantic exchange in the late Miocene, as well as the overarching themes of the interrelationships between marginal and deep settings and how radiogenic isotopes are preserved in the marine environments typical to the Mediterranean region. These theoretical issues are often compounded by analytical difficulties, which preclude record development in the first place. From an analytical point of view, the author would recommend the following:

- Acid-reductive bulk sediment leachate experiments, particularly those intended to determine seawater Nd isotopes and performed on sediments deposited in shallow and marginal settings, should be performed in stages. The first stage must be a small set of samples accompanied by strong leach and total dissolution samples, as well as fish teeth and elemental ratio analysis of the extracted solution from all archives. This suggestion may not seem innovative; however, it is imperative for good experimental planning when dealing with archives of past seawater Nd isotopes, and thus is stated here.
- Though the TOC for samples used in this thesis was expected to be less than 2%, organic matter proved to be a serious problem during attempts at total sample dissolution. Relatively large volumes of oxidizing agents were required to perform chemical oxidation, which increased the Pb blank contribution to a level requiring blank correction (~1-3%). Advice from colleagues indicated that the organic matter appeared kerogen-like, although analyses to identify the compounds were not performed due to time constraints. Ashing (or 'roasting' [*Bayon et al.*, 2002]) at high temperature or using a plasma asher may be a cleaner way to remove this

material. The effect on the detrital Nd and Pb isotope signal should be minimal, although this may warrant testing.

Further to improvements in laboratory procedure or experimental design, a more complete understanding of the Al/Nd ratio of the FeMn oxyhydroxide fraction in shallow settings such as the Sorbas Basin would be ideal. This elemental ratio appears to be useful to test whether the ε_{Nd} of acid-reductive bulk sediment leachates are contaminated by the detrital fraction, specifically for sediments from open settings with 'normal' marine sedimentation (i.e., sediments primarily composed of fine grained siliclastics and biogenic carbonates deposited in relatively quiet environments) [*Blaser et al.*, 2016]. However, the different relationships observed between ε_{Nd} and Al/Nd in the Sorbas Basin indicate that a greater understanding of how Al is transported away from the coast and how it combines with authigenic oxyhydroxides is required to allow more direct usage of the Al/Nd proxy in shallow settings.

7.5.2 Pb isotopes as a stratigraphic tool in the Mediterranean: where to sample?

Besides recovery of deep deposits below the Mediterranean halite units (see section 7.5.4 below), there are many relatively accessible locations which should be investigated for sea water Pb isotope records. As outlined in Appendix 3, a few samples from Ain el Beida (Atlantic Morocco), Monte dei Corvi (Northern Italy), and Metochia (Crete) were analysed for Pb isotope ratios. The results from all three sections suggest that there may be variability with insolation, similarly to the sections investigated in Ch. 5. In order to determine whether there is a Mediterranean-wide signal at insolation minima which can be observed using Pb isotopes, and whether or not this could be a useful stratigraphic proxy, these sections, and others known to have clear precessional sedimentary variability, should be investigated. For sediments younger than the Miocene, the Trubi Formation and Capo Rosello on Sicily are also prime candidates, as are any which were used by *Lourens et al.* [1996] to develop the Pliocene to recent Mediterranean stratigraphy. It is possible to acquire samples from Dr Frits Hilgen at Utrecht University, although most marginal locations around Southern Europe are accessible for sampling. The Pissouri section on Cyprus [*Krijgsman et al.,* 2002] is another viable location which could extend the spatial coverage further east. Although today's socio-political events currently prohibit investigation in many regions of North Africa, there are likely to be many locations which are appropriate to investigate. Besides the deposited sediments, the dust sources

themselves must be thoroughly sampled, in order to overcome problems due to anthropogenic contamination. Additionally, the deposits in locations such as Mega Lake Chad require the development of high-resolution stratigraphic frameworks in order to understand both what material was available for dust production at what times, as well as the more important issue of climate cyclicity and teleconnections between water bodies.

Further to the sections mentioned, there are several Pliocene and younger ODP cores which have good age constraints and show cyclical sedimentation from within the Mediterranean. The most appropriate times to begin a record for proof-of-concept studies should include both eccentricity maxima and eccentricity minima (where the insolation curve has its highest and lowest amplitudes, respectively). This approach will allow testing this potential proxy under the most and least optimal conditions.

7.5.3 What is needed for numerical modeling with Pb?

Box model experiments, such as those performed in Chapter 3, would be invaluable for furthering our understanding of how Pb isotopes behave in the Mediterranean and its marginal basins. Modeling Pb isotopes in the oceans has been perfomed using GCM type simulations previously where ^{210}Pb was used to judge the model's accuracy [e.g., *Henderson and Maier-Reimer*, 2002]. Such studies could provide the means to determine whether or not dust is responsible for the excursions observed at Sorbas, Falconara, and Monte del Casino, for example. This could be undertaken with a GCM; however, low-complexity models like the box model approach employed here (Ch. 3) is more accessible and easier to perform, due to the lower computational requirements. Furthermore, box modeling can provide more direct interpretations, if the goal is to provide insight into specific mechanisms at specific locations, rather than on the complete Earth system level. Several constraints are necessary for box modelling, which at the moment are not available. This is primarily due to the problem of anthropogenic contamination of the natural Pb cycle, such that modern seawater, riverwater, and dust measurements do not reflect the natural isotopic signals. As Nd and Sr do not suffer from this issue, these systems are much easier to estimate for times in the past, particularly for dust and fluvial inputs as only major changes in exposed catchment geology are expected to alter these compositions, while late Miocene catchments are not expected to be so different from today in many areas around the Mediterranean. As discussed in Ch. 5, it may be more useful to estimate dust Pb isotope compositions directly from source materials; in the

modern environment, the most significant dust sources are relatively well known. Samples of silt and easily deflatable material should be sampled from fresh exposures to measure Pb isotope compositions directly; this information could be tabulated, potentially alongside annually averaged back-trajectories, to estimate the isotopic compositions of dust being transported to various areas. Another important aspect which needs to be better constrained is the amount of natural Pb transferred from dust particles to seawater, and the true variability in this parameter. Again, as anthropogenic contamination has impacted the natural Pb cycle, it is unclear how much the Pb observed to transfer from aerosols to seawater is due to easily desorbed ions which adhered during subaerial transport of the particles. Sensitivity experiments testing how a response in seawater Pb isotope signatures scale to inputs depending on the amount of Pb dissolution could help provide further constraints on this issue.

7.5.4 The importance of deep section recovery: the DREAM project

As alluded to several times throughout this thesis, it is imperative to our understanding of the Messinian Salinity Crisis, and the state of Atlantic-Mediterranean exchange leading up to this event, to recover deep basin sediments, including the evaporites themselves as well as pre-MSC sediments. Several key pieces of information can only be garnered from the deep basin. One of these key concerns is the relationship between the marginal and deep deposits, only understood through indirect geophysical information such as seismic images until very recently [e.g., *Ochoa et al.*, 2015].

While correlation between marginal and deep basin sedimentary units is not the focus of this thesis, it is a very important detail in any study employing and relating data garnered from these different settings. For example, it would be useful to determine the open Mediterranean salinity, particularly in the Western Mediterranean (but also in the east), across several precessional cycles leading up to the MSC. This would allow for the acceptance or rejection of the hypothesis that open Mediterranean salinity was gradually increasing several precessional cycles prior to MSC onset during the so-called aplanktic marls of the Sorbas Basin (Ch. 3, section 3.4.5). Since stratigraphic relationships are important in combining datasets from different locations, proving that two records are temporally consistent is of paramount importance, particularly when high resolution is required.

Another important aspect would be to determine if the Pb isotope variability observed in relatively shallow settings, such as the sections investigated here, extends to the deep basin. Besides furthering our understanding in general of the behavior of Pb isotopes in seawater, this could confirm or deny whether the signatures observed during insolation minima are basin-wide, and thus if Pb isotope compositions in seawater are a useful stratigraphic tool. If cores have poor 'datability' due to a lack of fossil information, potential reworking, or poor magnetic susceptibility, the theory that Pb isotopes could be used to aid in astronomical tuning and cyclostratigraphy, in a similar manner to stable isotopes, could be put to the test. This is a particularly exciting possibility, as it has been long recognized that there are difficulties matching stable isotope records from within the Mediterranean to open ocean records because of the extreme differences in local signals, particularly leading up to the MSC after the onset of restriction at about 6.8 Ma [*Sierro et al.*, 2003].

As emphasized by the radiogenic isotope records of Sr and Nd (Chs. 3 and 4), marginal Mediterranean records are not expected to be the same as the open Mediterranean basins, whether these are related to the preserved seawater radiogenic isotope signatures, salinity, or lithological cyclicity. However, the Sr isotope record and box modeling results suggest that the main basins drive the marginal basins, at least in terms of longer term or average trends. Recovery of sedimentary material from the deep basins will provide the ability to look at this relationship in earnest, as well as potentially provide appropriate material to accomplish the original goal of this thesis, which was to understand water mass exchange prior to and during the MSC, primarily with Nd isotopes.

7.5.5 A better salinity proxy

For the Sr isotope box model, salinity constraints needed to be assumed. The best available means to do so was to look at the foraminiferal assemblages, which do not provide an accurate idea of salinity, only a large range. At the moment, there are no proven proxies for salinity changes which will work within the Mediterranean leading up to and during the MSC; stable oxygen isotope records, for example, cannot be interpreted in a straightforward manner due to the extreme influence of local inputs. Thus, it is essential to develop a proxy which can work independently to determine changes in salinity, in addition to working out the stratigraphic relationships between deep and marginal deposits. Understanding changes in salinity at various locations will not only prove invaluable for

reconstructing Mediterranean exchange, but also climate changes nearer the poles, for example over glacial/interglacial cycles.

7.5.6 Where can we find ideal records for reconstructing global ocean circulation?

As shown by many researchers, Nd isotopes can be very useful for reconstructing ocean circulation in deep and distal locations. Several such Nd records have been produced, either on their own or in combination with other proxies [e.g., *Abouchami et al.,* 1999; *Muiños et al.,* 2008; *Roberts et al.,* 2010; *Khélifi et al.,* 2009, 2014; *Böhm et al.,* 2015]. The key to using Nd isotopes as a proxy for changes in the open ocean is location and methodology; sites far from the ocean margins, and appropriate materials which allow careful selection of the authigenic signal. In terms of the Mediterranean Outflow, deep deposits buried beneath the halite may be of use for future studies. Preferably, sites near to the Gibraltar region are ideal; however, seismic profiles indicate that deposits in the Alborán Sea are mostly not ideal [*Shipboard Scientific Party*, 1996]. Thus, it is more likely that deeper deposits in the Balearic Basin need to be drilled to make use of this isotope system. This may preclude direct observations of changes in Levantine Intermediate Water (LIW), due to the fact that this water mass is generally found above 2000 m, but should still allow for an understanding of the longer term effects through time of restriction in Mediterranean circulation. Deposits outwith the Mediterranean which are directly associated with Mediterranean Outflow tend to be coarse grained due to the high current speeds, and are constantly being reworked; thus, Nd isotopes are not likely to be of use.

As mentioned in Ch. 6 (section 6.6.1), the closure of the Panama gateway likely had a strong influence on global ocean circulation. The timing of closure of this gateway is still debated, which hinders both GCM past climate reconstructions as well as the interpretation of long-term records including the period between 6 and 3 Ma. The ^{10}Be results (Ch. 6) suggest that, during major gateway reorganization or closure, the ^{10}Be/^{9}Be record in a crust may be affected. If a FeMn crust with a long enough growth period could be found, which accreted in the appropriate region, the ^{10}Be/^{9}Be record is a likely means of furthering our understanding of the timing of the closure of this gateway.

References

Abbott, A. N., B. A. Haley, and J. McManus (2015a), Bottoms up: Sedimentary control of the deep North Pacific Ocean's εNd signature, *Geology*, *43*(11), 1035–1038, doi:10.1130/G37114.1.

Abbott, A. N., B. A. Haley, J. McManus, and C. E. Reimers (2015b), The sedimentary flux of dissolved rare earth elements to the ocean, *Geochim. Cosmochim. Acta*, *154*, 186–200, doi:10.1016/j.gca.2015.01.010.

Abouchami, W. et al. (2013), Geochemical and isotopic characterization of the bodélé depression dust source and implications for transatlantic dust transport to the Amazon basin, *Earth Planet. Sci. Lett.*, *380*, 112–123, doi:10.1016/j.epsl.2013.08.028.

Abouchami, W., and M. Zabel (2003), Climate forcing of the Pb isotope record of terrigenous input into the Equatorial Atlantic, *Earth Planet. Sci. Lett.*, *213*(3-4), 221–234, doi:10.1016/S0012-821X(03)00304-2.

Abouchami, W., S. L. Goldstein, S. J. G. Gazer, A. Eisenhauer, and A. Mangini (1997), Secular changes of lead and neodymium in central Pacific seawater recorded by a Fe-Mn crust, *Geochim. Cosmochim. Acta*, *61*(18), 3957–3974, doi:10.1016/S0016-7037(97)00218-4.

Abouchami, W., S. J. . S. Galer, and A. Koschinsky (1999), Pb and Nd isotopes in NE Atlantic Fe-Mn crusts: Proxies for trace metal paleosources and paleocean circulation, *Geochim. Cosmochim.*, *63*(10), 1489–1505, doi:10.1016/S0016-7037(99)00068-X.

Abu-Zied, R. H., E. J. Rohling, F. J. Jorissen, C. Fontanier, J. S. L. Casford, and S. Cooke (2008), Benthic foraminiferal response to changes in bottom-water oxygenation and organic carbon flux in the eastern Mediterranean during LGM to Recent times, *Mar. Micropaleontol.*, *67*(1-2), 46–68, doi:10.1016/j.marmicro.2007.08.006.

Adams, C. G., R. H. Benson, R. B. Kidd, W. B. F. Ryan, and R. C. Wright (1977), The Messinian salinity crisis and evidence of late Miocene eustatic changes in the world ocean, *Nature*, *269*, 383–386, doi:10.1038/269383a0.

Van Aken, H. M. (2001), The hydrography of the mid-latitude Northeast Atlantic Ocean - Part III: The subducted thermocline water mass, *Deep. Res. Part I Oceanogr. Res. Pap.*, *48*, 237–267, doi:10.1016/S0967-0637(00)00059-5.

Albarede, F., and A. Michard (1987), Evidence for slowly changing 87Sr/86Sr in runoff from freshwater limestones of southern France, *Chem. Geol.*, *64*(1-2), 55–65, doi:10.1016/0009-2541(87)90151-3.

Ambar, I., N. Serra, M. . J. Brogueira, G. Cabeçadas, F. Abrantes, P. Freitas, C. Gonçalves, and N. Gonzalez (2002), Physical, chemical and sedimentological aspects of the Mediterranean outflow off Iberia, *Deep. Res. Part II Top. Stud. Oceanogr.*, *49*(19), 4163–4177, doi:10.1016/S0967-0645(02)00148-0.

Andersen, M. B., C. H. Stirling, B. Zimmermann, and A. N. Halliday (2010), Precise determination of the open ocean 234U/238U composition, *Geochemistry, Geophys. Geosystems*, *11*(12), doi:10.1029/2010GC003318.

Andersen, M. B., S. Romaniello, D. Vance, S. H. Little, R. Herdman, and T. W. Lyons (2014), A modern framework for the interpretation of 238U/235U in studies of ancient ocean redox, *Earth Planet. Sci. Lett.*, *400*, 184–194, doi:10.1016/j.epsl.2014.05.051.

van Assen, E., K. F. Kuiper, N. Barhoun, W. Krijgsman, and F. J. Sierro (2006), Messinian astrochronology of the Melilla Basin: Stepwise restriction of the Mediterranean–Atlantic connection through Morocco, *Palaeogeogr. Palaeoclimatol. Palaeoecol.*, *238*(1-4), 15–31, doi:10.1016/j.palaeo.2006.03.014.

Aufgebauer, A., and T. McCann (2010), Messinian to Pliocene transition in the deep part of the Sorbas Basin, SE Spain – a new description of the depositional environment during the Messinian Salinity Crisis, *Neues Jahrb. für Geol. und Paläontologie - Abhandlungen*, *259*(2), 177–195, doi:10.1127/0077-7749/2010/0112.

Bacon, M. P., D. W. Spencer, and P. G. Brewer (1976), 210Pb/226Ra and 210Po/210Pb disequilibria in seawater and suspended particulate matter, *Earth Planet. Sci. Lett.*, *32*, 277–296.

Bacon, M. P., W. Roether, and H. Elderfield (1988), Tracers of Chemical Scavenging in the Ocean: Boundary Effects and Large-Scale Chemical Fractionation [and Discussion], *Philos. Trans. R. Soc. A Math. Phys. Eng. Sci.*, *325*(1583), 147–160, doi:10.1098/rsta.1988.0048.

Baggley, K. A. (2000), The late Tortonian-Early Messinian foraminiferal record of the Abad

Member (Turre formation), Sorbas Basin, Almería, South-East Spain, *Palaeontology*, *43*(6), 1069–1112, doi:10.1111/1475-4983.00162.
Baker, J., D. Peate, T. Waight, and C. Meyzen (2004), Pb isotopic analysis of standards and samples using a 207Pb-204Pb double spike and thallium to correct for mass bias with a double-focusing MC-ICP-MS, *Chem. Geol.*, *211*(3-4), 275–303, doi:10.1016/j.chemgeo.2004.06.030.
Baker, P. A., J. M. Gieskes, and H. Elderfield (1982), Diagenesis of carbonates in deep-sea sediments - evidence from Sr/Ca ratios and interstitial dissolved Sr data., *J. Sediment. Petrol.*, *52*(1), 71–82, doi:10.1306/212F7EE1-2B24-11D7-8648000102C1865D.
Baringer, M. O., and J. F. Price (1999), A review of the physical oceanography of the Mediterranean outflow, *Mar. Geol.*, *155*(1-2), 63–82, doi:10.1016/S0025-3227(98)00141-8.
Barnaba, F., and G. P. Gobbi (2004), Aerosol seasonal variability over the Mediterranean region and relative impact of maritime, continental and Saharan dust particles over the basin from MODIS data in the year 2001, *Atmos. Chem. Phys. Discuss.*, *4*(4), 4285–4337, doi:10.5194/acpd-4-4285-2004.
Barrett, T. J., P. N. Taylor, and J. Lugowski (1987), Metalliferous sediments from DSDP Leg 92: The East Pacific Rise transect, *Geochim. Cosmochim. Acta*, *51*, 2241–2253.
Basak, C., E. E. Martin, and G. D. Kamenov (2011), Seawater Pb isotopes extracted from Cenozoic marine sediments, *Chem. Geol.*, *286*(3-4), 94–108, doi:10.1016/j.chemgeo.2011.04.007.
Baumgarten, H., and T. Wonik (2014), Cyclostratigraphic studies of sediments from Lake Van (Turkey) based on their uranium contents obtained from downhole logging and paleoclimatic implications, *Int. J. Earth Sci.*, *104*, 1639–1654, doi:10.1007/s00531-014-1082-x.
Bayon, G., C. R. German, R. M. Boella, J. A. Milton, R. N. Taylor, and R. W. Nesbitt (2002), An improved method for extracting marine sediment fractions and its application to Sr and Nd isotopic analysis, *Chem. Geol.*, *187*, 179–199, doi:10.1016/S0009-2541(01)00416-8.
Bayon, G., C. R. German, K. W. Burton, R. W. Nesbitt, and N. Rogers (2004), Sedimentary Fe-Mn oxyhydroxides as paleoceanographic archives and the role of aeolian flux in regulating oceanic dissolved REE, *Earth Planet. Sci. Lett.*, *224*(3-4), 477–492, doi:10.1016/j.epsl.2004.05.033.
Beets, C. J., and M. J. De Ruig (1992), 87Sr/86Sr dating of coralline algal limestones and its implications for the tectono-stratigraphic evolution of the eastern Prebetic (Spain), *Sediment. Geol.*, *78*(3-4), 233–250, doi:10.1016/0037-0738(92)90022-J.
Begemann, F., K. R. Ludwig, G. W. Lugmair, K. Min, L. E. Nyquist, P. J. Patchett, P. R. Renne, C. Y. Shih, I. M. Villa, and R. J. Walker (2001), Call for an improved set of decay constants for geochronological use, *Geochim. Cosmochim. Acta*, *65*(1), 111–121, doi:10.1016/S0016-7037(00)00512-3.
Benito, R., J. López-Ruiz, J. M. Cebriá, J. Hertogen, M. Doblas, R. Oyarzun, and D. Demaiffe (1999), Sr and O isotope constraints on source and crustal contamination in the high-K calc-alkaline and shoshonitic neogene volcanic rocks of SE Spain, *Lithos*, *46*(4), 773–802, doi:10.1016/S0024-4937(99)00003-1.
Benson, R., K. R.-E. Bied, and G. Bonaduce (1991), An important current reversal (influx) in the Rifian corridor (Morocco) at the Tortonian-Messinian boundary: the end of the Tethys Ocean, *Paleoceanography*, *6*(1), 164–192, doi:10.1029/90PA00756.
Bergametti, G., L. Gomes, G. Coudé-Gaussen, P. Rognon, and M.-N. Le Coustumer (1989), African dust observed over Canary Islands: Source-regions identification and transport pattern for some summer situations, *J. Geophys. Res.*, *94*(D12), 14855–14864, doi:10.1029/JD094iD12p14855.
Berger, A., and M. F. Loutre (1992), Astronomical solutions for paleoclimate studies over the last 3 million years, *Earth Planet. Sci. Lett.*, *111*(2-4), 369–382, doi:10.1016/0012-821X(92)90190-7.
Berggren, A. M., J. Beer, G. Possnert, A. Aldahan, P. Kubik, M. Christl, S. J. Johnsen, J. Abreu, and B. M. Vinther (2009), A 600-year annual 10Be record from the NGRIP ice core, Greenland, *Geophys. Res. Lett.*, *36*(11), 1–5, doi:10.1029/2009GL038004.
Betzler, C., J. C. Braga, J. M. Martín, I. M. Sánchez-Almazo, and S. Lindhorst (2006), Closure of a seaway: stratigraphic record and facies (Guadix basin, Southern Spain), *Int. J. Earth Sci.*, *95*(5), 903–910, doi:10.1007/s00531-006-0073-y.
Bigg, G. R., T. D. Jickells, P. S. Liss, and T. J. Osborn (2003), The role of the oceans in climate, *Int. J. Climatol.*, *23*(10), 1127–1159, doi:10.1002/joc.926.

Bijma, J., W. W. Faber, and C. Hemleben (1990), Temperature and salinity limits for growth and survival of some planktonic foraminifers in laboratory cultures, *J. Foraminifer. Res.*, *20*(2), 95–116, doi:10.2113/gsjfr.20.2.95.

Blanc, P. L. (2000), Of sills and straits: A quantitative assessment of the Messinian Salinity Crisis, *Deep. Res. Part I Oceanogr. Res. Pap.*, *47*(8), 1429–1460, doi:10.1016/S0967-0637(99)00113-2.

von Blanckenburg, F., R. K. O'Nions, N. S. Belshaw, A. Gibb, and J. R. Hein (1996), Global distribution of beryllium isotopes in deep ocean water as derived from Fe-Mn crusts, *Earth Planet. Sci. Lett.*, *141*(1-4), 213–226, doi:10.1016/0012-821X(96)00059-3.

von Blanckenburg, F., J. Bouchez, D. E. Ibarra, and K. Maher (2015), Stable runoff and weathering fluxes into the oceans over Quaternary climate cycles, *Nat. Geosci.*, *8*(July), doi:10.1038/ngeo2452.

Blaser, P., J. Lippold, M. Gutjahr, N. Frank, J. M. Link, and M. Frank (2016), Extracting foraminiferal Nd isotope signatures from bulk deep sea sediment by chemical leaching, *Chem. Geol.*, *439*, 189–204, doi:10.1016/j.chemgeo.2016.06.024.

Blum, J. D., and Y. Erel (1997), Rb-Sr isotope systematics of a granitic soil chronosequence: The importance of biotite weathering, *Geochim. Cosmochim. Acta*, *61*(15), 3193–3204, doi:10.1016/S0016-7037(97)00148-8.

Blum, J. D., and Y. Erel (1997), Rb-Sr isotope systematics of a granitic soil chronosequence: The importance of biotite weathering, *Geochim. Cosmochim. Acta*, *61*(15), 3193–3204, doi:10.1016/S0016-7037(97)00148-8.

Blum, J. D., C. A. Gazis, A. D. Jacobson, and C. P. Chamberlain (1998), Carbonate versus silicate weathering in the Raikhot watershed within the High Himalayan Crystalline Series, *Geology*, *26*(5), 411–414, doi:10.1130/0091-7613(1998)026<0411:CVSWIT>2.3.CO.

Bollhofer, A., and K. J. R. Rosman (2001), Isotopic source signatures for atmospheric lead: The Northern Hemisphere, *Geochim. Cosmochim. Acta*, *65*(11), 1727–1740.

Böhm, E., J. Lippold, M. Gutjahr, M. Frank, P. Blaser, B. Antz, J. Fohlmeister, N. Frank, M. B. Andersen, and M. Deininger (2015), Strong and deep Atlantic meridional overturning circulation during the last glacial cycle, *Nature*, *517*(7534), 73–76, doi:10.1038/nature14059.

Bosmans, J. H. C., F. J. Hilgen, E. Tuenter, and L. J. Lourens (2015a), Obliquity forcing of low-latitude climate, *Clim. Past*, *11*(10), 1335–1346, doi:10.5194/cp-11-1335-2015.

Bosmans, J. H. C., S. S. Drijfhout, E. Tuenter, F. J. Hilgen, and L. J. Lourens (2015b), Response of the North African summer monsoon to precession and obliquity forcings in the EC-Earth GCM, *Clim. Dyn.*, *44*(1-2), 279–297, doi:10.1007/s00382-014-2260-z.

Bosmans, J. H. C., S. S. Drijfhout, E. Tuenter, F. J. Hilgen, L. J. Lourens, and E. J. Rohling (2015c), Precession and obliquity forcing of the freshwater budget over the Mediterranean, *Quat. Sci. Rev.*, *123*, 16–30, doi:10.1016/j.quascirev.2015.06.008.

Bradshaw, C. D., D. J. Lunt, R. Flecker, U. Salzmann, M. J. Pound, A. M. Haywood, and J. T. Eronen (2012), The relative roles of CO2 and palaeogeography in determining late Miocene climate: Results from a terrestrial model-data comparison, *Clim. Past*, *8*, 1257–1285, doi:10.5194/cp-8-1257-2012.

Braga, J. C., and J. M. Martin (1996), Geometries of reef advance in response to relative sea-level changes in a Messinian (uppermost Miocene) fringing reef (Cariatiz reef, Sorbas Basin, SE Spain), *Sediment. Geol.*, *107*, 61–81, doi:10.1016/S0037-0738(96)00019-X.

Braga, J. C., J. M. Martin, and J. L. Wood (2001), Submarine lobes and feeder channels of redeposited, temperate carbonate and mixed siliciclastic-carbonate platform deposits (Vera Basin, Almeria, southern Spain), *Sedimentology*, *48*, 99–116, doi:10.1046/j.1365-3091.2001.00353.x.

Brass, G. W. (1976), The variation of the marine 87Sr/86Sr ratio during Phanerozoic time: interpretation using a flux model, *Geochim. Cosmochim. Acta*, *40*, 721–730, doi:10.1016/0016-7037(76)90025-9.

Broecker, W. S., and T.-H. Peng (1982), *Tracers in the Sea*, Lamont-Doherty Geological Observatory, Columbia University, Pallisades, NY.

Bryden, H. L., and T. H. Kinder (1991), Steady two-layer exchange through the Strait of Gibraltar, *Deep Sea Res. Part A. Oceanogr. Res. Pap.*, *38*, S445–S463, doi:10.1016/S0198-0149(12)80020-3.

Bryden, H. L., and H. M. Stommel (1984), Limiting processes that determine basic features of the circulation in the Mediterranean Sea, *Oceanol. Acta*, *7*(3), 289–296.

Camerlenghi, A. et al. (2014), Uncovering a Salt Giant. Deep-Sea Record of Mediterranean Messinian Events (DREAM) multi-phase drilling project, *Geophys. Res. Abstr.*, *16*, 7443.
Cantalejo, B., and K. T. Pickering (2015), Orbital forcing as principal driver for fine-grained deep-marine siliciclastic sedimentation, Middle-Eocene Ainsa Basin, Spanish Pyrenees, *Palaeogeogr. Palaeoclimatol. Palaeoecol.*, *421*, 24–47, doi:10.1016/j.palaeo.2015.01.008.
Carmignani, L., and R. Kligfield (1990), Crustal extension in the northern Apennines: the transition from compression to extension in the Alpi Apuane core complex, *Tectonics*, *9*(6), 1275–1303.
Chabaux, F., A. S. Cohen, R. K. Onions, and J. R. Hein (1995), 238U-234U-230Th chronometry of FeMn crusts: Growth processes and recovery of thorium isotopic ratios of seawater, *Geochim. Cosmochim. Acta*, *59*(3), 633–638, doi:10.1016/0016-7037(94)00379-Z.
Charbonnier, G. et al. (2012), Reconstruction of the Nd isotope composition of seawater on epicontinental seas: Testing the potential of Fe-Mn oxyhydroxide coatings on foraminifera tests for deep-time investigations, *Geochim. Cosmochim. Acta*, *99*, 39–56, doi:10.1016/j.gca.2012.09.012.
Chen, J. H., R. L. Edwards, and G. J. Wasserburg (1986), 238U, 234U and 232Th in seawater, *Earth Planet. Sci. Lett.*, *80*, 241–251.
Chen, J. H., G. J. Wasserburg, K. L. Von Damm, and J. M. Edmond (1986), The U-Th-Pb systematics in hot springs on the East Pacific Rise at 21N and Guaymas Basin, *Geochim. Cosmochim. Acta*, *50*(11), 2467–2479, doi:10.1016/0016-7037(86)90030-X.
Cheng, H. et al. (2013), Improvements in Th-230 dating, Th-230 and U-234 half-life values, and U-Th isotopic measurements by multi-collector inductively coupled plasma mass spectrometry, *Earth Planet. Sci. Lett.*, *371*, 82–91, doi:10.1016/j.epsl.2013.04.006.
Chiapello, I., G. Bergametti, B. Chatenet, P. Bousquet, F. Dulac, and E. Santos Soares (1997), Origins of African dust transported over the northeastern tropical Atlantic, *J. Geophys. Res.*, *102*(D12), 13,701–713,709, doi:10.1029/97JD00259.
Chmeleff, J., F. von Blanckenburg, K. Kossert, and D. Jakob (2010), Determination of the 10Be half-life by multicollector ICP-MS and liquid scintillation counting, *Nucl. Instruments Methods Phys. Res. Sect. B Beam Interact. with Mater. Atoms*, *268*(2), 192–199, doi:10.1016/j.nimb.2009.09.012.
Chow, T. J., and C. C. Patterson (1962), The occurrence and significance of lead isotopes in pelagic sediments, *Geochim. Cosmochim. Acta*, *26*(2), 263–308, doi:10.1016/0016-7037(62)90016-9.
Christensen, J. N., A. N. Halliday, L. V. Godfrey, J. R. Hein, and D. K. Rea (1997), Climate and Ocean Dynamics and the Lead Isotopic Records in Pacific Ferromanganese Crusts, *Science (80-.).*, *277*(5328), 913–918, doi:10.1126/science.277.5328.913.
CIESM (2008), The Messinian Salinity Crisis from mega-deposits to microbiology - A consensus report, in *No. 33 in CIESM Workshop Monographs*, edited by F. Briand, p. 168, CIESM, Monaco.
Clark, P. U., D. Archer, D. Pollard, J. D. Blum, J. A. Rial, V. Brovkin, A. C. Mix, N. G. Pisias, and M. Roy (2006), The middle Pleistocene transition: characteristics, mechanisms, and implications for long-term changes in atmospheric pCO2, *Quat. Sci. Rev.*, *25*, 3150–3184, doi:10.1016/j.quascirev.2006.07.008.
Claude, C., G. Suhr, A. W. Hofmann, and A. Koschinsky (2005), U-Th chronology and paleoceanographic record in a Fe-Mn crust from the NE Atlantic over the last 700 ka, *Geochim. Cosmochim. Acta*, *69*(20), 4845–4854, doi:10.1016/j.gca.2005.05.016.
Clauzon, G. et al. (2015), New insights on the Sorbas Basin (SE Spain): the onshore reference of the Messinian Salinity Crisis, *Mar. Pet. Geol.*, *66*, 71–100, doi:10.1016/j.marpetgeo.2015.02.016.
Cochran, J. K. (1992), The oceanic chemistry of the uranium and thorium series nuclides, in *Uranium-series disequilibrium: Applications to earth, marine, and environmental sciences*, edited by M. Ivanovich and R. S. Harmon, pp. 334–395.
Cochran, J. K., A. E. Carey, E. R. Sholkovitz, and L. D. Surprenant (1986), The Geochemistry of Uranium and Thorium in Coastal Marine-Sediments and Sediment Pore Waters, *Geochim. Cosmochim. Acta*, *50*(5), 663–680.
Colin, C. et al. (2014), Late Miocene to early Pliocene climate variability off NW Africa (ODP Site 659), *Palaeogeogr. Palaeoclimatol. Palaeoecol.*, *401*, 81–95, doi:10.1016/j.palaeo.2014.02.015.
Conticelli, S. et al. (2009), Trace elements and Sr-Nd-Pb isotopes of K-rich, shoshonitic, and calc-

alkaline magmatism of the Western Mediterranean Region: Genesis of ultrapotassic to calc-alkaline magmatic associations in a post-collisional geodynamic setting, *Lithos*, *107*(1-2), 68–92, doi:10.1016/j.lithos.2008.07.016.

Coude-Gaussen, G., P. Rognon, G. Bergametti, L. Gomes, B. Strauss, J. M. Gros, and M. N. Le Coustumer (1987), Saharan dust on Fuerteventura Island (Canaries): chemical and mineralogical characteristics, air mass trajectories, and probable sources, *J. Geophys. Res.*, *92*(D8), 9753–9771.

Criado-Aldeanueva, F., J. García-Lafuente, J. M. Vargas, J. Del Río, a. Vázquez, a. Reul, and a. Sánchez (2006), Distribution and circulation of water masses in the Gulf of Cadiz from in situ observations, *Deep. Res. Part II Top. Stud. Oceanogr.*, *53*(11-13), 1144–1160, doi:10.1016/j.dsr2.2006.04.012.

Craig, H., S. Krishnaswami, and B. L. K. Somayajulu (1973), 210Pb-226Ra: radioactive disequilibrium in the deep sea, *Earth Planet. Sci. Lett.*, *17*, 295–305.

Debenedetti, A. (1976), Messinian salt deposits in the Mediterranean: evaporites or precipitates?, *Boll. della Soc. Geol. Ital.*, *95*(5), 941–948.

Decima, A., and F. C. Wezel (1973), Late Miocene evaporites of the Central Sicilian Basin, Italy, DSDP Leg 13, in *Initial Reports of the Deep Sea Drilling Project, Volume XIII*, edited by W. B. F. Ryan, K. J. Hsü, M. B. Cita, P. Dumitrica, J. M. Lort, W. Mayne, W. D. Nesteroff, G. Pautot, H. Stradner, and F. C. Wezel, pp. 1234–1256, U.S. Government Printing Office, Washington.

Dela Pierre, F. et al. (2011), The record of the Messinian salinity crisis in the Tertiary Piedmont Basin (NW Italy): The Alba section revisited, *Palaeogeogr. Palaeoclimatol. Palaeoecol.*, *310*(3-4), 238–255, doi:10.1016/j.palaeo.2011.07.017.

Dickin, A. P. (2005), *Radiogenic Isotope Geology*, 2nd Edition, Cambridge University Press.

Do Couto, D., C. Gumiaux, L. Jolivet, R. Augier, N. Lebret, N. Folcher, G. Jouannic, J.-P. Suc, and C. Gorini (2014), 3D modelling of the Sorbas Basin (Spain): New constraints on the Messinian Erosional Surface morphology, *Mar. Pet. Geol.*, 1–16, doi:10.1016/j.marpetgeo.2014.12.011.

Dronkert, H. (1976), Late Miocene evaporites in the Sorbas Basin and adjoining areas, *Mem. Soc. Geol. Italy*, 341–361.

Duce, R. A. et al. (1991), The atmospheric input of trace species to the world ocean, *Global Biogeochem. Cycles*, *5*(3), 193–259, doi:10.1029/91gb01778.

Duggen, S., K. Hoernle, A. Klügel, J. Geldmacher, M. Thirlwall, F. Hauff, D. Lowry, and N. Oates (2008), Geochemical zonation of the Miocene Alborán Basin volcanism (westernmost Mediterranean): Geodynamic implications, *Contrib. to Mineral. Petrol.*, *156*, 577–593, doi:10.1007/s00410-008-0302-4.

Duggen, S., K. Hoernle, and P. Van Den Bogaard (2003), Deep roots of the Messinian salinity crisis, *Nature*, *422*(April), doi:10.1038/nature01551.1.

Elderfield, H. (1986), Strontium isotope stratigraphy, *Palaeogeogr. Palaeoclimatol. Palaeoecol.*, 57, 71-90, doi: 10.1016/0031-0182(86)90007-6.

Elmore, A. C., A. M. Piotrowski, J. D. Wright, and A. E. Scrivner (2011), Testing the extraction of past seawater Nd isotopic composition from North Atlantic deep sea sediments and foraminifera, *Geochemistry, Geophys. Geosystems*, *12*(9), n/a–n/a, doi:10.1029/2011GC003741.

Emeis, K. C., U. Struck, H. M. Schulz, R. Rosenberg, S. Bernasconi, H. Erlenkeuser, T. Sakamato, and F. Martinez-Ruiz (2000), Temperature and salinity variationsof Mediterranea Sea surface waters over the last 16,000 years from records of planktonic stable oxygen isotopes and alkenone unsaturation ratios, *Palaeogeogr. Palaeoclimatol. Palaeoecol.*, *158*, 259–280, doi:10.1016/S0031-0182(00)00053-5.

Engelstaedter, S., I. Tegen, and R. Washington (2006), North African dust emissions and transport, *Earth-Science Rev.*, *79*(1-2), 73–100, doi:10.1016/j.earscirev.2006.06.004.

English, N. B., J. Quade, P. G. DeCelles, and C. N. Garzione (2000), Geologic control of Sr and major element chemistry in Himalayan Rivers, Nepal, *Geochim. Cosmochim. Acta*, *64*(15), 2549–2566, doi:10.1016/S0016-7037(00)00379-3.

Erel, Y., Y. Harlavan, and J. D. Blum (1994), Lead isotope systematics of granitoid weathering, *Geochim. Cosmochim. Acta*, *58*(23), 5299–5306, doi:10.1016/0016-7037(94)90313-1.

Esteban, M., J. C. Braga, J. Martin, and C. De Santisteban (1996), Western Mediterranean reef complexes, in *Models for Carbonate Stratigraphy from Miocene Reef Complexes of*

Mediterranean Regions, SEPM Concepts in Sedimentology and Paleontology #5, pp. 55–72, SEPM (Society for Sedimentary Geology), Tulsa.

Evans, N. P., A. V. Turchyn, F. Gázquez, R. R. Bontognali, H. J. Chapman, and D. A. Hodell (2015), Coupled measurements of δ18O and δD of hydration water and salinity of fluid inclusions in gypsum from the Messinian Yesares Member , Sorbas Basin (SE Spain), *Earth Planet. Sci. Lett.*, *430*, 499–510, doi:10.1016/j.epsl.2015.07.071.

Fauquette, S. et al. (2006), How much did climate force the Messinian salinity crisis? Quantified climatic conditions from pollen records in the Mediterranean region, *Palaeogeogr. Palaeoclimatol. Palaeoecol.*, *238*(1-4), 281–301, doi:10.1016/j.palaeo.2006.03.029.

Fenton, M., S. Geiselhart, E. J. Rohling, and C. Hemleben (2000), Aplanktonic zones in the Red Sea, *Mar. Micropaleontol.*, *40*(3), 277–294, doi:10.1016/S0377-8398(00)00042-6.

Filippelli, G. M., F. J. Sierro, J. a. Flores, a. Vázquez, R. Utrilla, M. Pérez-Folgado, and J. C. Latimer (2003), A sediment-nutrient-oxygen feedback responsible for productivity variations in Late Miocene sapropel sequences of the western Mediterranean, *Palaeogeogr. Palaeoclimatol. Palaeoecol.*, *190*, 335–348, doi:10.1016/S0031-0182(02)00613-2.

Flanagan, F. J., and D. Gottfried (1980), *USGS Rock Standards, III: Manganese-Nodule Reference Samples USGS-Nod-A-1 and USGS-Nod-P-1*, Washington, D.C.

Flecker, R., and R. M. Ellam (1999), Distinguishing climatic and tectonic signals in the sedimentary successions of marginal basins using Sr isotopes: an example from the Messinian salinity crisis, Eastern Mediterranean, *J. Geol. Soc. London.*, *156*(4), 847–854, doi:10.1144/gsjgs.156.4.0847.

Flecker, R., and R. M. Ellam (2006), Identifying Late Miocene episodes of connection and isolation in the Mediterranean–Paratethyan realm using Sr isotopes, *Sediment. Geol.*, *188-189*, 189–203, doi:10.1016/j.sedgeo.2006.03.005.

Flecker, R., R. M. Ellam, C. Muller, A. Poisson, A. Robertson, and J. Turner (1998), Application of Sr isotope stratigraphy and sedimentary analysis to the origin and evolution of the Neogene basins in the Isparta Angle, southern Turkey, *Tectonophysics*, *298*, 83–101.

Flecker, R., S. de Villiers, and R. M. Ellam (2002), Modelling the effect of evaporation on the salinity - 87Sr/86Sr relationship in modern and ancient marginal-marine systems: the Mediterranean Messinian Salinity Crisis, *Earth Planet. Sci. Lett.*, *203*, 221–233, doi:10.1016/S0012-821X(02)00848-8.

Flecker, R. et al. (2015), Evolution of the Late Miocene Mediterranean–Atlantic gateways and their impact on regional and global environmental change, *Earth-Science Rev.*, *150*, 365–392, doi:10.1016/j.earscirev.2015.08.007.

van de Flierdt, T., M. Frank, A. N. Halliday, J. R. Hein, B. Hattendorf, D. Günther, and P. W. Kubik (2003), Lead isotopes in North Pacific deep water – implications for past changes in input sources and circulation patterns, *Earth Planet. Sci. Lett.*, *209*(1-2), 149–164, doi:10.1016/S0012-821X(03)00069-4.

van de Flierdt, T., M. Frank, A. N. Halliday, J. R. Hein, B. Hattendorf, D. Günther, and P. W. Kubik (2004), Tracing the history of submarine hydrothermal inputs and the significance of hydrothermal hafnium for the seawater budget - A combined Pb-Hf-Nd isotope approach, *Earth Planet. Sci. Lett.*, *222*, 259–273, doi:10.1016/j.epsl.2004.02.025.

van de Flierdt, T., K. Pahnke, H. Amakawa, P. Andersson, C. Basak, B. Coles, C. Colin, K. Crocket, M. Frank, and N. Frank (2012), GEOTRACES intercalibration of neodymium isotopes and rare earth element concentrations in seawater and suspended particles. Part 1: reproducibility of results for the international intercomparison, *Limnol. Oceanogr. Methods*, *10*, 234–251, doi:10.4319/lom.2012.10.234.

Fortuin, A. R., J. M. D. Kelling, and T. B. Roep (1995), The enigmatic Messinian-Pliocene section of Cuevas del Almanzora (Vera Basin, SE Spain) revisited—erosional features and strontium isotope ages, *Sediment. Geol.*, *97*(3-4), 177–201, doi:10.1016/0037-0738(95)00009-W.

Foster, G. L., and D. Vance (2006), Negligible glacial–interglacial variation in continental chemical weathering rates, *Nature*, *444*(7121), 918–921, doi:10.1038/nature05365.

Frank, M. (2002), Radiogenic isotopes: tracers of past ocean circulation and erosional input, *Rev. Geophys.*, *40*(1), 1–38, doi:10.1029/2000RG000094.

Frank, M., R. K. O'nions, J. R. Hein, and V. K. Banakar (1999a), 60 Myr records of major elements and Pb – Nd isotopes from hydrogenous ferromanganese crusts: Reconstruction of seawater paleochemistry, *Geochim. Cosmochim. ...*, *63*(11), 1689–1708.

Frank, M., B. C. Reynolds, and R. Keith O'Nions (1999b), Nd and Pb isotopes in atlantic and

Pacific water masses before and after closure of the Panama gateway, *Geology*, *27*(12), 1147–1150, doi:10.1130/0091-7613(1999)027<1147:NAPIIA>2.3.CO;2.
Frank, M., T. van de Flierdt, A. N. Halliday, P. . Kubik, B. Hattendorf, and D. Gunther (2003), Evolution of deepwater mixing and weathering inputs in the central Atlantic Ocean over the past 33 Myr, *Paleoceanography*, *18*(4), doi:10.1029/2003PA000919.
Frigola, J., A. Moreno, I. Cacho, M. Canals, F. J. Sierro, J. A. Flores, and J. O. Grimalt (2008), Evidence of abrupt changes in Western Mediterranean Deep Water circulation during the last 50kyr: A high-resolution marine record from the Balearic Sea, *Quat. Int.*, *181*(1), 88–104, doi:10.1016/j.quaint.2007.06.016.
Frost, C. D., R. K. O'Nions, and S. L. Goldstein (1986), Mass balance for Nd in the Mediterranean Sea, *Chem. Geol.*, *55*(1-2), 45–50, doi:10.1016/0009-2541(86)90126-9.
Gadde, R. R., and H. A. Laitinen (1974), Studies of heavy metal adsorption by hydrous Iron and Manganese oxides, *Anal. Chem.*, *46*(13), 2022–2026, doi:10.1021/ac60349a004.
Garcés, M., W. Krijgsman, and J. Agustí (1998), Chronology of the late Turolian deposits of the Fortuna basin (SE Spain): implications for the Messinian evolution of the eastern Betics, *Earth Planet. Sci. Lett.*, *163*, 69–81.
Garcia-Lafuente, J., A. Sanchez-Roman, C. Naranjo, and J. C. Sanchez-Garrido (2011), The very first transformation of the Mediterranean outflow in the Strait of Gibraltar, *J. Geophys. Res. Ocean.*, *116*(7), 1–7, doi:10.1029/2011JC006967.
Ghoneim, E., M. Benedetti, and F. El-Baz (2012), An integrated remote sensing and GIS analysis of the Kufrah Paleoriver, Eastern Sahara, *Geomorphology*, *139-140*, 242–257, doi:10.1016/j.geomorph.2011.10.025.
Gladstone, R., R. Flecker, P. Valdes, D. Lunt, and P. Markwick (2007), The Mediterranean hydrologic budget from a Late Miocene global climate simulation, *Palaeogeogr. Palaeoclimatol. Palaeoecol.*, *251*(2), 254–267, doi:10.1016/j.palaeo.2007.03.050.
Goldstein, S. L., R. K. Onions, and P. J. Hamilton (1984), A Sm-Nd isotopic study of atmospheric dusts and particulates from major river systems, , *70*, 221–236, doi:10.1016/0012-821X(84)90007-4.
Goldstein, S. J., and S. B. Jacobsen (1987), The Nd and Sr isotopic systematics of river-water dissolved material: implications for the sources of Nd and Sr in seawater, *Chem. Geol.*, *66*, 245–272, doi:10.1016/0168-9622(87)90045-5.
Goldstein, S. L., and S. R. Hemming (2003), Long-lived isotopic tracers in oceanography, paleoceanography, and ice-sheet dynamics, *Treatise on geochemistry*, 453–489, doi:10.1016/B0-08-043751-6/06179-X.
Goudie, A. S., and N. J. Middleton (2001), Saharan dust storms: Nature and Consecuences, *Earth-Science Rev.*, *56*, 179–204.
Govers, R. (2009), Choking the Mediterranean to dehydration: The Messinian salinity crisis, *Geology*, *37*(2), 167–170, doi:10.1130/G25141A.1. Gradstein, F. M., J. G. Ogg, M. D. Schmitz, and G. M. Ogg (2012), *The Geologic Time Scale*, Elsevier B.V., Boston.
Greaves, M., P. Statham, and H. Elderfield (1994), Rare earth element mobilization from marine atmospheric dust into seawater, *Mar. Chem.*, *46*, 255–260.
Greaves, M. J., M. Rudnicki, and H. Elderfield (1991), Rare earth elements in the Mediterranean Sea and mixing in the Mediterranean outflow, *Earth Planet. Sci. Lett.*, *103*(1-4), 169–181, doi:10.1016/0012-821X(91)90158-E.
Griffin, D. L. (2002), Aridity and humidity: Two aspects of the late Miocene climate of North Africa and the Mediterranean, *Palaeogeogr. Palaeoclimatol. Palaeoecol.*, *182*(1-2), 65–91, doi:10.1016/S0031-0182(01)00453-9.
Griffin, D. L. (2006), The late Neogene Sahabi rivers of the Sahara and their climatic and environmental implications for the Chad Basin, *J. Geol. Soc. London.*, *163*, 905–921, doi:10.1144/0016-76492005-049.
Griffin, D. L. (2011), The late neogene sahabi rivers of the sahara and the hamadas of the eastern libya-chad border area, *Palaeogeogr. Palaeoclimatol. Palaeoecol.*, *309*(3-4), 176–185, doi:10.1016/j.palaeo.2011.05.007.
Grousset, F. E., and P. E. Biscaye (2005), Tracing dust sources and transport patterns using Sr, Nd and Pb isotopes, *Chem. Geol.*, *222*(3-4), 149–167, doi:10.1016/j.chemgeo.2005.05.006.
Grousset, F. E., P. E. Biscaye, A. Zindler, J. Prospero, and R. Chester (1988), Neodymium isotopes as tracers in marine sediments and aerosols: North Atlantic, *Earth Planet. Sci. Lett.*, *87*(4), 367–378, doi:10.1016/0012-821X(88)90001-5.

Grousset, F. E., F. Henry, J. F. Minster, and a. Monaco (1990), Nd isotopes as tracers in water column particles: the western Mediterranean Sea, *Mar. Chem.*, *30*, 389–407, doi:10.1016/0304-4203(90)90083-O.

Grousset, F. E., P. Rognon, G. Coudé-Gaussen, and P. Pédemay (1992), Origins of peri-Saharan dust deposits traced by their Nd and Sr isotopic composition, *Palaeogeogr. Palaeoclimatol. Palaeoecol.*, *93*(3-4), 203–212, doi:10.1016/0031-0182(92)90097-O.

Gutjahr, M. (2006), Reconstruction of changes in ocean circulation and continental weathering using radiogenic isotopes in marine sediments, ETH.

Gutjahr, M., M. Frank, C. Stirling, V. Klemm, T. van de Flierdt, and A. N. Halliday (2007), Reliable extraction of a deepwater trace metal isotope signal from Fe–Mn oxyhydroxide coatings of marine sediments, *Chem. Geol.*, *242*(3-4), 351–370, doi:10.1016/j.chemgeo.2007.03.021.

Gutjahr, M., M. Frank, C. H. Stirling, L. D. Keigwin, and A. N. Halliday (2008), Tracing the Nd isotope evolution of North Atlantic Deep and Intermediate Waters in the western North Atlantic since the Last Glacial Maximum from Blake Ridge sediments, *Earth Planet. Sci. Lett.*, *266*(1-2), 61–77, doi:10.1016/j.epsl.2007.10.037.

Gutjahr, M., M. Frank, A. N. Halliday, and L. D. Keigwin (2009), Retreat of the Laurentide ice sheet tracked by the isotopic composition of Pb in western North Atlantic seawater during termination 1, *Earth Planet. Sci. Lett.*, *286*(3-4), 546–555, doi:10.1016/j.epsl.2009.07.020.

Haley, B. A, G. P. Klinkhammer, and J. McManus (2004), Rare earth elements in pore waters of marine sediments, *Geochim. Cosmochim. Acta*, *68*(6), 1265–1279, doi:10.1016/j.gca.2003.09.012.

Halliday, A. N., J. P. Davidson, P. Holden, R. M. Owen, and A. M. Olivarez (1992), Metalliferous sediments and the scavenging residence time of Nd near hydrothermal vents, *Geophys. Res. Lett.*, *19*(8), 761–764, doi:10.1029/92GL00393.

Hamelin, B., F. E. Grousset, P. E. Biscaye, A. Zindler, and J. M. Prospero (1989), Lead isotopes in trade wind aerosols at Barbados: The influence of European emissions over the North Atlantic, *J. Geophys. Res.*, *94*(C11), 16243–16250, doi:10.1029/JC094iC11p16243.

Hamilton, P. J., R. K. O'Nions, D. Bridgwater, and A. Nutman (1983), Sm-Nd studies of Archaean metasediments and metavolcanics from West Greenland and their implications for the Earth's early history, *Earth Planet. Sci. Lett.*, *62*(2), 263–272, doi:10.1016/0012-821X(83)90089-4.

Hamon, N., P. Sepulchre, V. Lefebvre, and G. Ramstein (2013), The role of eastern tethys seaway closure in the middle miocene climatic transition (ca. 14 Ma), *Clim. Past*, *9*(6), 2687–2702, doi:10.5194/cp-9-2687-2013.

Harlavan, Y., and Y. Erel (2002), The release of Pb and REE from granitoids by the dissolution of accessory phases, *Geochim. Cosmochim. Acta*, *66*(5), 837–848.

Harlavan, Y., Y. Erel, and J. Blum (1998), Systematic changes in lead isotopic composition with soil age in glacial granitic terrains, *Geochim. Cosmochim. Acta*, *62*(1), 33–46.

Harlavan, Y., Y. Erel, and J. D. Blum (2009), The coupled release of REE and Pb to the soil labile pool with time by weathering of accessory phases, Wind River Mountains, WY, *Geochim. Cosmochim. Acta*, *73*(2), 320–336, doi:10.1016/j.gca.2008.11.002.

Hayes, C. T., A. Martínez-garcía, A. P. Hasenfratz, S. L. Jaccard, D. A. Hodell, D. M. Sigman, G. H. Haug, and R. F. Anderson (2014), A stagnation event in the deep South Atlantic during the last interglacial period, *Science (80-.).*, *346*(6216), 1514–1516, doi:10.1126/science.1256620.

Hays, J. D., J. Imbrie, and N. J. J. . Shackleton (1976), Variations in the Earth ' s Orbit : Pacemaker of the Ice Ages, *Science (80-.).*, *194*(4270), 1121–1132, doi:10.1126/science.194.4270.1121.

Hazeleger, W. et al. (2010), EC-Earth: A seamless Earth-system prediction approach in action, *Bull. Am. Meteorol. Soc.*, *91*(10), 1357–1363, doi:10.1175/2010BAMS2877.1.

Hebeda, E. H., N. A. I. M. Boelrijk, H. N. A. Priem, E. A. T. Verdurmen, R. H. Vershure, and O. J. Simon (1980), Excess radiogenic Ar and undisturbed Rb-Sr systems in basic intrusives subjected to alpine metamorphism in southeastern Spain, *Earth Planet. Sci. Lett.*, *47*, 81–90, doi:10.1016/0012-821X(80)90106-5.

Hein, J. R., A. Koschinsky, and A. N. Halliday (2003), Global occurrence of tellurium-rich ferromanganese crusts and a model for the enrichment of tellurium, *Geochim. Cosmochim. Acta*, *67*(6), 1117–1127, doi:10.1016/S0016-7037(00)01279-6.

Henderson, G. M., D. J. Martel, R. K. O'Nions, and N. J. Shackleton (1994), Evolution of seawater 87Sr/86Sr over the last 400 ka: the absence of glacial/interglacial cycles, *Earth Planet. Sci. Lett.*, *128*, 643–651, doi:10.1016/0012-821X(94)90176-7.

Henderson, G. M., and K. W. Burton (1999), Using (234U/238U) to assess diffusion rates of isotope tracers in ferromanganese crusts, *Earth Planet. Sci. Lett.*, *170*(3), 169–179, doi:10.1016/S0012-821X(99)00104-1.

Henderson, G. M., and E. Maier-Reimer (2002), Advection and removal of Pb and stable Pb isotopes in the oceans: a general circulation model study, *Geochim. Cosmochim. Acta*, *66*(2), 257–272.

Henry, F., C. Jeandel, B. Dupre, and J. Minster (1994), Particulate and dissolved Nd in the western Mediterranean Sea: sources, fate and budget, *Mar. Chem.*, *45*, 283–305.

Hernández-Molina, F. J. et al. (2014a), Contourite processes associated with the Mediterranean Outflow Water after its exit from the Strait of Gibraltar: Global and conceptual implications, *Geology*, *42*(3), 227–230, doi:10.1130/G35083.1.

Hernández-Molina, F. J. et al. (2014b), Onset of Mediterranean outflow into the North Atlantic, *Science (80-.).*, *344*(6189), 1244–50, doi:10.1126/science.1251306.

Hernández-Molina, F. J., N. Serra, D. A. V. Stow, E. Llave, G. Ercilla, and D. Rooij (2011), Along-slope oceanographic processes and sedimentary products around the Iberian margin, *Geo-Marine Lett.*, *31*(5-6), 315–341, doi:10.1007/s00367-011-0242-2.

Hillbrecht, H. (1996), *Extant planktic foraminifera and the physical environment in the Atlantic and Indian Oceans: an atlas based on Climap and Levitus (1982) data*, Zürich.

Hilgen, F., K. Kuiper, W. Krijgsman, E. Snel, and E. van der Laan (2007), Astronomical tuning as the basis for high resolution chronostratigraphy: the intricate history of the Messinian Salinity Crisis, *Stratigraphy*, *4*(2-3), 231–238.

Hilgen, F. J. et al. (1999), Present status of the astronomical (polarity) time-scale for the Mediterranean Late Neogene, *Philos. Trans. R. Soc. A Math. Phys. Eng. Sci.*, *357*(1757), 1931–1947, doi:10.1098/rsta.1999.0408.

Hilgen, F. J., and W. Krijgsman (1999), Cyclostratigraphy and astrochronology of the Tripoli diatomite formation (pre-evaporite Messinian, Sicily, Italy), *Terra Nov.*, *11*(1), 16–22, doi:10.1046/j.1365-3121.1999.00221.x.

Van Hinsbergen, D. J. J., T. J. Kouwenhoven, and G. J. Van Der Zwaan (2005), Paleobathymetry in the backstripping procedure: Correction for oxygenation effects on depth estimates, *Palaeogeogr. Palaeoclimatol. Palaeoecol.*, *221*(3-4), 245–265, doi:10.1016/j.palaeo.2005.02.013.

Hodell, D. A., K. M. Elmstrom, and J. P. Kennett (1986), Latest Miocene δ18O changes, global ice volume, sea level and the "Messinian salinity crisis," *Nature*, *320*(3), 411–414.

Hodell, D. A., J. H. Curtis, F. J. Sierro, and M. E. Raymo (2001), Correlation of late Miocene to early Pliocene sequences between the Mediterranean and North Atlantic, *Paleoceanography*, *16*(2), 164–178, doi:10.1029/1999PA000487.

Hodell, D. A., R. H. Benson, J. P. Kennett, and K. Rakic-El Beid (1989), Stable isotope stratigraphy of the latest Miocene sequences in northwest Morocco: the Bou Regreg Section, *Paleoceanography*, *4*(4), 467–482.

Hodell, D. A., G. A. Mead, and P. A. Mueller (1990), Variation in the strontium isotopic composition of seawater (8 Ma to present): Implications for chemical weathering rates and dissolved fluxes to the oceans, *Chem. Geol.*, *80*, 291–307.

Hoernle, K. et al. (2003), *Part 1: Cruise No. M51, Leg 1, 12 September - 15 October 2001, Warnemünde-Malaga*, Hamburg.

Howarth, R. J., and J. M. McArthur (1997), Statistics For Strontium Isotope Stratigraphy: A Robust Lowess Fit to the Marine Sr-Isotope Curve For 0 to 206 Ma, With Look-Up Table For Derivation of Numeric Age, *J. Geol.*, *105*(4), 441–456, doi:10.1086/515938.

Hsü, K. J., W. B. F. Ryan, and M. B. Cita (1973), Late Miocene dessication of the Mediterranean, *Nature*, *242*, 240–244, doi:10.1038/242240a0.

Hüsing, S. K., K. F. Kuiper, W. Link, F. J. Hilgen, and W. Krijgsman (2009), The upper Tortonian–lower Messinian at Monte dei Corvi (Northern Apennines, Italy): Completing a Mediterranean reference section for the Tortonian Stage, *Earth Planet. Sci. Lett.*, *282*(1-4), 140–157, doi:10.1016/j.epsl.2009.03.010.

Hydes, D. J. (1983), Distribution of aluminium in waters of the North East Atlantic 25 N to 35 N, *Geochim. Cosmochim. Acta*, *47*, 967–973.

Iaccarino, S. M., and A. Bossio (1999), Paleoenvironment of uppermost Messinian sequences in the western Mediterranean (Sites 974, 975, and 978), in *Proceedings of the Ocean Drilling*

Program, Scientific Results, 161, vol. 161, edited by R. Zahn, M. C. Comas, and A. Klaus, pp. 529–541, Ocean Drilling Program, College Station, TX (Ocean Drilling Program).
Imbrie, J., and J. Z. Imbrie (1980), Modeling the climatic response to orbital variations., *Science (80-.).*, *207*(4434), 943–953, doi:10.1126/science.207.4434.943.
Israelevich, P. L., E. Ganor, Z. Levin, and J. H. Joseph (2003), Annual variations of physical properties of desert dust over Israel, *J. Geophys. Res.*, *108*(D13), 1–9, doi:10.1029/2002JD003163.
Ivanovic, R. (2012), Did Mediterranean Outflow Water affect global climate during the Messinian?, University of Bristol.
Ivanoviç, R., R. Flecker, M. Gutjahr, and P. J. Valdes (2013), First Nd isotope record of Mediterranean-Atlantic water exchange through the Moroccan Rifian Corridor during the Messinian Salinity Crisis, *Earth Planet. Sci. Lett.*, *368*, 163–174, doi:10.1016/j.epsl.2013.03.010.
Ivanoviç, R. F., P. J. Valdes, R. Flecker, and M. Gutjahr (2014), Modelling global-scale climate impacts of the late Miocene Messinian Salinity Crisis, *Clim. Past*, *10*(2), 607–622, doi:10.5194/cp-10-607-2014.
Ivanovich, M., and R. S. Harmon (1992), *Uranium series disequilibrium: Applications to Earth, Marine, and Environmental Sciences*, 2nd ed., Clarendon Press, Oxford.
Jackson, S. E., N. J. Pearson, W. L. Griffin, and E. A. Belousova (2004), The application of laser ablation-inductively coupled plasma-mass spectrometry to in situ U-Pb zircon geochronology, *Chem. Geol.*, *211*, 47–69, doi:10.1016/j.chemgeo.2004.06.017.
Jacobsen, S. B., and G. J. Wasserburg (1980), Sm-Nd isotopic evolution of chondrites, *Earth Planet. Sci. Lett.*, *50*, 139–155.
Jacobson, A. D., and J. D. Blum (2000), Ca/Sr and 87Sr/86Sr geochemistry of disseminated calcite in Himalayan silicate rocks from Nanga Parbat: Influence on river-water chemistry, *Geol.* , *28* (5), 463–466, doi:10.1130/0091-7613(2000)28<463:SASGOD>2.0.CO;2.
Jaffey, A. H., K. F. Flynn, L. E. Glendenin, W. C. Bentley, and A. M. Essling (1971), Precision measurement of half-lives and specific activities of 235U and 238U, *Phys. Rev. C*, *4*(5), 1889–1906.
Jeandel, C. (1993), Concentration and isotopic composition of Nd in the South Atlantic Ocean, *Earth Planet. Sci. Lett.*, *117*, 581–591.
Jeandel, C., T. Arsouze, F. Lacan, P. Techine, and J. Dutay (2007), Isotopic Nd compositions and concentrations of the lithogenic inputs into the ocean: A compilation, with an emphasis on the margins, *Chem. Geol.*, *239*(1-2), 156–164, doi:10.1016/j.chemgeo.2006.11.013.
de Jong, K. (2003), Very fast exhumation of high-pressure metamorphic rocks with excess 40Ar and inherited 87Sr, Betic Cordilleras, southern Spain, *Lithos*, *70*(3-4), 91–110, doi:10.1016/S0024-4937(03)00094-X.
Kerr, S., and R. G. Newell (2003), Policy-induced technology adoption: evidence from the U.S. Lead phasedown, *J. Ind. Econ.*, *LI*(3), 317–343.
Khélifi, N. et al. (2009), A major and long-term Pliocene intensification of the Mediterranean outflow, 3.5-3.3 Ma ago, *Geology*, *37*(9), 811–814, doi:10.1130/G30058A.1.
Khélifi, N., M. Sarnthein, M. Frank, N. Andersen, and D. Garbe-Schönberg (2014), Late Pliocene variations of the Mediterranean outflow, *Mar. Geol.*, *357*, 182–194, doi:10.1016/j.margeo.2014.07.006.
Kidd, R. B., M. B. Cita, and W. B. F. Ryan (1978), Stratigraphy of Eastern Mediterranean Sapropel Sequences Recovered during DSDP Leg 42A and Their Paleoenvironmental Significance, *Initial Reports Deep Sea Drill. Proj. 42 Pt. 1*, (DSDP 42A), 421–443, doi:10.2973/dsdp.proc.42-1.113-1.1978.
Kinder, T., and G. Parrilla (1987), Yes, some of the Mediterranean Outflow does come from great depth, *J. Geophys. Res.*, *92*(C3), 2901–2906.
Klinkhammer, G. P., and M. R. Palmer (1991), Uranium in the ocean: where it goes and why, *Geochim. Cosmochim. Acta*, *55*, 1799–1806.
Koho, K. A., and E. Piña-Ochoa (2012), Benthic Foraminifera: Inhabitants of Low-Oxygen Environments, in *Anoxia: Evidence for Eukaryote Survival and Paleontological Strategies*, edited by A. V. Altenbach, J. M. Bernhard, and J. Seckbach, pp. 249–285, Springer Netherlands.
Koho, K. A., E. Piña-Ochoa, E. Geslin, and N. Risgaard-Petersen (2011), Vertical migration, nitrate uptake and denitrification: survival mechanisms of foraminifers (Globobulimina

turgida) under low oxygen conditions., *FEMS Microbiol. Ecol.*, *75*(2), 273–83, doi:10.1111/j.1574-6941.2010.01010.x.
Koschinsky, A., and P. Halbach (1995), Sequential leaching of marine ferromanganese precipitates: Genetic implications, *Geochim. Cosmochim. Acta*, *59*(24), 5113–5132, doi:10.1016/0016-7037(95)00358-4.
Koschinsky, A., P. Halbach, J. R. Hein, and A. Mangini (1996), Ferromanganese crusts as indicators for paleoceanographic events in the NE Atlantic, *Geol. Rundschau*, *85*(3), 567–576, doi:10.1007/BF02369011.
Kouwenhoven, T., M. Seidenkrantz, and G. van der Zwaan (1999), Deep-water changes: the near-synchronous disappearance of a group of benthic foraminifera from the Late Miocene Mediterranean, *Palaeogeography,*, *152*, 259–281.
Kouwenhoven, T. J., F. J. Hilgen, and G. J. van der Zwaan (2003), Late Tortonian–early Messinian stepwise disruption of the Mediterranean–Atlantic connections: constraints from benthic foraminiferal and geochemical data, *Palaeogeogr. Palaeoclimatol. Palaeoecol.*, *198*(3-4), 303–319, doi:10.1016/S0031-0182(03)00472-3.
Kraft, S., M. Frank, E. C. Hathorne, and S. Weldeab (2013), Assessment of seawater Nd isotope signatures extracted from foraminiferal shells and authigenic phases of Gulf of Guinea sediments, *Geochim. Cosmochim. Acta*, *121*, 414–435, doi:10.1016/j.gca.2013.07.029.
Krijgsman, W., A. R. Fortuin, F. J. Hilgen, and F. J. Sierro (2001), Astrochronology for the Messinian Sorbas basin (SE Spain) and orbital (precessional) forcing for evaporite cyclicity, *Sediment. Geol.*, *140*(1-2), 43–60, doi:10.1016/S0037-0738(00)00171-8.
Krijgsman, W., M. E. Leewis, M. Garcés, T. J. Kouwenhoven, K. F. Kuiper, and F. J. Sierro (2006), Tectonic control for evaporite formation in the Eastern Betics (Tortonian; Spain), *Sediment. Geol.*, *188-189*, 155–170, doi:10.1016/j.sedgeo.2006.03.003.
Krijgsman, W., and P. T. Meijer (2008), Depositional environments of the Mediterranean "Lower Evaporites" of the Messinian salinity crisis: Constraints from quantitative analyses, *Mar. Geol.*, *253*(3-4), 73–81, doi:10.1016/j.margeo.2008.04.010.
Krijgsman, W., F. J. Hilgen, I. Raffi, and F. J. Sierro (1999a), Chronology, causes and progression of the Messinian salinity crisis, *Nature*, *400*(August), doi:10.1038/2323.
Krijgsman, W., C. G. Langereis, W. J. Zachariasse, M. Boccaletti, G. Moratti, R. Gelati, S. Iaccarino, G. Papani, and G. Villa (1999b), Late Neogene evolution of the Taza – Guercif Basin (Rifian Corridor, Morocco) and implications for the Messinian salinity crisis, *Mar. Geol.*, *153*(1-4), 147–160, doi:10.1016/S0025-3227(98)00084-X.
Krijgsman, W., F. J. Hilgen, A. Negri, J. R. Wijbrans, and W. J. Zachariasse (1997), The Monte del Casino section (Northern Appenines, Italy): a potential Tortonian/Messinian boundary stratotype?, *Palaeogeogr. Palaeoclimatol. Palaeoecol.*, *133*, 27–47.
Krijgsman, W., M.-M. Blanc-Valleron, R. Flecker, F. J. Hilgen, T. J. Kouwenhoven, D. Merle, F. Orszag-Sperber, and J.-M. Rouchy (2002), The onset of the Messinian salinity crisis in the Eastern Mediterranean (Pissouri Basin, Cyprus), *Earth Planet. Sci. Lett.*, *194*(3-4), 299–310, doi:10.1016/S0012-821X(01)00574-X.
Krijgsman, W., S. Gaboardi, F. J. Hilgen, S. Iaccarino, E. De Kaenel, and E. van der Laan (2004), Revised astrochronology for the Ain el Beida section (Atlantic Morocco): No glacio-eustatic control for the onset of the Messinian Salinity Crisis, *Stratigraphy*, *1*(1), 87–101.
Kuhlbrodt, T., A. Griesel, M. Montoya, A. Levermann, M. Hofmann, and S. Rahmstorf (2007), On the driving processes of the Atlantic meridional overturning circulation, *Rev. Geophys.*, *45*(2), RG2001000166, doi:10.1029/2004RG000166.1.INTRODUCTION.
Kurzweil, F., M. Gutjahr, D. Vance, and L. Keigwin (2010), Authigenic Pb isotopes from the Laurentian Fan: Changes in chemical weathering and patterns of North American freshwater runoff during the last deglaciation, *Earth Planet. Sci. Lett.*, *299*(3-4), 458–465, doi:10.1016/j.epsl.2010.09.031.
de la Vara, A., R. P. M. Topper, P. T. Meijer, and T. J. Kouwenhoven (2015), Water exchange through the Betic and Rifian corridors prior to the Messinian Salinity Crisis: A model study, *Paleoceanography*, 548–557, doi:10.1002/2014PA002719.
van der Laan, E., E. Snel, E. de Kaenel, F. J. Hilgen, and W. Krijgsman (2006), No major deglaciation across the Miocene-Pliocene boundary: Integrated stratigraphy and astronomical tuning of the Loulja sections (Bou Regreg area, NW Morocco), *Paleoceanography*, *21*(3), n/a–n/a, doi:10.1029/2005PA001193.
Lacan, F., and C. Jeandel (2005), Neodymium isotopes as a new tool for quantifying exchange

fluxes at the continent–ocean interface, *Earth Planet. Sci. Lett.*, *232*(3-4), 245–257, doi:10.1016/j.epsl.2005.01.004.
Lalou, C., T. L. Ku, E. Brichet, G. Poupeau, and P. Romary (1979), Techno encrustation Part I: Radiometric studies, in *La Genèse Des Nodules de Manganèse*, edited by C. Lalou and B. M. Sorensen, pp. 261–269, Centre Océanologique de Bretagne, Gif-sur-Yvette, France.
Lambelet, M., T. van de Flierdt, K. Crocket, M. Rehkämper, K. Kreissig, B. Coles, M. J. A. Rijkenberg, L. J. A. Gerringa, H. J. W. de Baar, and R. Steinfeldt (2015), Neodymium isotopic composition and concentration in the western North Atlantic Ocean: results from the GEOTRACES GA02 section, *Geochim. Cosmochim. Acta*, *177*, 1–29, doi:10.1016/j.gca.2015.12.019.
Langlet, D., C. Baal, E. Geslin, E. Metzger, M. Zuschin, B. Riedel, N. Risgaard-Petersen, M. Stachowitsch, and F. J. Jorissen (2014), Foraminiferal species responses to in situ, experimentally induced anoxia in the Adriatic Sea, *Biogeosciences*, *11*(7), 1775–1797, doi:10.5194/bg-11-1775-2014.
Langmuir, D. (1978), Uranium solution-mineral equilibria at low temperatures with applications to sedimentary ore deposits, *Geochim. Cosmochim. Acta*, *42*, 547–569, doi:10.1016/0016-7037(78)90001-7.
Larrasoaña, J. C., A. P. Roberts, E. J. Rohling, M. Winklhofer, and R. Wehausen (2003), Three million years of monsoon variability over the northern Sahara, *Clim. Dyn.*, *21*(7-8), 689–698, doi:10.1007/s00382-003-0355-z.
Laskar, J. (1990), The Chaotic Motion of the Solar System: A Numerical Estimate of the Size of the Chaotic Zones, *Icarus*, *88*, 266–291.
Laskar, J. (1993), Frequency analysis for multi-dimensional systems. Global dynamics and diffusion, *Phys. D*, *67*, 257–281.
Laskar, J., P. Robutel, F. Joutel, M. Gastineau, A. C. M. Correia, and B. Levrard (2004), A long-term numerical solution for the insolation quantities of the Earth, *Astron. Astrophys.*, *428*, 261–285, doi:10.1051/0004-6361:20041335.
Laskar, J., A. Fienga, M. Gastineau, and H. Manche (2011), La2010: A new orbital solution for the long term motion of the Earth, *Astron. Astrophys.*, *4*, 17, doi:10.1051/0004-6361/201116836.
Leuschner, D. C., and F. Sirocko (2003), Orbital insolation forcing of the Indian Monsoon - A motor for global climate changes?, *Palaeogeogr. Palaeoclimatol. Palaeoecol.*, *197*(1-2), 83–95, doi:10.1016/S0031-0182(03)00387-0.
Levitus, S., and T. P. Boyer (1994), *World Ocean Atlas 1994. Volume 4. Temperature*, National Environmental Satellite, Data, and Information Service (NOAA), Washington, D.C.
Li, G., J. Chen, J. Ji, L. Liu, J. Yang, and X. Sheng (2007), Global cooling forced increase in marine strontium isotopic ratios: Importance of mica weathering and a kinetic approach, *Earth Planet. Sci. Lett.*, *254*(3-4), 303–312, doi:10.1016/j.epsl.2006.11.045.
Lisiecki, L. E., and M. E. Raymo (2005), A Pliocene-Pleistocene stack of 57 globally distributed benthic δ 18 O records, *Paleoceanography*, *20*(1), 1–17, doi:10.1029/2004PA001071.
Lofi, J., C. Gorini, S. Berné, G. Clauzon, A. Tadeu Dos Reis, W. B. F. Ryan, and M. S. Steckler (2005), Erosional processes and paleo-environmental changes in the Western Gulf of Lions (SW France) during the Messinian Salinity Crisis, *Mar. Geol.*, *217*(1-2), 1–30, doi:10.1016/j.margeo.2005.02.014.
Lourens, L. J., A. Antonarakou, and F. J. Hilgen (1996), Evaluation of the Plio-Pleistocene astronomical timescale, *Paleoceanography*, *11*(4), 391–413, doi:10.1029/96PA01125.
Lourens, L. J., F. J. Hilgen, N. J. Shackleton, J. Laskar, and D. Wilson (2004), The Neogene Period, edited by F. M. Gradstein, J. G. Ogg, and A. G. Smith, *A Geol. Time Scale*, 409–440, doi:10.1016/B978-0-444-59425-9.00029-9.
Lucchi, F. R. (1986), The Oligocene to Recent foreland basins of the northern Apennines, in *Foreland Basins, Special Publication of the International Association of Sedimentologists*, pp. 105–139, Oxford Blackwell.
Lugli, S., M. A. Bassetti, V. Manzi, M. Barbieri, a. Longinelli, and M. Roveri (2007), The Messinian "Vena del Gesso" evaporites revisited: characterization of isotopic composition and organic matter, *Geol. Soc. London, Spec. Publ.*, *285*(1), 179–190, doi:10.1144/SP285.11.
Lugli, S., V. Manzi, M. Roveri, and C. B. Schreiber (2010), The Primary Lower Gypsum in the Mediterranean: A new facies interpretation for the first stage of the Messinian salinity crisis, *Palaeogeogr. Palaeoclimatol. Palaeoecol.*, *297*(1), 83–99, doi:10.1016/j.palaeo.2010.07.017.
Lugmair, G., and K. Marti (1978), Lunar initial 143 Nd/ 144 Nd: Differential evolution of the lunar

crust and mantle, *Earth Planet. Sci. Lett.*, *39*, 349–357.
Maden, C., P. A. F. Anastasi, A. Dougans, S. P. H. T. Freeman, R. Kitchen, G. Klody, C. Schnabel, M. Sundquist, K. Vanner, and S. Xu (2007), SUERC AMS ion detection, *Nucl. Instruments Methods Phys. Res. Sect. B Beam Interact. with Mater. Atoms*, *259*, 131–139, doi:10.1016/j.nimb.2007.01.151.
Manheim, F. T. (1980), Resources Cobalt in the Ocean Ferromanganese,
Mann, H., and W. S. Fyfe (1985), Uranium uptake by algae: experimental and natural environments, *Can. J. Earth Sci.*, *22*, 1899–1903.
Manzi, V. et al. (2007), The deep-water counterpart of the Messinian Lower Evaporites in the Apennine foredeep: The Fanantello section (Northern Apennines, Italy), *Palaeogeogr. Palaeoclimatol. Palaeoecol.*, *251*(3-4), 470–499, doi:10.1016/j.palaeo.2007.04.012.
Manzi, V., R. Gennari, F. Hilgen, W. Krijgsman, S. Lugli, M. Roveri, and F. J. Sierro (2013), Age refinement of the Messinian salinity crisis onset in the Mediterranean, *Terra Nov.*, *0*(0), 1–8, doi:10.1111/ter.12038.
Manzi, V., S. Lugli, M. Roveri, F. Dela Pierre, R. Gennari, F. Lozar, M. Natalicchio, B. C. Schreiber, M. Taviani, and E. Turco (2016), The Messinian salinity crisis in Cyprus: A further step towards a new stratigraphic framework for Eastern Mediterranean, *Basin Res.*, *28*, 207–236, doi:10.1111/bre.12107.
Maring, H. B., and R. A. Duce (1990), The Impact of Atmospheric Aerosols on Trace Metal Chemistry In Open Ocean Surface Seawater 3. Lead, *J. Geophys. Res.*, *95*(C4), 5341–5347.
Mariotti, A., M. V. Struglia, N. Zeng, and K. M. Lau (2002), The Hydrological Cycle in the Mediterranean Region and Implications for the Water Budget of the Mediterranean Sea, *J. Clim.*, *15*(13), 1674–1690, doi:10.1175/1520-0442(2002)015<1674:THCITM>2.0.CO;2.
Martin, E. E., and H. D. Scher (2004), Preservation of seawater Sr and Nd isotopes in fossil fish teeth: bad news and good news, *Earth Planet. Sci. Lett.*, *220*(1-2), 25–39, doi:10.1016/S0012-821X(04)00030-5.
Martin, J. M., and J. C. Braga (1994), Messinian events in the Sorbas Basin in Southeastern Spain and their implications in the recent history of the Mediterranean, *Sediment. Geol.*, *90*(3-4), 257–268, doi:10.1016/0037-0738(94)90042-6.
Martin, J. M., J. C. Braga, and C. Betzler (2001), The Messinian Guadalhorce corridor: the last northern, Atlantic-Mediterranean gateway, *Terra Nov.*, *13*(6), 418–424, doi:10.1046/j.1365-3121.2001.00376.x.
Martín, J. M., J. C. Braga, J. Aguirre, and Á. Puga-Bernabéu (2009), History and evolution of the North-Betic Strait (Prebetic Zone, Betic Cordillera): A narrow, early Tortonian, tidal-dominated, Atlantic–Mediterranean marine passage, *Sediment. Geol.*, *216*(3-4), 80–90, doi:10.1016/j.sedgeo.2009.01.005.
Martin-Suarez, E., M. Freudenthal, W. Krijgsman, and A. R. Fortuin (2000), On the age of the continental deposits of the Zorreras Member (Sorbas Basin, SE Spain), *Geobios*, *33*(4), 505–512, doi:10.1016/S0016-6995(00)80084-4.
Martínez-Ruíz, F., M. C. Comas, and B. Alonso (1999), Mineral associations and geochemical indicators in upper Miocene to Pleistocene sediments in the Alboran Basin, in *Proceedings of the Ocean Drilling Program, 161 Scientific Results*, vol. 161, edited by R. Zahn, M. C. Comas, and A. Klaus, pp. 21–36, Ocean Drilling Program, College Station, TX.
Marzocchi, A. (2016), Modelling the impact of orbital forcing on late Miocene climate: implications for the Mediterranean Sea and the Messinian Salinity Crisis, Ph.D. Thesis, University of Bristol.
Marzocchi, A., D. J. Lunt, R. Flecker, C. D. Bradshaw, A. Farnsworth, and F. J. Hilgen (2015), Orbital control on late Miocene climate and the North African monsoon: insight from an ensemble of sub-precessional simulations, *Clim. Past*, *11*(10), 1271–1295, doi:10.5194/cp-11-1271-2015.
Marzocchi, A., R. Flecker, D. J. Lunt, F. J. Hilgen, W. Krijgsman, and R. Gladstone (2016), Precessional drivers of the Mediterranean freshwater budget and implications for sapropel formation: African monsoon and Atlantic storm tracks, *Earth Planet. Sci. Lett.*, submitted.
Mather, A. E. (2000), Adjustment of a drainage network to capture induced base-level change: An example from the Sorbas Basin, SE Spain, *Geomorphology*, *34*(3-4), 271–289, doi:10.1016/S0169-555X(00)00013-1.
Matthiesen, S., and K. Haines (2003), A hydraulic box model study of the Mediterranean response to postglacial sea-level rise, *Paleoceanography*, *18*(4), 1084, doi:10.1029/2003PA000880.

Mauritzen, C., Y. Morel, and J. Paillet (2001), On the influence of Mediterranean Water on the Central Waters of the North Atlantic Ocean, *Deep Sea Res. Part I*, *48*, 347–381.
Maury, R. C. et al. (2000), Post-collisional Neogene magmatism of the Mediterranean Maghreb margin: A consequence of slab breakoff, *Comptes Rendus l'Academie Sci. - Ser. IIA-Earth Planet. Sci.*, *331*, 159–173, doi:10.1016/S1251-8050(00)01406-3.
McArthur, J. M., R. J. Howarth, and G. A. Shields (2012), Strontium Isotope Stratigraphy, in *The Geologic Time Scale 2012*, edited by F. M. Gradstein, J. G. Ogg, M. Schmitz, and G. Ogg, pp. 127–144, Elsevier B.V.
McCulloch, M., and P. De Deckker (1989), Sr isotope constraints on the Mediterranean environment at the end of the Messinian salinity crisis, *Nature*, *342*, 62–65, doi:10.1038/342062a0.
McKenzie, J. A. (1999), From desert to deluge in the Mediterranean, *Nature*, *400*(August), 613–614, doi:10.1038/23131.
Measures, C. I., and J. M. Edmond (1988), Aluminium as a tracer of the deep outflow from the Mediterranean, *J. Geophys. Res.*, *93*(C1), 591, doi:10.1029/JC093iC01p00591.
Meijer, P. T. (2006), A box model of the blocked-outflow scenario for the Messinian Salinity Crisis, *Earth Planet. Sci. Lett.*, *248*(1-2), 486–494, doi:10.1016/j.epsl.2006.06.013.
Melezhik, V. A., I. M. Gorokhov, A. B. Kuznetsov, and A. E. Fallick (2001), Chemostratigraphy of Neoproterozoic carbonates: implications for "blind dating," *Terra Nov.*, *13*, 1–11, doi:10.1046/j.1365-3121.2001.00318.x.
de Menocal, P. B. (2004), African climate change and faunal evolution during the Pliocene-Pleistocene, *Earth Planet. Sci. Lett.*, *220*(1-2), 3–24, doi:10.1016/S0012-821X(04)00003-2.
Millot, C. (1999), Circulation in the Western Mediterranean Sea, *J. Mar. Syst.*, *20*(1-4), 423–442, doi:10.1016/S0924-7963(98)00078-5.
Minster, J.-F., J.-L. Birck, and C. J. Allegre (1982), Absolute age of formation of chondrites studied by the 87Rb-87Sr method, *Nature*, *300*, 414 – 419, doi:10.1017/CBO9781107415324.004.
Montanari, A., B. Beaudoin, L. S. Chan, R. Coccioni, A. Deino, D. J. De Paolo, L. Emmanuel, E. Fornaciari, M. Kruge, and S. Lundblad (1997), Integrated stratigraphy of the Middle and Upper Miocene pelagic sequence of the Cònero Riviera (Marche region, Italy), in *Miocene stratigraphy: An integrated approach*, vol. 15, edited by A. Montanari, G. Odin, and R. Coccioni, pp. 409–450, Elsevier Science, Amsterdam.
Muiños, S. B., M. Frank, C. Maden, J. R. Hein, T. van de Flierdt, S. M. Lebreiro, L. Gaspar, J. H. Monteiro, and A. N. Halliday (2008), New constraints on the Pb and Nd isotopic evolution of NE Atlantic water masses, *Geochem. Geophys. Geosyst.*, *9*(2), Q02007, doi:10.1029/2007GC001766.
Muiños, S. B. et al. (2013), Deep-sea Fe-Mn Crusts from the Northeast Atlantic Ocean: Composition and Resource Considerations, *Mar. Georesources Geotechnol.*, *31*(1), 40–70, doi:10.1080/1064119x.2012.661215.
Müller, D. W., and P. A. Mueller (1991), Origin and age of the Mediterranean Messinian evaporites: implications from Sr isotopes, *Earth Planet. Sci. Lett.*, *107*(1), 1–12, doi:10.1016/0012-821X(91)90039-K.
Murat, A. (1999), 41 . Pliocene-Pleistocene occurrence of sapropels in the Western Mediterranean Sea and their relation to Eastern Mediterranean Sapropels, in *Proceedings of the Ocean Drilling Program, Scientific Results*, vol. 161, edited by R. Zahn, M. C. Comas, and A. Klaus, pp. 519–527, Ocean Drilling Program, College Station, TX.
Natalicchio, M., F. Dela Pierre, S. Lugli, T. K. Lowenstein, S. J. Feiner, S. Ferrando, V. Manzi, M. Roveri, and P. Clari (2014), Did Late Miocene (Messinian) gypsum precipitate from evaporated marine brines? Insights from the Piedmont Basin (Italy), *Geology*, *42*(3), 179–182, doi:10.1130/G34986.1.
Nesbitt, H. W., G. Markovics, and R. C. Price (1980), Chemical processes affecting alkalies and alkaline earths during continental weathering, *Geochim. Cosmochim. Acta*, *44*, 1659–1666, doi:10.1016/0016-7037(80)90218-5.
Negri, A., S. Giunta, F. Hilgen, W. Krijgsman, and G. B. Vai (1999), Calcareous nannofossil biostratigraphy of the M. del Casino section (northern Apennines, Italy) and paleoceanographic conditions at times of Late Miocene sapropel formation, *Mar. Micropaleontol.*, *36*(1), 13–30, doi:10.1016/S0377-8398(98)00024-3.
Nesteroff, W. D. (1973), Un modèle pour les évaporites messiniennes en Méditerranée, des bassins

peu profonds avec des dépôts d'évaporites lagunaires, in *Messinian Events in the Mediterranean, Geodynamics Scientific Report no. 7*, edited by C. W. Drooger, pp. 68–81, Proceedings of the Koninklijke Nederlandse Academie van Wetenschappen, Amsterdam.

Nielsen, J. N. (1912), Hydrography of the Mediterranean and adjacent waters. *Report on the Danish Oceanographical Expeditions 1908~1910*. 1, 77-191.

Nier, A. O. (1938), The isotopic constitution of Strontium, Barium, Bismuth, Thallium and Mercury. *Phys. Rev.* 54, 275–278.

Noble, A. E., Y. Echegoyen-Sanz, E. A. Boyle, D. C. Ohnemus, P. J. Lam, R. Kayser, M. Reuer, J. Wu, and W. Smethie (2015), Dynamic variability of dissolved Pb and Pb isotope composition from the U.S. North Atlantic GEOTRACES transect, *Deep. Res. Part II Top. Stud. Oceanogr.*, *116*, 208–225, doi:10.1016/j.dsr2.2014.11.011.

Nolet, G. J., and B. H. Corliss (1990), Benthic foraminiferal evidence for reduced deep-water circulation during sapropel deposition in the eastern Mediterranean, *Mar. Geol.*, *94*, 109–130, doi:10.1016/0025-3227(90)90106-T.

Nozaki, Y., J. Thomson, and K. K. Turekian (1976), The distribution of 210Pb and 210Po in the surface waters of the Pacific ocean, *Earth Planet. Sci. Lett.*, *32*(86), 304–312.

Ochoa, D., F. J. Sierro, J. Lofi, A. Maillard, J. A. Flores, and M. Suarez (2015), Synchronous onset of the Messinian evaporite precipitation: First Mediterranean offshore evidence, *Earth Planet. Sci. Lett.*, *427*, 112–124, doi:10.1016/j.epsl.2015.06.059.

Oelkers, E. H., S. R. Gislason, E. S. Eiriksdottir, M. Jones, C. R. Pearce, and C. Jeandel (2011), The role of riverine particulate material on the global cycles of the elements, *Appl. Geochemistry*, *26*, S365–S369, doi:10.1016/j.apgeochem.2011.03.062.

Ohneiser, C., F. Florindo, P. Stocchi, A. P. Roberts, R. M. DeConto, and D. Pollard (2015), Antarctic glacio-eustatic contributions to late Miocene Mediterranean desiccation and reflooding, *Nat. Commun.*, *6*, 8765, doi:10.1038/ncomms9765.

O'Nions, R. ., M. Frank, F. von Blanckenburg, and H.-F. Ling (1998), Secular variation of Nd and Pb isotopes in ferromanganese crusts from the Atlantic, Indian and Pacific Oceans, *Earth Planet. Sci. Lett.*, *155*(1-2), 15–28, doi:10.1016/S0012-821X(97)00207-0.

O'Nions, R. K., P. J. Hamilton, and N. M. Evensen (1977), Variations in 143Nd/144Nd and 87Sr/86Sr ratios in oceanic basalts, *Earth Planet. Sci. Lett.*, *34*(1), 13–22.

Ortiz, J. D., and A. C. Mix (1992), The spatial distribution and seasonal succession of planktonic foraminifera in the California Current off Oregon, September 1987 - September 1988, in *Upwelling Systems: Evolution Since the Early Miocene*, vol. 64, edited by C. P. Summerhayes, W. L. Prell, and K. C. Emeis, pp. 197–213, Geological Society Special Publication.

Ortiz, J. D., A. C. Mix, and R. W. Collier (1995), Environmental control of living symbiotic and asymbiotic foraminifera of the California Current, *Paleoceanography*, *10*(6), 987–1009, doi:10.1029/95PA02088.

Osborne, A. H., D. Vance, E. J. Rohling, N. Barton, M. Rogerson, and N. Fello (2008), A humid corridor across the Sahara for the migration of early modern humans out of Africa 120,000 years ago., *Proc. Natl. Acad. Sci. U. S. A.*, *105*(43), 16444–7, doi:10.1073/pnas.0804472105.

Osborne, A. H., G. Marino, D. Vance, and E. J. Rohling (2010), Eastern Mediterranean surface water Nd during Eemian sapropel S5: monitoring northerly (mid-latitude) versus southerly (sub-tropical) freshwater contributions, *Quat. Sci. Rev.*, *29*(19-20), 2473–2483, doi:10.1016/j.quascirev.2010.05.015.

Osborne, A. H., B. a. Haley, E. C. Hathorne, S. Flögel, and M. Frank (2014a), Neodymium isotopes and concentrations in Caribbean seawater: Tracing water mass mixing and continental input in a semi-enclosed ocean basin, *Earth Planet. Sci. Lett.*, *406*, 174–186, doi:10.1016/j.epsl.2014.09.011.

Osborne, A. H., D. R. Newkirk, J. Groeneveld, E. E. Martin, R. Tiedemann, and M. Frank (2014b), The seawater neodymium and lead isotope record of the final stages of Central American Seaway closure, *Paleoceanography*, *29*(7), 715–729, doi:10.1002/2014PA002676.

Paillou, P., M. Schuster, S. Tooth, T. Farr, A. Rosenqvist, S. Lopez, and J. M. Malezieux (2009), Mapping of a major paleodrainage system in eastern Libya using orbital imaging radar: The Kufrah River, *Earth Planet. Sci. Lett.*, *277*(3-4), 327–333, doi:10.1016/j.epsl.2008.10.029.

Paillou, P., S. Tooth, and S. Lopez (2012), The Kufrah paleodrainage system in Libya: A past connection to the Mediterranean Sea?, *Comptes Rendus - Geosci.*, *344*(8), 406–414, doi:10.1016/j.crte.2012.07.002.

Palmer, M. R., and H. Elderfield (1985), Variations in the Nd isotopic composition of foraminifera from Atlantic Ocean sediments, *Earth Planet. Sci. Lett.*, *73*(2-4), 299–305, doi:10.1016/0012-821X(85)90078-0.

Palmer, M. R., and J. M. Edmond (1989), The strontium isotope budget of the modern ocean, *Earth Planet. Sci. Lett.*, *92*, 11–26, doi:10.1016/0012-821X(89)90017-4.

Pearce, C. R., M. T. Jones, E. H. Oelkers, C. Pradoux, and C. Jeandel (2013), The effect of particulate dissolution on the neodymium (Nd) isotope and Rare Earth Element (REE) composition of seawater, *Earth Planet. Sci. Lett.*, *369-370*, 138–147, doi:10.1016/j.epsl.2013.03.023.

Peixoto, J. P., and M. A. Kettani (1973), The control of the water cycle, *Sci. Am.*, *228*(4), 46–61, doi:10.1038/scientificamerican0473-46.

Pérez-Folgado, M., F. J. Sierro, M. A. Bárcena, J. A. Flores, A. Vázquez, R. Utrilla, F. J. Hilgen, W. Krijgsman, and G. M. Filippelli (2003), Western versus eastern Mediterranean paleoceanographic response to astronomical forcing: A high-resolution microplankton study of precession-controlled sedimentary cycles during the Messinian, *Palaeogeogr. Palaeoclimatol. Palaeoecol.*, *190*, 317–334, doi:10.1016/S0031-0182(02)00612-0.

Peros, M. C., E. G. Reinhardt, H. P. Schwarcz, and A. M. Davis (2007), High-resolution paleosalinity reconstruction from Laguna de la Leche, north coastal Cuba, using Sr, O, and C isotopes, *Palaeogeogr. Palaeoclimatol. Palaeoecol.*, *245*, 535–550, doi:10.1016/j.palaeo.2006.09.006.

Petit, R. et al. (1999), Climate and atmospheric history of the past 420,000 years from the Vostok ice core, Antarctica, *Nature*, *399*, 429–436, doi:10.1038/20859.

Piepgras, D. J., and G. J. Wasserburg (1983), Influence of the Mediterranean Outflow on the Isotopic Composition of Neodymium in Waters of the North Atlantic, *J. Geophys. Res.*, *88*(C10), 5997–6006.

Piotrowski, A. M., S. L. Goldstein, S. R. Hemming, and R. G. Fairbanks (2004), Intensification and variability of ocean thermohaline circulation through the last deglaciation, *Earth Planet. Sci. Lett.*, *225*(1-2), 205–220, doi:10.1016/j.epsl.2004.06.002.

Piotrowski, A. M., S. L. Goldstein, S. R. Hemming, and R. G. Fairbanks (2005), Temporal relationships of carbon cycling and ocean circulation at glacial boundaries., *Science*, *307*(5717), 1933–8, doi:10.1126/science.1104883.

Poisson, A. M., J. L. Morel, J. Andrieux, M. Coulon, R. Wernli, and C. Guernet (1999), The origin and development of Neogene basins in the SE Betic Cordillera (SE Spain): a case study of the Tabernas-Sorbas and Huercal Overa Basins, *J. Pet. Geol.*, *22*(1), 97–114, doi:10.1111/j.1747-5457.1999.tb00461.x.

Powell, J. L., and K. Bell (1970), Strontium isotopic studies of alkalic rocks: localities from Australia, Spain, and the Western United States, *Contrib. to Mineral. Petrol.*, *27*, 1–10, doi:10.1007/BF00539537.

Prospero, J. M. (1996), Saharan dust transport over the North Atlantic Ocean and Mediterranean: an overview, in *The impact of desert dust across the Mediterranean*, edited by S. Guerzoni and R. Chester, pp. 133–151, Kluwer Academic Publishers, Netherlands.

Prospero, J. M., P. Ginoux, O. Torres, S. E. Nicholson, and T. E. Gill (2002), Environmental characterization of global sources of atmospheric soil dust identified with the NIMBUS 7 Total Ozone Mapping Spectrometer (TOMS) absorbing aerosol product, *Rev. Geophys.*, *40*(1), 1–31, doi:10.1029/2000RG000095.

Pulido-Bosch, A. (1997), Los recursos hídricos de la Provincia de Almería, in *Actas del I y II seminario del agua*, edited by A. Pascual-Molina, pp. 65–89, Instituto de Estudios Almerienses, Almeria, Spain.

Puteanus, D., and P. Halbach (1988), Correlation of Co concentration and growth rate--A method for age determination of ferromanganese crusts, *Chem. Geol.*, *69*(1-2), 73–85, doi:10.1016/0009-2541(88)90159-3.

Raffi, I., C. Mozzato, E. Fornaciari, F. J. Hilgen, and D. Rio (2003), Late Miocene calcareous nannofossil biotratigraphy and astrobiochronology for the Mediterranean region, *Micropaleontology*, *49*(1), 1–26, doi:10.2113/49.1.1.

Rahmstorf, S. (1998), Influence of Mediterranean Outflow on climate, *Eos (Washington. DC).*, *79*(24), 281–282, doi:10.1029/98EO00218.

Reichart, G.-J. (1997), Late Quaternary variability of the Arabian Sea monsoon and oxygen minimum zone, Ph.D. Thesis, Utrecht University.

Reinhardt, E. G., D. J. Stanley, and R. T. Patterson (1998), Strontium isotopic-paleontological method as a high-resolution paleosalinity tool for lagoonal environments, *Geology*, *26*(11), 1003–1006, doi:10.1130/0091-7613(1998)026<1003:SIPMAA>2.3.CO;2.

Rempfer, J., T. F. Stocker, F. Joos, and J. C. Dutay (2012), Sensitivity of Nd isotopic composition in seawater to changes in Nd sources and paleoceanographic implications, *J. Geophys. Res. Ocean.*, *117*(12), 1–12, doi:10.1029/2012JC008161.

Reynolds, B. C., M. Frank, and R. K. O'Nions (1999), Nd- and Pb-isotope time series from Atlantic ferromanganese crusts: implications for changes in provenance and paleocirculation over the last 8 Myr, *Earth Planet. Sci. Lett.*, *173*(4), 381–396, doi:10.1016/S0012-821X(99)00243-5.

Rickli, J., M. Frank, and A. N. Halliday (2009), The hafnium–neodymium isotopic composition of Atlantic seawater, *Earth Planet. Sci. Lett.*, *280*(1-4), 118–127, doi:10.1016/j.epsl.2009.01.026.

Rickli, J., M. Gutjahr, D. Vance, M. Fischer-Godde, C. D. Hillenbrand, and G. Kuhn (2014), Neodymium and hafnium boundary contributions to seawater along the West Antarctic continental margin, *Earth Planet. Sci. Lett.*, *394*, 99–110, doi:10.1016/j.epsl.2014.03.008.

Riding, R., J. Braga, J. Martín, and I. Sánchez-Almazo (1998), Mediterranean Messinian Salinity Crisis: constraints from a coeval marginal basin, Sorbas, southeastern Spain, *Mar. Geol.*, *146*, 1–20, doi:10.1016/S0025-3227(97)00136-9.

Rivera, T. A., M. Storey, C. Zeeden, F. J. Hilgen, and K. Kuiper (2011), A refined astronomically calibrated 40Ar/39Ar age for Fish Canyon sanidine, *Earth Planet. Sci. Lett.*, *311*(3-4), 420–426, doi:10.1016/j.epsl.2011.09.017.

Roberts, N. L., A. M. Piotrowski, H. Elderfield, T. I. Eglinton, and M. W. Lomas (2012), Rare earth element association with foraminifera, *Geochim. Cosmochim. Acta*, doi:10.1016/j.gca.2012.07.009.

Roberts, N. L., A. M. Piotrowski, J. F. Mcmanus, and L. D. Keigwin (2010), Synchronous deglacial overturning and water mass source changes, *Science*, *327*, 75–78, doi:10.1126/science.1178068.

Rodrigo-Gámiz, M., F. Martínez-Ruiz, M. Chiaradia, F. J. Jiménez-Espejo, and D. Ariztegui (2015), Radiogenic isotopes for deciphering terrigenous input provenance in the western Mediterranean, *Chem. Geol.*, *410*, 237–250, doi:10.1016/j.chemgeo.2015.06.004.

Roep, T. B., C. J. Dabrio, A. R. Fortuin, and M. D. Polo (1998), Late highstand patterns of shifting and stepping coastal barriers and washover-fans (late Messinian, Sorbas Basin, SE Spain), *Sediment. Geol.*, *116*, 27–56, doi:10.1016/S0037-0738(97)00111-5.

Roep, T. B., and D. van Harten (1979), Sedimentological and ostracodological observations on Messinian post-evaporite deposits of some southeastern Spanish basins, *Ann. Géologiques des Pays Helléniques*, *3*, 1037–1044.

Rogerson, M., E. Rohling, G. R. Bigg, and J. Ramirez (2012), Paleoceanography of the Atlantic-Mediterranean exchange: overview and first quantitative assessment of climatic forcing, *Rev. Geophys.*, (50), doi:10.1029/2011RG000376.

Rognon, P., G. Coude-Gaussen, M. Revel, F. E. Grousset, and P. Pedemay (1996), Holocene Saharan dust deposition on the Cape Verde Islands: Sedimentological and Nd-Sr isotopic evidence, *Sedimentology*, *43*, 359–366, doi:10.1046/j.1365-3091.1996.d01-8.x.

Rohling, E. J. (1994), Review and new aspects concerning the formation of eastern Mediterranean sapropels, *Mar. Geol.*, *122*(1-2), 1–28, doi:10.1016/0025-3227(94)90202-X.

Rohling, E. J., R. Schiebel, and M. Siddall (2008), Controls on Messinian Lower Evaporite cycles in the Mediterranean, *Earth Planet. Sci. Lett.*, *275*(1-2), 165–171, doi:10.1016/j.epsl.2008.08.022.

Rohling, E. J., G. Marino, and K. M. Grant (2015), Mediterranean climate and oceanography, and the periodic development of anoxic events (sapropels), *Earth-Science Rev.*, *143*, 62–97, doi:10.1016/j.earscirev.2015.01.008.

Rossignol-Strick, M. (1985), Mediterranean Quaternary sapropels, an immediate response of the African monsoon to variation of insolation, *Palaeogeogr. Palaeoclimatol. Palaeoecol.*, *49*(3-4), 237–263, doi:10.1016/0031-0182(85)90056-2.

Rossignol-Strick, M., and N. Planchais (1989), Climate patterns revealed by pollen and oxygen isotope records of a Tyrrhenian sea core, *Nature*, *342*, 413–416, doi:10.1038/342413a0.

Rousseau, T. C. C., J. E. Sonke, J. Chmeleff, P. van Beek, M. Souhaut, G. Boaventura, P. Seyler, and C. Jeandel (2015), Rapid neodymium release to marine waters from lithogenic sediments

in the Amazon estuary., *Nat. Commun.*, *6*, 7592, doi:10.1038/ncomms8592.
Roveri, M., S. Lugli, V. Manzi, and B. C. Schreiber (2008), The Messinian Sicilian stratigraphy revisited: new insights for the Messinian salinity crisis, *Terra Nov.*, *20*(6), 483–488, doi:10.1111/j.1365-3121.2008.00842.x.
Roveri, M., S. Lugli, V. Manzi, R. Gennari, and B. C. Schreiber (2014), High-resolution strontium isotope stratigraphy of the Messinian deep Mediterranean basins: Implications for marginal to central basins correlation, *Mar. Geol.*, *349*, 113–125, doi:10.1016/j.margeo.2014.01.002.
Roy-Barman, M., L. Coppola, and M. Souhaut (2002), Thorium isotopes in the western Mediterranean Sea: an insight into the marine particle dynamics, *Earth Planet. Sci. Lett.*, *196*, 161–174.
Rutberg, R. L., S. R. Hemming, and S. L. Goldstein (2000), Reduced North Atlantic Deep Water flux to the glacial Southern Ocean inferred from neodymium isotope ratios, *Nature*, *405*(6789), 935–938, doi:10.1038/35016049.
Ryan, W. B. F. (2008), Modeling the magnitude and timing of evaporative drawdown during the Messinian salinity crisis, *Stratigraphy*, *5*(3-4), 227–243.
Santisteban, C., and C. Taberner (1983), Shallow marine and continental conglomerates derived from coral reef complexes after desiccation of a deep marine basin: the Tortonian-Messinian deposits of the Fortuna Basin, SE Spain, *J. Geol. Soc. London.*, *140*(3), 401–411, doi:10.1144/gsjgs.140.3.0401.
Santschi, P. H., J. W. Murray, M. Baskaran, C. R. Benitez-Nelson, L. D. Guo, C. C. Hung, C. Lamborg, S. B. Moran, U. Passow, and M. Roy-Barman (2006), Thorium speciation in seawater, *Mar. Chem.*, *100*(3-4 SPEC. ISS.), 250–268, doi:10.1016/j.marchem.2005.10.024.
Shackleton, N. J., and M. A. Hall (1997), 24. The Late Miocene stable isotope record, Site 926, in *Proceedings of the Ocean Drilling Program, Scientific Results*, vol. 154, edited by N. J. Shackleton, W. B. Curry, C. Richter, and T. J. Bralower, pp. 367–373, Ocean Drilling Program, College Station, TX.
Scheuvens, D., L. Schütz, K. Kandler, M. Ebert, and S. Weinbruch (2013), Bulk composition of northern African dust and its source sediments — A compilation, *Earth-Science Rev.*, *116*, 170–194, doi:10.1016/j.earscirev.2012.08.005.
Schmiedl, G., A. Mitschele, S. Beck, K. C. Emeis, C. Hemleben, H. Schulz, M. Sperling, and S. Weldeab (2003), Benthic foraminiferal record of ecosystem variability in the eastern Mediterranean Sea during times of sapropel S5 and S6 deposition, *Palaeogeogr. Palaeoclimatol. Palaeoecol.*, *190*, 139–164, doi:10.1016/S0031-0182(02)00603-X.
Schmiedl, G., T. Kuhnt, W. Ehrmann, K. C. Emeis, Y. Hamann, U. Kotthoff, P. Dulski, and J. Pross (2010), Climatic forcing of eastern Mediterranean deep-water formation and benthic ecosystems during the past 22 000 years, *Quat. Sci. Rev.*, *29*(23-24), 3006–3020, doi:10.1016/j.quascirev.2010.07.002.
Schmitz, W. J. (1996), *On the World Ocean Circulation: Volume 1. Some Global Features/North Atlantic Circulation*, Woods Hole Oceanographic Institution, Woods Hole, Massachusetts.
Schröder, K., G. P. Gasparini, M. Tangherlini, and M. Astraldi (2006), Deep and intermediate water in the western Mediterranean under the influence of the Eastern Mediterranean Transient, *Geophys. Res. Lett.*, *33*(21), 2–7, doi:10.1029/2006GL027121.
Schroeder, K., a. Ribotti, M. Borghini, R. Sorgente, a. Perilli, and G. P. Gasparini (2008), An extensive western Mediterranean deep water renewal between 2004 and 2006, *Geophys. Res. Lett.*, *35*(18), 1–7, doi:10.1029/2008GL035146.
Schroeder, K., J. Chiggiato, H. L. Bryden, M. Borghini, and S. Ben Ismail (2016), Abrupt climate shift in the Western Mediterranean Sea, *Sci. Rep.*, *6*, 23009, doi:10.1038/srep23009.
Schuster, M., P. Duringer, J.-F. Ghienne, P. Vignaud, H. T. Mackaye, A. Likius, and M. Brunet (2006), The age of the Sahara desert, *Science (80-.).*, *311*(5762), 821, doi:10.1126/science.1120161.
Scrivner, A. E., D. Vance, and E. J. Rohling (2004), New neodymium isotope data quantify Nile involvement in Mediterranean anoxic episodes, *Geology*, *32*(7), 565–568, doi:10.1130/G20419.1.
Segl, M., A. Mangini, G. Bonani, and H. Hofmann (1984), 10Be-dating of a manganese crust from Central North Pacific and implications for ocean palaeocirculation, *Nature*, *309*(7), 540–543.
Seidenkrantz, M.-S., T. . Kouwenhoven, F. . Jorissen, N. . Shackleton, and G. . van der Zwaan (2000), Benthic foraminifera as indicators of changing Mediterranean–Atlantic water exchange in the late Miocene, *Mar. Geol.*, *163*(1-4), 387–407.

Selli, R. (1973), An outline of the Italian Messinian, in *Messinian Events in the Mediterranean, Geodynamics Scientific Report no. 7*, edited by C. W. Drooger, pp. 150–171, Proceedings of the Koninklijke Nederlandse Academie van Wetenschappen, Amsterdam.

Settle, D. M., and C. C. Patterson (1982), Magnitudes and sources of precipitation and dry deposition fluxes of industrial and natural leads to the North Pacific at Enewetak, *J. Geophys. Res.*, *87*(11), 8857–8869.

Shipboard Scientific Party (1996), Site 978, in *Proceedings of the Ocean Drilling Program, Initial Reports*, vol. 161, edited by M. C. Comas, R. Zahn, A. Klaus, and E. Al., pp. 355–388, College Station, TX (Ocean Drilling Program).

Sholkovitz, E. R. (1993), The geochemistry of rare earth elements in the Amazon River estuary, *Geochim. Cosmochim. Acta*, *57*(10), 2181–2190, doi:10.1016/0016-7037(93)90559-F.

Sholkovitz, E., and R. Szymczak (2000), The estuarine chemistry of rare earth elements: Comparison of the Amazon, Fly, Sepik and the Gulf of Papua systems, *Earth Planet. Sci. Lett.*, *179*(2), 299–309, doi:10.1016/S0012-821X(00)00112-6.

Siddall, M., S. Khatiwala, T. van de Flierdt, K. Jones, S. L. Goldstein, S. Hemming, and R. F. Anderson (2008), Towards explaining the Nd paradox using reversible scavenging in an ocean general circulation model, *Earth Planet. Sci. Lett.*, *274*(3-4), 448–461, doi:10.1016/j.epsl.2008.07.044.

Sierro, F. J., J. A. Flores, I. Zamarreno, A. Vazquez, R. Utrilla, G. Frances, F. J. Hilgen, and W. Krijgsman (1997), Astronomical cyclicity and sapropels in the pre-evaporitic Messinian of the Sorbas basin (Western Mediterranean), *Geogaceta*, *21*, 199–202.

Sierro, F. J., J. A. Flores, I. Zamarreno, and A. Vazquez (1999), Messinian pre-evaporite sapropels and precession-induced oscillations in western Mediterranean climate, *Mar. Geol.*, *153*, 137–146.

Sierro, F. J., F. J. Hilgen, W. Krijgsman, and J. A. Flores (2001), The Abad composite (SE Spain): a Messinian reference section for the Mediterranean and the APTS, *Palaeogeogr. Palaeoclimatol. Palaeoecol.*, *168*(1-2), 141–169, doi:10.1016/S0031-0182(00)00253-4.

Sierro, F. J., J. A. Flores, G. Francés, A. Vazquez, R. Utrilla, I. Zamarreño, H. Erlenkeuser, and M. A. Barcena (2003), Orbitally-controlled oscillations in planktic communities and cyclic changes in western Mediterranean hydrography during the Messinian, *Palaeogeogr. Palaeoclimatol. Palaeoecol.*, *190*, 289–316, doi:10.1016/S0031-0182(02)00611-9.

Simon, D., and P. Meijer (2015), Dimensions of the Atlantic–Mediterranean connection that caused the Messinian Salinity Crisis, *Mar. Geol.*, *364*, 53–64, doi:10.1016/j.margeo.2015.02.004.

Spivack, A. J., and G. . Wasserburg (1988), Neodymium isotopic composition of the Mediterranean outflow and the eastern North Atlantic, *Geochim. Cosmochim. Acta*, *52*(12), 2767–2773, doi:10.1016/0016-7037(88)90144-5.

Steiger, R. H., and E. Jager (1977), Subcommission on Geochronology: convention on the use of decay constants in geo- and cosmochronology, *Earth Planet. Sci. Lett.*, *36*, 359–362.

Stichel, T., A. E. Hartman, B. Duggan, S. L. Goldstein, H. Scher, and K. Pahnke (2015), Separating biogeochemical cycling of neodymium from water mass mixing in the Eastern North Atlantic, *Earth Planet. Sci. Lett.*, *412*, 245–260, doi:10.1016/j.epsl.2014.12.008.

Stirling, C. H., D. C. Lee, J. N. Christensen, and A. N. Halliday (2000), High-precision in situ 238U-234U-230Th isotopic analysis using laser ablation multiple-collector ICPMS, *Geochim. Cosmochim. Acta*, *64*(21), 3737–3750, doi:10.1016/S0016-7037(00)00457-9.

Stirling, C. H., M. B. Andersen, E. K. Potter, and A. N. Halliday (2007), Low-temperature isotopic fractionation of uranium, *Earth Planet. Sci. Lett.*, *264*, 208–225, doi:10.1016/j.epsl.2007.09.019.

Stumpf, R., M. Frank, J. Schönfeld, and B. A. Haley (2010), Late Quaternary variability of Mediterranean Outflow Water from radiogenic Nd and Pb isotopes, *Quat. Sci. Rev.*, *29*(19-20), 2462–2472, doi:10.1016/j.quascirev.2010.06.021.

Sun, S. (1980), Lead isotopic study of young volcanic rocks from mid-ocean ridges, ocean islands and island arcs, *Philos. Trans. R. Soc. B*, *297*, 409–445.

Tachikawa, K., A. M. Piotrowski, and G. Bayon (2014), Neodymium associated with foraminiferal carbonate as a recorder of seawater isotopic signatures, *Quat. Sci. Rev.*, *88*, 1–13, doi:10.1016/j.quascirev.2013.12.027.

Tachikawa, K., C. Jeandel, and M. Roy-Barman (1999), A new approach to the Nd residence time in the ocean: the role of atmospheric inputs, *Earth Planet. Sci. Lett.*, *170*, 433–446.

Tachikawa, K., M. Roy-Barman, A. Michard, D. Thouron, D. Yeghicheyan, and C. Jeandel

(2004), Neodymium isotopes in the Mediterranean Sea: comparison between seawater and sediment signals, *Geochim. Cosmochim. Acta*, *68*(14), 3095–3106, doi:10.1016/j.gca.2004.01.024.
Tanaka, T. et al. (2000), JNdi-1: a neodymium isotopic reference in consistency with LaJolla neodymium, *Chem. Geol.*, *168*(3-4), 279–281, doi:10.1016/S0009-2541(00)00198-4.
Tessier, A., P. G. C. Campbell, and M. Bisson (1979), Sequential Extraction Procedure for the Speciation of Particulate Trace Metals, *Anal. Chem.*, *51*(7), 844–851, doi:10.1021/ac50043a017.
Topper, R. P. M. (2013), A model analysis of atypical marine sedimentation in mediterranean basins, Ph.D. Thesis, Utrecht University.
Topper, R. P. M., and P. T. Meijer (2015), The precessional phase lag of Messinian gypsum deposition in Mediterranean marginal basins, *Palaeogeogr. Palaeoclimatol. Palaeoecol.*, *417*, 6–16, doi:10.1016/j.palaeo.2014.10.025.
Topper, R. P. M., R. Flecker, P. T. Meijer, and M. J. R. Wortel (2011), A box model of the Late Miocene Mediterranean Sea: Implications from combined 87 Sr/ 86 Sr and salinity data, *Paleoceanography*, *26*, PA3223, doi:10.1029/2010PA002063.
Topper, R. P. M., S. Lugli, V. Manzi, M. Roveri, and P. T. Meijer (2014), Precessional control of Sr ratios in marginal basins during the Messinian Salinity Crisis?, *Geochemistry, Geophys. Geosystems*, *15*, 1926–1944, doi:10.1002/2013GC005192.
Toscani, L., G. Venturelli, M. Barbieri, S. Capedri, J. M. Fernandez Soler, and M. Oddone (1990), Geochemistry and petrogenesis of two-pyroxene andesites from Sierra de Gata (SE Spain), *Mineral. Petrol.*, *41*, 199–213, doi:10.1007/BF01168495.
Toucanne, S., C. M. Angue Minto'o, C. Fontanier, M.-A. Bassetti, S. J. Jorry, and G. Jouet (2015), Tracking rainfall in the northern Mediterranean borderlands during sapropel deposition, *Quat. Sci. Rev.*, *129*, 178–195, doi:10.1016/j.quascirev.2015.10.016.
Troelstra, S. R., H. M. van der Poel, C. H. A. Huisman, L. P. A. Geerlings, and H. Dronkert (1980), Paleoecological changes in the latest Miocene of the Sorbas Basin, SE Spain, *Géologie Méditerranienne*, *7*, 115–126.
Tsimplis, M. N., and H. L. Bryden (2000), Estimation of the transports through the Strait of Gibraltar, *Deep. Res. Part I Oceanogr. Res. Pap.*, *47*(12), 2219–2242, doi:10.1016/S0967-0637(00)00024-8.
Tuenter, E., S. L. Weber, F. J. Hilgen, and L. J. Lourens (2003), The response of the African summer monsoon to remote and local forcing due to precession and obliquity, *Glob. Planet. Change*, *36*(4), 219–235, doi:10.1016/S0921-8181(02)00196-0.
Vai, G. B., and I. P. Martini (2001), *Anatomy of an Orogen: The Apennines and Adjacent Mediterranean Basins*, Springer Science & Business Media.
Vazquez, M., A. Jabaloy, L. Barbero, and F. M. Stuart (2011), Deciphering tectonic- and erosion-driven exhumation of the Nevado-Filabride Complex (Betic Cordillera, Southern Spain) by low temperature thermochronology, *Terra Nov.*, *23*(4), 257–263, doi:10.1111/j.1365-3121.2011.01007.x.
Vázquez, A., R. Utrilla, I. Zamarreño, F. J. Sierro, J. A. Flores, G. Francés, and M. A. Bárcena (2000), Precession-related sapropelites of the Messinian Sorbas Basin (South Spain): Paleoenvironmental significance, *Palaeogeogr. Palaeoclimatol. Palaeoecol.*, *158*(3-4), 353–370, doi:10.1016/S0031-0182(00)00058-4.
Veizer, J. (1989), Strontium isotopes in seawater through time, *Annu. Rev. Earth Planet. Sci.*, *17*, 141–167, doi:10.1017/CBO9781107415324.004.
Vignaud, P. et al. (2002), Geology and palaeontology of the upper miocene toros-menalla hominid locality, chad, *Nature*, *418*(6894), 152–155.
Voelker, A. H. L., A. Colman, G. Olack, J. J. Waniek, and D. Hodell (2015), Oxygen and hydrogen isotope signatures of Northeast Atlantic water masses, *Deep Sea Res. Part II Top. Stud. Oceanogr.*, *116*, 89–106, doi:10.1016/j.dsr2.2014.11.006.
Vonhof, H. B., F. P. Wesselingh, and G. M. Ganssen (1998), Reconstruction of the Miocene western Amazonian aquatic system using molluscan isotopic signatures, *Palaeogeogr. Palaeoclimatol. Palaeoecol.*, *141*, 85–93, doi:10.1016/S0031-0182(98)00010-8.
Washington, R., M. Todd, N. J. Middleton, and A. S. Goudie (2003), Dust-storm source areas determined by the total ozone monitoring spectrometer and surface observations, *Ann. Assoc. Am. Geogr.*, *93*(2), 297–313, doi:10.1111/1467-8306.9302003.
Washington, R., C. Bouet, G. Cautenet, E. Mackenzie, I. Ashpole, S. Engelstaedter, G. Lizcano, G.

M. Henderson, K. Schepanski, and I. Tegen (2009), Dust as a tipping element: the Bodele Depression, Chad., *Proc. Natl. Acad. Sci. U. S. A.*, *106*(49), 20564–20571, doi:10.1073/pnas.0711850106.

Weber, S. L., and E. Tuenter (2011), The impact of varying ice sheets and greenhouse gases on the intensity and timing of boreal summer monsoons, *Quat. Sci. Rev.*, *30*(3-4), 469–479, doi:10.1016/j.quascirev.2010.12.009.

Weijermars, R. (1988), Neogene tectonics in the Western Mediterranean may have caused the Messinian salinity crisis and an associated glacial event, *Tectonophysics*, *148*, 211–219, doi:10.1016/0040-1951(88)90129-1.

Weldeab, S., K.-C. Emeis, C. Hemleben, and W. Siebel (2002), Provenance of lithogenic surface sediments and pathways of riverine suspended matter in the Eastern Mediterranean Sea: evidence from 143Nd/144Nd and 87Sr/86Sr ratios, *Chem. Geol.*, *186*(1–2), 139–149, doi:10.1016/S0009-2541(01)00415-6.

Westerhold, T., T. Bickert, and U. Röhl (2005), Middle to late Miocene oxygen isotope stratigraphy of ODP site 1085 (SE Atlantic): New constrains on Miocene climate variability and sea-level fluctuations, *Palaeogeogr. Palaeoclimatol. Palaeoecol.*, *217*(3-4), 205–222, doi:10.1016/j.palaeo.2004.12.001.

Weyer, S., A. D. Anbar, A. Gerdes, G. W. Gordon, T. J. Algeo, and E. A. Boyle (2008), Natural fractionation of 238U/235U, *Geochim. Cosmochim. Acta*, *72*, 345–359, doi:10.1016/j.gca.2007.11.012.

Willenbring, J. K., and F. von Blanckenburg (2010), Long-term stability of global erosion rates and weathering during late-Cenozoic cooling., *Nature*, *465*(7295), 211–4, doi:10.1038/nature09044.

Wilson, D. J., A. M. Piotrowski, A. Galy, and I. N. McCave (2012), A boundary exchange influence on deglacial neodymium isotope records from the deep western Indian Ocean, *Earth Planet. Sci. Lett.*, *341-344*, 35–47, doi:10.1016/j.epsl.2012.06.009.

Wilson, D. J., A. M. Piotrowski, A. Galy, and J. A. Clegg (2013), Reactivity of neodymium carriers in deep sea sediments: Implications for boundary exchange and paleoceanography, *Geochim. Cosmochim. Acta*, *109*, 197–221, doi:10.1016/j.gca.2013.01.042.

Wu, P., and K. Haines (1996), Modeling the dispersal of Levantine Intermediate Water and its role in Mediterranean deep water formation, *J. Geophys. Res.*, *101*(C3), 6591–6607, doi:10.1029/95JC03555.

Xu, S., A. B. Dougans, S. P. H. T. Freeman, C. Schnabel, and K. M. Wilcken (2010), Improved 10Be and 26Al-AMS with a 5MV spectrometer, *Nucl. Instruments Methods Phys. Res. Sect. B Beam Interact. with Mater. Atoms*, *268*, 736–738, doi:10.1016/j.nimb.2009.10.018.

Zachos, J. C., N. J. Shackleton, J. S. Revenaugh, H. Palike, and B. P. Flower (2001), Climate response to orbital forcing across the Oligocene-Miocene boundary, *Science*, *292*, 274–278, doi:10.1126/science.1058288.

Zeck, H. P., F. Albat, B. T. Hansen, L. R. Torres-Roldán, A. Garciá-Casco, and A. Martín-Algarra (1989), A 21 ± 2 Ma age for the termination of the ductile alpine deformation in the internal zone of the betic cordilleras, South Spain, *Tectonophysics*, *169*, 215–220, doi:10.1016/0040-1951(89)90196-0.

Zhang, Z., G. Ramstein, M. Schuster, C. Li, C. Contoux, and Q. Yan (2014), Aridification of the Sahara desert caused by Tethys Sea shrinkage during the Late Miocene., *Nature*, *513*(7518), 401–4, doi:10.1038/nature13705.

Zheng, Y., R. F. Anderson, A. van Geen, and M. Q. Fleisher (2002), Remobilization of authigenic uranium in marine sediments by bioturbation, *Geochim. Cosmochim. Acta*, *66*(10), 1759–1772, doi:10.1016/S0016-7037(01)00886-9.

van der Zwaan, G. J., F. J. Jorissen, and H. C. de Stigter (1990), The depth dependency of planktonic/benthic foraminiferal ratios: Constraints and applications, *Mar. Geol.*, *95*(1), 1–16, doi:10.1016/0025-3227(90)90016-D.

Appendix 1: *Letters of permission and credit to contributors*

Due to the interdisciplinarity of the MEDGATE project, within which this thesis was generated, data produced by other research group members has been included in this thesis. Moreover, individuals other than my own supervisors have contributed significantly to my training, specifically in data reduction using Matlab and mass spectrometric measurements. The individuals and their contributions are summarized in Table A1.1. Letters of permission for data usage are included from relevant individuals follow the table.

Table A1.1. Contributors and details of their contributions to this thesis.

Contributor	Contribution
Dr. Alice Marzocchi (University of Bristol, now at University of Chicago)	Data: evaporation, precipitation, and river runoff results from GCM HadCM3L experiments for the Western and Eastern Mediterranean basins (Ch. 2, Table 2.6).
Dr. Tanja Kouwenhoven (Utrecht University)	Data: benthic foraminifera counting/assemblages for 12 samples of washed and prepared late Miocene sediment from the Sorbas Basin (Ch. 3, Table 3.2).
Dr. Marlies van der Schee (University of Salamanca)	Data: Nd and Pb isotope analyses of bulk sediment acid-reductive leachates from 6 samples of ODP Site 978 in the Alborán Sea (Ch. 4, Table 4.1; Ch. 5, Table 5.2).
Dr. Ángel Rodés (SUERC)	Guidance/assistance with $^{10}Be/^{9}Be$ analyses and generation of Matlab data reduction script.
Dr. Jan Fietzke (GEOMAR Helmholtz Centre for Ocean Research Kiel)	Guidance/assistance with LA-MC-ICPMS measurements of ferromanganese crust 3514-6.
Anne Kelly (SUERC)	Guidance/assistance with column chemistry for Sr purification and general clean lab protocols.
Vincent Gallagher (SUERC)	Guidance/assistance with TIMS mass spectrometry for Sr isotope analysis.

06 February 2016

To whom it may concern,

I, Alice Marzocchi (PhD Candidate, Bristol University), hereby give permission to Sevasti Eleni Modestou to use data generated by me for her thesis. Specifically, the data in question are global circulation model results from the model HadCM3L. These data are not explicitly published elsewhere as of yet.

These data were initially generated for the purpose of studying the relationship between model results and other data when varying orbital parameters in the model throughout a precessional cycle and are fundamental to my own research. However, a subset (specifically, evaporation, precipitation, and river runoff values for the Mediterranean region) have also proven useful for Sevasti's research project. We are colleagues who actively collaborate through the MEDGATE ITN. One of the major aims of our research group was to facilitate collaboration and interdisciplinary research.

I have had many general conversations with Sevasti regarding the format of the data and other applications, but have not had any input in the interpretation or use of the data in her specific applications.

Contact email: alice.marzocchi@bristol.ac.uk

Sincerely,

Alice Marzocchi

13 January 2016

To whom it may concern,

I, Tanja J. Kouwenhoven, hereby give permission to Sevasti Eleni Modestou to use data generated by me for her thesis.

Specifically, I counted 12 samples of washed sediment for benthic foraminifera. I am a benthic foraminifer specialist. After analysis of the samples, I spent time with Sevasti at a microscope to explain the results and show her the important details first hand (i.e., how important fossils look, what certain species imply about environmental conditions, and assessment of fossil preservation). I provided Sevasti with a data table and explained the results. Together, we discussed the potential implications of this data, following which Sevasti wrote up the results for publication and I assessed the text for accuracy.

These data were generated for the purpose of estimating water depth and infer information about palaeoenvironmental conditions in a basin ~6.5 Ma. We are colleagues who actively collaborate through the MEDGATE ITN.

Contact email: T.J.Kouwenhoven@uu.nl

Sincerely,

Tanja J. Kouwenhoven

13 January 2016

To whom it may concern,

I, Marlies van der Schee, hereby give permission to Sevasti Eleni Modestou to use data generated by me for her thesis. Specifically, the data in question are neodymium and lead isotope measurements from Late Miocene and Early Pliocene sediments sampled from a marine sediment core from Site 978, ODP Leg 161, Alboran Sea (Western Mediterranean).

These data were generated for the purpose of estimating water mass signatures which are useful for both my own and Sevasti's research projects, as we are colleagues who actively collaborate through the MEDGATE ITN. Sevasti was involved in the process to a small degree, in terms of selection of the samples, but I did most of the work involved in processing and measuring. Interpretation of the data has been a joint effort as we are both working towards similar problems.

Contact email: marliesvanderschee@gmail.com

Sincerely,

Marlies van der Schee

Appendix 2: *Corrected secondary standard data*

The following figure shows the secondary standard measurements performed during LA-MC-ICPMS measurement of ferromanganese crust 3514-6. The y-axis is number of measurements.

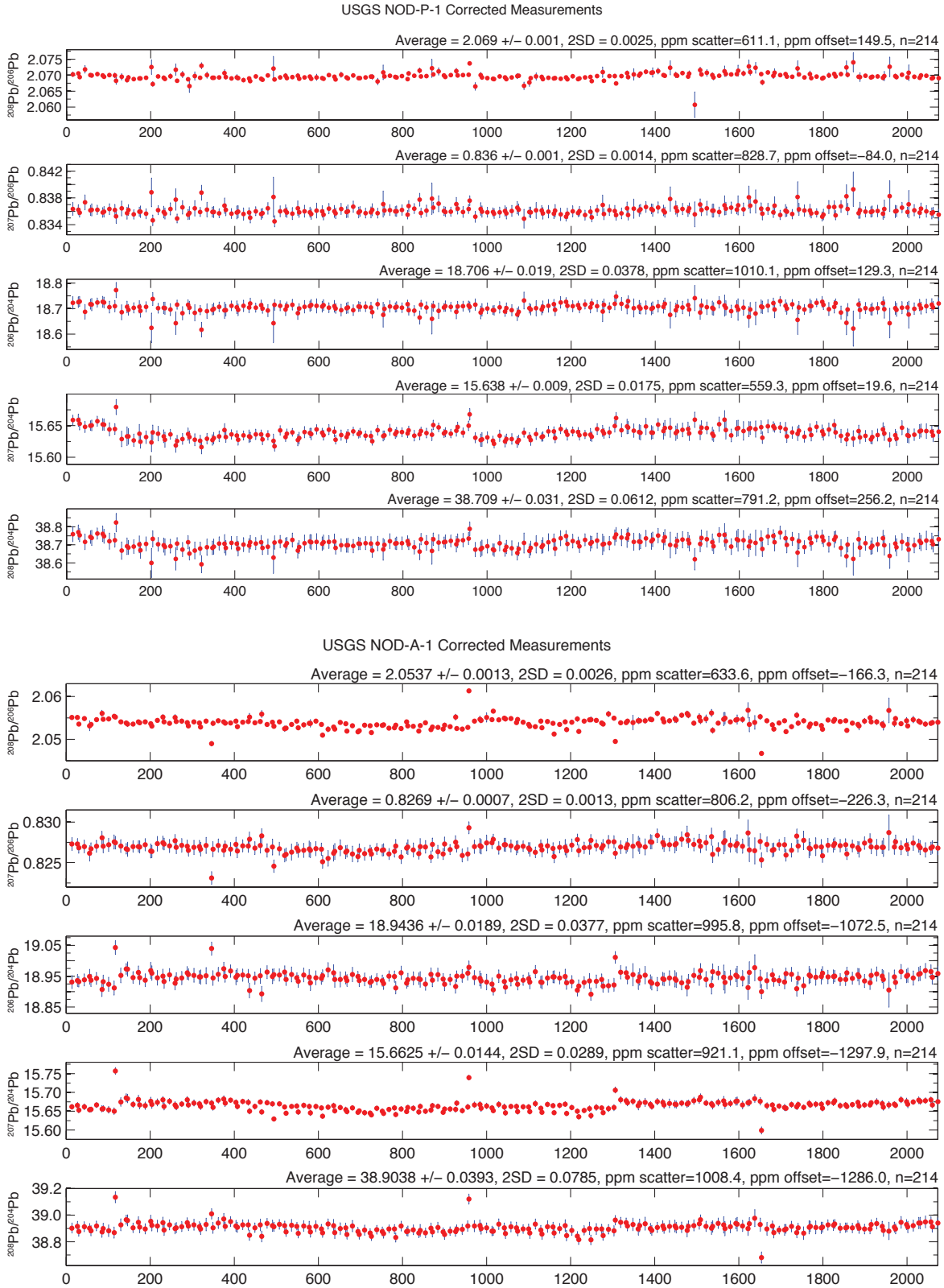

Appendix 3: *Additional results: Nd and Pb across the Mediterranean*

Some additional Nd and Pb isotope data for sections around the Mediterranean were generated over the course of this project which did not fit appropriately into the results and discussion chapters. However, do they provide some insight into the different relationships between Nd and Pb to the isotope composition of Mediterranean seawater during the Late Miocene. The additional data was generated from samples from Ain el Beida, Metochia, and Monte dei Corvi, in addition to Sorbas, Falconara, Monte dei Corvi and ODP Site 978 (summarized in Tables A3.1, A3.2, Fig. A3.1).

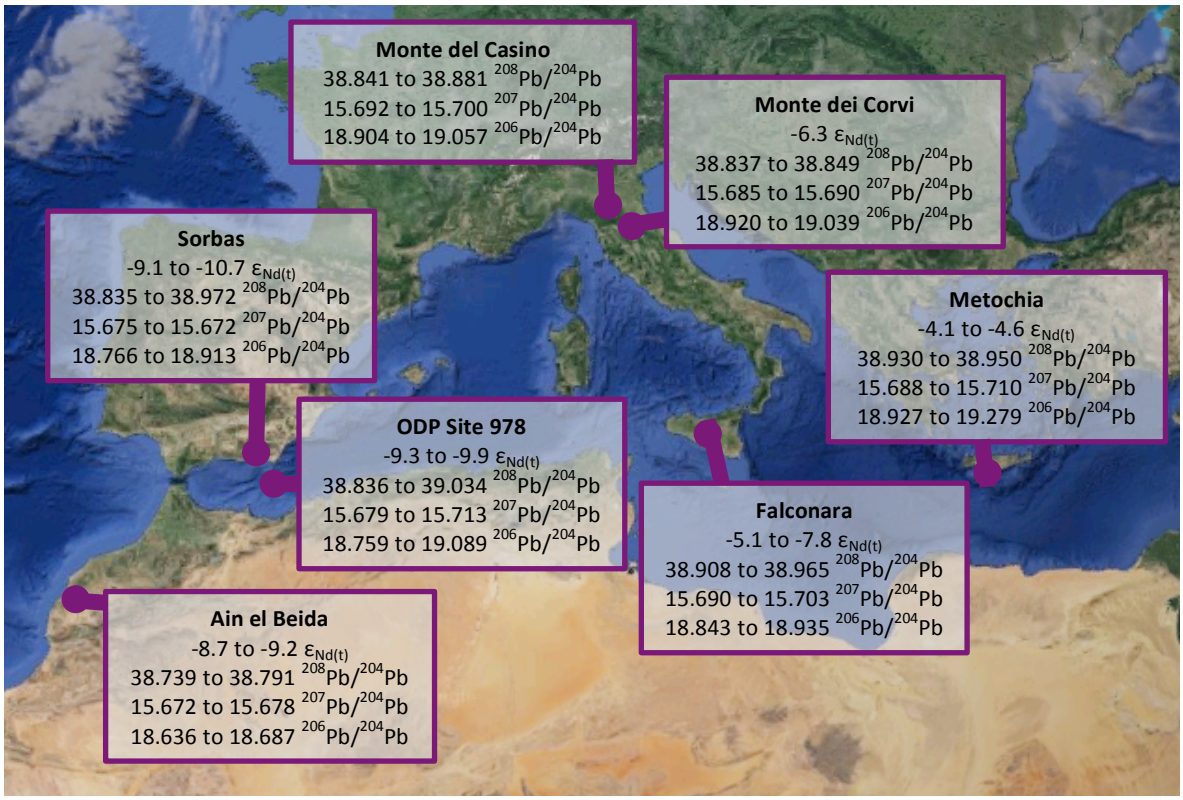

Fig. A3.1. Map of Mediterranean region showing range of seawater Nd and Pb isotopic compositions measured for each location, including data for sections only shown in this appendix as well as data for Sorbas, Falconara, Metochia and ODP Site 978 shown in chapters 4 and 5. See Tables A3.1 and A3.2 for 2σ external reproducibility of Monte dei Corvi, Metochia, and Ain el Beida.

Table A3.1. ε_{Nd} from Metochia, Falconara, Ain el Beida, and Monte dei Corvi. Error of ratio is 2σ internal reproducibility; error of $\varepsilon_{Nd(t)}$ is 2σ external reproducibility based on secondary standard measurements.

Sample	Age Ma	$^{143}Nd/^{144}Nd$	eNd(t)
Metochia			
9780 FT	6.650	0.512400 ±10	-4.65 ±0.42
9788 FT	6.677	0.512411 ±13	-4.44 ±0.42
9788 BSL4	6.677	0.512415 ±13	-4.35 ±0.42
9792 BSL4	6.697	0.512427 ±13	-4.11 ±0.42
Falconara			
18.892 FT	6.605	0.512303 ±15	-6.48 ±0.42
18.907 FT	6.582	0.512377 ±13	-5.05 ±0.42
18.907 BSL4	6.582	0.512370 ±14	-5.18 ±0.42
18.913 FT	6.573	0.512237 ±13	-7.77 ±0.42
Ain el Beida			
MA305 BSL4	6.301	0.512175 ±5	-8.99 ±0.18
MA347 BSL4	6.184	0.512191 ±4	-8.67 ±0.18
MA348 BSL4	6.181	0.512171 ±4	-9.06 ±0.18
MA349 BSL4	6.179	0.512164 ±9	-9.19 ±0.18
Monte dei Corvi			
22.464 FT	6.576	0.512313 ±17	-6.29 ±0.42

Metochia, Falconara, and Monte dei Corvi analytical session 3 – Nu Plasma, GEOMAR, November 2014. Ain el Beida analytical session 4 – Neptune Plus, GEOMAR, September 2015.

The Nd isotope compositions display a wide range, from -4.1 $\varepsilon_{Nd(t)}$ in the East at Metochia to -9.2 outside the Mediterranean at Ain el Beida (all ± 0.42 ε_{Nd}). The general trend towards less radiogenic values westwards is consistent with modern Mediterranean water mass Nd signatures (Ch. 1, Fig. 1.14; [*Henry et al.*, 1994; *Tachikawa et al.*, 2004]). As no investigation of detrital material has been performed, it is unknown if there is influence due to local inputs at these sites; however, several deep sites in the Eastern Mediterranean [*Osborne et al.*, 2010] have shown similarly radiogenic signatures to those observed from these new analyses at Metochia. Although more analysis is required to confirm, this suggests the radiogenic values at Metochia are consistent with a water signature. In contrast to the Nd results, there is no consistent spatial shift in the Pb isotope signatures. This supports the hypothesis that at least one end member of the observed values at all the sites approaches that of North African dust, which seems to have a strong control over seawater values all over the Mediterranean, particularly during insolation minima.

Table A3.2. Radiogenic Pb isotope data from acid-reductive bulk sediment leachates from Monte dei Corvi, Ain el Beida and Metochia sections. Duplicate samples and their averages are shown. Errors shown are 2σ external reproducibility for respective analytical sessions.

Sample	Age Ma	$^{208}Pb/^{204}Pb$	$^{207}Pb/^{204}Pb$	$^{206}Pb/^{204}Pb$	$^{208}Pb/^{206}Pb$	$^{207}Pb/^{206}Pb$
Ain el Beida						
MA305	6.3012	38.741 ±7	15.673 ±2	18.637 ±2	2.0787 ±2	0.84095 ±4
MA305	6.3012	38.738 ±7	15.672 ±2	18.635 ±2	2.0788 ±2	0.84098 ±4
MA305	6.3012	38.733 ±7	15.670 ±2	18.634 ±2	2.0786 ±2	0.84094 ±4
	Average	*38.738* ±7	*15.672* ±2	*18.639* ±2	*2.0787* ±2	*0.84095* ±4
MA307	6.1836	38.742 ±7	15.674 ±2	18.643 ±2	2.0781 ±2	0.84077 ±4
MA307	6.1836	38.740 ±7	15.674 ±2	18.642 ±2	2.0781 ±2	0.84075 ±4
MA307	6.1836	38.734 ±7	15.672 ±2	18.641 ±2	2.0779 ±2	0.84072 ±4
MA307	6.1836	38.741 ±7	15.675 ±2	18.644 ±2	2.0780 ±2	0.84075 ±4
	Average	*38.740* ±7	*15.674* ±2	*18.643* ±2	*2.0780* ±2	*0.84075* ±4
MA311	6.1812	38.794 ±7	15.679 ±2	18.688 ±2	2.0759 ±2	0.83900 ±4
MA311	6.1812	38.788 ±7	15.677 ±2	18.687 ±2	2.0757 ±2	0.83894 ±4
	Average	*38.791* ±7	*15.678* ±2	*18.687* ±2	*2.0758* ±2	*0.83897* ±4
MA312	6.1786	38.776 ±7	15.678 ±2	18.674 ±2	2.0764 ±2	0.83955 ±4
MA312	6.1786	38.777 ±7	15.678 ±2	18.675 ±2	2.0764 ±2	0.83950 ±4
MA312	6.1786	38.770 ±7	15.676 ±2	18.673 ±2	2.0762 ±2	0.83948 ±4
MA312	6.1786	38.779 ±7	15.679 ±2	18.676 ±2	2.0764 ±2	0.83950 ±4
	Average	*38.776* ±7	*15.678* ±2	*18.674* ±2	*2.0764* ±2	*0.83952* ±4
Monte dei Corvi						
22.460	6.6040	38.837 ±14	15.685 ±6	18.920 ±18	2.0527 ±4	0.82899 ±13
22.461	6.5982	38.845 ±14	15.689 ±6	19.012 ±18	2.0433 ±4	0.82522 ±13
22.463	6.5830	38.849 ±14	15.690 ±6	19.039 ±18	2.0405 ±4	0.82412 ±13
Metochia						
9780	6.6483	38.931 ±14	15.688 ±6	18.927 ±18	2.0569 ±4	0.82885 ±13
9788	6.6775	38.937 ±14	15.709 ±6	19.279 ±18	2.0196 ±4	0.81481 ±13
9790	6.6919	38.945 ±14	15.694 ±6	18.997 ±18	2.0500 ±4	0.82613 ±13
9790	6.6919	38.950 ±14	15.696 ±6	18.999 ±18	2.0502 ±4	0.82618 ±13
	Average	*38.947* ±14	*15.695* ±6	*18.998* ±18	*2.0501* ±4	*0.82615* ±13
9792	6.6975	38.950 ±14	15.710 ±6	19.264 ±18	2.0219 ±4	0.81548 ±13

Monte dei Corvi, Metochia analytical session 3 - Nu Plasma, GEOMAR, November 2014. Ain el Beida analytical session 4 - Neptune Plus, GEOMAR, September 2015.

The Pb isotope data for Monte dei Corvi are very similar to the Monte del Casino values. For the former section, four samples were selected, from periods of both insolation minima and maxima. From these, the samples selected from insolation maxima are consistent at both sites, while samples from insolation minima are also consistent at both sites. This suggests that if a high temporal resolution study were performed for Monte dei Corvi, it is likely that the precessional variability observed would follow the same pattern as Monte del Casino. This is consistent with the fact these locations are near each other (both located within the Northern Apennines fore-arc basin) and the expected influence of local inputs

on the Pb isotope composition of seawater. The four samples from Ain el Beida also suggest precessional variability, with more radiogenic values observed at insolation minima, although this site is from the Atlantic side of the Rifian corridor. This could suggest that the Pb isotope composition of water at Ain el Beida is also strongly correlated to dust production, although the signatures are different, suggesting a different overall dust composition. Follow-up studies comparing high resolution seawater fluctuations from the Atlantic side of both the Betic and Rifian corridors, for sites such as Ain el Beida, could potentially provide more information about how the climate of the Mediterranean and the buffering effect of the Atlantic combine. This would have implications for understanding how the stratigraphy and sedimentology of the extra-Mediterranean sections, which are key to Messinian salinity crisis chronology, are related to intra-Mediterranean deposition.

Appendix 4: *Elemental ratio data*

Table A4.1. Elemental ratio data from acid-reductive leachates, referred to in Ch. 4. Errors are percent relative standard deviation. This table covers several pages, and as such this header will not be repeated.

Sample	Mn/Nd	%RSD	Fe/Nd	%RSD	Al/Nd	%RSD	Nd/Ti	%RSD	Mn/Pb	%RSD	Fe/Pb	%RSD	Pb/Ti	%RSD	Fe/Al	%RSD	Mn/Al	%RSD
17.776 R3S2	48.12	0.65	63.99	2.59	21.98	1.64	1.80	0.13	157.13	6.46	28.95	11.68	0.55	0.22	2.91	0.25	2.19	0.16
17.776 R3S3	47.50	0.26													3.47	8.80	2.45	5.98
17.776 R3S3	48.37	0.34			19.59	6.32									3.53	11.28	2.47	7.60
17.777 R3S2	114.49	0.23	83.12	2.36	35.84	11.20	1.59	0.60	19.77	2.59	138.50	4.20	0.96	0.32	2.32	0.72	3.19	0.98
17.777 R3S3	118.83	0.42													2.76	6.37	3.59	7.76
17.779 BSL4							2.84	0.27										
17.779 BSL4 R2									25.45	0.38	176.55	0.59						
17.779 R3S2	1.77	0.44	66.52	0.32	26.42	9.43	2.21	0.26	195.53	0.61	129.84	0.49	1.14	0.13	2.52	0.90	3.82	1.36
17.779 R3S3	15.17	0.17							218.18	14.64					2.95	8.60	4.22	12.13
17.779 R3S3	15.50	0.22													3.30	2.84		
17.78 R3S2	33.14	0.23	94.99	2.42	21.15	2.83	0.83	0.36	67.48	0.43	192.30	5.36	0.49	0.32	4.49	0.61	1.57	0.30
17.78 R3S3	33.43	0.27					0.79	0.18					0.38	0.14	5.26	3.22	1.70	9.68
17.781 BSL4							0.75	0.28										
17.781 BSL4 R2									6.86	0.48	32.78	4.15						
17.781 R3S2	31.67	0.72	76.68	0.67	21.83	5.17	0.76	0.42	76.36	0.34	184.88	1.78	0.31	0.21	3.51	0.83	1.46	0.34
17.781 R3S3	31.53	0.27					0.80	0.20					0.33	0.82	4.37	6.35	1.66	2.38
17.782 R3S2	43.94	0.27	69.66	0.47	22.19	4.96	1.76	0.36	133.57	1.80	211.74	2.98	0.58	0.12	3.14	0.58	1.99	0.37
17.782 R3S3	43.57	0.47							138.47	8.34							2.31	14.54
17.783 BSL4							2.19	0.17										
17.783 BSL4 R2									22.18	0.30	228.57	1.36						
17.783 R3S2	129.25	0.45	88.95	2.87	38.73	1.73	1.54	0.77	195.91	2.87	134.87	4.56	1.18	0.53	2.30	0.65	3.34	0.92
17.783 R3S3	13.60	0.21									142.45	11.67			2.66	6.73	3.68	8.96
17.784 R3S2	87.83	0.53	73.67	3.57	26.87	1.37	2.55	0.50	139.88	1.72	117.36	5.73	1.29	0.34	2.74	1.66	3.27	1.27
17.784 R3S2	87.73	0.32	72.42	5.63	27.00	11.96	2.48	0.34	14.88	1.57	116.33	9.81	1.28	0.25	2.68	1.26	3.25	1.44
17.784 R3S3	9.76	0.21	8.33	14.95											3.31	3.89	3.73	4.35
17.785 BSL4					57.59	3.47	2.78	0.22										
17.785 BSL4					56.22	1.15	2.84	0.12										
17.785 BSL4					56.90	2.45	2.82	0.15					13.59	0.70				
17.785 BSL4 R2									9.13	0.35	471.82	1.95						
17.785 BSL4 R2									9.17	0.46	482.23	3.51						
17.785 R3S2	32.64	0.66	64.44	1.46	19.33	7.63	0.98	0.26	119.65	2.11	236.24	6.78	0.27	0.47	3.33	1.32	1.69	0.67
17.785 R3S3	33.74	0.13					0.92	0.23					0.22	0.11			1.84	8.39

Sample	Mn/Nd	%RSD	Fe/Nd	%RSD	Al/Nd	%RSD	Nd/Ti	%RSD	Mn/Pb	%RSD	Fe/Pb	%RSD	Pb/Ti	%RSD	Fe/Al	%RSD	Mn/Al	%RSD
17.786 R3S2	41.84	0.17	75.46	1.54	2.21	3.53	0.79	0.34	139.38	4.68	251.38	9.83	0.24	0.79	3.73	0.66	2.70	0.37
17.786 R3S3	42.46	0.98					0.78	0.19					0.23	0.12	4.46	12.50	2.34	6.43
17.787 R3S2	49.46	0.13	83.78	3.64	23.79	2.99	1.78	0.25	113.70	1.23	192.60	8.62	0.77	0.13	3.52	0.47	2.79	0.27
17.787 R3S3	51.76	0.72	94.34	3.64							236.28	12.51			4.16	8.51	2.24	4.63
17.788 R3S2	8.63	0.42	8.81	4.16	27.65	5.67	1.80	0.14	15.84	0.53	151.17	7.77	0.96	0.65	2.92	0.62	2.92	0.60
17.788 R3S3	82.77	0.87													3.42	4.94	3.23	4.58
17.789 R3S2	75.75	0.22	88.64	3.90	29.17	5.37	1.69	0.39	185.34	3.59	216.86	8.63	0.69	0.24	3.39	0.57	2.60	0.48
17.789 R3S3	77.69	0.12													3.76	7.89	2.98	6.79
17.789 R3S3	76.69	0.44													3.62	9.76	2.88	7.76
17.79 R3S2	33.58	0.68	75.48	3.86	18.76	7.11	0.90	0.44	99.39	1.27	223.44	9.56	0.34	0.41	4.23	1.53	1.79	0.68
17.79 R3S3	34.75	0.14	84.96	4.71			0.88	0.19	16.53	11.47			0.29	0.69				
17.791 R3S2	46.24	0.46	11.25	1.94	19.47	5.42	0.62	0.44	98.67	0.78	216.43	4.47	0.29	0.38	5.22	1.47	2.38	0.67
17.791 R3S3	49.13	0.19					0.55	0.39	18.14	4.24			0.25	0.95	6.40	8.62	2.54	3.59
17.791 R3S3	47.38	0.19					0.62	0.72					0.29	0.86	6.22	6.84	2.63	2.86
17.792 R3S2	56.55	0.70	85.22	2.58	2.92	8.54	1.94	0.48	136.29	0.99	27.20	6.45	0.80	0.27	4.73	1.66	2.68	1.89
17.792 R3S3	56.50	0.26	93.18	12.53														
17.793 R3S2	53.62	0.13	79.63	1.75	21.73	11.23	1.71	0.47	161.40	2.64	239.69	6.84	0.57	0.17	3.66	1.90	2.47	1.28
17.793 R3S2	53.73	0.21	79.19	2.38	22.47	6.45	1.69	0.67	163.26	2.60	24.60	8.13	0.56	0.24	3.59	1.56	2.44	0.71
17.793 R3S3	55.75	0.67													4.39	12.84	2.72	7.77
17.794 R3S2	48.54	0.35	8.93	2.52	25.77	7.73	1.56	0.50	133.15	3.74	224.23	9.26	0.56	0.24	3.14	0.87	1.86	0.51
17.794 R3S3	49.46	0.55					0.99	0.15					0.33	0.14			2.16	8.44
17.795 R3S2	57.24	0.96	81.37	1.18	2.97	11.28	0.73	0.11	132.44	4.59	188.97	6.23	0.32	0.97	3.88	2.87	2.72	1.46
17.795 R3S3	59.78	0.82					0.61	0.75					0.27	0.32			3.12	11.85
17.796 R3S2	49.78	0.12	7.98	0.76	21.92	4.34	0.74	0.29	171.47	4.23	247.98	6.37	0.21	0.50	3.24	0.64	2.24	0.44
17.796 R3S3	51.89	0.88					0.67	0.12					0.18	0.41	3.75	6.73	2.42	3.68
17.797 R3S2	53.78	0.26	89.35	3.53	27.24	2.79	1.69	0.42	15.74	2.83	25.37	9.68	0.61	0.18	3.28	0.35	1.97	0.22
17.797 R3S3	55.24	0.32													3.88	7.57	2.21	4.25
17.798 R3S2	58.11	0.91	84.35	4.65	25.78	7.78	1.69	0.40	22.57	1.19			0.48	0.27	3.27	1.45	2.25	0.69
17.798 R3S3	59.93	0.18													3.85	5.43	2.56	3.51
18.892 BSL4					21.42	2.32	2.83	0.99										
18.892 BSL4					2.84	4.18	2.78	0.54										
18.892 BSL4					2.94	1.92	2.85	0.86					4.39	0.12				

Sample	Mn/Nd	%RSD	Fe/Nd	%RSD	Al/Nd	%RSD	Nd/Ti	%RSD	Mn/Pb	%RSD	Fe/Pb	%RSD	Pb/Ti	%RSD	Fe/Al	%RSD	Mn/Al	%RSD
18.892 BSL4 R2									28.68	0.34	634.86	7.82						
18.892 BSL4 R2									28.44	0.52	638.24	11.97						
18.899 BSL4							0.14	0.18					0.39	0.77				
18.899 BSL4							0.13	0.61					0.39	0.69				
18.899 BSL4							0.13	0.31					0.39	0.12				
18.899 BSL4 R2																		
18.899 BSL4 R2																		
18.91 D1 R3S3	27.56	0.37			29.99	13.85			34.68	5.65					4.21	14.57	0.92	3.18
18.91 R3S3	26.22	0.52	14.27	3.97	28.17	6.60	1.82	0.17	32.95	0.13	132.12	5.46	1.44	0.13	3.71	0.87	0.92	0.21
18.911 D1 R3S3	32.98	0.68													1.12	2.75	0.82	1.37
18.911 R3S3	3.13	0.76	38.72	5.86	37.72	5.53	2.29	0.22	6.85	1.59	78.17	11.91	1.13	0.17	1.27	0.22	0.80	0.12
18.912 D1 R3S3	48.63	0.78													0.57	1.39	0.69	0.99
18.912 R3S3	45.16	0.58	47.24	3.42	7.67	5.31	2.14	0.57	6.38	0.61	63.16	4.55	1.50	0.41	0.67	0.67	0.64	0.45
18.913 BSL4							0.46	0.87					1.17	0.16				
18.913 BSL4 R2																		
18.914 D1 R3S3	43.76	0.16					1.35	0.54	45.99	1.51			1.28	0.59	3.93	13.18	2.60	8.66
18.914 R3S3	42.67	0.64	58.17	0.68	17.89	12.73	1.47	0.82	44.87	0.14	61.17	0.74	1.40	0.88	3.25	2.40	2.39	1.69
18.915 D1 R3S3	87.42	0.62			38.69	1.17	0.74	0.78	76.98	1.85	1.34	4.83	0.85	0.14	2.99	7.96	2.30	6.43
18.915 R3S3	83.51	0.48	97.79	2.50			0.76	0.64	96.88	0.82	113.45	2.98	0.66	0.68	2.48	0.97	2.12	0.83
18.916 D1 R3S3	88.73	0.44							147.24	14.94					1.95	13.72		
18.916 R3S3	84.68	0.25	5.67	7.12			0.68	0.13	14.60	2.38	84.75	11.86	0.46	0.12	1.65	2.28	2.74	3.76
18.917 R3S3	19.99	0.76	59.83	6.65			0.68	0.23	152.34	5.55	82.85	8.97	0.44	0.23	1.41	0.60	2.58	1.76
18.917D1 R3S3	116.98	0.25					0.68	0.20					0.43	0.36				
18.918 D1 R3S3	75.76	0.12					0.78	0.19	12.55	14.51			0.49	0.99	1.57	8.35	2.87	11.38
18.918 D1 R3S3	7.93	0.52	5.39	1.40	35.60	3.24	0.83	0.84	19.90	0.84	78.77	2.18	0.54	0.55	1.42	0.13	1.99	0.18
18.918 R3S3	7.68	0.24	5.61	3.14	36.17	12.15	0.83	0.25	19.64	1.61	79.20	5.35	0.53	0.18	1.40	0.48	1.94	0.66
18.919 R3S2	28.86	0.73	36.24	0.60	22.80	2.76	1.73	0.15	5.24	0.29	63.69	1.96	0.99	0.11	1.59	0.19	1.27	0.15
18.919 R3S3	29.76	0.12	37.53	9.73					5.41	6.48					1.87	12.70	1.43	1.65
18.919 R3S3	29.19	0.28							5.43	9.64	65.62	5.72			1.74	7.25	1.34	5.49
18.92 R3S2	12.24	0.60	85.15	1.76	24.77	4.61	2.34	0.46	21.85	0.42	152.44	3.67	1.32	0.25	3.44	0.64	0.49	0.92
18.92 R3S3	11.99	0.69	10.00	13.36					2.13	0.99					4.23	8.18	0.55	1.67
18.92 R3S3	12.49	0.58							22.90	3.25					4.11	9.43	0.54	1.19

Sample	Mn/Nd	%RSD	Fe/Nd	%RSD	Al/Nd	%RSD	Nd/Ti	%RSD	Mn/Pb	%RSD	Fe/Pb	%RSD	Pb/Ti	%RSD	Fe/Al	%RSD	Mn/Al	%RSD
18.921 R3S2	11.46	0.34	93.42	1.28	22.12	4.25	2.45	0.48	17.19	0.12	145.41	2.20	1.58	0.33	4.22	0.81	0.50	0.96
18.921 R3S3	1.78	0.64							15.87	1.34					5.13	7.48	0.55	0.78
18.922 R3S2	2.83	0.69	125.77	1.64	23.85	4.14	2.57	0.14	25.76	0.16	155.73	2.67	1.66	0.13	5.45	0.98	0.91	0.16
18.922 R3S3	2.38	0.14							23.52	2.47							0.93	2.35
18.923 R3S2	36.49	0.66	62.15	2.53	15.87	5.48	2.94	0.56	36.36	0.13	61.91	2.54	2.95	0.57	3.92	1.37	2.30	0.79
18.923 R3S3	36.19	0.12	65.81	14.76					33.78	1.59	61.56	13.97					2.72	11.71
18.924 R3S2	13.74	0.17	4.69	2.18	18.19	7.26	2.87	0.33	26.52	0.57	77.33	4.20	1.49	0.17	2.22	0.95	0.76	0.37
18.924 R3S3	13.60	0.74	42.24	13.50					25.88	1.67							0.88	8.28
18.925 R3S2	99.38	0.54	43.60	2.86	4.55	13.47	2.25	0.22	73.54	0.33	32.26	2.11	2.74	0.28	1.75	0.35	2.46	0.79
18.925 R3S3	13.54	0.86			38.79	9.37			72.34	7.72					1.19	3.25	2.72	6.45
18.926 R3S2	85.74	0.35	45.38	4.41	61.36	12.66	1.66	0.76	63.83	0.51	33.79	3.29	2.16	0.12	0.74	0.17	1.40	0.29
18.926 R3S3	88.67	0.16							12.51	0.72					0.74	2.29	1.50	2.25
18.927 R3S2	18.42	0.17	2.96	1.40	31.40	5.33	1.85	0.27	37.49	0.30	42.55	2.85	0.91	0.15	0.68	0.12	0.59	0.12
18.927 R3S2	19.17	0.40	21.59	1.12	31.99	2.48	1.85	0.19	38.26	0.29	43.83	2.46	0.92	0.12	0.67	0.62	0.60	0.46
18.927 R3S3	18.77	0.59							37.38	7.23					0.68	1.83	0.67	1.62
18.928 R3S2	48.32	0.27	88.47	3.96	32.49	5.67	1.25	0.15	34.58	0.11	63.39	2.79	1.74	0.19	2.72	0.49	1.49	0.26
18.928 R3S3	49.28	0.64							33.37	1.36					3.25	5.61	1.64	2.83
18.928 R3S3	48.79	0.48							33.85	0.69					3.24	9.32	1.63	4.70
18.929 R3S2	24.79	0.78	75.22	0.99	24.00	1.85	1.60	0.19	33.83	0.65	12.67	1.33	1.17	0.14	3.13	0.24	1.34	0.80
18.929 R3S3	24.70	0.12	81.89	5.76					32.56	1.15	17.96	6.44			3.77	5.99	1.14	1.84
18.929 R3S3	25.38	0.29	83.35	1.82	23.54	1.27	1.47	0.39	34.33	2.65	112.74	14.24	1.89	0.28	3.55	1.56	1.78	0.46
18.93 R3S2	26.89	0.23	112.94	2.42	34.84	8.56	1.62	0.14	28.50	0.33	119.68	2.48	1.53	0.64	3.24	0.80	0.77	0.19
18.93 R3S3	26.68	0.22			3.79	2.63			27.60	1.46					3.97	2.85	0.87	0.58
18.93 R3S3	27.65	0.27	127.20	14.94					28.92	5.33					3.69	5.12	0.83	1.18
18.931 R3S2	58.94	0.14	1.28	3.60	2.96	5.88	2.23	0.16	85.24	0.14	145.32	4.42	1.54	0.19	4.99	1.47	2.93	0.86
18.931 R3S3	59.23	0.19	19.92	3.98					83.73	3.43					6.12	9.87	3.30	5.24
18.932 R3S2	63.58	0.18	142.59	4.60	27.90	4.64	0.91	0.79	68.15	0.13	152.83	4.35	0.85	0.74	5.12	0.86	2.28	0.38
18.932 R3S3	65.98	0.46					0.84	0.18	6.94	12.17			0.92	0.26	6.56	12.88	2.42	4.75
18.933 R3S2	18.57	0.66	83.53	5.57			0.87	0.14	75.93	0.32	58.40	3.89	1.25	0.20	1.13	0.29	1.47	0.36
18.933 R3S3	11.69	0.29													1.26	0.93	1.62	0.97
18.934 R3S2	46.17	0.72	61.13	1.98			0.79	0.13	57.20	1.56	75.70	13.63	0.64	0.13	0.97	0.33	0.73	0.29
18.934 R3S3	46.17	0.15													1.38	1.70	0.79	0.89

Sample	Mn/Nd	%RSD	Fe/Nd	%RSD	Al/Nd	%RSD	Nd/Ti	%RSD	Mn/Pb	%RSD	Fe/Pb	%RSD	Pb/Ti	%RSD	Fe/Al	%RSD	Mn/Al	%RSD
18.935 R3S2	123.31	0.49	88.79	6.84			0.53	0.39	143.85	0.63	13.59	7.99	0.46	0.34	1.77	0.69	2.46	0.94
18.935 R3S3	127.96	0.24	93.35	4.79			0.54	0.27					0.45	0.38	2.15	7.67	2.96	1.49
18.936 R3S2	11.21	0.63	118.00	3.43	56.57	4.52	0.56	0.56	143.29	1.19	153.46	4.53	0.43	0.48	2.86	0.18	1.95	0.16
18.936 R3S2	11.25	0.74	117.69	7.73	56.38	7.51	0.57	0.76	144.96	0.48	153.93	1.12	0.43	0.52	2.77	0.38	1.96	0.26
18.936 R3S3	111.59	0.15					0.57	0.22	144.17	1.78			0.44	0.16	2.48	3.73	2.18	3.16
18.936 R3S3	117.43	0.23	134.61	3.85			0.55	0.12	161.86	9.88			0.40	0.49	2.37	0.95	2.67	0.79
18.937 R3S2	46.55	0.14	94.86	2.27	38.37	9.55	1.22	0.13	63.36	0.33	129.13	3.52	0.90	0.11	2.47	0.62	1.21	0.32
18.937 R3S3	45.49	0.82							62.77	14.14					2.92	2.76	1.34	9.54
18.937 R3S3	47.92	0.69													2.93	5.82	1.34	2.60
18.97 BSL4					16.32	0.99	2.49	0.13										
18.97 BSL4 R2	33.87	0.24	976.59	9.72					14.64	0.31	422.14	3.32						
22.46 BSL4					29.82	5.59	6.88	1.88										
22.46 BSL4 R2									7.48	0.71	644.78	6.38						
22.461 BSL4					2.68	0.65	7.74	0.26										
22.461 BSL4 R2									16.99	0.22	936.95	12.40						
22.463 BSL4					55.30	2.99	1.71	0.64										
22.463 BSL4 R2									11.76	0.29	422.64	3.54						
22.464 BSL4							4.24	0.54										
22.464 BSL4 R2									38.53	0.34	483.36	9.50						
33-15 BSL3							0.44	0.85										
33-15 BSL3							0.44	0.87										
33-15 BSL3							0.44	0.12					2.54	0.24				
33-15 BSL3 R2									37.63	0.16	19.92	3.37	3.52	0.12				
33-15 BSL3 R2									38.35	0.17	111.20	4.27	3.31	0.51	6.48	2.81	2.24	0.97
33-15 SLL1 R3S1	17.78	1.11																
33-15 SLL1 R3S2									23.65	12.93					3.73	12.13	0.25	0.98
33-15 SLL2 R3S1	7.43	0.28	194.99	0.93	17.97	6.70	1.00	0.64	15.82	0.17	413.88	4.66	0.47	0.57	1.84	4.27	0.41	0.15
33-15 SLL3 R3S1	6.49	0.19	1378.16	5.98			0.19	0.74	3.25	0.21			0.37	0.26			0.84	0.17
33-15 SLL3 R3S1	6.38	0.44					0.18	0.13	3.23	0.24			0.36	0.23	17.97	1.63	0.83	0.49
33-15 SLSL R3S1	5.95	0.14	295.96	6.35	671.14	6.82	0.61	0.14	7.58	0.50			0.47	0.39	3.12	0.32	0.89	0.88
33-15 SLSL R3S2	6.31	0.36			719.22	6.94	0.55	0.26	7.30	0.99			0.48	0.64	3.93	0.23	0.88	0.64
33-15 TDL1 R3S1	45.51	0.75							45.37	13.42					4.23	3.90	1.38	1.13

Sample	Mn/Nd	%RSD	Fe/Nd	%RSD	Al/Nd	%RSD	Nd/Ti	%RSD	Mn/Pb	%RSD	Fe/Pb	%RSD	Pb/Ti	%RSD	Fe/Al	%RSD	Mn/Al	%RSD
33-15 TDL1 R3S2	48.87	0.56	141.11	6.42	3.23	4.83	1.35	0.74	46.24	0.67	133.53	6.20	1.42	0.79	4.67	0.77	1.62	0.26
33-15 TDL1 R3S2	5.87	0.14	144.82	13.40			1.29	0.25	49.35	1.18	14.33	12.86	1.33	0.26	4.50	2.56	1.58	0.89
33-15 TDL1 R3S4	47.51	0.14							48.33	11.85							1.16	3.74
33-15 TDL1 R3S4	46.83	0.17							33.79	7.00							1.27	4.20
33-15 TDL2 R3S1	8.42	0.12	2.23	2.66	17.79	5.56	1.29	0.13	17.15	0.18	425.44	6.20	0.48	0.69	11.30	3.55	0.45	0.14
33-15 TDL3 R3S1	6.69	0.89					0.19	0.25	3.50	0.14			0.36	0.16			0.87	0.88
33-27 BSL3							0.46	0.19										
33-27 BSL3							0.46	0.18										
33-27 BSL3							0.46	0.16					2.28	0.50				
33-27 BSL3 R2									98.72	0.83	288.63	4.42						
33-27 BSL3 R2									13.35	0.96	294.77	3.89						
33-27 SLL1 R3S1	37.62	1.16																
33-27 SLL1 R3S2	54.14	0.39					0.42	0.25					0.49	0.24	5.71	7.11	0.64	0.79
33-27 SLL1 R3S4																		
33-27 SLL2 R3S1	21.45	0.58	317.27	3.48	16.39	5.34	0.73	0.80	37.89	0.33	572.38	7.85	0.44	0.52	19.36	6.36	1.28	0.42
33-27 SLL3 R3S1	13.92	0.77					0.15	0.88	7.18	0.23			0.30	0.18			0.22	0.13
33-27 SLSL R3S1	8.54	0.72			867.82	9.13	0.42	0.35	7.94	0.11			0.45	0.64	3.73	0.25	0.99	0.64
33-27 SLSL R3S2	9.43	0.16					0.38	0.68	7.19	1.49			0.48	0.99	3.65	0.40	0.97	0.84
33-27 TDL1 R3S1	83.39	0.77					0.52	0.90	86.52	3.74			0.58	0.76	6.43	5.59	1.34	1.16
33-27 TDL1 R3S2	86.94	0.24	41.63	5.34	73.53	6.44	0.41	0.12	86.83	1.62	41.57	9.24	0.42	0.14	5.58	0.49	1.18	0.13
33-27 TDL1 R3S3	88.28	0.15	384.56	12.87			0.51	0.17	88.43	3.45			0.52	0.25	6.00	3.47	1.38	0.79
33-27 TDL2 R3S1	22.42	0.86	322.38	2.96	16.57	1.72	0.71	0.67	39.27	0.45	564.66	8.30	0.47	0.58	19.46	12.59	1.35	0.88
33-27 TDL3 R3S1	15.73	0.72			59.27	2.69	0.17	0.82	7.78	0.13	829.58	14.50	0.32	0.72	27.13	9.39	0.25	0.88
33-6 SLL1 R3S1	21.57	0.55																
33-6 SLL1 R3S1	2.98	0.67																
33-6 SLL1 R3S2	36.76	0.42													6.16	1.18	0.48	0.79
33-6 SLL1 R3S2	29.20	0.13																
33-6 SLL2 R3S1	7.34	0.13	379.29	3.00	12.98	4.78	0.77	0.48	1.46	0.75	54.60	5.65	0.54	0.50	29.24	9.20	0.57	0.18
33-6 SLL3 R3S1	7.85	0.47					0.23	0.16	4.52	0.25			0.48	0.25			0.15	0.27
33-6 SLSL R3S1	7.55	0.20	2538.58	7.66	885.65	6.51	0.44	0.12	11.37	0.13			0.29	0.32	2.87	0.21	0.85	0.59
33-6 SLSL R3S2	8.15	0.17					0.39	0.84	1.65	2.79			0.30	0.79	2.90	0.29	0.83	0.86
33-6 SLSL R3S2	8.24	0.98					0.47	0.49	12.28	3.75			0.27	0.83	2.82	0.94	0.86	0.36

Sample	Mn/Nd	%RSD	Fe/Nd	%RSD	Al/Nd	%RSD	Nd/Ti	%RSD	Mn/Pb	%RSD	Fe/Pb	%RSD	Pb/Ti	%RSD	Fe/Al	%RSD	Mn/Al	%RSD
33-6 TDL1 R3S1	33.33	0.49																
33-6 TDL1 R3S2	39.19	0.42			43.38	9.89	0.68	0.21	47.49	5.00			0.56	0.18	6.94	14.52	0.93	1.90
33-6 TDL2 R3S1	7.51	0.29	38.42	1.79	13.47	4.33	0.75	0.32	11.64	0.59	56.28	3.34	0.51	0.28	29.16	9.11	0.58	0.18
33-6 TDL3 R3S1	7.98	0.43					0.22	0.82	4.68	0.28			0.44	0.34	32.20	9.60	0.16	0.46
34-12 BSL1	38.52	0.45	199.40	5.23	9.25	5.72	1.35	0.19	45.38	0.79	234.92	6.89	0.88	0.20	21.55	13.32	4.16	2.57
34-12 BSL1	37.91	0.27	183.62	9.28	8.39	7.56	1.96	0.17	42.72	0.78	26.89	11.17	0.97	0.23			4.52	4.41
34-12 BSL1	38.21	0.49					1.65	0.34	44.17	2.49	22.51	5.70	0.92	0.58				
34-12 BSL1 R2																		
34-12 BSL1 R2																		
34-16 SLL1 R3S1	27.28	0.11													0.68	0.34	0.12	0.13
34-16 SLL1 R3S2	28.44	0.12					1.72	0.20	38.63	0.88			0.79	0.14	4.79	2.46	0.88	0.44
34-16 SLL1 R3S3	29.29	0.28			33.41	6.88	1.23	0.13	41.74	12.36			0.71	0.22	5.44	9.19	0.87	1.59
34-16 SLL2 R3S1	5.53	0.45	183.59	4.65	14.30	3.94	0.95	0.86	12.55	0.17	399.58	11.16	0.43	0.63	12.85	3.55	0.39	0.17
34-16 SLL2 R3S1	5.59	0.97	184.27	1.31	14.55	3.30	0.92	0.23	12.12	0.12	399.33	4.71	0.42	0.41	12.67	2.88	0.38	0.87
34-16 SLL3 R3S1	6.34	0.48					0.15	0.12	2.64	0.15			0.37	0.21	22.45	7.12	0.98	0.32
34-16 SLSL R3S1	7.27	0.47			775.24	11.28	0.52	0.35	9.91	0.72			0.44	0.32	3.15	0.50	0.96	0.12
34-16 SLSL R3S2	7.48	0.19					0.48	0.69	8.34	1.69			0.43	0.87	3.12	0.24	0.91	0.69
34-16 TDL1 R3S1	26.85	0.53																
34-16 TDL1 R3S2	29.63	0.15	143.58	1.86			1.25	0.26	39.62	2.72			0.93	0.20	5.31	4.68	1.94	0.96
34-16 TDL1 R3S3	3.57	0.27			26.75	6.32	1.20	0.50	43.19	3.39			0.85	0.35	5.34	12.12	1.14	2.57
34-16 TDL2 R3S1	5.52	0.24	184.47	3.32	14.86	6.64	0.94	0.11	11.95	0.12	399.23	8.12	0.43	0.66	12.42	5.56	0.37	0.17
34-16 TDL3 R3S1	5.99	0.23			56.57	12.41	0.18	0.70	2.77	0.17			0.39	0.23	22.14	4.68	0.16	0.22
34-3 BSL3							0.15	0.67										
34-3 BSL3 R2									95.86	0.50	292.99	2.23	1.55	0.54	12.62	9.59	4.14	2.97
34-3 BSL3 R2									99.25	1.56	297.16	4.49	1.38	0.18	12.27	6.15	5.00	2.86
34-43 BSL3							0.49	0.25										
34-43 BSL3 R2	81.92	0.53	196.17	3.44			1.12	0.42	99.41	1.00	24.49	4.65	0.91	0.35				
34-43 BSL3 R2	82.23	0.50	198.55	8.34			1.12	0.14	12.95	1.25	246.54	1.69	0.89	0.15				
34-45 BSL3							0.52	0.39										
34-45 BSL3 R2									96.85	1.50	29.86	9.19						

Sample	Mn/Nd	%RSD	Fe/Nd	%RSD	Al/Nd	%RSD	Nd/Ti	%RSD	Mn/Pb	%RSD	Fe/Pb	%RSD	Pb/Ti	%RSD	Fe/Al	%RSD	Mn/Al	%RSD
34-45 SLL1 R3S1	51.44	0.47																
34-45 SLL1 R3S2	58.47	0.31	282.37	4.92			0.60	0.39					0.41	0.88	4.57	1.47	0.95	0.28
34-45 SLL1 R3S3	6.52	0.18	299.76	12.86			0.59	0.28					0.43	0.12	4.82	11.56	0.97	2.33
34-45 SLL2 R3S1	17.86	0.15	27.29	9.89	16.82	7.27	0.94	0.12	48.89	0.97			0.33	0.76	12.32	5.35	1.62	0.46
34-45 SLL3 R3S1	12.65	0.35					0.19	0.71	9.85	0.86			0.24	0.22	2.96	12.92	0.21	0.13
34-45 SLSL R3S1	8.79	0.42	2912.54	14.19	76.38	4.67	0.54	0.26	8.61	0.15			0.55	0.67	4.13	0.20	0.12	0.57
34-45 SLSL R3S2	9.75	0.13					0.59	0.72	7.67	1.57			0.62	0.12	4.49	0.72	0.12	0.22
34-45 TDL1 R3S1	48.49	0.57																
34-45 TDL1 R3S2	59.34	0.49					0.89	0.11	84.34	9.84			0.63	0.95			1.74	4.14
34-45 TDL1 R3S3	64.80	0.27	239.22	11.48													1.71	4.82
34-45 TDL2 R3S1	17.81	0.61	211.35	2.19	17.57	7.78	0.88	0.35	49.23	0.23	584.51	6.23	0.32	0.15	12.40	5.66	1.44	0.48
34-45 TDL3 R3S1	12.32	0.72	127.53	8.27			0.19	0.14	9.51	0.94			0.25	0.26			0.27	0.19
34-6 BSL1	5.78	0.78	165.21	7.13	1.45	14.54	1.66	0.12	64.39	0.99	29.52	9.42	1.32	0.94			4.86	6.76
34-6 BSL1	49.11	0.98	155.64	5.56			1.72	0.13	6.58	1.85	191.98	8.19	1.38	0.19			5.28	2.56
34-6 BSL1	49.94	0.49			9.88	7.13	1.68	0.29	62.45	2.86			1.34	0.63				
34-6 BSL1 R2																		
34-6 BSL1 R2																		
34-9 BSL1	52.72	0.97	2.78	4.88	12.39	8.30	1.43	0.45	83.19	3.45	316.85	14.73	0.99	0.44	16.22	1.85	4.25	2.85
34-9 BSL1	5.26	0.69	189.62	9.11	1.92	8.34	1.52	0.56	74.83	1.36	282.31	13.98	1.25	0.39	17.36	12.79	4.62	3.38
34-9 BSL1	51.49	0.34					1.48	0.97	78.91	6.58			0.96	0.12				
34-9 BSL1 R2																		
34-9 BSL1 R2																		
35-11 BSL1	25.53	0.36	98.18	2.89	14.18	5.88	1.53	0.41	41.18	0.90	158.76	5.36	0.95	0.38	6.92	2.88	1.83	0.75
35-11 BSL1 R2																		
35-19 BSL3							0.19	0.12										
35-19 BSL3							0.18	0.70										
35-19 BSL3							0.18	0.15					1.47	0.23				
35-19 BSL3 R2									42.51	0.16	161.65	8.15			6.82	0.57	1.60	0.12
35-19 BSL3 R2									42.54	0.36	161.41	1.58			6.17	1.69	1.59	0.44
35-19 SLL1 R3S1	19.97	0.64																
35-19 SLL1 R3S2	26.93	0.33			151.27	1.78	0.27	0.70					0.19	0.18	3.20	2.12	0.18	0.12
35-19 SLL2 R3S1	6.74	0.69	234.94	4.66	16.58	2.18	0.96	0.11	12.69	0.19	442.17	1.86	0.48	0.82	14.17	1.87	0.47	0.53

Sample	Mn/Nd	%RSD	Fe/Nd	%RSD	Al/Nd	%RSD	Nd/Ti	%RSD	Mn/Pb	%RSD	Fe/Pb	%RSD	Pb/Ti	%RSD	Fe/Al	%RSD	Mn/Al	%RSD
35-19 SLL3 R3S1	6.49	0.96					0.16	0.25	2.44	0.92			0.44	0.20			0.95	0.13
35-19 SLSL R3S1	6.64	0.71	2397.89	3.32	77.53	3.87	0.59	0.55	8.79	0.23	3474.65	9.34	0.47	0.13	3.39	0.19	0.86	0.47
35-19 SLSL R3S2	6.22	0.19					0.55	0.96	7.45	0.66			0.46	0.47	3.31	0.39	0.85	0.98
35-19 SLSL R3S4	6.72	0.37	549.35	3.48	667.95	4.39	0.59	0.30	8.47	0.11	766.57	9.62	0.42	0.52	0.82	0.42	0.99	0.33
35-19 TDL1 R3S1	25.59	0.12																
35-19 TDL1 R3S2	3.37	0.46					0.50	0.62	4.35	6.19			0.38	0.48	3.59	8.43	0.33	0.77
35-19 TDL2 R3S1	7.56	0.44	225.72	1.94	16.46	6.93	0.94	0.12	13.53	0.14	432.94	5.24	0.49	0.74	13.71	5.75	0.43	0.18
35-19 TDL3 R3S1	6.55	0.77					0.17	0.27	2.69	0.68			0.44	0.13			0.14	0.19
35-21 BSL3							0.25	0.42										
35-21 BSL3							0.27	0.56										
35-21 BSL3							0.27	0.28					3.25	0.33				
35-21 BSL3 R2									43.37	0.41	124.43	7.13						
35-21 BSL3 R2									44.65	0.40	127.33	6.75						
35-27 SLL1 R3S1	32.46	0.14													2.13	8.63	0.25	1.66
35-27 SLL1 R3S2	39.15	0.32					0.37	0.39	37.52	3.24			0.39	0.50	2.68	1.42	0.37	0.19
35-27 SLL2 R3S1	7.74	0.13	246.38	1.24	19.39	4.73	0.65	0.12	11.52	0.12	366.66	3.67	0.44	0.38	12.75	3.98	0.40	0.97
35-27 SLL3 R3S1	7.58	0.26			77.92	12.69	0.17	0.38	2.18	0.17	532.47	4.83	0.37	0.32	23.76	3.78	0.97	0.15
35-27 SLSL R3S2	6.73	0.23			774.48	11.96	0.52	0.16	6.77	0.44			0.52	0.30	3.56	0.46	0.87	0.11
35-27 SLSL R3S4	6.49	0.34	442.16	4.12	72.37	4.42	0.57	0.29	7.80	0.81	53.47	6.88	0.47	0.49	0.63	0.53	0.92	0.33
35-27 TDL1 R3S1	17.97	0.74																
35-27 TDL1 R3S2	3.21	0.37													2.99	4.00	0.19	0.24
35-27 TDL2 R3S1	7.55	0.42	254.36	2.64	19.68	2.37	0.63	0.42	1.46	0.96	352.37	4.48	0.45	0.45	12.93	1.56	0.38	0.47
35-27 TDL2 R3S1	7.59	0.36	253.58	3.64	18.83	4.54	0.65	0.37	1.54	0.53	352.93	5.98	0.47	0.28	13.46	3.24	0.43	0.97
35-27 TDL2 R3S4	7.99	0.26			2.41	4.22	0.62	0.39	11.28	0.72			0.44	0.36			0.39	0.88
35-27 TDL3 R3S1	7.59	0.97			83.42	12.64	0.11	0.13	2.13	0.26	554.59	6.76	0.36	0.42	23.71	1.93	1.00	0.73
35-39 SLL1 R3S1	51.12	0.29																
35-39 SLL1 R3S2	58.44	0.12	25.46	13.56			0.59	0.31	76.23	4.77			0.45	0.23	4.59	3.15	1.15	0.89
35-39 SLL2 R3S1	13.94	0.22	24.28	3.55	22.89	5.78	0.68	0.13	3.18	0.32	442.34	9.77	0.32	0.35	8.92	2.26	0.69	0.15
35-39 SLL2 R3S4	14.55	0.12			23.73	6.98	0.68	0.85	31.38	0.79			0.32	0.83			0.63	0.19
35-39 SLL3 R3S1	11.89	0.99					0.13	0.86	6.74	0.26			0.20	0.89	17.54	1.34	0.12	0.72
35-39 SLSL R3S2	8.23	0.19					0.52	0.66	5.90	0.48			0.70	0.57	4.75	0.46	0.18	0.15
35-39 SLSL R3S4	7.72	0.84	335.47	7.12	667.18	9.98	0.56	0.62	6.67	0.52	289.38	5.74	0.66	0.58	0.53	0.15	0.12	0.12

Sample	Mn/Nd	%RSD	Fe/Nd	%RSD	Al/Nd	%RSD	Nd/Ti	%RSD	Mn/Pb	%RSD	Fe/Pb	%RSD	Pb/Ti	%RSD	Fe/Al	%RSD	Mn/Al	%RSD
35-39 TDL1 R3S1	53.16	0.25													2.95	4.78	0.76	1.12
35-39 TDL1 R3S2	6.75	0.27	236.95	14.31			0.52	0.59	76.68	4.66			0.40	0.50	3.52	7.90	0.91	2.23
35-39 TDL2 R3S1	13.73	0.12	211.32	3.72	22.92	7.37	0.66	0.58	28.49	0.18	438.27	7.55	0.32	0.26	9.22	2.98	0.60	0.19
35-39 TDL3 R3S1	11.94	0.21					0.96	0.17	5.73	0.56			0.24	0.20	18.62	11.50	0.12	0.73
35-48 SLL1 R3S1	63.24	0.17					0.12	0.37	64.67	11.45			0.11	0.27	2.43	5.20	0.25	0.62
35-48 SLL1 R3S2	73.59	0.24					0.23	0.12	67.78	1.95			0.25	0.13	3.95	0.81	0.46	0.12
35-48 SLL2 R3S1	18.19	0.86	32.14	4.35	19.27	13.64	0.68	0.64	25.25	0.38	419.45	7.66	0.44	0.66	15.67	11.96	0.94	0.67
35-48 SLL3 R3S1	12.22	0.72					0.18	0.63	3.70	0.63	714.78	14.46	0.35	0.61			0.16	0.28
35-48 SLSL R3S2	7.61	0.29					0.45	0.17	6.80	0.75			0.57	0.68	4.18	0.72	0.91	0.16
35-48 SLSL R3S4	7.37	0.34	272.47	2.59	748.23	1.13	0.49	0.22	7.25	0.58	268.31	3.91	0.50	0.40	0.36	0.56	0.98	0.13
35-48 TDL1 R3S1	71.99	0.59					0.33	0.17	7.86	3.69			0.38	0.18	3.56	2.52	0.75	0.54
35-48 TDL1 R3S1	72.90	0.76					0.34	0.72	7.55	3.68			0.36	0.67	3.52	7.59	0.75	1.64
35-48 TDL1 R3S2	78.30	0.40	351.58	2.79	96.82	2.51	0.36	0.24	76.84	0.55	341.65	3.65	0.37	0.28	3.63	0.77	0.89	0.17
35-48 TDL2 R3S1	18.40	0.74	288.52	2.44	18.88	2.57	0.64	0.37	26.53	0.29	416.47	5.37	0.44	0.52	15.28	2.31	0.97	0.13
35-48 TDL3 R3S1	12.47	0.12					0.17	0.18	3.85	0.13	718.29	4.25	0.34	0.78			0.17	0.15
35-5 BSL1			192.25	7.42	13.25	5.11	1.61	0.13			232.70	9.34	0.88	0.14	14.59	5.63		
35-5 BSL1 R2																		
35-8 BSL1	31.27	0.36	123.67	4.27	11.53	3.46	1.32	0.24	4.56	0.22	16.38	5.30	1.14	0.18	11.19	3.52	2.83	0.89
35-8 BSL1 R2																		
35-9 SLL1 R3S1	21.73	0.58													2.58	8.79	0.18	0.73
35-9 SLL1 R3S1	19.24	0.93													2.14	14.56	0.18	1.23
35-9 SLL1 R3S2	26.60	0.37					0.32	0.44					0.16	0.66	2.67	3.12	0.22	0.87
35-9 SLL1 R3S3	27.17	0.19					0.30	0.24					0.12	0.18	2.74	1.85	0.22	0.14
35-9 SLL1 R3S3	27.13	0.12					0.33	0.12					0.12	0.15	2.87	3.60	0.22	0.22
35-9 SLL2 R3S1	6.93	0.44	14.89	1.92	16.55	12.62	0.85	0.95	23.37	0.67	474.92	14.87	0.25	0.76	8.51	6.49	0.42	0.32
35-9 SLL3 R3S1	8.17	0.19			51.55	3.72	0.19	0.59	5.75	0.34	58.87	4.68	0.34	0.22	15.88	1.29	0.16	0.11
35-9 SLSL R3S1	5.33	0.32			642.88	7.42	0.71	0.43	9.92	0.98			0.38	0.38	3.97	0.39	0.83	0.82
35-9 SLSL R3S2	5.45	0.65					0.68	0.76	7.95	2.28			0.47	0.13	3.96	0.52	0.82	0.11
35-9 TDL1 R3S1	11.75	0.16																
35-9 TDL1 R3S2	17.57	0.52					0.24	0.79							3.24	6.68	0.12	0.19
35-9 TDL2 R3S1	6.95	0.29	146.54	3.56	16.81	6.78	0.82	0.64	22.12	0.67			0.26	0.80	8.72	3.53	0.42	0.17
35-9 TDL3 R3S1	7.99	0.78					0.22	0.24	6.89	0.25	642.54	12.34	0.25	0.60	16.93	7.26	0.18	0.79

Sample	Mn/Nd	%RSD	Fe/Nd	%RSD	Al/Nd	%RSD	Nd/Ti	%RSD	Mn/Pb	%RSD	Fe/Pb	%RSD	Pb/Ti	%RSD	Fe/Al	%RSD	Mn/Al	%RSD
35-9 TDL3 R3S1	7.72	0.65					0.21	0.18	6.60	0.64			0.25	0.23			0.17	0.34
36-11 BSL1	39.14	0.66	13.54	8.71	11.63	14.29	1.62	0.38	7.95	2.99			0.90	0.41	11.23	13.57	3.37	4.61
36-11 BSL1 R2																		
36-11 SLL1 R3S1	19.44	0.23																
36-11 SLL2 R3S1	13.17	0.40	131.59	14.75			0.82	0.42	41.75	5.24			0.26	0.35	5.73	3.87	0.57	0.38
36-11 SLL3 R3S1	1.34	0.39					0.19	0.61	1.48	8.29			0.19	0.15			0.12	0.28
36-11 SLSL R3S2	5.48	0.25					0.62	0.27	8.77	3.45	2635.45	14.89	0.39	0.15	2.37	0.87	0.79	0.29
36-11 SLSL R3S2	5.78	0.19					0.62	0.24	1.52	3.57			0.34	0.12	2.38	0.33	0.84	0.12
36-11 SLSL R3S4	5.19	0.27	122.42	2.80	573.81	4.44	0.72	0.37	13.34	0.22	314.34	8.47	0.28	0.43	0.21	0.49	0.95	0.53
36-11 TDL1 R3S1	17.39	0.50																
36-11 TDL1 R3S3	28.23	0.38													1.87	4.67	0.15	0.33
36-11 TDL1 R3S3	28.19	0.84					0.22	0.76							1.86	1.51	0.14	0.20
36-11 TDL2 R3S1	14.32	1.00	142.27	5.74			0.77	0.14	41.68	2.64	413.94	3.97	0.27	0.17	5.75	5.57	0.58	0.56
36-11 TDL3 R3S1	1.61	0.55					0.18	0.98	8.78	7.53			0.22	0.19	5.97	9.68	0.14	0.17
36-9 BSL1	45.16	0.17	426.79	2.95	13.34	9.26	1.78	0.11	48.27	0.54	456.24	5.72	1.17	0.14			3.39	2.36
36-9 BSL1 R2																		
978 BSL4			12.30	3.52	7.22	3.56	0.74	0.40			231.56	7.95	0.39	0.47	1.71	0.99		
978 BSL4			122.75	2.14	64.95	4.23	0.75	0.27			236.39	4.34	0.40	0.27	1.89	0.13		
978 BSL4			121.49	2.13			0.75	0.62			233.96	4.56	0.39	0.46	1.80	0.67		
978 BSL4 R2																		
978 BSL4 R2																		
9788 BSL4					3.33	0.96	1.45	0.18					0.36	0.15				
9788 BSL4					29.46	0.18	1.57	0.12					0.36	0.21				
9788 BSL4					29.87	2.85	1.47	0.98					0.36	0.17				
9788 BSL4 R2	78.46	0.13	161.27	6.26														
9788 BSL4 R2	78.55	0.30	161.34	7.45														
979 BSL4			9.70	1.33			1.68	0.66			243.12	3.89	0.63	0.47				
979 BSL4			89.58	0.75			1.73	0.67			236.94	2.78	0.65	0.59				
979 BSL4			9.14	2.34			1.74	0.13			24.18	6.35	0.64	0.54				
979 BSL4 R2																		
979 BSL4 R2																		
9792 BSL4							2.35	0.72					0.72	0.72				

Sample	Mn/Nd	%RSD	Fe/Nd	%RSD	Al/Nd	%RSD	Nd/Ti	%RSD	Mn/Pb	%RSD	Fe/Pb	%RSD	Pb/Ti	%RSD	Fe/Al	%RSD	Mn/Al	%RSD
9792 BSL4 R2	93.28	0.74	177.79	4.46														
H131-1							0.71	0.56					0.54	2.38	0.79	6.63		
H131-1 R2																		
H131-2			9.21	0.88	12.33	1.41	7.28	0.22					0.72	0.36	0.77	0.12		
H131-2 R2	76.64	0.16																
H131-3			112.49	8.48	5.86	7.48	3.98	2.29					0.37	0.59	2.21	0.36		
H131-3 R2																		
H131-4 R2	1.24	0.53	1513.36	8.88	441.76	2.98	0.59	0.36	9.27	0.46	1374.44	8.86	0.65	0.34	3.43	0.20	0.24	0.20
H15							9.18	1.76					0.40	0.79				
H15 R2	89.55	0.53	189.98	4.62														
H151-1	1674.45	7.52					0.24	0.23					0.29	1.75	2.17	4.18		
H151-1 R2																		
H151-2							13.24	0.20					0.53	0.14				
H151-2 R2	82.90	0.13	174.96	6.80														
H151-3			31.98	1.57			8.76	1.97					0.32	0.88				
H151-3 R2																		
H151-4 R2	11.97	0.14	221.44	3.33	72.82	1.67	0.55	0.12	7.89	0.28	1571.13	4.19	0.77	0.24	3.67	0.58	0.15	0.28
H152	38.66	2.69					0.65	4.74					0.35	1.84				
H152 R2																		
H154			23.20	0.47	21.44	2.52	9.91	0.48					0.15	0.28	1.82	0.13		
H154 R2	74.13	0.16																
NODA BSL1	192.14	0.27							442.87	0.22								
NODA BSL1 R2			756.61	2.84			0.12	0.26			164.85	1.31	0.47	0.16				
NODA BSL1 R2	1877.53	0.24	744.64	9.65			0.14	0.14	42.99	1.66	159.83	0.79	0.48	0.27				
NODA BSL1 R2	1916.00	0.99	753.20	13.64			0.15	0.56	414.68	1.44	162.99	2.89	0.49	0.18				
NODA BSL1 R2	1891.63	0.51					0.14	0.27	41.20	1.54	165.27	2.98	0.46	0.22	6.84	1.45	16.95	3.48
NODA BSL1 R2	197.55	0.26	754.61	11.16			0.99	0.14	423.94	0.76	167.76	1.25	0.45	0.84	6.76	1.61	17.85	4.79
NODA BSL1 R2	1914.55	0.22	764.78	12.86	112.26	12.71	0.99	0.11	42.80	1.32	168.91	2.16	0.45	0.15	6.81	0.77	17.55	1.92
NODA BSL1 R2	1893.45	0.32					0.12	0.18	47.13	0.65	162.57	2.88	0.48	0.94	6.76	2.97	16.92	5.23
NODA BSL1 R2							0.12	0.14			164.44	3.82	0.47	0.31	6.78	0.96		
NODA BSL3 R2			75.30	0.38	131.76	0.72	0.21	0.12			176.26	0.79	0.99	0.44	5.69	0.31		
NODA BSL3 R2			751.64	0.82	135.18	1.31	0.26	1.00			18.86	0.18	0.86	0.19	5.56	0.54		

Sample	Mn/Nd	%RSD	Fe/Nd	%RSD	Al/Nd	%RSD	Nd/Ti	%RSD	Mn/Pb	%RSD	Fe/Pb	%RSD	Pb/Ti	%RSD	Fe/Al	%RSD	Mn/Al	%RSD
NODA BSL4							0.28	0.36										
NODA BSL4							0.28	0.67										
NODA BSL4 R2							0.33	0.63			32.49	5.85	1.14	0.82	7.71	0.76		
NODA BSL4 R2					161.24	7.96	0.28	0.71			331.55	2.59	1.69	0.82	7.72	0.34		
NODA5 ER R3S3	1946.17	0.18	657.14	8.73	114.60	6.51	0.32	0.32	338.77	0.23	114.40	1.71	1.82	0.60	5.74	0.33	17.00	0.95
NODA5 ER R3S3	1966.22	4.87					0.39	0.83	318.44	3.89	19.29	11.65	1.99	0.15	6.29	4.99	18.34	14.40
NODA6 ER R3S3	267.43	0.39	761.94	1.65			0.27	0.32	258.94	7.49	95.42	12.78	2.15	0.24				
NODA6 ER R3S3	1938.54	0.18	695.63	6.82			0.30	0.19	248.61	0.78	89.23	0.77	2.33	0.15	5.83	1.15	16.25	3.21
NODA6 ER R3S3	248.15	4.38					0.27	0.59	255.38	3.25	94.36	9.57	2.19	0.58	6.79	1.48	16.46	3.68
NODP BSL1							0.75	0.89					0.41	0.69				
NODP BSL1					39.16	2.74	0.76	0.23					0.43	0.21				
NODP BSL1					39.52	3.31	0.74	0.15					0.41	0.13				
NODP BSL1					39.95	1.52	0.74	0.68					0.42	0.90				
NODP BSL1					4.46	1.17	0.73	0.14					0.44	0.13				
NODP BSL1					39.99	3.98	0.74	0.19					0.41	0.17				
NODP BSL1 R2			235.00	9.15			0.79	0.15										
NODP BSL1 R2			239.78	12.85			0.80	0.38										
NODP BSL1 R2			241.99	7.89			0.78	0.28										
NODP BSL1 R2			242.56	11.13			0.78	0.31										
NODP BSL1 R2			237.57	6.74			0.78	0.12										
NODP BSL1 R2			239.25	14.31			0.79	0.16										
NODP BSL3 R2			263.19	0.26	5.57	1.35	0.20	0.90			16.73	0.98	0.48	0.16	5.22	0.13		
NODP BSL3 R2			263.70	0.58	49.94	0.97	0.20	0.13			17.32	0.22	0.49	0.12	5.29	0.13		
NODP BSL4							1.83	0.19					0.38	0.17				
NODP BSL4							1.88	0.25					0.37	0.16				
NODP BSL4 R2			39.22	4.30	39.39	1.63	1.93	0.69							7.85	2.12		
NODP BSL4 R2			311.19	2.90	39.94	6.24	1.86	0.15							7.79	1.22		
NODP5 ER R3S3	1919.55	0.12	221.35	1.95	41.58	3.68	0.44	0.30	1266.28	6.23	146.22	1.25	0.67	0.43	5.33	0.47	46.25	4.97
NODP5 ER R3S3	1958.73	3.91					0.42	0.88					0.61	0.60	6.15	3.15		
NODP6 ER R3S3	1913.82	0.22	227.15	7.78	41.48	12.58	0.20	0.23	917.87	3.29	18.94	3.18	0.41	0.18	5.48	1.67	46.14	13.99
NODP6 ER R3S3	199.55	5.19			43.79	14.00	0.18	0.48					0.37	0.24	6.26	14.83		

Sample	Sr/Ca	%RSD	Sr/Ti	%RSD	Mn/Ti	%RSD	Ba/Ti	%RSD	U/Al	%RSD	U/Ti	%RSD	Th/Al	%RSD	Th/Ti	%RSD
17.776 R3S2			121.72	0.87	86.42	0.62	7.23	0.52	0.14	0.18	0.56	0.16	0.25	0.15	0.89	0.79
17.776 R3S3	0.34	0.00							0.16	0.40			0.23	0.56		
17.776 R3S3	0.33	0.00							0.16	0.57			0.23	0.79		
17.777 R3S2			145.59	4.63	182.48	5.82	6.25	0.20	0.90	0.28	0.51	0.25	0.12	0.38	0.75	0.29
17.777 R3S3	0.23	0.00							0.12	0.23			0.14	0.30		
17.779 BSL4							1.35	0.99							0.87	0.12
17.779 BSL4 R2	0.15	0.20														
17.779 R3S2			172.30	1.85	222.83	2.39	6.64	0.71	0.86	0.39	0.53	0.16	0.15	0.53	0.86	0.17
17.779 R3S3	0.25	0.00							0.91	0.26			0.15	0.45		
17.779 R3S3	0.24	0.11							0.96	0.66			0.16	0.17		
17.78 R3S2			41.35	0.18	27.42	0.12	1.25	0.56	0.23	0.39	0.41	0.65	0.19	0.27	0.34	0.26
17.78 R3S3	0.35	0.12	39.75	8.20	26.46	5.46	1.42	0.22	0.24	0.14	0.38	0.94	0.26	0.12	0.32	0.79
17.781 BSL4							0.92	0.35							0.24	0.20
17.781 BSL4 R2	0.25	0.75														
17.781 R3S2			27.63	0.14	23.98	0.12	0.96	0.55	0.27	0.63	0.44	0.26	0.18	0.44	0.28	0.26
17.781 R3S3	0.32	0.14	28.67	3.73	25.15	2.70	0.85	0.14	0.32	0.46	0.48	0.53	0.20	0.29	0.39	0.65
17.782 R3S2			117.36	1.92	77.26	1.26	6.30	0.13	0.16	0.30	0.63	0.17	0.19	0.36	0.76	0.15
17.782 R3S3	0.38	0.14							0.21	0.13			0.25	0.15		
17.783 BSL4							9.76	0.75							0.74	0.59
17.783 BSL4 R2	0.16	0.92														
17.783 R3S2			135.68	6.79	199.37	9.98	5.76	0.29	0.49	0.14	0.29	0.19	0.19	0.32	0.65	0.33
17.783 R3S3	0.24	0.00							0.58	0.15			0.12	0.28		
17.784 R3S2			141.24	3.33	18.46	4.25	5.54	0.14	0.79	0.38	0.44	0.28	0.17	0.66	0.95	0.25
17.784 R3S2			138.35	2.25	179.64	2.92	5.47	0.89	0.79	0.35	0.44	0.86	0.17	0.74	0.93	0.16
17.784 R3S3	0.26	0.47							0.89	0.11			0.20	0.22		
17.785 BSL4							3.88	0.48					0.47	0.28	0.57	0.72
17.785 BSL4							3.87	0.21					0.50	0.98	0.58	0.36
17.785 BSL4							3.88	0.24	0.13	0.58	1.57	0.18	0.49	0.34	0.58	0.26
17.785 BSL4 R2	0.23	0.50														
17.785 BSL4 R2	0.24	0.47														
17.785 R3S2			39.51	0.66	32.34	0.54	1.50	0.46	0.26	0.11	0.49	0.35	0.25	0.81	0.39	0.19
17.785 R3S3	0.40	0.12	37.86	9.33	31.23	7.64	1.27	0.31	0.27	0.13	0.46	0.12	0.21	0.98	0.37	0.12

Sample	Sr/Ca	%RSD	Sr/Ti	%RSD	Mn/Ti	%RSD	Ba/Ti	%RSD	U/Al	%RSD	U/Ti	%RSD	Th/Al	%RSD	Th/Ti	%RSD
17.786 R3S2			39.34	0.44	32.99	0.37	1.64	0.30	0.39	0.69	0.63	0.52	0.18	0.32	0.29	0.18
17.786 R3S3	0.33	0.12	38.75	9.50	32.99	8.86	1.52	0.38	0.45	0.13	0.64	0.17	0.25	0.57	0.29	0.94
17.787 R3S2			113.24	1.27	87.93	0.98	7.38	0.82	0.17	0.21	0.71	0.16	0.19	0.24	0.82	0.14
17.787 R3S3	0.34	0.18							0.17	0.36			0.19	0.44		
17.788 R3S2			124.87	0.73	144.78	0.84	8.14	0.48	0.82	0.17	0.42	0.90	0.17	0.35	0.82	0.99
17.788 R3S3	0.26	0.00							0.92	0.14			0.18	0.26		
17.789 R3S2			126.88	2.83	128.15	2.85	6.72	0.15	0.77	0.14	0.38	0.15	0.15	0.29	0.76	0.18
17.789 R3S3	0.28	0.00							1.00	0.19			0.18	0.36		
17.789 R3S3	0.27	0.00							0.85	0.23			0.17	0.45		
17.79 R3S2			31.98	0.14	3.19	0.14	1.72	0.84	0.31	0.12	0.53	0.34	0.24	0.77	0.34	0.40
17.79 R3S3	0.28	0.23	31.91	6.95	3.46	6.63	1.55	0.35	0.34	0.30	0.53	0.15	0.27	0.18	0.32	0.88
17.791 R3S2			3.84	0.21	28.55	0.23	1.39	0.99	0.42	0.12	0.57	0.43	0.22	0.57	0.24	0.44
17.791 R3S3	0.32	0.27	28.12	1.64	27.21	1.60	1.17	0.81	0.43	0.69	0.46	0.34	0.30	0.28	0.22	0.20
17.791 R3S3	0.34	0.00	3.52	3.34	29.51	3.23	1.31	0.16	0.47	0.60	0.52	0.62	0.22	0.24	0.24	0.39
17.792 R3S2			114.18	2.85	18.57	2.71	8.27	0.25	0.16	0.66	0.66	0.22	0.22	0.89	0.88	0.23
17.792 R3S3	0.30	0.00							0.18	0.96			0.23	0.13		
17.793 R3S2			88.69	2.44	91.90	2.53	5.46	0.15	0.17	0.87	0.63	0.19	0.22	0.12	0.84	0.23
17.793 R3S2			86.94	3.42	9.89	3.56	5.34	0.29	0.16	0.49	0.61	0.24	0.22	0.64	0.82	0.32
17.793 R3S3	0.24	0.00							0.18	0.52			0.23	0.67		
17.794 R3S2			82.86	2.55	75.16	2.32	3.85	0.12	0.14	0.39	0.57	0.22	0.18	0.48	0.80	0.23
17.794 R3S3	0.26	0.80	51.96	5.26	48.58	4.92	2.19	0.25	0.17	0.66	0.38	0.99	0.20	0.78	0.45	0.70
17.795 R3S2			41.64	0.62	41.88	0.63	1.70	0.32	0.38	0.23	0.59	0.19	0.19	0.14	0.30	0.93
17.795 R3S3	0.24	0.00					1.30	1.49	0.42	0.16	0.55	0.58	0.20	0.78	0.24	0.28
17.796 R3S2			33.24	1.00	36.85	0.18	1.76	0.56	0.36	0.71	0.58	0.44	0.17	0.34	0.28	0.15
17.796 R3S3	0.25	0.00	31.21	1.98	34.43	2.19	1.50	0.99	0.38	0.56	0.54	0.49	0.17	0.26	0.25	0.54
17.797 R3S2			113.62	2.65	9.64	2.12	5.56	0.13	0.15	0.15	0.67	0.19	0.17	0.17	0.76	0.19
17.797 R3S3	0.29	0.00							0.17	0.32			0.19	0.36		
17.798 R3S2			124.75	2.92	98.83	2.30	5.48	0.12	0.16	0.48	0.69	0.19	0.17	0.52	0.75	0.18
17.798 R3S3	0.29	0.00							0.18	0.25			0.19	0.27		
18.892 BSL4							3.78	0.12								
18.892 BSL4							3.67	0.80					0.22	0.45	1.30	0.25
18.892 BSL4							3.72	0.12	0.66	0.67	3.89	0.11	0.22	0.21	1.29	0.79

Sample	Sr/Ca	%RSD	Sr/Ti	%RSD	Mn/Ti	%RSD	Ba/Ti	%RSD	U/Al	%RSD	U/Ti	%RSD	Th/Al	%RSD	Th/Ti	%RSD
18.892 BSL4 R2	0.24	0.35														
18.892 BSL4 R2	0.24	0.00														
18.899 BSL4							0.39	0.57							0.46	0.72
18.899 BSL4							0.39	0.59							0.47	0.32
18.899 BSL4							0.39	0.54			0.15	0.86			0.47	0.19
18.899 BSL4 R2	0.32	0.75	1.12	0.69	18.00	1.82					0.18	0.17				
18.899 BSL4 R2	0.31	0.16	9.85	0.26	17.28	0.45					0.17	0.11				
18.91 D1 R3S3	0.44	0.25							0.25	0.86			0.68	0.24		
18.91 R3S3	0.48	0.00	144.96	13.27	47.48	4.35	2.32	0.21	0.27	0.63	1.49	0.13	0.76	0.18	0.39	0.36
18.911 D1 R3S3	0.39	0.00							0.16	0.27			0.46	0.98		
18.911 R3S3	0.42	0.00			68.72	6.34	5.25	0.48	0.18	0.27	1.56	0.15	0.59	0.75	0.44	0.41
18.912 D1 R3S3	0.44	0.13							0.94	0.15			0.47	0.79		
18.912 R3S3	0.47	0.00	377.83	9.71	9.36	2.32	5.14	0.13	0.12	0.80	1.56	0.49	0.57	0.37	0.78	0.24
18.913 BSL4							1.11	0.19							0.23	0.11
18.913 BSL4 R2	0.25	0.12														
18.914 D1 R3S3	0.30	0.12					1.75	0.70	0.40	0.13	0.91	0.36	0.24	0.80	0.54	0.22
18.914 R3S3	0.32	0.00	63.78	0.34	62.86	0.34	2.23	0.13	0.39	0.28	1.22	0.12	0.23	0.16	0.62	0.96
18.915 D1 R3S3	0.28	0.00	6.64	4.78	65.18	5.54	1.67	0.15	0.27	0.54	0.59	0.78	0.89	0.23	0.26	0.66
18.915 R3S3	0.30	0.00	61.36	0.37	63.78	0.38	1.87	0.12	0.22	0.79	0.66	0.38	0.93	0.35	0.27	0.44
18.916 D1 R3S3	0.22	0.00							0.34	0.24			0.13	0.94		
18.916 R3S3	0.22	0.00	4.99	0.77	57.85	1.69	1.77	0.33	0.31	0.43	0.65	0.14	0.14	0.18	0.27	0.79
18.917 R3S3	0.23	0.00	42.34	1.59	66.92	2.56	1.80	0.68	0.27	0.12	0.69	0.30	0.69	0.29	0.18	0.14
18.917D1 R3S3	0.26	0.00	41.43	1.34			1.56	0.43	0.29	0.27	0.68	0.19	0.84	0.78	0.19	0.18
18.918 D1 R3S3	0.25	0.00	76.55	12.41	59.22	9.62	2.39	0.34	0.24	0.13	0.68	0.13	0.67	0.35	0.19	0.13
18.918 D1 R3S3	0.28	0.00	78.95	0.54	59.19	0.47	2.38	0.17	0.25	0.23	0.75	0.80	0.76	0.67	0.30	0.59
18.918 R3S3	0.27	0.00	79.79	2.49	58.39	1.76	2.36	0.71	0.24	0.82	0.74	0.24	0.69	0.23	0.28	0.11
18.919 R3S2			112.14	0.93	49.66	0.41	3.89	0.32	0.39	0.47	1.51	0.16	0.12	0.15	0.49	0.93
18.919 R3S3	0.29	0.16							0.43	0.32			0.13	0.95		
18.919 R3S3	0.30	0.00							0.41	0.17			0.13	0.53		
18.92 R3S2			127.75	2.46	28.44	0.55	2.29	0.46	0.53	0.94	2.97	0.58	0.87	0.16	0.55	0.15
18.92 R3S3	0.42	0.00							0.62	0.12			0.94	0.19		
18.92 R3S3	0.39	0.14							0.56	0.13			0.84	0.19		

Sample	Sr/Ca	%RSD	Sr/Ti	%RSD	Mn/Ti	%RSD	Ba/Ti	%RSD	U/Al	%RSD	U/Ti	%RSD	Th/Al	%RSD	Th/Ti	%RSD
18.921 R3S2			153.86	2.98	27.95	0.53	2.23	0.43	0.49	0.94	2.65	0.52	0.14	0.27	0.57	0.14
18.921 R3S3	0.44	0.00							0.58	0.83			0.12	0.18		
18.922 R3S2			46.60	0.28	42.65	0.26	1.74	0.17	0.46	0.83	2.20	0.15	0.13	0.24	0.63	0.51
18.922 R3S3	0.36	0.28							0.52	0.14			0.14	0.37		
18.923 R3S2			88.26	1.67	17.37	2.27	2.76	0.53	0.54	0.17	2.35	0.46	0.17	0.57	0.77	0.20
18.923 R3S3	0.36	0.18							0.64	0.27			0.23	0.87		
18.924 R3S2					39.39	4.49	2.84	0.32	0.48	0.19	2.49	0.28	0.12	0.48	0.69	0.80
18.924 R3S3	0.36	0.26							0.60	0.56			0.14	0.13		
18.925 R3S2					21.24	2.90	5.42	0.56	0.27	0.87	2.23	0.23	0.38	0.12	0.32	0.34
18.925 R3S3	0.41	0.00							0.30	0.79						
18.926 R3S2					137.73	6.41	5.41	0.25	0.19	0.40	1.95	0.90	0.47	0.96	0.47	0.22
18.926 R3S3	0.40	0.00							0.21	0.32			0.49	0.74		
18.927 R3S2			97.62	1.48	34.16	0.49	2.39	0.35	0.22	0.37	1.24	0.24	0.78	0.13	0.45	0.88
18.927 R3S2			99.48	1.38	35.38	0.37	2.42	0.26	0.22	0.16	1.25	0.16	0.77	0.62	0.46	0.14
18.927 R3S3	0.38	0.00							0.25	0.68			0.97	0.22		
18.928 R3S2			19.66	1.16	6.28	0.64	2.85	0.33	0.35	0.62	1.43	0.19	0.14	0.24	0.56	0.12
18.928 R3S3	0.37	0.00							0.42	0.69			0.15	0.26		
18.928 R3S3	0.35	0.16							0.44	0.12			0.15	0.44		
18.929 R3S2			68.45	0.80	39.64	0.46	2.38	0.24	0.36	0.28	1.38	0.19	0.13	0.15	0.49	0.90
18.929 R3S3	0.35	0.00							0.42	0.66			0.14	0.23		
18.929 R3S3	0.38	0.00			37.39	9.28	1.68	0.42	0.38	0.16	1.35	0.33	0.14	0.56	0.45	0.11
18.93 R3S2			7.29	0.28	43.64	0.17	2.48	0.17	0.37	0.90	2.68	0.93	0.12	0.29	0.66	0.86
18.93 R3S3	0.36	0.00							0.43	0.29			0.14	0.94		
18.93 R3S3	0.31	0.11							0.38	0.52			0.12	0.16		
18.931 R3S2			97.79	0.67	131.37	0.96	2.74	0.19	0.62	0.18	2.79	0.28	0.15	0.43	0.67	0.75
18.931 R3S3	0.36	0.00							0.72	0.11			0.15	0.24		
18.932 R3S2			85.52	0.72	58.38	0.49	2.36	0.27	0.34	0.56	0.86	0.94	0.56	0.94	0.14	0.53
18.932 R3S3	0.36	0.11			55.50	1.93	2.13	0.43	0.34	0.68	0.79	0.16	0.50	0.19	0.11	0.12
18.933 R3S2			239.67	3.66	94.92	1.45	4.48	0.69	0.21	0.53	1.38	0.24	0.42	0.15	0.27	0.13
18.933 R3S3	0.38	0.00							0.25	0.14			0.50	0.40		
18.934 R3S2			84.97	0.58	36.66	0.25	2.12	0.16	0.18	0.60	0.89	0.85	0.55	0.16	0.28	0.56
18.934 R3S3	0.34	0.00							0.21	0.23			0.60	0.94		

Sample	Sr/Ca	%RSD	Sr/Ti	%RSD	Mn/Ti	%RSD	Ba/Ti	%RSD	U/Al	%RSD	U/Ti	%RSD	Th/Al	%RSD	Th/Ti	%RSD
18.935 R3S2			76.82	0.47	65.72	0.44	2.27	0.14	0.16	0.63	0.44	0.56	0.68	0.26	0.19	0.45
18.935 R3S3	0.27	0.00					2.15	0.99	0.24	0.72	0.47	0.22	0.81	0.29	0.19	0.16
18.936 R3S2			93.25	0.77	61.64	0.53	2.44	0.20	0.16	0.13	0.50	0.74	0.62	0.51	0.20	0.44
18.936 R3S2			95.76	1.12	63.55	0.73	2.50	0.29	0.16	0.21	0.51	0.65	0.63	0.85	0.23	0.55
18.936 R3S3	0.30	0.00					2.31	0.83	0.18	0.26	0.53	0.20	0.69	0.13	0.24	0.97
18.936 R3S3	0.27	0.40	97.53	7.79	64.53	5.15	2.26	0.30	0.17	0.64	0.52	0.68	0.68	0.35	0.19	0.83
18.937 R3S2			126.94	1.28	56.71	0.57	2.50	0.25	0.27	0.66	1.24	0.14	0.94	0.24	0.45	0.99
18.937 R3S3	0.36	0.20							0.36	0.22			0.17	0.76		
18.937 R3S3	0.34	0.00							0.30	0.58			0.11	0.20		
18.97 BSL4							1.83	0.98								
18.97 BSL4 R2	0.29	0.00														
22.46 BSL4													0.79	0.15	1.62	0.44
22.46 BSL4 R2	0.36	0.95														
22.461 BSL4							98.46	3.24					0.77	0.23	1.13	0.39
22.461 BSL4 R2	0.31	0.82														
22.463 BSL4							22.85	0.68					0.47	0.26	0.44	0.29
22.463 BSL4 R2	0.37	0.00														
22.464 BSL4							46.20	0.59							0.94	0.12
22.464 BSL4 R2	0.30	0.00														
33-15 BSL3							5.87	0.64							0.13	0.32
33-15 BSL3							5.84	0.18							0.14	0.73
33-15 BSL3							5.85	0.35			0.52	0.16			0.13	0.19
33-15 BSL3 R2	0.33	0.00	181.78	5.95	132.55	4.35			0.14	0.28	0.81	0.29	0.35	0.89	0.22	0.25
33-15 BSL3 R2	0.33	0.97							0.13	0.58	0.76	0.12	0.33	0.15	0.19	0.45
33-15 SLL1 R3S1	0.28	0.72														
33-15 SLL1 R3S2									0.29	0.98						
33-15 SLL2 R3S1	0.32	0.00	9.88	0.52	7.42	0.39	0.70	0.68	0.66	0.23	0.19	0.68	0.28	0.14	0.50	0.35
33-15 SLL3 R3S1	0.92	0.13	5.55	0.15	1.21	0.32	0.38	0.91	0.27	0.36	0.38	0.16	0.79	0.11	0.11	0.13
33-15 SLL3 R3S1	0.92	0.92	5.36	0.76	1.15	0.19	0.29	0.15	0.26	0.19	0.37	0.16	0.79	0.48	0.19	0.12
33-15 SLSL R3S1	0.11	0.73	0.59	0.47	0.36	0.30	0.99	0.19	0.14	0.00	0.58	0.38	0.62	0.00	0.25	0.27
33-15 SLSL R3S2			0.58	0.11	0.35	0.58	0.94	0.11	0.14	0.16	0.54	0.63	0.55	0.45	0.22	0.83
33-15 TDL1 R3S1	0.38	0.00							0.81	0.75			0.11	0.11		

Sample	Sr/Ca	%RSD	Sr/Ti	%RSD	Mn/Ti	%RSD	Ba/Ti	%RSD	U/Al	%RSD	U/Ti	%RSD	Th/Al	%RSD	Th/Ti	%RSD
33-15 TDL1 R3S2			83.30	4.48	65.89	3.55	3.65	0.20	0.95	0.18	0.39	0.42	0.13	0.23	0.53	0.42
33-15 TDL1 R3S2					65.75	12.58	3.51	0.67	0.86	0.48	0.36	0.69	0.12	0.68	0.50	0.15
33-15 TDL1 R3S4	0.29	0.27							0.67	0.23			0.88	0.29		
33-15 TDL1 R3S4	0.30	0.16							0.79	0.26			0.13	0.35		
33-15 TDL2 R3S1	0.33	0.00	11.96	0.11	8.27	0.82	0.67	0.74	0.63	0.20	0.11	0.70	0.28	0.88	0.51	0.69
33-15 TDL3 R3S1	0.98	0.30	5.83	0.19	1.25	0.25	0.32	0.14	0.26	0.32	0.37	0.25	0.78	0.79	0.11	0.13
33-27 BSL3															0.45	0.77
33-27 BSL3															0.47	0.13
33-27 BSL3											1.26	0.36			0.45	0.33
33-27 BSL3 R2	0.34	0.17														
33-27 BSL3 R2	0.34	0.13														
33-27 SLL1 R3S1	0.27	0.25														
33-27 SLL1 R3S2			16.92	2.87	22.62	3.83	1.15	0.22	0.59	0.77	0.28	0.97	0.44	0.60	0.16	0.86
33-27 SLL1 R3S4	0.30	0.25														
33-27 SLL2 R3S1	0.37	0.00	12.27	0.11	15.29	0.14	1.93	0.18	0.18	0.58	0.21	0.43	0.29	0.95	0.35	0.43
33-27 SLL3 R3S1	0.82	0.18	5.27	0.88	2.13	0.33	2.92	0.45	0.69	0.40	0.65	0.52	0.99	0.60	0.94	0.15
33-27 SLSL R3S1	0.16	0.33	0.93	0.17	0.36	0.37	1.59	0.28	0.22	0.14	0.79	0.59	0.47	0.00	0.17	0.32
33-27 SLSL R3S2			0.89	0.14	0.34	0.67	1.43	0.28	0.20	0.28	0.74	0.99	0.42	0.56	0.15	0.15
33-27 TDL1 R3S1	0.28	0.00	31.42	4.52	43.73	6.29	1.84	0.26	0.95	0.82	0.31	0.46	0.56	0.49	0.18	0.42
33-27 TDL1 R3S2			24.43	0.75	34.87	1.78	1.23	0.38	0.86	0.80	0.25	0.11	0.49	0.51	0.15	0.92
33-27 TDL1 R3S3	0.27	0.00	31.87	0.88	45.44	1.25	1.58	0.44	0.99	0.58	0.33	0.98	0.56	0.33	0.18	0.12
33-27 TDL2 R3S1	0.31	0.00	1.83	0.93	15.98	0.14	1.14	0.97	0.18	0.12	0.21	0.27	0.29	0.19	0.34	0.33
33-27 TDL3 R3S1	0.74	0.93	5.38	0.89	2.57	0.38	1.29	0.20	0.73	0.29	0.72	0.14	0.12	0.35	0.12	0.24
33-6 SLL1 R3S1	0.33	0.15														
33-6 SLL1 R3S1	0.32	0.19														
33-6 SLL1 R3S2									0.58	0.12			0.54	1.00		
33-6 SLL1 R3S2																
33-6 SLL2 R3S1	0.35	0.00	7.90	0.47	5.67	0.34	0.44	0.39	0.13	0.42	0.13	0.52	0.38	0.12	0.38	0.44
33-6 SLL3 R3S1	0.82	0.20	6.81	0.23	1.84	0.65	0.38	0.16	0.67	0.16	0.72	0.17	0.87	0.15	0.14	0.78
33-6 SLSL R3S1	0.74	0.37	0.66	0.60	0.33	0.66	0.99	0.13	0.21	0.00	0.83	0.59	0.43	0.00	0.17	0.14
33-6 SLSL R3S2			0.66	0.64	0.32	0.20	0.98	0.49	0.19	0.17	0.74	0.66	0.38	0.86	0.15	0.29
33-6 SLSL R3S2			0.65	0.92	0.33	0.44	0.94	0.57	0.20	0.23	0.76	0.88	0.38	0.15	0.15	0.56

Sample	Sr/Ca	%RSD	Sr/Ti	%RSD	Mn/Ti	%RSD	Ba/Ti	%RSD	U/Al	%RSD	U/Ti	%RSD	Th/Al	%RSD	Th/Ti	%RSD
33-6 TDL1 R3S1	0.34	0.27														
33-6 TDL1 R3S2					26.60	7.88	1.84	0.55	0.11	0.23	0.33	0.15	0.95	0.20	0.28	0.12
33-6 TDL2 R3S1	0.34	0.00	7.50	0.83	5.64	0.65	0.42	0.38	0.13	0.44	0.13	0.32	0.36	0.11	0.36	0.84
33-6 TDL3 R3S1	0.82	0.43	6.47	0.23	1.79	0.64	0.35	0.17	0.60	0.19	0.69	0.75	0.98	0.29	0.11	0.57
34-12 BSL1					39.88	0.55	2.73	0.38	0.71	0.44	0.68	0.18	0.46	0.28	0.44	0.18
34-12 BSL1					41.53	0.57	2.82	0.45	0.84	0.75	0.78	0.14	0.54	0.48	0.49	0.16
34-12 BSL1					4.69	1.18	2.77	0.89	0.78	0.46	0.73	0.55	0.49	0.29	0.46	0.44
34-12 BSL1 R2	0.37	0.13														
34-12 BSL1 R2	0.31	0.17														
34-16 SLL1 R3S1	0.39	0.53							0.12	0.15			0.13	0.91		
34-16 SLL1 R3S2			6.16	1.81	3.48	5.48	2.33	0.42	0.11	0.58	0.40	0.85	0.12	0.59	0.45	0.74
34-16 SLL1 R3S3	0.33	0.00	58.22	5.17	29.27	2.60	2.54	0.18	0.20	0.20	0.37	0.33	0.12	0.21	0.39	0.90
34-16 SLL2 R3S1	0.36	0.37	8.45	0.25	5.23	0.15	0.50	0.48	0.18	0.36	0.15	0.98	0.29	0.81	0.40	0.79
34-16 SLL2 R3S1	0.36	0.39	8.27	0.15	5.14	0.99	0.48	0.58	0.16	0.24	0.14	0.52	0.29	0.67	0.39	0.69
34-16 SLL3 R3S1	0.14	0.17	4.86	0.67	0.98	0.16	0.26	0.27	0.43	0.14	0.43	0.28	0.79	0.29	0.79	0.15
34-16 SLSL R3S1	0.83	0.48	0.63	0.57	0.37	0.17	0.93	0.16	0.14	0.00	0.56	0.34	0.49	0.00	0.23	0.28
34-16 SLSL R3S2			0.59	0.24	0.36	0.24	0.97	0.14	0.13	0.33	0.52	0.13	0.45	0.13	0.18	0.48
34-16 TDL1 R3S1	0.30	0.00														
34-16 TDL1 R3S2			72.29	14.53	36.97	7.43	2.79	0.56	0.14	0.12	0.46	0.11	0.14	0.12	0.48	0.13
34-16 TDL1 R3S3	0.37	0.72			36.59	14.86	2.35	0.96	0.14	0.33	0.45	0.22	0.14	0.33	0.46	0.31
34-16 TDL2 R3S1	0.37	0.00	8.49	0.96	5.18	0.58	0.79	0.96	0.13	0.46	0.14	0.52	0.29	0.13	0.40	0.57
34-16 TDL3 R3S1	0.97	0.55	4.86	0.20	1.52	0.26	0.27	0.85	0.47	0.17	0.47	0.14	0.89	0.22	0.88	0.99
34-3 BSL3															0.33	0.20
34-3 BSL3 R2	0.28	0.18	96.44	3.32	148.17	5.14	8.15	0.29	0.27	0.15	0.74	0.32				
34-3 BSL3 R2	0.28	0.00	89.52	11.66			7.48	0.97	0.20	0.97	0.66	0.89				
34-43 BSL3							1.84	0.66								
34-43 BSL3 R2	0.29	0.00	7.87	2.64	9.83	3.38					0.64	0.26			0.44	0.21
34-43 BSL3 R2	0.29	0.25	7.22	0.84	9.59	1.37					0.62	0.23			0.43	0.16
34-45 BSL3							5.43	0.39							0.60	0.14
34-45 BSL3 R2	0.44	0.17														

Sample	Sr/Ca	%RSD	Sr/Ti	%RSD	Mn/Ti	%RSD	Ba/Ti	%RSD	U/Al	%RSD	U/Ti	%RSD	Th/Al	%RSD	Th/Ti	%RSD
34-45 SLL1 R3S1	0.44	0.27														
34-45 SLL1 R3S2			61.33	2.36	34.96	1.35	1.65	0.83	0.16	0.46	0.57	0.33	0.56	0.16	0.19	0.22
34-45 SLL1 R3S3	0.43	0.18	61.78	11.42	35.52	6.57	1.44	0.29	0.17	0.39	0.59	0.12	0.52	0.13	0.19	0.86
34-45 SLL2 R3S1	0.38	0.00	15.54	0.18	16.13	0.20	0.77	0.92	0.28	0.12	0.42	0.54	0.27	0.12	0.41	0.67
34-45 SLL3 R3S1	0.97	0.16	6.87	0.18	2.35	0.63	0.33	0.97	0.93	0.58	1.00	0.14	0.93	0.60	0.12	0.19
34-45 SLSL R3S1	0.14	0.32	0.63	0.63	0.47	0.13	0.95	0.56	0.22	0.17	0.82	0.64	0.54	0.12	0.25	0.44
34-45 SLSL R3S2			0.59	0.76	0.46	0.67	1.00	0.17	0.21	0.18	0.78	0.65	0.59	0.14	0.19	0.41
34-45 TDL1 R3S1	0.43	0.24														
34-45 TDL1 R3S2			91.29	8.96	52.76	5.18	2.47	0.25	0.29	0.69	0.88	0.99	0.92	0.22	0.28	0.11
34-45 TDL1 R3S3	0.44	0.20							0.28	0.79			0.85	0.25		
34-45 TDL2 R3S1	0.38	0.00	15.32	0.32	15.74	0.33	0.68	0.62	0.26	0.12	0.40	0.42	0.27	0.12	0.45	0.68
34-45 TDL3 R3S1	0.12	0.22	7.40	0.32	2.29	0.16	0.34	0.27	0.89	0.84	0.98	0.19	0.90	0.84	1.00	0.56
34-6 BSL1					84.48	5.89	4.16	0.29	0.80	0.99	1.23	0.86	0.46	0.65	0.86	0.57
34-6 BSL1					83.57	6.85	4.17	0.34	0.84	0.33	1.33	0.17	0.55	0.21	0.87	0.74
34-6 BSL1					83.99	1.19	4.17	0.61	0.77	0.55	1.28	0.73	0.54	0.36	0.84	0.67
34-6 BSL1 R2	0.29	0.20														
34-6 BSL1 R2	0.29	0.18														
34-9 BSL1					75.62	1.93	4.34	0.11	0.83	0.56	1.48	0.42	0.35	0.23	0.62	0.22
34-9 BSL1					76.37	2.60	4.53	0.15	0.14	0.76	1.72	0.59	0.43	0.32	0.72	0.28
34-9 BSL1					75.98	4.92	4.44	0.29	0.93	0.74	1.60	0.14	0.39	0.39	0.67	0.94
34-9 BSL1 R2	0.27	0.14														
34-9 BSL1 R2	0.27	0.14														
35-11 BSL1					39.49	0.90	3.37	0.79	0.61	0.25	1.33	0.32	0.29	0.12	0.62	0.25
35-11 BSL1 R2	0.30	0.00														
35-19 BSL3							7.22	0.46							0.45	0.36
35-19 BSL3							6.90	0.66							0.43	0.39
35-19 BSL3							7.58	0.20			0.65	0.11			0.43	0.38
35-19 BSL3 R2	0.56	0.16							0.15	0.13						
35-19 BSL3 R2	0.55	0.00							0.15	0.43						
35-19 SLL1 R3S1	0.44	0.13														
35-19 SLL1 R3S2			22.36	5.13	7.14	1.66	0.73	0.29	0.25	0.52	0.12	0.28	0.35	0.28	0.12	0.81
35-19 SLL2 R3S1	0.52	0.00	14.84	0.11	6.12	0.46	0.67	0.88	0.96	0.14	0.14	0.12	0.36	0.46	0.46	0.11

Sample	Sr/Ca	%RSD	Sr/Ti	%RSD	Mn/Ti	%RSD	Ba/Ti	%RSD	U/Al	%RSD	U/Ti	%RSD	Th/Al	%RSD	Th/Ti	%RSD
35-19 SLL3 R3S1	0.12	0.47	6.66	0.17	1.69	0.39	0.34	0.35	0.47	0.66	0.52	0.19	0.95	0.13	0.17	0.15
35-19 SLSL R3S1	0.93	0.28	0.65	0.61	0.35	0.28	0.93	0.75	0.24	0.00	0.97	0.36	0.64	0.00	0.26	0.27
35-19 SLSL R3S2			0.63	0.22	0.34	0.22	0.91	0.92	0.22	0.16	0.88	0.64	0.60	0.24	0.25	0.93
35-19 SLSL R3S4	0.89	0.39	0.64	0.33	0.36	0.12	0.92	0.83	0.25	0.00	1.00	0.35	0.69	0.00	0.28	0.22
35-19 TDL1 R3S1	0.46	0.55														
35-19 TDL1 R3S2			38.41	0.75	12.44	0.24	1.94	0.49	0.42	0.97	0.16	0.74	0.46	0.19	0.17	0.13
35-19 TDL2 R3S1	0.52	0.14	16.85	0.18	6.61	0.73	0.66	0.73	0.92	0.39	0.14	0.64	0.34	0.13	0.47	0.55
35-19 TDL3 R3S1	0.11	0.35	6.96	0.14	1.15	0.27	0.33	0.76	0.47	0.86	0.52	0.50	0.96	0.17	0.16	0.15
35-21 BSL3							12.59	0.99							0.70	0.32
35-21 BSL3							12.54	0.95							0.65	0.52
35-21 BSL3							12.25	0.12			1.42	0.14			0.63	0.22
35-21 BSL3 R2	0.52	0.18														
35-21 BSL3 R2	0.51	0.00														
35-27 SLL1 R3S1	0.32	0.24							0.29	0.12						
35-27 SLL1 R3S2			22.20	1.37	14.57	0.89	0.87	0.55	0.39	0.21	0.15	0.26	0.33	0.19	0.14	0.22
35-27 SLL2 R3S1	0.36	0.00	7.48	0.43	5.19	0.46	0.40	0.50	0.78	0.20	0.97	0.67	0.23	0.57	0.29	0.41
35-27 SLL3 R3S1	0.99	0.94	3.32	0.20	0.89	0.57	0.17	0.24	0.37	0.18	0.37	0.68	0.85	0.18	0.78	0.98
35-27 SLSL R3S2			0.61	0.18	0.35	0.62	0.87	0.64	0.19	0.23	0.77	0.94	0.57	0.98	0.23	0.26
35-27 SLSL R3S4	0.91	0.25	0.61	0.35	0.36	0.19	0.87	0.29	0.21	0.93	0.85	0.36	0.68	0.11	0.27	0.44
35-27 TDL1 R3S1	0.28	0.23														
35-27 TDL1 R3S2									0.26	0.32						
35-27 TDL2 R3S1	0.37	0.00	7.63	0.29	4.75	0.18	0.42	0.28	0.79	1.00	0.98	0.39	0.23	0.28	0.29	0.64
35-27 TDL2 R3S1	0.40	0.79	7.69	0.25	4.91	0.16	0.43	0.48	0.83	0.22	0.11	0.30	0.25	0.59	0.30	0.39
35-27 TDL2 R3S4	0.36	0.00	7.58	0.45	4.91	0.26	0.38	0.60	0.76	0.16	0.96	0.35	0.23	0.47	0.29	0.36
35-27 TDL3 R3S1	0.13	0.13	3.36	0.66	0.77	0.36	0.18	0.55	0.35	0.19	0.29	0.16	0.87	0.15	0.68	0.11
35-39 SLL1 R3S1	0.31	0.20														
35-39 SLL1 R3S2							1.52	0.79	0.12	0.91	0.35	0.18	0.72	0.56	0.21	0.11
35-39 SLL2 R3S1	0.40	0.00	1.39	0.12	9.51	0.11	0.74	0.44	0.11	0.30	0.18	0.33	0.21	0.53	0.33	0.27
35-39 SLL2 R3S4	0.38	0.00	1.18	0.85	9.90	0.82	0.70	0.59	0.12	0.37	0.19	0.92	0.21	0.65	0.34	0.72
35-39 SLL3 R3S1	0.13	0.15	3.84	0.55	1.25	0.16	0.24	0.13	0.52	0.36	0.52	0.18	0.75	0.45	0.74	0.76
35-39 SLSL R3S2			0.57	0.20	0.41	0.26	0.84	0.61	0.27	0.17	0.12	0.62	0.63	0.21	0.24	0.78
35-39 SLSL R3S4	0.94	0.11	0.66	0.33	0.43	0.38	0.86	0.25	0.35	0.00	0.11	0.26	0.74	0.13	0.28	0.35

Sample	Sr/Ca	%RSD	Sr/Ti	%RSD	Mn/Ti	%RSD	Ba/Ti	%RSD	U/Al	%RSD	U/Ti	%RSD	Th/Al	%RSD	Th/Ti	%RSD
35-39 TDL1 R3S1	0.31	0.65							0.73	0.12			0.47	0.77		
35-39 TDL1 R3S2			27.14	2.95	3.46	3.32	1.36	0.15	0.95	0.22	0.34	0.46	0.56	0.12	0.19	0.26
35-39 TDL2 R3S1	0.37	0.00	8.50	0.42	9.19	0.44	0.56	0.37	0.11	0.37	0.17	0.31	0.21	0.68	0.32	0.39
35-39 TDL3 R3S1	0.15	0.24	3.58	0.28	1.15	0.94	0.22	0.15	0.53	0.35	0.51	0.14	0.73	0.47	0.71	0.18
35-48 SLL1 R3S1	0.33	0.14	7.43	1.14	7.34	1.13	0.42	0.79	0.32	0.77	0.91	0.16	0.18	0.45	0.52	0.28
35-48 SLL1 R3S2			16.36	0.76	16.68	0.78	0.56	0.27	0.56	0.15	0.23	0.13	0.21	0.57	0.77	0.62
35-48 SLL2 R3S1	0.32	0.00	8.85	0.77	11.62	0.97	0.48	0.49	0.19	0.13	0.22	0.48	0.24	0.17	0.29	0.32
35-48 SLL3 R3S1	0.93	0.34	3.68	0.22	1.39	0.13	0.19	0.69	0.80	0.12	0.57	0.18	0.85	0.14	0.65	0.73
35-48 SLSL R3S2			0.58	0.28	0.35	0.76	0.90	0.80	0.27	0.13	0.12	0.45	0.45	0.13	0.17	0.41
35-48 SLSL R3S4	0.12	0.24	0.62	0.32	0.37	0.21	0.92	0.46	0.38	0.16	0.11	0.37	0.53	0.00	0.19	0.13
35-48 TDL1 R3S1	0.32	0.00	22.11	12.23	21.83	12.32	0.87	0.48	0.92	0.65	0.27	0.15	0.33	0.24	0.95	0.54
35-48 TDL1 R3S1	0.32	0.00	25.32	4.63	25.58	4.58	0.98	0.18	0.92	0.20	0.37	0.58	0.33	0.77	0.18	0.26
35-48 TDL1 R3S2			26.97	0.11	27.46	0.12	0.86	0.48	0.94	0.20	0.32	0.22	0.34	0.72	0.11	0.12
35-48 TDL2 R3S1	0.32	0.00	9.36	0.38	11.74	0.48	0.49	0.48	0.19	0.26	0.23	0.49	0.25	0.33	0.30	0.37
35-48 TDL3 R3S1	0.95	0.23	3.92	0.88	1.32	0.30	0.23	0.88	0.68	0.63	0.54	0.25	0.79	0.73	0.62	0.30
35-5 BSL1							3.41	0.34					0.29	0.11	0.41	0.13
35-5 BSL1 R2	0.34	0.19														
35-8 BSL1					41.14	7.40	2.73	0.50					0.50	0.13	0.60	0.17
35-8 BSL1 R2	0.42	0.33														
35-9 SLL1 R3S1	0.36	0.68							0.89	0.37						
35-9 SLL1 R3S1	0.39	0.18							0.88	0.60						
35-9 SLL1 R3S2			25.90	0.44	8.60	0.15	0.71	0.36	0.17	0.43	0.42	0.17	0.36	0.18	0.15	0.45
35-9 SLL1 R3S3	0.37	0.15	24.94	11.16	8.25	3.70	0.55	0.39	0.11	0.72	0.49	0.23	0.37	0.47	0.14	0.16
35-9 SLL1 R3S3	0.35	0.22	24.42	1.72	8.22	0.58	0.53	0.12	0.11	0.11	0.42	0.90	0.36	0.57	0.13	0.17
35-9 SLL2 R3S1	0.45	0.16	11.97	0.11	5.88	0.57	0.55	0.86	0.44	0.34	0.62	0.77	0.29	0.22	0.41	0.54
35-9 SLL3 R3S1	0.98	0.12	6.94	0.16	1.55	0.38	0.38	0.23	0.19	0.24	0.18	0.20	0.93	0.24	0.99	0.22
35-9 SLSL R3S1	0.87	0.30	0.96	0.87	0.38	0.31	0.11	0.59	0.42	0.14	0.19	0.63	0.52	0.00	0.24	0.34
35-9 SLSL R3S2			0.93	0.26	0.37	0.16	0.19	0.83	0.44	0.20	0.18	0.86	0.48	0.97	0.22	0.34
35-9 TDL1 R3S1	0.37	0.24														
35-9 TDL1 R3S2			12.55	1.96	4.14	0.65	0.56	0.21	0.67	0.13	0.27	0.15				
35-9 TDL2 R3S1	0.44	0.00	11.28	0.74	5.64	0.37	0.50	0.17	0.43	0.18	0.60	0.84	0.29	0.11	0.39	0.79
35-9 TDL3 R3S1	0.15	0.16	7.39	0.13	1.75	0.66	0.37	0.24	0.21	1.00	0.22	0.12	0.11	0.58	0.18	0.38

Sample	Sr/Ca	%RSD	Sr/Ti	%RSD	Mn/Ti	%RSD	Ba/Ti	%RSD	U/Al	%RSD	U/Ti	%RSD	Th/Al	%RSD	Th/Ti	%RSD
35-9 TDL3 R3S1	0.16	0.76	7.41	0.36	1.65	0.19	0.36	0.27	0.30	0.42	0.22	0.26	0.20	0.22	0.16	0.14
36-11 BSL1					63.55	1.14	4.32	0.81	0.68	0.82	1.28	0.35	0.45	0.55	0.86	0.42
36-11 BSL1 R2	0.32	0.17														
36-11 SLL1 R3S1	0.33	0.75														
36-11 SLL2 R3S1	0.41	0.26	16.85	0.76	1.84	0.49	0.88	0.54	0.27	0.14	0.39	0.19	0.22	0.15	0.41	0.24
36-11 SLL3 R3S1	0.17	0.88	15.39	1.79	1.98	0.23	0.69	0.13	0.85	0.19	0.13	0.93	0.57	0.13	0.91	0.40
36-11 SLSL R3S2			0.68	0.17	0.34	0.80	0.12	0.17	0.17	0.22	0.74	0.93	0.45	0.25	0.20	0.79
36-11 SLSL R3S2			0.91	0.22	0.36	0.13	0.18	0.86	0.17	0.76	0.74	0.32	0.44	0.17	0.19	0.67
36-11 SLSL R3S4	0.15	0.12	0.73	0.25	0.38	0.30	0.11	0.36	0.22	0.00	0.87	0.89	0.57	0.00	0.24	0.27
36-11 TDL1 R3S1	0.33	0.17														
36-11 TDL1 R3S3	0.39	0.66							0.41	0.12						
36-11 TDL1 R3S3	0.31	0.36	11.75	1.95	6.32	1.53	0.46	0.25	0.37	0.33	0.17	0.74	0.27	0.24	0.12	0.53
36-11 TDL2 R3S1	0.42	0.18	17.35	0.29	11.56	0.19	0.89	0.25	0.19	0.18	0.35	0.16	0.19	0.19	0.37	0.14
36-11 TDL3 R3S1	0.16	0.70	16.17	2.62	2.00	0.32	0.78	0.14	0.64	0.12	0.12	0.91	0.44	0.96	0.89	0.12
36-9 BSL1					48.35	0.42	3.25	0.29	0.20	0.77	1.56	0.14	0.33	0.23	0.47	0.12
36-9 BSL1 R2	0.34	0.80														
978 BSL4							2.42	0.19	0.54	0.28	0.28	0.45	0.29	0.15	0.15	0.26
978 BSL4							2.47	0.54	0.59	0.39	0.29	0.30	0.31	0.26	0.15	0.19
978 BSL4							2.44	0.15	0.56	0.22	0.28	0.26	0.30	0.11	0.16	0.19
978 BSL4 R2	0.31	0.50														
978 BSL4 R2	0.37	0.30														
9788 BSL4							11.24	0.19					0.38	0.13	0.12	0.12
9788 BSL4							11.28	0.69					0.41	0.81	0.13	0.24
9788 BSL4							11.26	0.98	0.21	0.24	0.67	0.22	0.40	0.39	0.12	0.32
9788 BSL4 R2	0.30	0.16														
9788 BSL4 R2	0.29	0.00														
979 BSL4							26.95	0.15							0.36	0.17
979 BSL4							27.59	0.16							0.32	0.58
979 BSL4							27.26	0.20			0.95	0.75			0.38	0.52
979 BSL4 R2	0.29	0.46														
979 BSL4 R2	0.29	0.28														
9792 BSL4							2.88	0.57							0.42	0.52

Sample	Sr/Ca	%RSD	Sr/Ti	%RSD	Mn/Ti	%RSD	Ba/Ti	%RSD	U/Al	%RSD	U/Ti	%RSD	Th/Al	%RSD	Th/Ti	%RSD
9792 BSL4 R2	0.28	0.25														
H131-1									0.27	0.15	0.70	0.43	1.00	0.65	0.26	0.86
H131-1 R2	0.39	0.23														
H131-2							34.58	1.67	0.82	0.96	0.71	0.23	0.23	0.28	0.18	0.15
H131-2 R2	0.29	0.55														
H131-3									0.19	0.39	0.38	0.22	0.29	0.66	0.42	0.14
H131-3 R2	0.24	0.00														
H131-4 R2	0.39	0.58	1.11	0.31	6.51	0.11			0.12	0.67	0.31	0.18	0.12	0.17	0.27	0.42
H15							53.59	1.18							0.96	0.18
H15 R2	0.37	0.18														
H151-1									0.53	0.57	0.68	0.59	0.27	0.12	0.33	0.16
H151-1 R2	0.35	0.47														
H151-2							63.36	0.95							1.45	0.26
H151-2 R2	0.33	0.00														
H151-3							46.50	1.47			0.45	0.13			0.17	0.17
H151-3 R2	0.25	0.65														
H151-4 R2	0.47	0.40	0.71	0.17	6.12	0.17			0.78	0.00	0.31	0.26	0.61	0.79	0.24	0.31
H152							3.15	7.75	0.12	0.16	0.14	1.83	0.16	0.25	0.17	5.60
H152 R2																
H154							53.43	2.62					0.17	0.22	0.35	0.26
H154 R2	0.34	0.16														
NODA BSL1																
NODA BSL1 R2	0.12	0.88	1.63	0.44			1.33	0.38			0.88	0.39				
NODA BSL1 R2	0.13	0.18	1.65	0.63	194.83	0.73	1.35	0.55			0.98	0.53				
NODA BSL1 R2	0.13	0.13	1.66	0.26	199.37	0.38	1.35	0.29			0.88	0.37				
NODA BSL1 R2	0.12	0.18	1.62	0.69	189.93	0.77	1.33	0.54	0.78	0.25	0.88	0.22				
NODA BSL1 R2	0.12	0.75	1.59	0.85	189.47	0.95	1.28	0.85	0.75	0.44	0.83	0.46				
NODA BSL1 R2	0.12	0.15	1.60	0.30	189.97	0.23	1.30	0.24	0.76	0.19	0.85	0.19				
NODA BSL1 R2	0.12	0.13	1.64	0.22	193.90	0.23	1.34	0.23	0.78	0.25	0.89	0.87				
NODA BSL1 R2	0.12	0.19	1.63	0.69			1.32	0.58	0.77	0.45	0.87	0.44				
NODA BSL3 R2	0.14	0.88	2.62	0.87			3.34	0.17	0.53	0.12	0.15	0.31	0.16	0.18	0.45	0.45
NODA BSL3 R2	0.13	0.84	2.56	0.30			3.19	0.36	0.58	0.16	0.14	0.26	0.15	0.16	0.42	0.19

Sample	Sr/Ca	%RSD	Sr/Ti	%RSD	Mn/Ti	%RSD	Ba/Ti	%RSD	U/Al	%RSD	U/Ti	%RSD	Th/Al	%RSD	Th/Ti	%RSD
NODA BSL4							4.15	0.19			0.27	0.68			0.66	0.74
NODA BSL4							4.13	0.25			0.28	0.31			0.68	0.44
NODA BSL4 R2	0.13	0.85	4.48	0.36			4.37	0.34	0.66	0.29	0.31	0.13	0.15	0.28	0.76	0.12
NODA BSL4 R2	0.13	0.18	4.34	0.32			4.17	0.29	0.70	0.37	0.28	0.14	0.14	0.25	0.66	0.11
NODA5 ER R3S3	0.11	0.80	5.27	0.16	614.95	1.98	3.49	0.11	0.69	0.96	0.25	0.32	0.16	0.14	0.60	0.39
NODA5 ER R3S3	0.18	0.77	4.96	0.39			3.43	0.27	0.76	0.18	0.25	0.53				
NODA6 ER R3S3	0.91	0.29	4.28	0.44			3.90	0.42	0.58	0.42	0.26	0.13	0.16	0.61	0.55	0.12
NODA6 ER R3S3	0.13	0.19	4.16	0.14	578.37	1.88	4.14	0.14	0.63	0.19	0.22	0.54	0.18	0.41	0.62	0.80
NODA6 ER R3S3	0.94	0.38	4.65	0.14	559.86	12.97	3.88	0.90	0.68	0.39	0.27	0.13				
NODP BSL1							3.78	0.14			0.25	0.22			0.57	0.60
NODP BSL1							3.83	0.63	0.87	0.61	0.26	0.18	0.20	0.15	0.59	0.25
NODP BSL1							3.71	0.53	0.87	0.77	0.25	0.77	0.19	0.16	0.57	0.89
NODP BSL1							3.73	0.15	0.85	0.36	0.25	0.46	0.19	0.94	0.57	0.18
NODP BSL1							3.63	0.68	0.83	0.32	0.24	0.61	0.19	0.72	0.56	0.14
NODP BSL1							3.73	0.92	0.85	0.76	0.25	0.11	0.19	0.16	0.58	0.77
NODP BSL1 R2	0.34	0.58	3.84	0.56							0.29	0.21				
NODP BSL1 R2	0.33	0.28	3.87	0.14							0.28	0.37				
NODP BSL1 R2	0.35	0.39	3.88	0.12							0.28	0.67				
NODP BSL1 R2	0.34	0.27	3.85	0.14							0.27	0.40				
NODP BSL1 R2	0.34	0.23	3.89	0.46							0.27	0.17				
NODP BSL1 R2	0.34	0.45	3.85	0.59							0.28	0.32				
NODP BSL3 R2	0.41	0.39	1.52	0.37			2.28	0.67	0.69	0.25	0.69	0.17	0.19	0.57	0.19	0.28
NODP BSL3 R2	0.42	0.28	1.72	0.26			2.25	0.46	0.69	0.29	0.69	0.26	0.19	0.39	0.19	0.20
NODP BSL4							6.64	0.46			0.81	0.13			0.78	0.17
NODP BSL4							6.54	0.90			0.89	0.98			0.79	0.11
NODP BSL4 R2	0.38	0.12	11.43	0.35					0.12	0.43	0.88	0.22				
NODP BSL4 R2	0.38	0.95	11.61	0.87					0.11	0.35	0.83	0.23				
NODP5 ER R3S3	0.31	0.15	2.36	0.13	842.15	3.53	2.50	0.17	0.86	0.45	0.16	0.85	0.25	0.37	0.37	0.57
NODP5 ER R3S3	0.14	0.20	2.34	0.19			2.33	0.19	0.86	0.92	0.15	0.16				
NODP6 ER R3S3	0.34	0.24	1.55	0.36	379.89	0.89	1.40	0.36	0.82	0.30	0.68	0.13	0.22	0.70	0.19	0.17
NODP6 ER R3S3	0.15	0.22	1.56	0.29	363.40	8.95	1.29	0.34	0.78	0.12	0.62	0.98				

Appendix 5: *Pb isotope data including individual measurements*

In Chapter 5, Pb isotope data from the Sorbas Basin, Falconara and Monte del Casino sections are given. This appendix is an expanded version, including the data from individual measurements of the same samples (Chapter 5 data includes only averages). Analytical session (AS) information is listed in Ch. 5.

Table A5.1. Pb isotope ratios of acid-reductive bulk sediment leachates from the Sorbas Basin, Falconara and Monte del Casino sections.

Sample	Age (Ma)	$^{208}Pb/^{204}Pb$	$^{207}Pb/^{204}Pb$	$^{206}Pb/^{204}Pb$	$^{208}Pb/^{206}Pb$	$^{207}Pb/^{206}Pb$	AS
(Sorbas)							
33-03 BSL2	6.6126	38.911 ±14	15.692 ±6	18.806 ±18	2.0692 ±4	0.83443 ±13	2
33-06 BSL2	6.6114	38.899 ±14	15.686 ±6	18.795 ±18	2.0698 ±4	0.83459 ±13	2
33-06 SL L1	6.6114	38.945 ±7	15.693 ±2	18.814 ±2	2.0700 ±2	0.83410 ±4	4
33-06 SL L1	6.6114	38.940 ±7	15.691 ±2	18.814 ±2	2.0698 ±2	0.83406 ±4	4
33-06 SL L1	6.6114	38.945 ±7	15.693 ±2	18.815 ±2	2.0699 ±2	0.83409 ±4	4
33-06 TD L1	6.6114	38.948 ±7	15.694 ±2	18.813 ±2	2.0703 ±2	0.83424 ±4	4
	Average	38.930 ±14	15.691 ±6	18.807 ±18	2.0700 ±4	0.83431 ±13	
33-12 BSL2	6.6092	38.876 ±14	15.686 ±6	18.776 ±18	2.0707 ±4	0.83547 ±13	2
33-15 BSL3	6.6080	38.890 ±14	15.682 ±6	18.786 ±18	2.0702 ±4	0.83475 ±13	3
33-15 BSL3	6.6080	38.886 ±14	15.681 ±6	18.785 ±18	2.0700 ±4	0.83472 ±13	3
33-15 SL L1	6.6080	38.936 ±7	15.695 ±2	18.800 ±2	2.0711 ±2	0.83486 ±4	4
33-15 SL L1	6.6080	38.931 ±7	15.6945 ±2	18.799 ±2	2.0709 ±2	0.83483 ±4	4
33-15 SL L1	6.6080	38.935 ±7	15.6955 ±2	18.800 ±2	2.0710 ±2	0.83485 ±4	4
33-15 TD L1	6.6080	38.934 ±7	15.6955 ±2	18.799 ±2	2.0710 ±2	0.83487 ±4	4
	Average	38.919 ±14	15.6905 ±6	18.795 ±18	2.0707 ±4	0.83482 ±13	
33-21 BSL2	6.6055	38.859 ±14	15.676 ±6	18.766 ±18	2.0708 ±4	0.83530 ±13	2
33-27 BSL3	6.6030	38.907 ±14	15.684 ±6	18.798 ±18	2.0697 ±4	0.83437 ±13	3
33-27 BSL3	6.6030	38.909 ±14	15.685 ±6	18.798 ±18	2.0699 ±4	0.83443 ±13	3
33-27 SL L1	6.6030	38.946 ±7	15.697 ±2	18.811 ±2	2.0704 ±4	0.83444 ±4	4
33-27 TD L1	6.6030	38.943 ±7	15.696 ±2	18.811 ±2	2.0703 ±4	0.83440 ±4	4
	Average	38.932 ±14	15.692 ±6	18.806 ±18	2.0702 ±4	0.83441 ±13	
34-01 BSL2	6.5978	38.906 ±14	15.685 ±6	18.776 ±18	2.0722 ±4	0.83538 ±13	2
34-02 BSL2	6.5974	38.948 ±14	15.682 ±6	18.789 ±18	2.0730 ±4	0.83465 ±13	2
34-06 BSL1	6.5958	38.957 ±14	15.694 ±6	18.848 ±18	2.0669 ±4	0.83267 ±13	1
34-09 BSL1	6.5945	38.944 ±14	15.701 ±6	18.913 ±18	2.0591 ±4	0.83014 ±13	1
34-10 BSL2	6.5939	38.895 ±14	15.682 ±6	18.815 ±18	2.0673 ±4	0.83349 ±13	2
34-12 BSL1	6.5928	38.933 ±14	15.691 ±6	18.843 ±18	2.0663 ±4	0.83274 ±13	1
34-13 BSL2	6.5919	38.889 ±14	15.687 ±6	18.793 ±18	2.0694 ±4	0.83471 ±13	2
34-16 BSL2	6.5908	38.906 ±14	15.684 ±6	18.784 ±18	2.0714 ±4	0.83498 ±13	2

Table A5.1 cont'd.

Sample	Age (Ma)	$^{208}Pb/^{204}Pb$	$^{207}Pb/^{204}Pb$	$^{206}Pb/^{204}Pb$	$^{208}Pb/^{206}Pb$	$^{207}Pb/^{206}Pb$	AS
(Sorbas cont'd)							
34-16 SL L1	6.5908	38.961 ±7	15.695 ±2	18.817 ±2	2.0705 ±2	0.83410 ±4	4
34-16 TD L1	6.5908	38.954 ±7	15.693 ±2	18.815 ±2	2.0704 ±2	0.83406 ±4	4
	Average	38.940 ±14	15.691 ±6	18.805 ±18	2.0708 ±4	0.83438 ±13	
34-18 BSL2	6.5901	38.885 ±14	15.685 ±6	18.781 ±18	2.0705 ±4	0.83517 ±13	2
34-19 BSL2	6.5897	38.881 ±14	15.682 ±6	18.790 ±18	2.0693 ±4	0.83457 ±13	2
34-21 BSL2	6.5890	38.896 ±14	15.685 ±6	18.782 ±18	2.0710 ±4	0.83512 ±13	2
34-28 BSL2	6.5861	38.893 ±14	15.688 ±6	18.773 ±18	2.0719 ±4	0.83568 ±13	2
34-30 BSL3	6.5853	38.901 ±14	15.685 ±6	18.787 ±18	2.0705 ±4	0.83487 ±13	3
34-43 BSL3	6.5803	38.922 ±14	15.689 ±6	18.806 ±18	2.0697 ±4	0.83429 ±13	3
34-45 SL L1	6.5795	38.948 ±7	15.698 ±2	18.861 ±2	2.0651 ±2	0.83232 ±4	4
34-45 SL L1	6.5795	38.942 ±7	15.696 ±2	18.859 ±2	2.0649 ±2	0.83229 ±4	4
34-45 SL L1	6.5795	38.948 ±7	15.698 ±2	18.860 ±2	2.0651 ±2	0.83235 ±4	4
34-45 TD L1	6.5795	38.943 ±7	15.696 ±2	18.860 ±2	2.0648 ±2	0.83225 ±4	4
	Average	38.944 ±7	15.697 ±2	18.860 ±2	2.0649 ±2	0.83229 ±4	
35-05 BSL1	6.5741	38.903 ±14	15.683 ±6	18.869 ±18	2.0617 ±4	0.83113 ±13	1
35-08 BSL1	6.5726	38.972 ±14	15.696 ±6	18.887 ±18	2.0634 ±4	0.83104 ±13	1
35-09 BSL2	6.5721	38.909 ±14	15.690 ±6	18.892 ±18	2.0597 ±4	0.83050 ±13	2
35-09 SL L1	6.5721	38.978 ±7	15.701 ±2	18.923 ±2	2.0598 ±2	0.82973 ±4	4
35-09 SL L1	6.5721	38.967 ±7	15.697 ±2	18.920 ±2	2.0595 ±2	0.82966 ±4	4
35-09 SL L1	6.5721	38.976 ±7	15.700 ±2	18.923 ±2	2.0597 ±2	0.82968 ±4	4
35-09 TD L1	6.5721	38.974 ±7	15.700 ±2	18.923 ±2	2.0596 ±2	0.82967 ±4	4
	Average	38.953 ±14	15.696 ±6	18.912 ±18	2.0597 ±4	0.82995 ±13	
35-10 BSL2	6.5716	38.901 ±14	15.688 ±6	18.875 ±18	2.0610 ±4	0.83112 ±13	2
35-11 BSL1	6.5711	38.954 ±14	15.696 ±6	18.873 ±18	2.0641 ±4	0.83169 ±13	1
35-19 BSL3	6.5683	38.911 ±14	15.685 ±6	18.802 ±18	2.0695 ±4	0.83423 ±13	3
35-19 SL L1	6.5683	38.944 ±7	15.696 ±2	18.811 ±2	2.0703 ±2	0.83440 ±4	4
35-19 TD L1	6.5683	38.938 ±7	15.693 ±2	18.811 ±2	2.0700 ±2	0.83428 ±4	4
	Average	38.931 ±14	15.691 ±6	18.808 ±18	2.0699 ±4	0.83430 ±13	
35-21 BSL3	6.5676	38.884 ±14	15.683 ±6	18.770 ±18	2.0715 ±4	0.83551 ±13	3
35-22 BSL2	6.5672	38.891 ±14	15.685 ±6	18.786 ±18	2.0703 ±4	0.83488 ±13	2
35-25 BSL2	6.5662	38.864 ±14	15.686 ±6	18.768 ±18	2.0710 ±4	0.83585 ±13	2
35-27 BSL2	6.5655	38.893 ±14	15.685 ±6	18.784 ±18	2.0706 ±4	0.83502 ±13	2
35-27 SL L1	6.5655	38.934 ±7	15.694 ±2	18.800 ±2	2.0710 ±2	0.83480 ±4	4
35-27 TD L1	6.5655	38.929 ±7	15.693 ±2	18.798 ±2	2.0709 ±2	0.83480 ±4	4
	Average	38.919 ±14	15.691 ±6	18.794 ±18	2.0708 ±4	0.83487 ±13	
35-39 BSL2	6.5616	38.881 ±14	15.677 ±6	18.769 ±18	2.0717 ±4	0.83529 ±13	2

Table A5.1 cont'd.

Sample	Age (Ma)	$^{208}Pb/^{204}Pb$	$^{207}Pb/^{204}Pb$	$^{206}Pb/^{204}Pb$	$^{208}Pb/^{206}Pb$	$^{207}Pb/^{206}Pb$	AS
(Sorbas cont'd)							
35-39 SL L1	6.5616	38.956 ±7	15.695 ±2	18.804 ±2	2.0717 ±2	0.83468 ±4	4
35-39 TD L1	6.5616	38.952 ±7	15.694 ±2	18.803 ±2	2.0716 ±2	0.83466 ±4	4
	Average	38.930 ±14	15.689 ±6	18.792 ±18	2.0716 ±2	0.83488 ±13	
35-48 BSL2	6.5582	38.911 ±14	15.685 ±6	18.795 ±18	2.0704 ±4	0.83456 ±13	2
35-48 SL L1	6.5582	38.955 ±7	15.694 ±2	18.818 ±2	2.0701 ±2	0.83397 ±4	4
35-48 TD L1	6.5582	38.953 ±7	15.694 ±2	18.817 ±2	2.0701 ±2	0.83402 ±4	4
	Average	38.940 ±14	15.691 ±6	18.810 ±18	2.0702 ±4	0.83418 ±13	
36-09 BSL1	6.5536	38.952 ±14	15.694 ±6	18.868 ±18	2.0644 ±4	0.83176 ±13	1
36-11 BSL1	6.5529	38.948 ±14	15.696 ±6	18.878 ±18	2.0632 ±4	0.83145 ±13	1
36-11 SL L1	6.5529	38.971 ±7	15.699 ±2	18.857 ±2	2.0667 ±2	0.83255 ±4	4
36-11 TD L1	6.5529	38.965 ±7	15.698 ±2	18.861 ±2	2.0659 ±2	0.83229 ±4	4
	Average	38.961 ±14	15.698 ±6	18.865 ±18	2.0652 ±4	0.83209 ±13	
(Falconara)							
18.887 BSL5	6.6122	38.922 ±7	15.696 ±2	18.871 ±2	2.0625 ±2	0.83175 ±4	4
18.888 BSL5	6.6112	38.941 ±7	15.695 ±2	18.861 ±2	2.0646 ±2	0.83214 ±4	4
18.889 BSL5	6.6098	38.959 ±7	15.697 ±2	18.875 ±2	2.0641 ±2	0.83163 ±4	4
18.890 BSL5	6.6082	38.965 ±7	15.698 ±2	18.857 ±2	2.0664 ±2	0.83249 ±4	4
18.891 BSL5	6.6068	38.963 ±7	15.698 ±2	18.852 ±2	2.0668 ±2	0.83272 ±4	4
18.892 BSL4	6.6053	38.936 ±14	15.692 ±6	18.853 ±18	2.0652 ±4	0.83232 ±13	3
18.893 BSL5	6.6045	38.941 ±7	15.700 ±2	18.897 ±2	2.0607 ±2	0.83082 ±4	4
18.894 BSL5	6.6026	38.934 ±7	15.699 ±2	18.866 ±2	2.0637 ±2	0.83212 ±4	4
18.895 BSL5	6.6004	38.935 ±7	15.698 ±2	18.857 ±2	2.0648 ±2	0.83250 ±4	4
18.896 BSL5	6.5989	38.941 ±7	15.703 ±2	18.935 ±2	2.0565 ±2	0.82933 ±4	4
18.897 BSL5	6.5973	38.939 ±7	15.700 ±2	18.894 ±2	2.0609 ±2	0.83097 ±4	4
18.898 BSL5	6.5958	38.939 ±7	15.701 ±2	18.901 ±2	2.0601 ±2	0.83072 ±4	4
18.899 BSL4	6.5943	38.915 ±14	15.695 ±6	18.898 ±18	2.0592 ±4	0.83048 ±13	3
18.900 BSL5	6.5929	38.928 ±7	15.699 ±2	18.893 ±2	2.0604 ±2	0.83095 ±4	4
18.901 BSL5	6.5911	38.945 ±7	15.698 ±2	18.875 ±2	2.0633 ±2	0.83168 ±4	4
18.902 BSL5	6.5899	38.965 ±7	15.699 ±2	18.872 ±2	2.0646 ±2	0.83183 ±4	4
18.903 BSL5	6.5883	38.959 ±7	15.697 ±2	18.858 ±2	2.0659 ±2	0.83234 ±4	4
18.904 BSL5	6.5865	38.961 ±7	15.698 ±2	18.857 ±2	2.0661 ±2	0.83249 ±4	4
18.905 BSL5	6.5844	38.944 ±7	15.698 ±2	18.849 ±2	2.0661 ±2	0.83285 ±4	4
18.906 BSL5	6.5838	38.944 ±7	15.700 ±2	18.866 ±2	2.0642 ±2	0.83219 ±4	4
18.907 BSL4	6.5824	38.908 ±14	15.690 ±6	18.862 ±18	2.0627 ±4	0.83182 ±13	3
18.907 BSL4	6.5824	38.893 ±14	15.685 ±6	18.858 ±18	2.0624 ±4	0.83176 ±13	3
	Average	38.900 ±14	15.688 ±6	18.860 ±18	2.0626 ±4	0.83179 ±13	

Table A5.1 cont'd.

Sample	Age (Ma)	$^{208}Pb/^{204}Pb$	$^{207}Pb/^{204}Pb$	$^{206}Pb/^{204}Pb$	$^{208}Pb/^{206}Pb$	$^{207}Pb/^{206}Pb$	AS
(Falconara cont'd)							
18.908 BSL5	6.5807	38.935 ±7	15.699 ±2	18.859 ±2	2.0646 ±2	0.83248 ±4	4
18.909 BSL5	6.5796	38.935 ±7	15.701 ±2	18.894 ±2	2.0606 ±2	0.83096 ±4	4
18.910 BSL5	6.5781	38.932 ±7	15.699 ±2	18.880 ±2	2.0621 ±2	0.83151 ±4	4
18.911 BSL5	6.5762	38.941 ±7	15.702 ±2	18.922 ±2	2.0580 ±2	0.82980 ±4	4
18.912 BSL5	6.5742	38.965 ±7	15.699 ±2	18.921 ±2	2.0593 ±2	0.82972 ±4	4
18.913 BSL4	6.5725	38.915 ±14	15.685 ±6	18.855 ±18	2.0639 ±4	0.83186 ±13	3
18.914 BSL5	6.5708	38.943 ±7	15.698 ±2	18.863 ±2	2.0645 ±2	0.83220 ±4	4
18.915 BSL5	6.5697	38.929 ±7	15.693 ±2	18.855 ±2	2.0647 ±2	0.83231 ±4	4
18.916 BSL5	6.5684	38.939 ±7	15.694 ±2	18.848 ±2	2.0659 ±2	0.83264 ±4	4
18.917 BSL5	6.5670	38.944 ±7	15.695 ±2	18.844 ±2	2.0667 ±2	0.83287 ±4	4
18.918 BSL5	6.5657	38.949 ±7	15.696 ±2	18.849 ±2	2.0663 ±2	0.83273 ±4	4
18.919 BSL5	6.5645	38.952 ±7	15.698 ±2	18.870 ±2	2.0643 ±2	0.83189 ±4	4
18.920 BSL5	6.5630	38.943 ±7	15.699 ±2	18.866 ±2	2.0641 ±2	0.83210 ±4	4
18.921 BSL5	6.5624	38.940 ±7	15.698 ±2	18.865 ±2	2.0642 ±2	0.83212 ±4	4
18.922 BSL5	6.5610	38.941 ±7	15.697 ±2	18.847 ±2	2.0662 ±2	0.83289 ±4	4
18.923 BSL5	6.5597	38.937 ±7	15.697 ±2	18.872 ±2	2.0632 ±2	0.83177 ±4	4
18.924 BSL5	6.5579	38.941 ±7	15.700 ±2	18.935 ±2	2.0565 ±2	0.82916 ±4	4
18.925 BSL5	6.5554	38.934 ±7	15.699 ±2	18.923 ±2	2.0575 ±2	0.82961 ±4	4
18.926 BSL5	6.5525	38.938 ±7	15.696 ±2	18.898 ±2	2.0603 ±2	0.83056 ±4	4
18.927 BSL5	6.5496	38.958 ±7	15.699 ±2	18.891 ±2	2.0622 ±2	0.83100 ±4	4
18.928 BSL5	6.5468	38.951 ±7	15.697 ±2	18.871 ±2	2.0641 ±2	0.83182 ±4	4
18.929 BSL5	6.5459	38.945 ±7	15.697 ±2	18.868 ±2	2.0641 ±2	0.83195 ±4	4
18.930 BSL5	6.5445	38.958 ±7	15.697 ±2	18.843 ±2	2.0675 ±2	0.83301 ±4	4
18.931 BSL5	6.5424	38.942 ±7	15.697 ±2	18.869 ±2	2.0637 ±2	0.83185 ±4	4
18.932 BSL5	6.5389	38.934 ±7	15.698 ±2	18.890 ±2	2.0611 ±2	0.83105 ±4	4
18.933 BSL5	6.5359	38.931 ±7	15.697 ±2	18.902 ±2	2.0597 ±2	0.83044 ±4	4
18.934 BSL5	6.5330	38.939 ±7	15.698 ±2	18.900 ±2	2.0602 ±2	0.83057 ±4	4
18.935 BSL5	6.5304	38.941 ±7	15.697 ±2	18.877 ±2	2.0629 ±2	0.83153 ±4	4
18.936 BSL5	6.5289	38.939 ±7	15.694 ±2	18.863 ±2	2.0643 ±2	0.83197 ±4	4
18.936 BSL5	6.5289	38.927 ±7	15.690 ±2	18.859 ±2	2.0641 ±2	0.83193 ±4	4
18.936 BSL5	6.5289	38.947 ±7	15.697 ±2	18.869 ±2	2.0641 ±2	0.83190 ±4	4
	Average	38.938 ±7	15.694 ±2	18.864 ±2	2.0642 ±2	0.83193 ±4	
18.937 BSL5	6.5273	38.949 ±7	15.696 ±2	18.861 ±2	2.0650 ±2	0.83216 ±4	4
18.937 BSL5	6.5273	38.942 ±7	15.693 ±2	18.859 ±2	2.0648 ±2	0.83212 ±4	4
18.937 BSL5	6.5273	38.945 ±7	15.694 ±2	18.859 ±2	2.0651 ±2	0.83219 ±4	4
	Average	38.945 ±7	15.694 ±2	18.860 ±2	2.0650 ±2	0.83216 ±4	

Table A5.1 cont'd.

Sample	Age (Ma)	$^{208}Pb/^{204}Pb$	$^{207}Pb/^{204}Pb$	$^{206}Pb/^{204}Pb$	$^{208}Pb/^{206}Pb$	$^{207}Pb/^{206}Pb$	AS
(Monte del Casino)							
17.776 BSL6	6.6223	38.868 ±7	15.697 ±2	18.992 ±2	2.0466 ±2	0.82649 ±4	4
17.776 BSL6	6.6223	38.874 ±7	15.699 ±2	18.994 ±2	2.0467 ±2	0.82653 ±4	4
	Average	38.871 ±7	15.698 ±2	18.993 ±2	2.0466 ±2	0.82651 ±4	
17.777 BSL6	6.6183	38.870 ±7	15.693 ±2	18.909 ±2	2.0556 ±2	0.82991 ±4	4
17.779 BSL4	6.6142	38.817 ±14	15.678 ±6	18.901 ±18	2.0537 ±4	0.82947 ±13	3
17.779 BSL6	6.6142	38.864 ±7	15.693 ±2	18.907 ±2	2.0555 ±2	0.83002 ±4	4
	Average	38.841 ±14	15.686 ±6	18.904 ±18	2.0546 ±4	0.82975 ±13	
17.780 BSL6	6.6075	38.844 ±7	15.693 ±2	18.948	2.0500 ±2	0.82821 ±4	4
17.781 BSL4	6.6019	38.839 ±14	15.690 ±6	18.973 ±18	2.0471 ±4	0.82698 ±13	3
17.781 BSL6	6.6019	38.854 ±7	15.695 ±2	18.960 ±2	2.0492 ±2	0.82777 ±4	4
	Average	38.846 ±14	15.692 ±6	18.966 ±18	2.0482 ±4	0.82738 ±13	
17.782 BSL6	6.5982	38.865 ±7	15.696 ±2	18.982 ±2	2.0474 ±2	0.82686 ±4	4
17.783 BSL4	6.5963	38.871 ±14	15.690 ±6	18.909 ±18	2.0557 ±4	0.82981 ±13	3
17.783 BSL6	6.5963	38.872 ±7	15.692 ±2	18.904 ±2	2.0563 ±2	0.83007 ±4	4
	Average	38.871 ±14	15.691 ±6	18.906 ±18	2.0560 ±4	0.82994 ±13	
17.784 BSL6	6.5941	38.881 ±7	15.694 ±2	18.918 ±2	2.0552 ±2	0.82961 ±4	4
17.785 BSL4	6.5877	38.850 ±14	15.690 ±6	19.000 ±18	2.0448 ±4	0.82580 ±13	3
17.785 BSL6	6.5877	38.871 ±7	15.698 ±2	18.997 ±2	2.0462 ±2	0.82634 ±4	4
	Average	38.860 ±14	15.694 ±6	18.998 ±18	2.0455 ±4	0.82607 ±13	4
17.786 BSL6	6.5781	38.841 ±7	15.696 ±2	19.003 ±2	2.0439 ±2	0.82596 ±4	4
17.787 BSL6	6.5728	38.861 ±7	15.695 ±2	18.945 ±2	2.0512 ±2	0.82845 ±4	4
17.788 BSL6	6.5708	38.874 ±7	15.694 ±2	18.910 ±2	2.0557 ±2	0.82992 ±4	4
17.789 BSL6	6.5688	38.871 ±7	15.694 ±2	18.938 ±2	2.0525 ±2	0.82868 ±4	4
17.789 BSL6	6.5688	38.876 ±7	15.696 ±2	18.939 ±2	2.0527 ±2	0.82873 ±4	4
	Average	38.873 ±7	15.695 ±2	18.939 ±2	2.0526 ±2	0.82871 ±4	
17.790 BSL6	6.5644	38.859 ±7	15.696 ±2	18.987 ±2	2.0467 ±2	0.82672 ±4	4
17.791 BSL6	6.5594	38.850 ±7	15.694 ±2	18.962 ±2	2.0489 ±2	0.82770 ±4	4
17.792 BSL6	6.5538	38.858 ±7	15.692 ±2	18.949 ±2	2.0507 ±2	0.82817 ±4	4
17.792 BSL6	6.5538	38.864 ±7	15.695 ±2	18.950 ±2	2.0509 ±2	0.82821 ±4	4
	Average	38.861 ±7	15.694 ±2	18.949 ±2	2.0508 ±2	0.82819 ±4	
17.793 BSL6	6.5522	38.873 ±7	15.697 ±2	18.993 ±2	2.0468 ±2	0.82648 ±4	4
17.794 BSL6	6.5506	38.869 ±7	15.696 ±2	18.975 ±2	2.0484 ±2	0.82722 ±4	4
17.795 BSL6	6.5451	38.853 ±7	15.696 ±2	18.994 ±2	2.0455 ±2	0.82638 ±4	4
17.796 BSL6	6.5394	38.861 ±7	15.699 ±2	19.055 ±2	2.0394 ±2	0.82385 ±4	4
17.796 BSL6	6.5394	38.870 ±7	15.701 ±2	19.058 ±2	2.0396 ±2	0.82388 ±4	4
	Average	38.866 ±7	15.700 ±2	19.057 ±2	2.0395 ±2	0.82386 ±4	

Table A5.1 cont'd.

Sample	Age (Ma)	$^{208}Pb/^{204}Pb$	$^{207}Pb/^{204}Pb$	$^{206}Pb/^{204}Pb$	$^{208}Pb/^{206}Pb$	$^{207}Pb/^{206}Pb$	AS
(Monte del Casino cont'd)							
17.797 BSL6	6.5334	38.874 ±7	15.697 ±2	18.988 ±2	2.0473 ±2	0.82670 ±4	4
17.798 BSL6	6.5310	38.877 ±7	15.698 ±2	19.020 ±2	2.0440 ±2	0.82533 ±4	4

Appendix 6: $^{230}Th^{excess}$ plots

Activity vs. depth and $^{230}Th_{excess}$ growth rate calculation for all ablation lines. The plots are in pairs, with the activity vs. depth plot above the slope calculation plot for each ablation line.